DYNAMICAL SYSTEMS

Control and Stability

Editors

J. AWREJCEWICZ
M. KAŹMIERCZAK
J. MROZOWSKI
P. OLEJNIK

DSTA 2015

DYNAMICAL SYSTEMS

Control and Stability

Editors

JAN AWREJCEWICZ, MAREK KAŹMIERCZAK
JERZY MROZOWSKI, PAWEŁ OLEJNIK

PREFACE

This is the thirteen time when the conference "Dynamical Systems: Theory and Applications" gathers a numerous group of outstanding scientists and engineers, who deal with widely understood problems of dynamics met in daily life.

Organization of the conference would not have been possible without a great effort of the staff of the Department of Automation, Biomechanics and Mechatronics, as well as Committee of Mechanics of the Polish Academy of Sciences. The financial support has been given by the Polish Academy of Sciences.

It is a great pleasure that our invitation has been accepted by recording in the history of our conference number of people, including good colleagues and friends as well as a large group of researchers and scientists, who decided to participate in the conference for the first time. With proud and satisfaction we welcomed over **180** persons from **29** countries all over the world. They decided to share the results of their research and many years experiences in a discipline of dynamical systems by submitting many very interesting papers.

This year, the DSTA Conference Proceedings were split into three volumes entitled "Dynamical Systems" with respective subtitles: *Mathematical and numerical approaches*; *Mechatronics and life sciences* and vol. 3 *Control and stability*. Additionally there will be also published two volumes of Springer Proceedings in Mathematics and Statistics entitled "*Dynamical Systems. Modelling*" and "*Dynamical Systems. Theoretical and Experimental Analysis*".

These books include the invited papers and regular papers dealing with the following topics:
- control in dynamical systems,
- stability of dynamical systems,
- asymptotic methods in nonlinear dynamics,
- mathematical approaches to dynamical systems,
- dynamics in life sciences and bioengineering,
- engineering systems and differential equations,
- original numerical methods of vibration analysis,
- bifurcations and chaos in dynamical systems,
- vibrations of lumped and continuous systems,
- non-smooth systems,
- other problems.

Proceedings of the 13th Conference „Dynamical Systems - Theory and Applications" summarize **164** and the Springer Proceedings summarize **60** best papers of university teachers and students, researchers and engineers from whole the world. The papers were chosen by the International Scientific Committee from **315** papers submitted to the conference. The reader thus obtains an overview of the recent developments of dynamical systems and can study the most progressive tendencies in this field of science.

Our previous experience shows that an extensive thematic scope comprising dynamical systems stimulates a wide exchange of opinions among researchers dealing with different branches of dynamics. We think that vivid discussions will influence positively the creativity and will result in effective solutions of many problems of dynamical systems in mechanics and physics, both in terms of theory and applications.

We do hope that DSTA 2015 will contribute to the same extent as all the previous conferences to establishing new and tightening the already existing relations and scientific and technological co-operation between both Polish and foreign institutions.

On behalf of both
Scientific and Organizing Committees

Chairman
Professor Jan Awrejcewicz

CONTENTS

Influence of a volumetric chemical reaction of the convective diffusion near a drop
(ASY095-15)

Rustyam Akhmetov, Ruslan Kutluev

Abstract: The problem of steady convective diffusion around a drop in view of the distributed chemical reaction is a streamlined flow of a viscous incompressible fluid. The characteristic feature of the problem is the presence of two dimensionless parameters: k_v is rate constant of the chemical reaction, *Pe* is Peclet number, which determine the concentration distribution in the flow. The quantity of rate constant of the chemical reaction and Peclet number is assumed to have a constant value. It is a boundary value problem for a quasilinear elliptic partial differential equation with a small parameter multiplying in higher derivatives. The additional boundary layer arises in the neighborhood of the saddle point. The asymptotic expansion of solution is constructed in the boundary layer near the rear stagnation point of the drop as the solution for the quasilinear ordinary differential equation. The asymptotics of the solution are obtained near a spherical drop.

1. Introduction

The boundary value problem is considered as

$$\varepsilon^2 \Delta u - \frac{1}{r^2 \sin\theta}\left(\frac{\partial u}{\partial r}\frac{\partial \psi}{\partial \theta} - \frac{\partial u}{\partial \theta}\frac{\partial \psi}{\partial r}\right) - \mu F(u) = 0, \tag{1}$$

$$u = 1 \text{ if } r = 1; \ u \to 0 \text{ if } r \to \infty, \ \partial u/\partial \theta = 0 \text{ if } \theta = \pi \text{ and } \theta = 0, \tag{2}$$

where $\varepsilon = Pe^{-1/2}$ is the small parameter, $\psi(r,\theta)$ is the stream function, r and θ are spherical coordinates $(0 \le \theta \le \pi)$, Δ is the Laplace operator. $\mu = k_v \cdot Pe^{-1}$ is the constant value, where *Pe* is the Peclet number, and k_v is parameter depending on the chemical reaction rate.

The function of the current in the Stokes approximation has the form

$$\psi(r,\theta) = \sin^2\theta(r-1)\left(2r - \frac{\lambda}{\lambda+1}\left(1 + \frac{1}{r}\right)\right)/4, \text{ where } \lambda - const. \tag{3}$$

The natural variables in the diffusion boundary layer are $x = \varepsilon^{-1}(\lambda+1)^{-1/2}(r-1)$, θ, then the asymptotics of the solution $u(x,\theta,\varepsilon)$ is sought as

$$u(x, \theta, \varepsilon) = u_0(x, \theta) + O(\varepsilon). \tag{4}$$

From Eqs. (1) – (4) at the variables x, θ for determining $u_0(x, \theta)$ we obtain the problem

$$\frac{\partial^2 u_0}{\partial x^2} - x \cos\theta \frac{\partial u_0}{\partial x} + \sin\theta \frac{\partial u_0}{\partial \theta} - \mu F(u_0) = 0,$$

$$u_0(0, \theta) = 1; \ u_0(x, \theta) \to 0 \text{ if } x \to \infty.$$

The asymptotics $u_0(x, \theta)$ as $\theta \to \pi$ is sought as

$$u_0(x, \theta) = u_{0,0}(x) + O\left((\pi - \theta)^2 \exp\left(-\gamma x^2\right)\right) \text{ for some } \gamma > 0.$$

In area $D = \left\{x, \theta : x \geq 0, \gamma_1 \varepsilon^v \leq \theta \leq \pi\right\}$ the assessment is fair

$$|u_0(x, \theta)| \leq M \exp\left(-\gamma x^2\right) \text{ for some } M > 0, \ v \in (0,1) \text{ and } \gamma_1 > 0.$$

2. The Asymptotics $u_0(x, \theta)$ when $\theta \to 0$

Let us assume that $F(u)$ taking into account

$$F(u) = u^\alpha g(u), \ g(u) \in C^\infty(\mathbf{R}), \ g(0) > 0, \ \alpha > 1, \tag{5}$$

where the function $g(u)$ has an asymptotic

$$g(u) = 1 + g_1 u + g_2 u^2 + g_3 u^3 + g_4 u^4 + g_5 u^5 + O\left(u^6\right) \text{ for } u \to 0, \tag{6}$$

In work [1] the asymptotic behavior of the solutions near a spherical particle, when the bulk chemical reaction has the following forma: $F(u) = u^\alpha \left(g(u) \equiv 1\right)$. In a case $\alpha > 1$ and α - not whole, with conditions (5) and (6) when $g_{2k+1} = 0$, $k = 1, 2, \dots$, it is constructed in work [2].

The asymptotics of the function $u_0(x, \theta)$ when $\theta \to 0$ is sought as

$$u_0(x, \theta) = v_0(x) + O\left(\theta^2\right),$$

where the function $v_0(x)$ is constructed as the solution for the problem

$$v_0''(x) - x v_0'(x) - \mu F(v_0(x)) = 0, \tag{7}$$

$$v_0(0) = 1, \ v_0(x) = O(1) \text{ при } x \geq 0. \tag{8}$$

Formal asymptotic decomposition $v_0(x)$ of the decision (7), (8) is sought as

$$v_0(x) = \sum_{k=0}^{\infty}\sum_{m=1}^{\infty} C_{k,m}\frac{\ln^k\big((\alpha-1)\mu\ln x + c\big)}{\big((\alpha-1)\mu\ln x + c\big)^{md+k}} + O\!\left(\frac{1}{x^2}\right),\ \text{where}\ d = 1/(\alpha-1). \tag{9}$$

We will substitute ranks (5), (6) and (9) in the equation (7). We will equate coefficients at identical degrees $(\alpha-1)\mu\ln x + c$ (for convenience we will enter designation $r = (\alpha-1)\mu\ln x + c$) and receive expressions

$r^{-d-1}:\ \mu C_{0,1} - \mu C_{0,1}^{\alpha} = 0$,

$r^{-2d-1}:\ 2\mu C_{0,2} - \mu C_{0,1}^{\alpha}\big(\alpha C_{0,2} + g_1 C_{0,1}\big) = 0$,

$r^{-3d-1}:\ 3\mu C_{0,3} - \mu C_{0,1}^{\alpha}\big(\alpha C_{0,3} + \alpha_2 C_{0,2}^2 + g_1\big(C_{0,2} + \alpha C_{0,1}C_{0,2}\big) + g_2 C_{0,1}^2\big) = 0$,

$r^{-4d-1}:\ 4\mu C_{0,4} - \mu C_{0,1}^{\alpha}\Big(\alpha C_{0,4} + \alpha_2 2C_{0,2}C_{0,3} + \alpha_3 C_{0,2}^2 + g_1\big(C_{0,3} + \alpha\big(C_{0,2}^2 + C_{0,1}C_{0,3}\big) +$

$\qquad + \alpha_2 C_{0,1}C_{0,2}^2\big) + g_2\big(2C_{0,1}C_{0,2} + \alpha C_{0,2}C_{0,1}^2\big) + g_3 C_{0,1}^3\Big) = 0$,

$r^{-d-2}\ln r:\ \alpha\mu C_{1,1} - \mu C_{0,1}^{\alpha}\alpha C_{1,1} = 0$,

$r^{-2d-2}\ln r:\ (\alpha+1)\mu C_{1,2} - \mu C_{0,1}^{\alpha}\big(\alpha C_{1,2} + \alpha_2 2C_{0,2}C_{1,1} + g_1\big(C_{1,1} + \alpha C_{0,1}C_{1,1}\big)\big) = 0$, \hfill (10)

$r^{-3d-2}\ln r:\ (\alpha+2)\mu C_{1,3} - \mu C_{0,1}^{\alpha}\Big(\alpha C_{1,3} + \alpha_2\big(2C_{0,3}C_{1,1} + 2C_{0,2}C_{1,2}\big) + \alpha_3 3C_{0,2}^2 C_{1,1}\big) + g_1\big(C_{1,2} +$

$\qquad + \alpha\big(2C_{0,2}C_{1,1} + C_{0,1}C_{1,2}\big)\big) + \alpha_2 2C_{0,1}C_{0,2}C_{1,1} + g_2\big(2C_{0,1}C_{1,1} + \alpha C_{0,1}^2 C_{1,1}\big)\Big) = 0$,

$r^{-d-3}\ln^2 r:\ (2\alpha-1)\mu C_{2,1} - \mu C_{0,1}^{\alpha}\big(\alpha C_{2,1} + \alpha_2 C_{1,1}^2\big) = 0$,

$r^{-2d-3}\ln^2 r:\ 2\alpha\mu C_{2,2} - \mu C_{0,1}^{\alpha}\Big(\alpha C_{2,2} + \alpha_2\big(2C_{0,2}C_{2,1} + 2C_{1,1}C_{1,2}\big) + \alpha_3 3C_{0,2}C_{1,1}^2 + g_1\big(C_{2,1} +$

$\qquad + \alpha\big(C_{1,1}^2 + C_{0,1}C_{2,1}\big) + \alpha_2 C_{0,1}C_{1,1}^2\big)\Big) = 0$,

$r^{-d-4}\ln^3 r:\ (3\alpha-2)\mu C_{3,1} - \mu C_{0,1}^{\alpha}\big(\alpha C_{3,1} + \alpha_2 2C_{1,1}C_{2,1} + \alpha_3 C_{1,1}^3\big) = 0$.

Where $\alpha_n = \dfrac{\alpha(\alpha-1)\cdot\ldots\cdot(\alpha-n+1)}{n!}$ - is binomial coefficient from on α on n.

From where equating to zero expression (10) we find coefficients $C_{k,m}$

$C_{0,1} = 1$, $C_{0,2}(2-\alpha) = g_1$, $C_{0,3}(3-\alpha) = \alpha_2 C_{0,2}^2 + g_1(\alpha+1)C_{0,2} + g_2$,

$C_{0,4}(4-\alpha) = \alpha_2 2C_{0,2}C_{0,3} + \alpha_3 C_{0,2}^2 + g_1\big((\alpha+1)C_{0,3} + (\alpha+\alpha_2)C_{0,2}^2\big) + g_2(\alpha+2)C_{0,2} + g_3$,

$$C_{1,1}(\alpha - \alpha) = 0, \quad C_{1,2} = 2\alpha_2 C_{0,2} C_{1,1} + g_1(\alpha + 1)C_{1,1}, \quad 2C_{1,3} = 2\alpha_2\left(C_{0,3}C_{1,1} + C_{0,2}C_{1,2}\right) +$$

$$+ 3\alpha_3 C_{0,2}^2 C_{1,1} + g_1\left(C_{1,2} + 2\alpha\left(C_{0,2}C_{1,1} + C_{1,2}\right)\right) + 2\alpha_2 C_{0,2}C_{1,1} + g_2(\alpha_1 + 2)C_{1,1},$$

$$C_{2,1}(\alpha - 1) = \alpha_2 C_{1,1}^2, \quad \alpha C_{2,2} = \alpha_2\left(2C_{0,2}C_{2,1} + 2C_{1,1}C_{1,2}\right) + \alpha_3 3C_{0,2}C_{1,1}^2 +$$

$$+ g_1\left(C_{2,1} + \alpha\left(C_{1,1}^2 + C_{0,1}C_{2,1}\right) + \alpha_2 C_{0,1}C_{1,1}^2\right), \quad \mu C_{3,1}(2\alpha - 2) = \alpha_2 2C_{1,1}C_{2,1} + \alpha_3 C_{1,1}^3.$$

From the equations (10) it isn't possible to find coefficients $C_{0,m}$ for the whole $\alpha > 1$, for example in a case $\alpha = 2$ the coefficient $C_{0,2}$ isn't defined. For resolvability of a task in cases of the whole $\alpha > 1$ it is necessary to add members of type $\ln^k r$. Then the structure of the decision becomes complicated, and there are the following expressions

$$r^{-d-2} : (1-\alpha)\mu C_{1,2},$$

$$r^{-2d-2} : (1-\alpha)\mu C_{1,3},$$

$$r^{-3d-2} : (1-\alpha)\mu C_{1,4}, \tag{11}$$

$$r^{-d-3}\ln r : 2(1-\alpha)\mu C_{2,1},$$

$$r^{-2d-3}\ln r : 2(1-\alpha)\mu C_{2,2},$$

$$r^{-d-4}\ln^2 r : 3(1-\alpha)\mu C_{3,1}.$$

It is possible to notice that for each whole $\alpha > 1$ indicators of degrees at which equalities are written out (10) coincide with indicators of degrees of equalities (11). For example for $\alpha = 2$

$$r^{-2d-1} = r^{-\frac{2}{\alpha-1}-1} = r^{-3} \quad \text{and} \quad r^{-d-2} = r^{-\frac{1}{\alpha-1}-2} = r^{-3}.$$

After addition of new members in cases $\alpha = 2$ for stay $C_{0,2}$ we receive the equation

$$r^{-3} : (2-2)C_{0,2} - g_1 + (1-2)C_{1,1} = 0, \text{ where } C_{0,2} \text{ - any, } C_{1,1} = -g_1.$$

The case when $\alpha = 2$ is considered in article [6]. We will consider the table of coincidence of degrees. We will consider table 1. In the first column r exponents in expressions are presented (10). In the second, third and j a column are presented r (11). Each element of 1 column coincides with one of the column j elements depending on value of α.

Table 1. Comparison of indicators of degrees $r = (\alpha - 1)\mu \ln x + c$.

α - the whole	$\alpha = 2$	$\alpha = 3$	$\cdots$	$\alpha = j$, $j \geq 2$, $j \in N$.
r^{-d-1}			$\cdots$	
r^{-2d-1}	r^{-d-2}		$\cdots$	
r^{-3d-1}	r^{-2d-2}	r^{-d-2}	$\cdots$	
$\cdots$	$\cdots$	$\cdots$	$\cdots$	$\cdots$
r^{-kd-1}	$r^{-(k-1)d-2}$	$r^{-(k-2)d-2}$	$\cdots$	$r^{-(k-l+1)d-2}$
$r^{-d-2}\ln r$			$\cdots$	
$r^{-2d-2}\ln r$	$r^{-d-3}\ln r$		$\cdots$	
$r^{-3d-2}\ln r$	$r^{-2d-3}\ln r$	$r^{-d-3}\ln r$	$\cdots$	
$\cdots$	$\cdots$	$\cdots$	$\cdots$	$\cdots$
$r^{-kd-2}\ln r$	$r^{-(k-1)d-3}\ln r$	$r^{-(k-2)d-3}\ln r$	$\cdots$	$r^{-(k-l+1)d-3}\ln r$
$\cdots$	$\cdots$	$\cdots$	$\cdots$	$\cdots$
$r^{-d-(t+1)}\ln^t r$			$\cdots$	
$r^{-2d-(t+1)}\ln^t r$	$r^{-d-(t+2)}\ln^t r$		$\cdots$	
$r^{-3d-(t+1)}\ln^t r$	$r^{-2d-(t+2)}\ln^t r$	$r^{-d-(t+2)}\ln^t r$	$\cdots$	
$\cdots$	$\cdots$	$\cdots$	$\cdots$	$\cdots$
$r^{-kd-(t+1)}\ln^t r$	$r^{-(k-1)d-(t+2)}\ln^t r$	$r^{-(k-2)d-(t+2)}\ln^t r$	$\cdots$	$r^{-(k-l+1)d-(t+2)}\ln^t r$

Theorem 1. *The function $F(u)$ satisfies conditions (5), (6) and $\mu - const$, then $x \to \infty$ for the solution of Eq. (7) asymptotics holds (9) and $v_0(x) > 0$, $v_0'(x) < 0$ at $x > 0$.*

Proof. The function $v_0(x)$ in the form of the sum is:

$$v_0(x) = \hat{v}_n(x) + w(x), \text{ where } x \geq 2, \ n \geq 2, \ \hat{v}_n(x) \in C(x \geq 0) \text{ and} \tag{12}$$

$$\hat{v}_n = \sum_{k=0}^{n}\sum_{m=1}^{N} C_{k,m} \frac{\ln^k((\alpha-1)\mu \ln x + c)}{((\alpha-1)\mu \ln x + c)^{md+k}}, \text{ where } N = 1 + (\alpha-1)(n-k).$$

Substituting the sum (12) in Eq. (7), we obtain the problem

$$w''(x) - xw'(x) - \mu\big(F(w + \hat{v}_n) - F(\hat{v}_n)\big) = h_n(x), \tag{13}$$

$$w(x) \to 0, \ w'(x) \to 0, \text{ for } x \to \infty, \text{ where} \tag{14}$$

$$|h_n(x)| \leq M(\ln t)^{-n-1}. \tag{15}$$

Equation (13) is transformed as

$$w''(x) - xw'(x) - \mu F'(\hat{v}_n(x))w(x) = \mu R(\hat{v}_n(x), w(x)) + h_n(x), \text{ where}$$

$$R(\hat{v}_n, w, x) = F(w(x) + \hat{v}_n(x)) - F(\hat{v}_n(x)) - F'(\hat{v}_n(x))w(x),$$

$$R(\hat{v}_n(x), w(x)) = O(F''(\hat{v}_n(x))w^2(x)), \tag{16}$$

$$|F''(\hat{v}_n(x))| \le B(\ln x)^{d(2-\alpha)} \text{ for } \alpha \in (1, 2). \tag{17}$$

The idea of that transformation was earlier used in Refs. [3], [4].

In order to construct the solution $w(x)$ of the problem (13), (14) we obtain an integral equation

$$w(x) = -\int_x^\infty W^{-1}(s)(\varphi_1(x)\varphi_2(s) - \varphi_1(s)\varphi_2(x))(\mu R(\hat{v}_n, w, s) + h_n(s))ds \tag{18}$$

where, $W(t) = \exp\left(\dfrac{t^2}{2}\right)$ is the Wronskian and $\varphi_1(x)$, $\varphi_2(x)$ are linearly independent solutions

$w'' - xw' - \mu F'(\hat{v}_n)w = 0$.

$$\varphi_1(x) = d_1((\alpha-1)\mu \ln x + c)^{-\alpha d} + O((\ln x)^{-2\alpha d}) \text{ for } x \to \infty,$$

$$\varphi_2(x) = q_1 x^{-1} e^{x^2/2}((\alpha-1)\mu \ln x + c)^{\alpha d}(1 + O((\ln x)^{-\alpha d})) \text{ for } x \to \infty, \text{ where } d_1, q_1 - const.$$

We apply the method of successive approximations for the solution for the solution of the integral Eq. (18). We choose $w_0 \equiv 0$, then, using (15) – (18), we find $w(x)$.

There exists $M_1 > 0$ that for solution of the Eq. (18) inequality

$$|w(x)| \le M_1(\ln x)^{-m}, \text{ where } m = n - (2-\alpha)d.$$

3. Numerical Solution and solution of the problem

We rewrite Eq. (7) in the form of the system

$$\begin{cases} v'(x) = z(x), \\ z'(x) = xz(x) + \mu F(v(x)). \end{cases} \tag{19}$$

Sufficient conditions of stability of the Runge-Kutta difference scheme for the system (19) are the inequalities [5]

$$|h \cdot \mu \cdot F'(x)| << 1, h < 0, |hX_0| < 1$$

16

This implies that one should take X_0 and integrate it backwards (i.e. with increments $h < 0$) in the interval $[0; X_0]$. The initial conditions at the point X_0 have the form

$$v_0(X_0) = V_0, \ z(X_0) = Z_0, \tag{20}$$

where V_0, Z_0 are frome (10), (11)

$$V_0(x) = \sum_{k=0}^{4} \sum_{m=1}^{1+(\alpha-1)(4-k)} C_{k,m} \frac{\ln^k((\alpha-1)\mu \ln x + c)}{((\alpha-1)\mu \ln x + c)^{md+k}},$$

$$Z_0(x) = \sum_{k=0}^{4} \sum_{m=1}^{1+(\alpha-1)(4-k)} \mu C_{k,m} \frac{-(\alpha-1)(md+k)\ln^k((\alpha-1)\mu \ln x + c)}{x((\alpha-1)\mu \ln x + c)^{md+k+1}} +$$

$$+ \sum_{k=1}^{4} \sum_{m=1}^{1+(\alpha-1)(4-k)} \mu C_{k,m} \frac{k(\alpha-1)\ln^{k-1}((\alpha-1)\mu \ln x + c)}{x((\alpha-1)\mu \ln x + c)^{md+k+1}}.$$

Coefficients of an $C_{k,m}$ are defined from (10), (11) for each α with the table. We will give results of the numerical analysis of a task (19), (20). It agrees with (5), (6) we will set an obvious look for function of an $F(u)$, for example: $F(u) = u^\alpha(1 + \ln(1 + u))$.
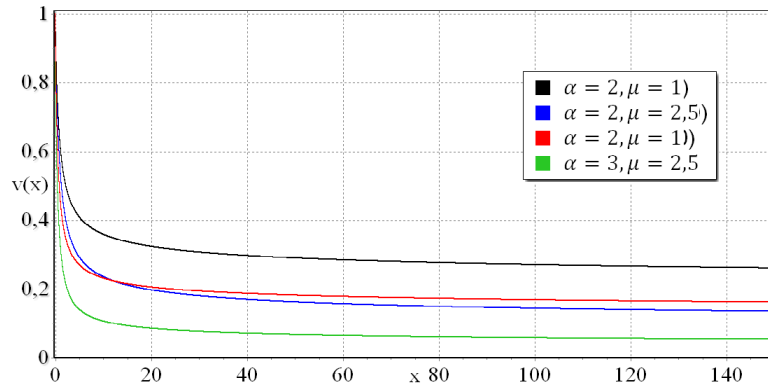
Figure 1. The graphical image of function $v(x)$.

Thus, the numerical solution of a task is constructed (7), (8).

In case of $\alpha = 2$:

$\mu = 1, c = 0,3697, z(0) = -0,8924; \quad \mu = 1,5, c = 0,2139, z(0) = -1,1341;$

$\mu = 2, c = 0,0817, z(0) = -1,3367; \quad \mu = 2,5, c = 0,0001, z(0) = -1,4107.$

In case of $\alpha = 3$:

$\mu = 1, c = 0,6299, z(0) = -0,7898; \quad \mu = 1,5, c = 0,5942, z(0) = -0,9991;$

$$\mu = 2, c = 0,5206, z(0) = -1,1745; \quad \mu = 2,5, c = 0,4008, z(0) = -1,3284.$$

4. Conclusion

The problem considered in this work describes the phenomenon of convective diffusion around a drop in view of distributed chemical reaction, a streamlined flow of a viscous incompressible fluid. It is well known that several boundary layers develop in the neighborhood of the particle (see [5]). In work [2] the main member of an asymptotics in a diffusive interface about a drop in the vicinity of a point of running off of liquid from a drop in case of $\alpha > 1$, with conditions (5) and (6) when $g_{2k+1} = 0$, $k \in N_0$ was constructed. In this work the result for the following members of an asymptotics, in cases of the whole $\alpha > 1$ is generalized. For finding coefficients of $C_{k,m}$ software mathematical packages, for example Maple are used. An analogous structure of the asymptotics (up to a linear change of variable x) takes place in the diffusive boundary layer of convection-diffusion problem around the cylinder, a streamlined cross-flow of ideal fluid (see [6] in cases $\alpha = 2$). Case $\alpha = 2$ shown for comparison.

References

[1] Akhmetov, R.G. Asymptotics of solutions for a class of quasilinear second-order ordinary differential equations, *Differ. Eq.,* 46(2), (2010), 159 – 166.

[2] Akhmetov, R.G., Kutluev, R.R. Influence of a volumetric chemical reaction on the convective mass transfer near a drop. *International Journal of Structural Stability and Dynamics*, 13(7), (2013). 1340002-1 – 1340002-8.

[3] Fedoruk M.V. WKB method for nonlinear second order equation, *Journ vychisl. math. and math. phys.* 26, (1986). 196-210.

[4] Kalyakin L.A. Justification of Asymptotic Expansion for the Principal Resonance Equation, *Proc. of the Steklov Inst. of Math. Suppl.* 1, (2003). 108-122.

[5] Akhmetov, R.G. Asymptotic behavior of the solution to the convective diffusion problem in the wake of a particle, *Comput. Math. Math. Phys.,* 46(5), (2006), 796 – 809.

[6] Maksimova, N.V., Akhmetov, R.G. The asymptotic solutions for boundary value problem to a convective diffusion equation with chemical reaction near a cylinder. *Latin American Journal of Solids and Structures*, 10(1), (2013), 123 – 131.

Rustyam G. Akhmetov, Professor: Chair of Mathematics and Computer Programming Bashkir State Pedagogical University named after M.Akmullah, 450000, Russia, Ufa, 3a Oktyabrskoy revolutsii st, Building 2, room 403, 62 R. Zorge st, apartment 12, RUSSIA (akhmetovrg@mail.ru).

Ruslan R. Kutluev (M.Sc.): Bashkir State Pedagogical University named after M.Akmullah, 450000, Russia, Ufa, 3a Oktyabrskoy revolutsii st, Building 2, room 403, RUSSIA (rus4652@yandex.ru).

Internal resonances in nonlinear vibrations of a continuous rod with microstructure
(ASY104-15)

Igor V. Andrianov, Jan Awrejcewicz, Vladyslav V. Danishevskyy, Bernd Markert

Abstract: Nonlinear longitudinal vibrations of a periodically heterogeneous rod are considered. Geometrical nonlinearity is described by the Cauchy–Green strain tensor. Physical nonlinearity is modelled expressing the energy of deformation as a series expansion in powers of the strains. The governing macroscopic dynamical equation is obtained by the higher-order asymptotic homogenization method. An asymptotic solution is developed by the method of multiple time scales. The effects of internal resonances and modes coupling are predicted. The specific objective of the paper is to analyse how the presence of the microstructure influences on the processes of mode interactions. It is shown that depending on a scaling relation between the amplitude of the vibrations and the size of the unit cell different scenarios of the modes coupling can be realised.

1. Introduction

The effect of internal resonances may arise in nonlinear multi-degree of freedom systems, when natural frequencies of the modes become commensurable with each other. Then, the presence of nonlinearity induces a coupling between different modes even in zero-order approximation. Complicated modal interactions occur, which may result in a self-generation of higher-order modes. In such a case, truncation to the modes having non-zero initial energy (which is usually applied studying vibrations of continuous structures) will not be valid and all resonant modes should be taken into account simultaneously.

The nonlinear phenomena of modes coupling and internal resonances have been intensively studied for homogeneous structures [1–3]. Meantime, the nonlinear dynamic behaviour of heterogeneous solids was considered significantly less. Several studies of nonlinear vibrations of composite structures were presented in [4–6]. However, many authors have focused on laminated plates and shells that include a small number of layers (usually only a few), so the influence of a microstructure was not investigated thoroughly. Only very recently, vibrations of a heterogeneous rod embedded in a nonlinear elastic medium were considered in [7].

In this paper, natural longitudinal vibrations of an elastic periodically heterogeneous rod are studied. Geometrical and physical nonlinearity of the problem is taken into account. We wish to predict how the presence of the microstructure affects the processes of internal resonances and mode

interactions. The governing macroscopic dynamical equation was obtained earlier with the help of the asymptotic homogenization method [8]. The method of multiple time scales [1–3] is applied for the analysis of nonlinear dynamical behaviour of the rod.

The paper is organized as follows. In Section 2, the input problem is formulated. In Section 3, the perturbation procedure for a homogeneous rod is introduced. In Section 4, the influence of the microstructure is analysed. Conclusion remarks are presented in Section 5.

2.   Input problem

We consider a periodically heterogeneous composite rod consisting of alternating layers of two different components $\Omega^{(1)}$ and $\Omega^{(2)}$ with a perfect bonding at the interface $\partial\Omega$ (figure 1). Natural longitudinal vibrations in the direction x are studied.
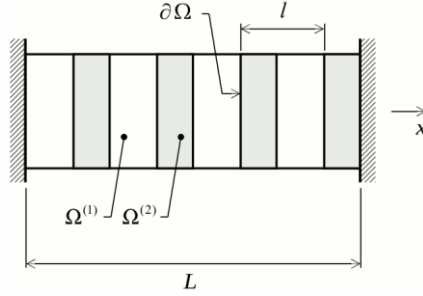
Figure 1. Heterogeneous rod under consideration.

Geometrical nonlinearity appears due to nonlinear relations between the elastic strains and the gradients of displacements and is described by the Cauchy–Green strain tensor [9]. Physical nonlinearity displays a deviation of the stress–strain relations from the proportional Hooke's law. It is modelled representing the energy of deformation as a series expansion in powers of invariants of the strain tensor and taking into account the higher-order terms. Such expansion is usually referred to as the Murnaghan elastic potential [10]. In our previous paper [8], we have obtained a macroscopic dynamical equation that describes nonlinear vibrations of heterogeneous layered structures. For the problem under consideration it can be written as follows:

$$E_1 \frac{\partial^2 u}{\partial x^2} + E_2 \frac{\partial u}{\partial x}\frac{\partial^2 u}{\partial x^2} + l^2 E_3 \frac{\partial^4 u}{\partial x^4} = \rho \frac{\partial^2 u}{\partial t^2},$$

(1)

where u is the displacement; l is the size of the unit cell; E_1, E_2, E_3 are the effective elastic coefficients; ρ is the effective mass density. In the l.h.s. of equation (1), the first term is associated

with a linear elastic response of a homogeneous solid. The second term accounts for nonlinear effects (both physical and geometrical). The third term describes the influence of the microstructure.

For the effective coefficients, explicit analytical expressions were derived [8]. The coefficients E_1, E_3 are always positive. E_2 is negative for the most industrial materials, but it will be positive in the case of a physically linear solid. The typical magnitudes of the elastic coefficients are as follows: $|E_2|/E_1 \sim 10$, $E_3/E_1 \sim 10^{-2}$.

Equation (1) presents an asymptotic approximation of the original problem. It is valid only if the size of the microstructure l is smaller than the macroscopic size L of the entire body, $l/L < 1$. It was shown [11] that a good accuracy is achieved for $l/L < 0.4$, i.e. $l^2/L^2 \leq 10^{-1}$.

Let us introduce non-dimensional variables $\bar{x} = x(\pi/L)$, $\bar{t} = t(\pi/L)\sqrt{E_1/\rho}$, $\bar{u} = u/A$, where A is the amplitude of the vibrations. For the simplicity, after the substitution we drop the over bars. Then, equation (1) reads

$$\frac{\partial^2 u}{\partial x^2} + \varepsilon \frac{\partial u}{\partial x} \frac{\partial^2 u}{\partial x^2} + \eta \frac{\partial^4 u}{\partial x^4} = \frac{\partial^2 u}{\partial t^2}, \tag{2}$$

where $\varepsilon = \pi(E_2/E_1)(A/L)$, $\eta = \pi^2(E_3/E_1)(l^2/L^2)$. Let us note that η is always positive, whereas the sign of ε depends on the properties of the material: $\varepsilon < 0$ if $E_3 < 0$ (soft nonlinearity) and $\varepsilon > 0$ if $E_3 > 0$ (hard nonlinearity). The variables η and ε may be considered as natural small parameters characterizing, accordingly, the rate of heterogeneity and the rate of nonlinearity.

Let us consider the case of clamped-clamped edges. The boundary and the initial conditions are:

$$u(0,t) = u(\pi,t) = 0, \quad u(x,0) = U_0(x), \quad \partial u(x,0)/\partial t = U_1(x). \tag{3}$$

It should be noted that equation (2) includes the fourth-order spatial derivative and, consequently, additional boundary conditions are required. This is a typical difficulty that arises when higher-order models, derived originally for infinite media, are applied to bounded domains. It has been shown [12] that general solutions of the higher-order models combine contributions of long-wave solutions associated with the macroscopic problem and short-wave solutions localised in the vicinity of boundaries. The latter are induced particularly by the presence of higher-order derivative terms. The short-wave solutions describe extraneous boundary layers that have no physical sense. Therefore, additional boundary conditions for equation (2) should be formulated in such a way to eliminate the effect of short-wave boundary layers. This principle yields [12]:

$$\partial^2 u(0,t)/\partial x^2 = \partial^2 u(\pi,t)/\partial x^2 = 0. \tag{4}$$

3. Vibrations of a homogeneous rod

The behaviour of the nonlinear problem (2)–(4) depends on the scaling relation between the small parameters η and ε, which, in its turn, is determined by the size l of the microstructure and by the amplitude A of the vibrations. If the size of the microstructure is considerably small, one can estimate $\eta \sim \varepsilon^2$. In such a case, $l^2/L^2 \sim 10^{-3}$ for $A/L \sim 10^{-4}$ and $l^2/L^2 \sim 10^{-1}$ for $A/L \sim 10^{-3}$. Up to $O(\varepsilon^2)$ approximation, the influence of the microstructure can be neglected, so equation (2) reads:

$$\frac{\partial^2 u}{\partial x^2} + \varepsilon \frac{\partial u}{\partial x} \frac{\partial^2 u}{\partial x^2} + O(\varepsilon^2) = \frac{\partial^2 u}{\partial t^2} \ . \tag{5}$$

Let us represent the displacement u as a Fourier-sine expansion:

$$u(x,t) = q_1(t)\sin(x) + q_2(t)\sin(2x) + q_3(t)\sin(3x)\ldots \ . \tag{6}$$

Substituting (6) into (5), we obtain:

$$\frac{d^2 q_1}{dt^2} + \omega_1^2 q_1 + \varepsilon(q_1 q_2 + 3q_2 q_3 + \ldots) = 0 \ , \tag{7}$$

$$\frac{d^2 q_2}{dt^2} + \omega_2^2 q_2 + \varepsilon\left(\frac{1}{2}q_1^2 + 3q_1 q_3 + \ldots\right) = 0 \ ,$$

$$\frac{d^2 q_3}{dt^2} + \omega_3^2 q_3 + \varepsilon(3q_1 q_2 + \ldots) = 0 \ , \quad \ldots \ ;$$

where ω_n is the frequency in the linear case, $\omega_n = n$; n is the number of the mode, $n = 1,2,3,\ldots$.

Let us introduce different time scales $t_0 = t$, $t_1 = \varepsilon t$ and represent q_n as an asymptotic expansion in powers of ε:

$$q_n(t) = q_{n0}(t_0,t_1) + \varepsilon q_{n1}(t_0,t_1) + O(\varepsilon^2) \ . \tag{8}$$

We note that $d^2/dt^2 = \partial^2/\partial t_0^2 + 2\varepsilon \partial^2/(\partial t_0 \partial t_1) + O(\varepsilon^2)$. Next we substitute expressions (8) into equations (7) and collect the coefficients at equal powers of ε.

In $O(\varepsilon^0)$ approximation we obtain

$$q_{n0} = a_n(t_1)\cos(\omega_n t_0) + b_n(t_1)\sin(\omega_n t_0) \ , \tag{9}$$

where $a_n(0) = (2/\pi)\int_0^\pi U_0(x)\sin(nx)dx$, $b_n(0) = [2/(\pi\omega_n)]\int_0^\pi U_1(x)\sin(nx)dx$.

In $O(\varepsilon^1)$ approximation equations (7) for give:

$$\frac{\partial^2 q_{11}}{\partial t_0^2} + \omega_1^2 q_{11} = -2\frac{\partial^2 q_{10}}{\partial t_0 \partial t_1} - q_{10}q_{20} - 3q_{20}q_{30} + \ldots, \tag{10}$$

$$\frac{\partial^2 q_{21}}{\partial t_0^2} + \omega_2^2 q_{21} = -2\frac{\partial^2 q_{20}}{\partial t_0 \partial t_1} - \frac{1}{2}q_{10}^2 - 3q_{10}q_{30} + \ldots,$$

$$\frac{\partial^2 q_{31}}{\partial t_0^2} + \omega_3^2 q_{31} = -2\frac{\partial^2 q_{30}}{\partial t_0 \partial t_1} - 3q_{10}q_{20} + \ldots, \quad \ldots;$$

A straightforward integration of system (10) will lead to the appearance of secular terms in the expressions for q_{n1}. Secular terms grow without a bound in time, which is inconsistent with the physical properties of the conservative system under consideration. In order to eliminate secular terms, the coefficients of $\cos(\omega_n t_0)$ and $\sin(\omega_n t_0)$ in the r.h.s. of equations (10) must be equal to zero. Substituting expressions (9) into equations (10) and fulfilling the aforementioned condition, we obtain a system of equations for a_n and b_n, which gives a possibility to investigate the interactions between different modes.

We note that in the problem under consideration an infinite number of modes can be involved into the resonant interactions. In this paper, we consider only two leading modes and examine in detail the internal resonance between the modes 1 and 2. Coupling between higher-order modes can be investigated in a similar way.

For the further analysis, it is convenient to introduce polar coordinates as follows: $a_n = r_n\cos(\varphi_n)$, $b_n = r_n\sin(\varphi_n)$, where r_n is the amplitude and φ_n is the phase. After routine transformations, the condition of the elimination of secular terms gives:

$$\frac{dr_1}{dt_1} = \frac{1}{4}r_1 r_2\sin(\varphi_2 - 2\varphi_1), \tag{11}$$

$$r_1\frac{d\varphi_1}{dt_1} = -\frac{1}{4}r_1 r_2\cos(\varphi_2 - 2\varphi_1), \tag{12}$$

$$\frac{dr_2}{dt_1} = -\frac{1}{16}r_1^2\sin(\varphi_2 - 2\varphi_1), \tag{13}$$

$$r_2\frac{d\varphi_2}{dt_1} = -\frac{1}{16}r_1^2\cos(\varphi_2 - 2\varphi_1). \tag{14}$$

A simple analysis shows that equations (11)–(14) allow vibrations by a single mode 2 ($r_2 \neq 0$, $r_1 = 0$). In this case the amplitude is constant in time, $r_2(t_1) = r_2(0)$. This is true up to the order $O(\varepsilon)$ for the time $t \leq O(\varepsilon^{-1})$. If we start with zero initial energy in the 1st mode, there will be no energy

present up to the order $O(\varepsilon)$ on the timescale $O(\varepsilon^{-1})$. On the other hand, vibrations by a single mode 1 are not possible, because system (11)–(14) does not hold for $r_1 \neq 0$, $r_2 = 0$. If there is initial energy present in the mode 1, energy transfers occur between the modes 1 and 2. Thereby, the modes 1 and 2 are coupled in $O(\varepsilon^0)$ approximation. This effect is called the internal resonance.

Multiplying equation (11) with r_1 and equation (13) with r_2, adding both equations and performing the integration, one obtains: $r_1^2 + 4r_2^2 = E^2$. This formula represents the energy conservation law, where E is the constant of integration having a physical sense of the full energy of the vibrations. Since in the input non-dimensional equation (2) the displacement u has been normalized to the amplitude A of the vibrations, without loss of generality we let $E = 1$. Then, equations (11)–(14) can be written as follows:

$$\frac{dr_2}{dt_1} = \frac{4r_2^2 - 1}{16}\sin(\psi),$$ (15)

$$\frac{d\psi}{dt_1} = \frac{12r_2^2 - 1}{16r_2}\cos(\psi);$$

where $\psi = \varphi_2 - 2\varphi_1$, $0 \leq r_2 \leq 1/2$.

We performed a numerical integration of system (15) using the Runge-Kutta fourth-order method; the obtained results are presented in (r_2, ϕ) phase plane in figure 2. The solution is 2π-periodic in ψ; the parts of the phase diagram at $r_2 > 0$ and at $r_2 < 0$ are symmetric with respect to the line $r_2 = 0$. The critical points are located at $r_2 = \pm\sqrt{3}/6$, $\psi = \pm\pi m$ (centres) and at $r_2 = \pm 1/2$, $\psi = \pi/2 \pm \pi m$ (saddles); $m = 0,1,2,...$. We can observe that the system oscillates around an equilibrium state with a periodic energy transfer between the modes 1 and 2.

4. Influence of the microstructure

As the size of the microstructure increases, the parameters η and ε become the same order of magnitude: $\eta \sim \varepsilon$. In such a case, $l^2/L^2 \sim 10^{-1}$ for $A/L \sim 10^{-4}$. The presence of the microstructure provides a kind of detuning effect for the phenomenon of internal resonance. Let us introduce the detuning parameter γ of the order $O(1)$ as follows: $\gamma = \eta/\varepsilon = \pi(E_3/E_2)(l^2/L^2)(L/A)$. The input dynamical equation (2) takes the form:
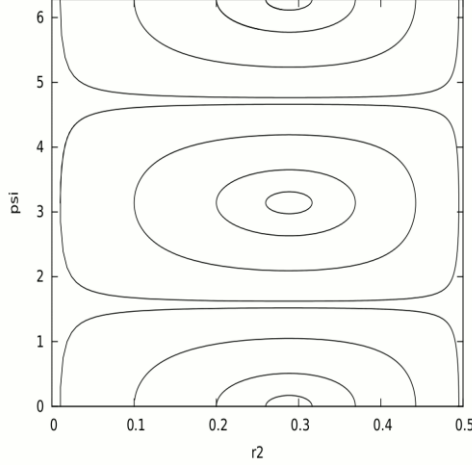
Figure 2. Phase plane in the case of a homogeneous rod.

$$\frac{\partial^2 u}{\partial x^2} + \varepsilon \frac{\partial u}{\partial x}\frac{\partial^2 u}{\partial x^2} + \varepsilon \gamma \frac{\partial^4 u}{\partial x^4} = \frac{\partial^2 u}{\partial t^2} .$$

Following the asymptotic procedure presented in Section 3, we obtain an additional contribution in system (15), which now reads:

$$\frac{dr_2}{dt_1} = \frac{4r_2^2 - 1}{16}\sin(\psi),$$ (16)

$$\frac{d\psi}{dt_1} = \frac{12r_2^2 - 1}{16r_2}\cos(\psi) + 3\gamma .$$

Let us examine the solution in the domain $0 \le r_2 \le 1/2$, $0 \le \psi \le 2\pi$, because for other values of r_2 and ψ it continues periodically.

In the case of soft nonlinearity, $\gamma < 0$, examples of the phase plane are shown in figure 3. As $|\gamma|$ increases, one centre moves left along the line $\psi = \pi$, whereas two centres move right along the lines $\psi = 0$, $\psi = 2\pi$. One saddle moves up and the other saddle moves down along the line $r_2 = 1/2$. For $\gamma = -1/12$, centres and saddles coincide at the points $r_2 = 1/2$, $\psi = 0$ and $r_2 = 1/2$, $\psi = 2\pi$ and then disappear. The only one centre remains and, with the further increase in $|\gamma|$, it continues moving left along the line $\psi = \pi$. The area of the periodic energy transfers between the modes 1 and 2 narrows.

In the case of hard nonlinearity, $\gamma > 0$, the behaviour of the system is illustrated in figure 4. As γ increases, one centre moves right along the line $\psi = \pi$ and two centres move left along the lines

$\psi = 0$, $\psi = 2\pi$. For $\gamma = 1/12$, one centre and two saddles coincide at the point $r_2 = 1/2$, $\psi = \pi$ and disappear. With the further increase in γ, two centres continues moving left along the lines $\psi = 0$, $\psi = 2\pi$ and the intensity of the energy transfers between the modes decreases.

For the both soft and hard nonlinearity, the increase of the size of the microstructure suppresses the energy exchange between the modes, so the effect of internal resonance becomes negligible.

$\gamma = -0.05$ $\gamma = -1$
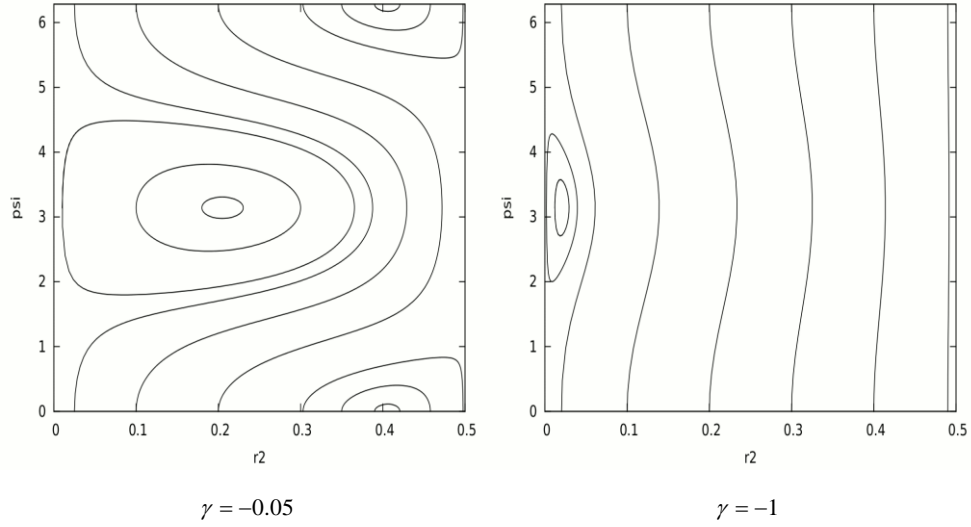
Figure 3. Phase plane in the case of soft nonlinearity.

$\gamma = 0.05$ $\gamma = 1$
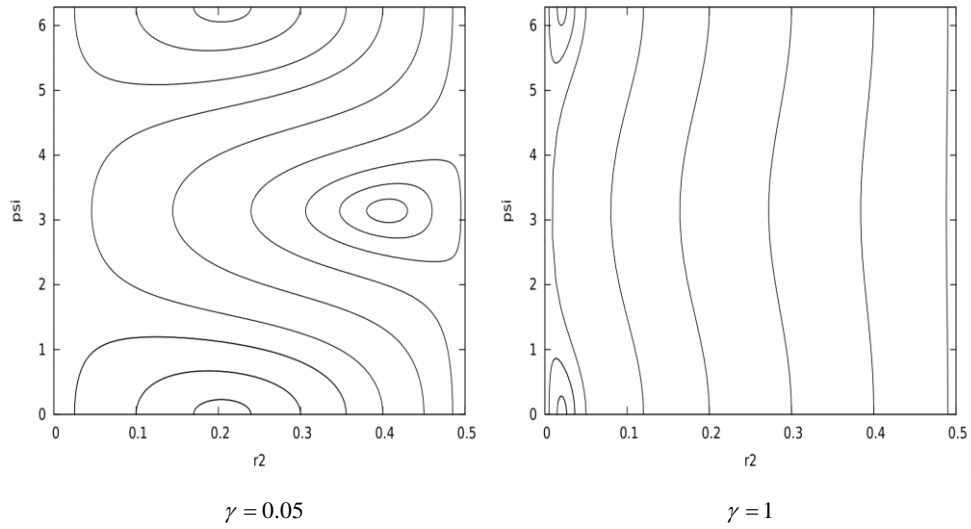
Figure 4. Phase plane in the case of hard nonlinearity.

5. Conclusions

Natural vibrations of a periodically heterogeneous rod are considered with an account for geometrical and physical nonlinearity. The governing dynamical equation was obtained earlier by the method of higher-order asymptotic homogenization. In this paper, we present the asymptotic analysis of the problem with the help of the method of multiple time scales.

If the size of the microstructure is relatively small in comparison to the amplitude of the vibrations, the effect of internal resonance takes place. It results in periodic energy transfers between different modes and in a modulation of their amplitudes. The resonant modes are coupled in $O(\varepsilon^0)$ approximation, so the truncation to the modes having non-zero initial energy is not possible. We studied in details the internal resonance between the leading modes 1 and 2, which is of primary importance for the engineering practice. The behaviour of the system was analysed in the phase plane using the Runge-Kutta fourth-order method and numerical results were presented.

If the size of the microstructure increases, the intensity of the energy transfers between different modes decreases and the effect of internal resonance is suppressed

The results presented in the paper can be applied to facilitate the development of new efficient methods of non-destructive testing. Measuring the characteristics of nonlinear vibrations at different amplitudes allows us to receive precise information about the internal structure of heterogeneous solids. This is sometimes that may be not possible within a linear framework.

Changing properties of the microstructure (e.g., using piezoelectric effects or saturation/desaturation of porous media) make it possible to tune the macroscopic dynamic response of nonlinear structures. This can be useful for a design of new active control devices in various branches of engineering.

Finally, we remark that the effect of internal resonance may be applied for the purposes of vibration damping. Nonlinear coupling between the vibrating modes may help to transfer mechanical energy from low- to high-order modes and, therefore, to decrease essentially the amplitude of the vibrations.

References

[1] Nayfeh, A.H., Mook D.T. *Nonlinear oscillations.* New York, Wiley, 1979.

[2] Boertjens, G.J., and van Horssen, W.T. On mode interactions for a weakly nonlinear beam equation. *Nonlinear Dynamics* 17 (1998), 23–40.

[3] Boertjens, G.J., and van Horssen, W.T. An asymptotic theory for a weakly nonlinear beam equation with a quadratic perturbation. *SIAM Journal on Applied Mathematics* 60 (2000), 602–632.

[4] Amabili, M. Internal resonances in non-linear vibrations of a laminated circular cylindrical shell. *Nonlinear Dynamics* 69 (2012), 755 –770.

[5] Rega, G., and Saetta, E. Nonlinear curvature-based model and resonant finite-amplitude vibrations of symmetric cross-ply laminates. *Journal of Sound and Vibration* 331 (2012), 2836–2855.

[6] Arvin, H., and Bakhtiari-Nejad, F. Nonlinear modal interaction in rotating composite Timoshenko beams. *Composite Structures* 96 (2013), 121–134.

[7] Andrianov, I.V., Danishevskyy, V.V., and Markert, B. Nonlinear vibrations and mode interactions for a continuous rod with microstructure. *Journal of Sound and Vibration* 351 (2015), 268–281.

[8] Andrianov, I.V., Danishevs'kyy, V.V., Ryzhkov, O.I., and Weichert D. Dynamic homogenization and wave propagation in a nonlinear 1D composite material. *Wave Motion* 50 (2013), 271–281.

[9] Lur'e, A.I. *Nonlinear theory of elasticity*. Amsterdam, North-Holland 1990.

[10] Murnaghan, F.D. *Finite deformation of an elastic solid.* New York, Wiley, 1951.

[11] Andrianov, I.V., Danishevs'kyy, V.V., Ryzhkov, O.I., and Weichert, D. Numerical study of formation of solitary strain waves in a nonlinear elastic layered composite material. *Wave Motion* 51 (2014), 405–417.

[12] Kaplunov, J.D., and Pichugin, A.V. On rational boundary conditions for higher-order long-wave models. *IUTAM Symposium on Scaling in Solid Mechanics. IUTAM Bookseries* 10 (2009), 81–90.

Igor V. Andrianov, Professor: RWTH Aachen University, Institute of General Mechanics, Templergraben 64, Aachen 52062, Germany (*igor_andrianov@hotmail.com*). The author gave a presentation of this paper during one of the conference sessions.

Jan Awrejcewicz, Professor: Technical University of Łódź, Department of Automation, Biomechanics and Mechatronics, Stefanowski St. 1/15, Łódź 90-924, Poland (*awrejcew@p.lodz.pl*).

Vladyslav V. Danishevskyy, Professor: Keele University, School of Computing and Mathematics, Staffordshire, ST5 5BG, UK (*v.danishevskyy@keele.ac.uk*).

Bernd Markert, Professor: RWTH Aachen University, Institute of General Mechanics, Templergraben 64, Aachen 52062, Germany (*markert@iam.rwth-aachen.de*).

Wave energy conversion with fully enclosed multi-axis inertial reaction mechanisms
(CON258-15)

I.A. Antoniadis, V. Georgoutsos

Abstract: A novel class of Wave Energy Converters is proposed, consisting from a class of fully enclosed appropriate internal body mechanisms, which provide inertial reaction against any multi-axis, multi-direction motion of an external vessel. This ensures maximum wave energy capture in comparison to other wave energy converters. The internal bodies are suspended from the external vessel body in such an appropriate geometrical configuration, that a symmetric four bar mechanism is essentially formed. The first advantage of this suspension geometry is that a linear trajectory results for the center of the mass of the suspended body with respect to the external vessel, enabling the introduction of a quite simple form of a Power Take Off (PTO) design. Moreover, the simplicity and the symmetry of the suspension geometry and of the PTO, ensure a quite simple and robust technological implementation, removing the restrictions of other linear, pendulum or gyroscopic variants of inertial reacting bodies. Furthermore, the mass and the inertia distribution of the internal body is optimized for the maximal conversion and storage of the wave energy. As a result, the dynamic behavior of the internal body assembly is essentially that of an equivalent vertical physical pendulum. However, the resulting equivalent pendulum length and inertia can far exceed those that can be achieved by an actual technical implementation of other pendulum variants, which results to a significant reduction of the suspended mass.

1. Introduction

Estimates for ocean wave power are of the same order as the global electricity production [1]. More than a thousand of patents and tenths (if not hundreds) of experimental prototypes of Wave Energy Converters are being tested in the sea [2]. However, no specific technological paradigm exists till today for efficient wave energy conversion. Among the WEC concepts with best perspectives, are those consisting from two-body configurations, in which only one body is in contact with the water and the other body is located above the water or is totally enclosed inside the wetted one. Numerous variants exist, such as the Frog and PS the Frog [3], which is a linear sliding mass enclosed inside a floating vessel. Interesting variants of this design include various pendulum forms, such as the SEAREV [4], inverted pendulum designs, or horizontal pendulum designs [5-8], all of which are associated with serious disadvantages.

29

A novel concept for the design of a general class of wave energy converters able to overcome all of these disadvantages is presented, based on fully enclosed internal body configurations, which provide inertial reaction against the motion of an external vessel. An example of such an arrangement is further analysed in details. An external vessel is subjected to simultaneous surge and pitch motion in all directions, ensuring thus maximum wave capture, in comparison for e.g. to heave only point absorbers. An inertial reacting body is enclosed internally, suspended appropriately from the external body in such a way that a symmetric 4bar mechanism is formed.

The first advantage of this suspension geometry is that the center of the mass of the suspended body moves in a linear trajectory with respect to the external vessel. This implies that the internal body appears to move essentially in linear way, like a simple mass in the conventional form of the PSFrog arrangements. This enables the introduction of a quite simple Power Take Off (PTO) system, as for e.g. hydraulic rams. Moreover, the simplicity and the symmetry of the suspension geometry and of the PTO, ensure a quite simple and robust technological implementation, contrary to all other known above variants of inertial reacting internal bodies.

The second advantage of this design is that the internal body behaves dynamically as a vertically suspended pendulum. However, the suspension geometry, in combination to the optimal mass and the inertia distribution of the internal body, ensure the maximal conversion and storage of the wave energy in the form of kinetic and potential energy. This is reflected to the resulting equivalent pendulum length and inertia of this design, which can far exceed those that can be achieved by an actual technical implementation either of a simple horizontal or of a vertical pendulum (suspended, or inverted). The direct consequence is significant reduction of the suspended mass.

The kinematic relations and the dynamic equations of motion are derived in section 2. In section 3 the equations of motion are linearized, an appropriate feedback law is proposed and the power that can be converted is estimated. Finally an indicative design of an 1MW WEC is presented in section 4.

2. Equations of motion

2.1. Kinematic relations

The assembly considered is depicted in Fig. 1, consisting from a floating external vessel V into which an internal symmetric four bar mechanism ABDE is suspended at a height α above the sea level. The waves induce to the vessel a simultaneous surge motion of magnitude u and a pitching motion of an angle θ with respect to the inertial coordinate system OXY. The center of mass G of the vessel V is located at a distance b below the level of the sea. The member DE of the internal four bar mechanism provides a basis onto which a solid body S is placed. The solid body provides a reaction mass to the motion of the external vessel, rotating with an angle φ about the Z axis of the inertial reference frame

OXY. The coordinate reference system RX_BY_B is rigidly attached to the vessel V, following its motion.

The basic geometrical configuration of the four bar mechanism is presented in Fig 2 and it is defined by the selection of the three independent lengths *d, c, l*. Following the fundamental kinematic analysis of 4 bar mechanisms, the angles γ and δ can be expressed as a function of the angle φ and of the three independent lengths *d, c, l*. The center of mass C of the body S is located at a distance *h* above the member DE.

The angular velocities of the mechanism can be expressed in the following compact form:

Figure 1. Schematic presentation of the assembly considered. An internally reacting body S is suspended by an appropriate 4bar mechanism ABDE from an external floating vessel V.

$$\dot{\gamma} = -\frac{2c}{l\sigma}\dot{\varphi} = -\mu\dot{\varphi} \tag{1}$$

$$\dot{\psi} = -\dot{\gamma} = \mu\dot{\varphi} \tag{2}$$
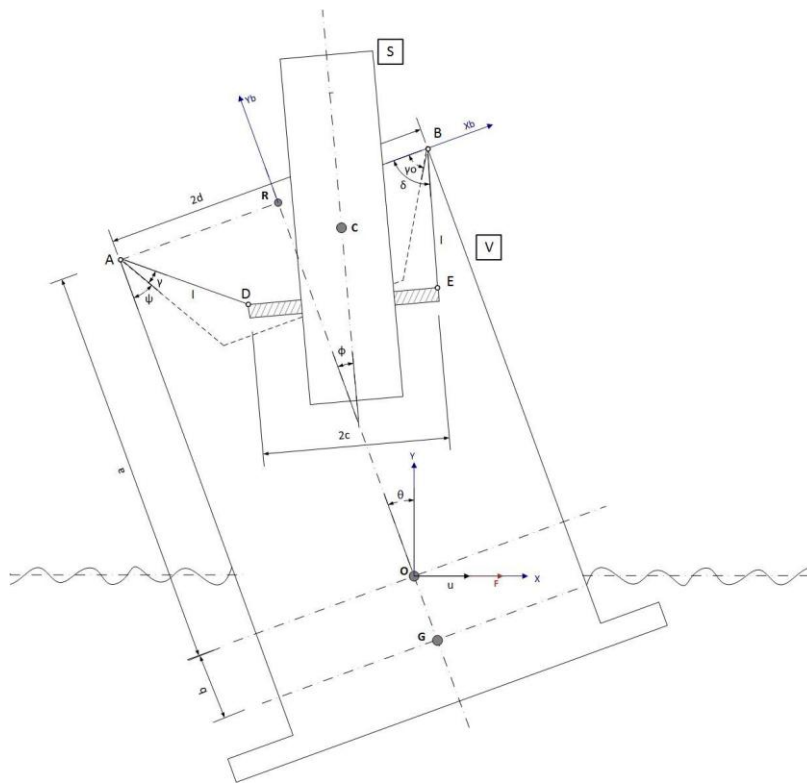
$$\mu = \frac{2c}{l\sigma} \tag{3}$$

$$\sigma = \frac{\sin(\gamma + \delta)}{\sin(\varphi + \delta)} \tag{4}$$

The coordinates x_B, y_B of the center of mass C of the body S with respect to the coordinate system RX_BY_B result as follows:

$$x = -d + l\cos\gamma + c\cos\varphi + h\sin\varphi \tag{5}$$

$$y_B = l\sin\gamma + c\sin\varphi - h\cos\varphi \tag{6}$$

A typical choice for h is:

$$h = l\sin\gamma_0 \tag{7}$$

It is easy to derive that y_B is equal to zero when $l=d=2c$, as it is the special case of the Roberts linkage. Therefore, the point C moves in a straight line over the segment AB.

The coordinates of the point G with respect to the inertial coordinate system are as follows:

$$x_G = u + b\sin\theta \tag{8}$$

$$y_G = -b\cos\theta \tag{9}$$

The translation of the center of mass C of the body S according to the system OXY is as follows:

$$x_M = x_R + x_B\cos\theta - y_B\sin\theta = u + x_B\cos\theta - (a + y_B)\sin\theta \tag{10}$$

$$y_M = y_R + x_B\sin\theta + y_B\cos\theta = x_B\sin\theta + (a + y_B)\cos\theta \tag{11}$$

2.2. Dynamic equations of motion

The kinetic energy captured from the bodies V and S can be written as:

$$T = \frac{1}{2}m_V\left(\dot{x}_G^2 + \dot{y}_G^2\right) + \frac{1}{2}I_V\dot\theta^2 + \frac{1}{2}m_s\left(\dot{x}_M^2 + \dot{y}_M^2\right) + \frac{1}{2}I_s(\dot\theta - \dot\varphi)^2 \tag{12}$$

where:

    m_V is the mass of the vessel V including the added mass of the water

    m_S is the mass of the body S

    I_V is the moment of inertia of the vessel V about O

    I_S is the moment of inertia of the reaction mass S about C.

The potential energy is as follows:

$$U = m_s g y_M + \frac{1}{2}K_V\theta^2 + m_V g y_G \tag{13}$$

where K_V is the hydrostatic stiffness in pitch (and/or roll) for the vessel about O.

The system presents three degrees of freedom:

$$r_1 = u \tag{14.a}$$

32

$$r_2 = \theta \tag{14.b}$$

$$r_3 = \varphi \tag{14.c}$$

The equations of motion of the system can be derived by the application of the following Lagrange principle:

$$\frac{d}{dt}\left(\frac{\partial L}{\partial \dot{r}_i}\right) - \left(\frac{\partial L}{\partial r_i}\right) = F_i \quad i = 1,3 \tag{15}$$

$$L = T - U \tag{16}$$

where Fi denote the external and the damping forces of the system.

After appropriate differentiations, the equations of motion result as:

$$\frac{d}{dt}P_u + R_u \dot{u} = F_w \tag{17.a}$$

$$\frac{d}{dt}P_\theta + K_v\theta + T_{v\theta} + T_{g\theta} = 0 \tag{17.b}$$

$$\frac{d}{dt}P_\varphi + T_{g\varphi} = T_p \tag{17.c}$$

where the momentum values P_u, P_θ, P_φ are defined as follows:

$$P_u = M_{uu}\dot{u} + M_{u\theta}\dot{\theta} + M_{u\varphi}\dot{\varphi} \tag{18.a}$$

$$P_\theta = M_{u\theta}\dot{u} + M_{\theta\theta}\dot{\theta} + M_{\theta\varphi}\dot{\varphi} \tag{18.b}$$

$$P_\varphi = M_{u\varphi}\dot{u} + M_{\theta\varphi}\dot{\theta} + M_{\varphi\varphi}\dot{\varphi} \tag{18.c}$$

with:

$$M_{uu} = m_v + m_s \tag{19.a}$$

$$M_{u\theta} = m_v b \cos\theta - m_s l_{xM} \tag{19.b}$$

$$M_{u\varphi} = m_s r_{xM} \tag{19.c}$$

$$M_{\theta\theta} = I_v + I_s + m_v b^2 + m_s\left(l_{xM}^2 + l_{yM}^2\right) \tag{19.d}$$

$$M_{\theta\varphi} = -\left[I_s + m_s\left(r_{xM}l_{xM} - r_{yM}l_{yM}\right)\right] \tag{19.e}$$

$$M_{\varphi\varphi} = I_s + m_s\left(r_{xM}^2 + r_{yM}^2\right) \tag{19.f}$$

$$\tag{20.a}$$

$$l_{xM} = (a + y_B)\cos\theta + x \; \sin\theta$$

$$l_{yM} = x \; \cos\theta - (\alpha + y_B)\sin\theta \tag{20.b}$$

$$r_{xM} = r_x \cos\theta - r_y\sin\theta \tag{21.a}$$

$$r_{yM} = r_x \sin\theta + r_y \cos\theta \qquad (21.b)$$

$$r_x = l\mu \sin\gamma - c \sin\varphi + h \cos\varphi \qquad (22.a)$$

$$r_y = -l\mu \cos\gamma + c \cos\varphi + h \sin\varphi \qquad (22.b)$$

The moments due to the gravity are:

$$T_{v\theta} = m_v g b \sin\theta \qquad (23.a)$$

$$T_{g\theta} = m_s g l_{ym} \qquad (23.b)$$

$$T_{g\varphi} = m_s g r_{ym} \qquad (23.c)$$

The rest of the terms are:

R_u is an added damping coefficient for the surge motion induced by the waves.

F_w is the force due to the incident and diffracted waves.

T_p is the reaction force of the PTO.

Under the assumption that the surge and pitch motion of the external vessel are known in the time domain, the equations of motion can be further simplified, retaining only the set of equations which refer to the mechanism itself:

$$\frac{d}{dt}\left(M_{\varphi\varphi}\dot{\varphi}\right) = -\frac{d}{dt}\left(M_{u\varphi}\dot{u} + M_{\theta\varphi}\dot{\theta}\right) - T_{g\varphi} + T_p \qquad (24)$$

3. Maximum power conversion capability

3.1. Linearization of the equations of motion

Under the assumption of small perturbations around the rest position of the mechanism, the following approximate relations hold for the angles $\alpha \in \{\varphi, \psi, \theta\}$ of the assembly:

$$\cos a \approx 1 \qquad (25.a)$$

$$\sin a \approx a \qquad (25.b)$$

which result to:

$$\cos\gamma = \cos(\gamma_o - \psi) \approx \cos\gamma_o + \psi \sin\gamma_o \qquad (26.a)$$

$$\sin\gamma = \sin(\gamma_o - \psi) \approx \sin\gamma_o - \psi \cos\gamma_o \qquad (26.b)$$

The equations of motion (5) and (6) can thus be simplified as follows:

$$x \approx l_p\varphi \qquad (27)$$

$$y_B \approx 0 \tag{28}$$

$$l_p = (\mu + 1)h \tag{29}$$

$$\mu \approx \mu_0 = \frac{2c}{l\sigma_0} = \frac{c}{l\cos\gamma_0} = \frac{1}{d/c - 1} \tag{30}$$

$$\sigma \approx \sigma_o = \frac{\sin 2\gamma_o}{\sin\gamma_o} = 2\cos\gamma_o \tag{31}$$

Equations (27),(28) imply that the physical motion of the center of the mass of the body is linear, exactly in the same way as the traditional designs of linear sliding mass WECs, as for e.g. in the form of PS Frog. Similar simplified relations hold for the factors r_x, r_y, l_{xM}, l_{yM}, r_{xM} and r_{yM}:

$$r_x \approx l_p \tag{32}$$

$$r_y \approx 0 \tag{33}$$

$$l_{xM} \approx a \tag{34}$$

$$l_{yM} \approx l_p\varphi \tag{35}$$

$$r_{xM} \approx l_p \tag{36}$$

$$r_{yM} \approx l_p\theta \tag{37}$$

as well as for the components of the matrix **M**:

$$M_{uu} \approx m_v \tag{38.a}$$

$$M_{u\theta} \approx m_v b \tag{38.b}$$

$$M_{u\varphi} \approx m_s l_p \tag{38.c}$$

$$M_{\theta\theta} \approx I_v + I_s + m_v b^2 \tag{38.d}$$

$$M_{\theta\varphi} \approx -I_\theta = -\left[I_s + m_s l_p a\right] \tag{38.e}$$

$$M_{\varphi\varphi} \approx I_\varphi = I_s + m_s l_p^2 \tag{38.f}$$

and the moments due to the gravity :

$$T_{v\theta} \approx 0 \tag{39.a}$$

$$T_{g\theta} \approx m_s g l_p \varphi \tag{39.b}$$

$$T_{g\varphi} \approx m_s g l_p \theta \tag{39.c}$$

3.2. Proposed form for the Power Take Off force and Feedback Law

In view of the non-linear equations of motion (17), the mechanism is inherent to an unstable behavior. For this reason, a feedback law of the following form is incorporated in the power take off force:

$$T_p = -K_p\varphi - R_p\dot{\varphi} + T_N \tag{40}$$

where K_p and R_p are constant linear feedback gains to be properly selected and T_N denotes an appropriate compensator for the non-linearity of the system in the form:

$$T_N = \frac{d}{dt}\left(P_\varphi - m_s l_p \dot{u} + I_\theta \dot{\theta} - I_\varphi \dot{\varphi}\right) + \left(T_{g\varphi} - m_s g l_p \theta\right) \tag{41}$$

which results to the following equation for motion of the internal body:

$$I_\varphi \ddot{\varphi} + R_p \dot{\varphi} + K_p \varphi = -m_s l_p \ddot{u} + I_\theta \ddot{\theta} - m_s g l_p \theta + T_N \tag{42}$$

Obviously T_N is equal to zero for a linearized system.

Equation (42) implies that the motion of the internal body is fully equivalent dynamically to that of a damped physical pendulum, with a mass m_s and inertia I_s about its CM, which is suspended at a distance l_p from its center of mass.

However, it should be stretched, that in view of equation (29), the equivalent length l_p of this pendulum can be many orders of magnitude higher than that expected by any other vertical pendulum, realized in the traditional natural technological way, as for e.g. in the form of SEAREV [4].

This pendulum can simultaneously convert three different forms of wave energy:

- The kinetic energy resulting from the surge motion
- The kinetic energy resulting from the pitching motion
- The potential energy resulting from the pitching motion

In view of equation (40), the selection of the feedback gains can be performed in a way to ensure stability of the system, optimal tuning of the natural periods of the system to the periods of the external source, as well as maximum power conversion capability.

3.3. Calculation of maximum power conversion capacity

The analysis of the power conversion capability can be performed independently for the surge and pitch motion of the converter. However, the design of the external vessel and the coupled form of equations [17] imply that a dependence exists in fact between them. Detailed analysis of such a dependence is performed in {5}. Following the outline of such an analysis, the vessel will be assumed to be subjected to a pitching motion of amplitude Θ_C and frequency ω:

$$\theta(t) = \Theta_C \cos \omega t \tag{43}$$

while the surge motion will depend on the pitch motion as follows:

$$u(t) = -b\theta(t) = -b\Theta_C \cos \omega t \tag{44}$$

As a result, the equation of motion (42) now becomes:

$$I_\varphi \ddot{\varphi} + R_p \dot{\varphi} + K_p \varphi = -M_e \Theta_C \cos \omega t \tag{45}$$

$$T_p = -K_p \varphi - R_p \dot{\varphi} \tag{46}$$

$$M_e = \omega^2 I_P + m_s g l_p \tag{47}$$

$$I_P = I_S + m_s l_p (a + b) \tag{48}$$

The steady state response of the system is a harmonic function with a frequency equal to ω and with a phase difference of π/2 with the excitation force, in order to maximize power capture from the excitation force:

$$\varphi(t) = -\Phi_S \sin \omega t \tag{49}$$

The minus sign is used to denote that for the positive θ angle, a negative φ angle should result, in order to ensure the stability of the vessel.

Substitution of equation (49) into equation (45) leads to the following results:

$$R_p = M_e \Theta_c / \omega \Phi_s \tag{50.a}$$

$$K_p = \omega^2 I_\varphi \tag{50.b}$$

The mean power absorbed by the Power Take Off is defined as follows:

$$P_{out} = \frac{1}{T_w} \int_0^{T_w} T_p \dot{\varphi} dt \tag{51}$$

$$T_w = 2\pi / \omega \tag{52}$$

Substitution of equations (46), (49) into (47) leads to the following expression

$$P_{out} = -\frac{1}{2} \omega M_e \Theta_c \Phi_s = -P_{in} \tag{53}$$

or alternatively to:

$$P_{out} = -\frac{1}{2} \omega \Theta_c m_s X_M a_e \tag{54}$$

where:

$$X_M = l_p \Phi_s \tag{55.a}$$

$$a_e = g + \omega^2 (a + b + l_I) \tag{55.b}$$

$$l_I = I_S / (m_s l_p) \tag{55.c}$$

and

ω : Frequency of the waves

Θ_c : Amplitude of the pitch motion

m_s : reaction mass

X_M : Amplitude of the linear motion of the center of mass of the oscillating body

Φ_s : maximum inclination of the mechanism

l_P : equivalent pendulum length

I_S : inertia of the oscillating body about its CM

a : distance of the mechanism suspension points from the sea level

b : distance of the vessel's CM from the sea level

Equation (54) is of paramount importance for the design and sizing of the mechanism, since it clearly defines the effect of the various design parameters on the expected power output. As for example, the power output is proportional to the frequency ω of the waves, which normally very low. Typically, this necessitates the usage of large oscillating masses m_S, travelling over long distances X_M. However, these typical design requirements can be reduced, due to the intelligent selection of the various factors appearing in a_e, equation (55.c)

4. Indicative implementation

An indicative mechanism for a standalone 1MW WEC is presented. A body S consisting of two unequal spheres and a beam that links them together will be used as an inertial mass. This body is suspended with three links inside a sealed vessel V. All the other additional components such as the hydraulic system and the rams are also enclosed in the vessel. This basic configuration has the form presented in Figure 2. As fig 2 indicates, the vessel is a fully sealed hull with a plate at the bottom for maximizing reaction, increasing the added mass and lowering the center of mass of the external vessel. The hydraulic system power pack can be placed at the bottom, while the rams operate in the same plane with the center of mass C of the oscillating body V. Assuming that the weight of the beam and the supporting brackets are negligible, the values of M_1= 64tn, r_1=2.5m and M_2=8 tn, r_2=20 m are reached, where M_1 and M_2 indicate the masses of the two spheres and r_1 , r_2 their distance measured from the center of mass C. Table 1 below includes the main dimensions of the configuration. It should be clarified, that the above values refer just to an indicative implementation of a mechanism for a WEC and they are by no means optimized. Such an approach is obviously necessary in full association to the design of an optimized external vessel.
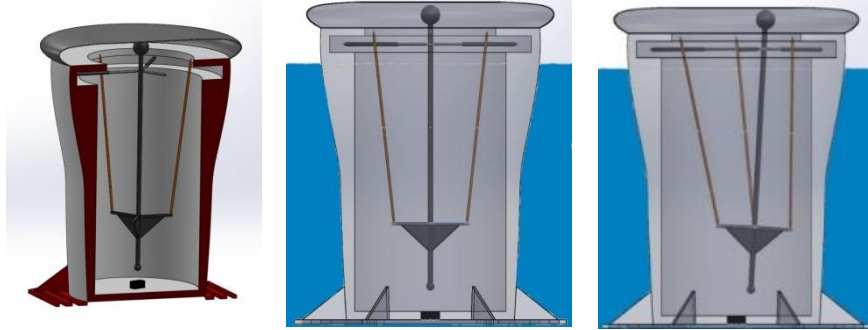
Figure 2: Rest position and limit position of the inertial mass

Table 1: Main design parameters of the Standalone WEC

Total mass (body)	72 tn
M_1	64 tn
M_2	8 tn
r_1 (distance of M_1 from C/CoM)	2.5 m
r_2 (distance of M_2 from C/CoM)	20 m
d(Mechanism)	7 m
c(Mechanism)	5 m
h (Mechanism)	18 m
a (Vessel)	5 m
b (Vessel)	2.5 m
T (period of waves)	8 s
Θ (Pitch ampltude)	25 deg
Φ (Internal mass inclination)	5 deg
Translation X_M (concerning C/CoM)	5.5 m
Rated Power Output	**1 MW**

The combined values of power and suspended mass in Table 1 compare more than favorably to those necessary for other types of internally reacting WECs, such as PSFrog [3] or SEAREV [4]. Far more important, the suspension geometry and the simplicity of the PTO render this design far more reliable and easily implementable than all other known types of internally reacting masses.

5. Conclusions

The novel class of Wave Energy Converters, consisting from fully enclosed inertially reacting bodies under appropriate suspension geometry from an external floating vessel can provide a reliable design, able to meet the severe conditions for survivability under extreme weather conditions.

The linear motion of the center of mass of the suspended body enables the introduction of a quite simple form of a Power Take Off (PTO) design. Moreover, the simplicity and the symmetry of the suspension geometry and of the PTO, ensure a quite simple and robust technological implementation. The optimal dynamic design of the geometry and the mass and the inertia distribution of the internal body ensure the maximal conversion and storage of the wave energy. This results to a significant reduction of the suspended mass, compared to other internal reacting designs.

The concept is flexible and parametrically designed, enabling its implementation in any form of floating vessels. A first option is as standalone WECs, fully enclosed in appropriately designed hulls. Moreover, an alternative direction for their implementation consists in properly embedding them in floating offshore platforms, supporting wind turbines. Such a design can drastically enhance the performance, the efficiency and the potential of floating offshore energy applications.

References

[1] K. Gunn, C. Stock-Williams, 2012, "*Quantifying the Global Wave Power Resource*," Renewable Energy*, N* 44, pp. 296-304, 2012.

[2] Antonio F. de O. Falcao, 2010, "Wave energy utilization: A review of the technologies. Renewable and Sustainable Energy Reviews", 14, 2010, 899-918.

[3] McCabe AP, Bradshaw A, Meadowcroft JAC, Aggidis G. 2006, Developments in the design of the PS Frog Mk 5 wave energy converter. Renewable Energy 2006;31:141–51.

[4] Babarit A, Clement AH, Gilloteaux JC. , 2005, "*Optimization and time-domain simulation of the SEAREV wave energy converter*". In: Proceedings of 24th International Conference Offshore Mechanics Arctic Engineering, Halkidiki, Greece, 2005, vol. 2, p. 703–712.

[5] M B Widden, M J French and G A Aggidis, 2008, "Analysis of a pitching-and-surging wave-energy converter that reacts against an internal mass, when operating in regular sinusoidal waves". Proc. IMechE Vol. 222 Part M: J. Engineering for the Maritime Environment, 2008, 153-161.

[6] http://www.wello.eu/penguin.php

[7] http://neptunewavepower.com

[8] D.Zhang, G. Aggidis, Y. Wang, A. McCabe, W. Li, 2013, Experimental results from wave tank trials of a multi-axis wave energy converter, APPLIED PHYSICS LETTERS 103, 103901 (2013)

I.A.Antoniadis, Professor
V.Georgoutsos, Research Assistant
Dynamics and Structures Laboratory, Mechanical Engineering Department, National Technical University of Athens, Email: antogian@central.ntua.gr

Hyperdamping properties of a novel stable non-linear oscillator concept, based on a statically unstable stiffness element (CON257-15)

Ioannis A Antoniadis, Konstantinos J Kyriakopoulos, Evangelos G Papadopoulos

Abstract: A novel concept of a non-linear oscillator is proposed, based on a bistable element, which operates around an unstable equilibrium point. Contrary to Quasi-Zero Stiffness oscillators, a totally different redistribution of the stiffness elements is followed, so that any level the required static stiffness can be maintained. This oscillator is designed to present the same overall (static) stiffness around the system equilibrium point, the same mass and to use the same damping element as a reference classical linear SDOF oscillator. Once such an oscillator is optimally designed, it is shown to exhibit an extraordinary apparent damping ratio, which is several orders of magnitude higher than that of the original SDOF system, especially in cases where the original damping of the SDOF system is extremely low. This damping behaviour is not a result of a novel additional extraordinary energy dissipation mechanism, but a result of the phase difference between the positive and the negative stiffness elastic forces; this is in turn a consequence of the proper redistribution of the stiffness and the damping elements. This fact ensures that an adequate level of elastic forces exists throughout the entire frequency range, able to counteract the inertial and the external excitation forces. Consequently, a resonance phenomenon, which is inherent in the original linear SDOF system, cannot emerge in the proposed oscillator.

1. Introduction

The concept of introducing negative stiffness elements (or 'anti-springs') for vibration isolation has a long history, being first introduced in the pioneering publication of Molyneaux [1] as well as in the milestone developments of Platus [2]. On a parallel approach, a quite interesting possibility towards achieving significant damping has been demonstrated to exist also in materials comprising a negative stiffness phase [3], not only at a material level [4], but also at macroscopic devices [5]. Quite interestingly, such a behaviour is combined with high stiffness properties. A theoretical approach has been performed for the analysis of the static and dynamic stability of composite materials, incorporating negative stiffness elements [6]. Recently, meta-material designs have appeared with negative effective moduli. An initial comprehensive review of such designs can be found in [7]. A rich variety of designs have been proposed for the realization of negative spring configurations, incorporating various structural elements such as post-buckled beams, plates, cells, pre-compressed springs, etc., arranged in appropriate geometrical configurations. Some interesting designs are described in [8],[9]. The central

concept of these approaches is to significantly reduce the stiffness of the isolator and consequently to reduce the natural frequency of the system even at almost zero levels [10]. In this way, the transmissibility of the system for all operating frequencies above the natural frequency is reduced, resulting to enhanced vibration isolation. Since then, numerous other applications have been reported in a diversity of engineering domains, such as automotive suspensions [11, 12, 13] or seismic isolation [14, 15]. From the dynamics point of view, many interesting improvements have been proposed, based on the non-linear properties of the elastic force of such designs [16, 17, 18, 19, 20]. However, all these designs suffer from their fundamental requirement for a drastic reduction of the stiffness of the structure almost to negligible levels, limiting thus the static load capacity of such structures.

In order to remove this drawback, a novel approach has been proposed [21], on how to optimally design a simple linear oscillator incorporating a negative stiffness element, which can exhibit extraordinary damping properties, without presenting the drawbacks of the traditional linear oscillator, or of the 'zero-stiffness' designs. This oscillator is designed to present the same overall (static) stiffness as a traditional reference original oscillator. In this way, it overcomes the inherent disadvantage of the known negative stiffness oscillators in requiring stiffness reduction. Moreover, it does not require any increase in the mass or the viscous damping of the original oscillator in order to increase the vibration isolation properties, as it is the case of the traditional linear vibration isolators. However, it differs both from the original SDoF oscillator, as well as from the known negative stiffness oscillators, by appropriately redistributing the individual stiffness elements and by reallocating the damping. Although the proposed oscillator incorporates a negative stiffness element, it is designed to be both statically and dynamically stable. Once such a system is designed according to the approach proposed in [21], it is shown to exhibit an extraordinary damping behaviour, with an apparent damping ratio to be even several orders of magnitude higher than that of the original system, especially in the cases where the original damping of the system is extremely low. Moreover, a drastic increase of several orders of magnitude has been observed for the damping ratio of the flexural waves propagating within layered periodic structures incorporating such negative stiffness oscillators [22].

In this paper, the concept of [21] is further generalized, by replacing the linear negative stiffness element by a non-linear bistable element, which operates around an unstable equilibrium point. This bistable element takes the form of two springs, which are oblique in their initial unstressed condition, while they allowed to oscillate around a stressed and unstable static equilibrium position, presenting thus a negative stiffness. When the properties of this oscillator are properly selected, it is shown to be statically and dynamically stable, presenting simultaneously an extraordinary damping behaviour and any level of required static stiffness.

2. The proposed non-linear oscillator system concept
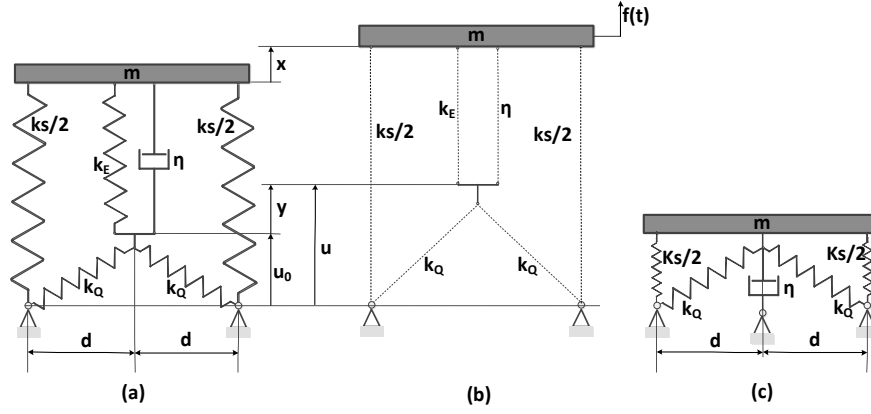
Figure 1. Schematic presentation of the oscillators considered. (a) Proposed non-linear oscillator at the static equilibrium point. (b) Notation concerning the perturbed behaviour of the oscillator. (c) Equivalent conventional Quasi-Zero Stiffness (QZS) non-linear oscillator.

The non-linear oscillator system under consideration is depicted in Figures 1(a) and 1(b). It consists from a mass m which is supported by two parallel linear springs with stiffness k_S and k_E respectively and by a damper with constant η. The damper η and the spring k_E are in turn supported by a set of two symmetric linear oblique springs with constants k_Q. The static equilibrium position of the system is depicted in Fig 1(a), when no external force is applied. The perturbed position after an external dynamic excitation f(t) is depicted in Fig 1(b), along with the necessary notion concerning the various displacements of the system. For comparison purposes, the structure of an equivalent conventional Quasi-Zero_Stiffness (QZS) non-linear oscillator is depicted in Fig 1(c).

The equations of motion of the proposed oscillator are:

$$m\ddot{x} + \eta(\dot{x} - \dot{y}) + k_S(l_S - l_{SI}) + k_E(l_E - l_{EI}) = f \tag{1.a}$$

$$-\eta(\dot{x} - \dot{y}) - k_E(l_E - l_{EI}) + f_N(u) = 0 \tag{1.b}$$

where:

l_S(t) is the length of the spring k_S, l_{SI} is the initial length of the un-deformed spring k_S, l_E(t) is the length of the spring k_E, l_{EI} is the initial length of the un-deformed spring k_E and $f_N(u)$ is the non-linear force exerted by the set of the two symmetric oblique springs k_Q.

The equations of the system at the static equilibrium point are derived by the set of equations (1):

$$k_S(l_{S0} - l_{SI}) + k_E(l_{E0} - l_{EI}) = 0 \tag{2.a}$$

$$-k_E(l_{E0} - l_{EI}) + f_N(u_0) = 0 \tag{2.b}$$

where the index ( )$_0$ is used to denote the static equilibrium point and l_{S0} is the length of the (normally deformed) spring k_S at the static equilibrium point, l_{E0} is the length of the (normally deformed) spring k_E at the static equilibrium point and $f_N(u_0)$ is the non-linear force exerted by the set of the two symmetric oblique springs k_Q at the static equilibrium point.

Denoting by:

$$v_S = l_{S0} - l_{SI} \tag{3.a}$$

$$v_E = l_{E0} - l_{EI} \tag{3.b}$$

$$f_{N0} = f_N(u_0) \tag{3.c}$$

the following equations result:

$$v_S = -f_{N0}/k_S \tag{4.a}$$

$$v_E = f_{N0}/k_E = -(k_S/k_E)v_S \tag{4.b}$$

Further elaboration of the sets of Eqs (2),(3),(4) and substitution in the set of Eqs (1) leads to the final set of equations of motion:

$$m\ddot{x} + k_S x + f_{Nd}(u) = f \tag{5.a}$$

$$-\eta(\dot{x} - \dot{y}) - k_E(x - y) + f_{Nd}(u) = 0 \tag{5.b}$$

where:

$$f_{Nd}(u) = f_N(u) - f_{N0} \tag{6.a}$$

$$u = u_0 + y \tag{6.b}$$

$$l_S = l_{S0} + x \tag{6.c}$$

The following expressions can be derived for the potential energy U_N, the non-linear force f_N and the equivalent non-liner stiffness k_N of the set of the oblique springs k_Q :

$$U_N[u(y)] = 2\frac{1}{2}k_Q(l_Q - l_{QI})^2 = k_Q l_{QI}^2 (1 - l_Q/l_{QI})^2 \tag{7}$$

$$f_N(u) = \frac{\partial U_N}{\partial y} = 2k_Q(1 - l_{QI}/l_Q)u \tag{8}$$

$$k_N = \frac{\partial f_N}{\partial y} = 2k_Q(1 - l_{QI}d^2/l_Q^3) = 2k_Q[1 - c_I^2(l_{QI}/l_Q)^3] \tag{9}$$

where l_{QI} is the initial length of the un-deformed springs k_Q, , $_Q(t)$ is the length of the springs k_Q,

$$l_Q = (u^2 + d^2)^{1/2} \tag{10}$$

and:

$$c_I = d/l_{QI} \leq 1 \tag{11}$$

Assuming that the operation of the non-linear set of springs is limited in the range:

$$l_Q \leq l_{QZ} \Leftrightarrow u \leq u_Z \tag{12.a}$$

where l_{QZ} is the value of l_Q were the stiffness k_N becomes zero,

$$l_{QZ} = l_{QI} c_I^{2/3} \leq l_{QI} \tag{12.b}$$

$$u_Z = (l_{QZ}^2 - d^2)^{1/2} = l_{QI}(c_I^{4/3} - c_I^2)^{1/2} \tag{12.c}$$

$$u_I = (l_{QI}^2 - d^2)^{1/2} = l_{QI}(1 - c_I^2)^{1/2} \geq u_Z \tag{12.d}$$

then the equivalent non-liner stiffness k_N of the set of the oblique springs k_Q is negative and reaches its peak value for u=0. Similarly, when $l_Q(t) < l_{QI}$ the non-linear force f_N is also negative.

By linearizing the non-linear part of the oscillator around the local static equilibrium point,

$$f_{Nd} = k_C y \tag{13.a}$$

$$k_C = k_N(u_0) = \frac{\partial f_N}{\partial y}(u = u_0) \tag{13.b}$$

equations (5) lead to the following linear dynamic system:

$$m\ddot{x} + k_S x + k_C y = f \tag{14.a}$$

$$-\eta(\dot{x} - \dot{y}) - k_E(x - y) + k_c y = 0 \tag{14.b}$$

which is exactly the type of oscillator analysed in [21].

The transfer function of the system in (14) is:

$$\frac{X}{F} = \frac{s\eta + (k_E + k_C)}{c_1 s^3 + c_2 s^2 + c_3 s + c_4} = \frac{s\eta + (k_E + k_C)}{m\eta(\sigma + \rho)(s^2 + 2\zeta_n \omega_n s + \omega_n^2)} \tag{15.a}$$

$$\frac{Y}{X} = \frac{s\eta + k_E}{s\eta + (k_E + k_C)} \tag{15.b}$$

with:

$$c_1 = m\eta \tag{16.a}$$

$$c_2 = m(k_E + k_C) \tag{16.b}$$

$$c_3 = \eta(k_S + k_C) \tag{16.c}$$

$$c_4 = k_S(k_E + k_C) + k_E k_C \tag{16.d}$$

The linearization of the dynamic system (5) enables the direct implementation of the systematic procedure for the selection of the parameters of the dynamic system of (14), and which is analytically described in [21].

3. A numerical example

According to the systematic design procedure described in [21], a reference SDOF linear oscillator is defined first, with a stiffness k_0, a mass m and a damper with a constant η. The natural frequency ω_0 and the damping factor ζ_0 of this reference linear oscillator are consequently:

$$\omega_0 = \sqrt{k_0/m} \tag{16.a}$$

$$\zeta_0 = \eta/2\sqrt{k_0 m} \tag{16.b}$$

In the subsequent numerical example, the reference oscillator is defined with a natural frequency of $\omega_0 = (2\pi)$ rad/sec, a damping factor of $\zeta_0 = 0.01$ and a stiffness of $k_0 = 1$ N/m.

The design procedure described in [21], essentially consists in an approach on how to redistribute the stiffness of the new oscillator by defining new stiffness constants k_S, k_E, k_C, in order to maximize its damping behaviour, while maintaining the same total stiffness k_0 the mass m and the damper η of the reference oscillator. The design steps, as detailed in section 2.2 of [21] are the following.

First, in order to retain the total original stiffness of the system, the following constraint must hold:

$$k_0 = k_S + \frac{k_E k_C}{k_E + k_C} \tag{17}$$

Next, since a high value of k_C can lead to a negative value of k_0, an engineering safety margin $\varepsilon > 0$ is defined, prohibiting the system from reaching such a statically unstable situation:

$$k_S + \frac{(1+\varepsilon)k_E k_C}{(1+\varepsilon)k_E + k_C} = 0 \tag{18}$$

Finally, a freely selectable design parameter α is defined:

$$k_S = \alpha k_0 \tag{19}$$

In view of (19), equations (17) and (18) become:

$$k_E = k_0 \frac{\varepsilon a(a-1)}{1+\varepsilon - a\varepsilon} \tag{20}$$

$$k_C = -k_0 \frac{\varepsilon a(a-1)}{1+\varepsilon} \tag{21}$$

Thus, after selecting a specific value of the safety margin ε, the design parameter α can be varied, so that a new maximum damping coefficient ζ_n is achieved for the modified negative stiffness oscillator.

In the numerical example considered, a safety factor of $\varepsilon = 5\%$ is selected. According to Fig 2, a new optimal damping factor of $\zeta_n = 0.158$ results for a value of $\alpha = 3$, increasing the initial damping factor $\zeta_0 = 0.01$ of the system by 16 times.
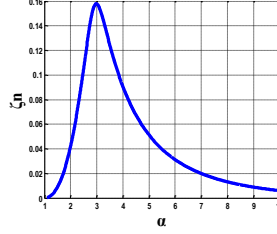
Figure 2: Variation of the new damping factor ζ_n with the parameter α.

The corresponding optimal values of the stiffness coefficients of the new linear oscillator result from equations (19),(20),(21) as k_S=3N/m, $k_E = 0.333$N/m and $k_C = -0.2857$N/m.

(a)   (b)
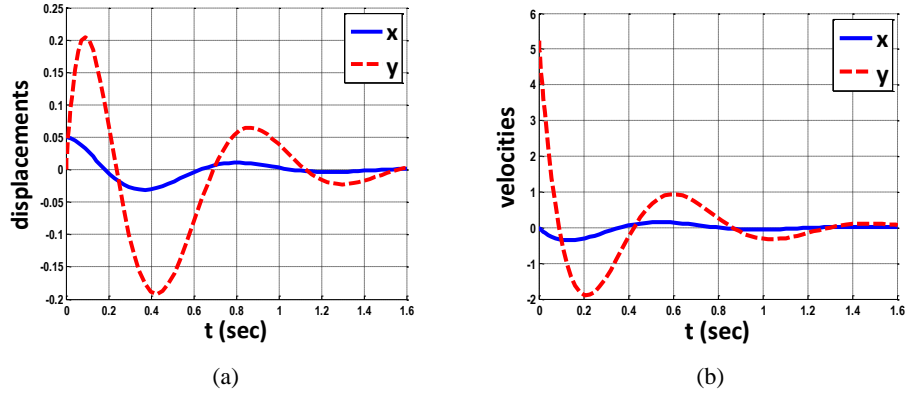
Figure 3. Response of the linear oscillator with a negative stiffness element: (a) Displacements (b) Velocities.

The response of this oscillator to an initial displacement of $x(0)$=0.05m is presented in fig. 3. As it can be observed, although the initial reference oscillator has a very low damping factor of ζ_0 =0.01, the new system with the negative stiffness element achieves a highly damped behaviour.

Next, a non-linear oscillator in the form of Fig. 1a is designed, were the negative stiffness spring of constant $k_C = -0.2857$N/m is replaced by a set of oblique springs. The necessary parameters of the oblique springs to be selected are the values of k_Q, l_{QI}, c_{QI}, as well as the position u_0.

For the proper selection of these parameters, first the maximum permissible amplitude of the excitation force is defined as $F_{MAX} = k_0 * X_{ST}$ with X_{ST} =0.05m. Thus, an initial estimate of the maximum response amplitudes of $x(t)$ and $y(t)$ to a harmonic excitation under F_{MAX} can be derived by the transfer function in eq. (15) as X_{MAX} =0.076m and Y_{MAX} =0.5326m. Thus, a conservative estimate for the maximum permissible value of $u(t)$ can be set as U_{MAX} =0.500m. Next the value of u_0 is selected as u_0=0.005m. This value is selected reasonably close to u_0=0 so that an almost symmetric response around u_0=0 is obtained.

The rest of the parameters of the oblique springs are selected so that $k_N(0)=1.02k_C$ and $k_N(U_{MAX})=0.96k_C$. Since $k_N(0)$ is the minimum value of K_N, this setting of $k_N(0)$ guarantees that in view of eq (17), the system of springs remains statically stable for the entire operating range. Parallel, the choice of $k_N(U_{MAX})$ guarantees that k_N retains a sufficient level of negative values in the entire operating range, so that the damping properties of the oscillator are not compromised. The resulting parameters of the oblique springs are $k_Q=1.3114$N/m , $l_{QI}=8.7719$ m, $c_{QI}=0.9$, $u_0=0.005$m.

The response of this oscillator to an initial displacement of $x(0)=0.05$m is presented in fig. 4. The system behaves almost exactly as the linear oscillator in Fig. 3, indicating also a highly damped behaviour. Figure 5a presents the variation of k_N over time and Fig 5.b as a function of the displacement u of the set of the oblique springs. As it can be observed, the negative stiffness remains within acceptable negative value limits.

(a)   (b)
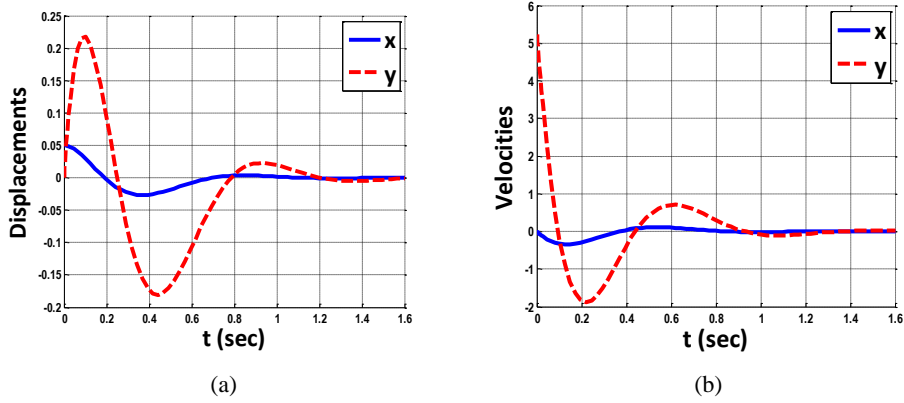
Figure 4 Response of the non-linear oscillator to $x(0)=0.05$m: (a) Displacements (b) Velocities.

(a)   (b)
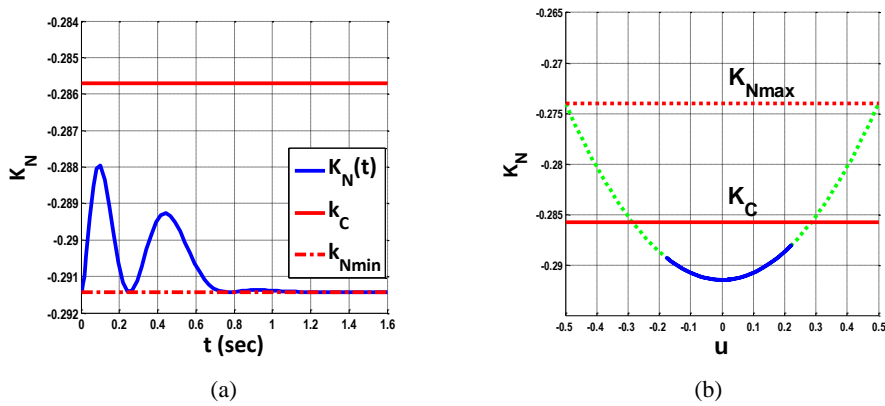
Figure 5. Variation of the non-linear stiffness k_N to to $x(0)=0.05$m. a) Variation in the time domain. b) Range of oscillation.

Next, the response of the proposed non-linear oscillator to a harmonic excitation force of $f(t)=F_e cos(2\pi f_e t)$ is considered, for a value of the excitation amplitude equal to $F_e = F_{MAX} = k_0 * X_{ST}$ with $X_{ST} = 0.05$m and for an excitation frequency of $f_e = f_0 = 1.0$Hz. The corresponding responses are presented in Figures 6 and 7.

(a)

(b)
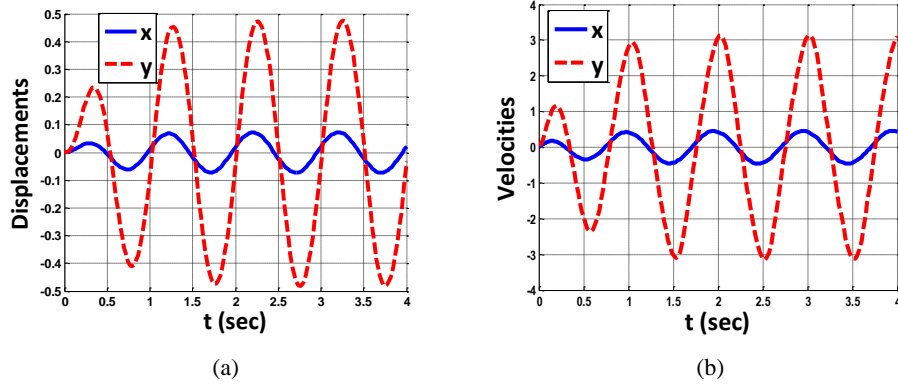
Figure 6 Response of the proposed non-linear oscillator to a harmonic excitation force of F_e=0.05N and f_e=1Hz: (a) Displacements (b) Velocities.

(a)

(b)
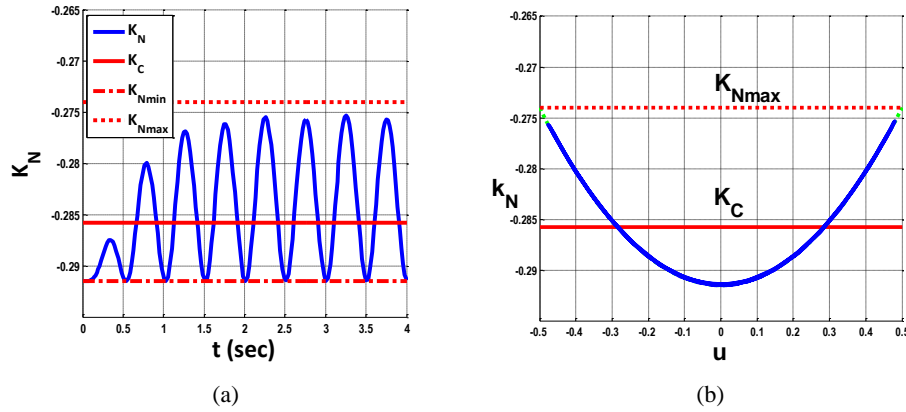
Figure 7. Variation of the non-linear stiffness k_N to a harmonic excitation force of F_e=0.05N and f_e=1Hz:. a) Variation in the time domain. b) Range of oscillation.

An essentially harmonic response is presented in Fig 6. The amplitude of $y(t)$ does not exceed the maximum value of Y_{MAX} =0.5m. Figure 7 verifies that the values of $k_N(t)$ remain within the specified maximum and minimum limits.

Fig. 8a presents the Frequency Response Functions of the displacement x of the proposed non-linear oscillator to a harmonic excitation force of F_e=F_{MAX}=0.05N. The FRF for x is in a very good agreement to that of the linear negative stiffness oscillator. The maximum deviation is observed for a

value of f_e=0.4Hz. The corresponding responses are shown in Fig. 9, indicating a significant non-linear behaviour, which requires further analysis.

(a)   (b)
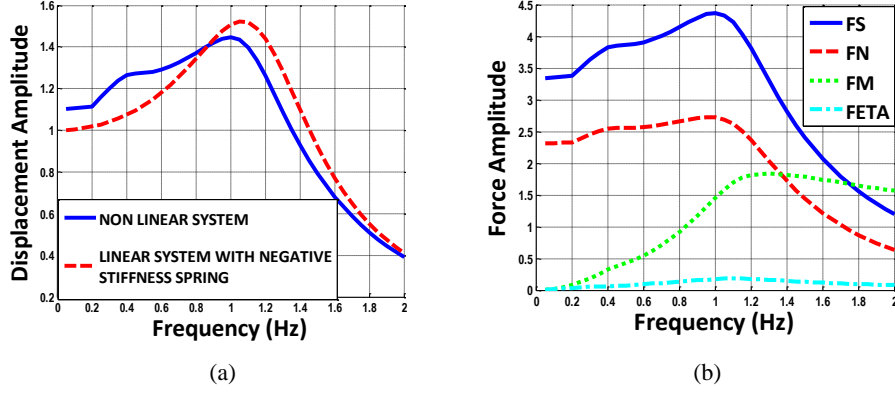
Figure 8 Frequency Response Functions of the proposed oscillator to a harmonic excitation force of F_e=F_{MAX}=0.05N a)Displacement x, b) Forces

(a)   (b)
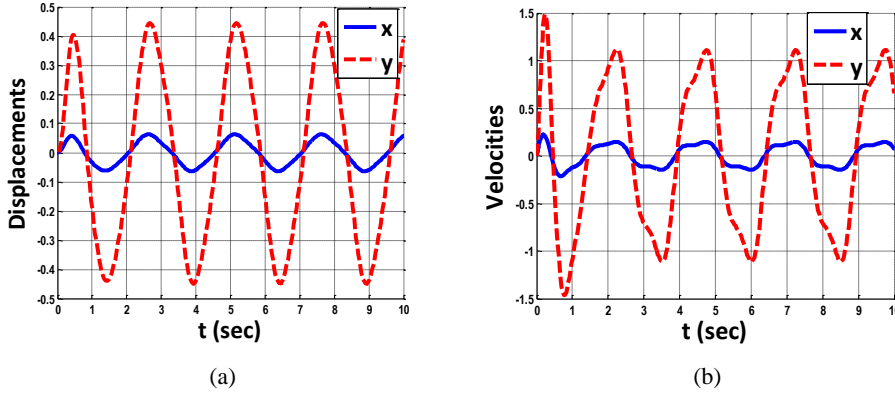
Figure 9 Response of the proposed non-linear oscillator to a harmonic excitation force of F_e=F_{MAX}=0.05N and f_e=0.4Hz: (a) Displacements (b) Velocities.

The FRFs of the forces in Fig 8.b and the waveforms in Fig 10 indicate that an adequate level of elastic forces exist throughout the entire frequency range, able to counteract the inertial and the external excitation forces. Consequently, a resonance phenomenon, which is inherent in the original linear SDOF system, cannot emerge in the proposed oscillator.

Conclusion

Stable non-linear oscillators, based on a bi-stable element which operate around an unstable equilibrium point can be designed, which exhibit an extraordinary damping behaviour. Contrary to

Quasi-Zero Stiffness oscillators, this damping behaviour can be achieved, so that any level of a required static stiffness can be maintained. Such an oscillator concept presents the potential for numerous implementations in a large variety of technological applications, either as a discrete vibration isolator, or in the form of periodic meta-materials and composite structures

| (a) | (b) |
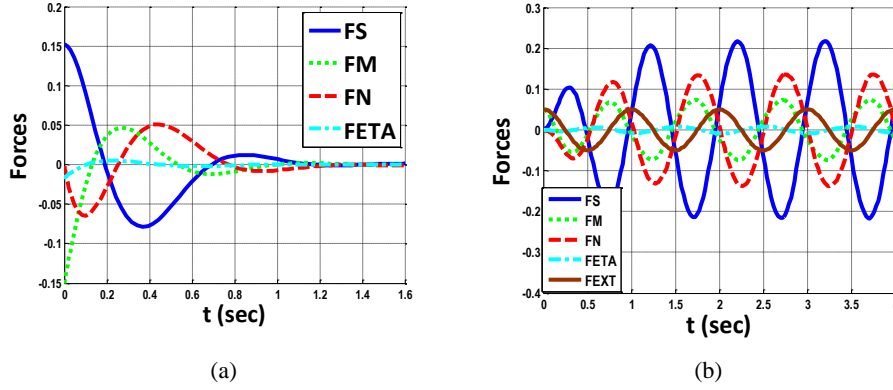
Figure 10 Forces of the non-linear oscillator a)Initial displacement x(0)=0.05m, b) Harmonic excitation force of $F_e=F_{MAX}$=0.05N and f_e=1.0Hz

References

[1] W. Molyneaux, Supports for vibration isolation, ARC/CP-322, Aero- nautical Research Council, Great Britain, 1957.

[2] D. L. Platus, Negative-stiffness-mechanism vibration isolation systems, In: SPIE's International Symposium on Optical Science, Engineering, and Instrumentation (1999) 98–105.

[3] R. Lakes, Extreme damping in composite materials with a negative stiffness phase, Physical Review Letters 86 (2001) 2897–8.

[4] T. Jaglinski, D. Kochmann, D. Stone, R. Lakes, Composite materials with viscoelastic stiffness greater than diamond, Science 315 (2007), 620–2.

[5] L. Dong, R. Lakes, Advanced damper with high stiffness and high hysteresis damping based on negative structural stiffness, International Journal of Solids and Structures 50 (2013) 2416–23.

[6] C. S. Wojnar, D. M. Kochmann, A negative-stiffness phase in elastic composites can produce stable extreme effective dynamic but not static stiffness, Philosophical Magazine 94 (2014) 532–55.

[7] H. Huang, C. Sun, G. Huang, On the negative effective mass density in acoustic metamaterials, International Journal of Engineering Science 47 (2009) 610–7.

[8] J. Winterflood, D. Blair, B. Slagmolen, High performance vibration isolation using springs in euler column buckling mode, Physics Letters A 300 (2002) 122–30.

[9] R. DeSalvo, Passive, nonlinear, mechanical structures for seismic attenuation, Journal of Computational and Nonlinear Dynamics 2 (2007), 290–8.

[10] A. Carrella, M. Brennan, T. Waters, Static analysis of a passive vibration isolator with quasi-zero-stiffness characteristic, Journal of Sound and Vibration 301 (2007) 678–89.

[11] C.M. Lee, V. Goverdovskiy, A. Temnikov, Design of springs with negative stiffness to improve vehicle driver vibration isolation, Journal of Sound and Vibration 302 (2007) 865–74.

[12] T. D. Le, K. K. Ahn, A vibration isolation system in low frequency excitation region using negative stiffness structure for vehicle seat, Journal of Sound and Vibration 330 (2011) 6311–35.

[13] C.-M. Lee, V. Goverdovskiy, A multi-stage high-speed railroad vibration isolation system with negative stiffness, Journal of Sound and Vibration, 331 (2012) 914–21.

[14] H. Iemura, M. H. Pradono, Advances in the development of pseudo- negative-stiffness dampers for seismic response control, Structural Control and Health Monitoring 16 (2009) 784–99.

[15] A. A. Sarlis, D. T. R. Pasala, M. Constantinou, A. Reinhorn, S. Nagarajaiah, D. Taylor, Negative stiffness device for seismic protection of structures, Journal of Structural Engineering 139 (2012) 1124–33.

[16] C.-M. Lee, V. Goverdovskiy, S. Samoilenko, Prediction of non-chaotic motion of the elastic system with small stiffness, Journal of Sound and Vibration 272 (2004) 643–55.

[17] A. Carrella, M. Brennan, T. Waters, V. Lopes Jr, Force and displacement transmissibility of a nonlinear isolator with high-static-low- dynamic-stiffness, International Journal of Mechanical Sciences 55 (2012) 22–9.

[18] I. Kovacic, M. J. Brennan, T. P. Waters, A study of a nonlinear vibration isolator with a quasi-zero stiffness characteristic, Journal of Sound and Vibration 315 (2008) 700–11.

[19] A. Shaw, S. Neild, D. Wagg, Dynamic analysis of high static low dynamic stiffness vibration isolation mounts, Journal of Sound Vibration, 332 (2013) 1437–55.

[20] X. Huang, X. Liu, J. Sun, Z. Zhang, H. Hua, Vibration isolation characteristics of a nonlinear isolator using Euler buckled beam as negative stiffness corrector: A theoretical and experimental study, Journal of Sound and Vibration 333 (2014) 1132–48.

[21] I. Antoniadis, D. Chronopoulos, V. Spitas, D. Koulocheris, "Hyper-damping properties of a stable linear oscillator with a negative stiffness element", Journal of Sound and Vibration, 2015, V346, pp 37-52.

[22] D. Chronopoulos, I. Antoniadis , M. Collet , M. Ichchou, "Enhancement of wave damping within metamaterials having embedded negative stiffness inclusions", 2015, Wave Motion, http://dx.doi.org/10.1016/j.wavemoti.2015.05.005.

Ioannis A Antoniadis, Professor, antogian@central.ntua.gr
Konstantinos J Kyriakopoulos, Professor, kkyria@mail.ntua.gr
Evangelos G Papadopoulos, Professor, egpapado@central.ntua.gr
Mechanical Design and Control Systems Section, Mechanical Engineering Department, National Technical University of Athens, Heroon Polytechniou 9, 15780 Zografou, Greece

Real-time drive functions optimisation of the satellite by using MLP and RBF neural network
(CON057-15)

Krzysztof Augustynek, Kornel Warwas

Abstract: The paper presents a method for determining optimal courses of drive functions which can be applied during satellite orientation change maneuver in real-time. Considered task has been realized in two steps. At first, a series of dynamic optimisation problem have been solved using the Nelder-Mead algorithm in order to calculate optimal driving functions. The optimisation problem requires the equations of motion to be integrated at each optimisation step and it can't be applied for controlling the motion of the system in real time. Therefore, in the next step multilayer perceptron (MLP) and radial basis function (RBF) networks have been proposed. The main task of the networks has been consisted in choosing drive functions in such a way that panels vibrations after maneuver are minimized in short time. Solutions of multiple dynamic optimisation tasks form training set of the neural network. In the paper, results obtained from dynamic optimisation, MLP and RBF neural networks have been presented and compared.

1. Introduction

Vibration control is one of the most important problems in satellite design. The orbiting attitude slewing or rapid rotational manoeuvres will introduce certain levels of vibration to flexible panels, which disturb work of the system and can lead to the damage its elements. Therefore, designing a control system which effectively suppress the induced vibration, creates a challenging problem for satellite designers. In [1] time invariant and periodic controllers have been proposed for simultaneous attitude control and vibration suppression using magnetic actuators. A comparative investigation designing the satellite Attitude Control System by the Linear Quadratic Regulator (LQR) and Linear Quadratic Gaussian (LQG) methods have been presented in [2]. In references [3, 4] adaptive fuzzy sliding mode control incorporating with I/O linearization have been applied on flexible satellite. Based on I/O linearization, decomposition method of MIMO (multi-input multi-output) system to single input single output using the fuzzy control rules has been applied. Classical controller based on Euler degrees' errors and two robust controllers of H_∞ and μ, by using internal feedback to resolve robust controller design problem, has been presented in [5]. Another approach to supress vibration of the satellite during its reorientation has been proposed in paper [6]. In this paper optimal torques have determined by formulation and solution of dynamic optimisation problem.

Many classical problems in satellite control use dynamic equations that are limited to rigid-body motion. In many works flexibility of the solar panels is reduced to linear spring element which are located in the joints [1, 2, 6]. Such assumption simplifies choice of a controller parameters. In [2] the interaction between the fuel slosh motion, the panel's flexible motion and the satellite rigid motion during translational and/or rotational manoeuvre have been additionally considered. In papers [3, 4] flexibility of the solar panels has been modelled by modal method. The complex spatial model of the satellite is shown in [7]. In this work flexibility of the panels has been modelled by means of the Rigid Finite Element (RFE) method [8]. The model presented takes into account flexibility of the joints.

In this paper model presented in [7] has been used to control a motion of the satellite during change orientation manoeuvre. Optimal driving functions have been calculated by solving dynamic optimisation task. Due to long time of single optimisation task calculation such approach is not suitable for application in real controllers [9]. Those problem has been solved by properly prepared artificial neural network which can be used in real-time systems. Training data for the neural network have been collected by solving multiple dynamic optimisation tasks for various input parameters. In this paper two kinds of the neural networks: Multilayer Perceptron and Radial Basis Function, have been considered.

2. Mathematical model of the satellite

In this paper it has been assumed that the satellite consists of central rigid body and four flexible panels (arms) (Figure 1). Central body has six degrees of freedom in relation to inertial frame. Generalized coordinates of this body are the components of the following vector:

$$\widetilde{\mathbf{q}}^{(1)} = \begin{bmatrix} \widetilde{x}^{(1)} & \widetilde{y}^{(1)} & \widetilde{z}^{(1)} & \widetilde{\varphi}_x^{(1)} & \widetilde{\varphi}_y^{(1)} & \widetilde{\varphi}_z^{(1)} \end{bmatrix}^T \tag{1}$$

For discretization of the flexible panels modification of the rigid finite element method has been used [7, 8]. In this method p link is replaced by a set of $m^{(p)}+1$ rigid finite elements (rfe) connected by $m^{(p)}$ massless and dimensionless spring-damping elements (sde).
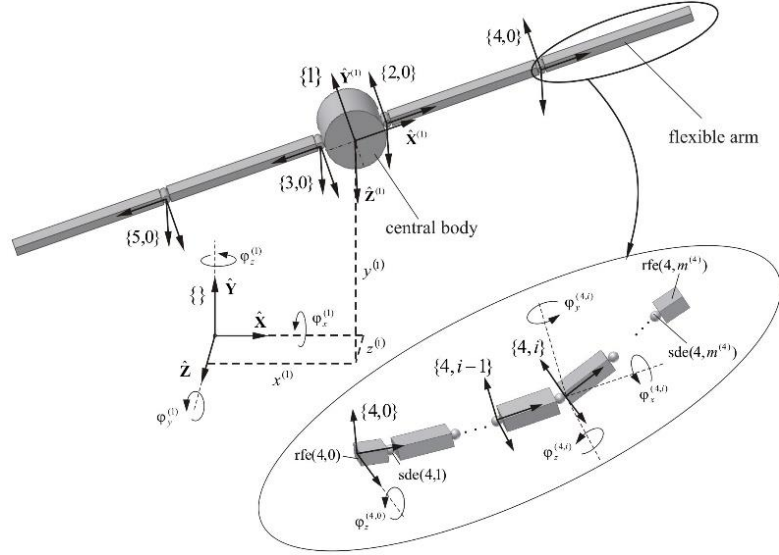
Figure 1. Discrete model of the satellite

Each rfe has three degrees of freedom in relation to preceding element in kinematic chain and its generalized coordinates vector are given by:

$$\widetilde{\mathbf{q}}^{(p,i)} = \begin{bmatrix} \widetilde{\varphi}_x^{(p,i)} & \widetilde{\varphi}_y^{(p,i)} & \widetilde{\varphi}_z^{(p,i)} \end{bmatrix}^T \tag{2}$$

where: $p = 2, \ldots, 5$, $i = 1, \ldots, m^{(p)}$.

Exception from this rule is rfe(p,0) which can only rotate in relation to preceding body as follows:

$$\widetilde{\mathbf{q}}^{(p,0)} = \begin{bmatrix} \widetilde{\varphi}_z^{(p,0)} \end{bmatrix} \tag{3}$$

Equations of motion are derived from Lagrange equations of the second kind [8]. Joint coordinates and homogenous transformation algorithms were used for generating equations of motion of the satellite with flexible panels. Equations of satellite motion have the following form [7]:

$$\mathbf{A}\ddot{\mathbf{q}} = \mathbf{f} \tag{4}$$

where: $\mathbf{A}$ - mass matrix,

$\mathbf{q}$ - vector of generalized coordinates of the satellite,

$\mathbf{f}$ - vector including centrifugal, gyroscopic and Coriolis forces and forces which follow from elastic deformations sdes.

Components of the vector **q** are generalized coordinates of the central rigid body and rfes, on which flexible links have been divided. In further consideration change orientation manoeuver of the satellite will be analysed. Configuration of the system before and after rotation is presented in figure 2.
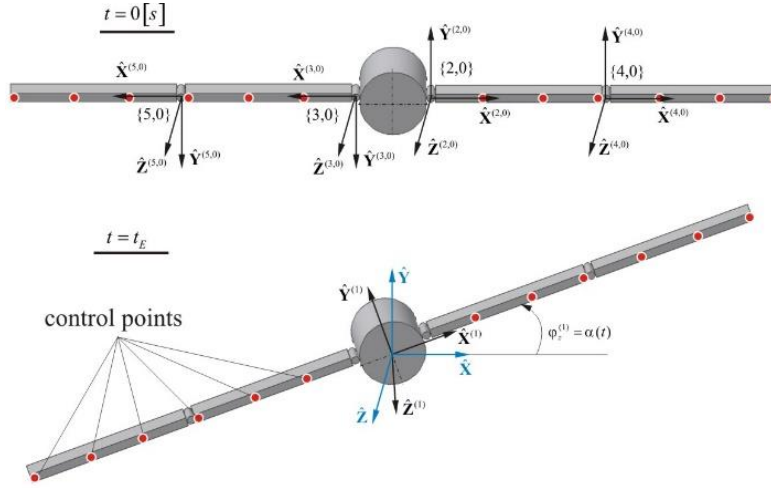
Figure 2. Initial and final configuration of the satellite in change orientation manoeuver

The motion of the satellite is realised by driving function $\alpha(t)$. It means that angle of rotation of the central body $\varphi_z^{(1)}$ is known function of time $\alpha(t)$:

$$\varphi_z^{(1)} = \alpha(t) \tag{5}$$

3. Dynamic optimisation problem

The aim of the optimisation is the choice of the driving function that vibration of the flexible panels after change orientation maneuver are minimized. Therefore objective function can be defined as follows [11]:

$$\Omega(\mathbf{u}) = \sum_{i=1}^{n_P} \Delta_i^{(d)} \rightarrow \min \tag{6}$$

where: **u** - vector of decisive variables,

n_p - number of control points,

$\Delta_i^{(d)}$ - RMS (Root Mean Square) value of the summary displacement, velocity and acceleration in i-th control point.

In considered case RMS value has a form:

$$\Delta_i^{(d)} = \sqrt{\frac{\int\limits_{t_E}^{t_K} \left(\tilde{y}_i^2 + \dot{\tilde{y}}_i^2 + \ddot{\tilde{y}}_i^2 \right) dt}{t_K - t_E}} \qquad (7)$$

where: $\tilde{y}_i$ - displacement of control point i in $\hat{\mathbf{Y}}^{(1)}$ direction,

$\dot{\tilde{y}}_i$ - velocity of control point i in $\hat{\mathbf{Y}}^{(1)}$ direction,

$\ddot{\tilde{y}}_i$ - acceleration of control point i in $\hat{\mathbf{Y}}^{(1)}$ direction,

t_E - time of the end of change orientation manoeuvre,

t_K - time of the simulation.

Dynamic optimisation can be performed for different input parameters which can be written as follows:

$$\mathbf{x} = \begin{bmatrix} t_E & \varphi_E \end{bmatrix}^T \qquad (8)$$

Decisive variables in dynamic optimisation problem are rotation angle about $\hat{\mathbf{Z}}^{(1)}$ axis of the central body in some discrete time steps:

$$\mathbf{u} = \mathbf{u}(\mathbf{x}) = \begin{bmatrix} u_1 & \dots & u_i & \dots & u_N \end{bmatrix}^T \qquad (9)$$

where $u_i = \alpha(t_i)$,

$t_i = i \cdot \dfrac{t_E}{N+1}$,

N - number of time steps.

Interpretation of the decisive variables are presented in [10]. It can be seen that optimal values of decisive variables depend on the input parameters vector **x.**

It is assumed that rotation angle of central body should change in specific range:

$$\mathbf{u}_{\min} \leq \mathbf{u} \leq \mathbf{u}_{\max} \qquad (10)$$

4. Neural networks

An artificial neural network is basically a computational system which receives an input, processes the data, and provides an output [12, 13]. Designing the neural network requires choice of the topology,

performance (transfer) function, learning algorithm and criteria to stop the learning process. In order to determine optimal driving function courses multilayer perceptron (MLP) and radial basis function (RBF) [12, 13] networks have been used. Both neural networks constructed for this problem (figure 3, figure 4) have three input signals which are time and angle of rotation of the satellite and coefficient, which is necessary to map output signal with corresponding timestamp. Only one output is necessary in considered case. It is rotation angle of the satellite in some discrete time which is connected with decisive variable of dynamic optimisation task. After the input has been entered into the neural network, the response is calculated using a transfer function.
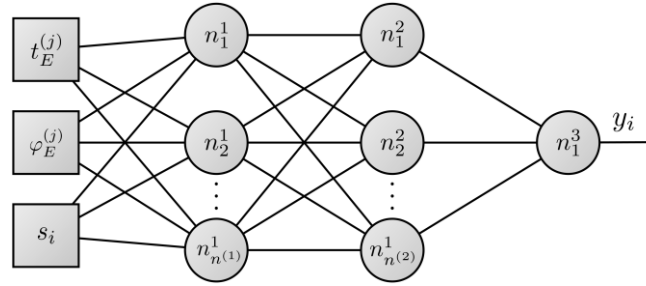
Figure 3. Topology of MLP neural network
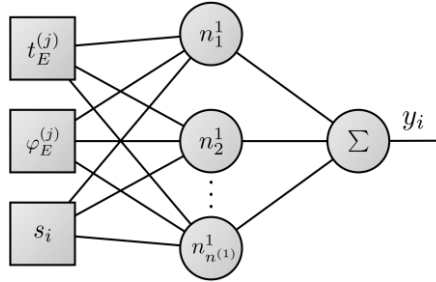
Figure 4. Topology of RBF neural network

Input signals from training set of the neural network can be written as follows:

$$\mathbf{Q} = \begin{bmatrix} \mathbf{q}_1 & \dots & \mathbf{q}_i & \dots & \mathbf{q}_m \end{bmatrix}^T, \tag{11}$$

where: $m = n_D \cdot N$ - number of rows in matrix $\mathbf{Q}$ which contains input signals from training set,

$\mathbf{q}_i = \begin{bmatrix} t_E^{(j)} & \varphi_E^{(j)} & s_i \end{bmatrix}^T$ - i-th row of input signals matrix,

$j = \theta(i)$ - describe dependency between i-th row of matrix $\mathbf{Q}$ and corresponding j-th optimisation task,

$$s_i \in \{1, \ldots, N\},$$

$$j = 1, \ldots, n_D,$$

n_D - number of optimisation tasks.

Driving function in discrete time t is determined in different manner for each type of neural network. In the case of multilayer perceptron response (output signal) of the network can be calculated according formula:

$$y_i = y(\mathbf{q}_i) = f\left(\sum_{j=0}^{n^{(n_L-1)}} w_{1,j}^{(n_L-1)} \phi_j^{(n_L-1)}(\mathbf{q}_i)\right) \tag{12}$$

where: $\phi_j^{(p)}(\mathbf{q}_i) = f\left(\sum_{l=0}^{n^{(p-1)}} w_{j,l}^{(p-1)} \phi_l^{(p-1)}(\mathbf{q}_i)\right)$ for $p = n_L - 1, \ldots, 1$,

$\boldsymbol{\varphi}^{(0)}(\mathbf{q}_i) = \mathbf{q}_i$ - input signals vector,

$w_{j,l}^{(p)}$ - weights of neurons in p layer for $j = 1, 2, \ldots, n^{(p)}$ and $l = 0, 1, \ldots, n^{(p-1)}$,

$n^{(p)}$ - number of neurons in p layer,

n_L - number of layers in neural network.

As the transfer functions the hyperbolic tangent and linear functions were used, for the hidden and output layer respectively. In RBF network each neuron in hidden layer is described by radial basis function. In this case driving function can be obtained from formula:

$$y(\mathbf{q}_i) = \sum_{j=1}^{k} w_j \cdot g_j(\mathbf{q}_i, \mathbf{c}_j) \tag{13}$$

where: w_j - weights associated with j-th neuron,

$g_j(\mathbf{q}_i, \mathbf{c}_j)$ - base function of the j-th center,

$k \leq m$ - number of centers $\mathbf{c}$,

$\mathbf{C} = [\mathbf{c}_1 \ \ldots \ \mathbf{c}_j \ \ldots \ \mathbf{c}_k]$, $\mathbf{c}_j = \left(c_l^{(j)}\right)_{l=1,2,3}$ - coordinates of the j-th center.

In calculations the Gauss radial basis function has been assumed:

$$g_j(\mathbf{q}_i, \mathbf{c}_j) = e^{-p_j} \tag{14}$$

where: $p_j = \dfrac{\left\| \mathbf{q}_i - \mathbf{c}_j \right\|^2}{2\sigma_j^2}$, σ_j - shape coefficient for the j-th center,

$$\left\| \mathbf{q}_i - \mathbf{c}_j \right\|^2 = \sum_{l=1}^{3} \left[q_{i,l} - c_l^{(j)} \right]^2 \ .$$

In order to train the RBF network the cumulative version of the iterative k-means algorithm was used. At the next step the shape coefficients for the centers obtained were calculated using information about position of other centers in the neighborhood (three closest centers) [13].

However, since the accuracy of the network response was not satisfactory (unacceptable errors were achieved for the validation set) the basis function was changed and the training process was repeated.

5. Numerical simulations and results

Algorithms related to formulation and solution flexible multibody system, its simulation and optimisation have been implemented in the own program [7] written in the C ++ language. In order to prepare and simulate neural networks also own programs have been written using Encog library [14] and its .NET implementation.

Physical parameters of the satellite model were taken from [7]. On the basis of results of the simulations it has been assumed division of the flexible panels into 4 rfes. Interpolation of the kinematic input has been performed for $m = 9$. 4th order Runge-Kutta [15] method with fixed step has been used for integration equations of motion. Step size used in calculations was 0.005 [s]. Time of single evaluation of the objective function was 5 [s].

Results obtained from multiple optimisation tasks have been used as learning sets for MLP and RBF networks. Each optimisation task has been solved by means of gradientlessness Nelder-Mead method [15, 16]. During simulations end time t_E and angle φ_E of rotation of the satellite was changed. It contains data for t_E from 1 [s] to 2 [s] with step 0,25 [s] and φ_E from 45° to 90° with step 5°.

It has been assumed that MLP network contains two hidden layers with 7 and 10 neurons respectively. The network has been trained using Resilient Propagation [12, 13, 14]. RBF network contains one hidden layer with 23 neurons. The transfer function for a radial basis neuron was Gaussian function [13].

After the training process an acceptable accuracy of network response has been obtained. Figure 9 and 10 show courses of the drive function calculated from the optimisation, MLP and RBF for data taken from learning set.
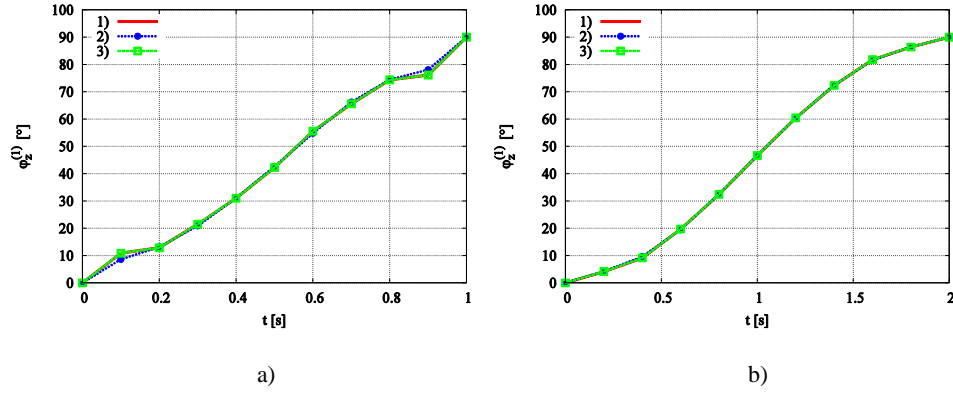
Figure 5. Courses of drive function calculated for $\varphi_E = 90°$ and a) $t_E = 1[\text{s}]$, b) $t_E = 2[\text{s}]$,

1) optimisation, 2) MLP, 3) RBF

Figure 11 and 12 show courses of the displacement tip of outer panel in local coordinate system of the central body before optimisation, obtained from the optimisation, MLP and RBF network for data taken from learning set.
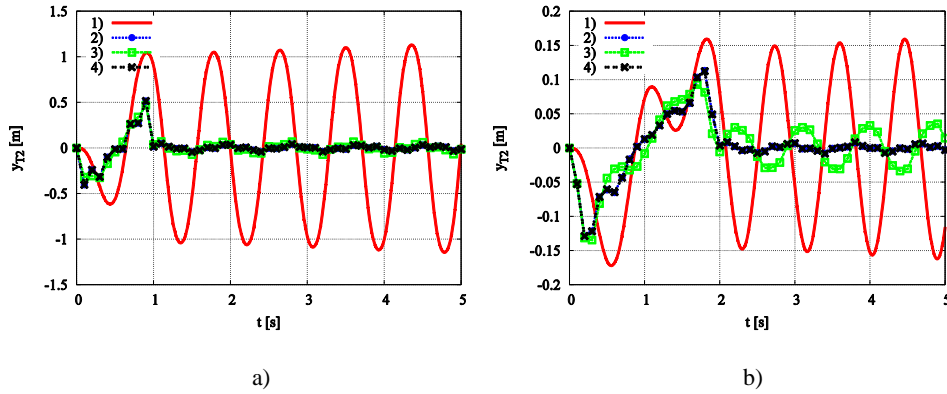
Figure 6. Courses of displacement tip of outer panel in local coordinate system of the central body for $\varphi_E = 90°$ and a) $t_E = 1[\text{s}]$, b) $t_E = 2[\text{s}]$,

1) before optimisation, 2) after optimisation, 3) MLP, 4) RBF

Figure 4 and 5 show results of RMS calculations for different time of maneuvers before and after optimisation task and from MLP and RBF networks.
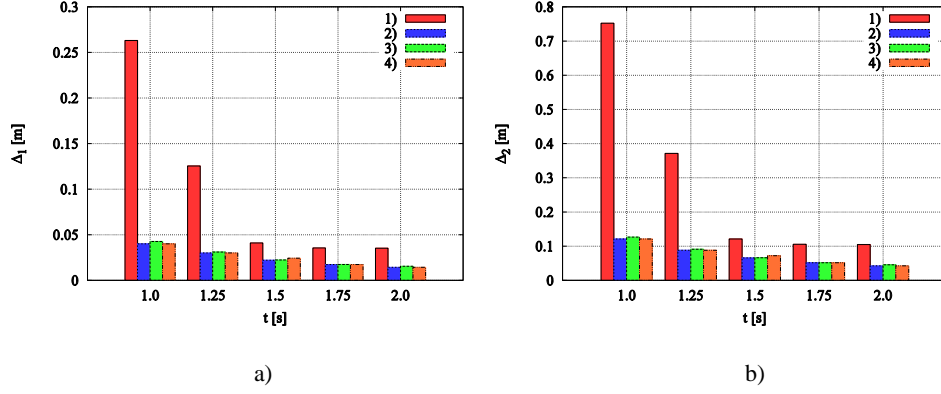
Figure 7. RMS values of a) inner, b) outer panel tip displacement obtained for different time of rotation t_E and $\varphi_E = 90°$, 1) before optimisation, 2) after optimisation, 3) MLP, 4) RBF

It can be seen large convergence for displacement courses and RMS value obtained from optimisation and neural networks. In order to numerically evaluate differences between courses obtained from optimisation and neural networks integral error and the Pearson correlation coefficient have been calculated [10]. Values of the coefficients for all training data are shown in Table 1.

Table 1. Comparison integral errors and Pearson correlation coefficients for courses obtained from trained network

t_E [s]	δ [‰]		R	
	MLP	RBF	MLP	RBF
1	0,5138	0.0064	0,9996	1.0000
1.25	0,4239	0.0112	0,9999	1.0000
1.5	0,5317	18.5094	0,9998	0.9997
1.75	1,3059	0.0145	0,9999	1.0000
2	0,5017	0.0102	0,9999	1.0000

After training neural networks can be used for simulation for input parameters different than in the learning set. Results of simulations for different time of change orientation manoeuvre t_E are presented on figure 8.
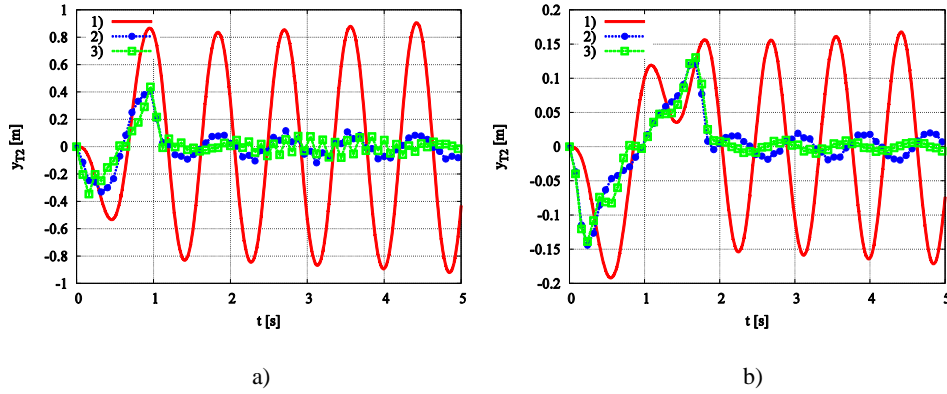
Figure 8. Courses of displacement tip of outer panel in local coordinate system of the central body for
$\varphi_E = 90°$, a) $t_E = 1.1\,[\text{s}]$, b) $t_E = 1.9\,[\text{s}]$ 1) before optimisation, 2) MLP, 3) RBF

For both analysed cases the output signals obtained from the simulation by MLP and RBF neural network are acceptable. Vibrations of outer panels, as in the case of dynamic optimisation, are significantly smaller than before optimisation. Preparation of training sets and then the training process are very time consuming, but the simulation using trained neural networks can be realised in real-time.

6. Conclusions

The paper presents algorithm of suppressing vibrations of the flexible elements of the satellite during change orientation manoeuvre. Because optimisation problem in considered case is a time consuming task and cannot be applied in order to control the satellite motion in real time. Application of the artificial neural networks can be solution of this problem. In presented approach results obtained from dynamic optimisation forms training set for the neural network. Results obtained from Multilayer Perceptron and Radial Basis Function network have been discussed and compared.

It has been shown that a properly trained neural network can obtain driving function courses close to those received from dynamic optimisation task. Application properly prepared and a trained neural network enables not only interpolation but also extrapolation driving function courses for input data from outside the training set. An essential feature of the neural network is that can give us results in real time. Presented results show that properly trained Multilayer Perceptron and Radial Basis Function network give results close to results obtained from optimisation. It is difficult to point which type neural networks is better in considered case. The authors experience shows that MLP network is easier to prepare and train than RBF network. Additionally MLP networks are more preferred by researchers and more often used in technical issues.

Although the analysis presented in the paper was concerned only with one type of a satellite and maneuvers, the method presented can be used in the analysis of any flexible multibody system. In order to control the stability in any conditions, the training set of optimal solution have to include results of the direct optimisation for other possible types of maneuvers.

References

[1]   Findlay E.J., Ruiter A., Forbes J.R., Liu H.H.Y., Damaren C.J., Lee J., *Magnetic Attitude Control of a Flexible Satellite*, Journal of Guidance, Control and Dynamics, Vol. 36, No. 5, 2013, pp.1522-1526.

[2]   Souza de A.G., Souza de L.C.G., *Satellite Attitude Control System Design Taking into Account the Fuel Slosh and Flexible Dynamics*, Mathematical Problems in Engineering, Vol. 2014, 2014.

[3]   Guan P., Liu X.J., Liu J.Z., *Flexible Satellite Attitude Control Via Sliding Mode Technique*, Proceedings of the 44th IEEE Conference on Decision and Control, and the European Control Conference 2005 Seville, Spain, 2005, pp. 1258-1263.

[4]   Hu Q., Xiao B., *Fault-tolerant sliding mode attitude control for flexible spacecraft under loss of actuator effectiveness*, Nonlinear Dynamics, Volume 64, Issue 1, 2011, pp. 13-23.

[5]   Mohsenipour R., Hossein N., Nasirian M., Nia A. K. *Attitude Control of a Flexible Satellite by Using Robust Control Design Methods*, Intelligent Control and Automation, 2013, 4, pp. 313-326.

[6]   Herber D., McDonald J., Alvarez-Salazar O., Krishnan G., Allison J. *Reducing Spacecraft Jitter During Satellite Reorientation Maneuvers via Solar Array Dynamics*, 15th AIAA/ISSMO Multidisciplinary Analysis and Optimization Conference, 16-20 June 2014, Atlanta, GA.

[7]   Augustynek K. *Analiza dynamiczna przestrzennych mechanizmów dźwigniowych o wiotkich członach*, PhD Thesis, University of Radom, 2010.

[8]   Wittbrodt E., Adamiec-Wójcik I., Wojciech S. *Dynamics of flexible multibody systems, Rigid finite element method*, Springer, 2006.

[9]   Warwas K., Augustynek K. An application of neural networks to control stability of an articulated *vehicle in real time*, Advances in Intelligent Systems and Computing, Springer, 2015 (in print).

[10] Augustynek K., Warwas K., Polański A. *Application of the genetic algorithms and distributed computing in task of the reduction of vibrations of a satellite*, 7th Conference Computer Methods and Systems, Kraków, 2009.

[11] Chong E., Zak S. *An Introduction to optimisation 4th Edition*, John Wiley & Sons, Inc., 2013.

[12] Haykin S. O. *Neural Networks and Learning Machines*, Prentice Hall, 2009.

[13] Du K., Swamy M. *Neural Networks and Statistical Learning 2014th Edition*, Springer, 2014.

[14] Heaton J. *Programming Neural Networks with Encog3 in C#*, Heaton Research, 2011.

[15] Press W., Teukolsky S., Vetterling W., Flannery B., *Numerical Recipes 3rd Edition: The Art of Scientific Computing*, Cambridge University Press, 2007.

[16] Luersen M., Le Riche R., *Globalized Nelder–Mead Method for Engineering Optimisation*, Computers and Structures, pp. 2251 -2260, 2004.

Experimental and numerical studies on the fatigue wear of an Mg-Al alloy with rare earth elements (STA055)

Henryk Bąkowski, Janusz Adamiec

Abstract: Fatigue wear is the type of wear, wherein the local loss of cohesion and the associated material losses are caused by fatigue due to the cyclic interaction of the contact stresses at the surface layer. During fatigue wear changes are multiple macroscopic elastic deformation, surface fatigue cracks arise in friction, typically under the influence of multiple elastic-plastic deformation or plastic. The magnesium alloys often occur casting defects and welding. These defects are repaired surfacing or welding methods. Welding technologies may also be used for connecting elements Mg alloys and to the regeneration operating after use. The most common reason for rejection or construction casting cracks generated in the process or operating conditions. The main difficulty in welding and weld Mg alloys is their tendency to crack during the crystallization of the hot weld. Occurring defects arising in the process influence on the ultimate service life under real conditions. Appearing cracks or microcracks in the material may cause the nucleation of defects and their propagation leading to the through cracks - particularly dangerous for the structure. The study used WE43 casting magnesium alloys to determine the fatigue strength on the stand bench for testing for unilateral bending and bilateral bending in a rotating motion. Casting of magnesium alloys with rare earths, for example, yttrium, zirconium, silver have high strength properties that are comparable with the properties of titanium alloys, or steel. The study compared the effects of the appearance of fatigue cracks (fatigue strength determination) based on the alloy composition, morphology, structure, both in experimental (laboratory) and the simulation using the FEM.

1. Introduction

Fatigue wear is the type of wearin which local loss of cohesion and the associated material losses are caused by fatigue as a result of cyclic impact of the contact stresses in the surface layer and friction associated components. Most often you add elements to magnesium alloys are aluminum, zinc and manganese. These alloys are characterized by good machinability and mechanical properties at ambient temperature, good corrosion resistance and low price. They are used for components which are required of good impact strength and fracture toughness combined with sufficient strength [1].
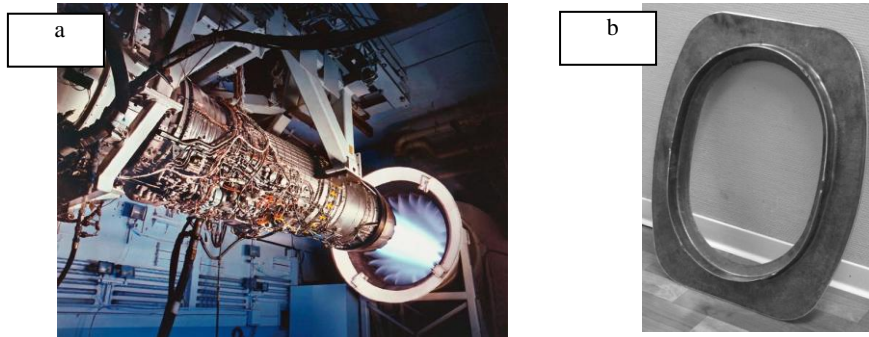
Figure 1. The application of magnesium alloy wrought: a) General Electric F110 engine [2],
b) a window frame AIRBUS A340 alloy AZ80 [3]

To increase the strength properties of the used heat treatment consisting of precipitation hardening. The disadvantage of magnesium alloys containing aluminum, zinc and manganese is their low resistance to creep, which limits the operating temperature to 125 °C. The addition of rare earth elements allows to improve the creep resistance of magnesium alloys [4]. This enables the use of alloys in automotive and aerospace, where the operating temperature of the gearbox housing is 175 °C, 200 °C engine block and pistons more than 300 °C [5]. Welding technology in magnesium alloys are used for joining metal components wrought and cast in the connecting structures. Joints made of magnesium alloy should have suitable properties to meet the requirements of the structure which they made of. In the literature there is no information on the properties of welded joints of cast magnesium alloys. There is therefore a need to define those properties in simulated conditions. To increase the strength properties at elevated temperatures are introduced rare earths and zirconium [6]. An example would be the alloy WE43 used to a temperature of 300 °C, which, after extrusion and heat treatment the obtained tensile strength Rm = 270 MPa, Re = yield strength of 195 MPa and an elongation A = 15% [7, 8]. To study were used for casting magnesium alloys with rare earth elements. The high strength properties are comparable to those of alloys of titanium or steel. Continuous development of magnesium alloys has meant that current yields are used in many fields of technology, and the maximum operating temperature is about 250 °C. The structure of the cast magnesium alloy parts are common to casting defects and welding. These defects are repaired surfacing or welding methods. Welding technologies may also be used for connecting the elements Mg alloy and the repair of cast after use operating.
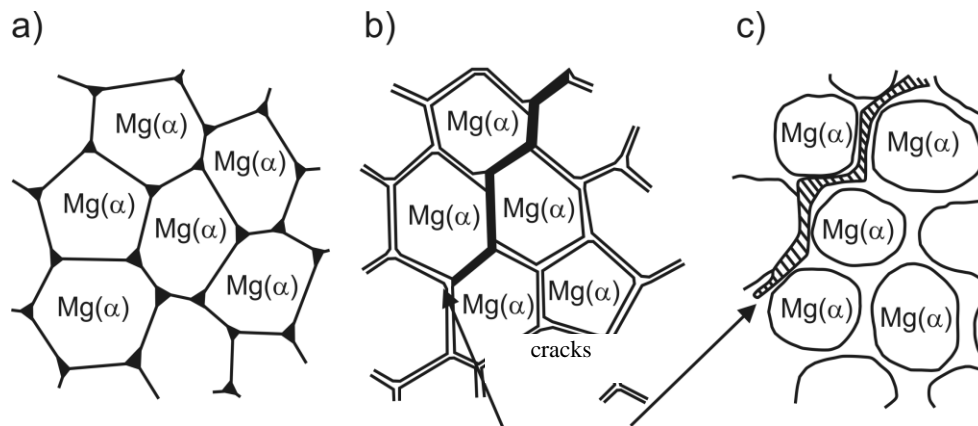
Figure 2. The structure of the Mg alloy in the process of crystallization: a) without a eutectic point, b) a small amount of the eutectic, c) with the amount of eutectic sufficient for the "healing" of cracks resulting hot [9]

Appearing cracks or microcracks in the alloy material also misruns casting and shrinkage porosity may causes the nucleation of defects and their propagation leading to a crack through - particularly dangerous for the structure.In the study used a casting magnesium alloy WE43 to determine the fatigue strength of the position to investigate unilateral bending. In this paper compared the impact of the emergence of fatigue cracks (determination of fatigue strength) using fatigue tests and simulation using Finite Element Method, depending on the morphology of the structure which determines the propensity for cracking.

1.1. Test equipment and parameters

For the quantitative evaluation of the structure of welded joints investigated alloys after heat treatment used software developed at the Department of Materials Science, Silesian University of Technology.

A- obraz wejściowy, LM	B – Korekcja cienia (A)
C – normalizacja (B)	D – binaryzacja (C)
E – inwersja, wypełnianie dziur	F – inwersja, skieletonizacja,
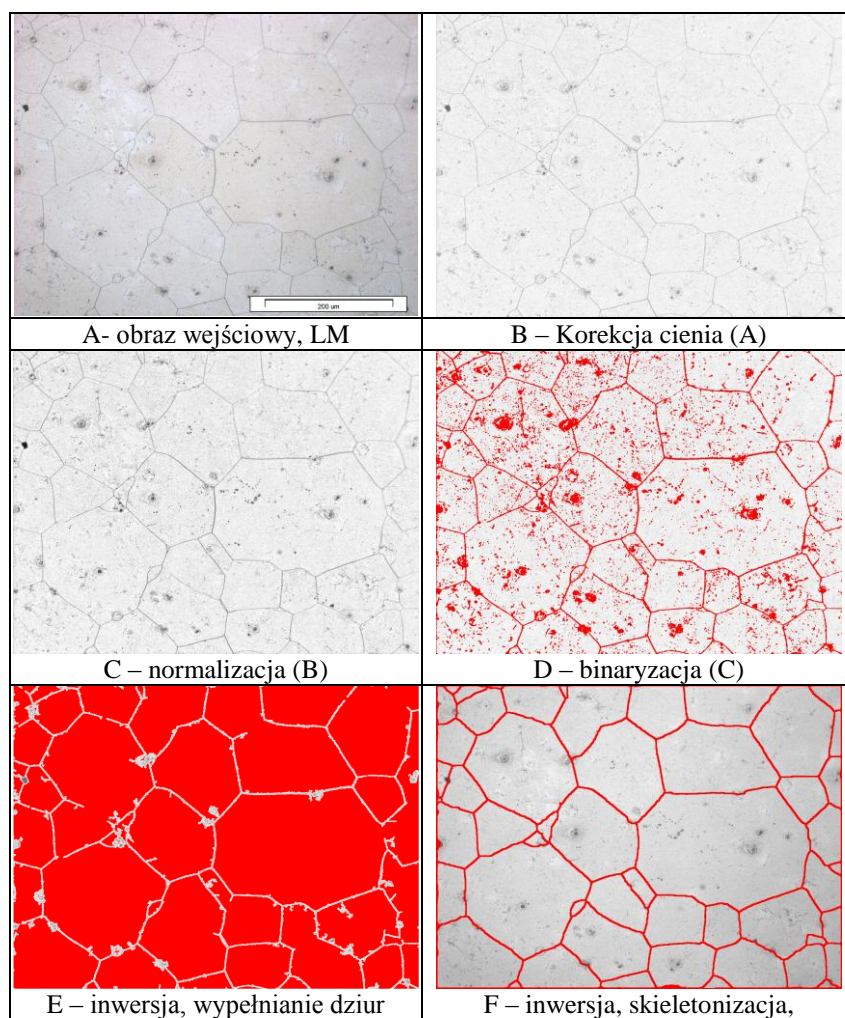
Figure 3. Detection of the grain boundaries of the home terminal material alloy WE43 after heat treatment (T6)

Therefore, an important factor determining the sampling strategy will be the resultant of: homogeneity of the chemical composition, size and shape of the casting and the technology of welding or surfacing by welding.
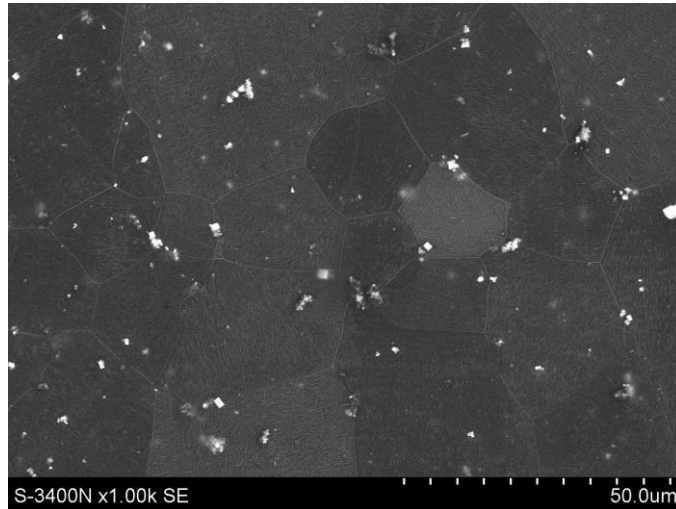
Figure 4. The structure of the weld joint alloy WE43 after heat treatment

The test machine is used for fatigue testing of samples of the tested metals (see figure 7). Test samples are subjected to one-sided - pulsating loads during pure bending. Elements that come into direct contact with the test sample rotate around its axis, so it can be said that the friction between them and the sample is very small and the study followed practically at the one-sided bending (see figure 5, 6).
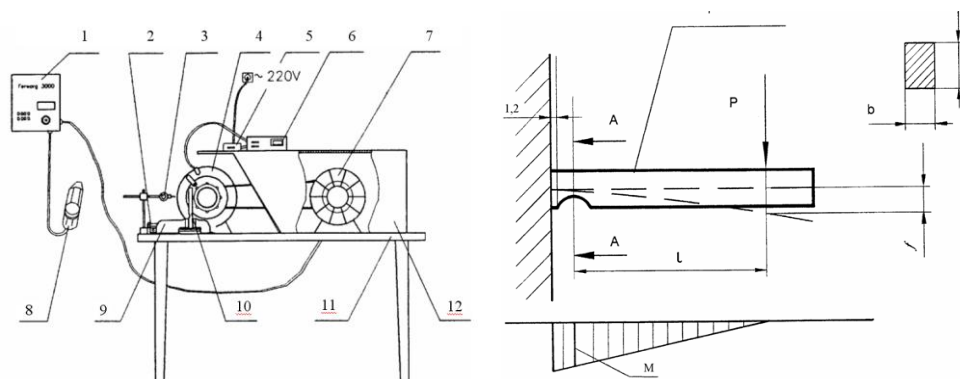
Figure 5. View of the machine: a) 1 - the inverter Ferwag 3000, 2 - screw set vices, 3 - the dial gauge, 4 - sample loading mechanism 5 – AC rev counter, 6 - rev counter, 7 - three-phase motor, 8 – slot Power RST 9 - vise, 10 - sample, 11 – table, 12 - protective casing; b) system testing and bending moment diagram
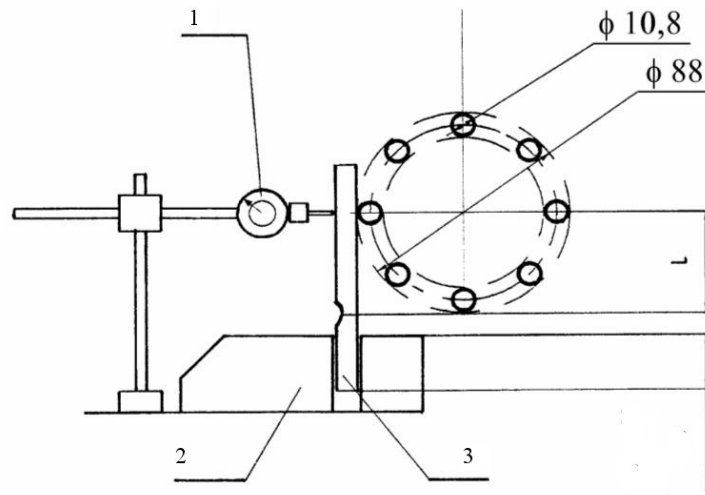
Figure 6. The view of the loading mechanism: 1 - the dial gauge, 2 - vise, 3 – sample

Figure 7. Sample

2. Results and discussion

Fatigue tests were carried out with a repetition of multiple in order to obtain fatigue strength diagram Wohler. For comparison used ZRE1 alloy containing zinc in order to illustrate the position of the fatigue curves in a Logsigma-LogN. It has been found that the joint of the WE43 alloy has a higher fatigue strength by additives Yttrium (see figure 8).

Metallographic at the macro level on the fracture surfaces of the fatigue revealed the presence of lines of fatigue characteristic for high cycle fatigue strength (see figure 9).
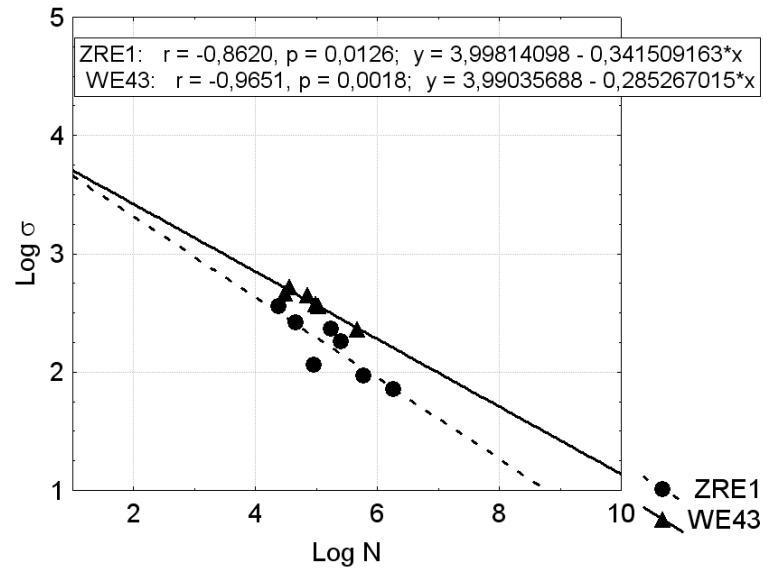
Figure 8. Curves of fatigue strength
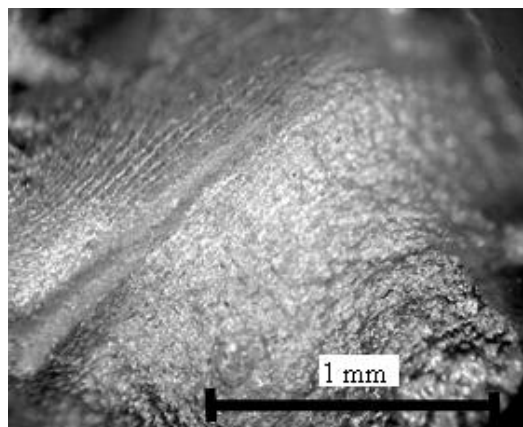
Figure 9. Surface farcture of fatigue

As a result of quantitative analysis of metallographic structure stereological WE43 defined features needed to create a geometric model which is similar to the real structure. Simulation calculations were carried out which showed that the places most likely to break are on the grain boundaries (see figure 10).
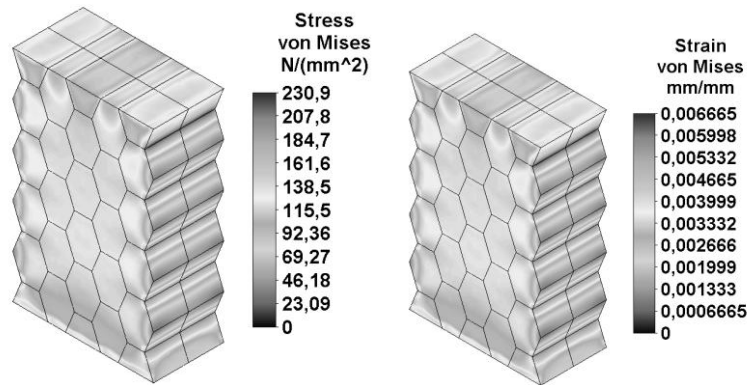
Figure 10. Distribution of stresses and strains in geometrical model of the structure WE43
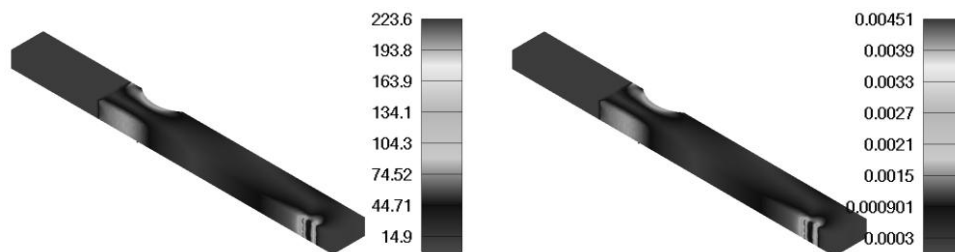
Figure 11. Distribution of stresses and strains of the sample under one-sided bending
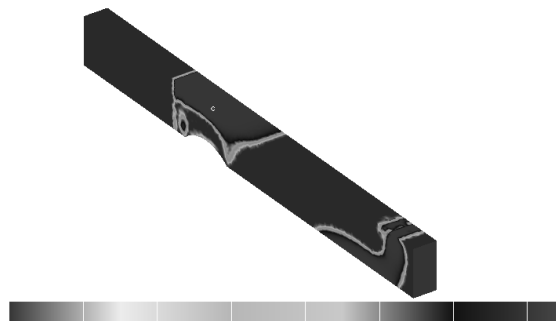
Figure 12.

Figure 13. Areas with higher risk for fatigue wear

FEM software is a comprehensive durability analysis and fatigue prediction. It provides a variety of "crack-initiation" life criteria for the calculation of material fatigue and the prediction of structural life.

3. Conclusion

Based on the the tests results analysis of welded joints of the alloy WE43 after heat treatment T6 indicates that the structure of the connector is composed of a base material characterized by a polygonal grain of the solid solution α-Mg, which is strain precipitation small dispersion intermetallic phases narrow heat-affected zone (HAZ), in which the grains feature a small dimensions relative to the base material, causing obtaining higher values of fatigue strength.

References

[1] Yang Z., Li J.P., Zhang J.X., Larimer G.W., Robson J.: Review and research and development of magnesium alloys, Acta Metallurgica Sinica 5, 2008, 313-328.

[2] http://www.defenseindustrydaily.com/442M-to-GE-for-F-16s-F110-Engine-Upgrades-05986/ 13.09.2015.

[3] http://smw.com/index.php?url=en/products/13/Aerospace-Components.html, 13.09.2015.

[4] Pekguleryuz M.O., Kaya A.A.: Creep resistant magnesium alloys for Powertrain applications, Proceedings of the 6th International Conference Magnesium Alloys and Their Applications, Edited by K.U.Keiner, Weinheim 2004.

[5] Yang Z., Li J.P., Zhang J.X., Larimer G.W., Robson J.: Review and research and development of magnesium alloys, Acta Metallurgica Sinica 5, 2008, 313-328.

[6] Yu Kun, Li Wen-xian, Wang Ri-chu, Mechanical properties and microstructure of as-cast and extruded Mg-(Ce, Nd)-Zn-Zr alloys, Journal Central South University Technology Vol. 12 No. 5, 2005, 499.

[7] Avedesian M., Baker H., Magnesium and Magnesium Alloys. ASM Speciality Handbook, 1999.

[8] Elektron WE43 wrought alloy, Data sheet 478, Magnesium Elektron, United Kongdom, 2006.

[9] Mordike B.L. Wiesner P.: Fugen von Magnesium Werkstoffen, DVS Verlag, 2005.

Henryk Bąkowski, Ph.D.: Silesian University of Technology, Faculty of Transport, Krasińskiego Street 8, 40-019, Katowice Poland (henryk.bakowski@polsl.pl, henryk.bakowski@gmail.com). The author gave a presentation of this paper during one of the conference sessions.

Janusz Adamiec, Professor.: Department of Materials Science, Department of Automotive Vehicle Service, Silesian University of Technology, Krasińskiego 8, 40-019 Katowice, Poland.

Stability of underactuated multibody systems subjected to periodic servo constraints
(CON082-15)

László Bencsik, László L. Kovács, Ambrus Zelei

Abstract: Motion control of underactuated multibody systems involves a lot of mathematical problems. This is mainly due to the fact that in case of underactuated systems the number of independent inputs are less than the degrees-of-freedom. Besides, the modelling of multibody systems is challenging in itself. Flexible manipulators, cranes and robots with passive joints can be mentioned as characteristic examples. Methods available in the literature are often provided to solve specific problems of specific systems. The general application of these method may lead to unstable dynamic behaviour. The present work assumes a general multibody description and proposes the use of periodic servo-constraints in order to enhance the dynamic properties of the system.

1. Introduction

In the motion simulation of multibody systems it is a standard procedure to use the non-minimum set of coordinates to describe the system [2]. Therefore between the dependent coordinates geometric constraints should be considered which leads to differential algebraic equations (DAE). Using this idea the control task is also can be formulated as an additional set of constraints that are called servo-constraint [4]. While the geometric or kinematic constraints are naturally satisfied, in some cases the servo-constrains cannot be fulfilled by different reasons. Several publications [6, 7] deal with the modification of the original servo-constraints in order to get a realizable task. In those cases the original task is simply modified using a linear combination of the newly selected set of servo-constraints considering the internal dynamics of the system. An other possible approach is the periodic variation of the servo-constraint. For underactuated robots the usefulness of the method was confirmed in [5]. The aim of this paper is to investigate the dynamic properties, the applicability of the periodic-servo constraint based control and to find the stable control parameters for the periodic servo-constraints. In the numerical studies a service-robotic application is used.

2. Problem Formulation

The equation of motion of an underactuated system can be derived using the non-minimum set of descriptor coordinates resulting the Lagrange equation of the first kind in the form:

$$\mathbf{M}\ddot{\mathbf{q}} + \mathbf{\Phi_q^T}\boldsymbol{\lambda} = \mathbf{Q} + \mathbf{Hu} \tag{1}$$

$$\boldsymbol{\phi}_g = \mathbf{0} \,, \tag{2}$$

where $\mathbf{M}(\mathbf{q}) \in \mathbb{R}^{n \times n}$ is the mass matrix, $\mathbf{\Phi_q}(\mathbf{q}) \in \mathbb{R}^{m \times n}$ is the Jacobian of geometric constraints $\boldsymbol{\phi}_g(\mathbf{q}, t) \in \mathbb{R}^m$ and $\boldsymbol{\lambda} \in \mathbb{R}^m$ is the vector of the Lagrangian multipliers. Matrix $\mathbf{H}(\mathbf{q}) \in \mathbb{R}^{n \times r}$ is the control input matrix and $\mathbf{u} \in \mathbb{R}^r$ contains the independent control inputs. In addition, $\mathbf{Q}(\mathbf{q}, \dot{\mathbf{q}}, t) \in \mathbb{R}^n$ denotes the remaining generalized forces. In similar form with geometric constraints (2) the desired motion also can be formulated as an additional constraint:

$$\boldsymbol{\phi}_S(\mathbf{q}, t) = \mathbf{0} \tag{3}$$

as a function of generalized coordinates and time, which called as servo constraint [4]. Using the method of Lagrange multipliers [2], the geometric constraints (2) should be considered on the level of acceleration in order to compute the acceleration $\ddot{\mathbf{q}}$, and the Lagrange multiplier $\boldsymbol{\lambda}$. As it is presented in [6] [9] additionally the servo constraints are also considered on the level of acceleration, while the control input $\mathbf{u}$ should satisfy the constraints which can be calculated as:

$$\begin{bmatrix} \mathbf{M} & \mathbf{\Phi_q^T} & -\mathbf{H} \\ 5\mathbf{\Phi_q} & \mathbf{0} & \mathbf{0} \\ \mathbf{G_q} & \mathbf{0} & \mathbf{0} \end{bmatrix} \begin{bmatrix} \ddot{\mathbf{q}} \\ \boldsymbol{\lambda} \\ \mathbf{u} \end{bmatrix} = \begin{bmatrix} \mathbf{Q} \\ -\dot{\mathbf{\Phi}}_\mathbf{q}\dot{\mathbf{q}} \\ -\dot{\mathbf{G}}_\mathbf{q}\dot{\mathbf{q}} - \dot{\mathbf{c}} - K_D\dot{\boldsymbol{\phi}}_s - K_P\boldsymbol{\phi}_s \end{bmatrix} . \tag{4}$$

In equation (4) the servo constraints are stabilized with a simple linear regulator where K_P and K_D are the proportional and derivative gains respectively. It is quite similar to the Baumgarte stabilization technique which is used in the solution of DAE equations of motion.

3. Periodic servo-constraints

Using the above explained *task based* formalism, the controlled- and the internal dynamics of the system can be separated. The internal dynamics it often referred ad passive dynamics which should be stable to ensure the stability of the system. However, the stability of the internal dynamics depend on the controlled task. If the stability of the internal dynamics can not be guaranteed, the original task (servo-constraint) should be modified slightly as it is presented in [7] and [8]. This modification makes the control stable with an acceptable violation of the original task. In reference [5] a different approach is introduced, when the
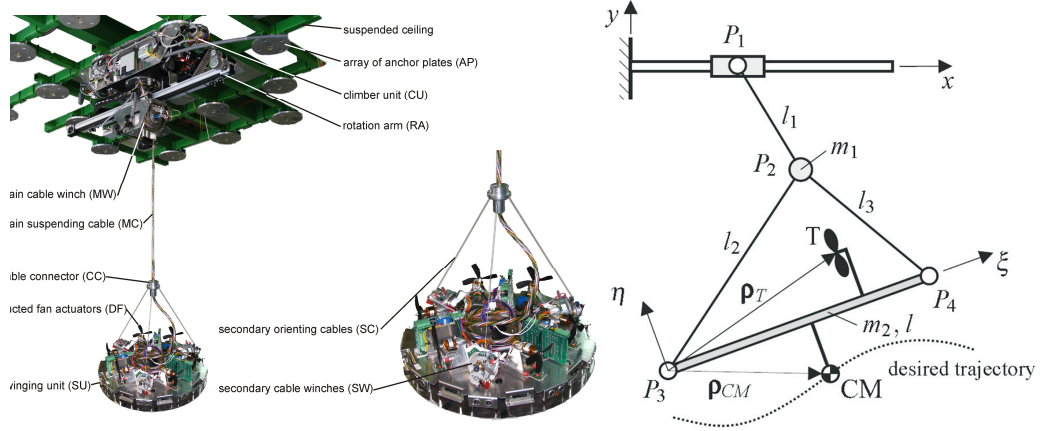
Figure 1. The prototype and the planar model of the ACROBOTER platform.

servo-constraint is not simply modified but also periodically changed in time. In one period the original servo-constraint is considered for realizing the desired motion, while in the subsequent period (typically shorter) a modified servo-constraint is applied to stabilize the unstable internal dynamics. Thus slightly modified servo constraints are applied to stabilize the otherwise unstable internal dynamics. This modification makes the stable control possible, and result in larger, but still acceptable, tracking errors. The goal of this paper is to investigate dynamic properties and the advantages of the periodic servo-constraint based control algorithm.

4. Stability and dynamics

The dynamics of the presented control approach will be investigated in case of service robot wich will be briefly introduced in the following.

4.1. Service robotic example

The introduced method will be presented via the example of the motion control of the AC-ROBOTER service robot [1] (see Fig. 1), which is a suspended pendulum like underactuated manipulator. The mechanical structure of ACROBOTER can be divided into two parts; the climber unit (CU) carries the swinging unit (SU), which hangs on the main cable (MC) and three orienting secondary cables (SC) as shown in Fig. 1. The length of the cables are adjusted by servo motors, and the positioning of the SU is assisted by ducted fan actuators. Despite of the large number of actuators the system is underactuated. In order to understand the behaviour of the control, the planar model of the system is investigated. The
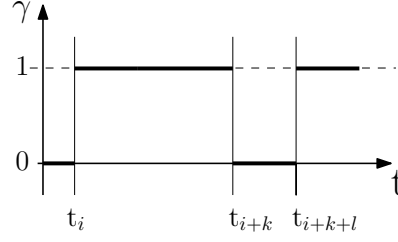
Figure 2. Servo constraint switching scheme.

planar model is shown on the right hand side of Fig. 1. While the model has five DoF and the number of independent actuators is four only thus it is still underactuated. To describe the geometry of the model depicted in Fig. 1 the most way convenient is to use Cartesian coordinates $\mathbf{q} = [x_2 \ y_2 \ x_3 \ y_3 \ x_4 \ y_4]^{\intercal}$, where the last four elements are the so-called natural coordinates that belong to the planar rigid body that represents the SU. Thus, according to [2], the mass matrix of the planar ACROBOTER model can be assembled as a constant block diagonal matrix $\mathbf{M} = \text{diag}(\mathbf{M}_{CC} \ \mathbf{M}_{SU})$. During the control tests the planar AC-ROBOTER has to follow a linear path with horizontal orientation, when the CC is above the SU with h_{CC}^d height. As it was mentioned the passive motion (lateral motion of the CC) should be stabilized by periodically changing servo constraints. Using the servo-constraint based formalism the modified task can be defined as:

$$
\phi_s = \begin{bmatrix} y_{CC} - \frac{y_3+y_4}{2} - h_{CC}^d \\ (1-\gamma)x_2 + \gamma\frac{x_3+x_4}{2} - x_{SU}^d \\ \frac{y_3+y_4}{2} - y_{SU}^d \\ y_3 - y_4 \end{bmatrix} .
\tag{5}
$$

In equation (5) the function γ is responsible for the switching of servo constraints as it is shown in Fig. 2. For l time steps $\gamma = 0$ the passive part of the motion is considered in the servo-constraint set, while for k time steps $\gamma = 1$ and the original task is realized in the control scheme.

4.2. Stability investigation

In order to chose an effective switching pattern linear stability analysis was carried out. Considering the discrete behaviour of the digitally controlled system a picewise solution of the equation of motion should constructed for eigenvalue analysis. This solution is known analytically if the system is linear, thus we have to linearize the system around the investigated configurations. During the stability investigation it is assumed that the control forces calculated at the nth time instant are based on the $(n-1)^{\text{th}}$ measured values which are held

78

by a zero-order-hold (ZOH) until the end of the $(n+1)^{\text{th}}$ sampling instant. The stability investigation is based on equation (2) where the input force $\mathbf{u}$ is calculated via the solution of equation (4).

The equation of motion can be linearized around an arbitrary configuration and after that the equation of the controlled system can be written in the general first order form:

$$\dot{\mathbf{x}}(t) = \mathbf{A}\mathbf{x}(t) + \mathbf{B}\mathbf{x}(t_{n-1}), \quad t \in [t_n, t_{n+1}]. \tag{6}$$

By using the state variables at the end of the nth sampling interval the solution can be calculated as:

$$\mathbf{x}(t_{n+1}) = \mathbf{A}_d \mathbf{x}(t_n) + \mathbf{B}_d(t_{n-1}), \tag{7}$$

where $\mathbf{A}_d$ and $\mathbf{B}_d$ can be calculated utilizing the following property [3]

$$e^{\mathbf{W}\Delta t} = \begin{bmatrix} \mathbf{A_d} & \mathbf{B_d} \\ \mathbf{0} & \mathbf{I} \end{bmatrix}, \tag{8}$$

where Δt is the sampling time of the digital controller, and the matrix W can be constructed as:

$$\mathbf{W} = \begin{bmatrix} \mathbf{A} & \mathbf{B} \\ \mathbf{0} & \mathbf{0} \end{bmatrix}. \tag{9}$$

Based on equation (7) the mapping $\mathbf{z}_{n+1} = \mathbf{H}\mathbf{z}_n$ can be composed where $\mathbf{z}_n = [\mathbf{x}_{n-1}, \mathbf{x}_n]^{\mathsf{T}}$. The control law is switched in time therefore the state-equation is also changed during the control. The discrete mapping for the whole pattern (see: Fig. 2) can be constructed as:

$$\mathbf{z}_{n+k+l} = \prod_{j=1}^{k+l} \mathbf{H}_{n+k+l-j}\, \mathbf{z}_n. \tag{10}$$

From the computed eigenvalues $\boldsymbol{\rho}$ of the mapping (10) the avaraged eigenvalue for one time step can be computed as:

$$\bar{\boldsymbol{\rho}} = \sqrt[k+l]{\boldsymbol{\rho}}. \tag{11}$$

In the stability analysis the internal dynamics is stabilized for $l = 1$ time step only. The stability charts in Fig. 3 show the stable domains of operation with different switching periods ($k = 1 \ldots 9$) in the plane of the control parameters K_P and K_D. It can be concluded that the area of the stable domains is the biggest, when $k = 5$. The fastest decay can be achieved when $k = 1$, which means that in every second time step the original constraint is repeated with the modified one.
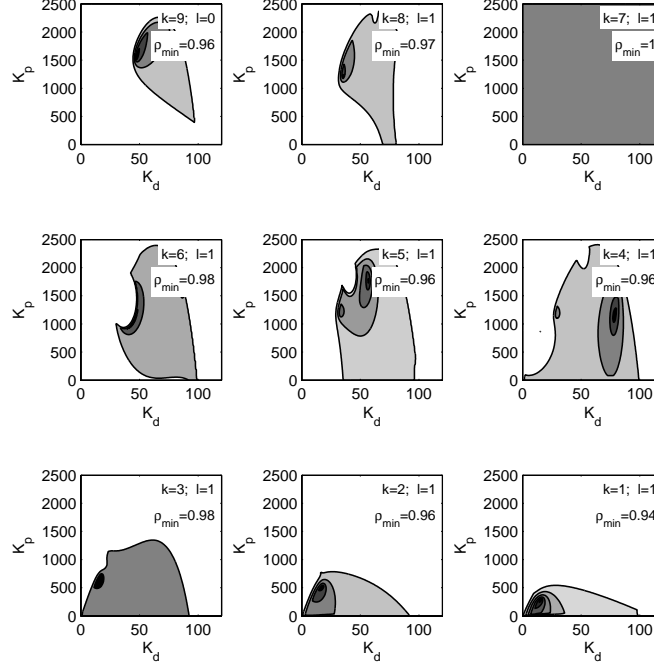
Figure 3. Stability charts in case of periodically switched servo constraints.

5. Simulation case study

We confirmed the results shown by the stability diagrams by numerical simulations of the original non-linear system. In the first simulation scenario the control command is computed using the original servo constraints only. In this case the position of the SU is controlled only during the motion. In order to check the robustness of the control a horizontal perturbation was applied on the CC at $t = 1.5s$. The result of the trajectory tracking is shown on Fig. 4. The violation of the servo-constraints clearly show that neglecting of the internal dynamics can lead to unstable dynamics behaviour.

In the second simulation scenario the periodic-servo constraints are used. It means that the horizontal displacement of the CC is used instead of the SU in the servo constraints at certain periodic time instances. The pattern was chosen based on the presented stability investigation (Sec. 4.2). The servo-constraints' violation is presented in Fig. 5. With the use of the same perturbation the results show that with the application of the periodic
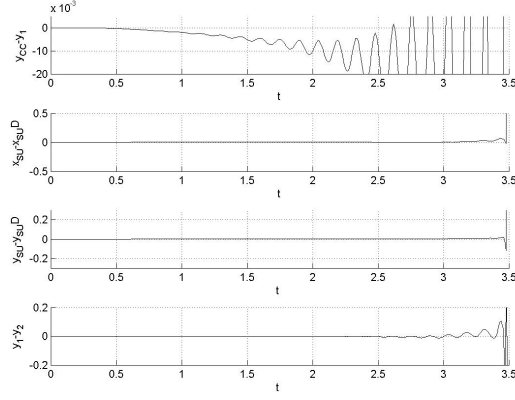
Figure 4. Simulation results with original servo constraints.
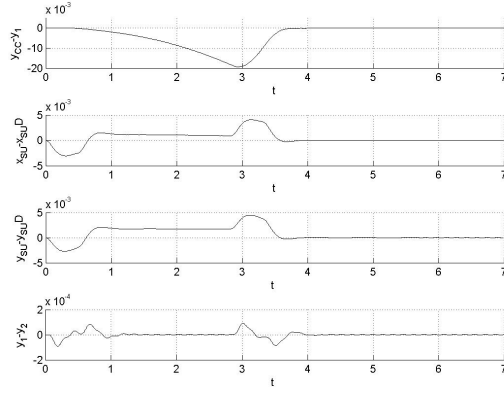
Figure 5. Simulation results with the periodic servo constraints

servo-constraints the investigated system can be controlled in stable way.

6. Conclusion

Present paper analysed the idea of periodic servo-constraints. Based on the stability analysis it can be concluded that the presented approach can effectively enhance the dynamical properties of the controlled system. The stability analysis was carried out in case of a service robot example. The result of that is applied in case of trajectory following problem which also shows that the application of periodic servo-constraints makes the original task feasible in stable way. For real-life application the optimal switching pattern requires a

further research in order avoid the numerically expensive stability investigation.

Acknowledgments

References

[1] A ZELEI, L BENCSIK, G. S. L. K. Dynamics and actuation of the acroboter platform. In *Book of Absrtacts of The 2nd Joint International Conference on Multibody System Dynamics-IMSD* (2012).

[2] DE JALÓN, J., AND BAYO, E. *Kinematic and dynamic simulation of multibody systems: the real-time challenge.* Springer-Verlag, 1994.

[3] DECARLO, R. *A State Variable Approach with Numerical Implementation.* Prentice Hall, 1989.

[4] KIRGETOV, V. I. The motion of controlled mechanical systems with prescribed constraints (servo constraints). *Prikl. Mat. Mekh. 31*, 3 (1967), 433–447.

[5] LÁSZLÓ BENCSIK, LÁSZLÓ L. KOVÁCS, A. Z. Periodic servo-constraints for stabilizing underactuated multibody systems. In *Book of Absrtacts of The 2nd Joint International Conference on Multibody System Dynamics-IMSD* (2014).

[6] LÁSZLÓ L. KOVÁCS, L. B. Stability case study of the acroboter underactuated service robot. *Theoretical and Applied Mechanics Letters. 2*, 4 (2012), 043004.

[7] R SEIFRIED, W. B. Analysis of servo-constraint problems for underactuated multibody systemss. *Mech. Sci 4* (2013), 113–19.

[8] W BLAJER, K. K. A case study of inverse dynamics control of manipulators with passive joints. *Journal of Theoretical and Applied Mechanics 52* (2014), 793–801.

[9] ZELEI, A. *Excitation for Underactuated Dynamical Systems.* PhD thesis, Budaopest University of Technology and Economics, 2015.

László Bencsik, (M.Sc., Research assistant): HAS-BME Research Group on Dynamics of Machines and Vehicles, Muegyetem rkp. 5, Budapest, H-1111, Hungary (*bencsik@mm.bme.hu*).

László L. Kovács, (Ph.D, Senior research associate): HAS-BME Research Group on Dynamics of Machines and Vehicles, Muegyetem rkp. 5, Budapest, H-1111, Hungary (*kovacs@mm.bme.hu*).

Ambrus Zelei, (Ph.D, Research associate): HAS-BME Research Group on Dynamics of Machines and Vehicles, Muegyetem rkp. 5, Budapest, H-1111, Hungary (*zelei@mm.bme.hu*).

Basic attractors and control
(CON263-15)

Björn Birnir

Abstract: In this talk we discuss the dynamical systems theory of dissipative nonlinear partial differential equations (PDEs), on a bounded domain, and connect it with the dynamical systems theory of ordinary differential equations (ODEs). A decomposition theorem says that attractors of PDEs can be decomposed into a basic attractor (a core) that attracts sets of positive measure, indeed it attracts a prevalent set in phase space, and a remainder whose basin, up to sets that are attracted to the basic attractor, is shy, or of zero measure. If the basic attractor is low-dimensional and the remainder high-dimensional, then the dynamics can still be analyzed up to transients that are exponentially decaying towards the attractor in time. The theory of basic attractors also makes it possible to develop a basic control theory creating the means to control instabilities in nonlinear PDEs. Thus basic attractors lead to basic control.

1. Introduction

In this paper we will give an introduction to the theory of *Basic Attractors and Control*, see [9]. We develop the dynamical systems theory of dissipative nonlinear partial differential equations (PDEs), on a bounded domain, and connect it with the dynamical systems theory of ordinary differential equations (ODEs). The latter theory was developed during the latter half of the twentieth century and has revolutionized modern science and engineering.

The attempts to develop a dynamical systems theory for PDEs in the late twentieth century, see [6, 7, 16, 18, 25], had some success. It was established that dissipative nonlinear PDEs had finite-dimensional attractors. These are set of solutions that attract all other solutions in the phase space of the PDEs as time becomes large. But a troublesome gap remained between the dimension of the attractors obtained in estimates, see [25], and the dimensions of solutions observed in experiments and numerical simulations. This prevented a meaningful application of the theory. We explain how this problem was resolved and how the analysis of the core of the attractors, called *Basic Attractors*, can be reduced to the theory of ODEs and the bifurcation theory of their solutions, see [9].

John Milnor [23] had proven in 1985 that the attractors of ODEs have a decomposition if the Lebesgue measure of their basin of attraction is taken into account. This raised the question whether a similar decomposition could be found for the attractors of PDEs and

whether the dimensions of their components that attracted positive measure in infinite-dimensional space were possibly small. Only these components were expected to play a role in most numerical simulations and experiments.

The first success in this direction was proving, see [7], that the breather solutions of the damped and driven sine-Gordon equation attracted sets of positive measure by a cumbersome projection onto a finite-dimensional subspace of the phase space of the PDE. The breathers constitute the dynamically interesting part of the sine-Gordon basic attractor. The reason why this was relatively complicated is that there is no straight-forward analog of Lebesgue measure that can be defined on the whole of an infinite-dimensional space. However, in 1992 Hunt, Sauer and York [17], developed a notion of measure zero, *shy*, and almost every, *prevalent*, in infinite dimensions. This set the stage for an elegant extension of Milnor's decomposition to attractors in infinite-dimensional space. After this development applications of the theory to many different types of PDEs became possible.

The decomposition theorem, Theorem 1 below, says that attractors of PDEs can be decomposed into a *basic attractor* (a core) that attracts sets of positive measure, indeed it attracts a prevalent set in phase space, and a *remainder* whose basin, up to sets that are attracted to the basic attractor, is shy. This offers an elegant closure of the gap discussed above. Namely, if the *basic attractor* is low-dimensional and the *remainder* high-dimensional, then the dynamics can still be analyzed up to transients that are exponentially decaying towards the attractor in time. The notion of the basin of attraction has to be generalized slightly and we do that by defining the *catchment* of a set below.

In [11, 13] we illustrated the theory by an application to the viscous Moore-Greitzer equation, see Chapter 7 in [9], describing the air flow through a jet engine. The viscous Moore-Greitzer basic attractor turns out to contain the flow for the desired operation of the jet engine, called *design flow*, but also two undesirable instabilities in the flow called *surge* and *stall*. The complete qualitative description of the design flow and those two instabilities is a great accomplishment of the theory.

The theory of basic attractors is however a perfectly general theory and in [9] we lay the foundation for nonlinear heat, dissipative wave equations and dissipative nonlinear Schrödinger equations. These details will not be repeated in the paper but we refer the interested reader to Chapter 4 in [9].

In this paper we define and prove the existence of the basic attractor, following Milnor's [23] results in finite dimensions. The decomposition of the global attractor, into a basic attractor and a reminder in infinite dimensions is proven. We refer the reader to [17] and [9] where the concepts of shy and prevalent sets, that are used in the definition of the basic attractor, are discussed in more detail. There we also give an example showing that there

exist basic attractors of arbitrarily high dimensions. Finally, we construct a "typical" basic attractor that is low-dimensional, and a reminder that is high-dimensional, using the damped and driven sine-Gordon equation in Chapter 5 in [9].

In [12, 14], the first impressive consequence of the theory of basic attractors is explored again by the example of the viscous Moore-Greitzer equation. The theory of basic attractors makes it possible to develop a *basic control theory* creating the means to control the surge and stall instabilities. Thus *basic attractors* lead to *basic control*, see [9]. This type of control is discussed below at the end of the paper.

In [15] and [9], Chapter 11, we also show how to approximate the general solution in the basic attractor by a finite basis of solutions from the basic attractor, these are called *basic approximations*. We prove in this chapter that the basic truncation basis consists of the first few Karhunen-Loeve (KL) [19] empirical eigenfunctions, when the motion is ergodic on the basic attractor. This was first observed numerically in [10]. Thus basic attractors provide an optimal low-dimensional truncation of the solutions to the nonlinear PDE and this also explains why the KL analysis works so surprisingly well on low-dimensional attractors of PDEs.

The numerical analysis of basic attractors has taken off in the last ten year with the availability of better numerical and symbolic programs, such as Matlab and Mathematica, see [9], especially in the engineering literature. Good examples are the papers on beam and shell dynamics by J. Awrejcewicz [1–5, 20–22] and his collaborators.

2. The Decomposition Theorem

A global attractor $\mathcal{A}$ of an ODE or a PDE is defined to be the omega limit set of an absorbing set, see [9]. If the absorbing set is convex and the phase space of the dynamical system is $\mathbb{R}^n$ or a Banach space, the global attractor is connected and compact, see [9]. The problem with $\mathcal{A}$ is that it tends to be large and high-dimensional, see [9]. Thus it is desirable to find a more restrictive notion of an attractor that permits a decomposition of $\mathcal{A}$ into more manageable parts. The first step is to work with sets that are more general than basins, namely sets that can also be closed or neither open nor closed and look for the omega limits sets of these sets. In order to do this Milnor defined the realm of a set. Milnor gives the following definition on page 179 in [23]:

Definition 1 *A closed subset $A \subset M$ (M a smooth compact manifold) will be called an attractor if it satisfies two conditions:*

1. *the realm of attraction $\rho(A)$ consisting of all points $x \in M$ for which $\omega(x) \subset A$, must have a strictly positive measure; and*

2. *there is no strictly smaller closed subset $A' \subset A$ such that $\rho(A')$ coinsides with $\rho(A)$ up to a set of measure zero.*

We want to generalize Milnor's notions to infinite dimensions and the first step is to define the generalization of the realm to infinite dimensions.

Definition 2 *The catchment of a set A consists of all points x, such that $\omega(x) \subset \bar{A}$.*

Catchment is the generalization of a realm of a set. Thus a catchment can be infinite dimensional and in finite-dimensions the catchment becomes the realm if the set is closed. However, catchment is slightly general than realm because it is also defined for open sets. Next we have to generalized the notion of Lebesgue measure zero and "almost every" to infinite dimensions. The problem is that there is no analog of Lebesgue measure in infinite dimensions. It is easy to see, [9] Chapter 5, that if there is a translation invariant measure defined on a separable Banach space such that the measure of a ball of radius $\epsilon > 0$ is finite, then either the whole space has measure zero or it is finite-dimensional.

Hunt, Sauer and Yorke [17], proposed that the notions of prevalent and shy could take the place of "almost every" and "measure zero" in infinite dimensions. They made the following definitions, see [9, 17]. Let X be a Banach space, μ a non-negative compactly supported measure defined on the Borel sets S of X and $S + x$ a translate of S by $x \in X$.

Definition 3 *The measure μ is transverse to S if $\mu(S+x) = 0$ for every $x \in X$ and μ, with (support μ) $< \infty$.*

Definition 4 *A Borel subset $S \subset X$ is said to be* shy *if there exists a measure transverse to S. Moreover, any subset of such an S is shy.*

Definition 5 *A Borel set S whose complement $X \setminus S$ is shy is said to be* prevalent.

It follows immediately from these definitions that if S is shy, so is every subset of S and every translate of S by constant vector $x_0 \in X$. Every shy Borel set has also clearly a finite transverse measure with compact support, see [9] Chapter 5, for more details.

Birnir gives the corresponding definition of a basic attractor $\mathcal{B}$ in [9]:

Definition 6 *A closed and compact set $\mathcal{B} \subset X$ (X is a complete metric space) is called a basic attractor if it satisfies the two conditions:*

1. *The catchment of $\mathcal{B}$ is not shy.*

2. *There exists no strictly smaller closed set $\mathcal{B}' \subset \mathcal{B}$ such that catchment $\mathcal{B} \subset$ catchment $\mathcal{B}'$ up to shy sets.*

Notice that this definition defines a more restricted notion of an "attractor" than the global attractor $\mathcal{A}$.

The proof follows Milnor's proof in [23] of the existence of the "likely limit set", that is the basic attractor in finite dimensions. Some details missing in Milnor's proof are supplied below, see [7–9]. Recall the decomposition theorem (of a global attractor $\mathcal{A}$) from [9]:

Theorem 1 *Let $\mathcal{A}$ be the global attractor of a continuous map T, with a convex absorbing set, on a separable Banach space X. Then $\mathcal{A}$ can be decomposed into a basic attractor $\mathcal{B}$ and a remainder $\mathcal{C}$, $\mathcal{A} = \mathcal{B} \cup \mathcal{C}$, such that the catchment of $\mathcal{B}$ is prevalent, but catchment $\mathcal{C} \setminus$ catchment $\mathcal{B}$ is shy.*

Proof:

1. Since X is separable there exists a countable cover of X by open balls $\{U_k, k \in \Omega\}$, where $\Omega \subset \mathbb{N}$ is an index set. We will extract a subcollection

$$U' = \bigcup_{k \in \Omega'} U_k,$$

where we have excludes all balls $U_k, k \in \Omega \setminus \Omega'$ that contain the omega limit set $\omega(x)$ of x in a set W that is not shy. If $\omega(x) \subset U_k, \ \forall x \in W_k, \ k \in \Omega'$, and the W_k are shy, then $W = \bigcup_{k \in \Omega'} W_k$ is shy, since a countable union of shy sets is shy, see Lemma 5.2 in [9]. Obviously, $x \in W$ implies $\omega(x) \subset U'$.

2. Consider the set $\mathcal{B} = X \setminus U'$. This set is closed. Moreover, $\mathcal{B} \subset \mathcal{A}$, since $\mathcal{A}$ contains the omega limit set of any set $W \subset X$, so if $W \cap \mathcal{A} = \emptyset$ then trivially $W \subset U'$. Now $\mathcal{A}$ is compact so $\mathcal{B}$ is compact.

3. The catchment of attraction of $\mathcal{B}$ is not shy because $\mathcal{B}$ contains the omega limit sets of sets that are not shy. Moreover, if $\mathcal{B}' \subset \mathcal{B}$, let $x \in \mathcal{B} \setminus \mathcal{B}'$, then if $W \subset$ catchment$\{x\}$ is not shy, $x \in \mathcal{B}$ by construction of $\mathcal{B}$. This shows that $\mathcal{B}$ is a basic attractor according to Definition 2 and minimal as such.

4. We now define the remainder $\mathcal{C}$ to be $\mathcal{C} = \mathcal{A} \setminus \mathcal{B}$. $\mathcal{B}$ can attract subsets of $\mathcal{C}$, but $\mathcal{C}$ cannot attract any points of $\mathcal{B}$. Thus since $\mathcal{A}$ attracts all of X , we have that $X =$ catchment $\mathcal{B} \cup$ catchment $\mathcal{C}$ and the disjoint union becomes $X =$ catchment $\mathcal{B} \cup$ {catchment $\mathcal{C} \setminus$ catchment $\mathcal{B}$}. This shows that catchment $\mathcal{B}$ should be prevalent (infinite-dimensional almost every), whereas the catchment $\mathcal{C}$, with the points that eventually are attracted to $\mathcal{B}$ are removed, should be shy. We now prove this.

5. Let $\mathcal{D} = \{\text{catchment } \mathcal{C} \setminus \text{catchment } \mathcal{B}\}$. By the above, to show that catchment $\mathcal{B}$ is prevalent it suffices to show that $\mathcal{D}$ is shy. Let $W \subset \mathcal{D}$ be so small that $\omega(x), \forall x \in W$ lies in a connected component of $\mathcal{D}$. W must be shy because only shy sets are attracted to $\mathcal{C}$ but not attracted to $\mathcal{B}$. W can be chosen to be open in the relative (strong) topology of $\mathcal{D}$ and since X is separable so is $\mathcal{D}$. This means that we can cover $\mathcal{D}$ by a countable union of shy sets and since, by Lemma 5.3 in [9], a countable union of shy sets is shy, and a subset of a shy set is shy, we conclude that $\mathcal{D}$ is shy.

This finishes the proof of the Theorem.

3. Comments and Examples

1. In [8] Birnir uses the definition $\mathcal{B} = \mathcal{A} \setminus U'$ to get the compactness of $\mathcal{B}$ and in [9] that the intersection of sets defining $\mathcal{B}$ can be made compact. The argument in the proof above is an improvement due to B. Pego.[1] Also using a countable basis of open balls, as Milnor does in his proof of Lemma 1 in [23], is adopted in the proof and removes the need to consider a refinement of the collection of balls.

2. It is really a very straight-forward argument to show that $\mathcal{B}$ satisfies Definition 6. It is both the minimal set in X with these properties and the maximal basic attractor.

3. To finish the proof of the decomposition one has to show that catchment $\mathcal{B}$ is prevalent and that catchment $\mathcal{C} \setminus$ catchment $\mathcal{B}$ is shy. It is not true that catchment $\mathcal{B} \cap$ catchment$\mathcal{C} = \emptyset$. In general, there is an overlap of these sets. However, only shy set have limit sets in $\mathcal{C}$, that are not eventually attracted to omega limit sets in $\mathcal{B}$. Thus we get a decomposition of X, and one only has to show that catchment $\mathcal{C} \setminus$ catchment $\mathcal{B}$ is shy. Since catchment $\mathcal{C} \setminus$ catchment $\mathcal{B}$ can be covered by shy sets it is shy.

Example 1: Consider the Example 5.1.1 in [9]. Here the global attractor $\mathcal{A}$ consists of a hyperbolic point P at the origin, two sinks $\{Q_1, Q_2\}$ at $(\pm 1, 0)$ and two heteroclinic connections connecting the hyperbolic point to the sinks. Here $\mathcal{B} = \{Q_1, Q_2\}$ and $\mathcal{C}$ consists of the hyperbolic point P along with the two heteroclinic connections. The heteroclinic connections themselves are attracted to the sinks. Thus catchment $\mathcal{C} = \mathbb{R}^2$, including the catchment of P that consists of its stable manifold $W^s(P)$ that has measure zero. We also see that catchment $\mathcal{B} = \mathbb{R}^2 \setminus W^s(P)$ and

$$X = \text{catchment } \mathcal{B} \cup \text{catchment } \mathcal{C} = \mathbb{R}^2 \setminus W^s(P) \cup \mathbb{R}^2 = \mathbb{R}^2.$$

---

[1] Private communication

However, the disjoint union becomes

$$X = \text{catchment } \mathcal{B} \cup \{\text{catchment } \mathcal{C} \setminus \text{catchment } \mathcal{B}\} = \mathbb{R}^2 \setminus W^s(P) \cup W^s(P) = \mathbb{R}^2,$$

because $\{\text{catchment } \mathcal{C} \setminus \text{catchment } \mathcal{B}\} = W^s(P)$. The last manifold has measure zero (shy), showing that the Decomposition Theorem 1 applies.

To understand the construction of $\mathcal{B}$ in this example one has to consider a refinement of the covering in Figure 1 (this can be considered to be a refinement by the smaller elements of the countable basis for the topology). Consider Figure 1. The top figure shows a simple cover of the global attractor $\mathcal{A}$, the bottom figure shows a refinement of the covering. Now in the construction of $\mathcal{B}$ above

$$U' = U_3 \cup U_5 \cup U_6$$

and $X \setminus U' = \overline{U_1 \cup U_2}$, where $X = \mathbb{R}^2$. We refine the covering as shown by the bottom figure in Figure 1 and get that

$$U' = U_3 \cup U_5 \cup U_6 \cup \bigcup_{k=7}^{n} U_k,$$

where $\{U_k, 7 \leq k \leq n\}$ is a covering of the heteroclinic connections with small disks. None of these disks contain an omega limit set so they get included in U'. In fact the omega limit set of the heteroclinic connections are the sinks so they are not included in the cover $\{U_k, 7 \leq k \leq n\}$. This is the case, in general, for homo- and heteroclinic connections, they get covered by a set $\{U_k\}$ that contains no omega limit sets.

However, this is not the end of the story, we have to consider all the sets in the basis of the topology and that includes the refinement where we let the diameters of the sets $\{U_1, U_2, U_3\}$ shrink to zero. This gives

$$U' = \lim_{d \to 0} U_3^d \cup U_5 \cup U_6 \cup \bigcup_{k=7}^{n(d)} U_k.$$

Thus we get $\mathcal{B} = X \setminus U' = \lim_{d \to 0} \bar{U}_1^d \cup \bar{U}_2^d = Q_1 \cup Q_2$ and $\mathcal{C} = \mathcal{A} \setminus \mathcal{B} = P \cup \{\text{heteroclinic connections}\}$.

Example 2:[2] Consider the phase space of an ODE consisting of a saddle P with a homoclinic connection encircling a source $\hat{Q}$ with the other part of the unstable manifold $W^u(P)$ going to a sink Q. The global attractor $\mathcal{A}$ consists of the three stationary solutions $\{P, Q, \hat{Q}\}$ and the homoclinic and the heteroclinic connection. This includes the whole disk around $\hat{Q}$ that is attracted to the homoclinic connection to P. A refinement of the covering of $\mathcal{A}$ similar to the

---

[2] This example is due to B. Pego, private communication.
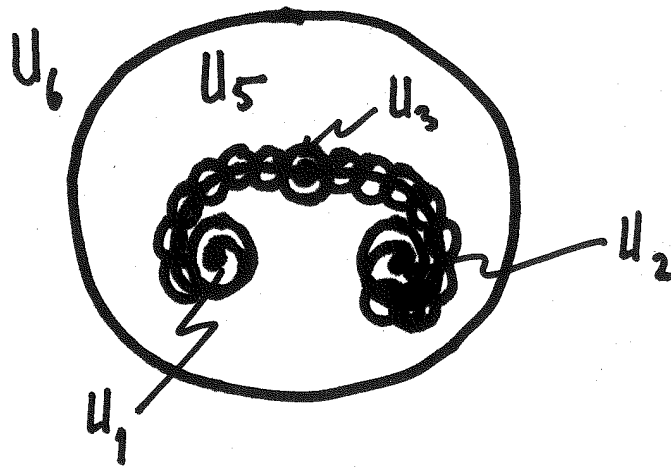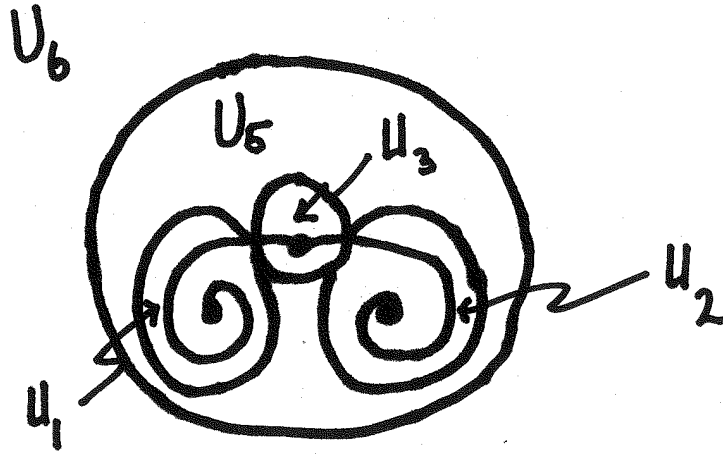
Figure 1. The refinement of the covering for Example 1. The top figure shows the original covering of the global attractor $\mathcal{A}$ and the bottom figure illustrates the refinement of the covering.

one in Example 1 above shows that $\mathcal{B} = \{P, Q\}$, and $\mathcal{C}$ consists of both the homoclinic and the heteroclinic connections, including the punctured disk inside the homoclinic connection to P and the source $\hat{Q}$. In fact, this is a nice example showing the some of the points of $\mathcal{B}$, namely P, may be hyperbolic and not attract a prevalent set of their neighborhood. The Decomposition Theorem 1 above applies and catchment $\mathcal{C} \setminus$ catchment $\mathcal{B} = \hat{Q}$, that is obviously shy. Here the point is that the inside of the unit disk is attracted to the homoclinic connection to P that eventually is attracted to $P \in \mathcal{B}$. The only set that is attracted to $\mathcal{C}$ and not eventually attracted to $\mathcal{B}$ is the stationary solution $\hat{Q}$. It has measure zero.

Example 2 verifies the statement that homo- and heteroclinic connections do not attract a set that is not shy in the sense of Milnor and Birnir (Definitions 1 and 2), unless these sets are ultimately attracted to $\mathcal{B}$. In fact, the argument given for Example 1 proves that these manifolds are not a part of $\mathcal{B}$. The same argument applies to unstable manifolds as long as they are smooth lower-dimensional (codimension 1 or greater) in X, and form a part of a homo- or heteroclinic connection in $\mathcal{A}$.

In two dimensions, the situation is rather simple because of the Poincaré-Bendixson Theorem, see for example [24]. The only omega limits sets of orbits are stationary solutions, periodic orbits or cycles of homo and heteroclinic connections and their stationary solutions. These connections cannot contain entire omega limit sets (the stationary solution is missing) and the reduction of $\mathcal{A}$ to $\mathcal{B}$ is obtained by discarding the connections and the hyperbolic stationary solutions, that do not attract a set of positive measure. Catchment $\mathcal{C} \setminus$ catchment $\mathcal{B}$ consists of the stable manifolds of the latter that have measure zero so the Decomposition Theorem 1 applies.

Example 3: The system in $\mathbb{R}^2$ consists of a source $\hat{Q}$ inside a stable periodic orbit that attracts $\mathbb{R}^2 \setminus \hat{Q}$. Here $\mathcal{A}$ is the periodic orbit and the disk inside it. $\mathcal{B}$ is the periodic orbit, $\mathcal{C}$ consists of the open disk inside the periodic orbit. The refinement of the covering in Example 1 shows that all the disks inside the periodic orbit are included in U' (they do not contain a omega limit set) and therefore excluded in the construction of $\mathcal{B}$. Again catchment $\mathcal{C} \setminus$ catchment $\mathcal{B} = \hat{Q}$, that is shy.

4. Basic Control

Let us consider now the issue of controllability. In finite dimensional control theory, a system is said to be controllable if for every two points $x_0, x_1 \in X$ and every two real numbers $t_0 < t_1$, there exists a control function u such that the unique solution of the equation

$$\dot{x} = F(x, u), \quad x(t_0) = x_0 \tag{1}$$

satisfies $x(t_1) = x_1$.

In infinite dimensional spaces this notion of controllability is too restrictive. For practical control applications one can never have more than finitely many control parameters, if for no other reason, the fundamentals of computing require computer outputs to be finite. There is therefore no hope that nonlinear evolution equations in infinite dimensional spaces will be controllable in this strict sense in practical applications.

If an evolution equation has an attractor and a basic attractor, its solutions will converge asymptotically to the attractor for all initial conditions and to the basic attractor for almost all (prevalent) initial conditions. The simplest thing one could ask of the control is that it makes all or almost all initial conditions give rise to solutions that converge to a given component in the basic attractor. A more stringent requirement on the control would be that it makes all or a prevalent set (almost all) of initial conditions initiate solutions that converge to a given component in the global attractor. This requires one to have enough control authority over the local unstable manifolds of the hyperbolic trajectories in the attractor to make them attractive. Consider the following definitions

Definition 7 *The equation (1) is* basically controllable *if for every bounded set M and every $\epsilon > 0$, there exists a finite time $T(M)$ and a control function $u(t)$, such that for every solution $x(t)$ with initial data $x_o \in M$ and any minimal component of the basic attractor $\mathcal{B}_j$*

$$\|x(t) - \mathcal{B}_j\| < \epsilon,$$

for $t > T(M)$.

This definition say that given an initial point one can steer to any component of the basic attractor in finite time. It is hopeless to get a finite T for x_o lying in a prevalent (full measure) set in the infinite-dimensional space, for the reason discussed above. It is also not wise to attempt to control every solution in the $\mathcal{A}$-attractor, because in general it $(\mathcal{C})$ contains many hyperbolic solutions and their heteroclinic connections.

5. Conclusions

If the basic attractor is low-dimensional and the remainder high-dimensional, then the dynamics can still be analyzed up to transients that are exponentially decaying towards the attractor in time, see for example [7, 9, 11, 13]. The theory of basic attractors also makes it possible to develop a basic control theory creating the means to control instabilities in nonlinear PDEs. This has been implemented for the Moore-Greitzer equations describing the flow through a jet engine, see [9, 12, 14]. But the theory also makes it possible to find the optimal low-dimensional basis, where the dynamics can be captured by a low-dimensional

system of ODEs, see [9]. Not surprisingly, this optimal low-dimensional basis turns out to consist of the Karhunen-Loeve empirical eigenfunctions. The property that these modes capture a prevalent catchment in infinite-dimensional space, implies that their representational entropy is maximal, see [9].

References

[1] AWREJCEWICZ, J. Dynamical systems theory and applications. *Communications in Nonlinear Science and Numerical Simulations 11* (Aug. 2006), 553–554.

[2] AWREJCEWICZ, J., KRYSKO, A. V., KUTEPOV, I. E., ZAGNIBORODA, N. A., DOBRIYAN, V., AND KRYSKO, V. A. Chaotic dynamics of flexible Euler-Bernoulli beams. *Chaos 23*, 4 (Dec. 2013), 043130.

[3] AWREJCEWICZ, J., KRYSKO, A. V., MROZOWSKI, J., SALTYKOVA, O. A., AND ZHIGALOV, M. V. Analysis of regular and chaotic dynamics of the Euler-Bernoulli beams using finite difference and finite element methods. *Acta Mechanica Sinica 27* (Feb. 2011), 36–43.

[4] AWREJCEWICZ, J., KRYSKO, A. V., AND SOLDATOV, V. On the Wavelet Transform Application to a Study of Chaotic Vibrations of the Infinite Length Flexible Panels Driven Longitudinally. *International Journal of Bifurcation and Chaos 19* (2009), 3347.

[5] AWREJCEWICZ, J., KRYSKO, V. A., AND NAZAR'IANTZ, V. Chaotic vibrations of flexible infinite length cylindrical panels using the Kirchhoff Love model. *Communications in Nonlinear Science and Numerical Simulations 12* (July 2007), 519–542.

[6] BABIN, A. V., AND VISHIK, M. I. *Attractors of Evolution Equations.* North Holland Amsterdam, 1992.

[7] B.BIRNIR, AND R.GRAUER. The global attractor of the damped and driven sine-Gordon equation. *Comm. Math. Phys. 162* (1994), 539–590.

[8] BIRNIR, B. Global attractors and basic turbulence. In *Nonlinear Coherent Structures in Physics and Biology* (New York, 1994), K. Spatschek and F.G.Mertens, Eds., vol. 329, NATO ASI Series.

[9] BIRNIR, B. *Basic Attractors and Control.* To be published by Springer, New York, 2016.

[10] BIRNIR, B., AND GRAUER, R. The center manifold and bifurcations of damped and driven sine-Gordon breathers. *Physica D 56* (1992), 165–184.

[11] BIRNIR, B., AND HAUKSSON, H. Finite dimensional attractor of the Moore-Greitzer PDE model. *SIAM J. of Applied Math. 59*, 2 (1998), 636–650.

[12] BIRNIR, B., AND HAUKSSON, H. The basic control of *SIAM Journ. Control and Optimization 38*, 5 (2000), 1554–1558.

[13] Birnir, B., and Hauksson, H. The basic attractor of the viscous Moore-Greitzer PDE equation. *J. Nonlinear Sci. 11*, 2 (2001), 169–192.

[14] Birnir, B., and Hauksson, H. Basic dynamical systems control of aeroengine flow. In *Proceedings of the 39th IEEE CDC conference, Sidney Des. 2000* (New Jersey, 2001), IEEE.

[15] Hauksson, H. A. *The Basic Attractor of the Viscous Moore-Greitzer Equations*. PhD thesis, UCSB, 1998.

[16] Henry, D. *Geometric Theory of Semilinear Parabolic Equations*. Springer, 1981.

[17] Hunt, B., Sauer, T., and Yorke, J. Prevalence: A translation-invariant "almost every" on ininite-dimensional spaces. *Bull. of the Am. Math. Soc. 27*, 2 (1992), 217–238.

[18] J.K.Hale. *Asymptotic Behavior of Dissipative Systems*. American Mathematical Society, 1988.

[19] Karhunen, K. Uber lineare methoden in der wahrscheinlichkeitsrechnung. *Ann. Acad. Sci. Fenn. 37* (1947).

[20] Krysko, A. V., Awrejcewicz, J., Kuznetsova, E. S., and Krysko, V. A. Chaotic Vibrations of Closed Cylindrical Shells in a Temperature Field. *International Journal of Bifurcation and Chaos 18* (2008), 1515.

[21] Krysko, V. A., Awrejcewicz, J., Kutepov, I. E., Zagniboroda, N. A., Papkova, I. V., Serebryakov, A. V., and Krysko, A. V. Chaotic dynamics of flexible beams with piezoelectric and temperature phenomena. *Physics Letters A 377* (Nov. 2013), 2058–2061.

[22] Krysko, V. A., Awrejcewicz, J., and Shchekaturova, T. V. Chaotic vibrations of spherical and conical axially symmetric shells. *Archive of Applied Mechanics 74* (Mar. 2005), 338–358.

[23] Milnor, J. On the concept of attractor. *Communications in Mathematical Physics 99* (1985), 177–195.

[24] Perko, L. *Differential equations and dynamical systems*, vol. 7. Springer Science & Business Media, 2013.

[25] R.Temam. *Infinite-Dimensional Dynamical Systems in Mechanics and Physics*. Springer, 1988.

Björn Birnir, Professor: Department of Mathematics and CNLS UC Santa Barbara and Department of Mathematics Univ. of Iceland, Dept. of Math. UCSB, Santa Barbara CA 93106, USA (*birnirb@gmail.com*). The author gave a presentation of this paper during one of the conference sessions.

Neuro-fuzzy control of structures with MR dampers
(CON253-15)

Manuel Braz-César, Rui Barros

Abstract: Over the last decades, soft computing based controllers have being widely explored as an alternative to conventional control systems in many engineering applications. The ability of Intelligent and adaptive control systems to deal with uncertain systems and to change the controller behavior at different operating conditions constitute decisive advantages over conventional control systems that allows for the development of robust controllers for complex vibration engineering problems. In this regard, this paper aims to analyze the performance of a neuro-fuzzy controller in reducing seismic-induced vibrations in building structures a using a MR damper. The plant is a three degree-of-freedom system, which represent a three-story shear building structure. The semi-active control system is derived from an optimal controller. This controller is used to command a MR damper located between the ground and the first floor, i.e., in a non-collocated configuration. The data obtained from the optimal controller is used as a reference to train a fuzzy based controller via an Adaptive Neuro-Fuzzy Inference System (ANFIS). The uncontrolled response is compared with passive and semi-active controlled responses in order to assess the effectiveness of the proposed neuro-fuzzy controller.

1. Introduction

Soft computing methods represent a relatively recent modeling technique of control devices and controllers that have been shown to be effective in dealing with complex and non-linear behavior of structural control systems. ANFIS is a hybrid learning algorithm that combines the backpropagation gradient descent and least squares methods to create a fuzzy inference system whose membership functions are iteratively adjusted according to a given set of input and output data [1,2]. The development of a neuro-fuzzy model of a control device or a neuro-fuzzy based controller typically involve four main steps:

1. Definition of input variables and the corresponding fuzzy inference system (FIS) membership functions (the FIS output is the desired control signal);

2. Selection of experimental or artificial data sets to generate training and checking data;

3. Use of ANFIS optimization algorithm for training the FIS membership function parameters to model the set of input/output data by mapping the relationship between inputs and outputs in order to generate a fuzzy model of the systems;

4. Validation of the resulting fuzzy model.

ANFIS system training procedure is summarized in the flowchart shown in Figure 1. The process begins by obtaining a training data set and checking data sets. The training data is used to find the premise parameters for the membership functions (MFs are dependent on the system designer). A threshold value for the error between the actual and desired output is determined. The consequent parameters are found using the least-squares method. If this error is larger than the threshold value, then the premise parameters are updated using the gradient decent method. The process end when the error becomes less than the threshold value. Checking data set can then be used to compare the model with the actual system.
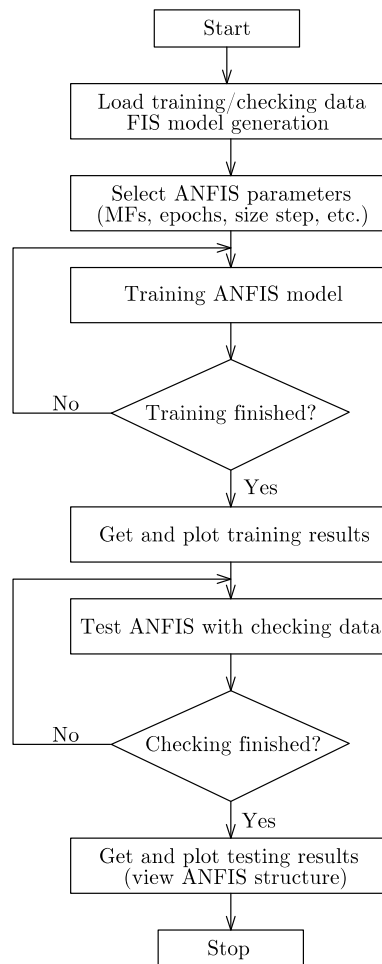
Figure 1. Flowchart of ANFIS training.

This paper aims to analyze the performance of a neuro-fuzzy controller in reducing seismic-induced vibrations in building structures a using a MR damper. The plant is a three degree-of-freedom system, which represent a three-story shear building structure. The semi-active control system is derived from an optimal controller. This controller is used to command a MR damper located between the ground and the first floor, i.e., in a non-collocated configuration. The data obtained from the optimal controller is used as a reference to train a fuzzy based controller via an Adaptive Neuro-Fuzzy Inference System (ANFIS). The uncontrolled response is compared with passive and semi-active controlled responses in order to assess the effectiveness of the proposed neuro-fuzzy controller.

2. Numerical model

Consider a semi-active controlled system subjected to an earthquake ground motion with a control force applied to the first mass (or the first DOF, x_1) as illustrated in Figure 2. The control force provided by a MR damper intends to reduce the response of the system and can be achieved placing an actuator between the base and the first mass. The damper force can be changed using a control system comprising a controller that monitors the system response and computes the required damping force that should be applied to the system changes the system response in order to improve its structural performance. An effective semi-active control system involves an appropriate control algorithm that can take advantage of the dissipative properties of the control device, i.e., the MR damper [3,4]. There are several approaches available in the literature to control semi-active devices including soft computing techniques such as neuro-fuzzy controllers.
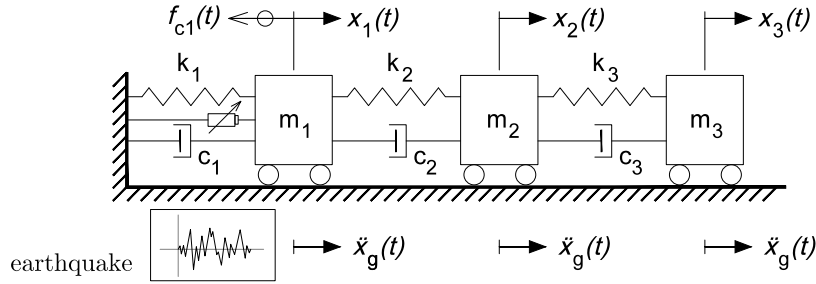
Figure 2. Schematic representation of a 3DOFs system under earthquake excitation - Semi-active control with a MR damper at the first floor.

The equation of motion of the controlled structure can be defined by a state space formulation as

$$\dot{z}(t) = Az(t) + Bf(t) + E\ddot{x}_g(t) \tag{1}$$

where matrix A represent the system matrix

$$A = \begin{bmatrix} 0 & I \\ -M^{-1}K & -M^{-1}C \end{bmatrix} \tag{2}$$

B is an additional matrix accounting for the position of the control forces in the structure and f is a column vector with the control forces. The location of the control forces is defined by a location matrix Γ within B. In this case there is only one control force applied to the first mass and therefore, it follows that

$$\Gamma = \left\{ 1, 0, 0 \right\}^T \tag{3}$$

and then

$$B = \left\{ 0, 0, 0, -\frac{1}{m_1}, 0, 0 \right\}^T \tag{4}$$

Finally, E is the disturbance vector that represents the location of the earthquake excitation and is given by

$$E = \left\{ 0, 0, 0, -1, -1, -1 \right\}^T \tag{5}$$

The response of the system can be determined using the state space output vector

$$y(t) = Cz(t) + Df(t) + F\ddot{x}_g(t) \tag{6}$$

where $\ddot{x}_g(t)$ represents the seismic excitation loading. If the system displacements, velocities and accelerations are required, then

$$C = \begin{bmatrix} I & 0 \\ 0 & I \\ -M^{-1}K & -M^{-1}C \end{bmatrix}, \quad D = \left\{ \begin{array}{c} 0 \\ -\lambda \end{array} \right\} \tag{7}$$

where λ represents the location of the earthquake excitation (i.e., the seismic acceleration).

In this study, the structure will be subjected to the El-Centro ground motion (1940 N-S component with a peak acceleration of 3.42 m/s2). Since the mechanical system seeks to represent a small-scale building, the earthquake signal needs to be decreased to represent the magnitude of displacements that would be observed in experiments tests. Thus, the time was scaled to 20% of the full-scale earthquake time history as shown in Figure 3.
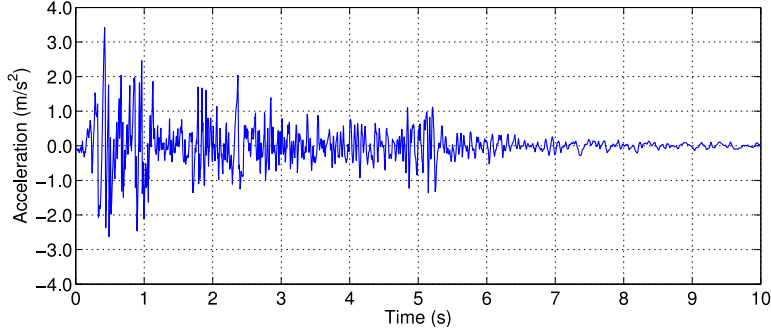
Figure 3. Time-scaled El-Centro NS earthquake ground motion (0.2t).

The mass (kg), damping (Ns/m) and stiffness (N/m) matrices of the model structure are given by

$$
\mathrm{M} = \begin{bmatrix} 100 & 0 & 0 \\ 0 & 100 & 0 \\ 0 & 0 & 100 \end{bmatrix}, \; \mathrm{C} = \begin{bmatrix} 175 & -50 & 0 \\ -50 & 100 & 0 \\ 0 & -50 & 50 \end{bmatrix}, \; \mathrm{K} = \begin{bmatrix} 12 & -6 & 0 \\ -6 & 12 & -6 \\ 0 & -6 & 6 \end{bmatrix} 10^{-5} \tag{8}
$$

The structure is equipped with a semi-active control system comprising a MR damper (Lord Corp., RD-1005-03 model) located between the ground floor and the first floor. The numerical formulation and the corresponding model parameters are presented in Table 1 [5].

Table 1. Modified Bouc-Wen model - Parameters of the RD-1005-3 MR damper.

Modified Bouc-Wen model

$$F(t) = c_1 \dot{y} + k_1(x - x_0)$$

$$\dot{y} = \frac{1}{c_0 + c_1} \left[\alpha z + c_0 \dot{x} + k_0(x - y)\right]$$

$$\dot{z}(t) = -\beta \left|\dot{x}(t)\right| z(t) \left|z(t)\right|^{n-1} - \gamma \dot{x}(t) \left|z(t)\right|^{n} + A\, \dot{x}(t)$$

Current **independent** parameters	A [-]	β [mm^{-1}]	γ [mm^{-1}]	k_0 [N/mm]	f_0 [N]	n
	10.013	3.044	0.103	1.121	40	2
Current **dependent** parameters	$\alpha(I) = -826.67I^3 + 905.14I^2 + 412.52I + 38.24$ [N] $c_0(I) = -11.73I^3 + 10.51I^2 + 11.02I + 0.59$ [N.s/mm] $c_1(I) = -54.40I^3 + 57.03I^2 + 64.57I + 4.73$ [N.s/mm]					

The MR damper can operate in two modes: as a passive energy dissipation device, i.e., without a control system (the properties of the actuator are constant during the simulation) and as a semi-active actuator whose control action is being commanded by a neuro-fuzzy based controller. In this case, the modified Bouc-Wen model was selected to simulate the behavior of the MR damper.

Besides, the first-order time lag involved in the current driver/electromagnet during a step command signal must be included in the numerical model of the device, which in this case is defined by a first order filter (η= 130 sec^{-1}).

Next, the results of the a neuro-fuzzy semi-active control system are compared with the uncontrolled, passive OFF and passive ON responses to evaluate the efficiency of the semi-active control scheme in reducing the structural response.

Using the state space formulation, the uncontrolled response of the 3DOFs system under the earthquake ground motion is displayed in Figure 4. It should be noted that the response was obtained with a high excitation level of the El Centro earthquake achieved by scaling up the amplitude of the earthquake signal in 150%.
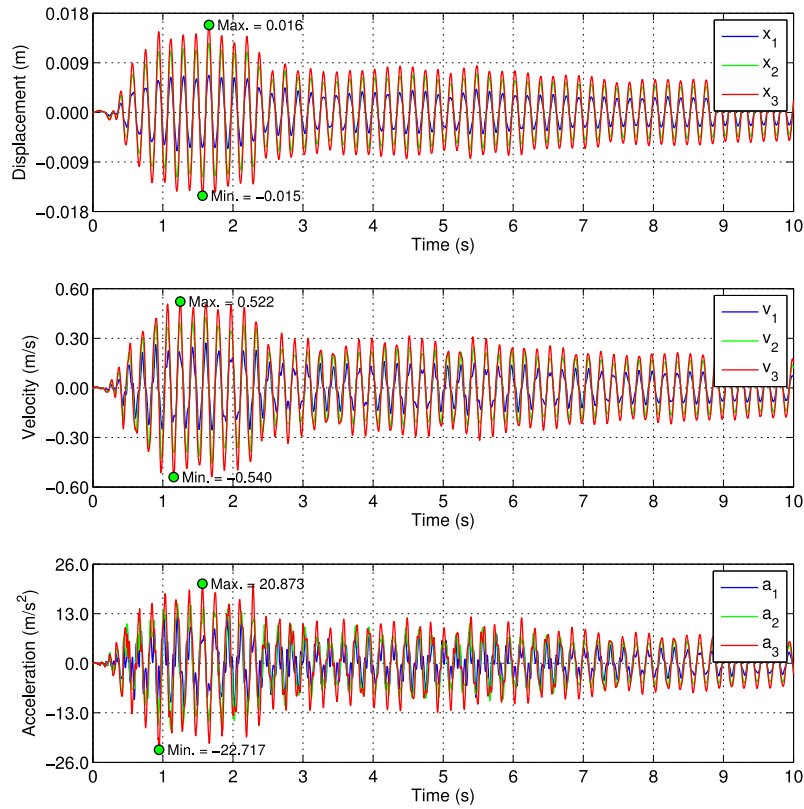
Figure 4. Uncontrolled responses of the 3DOFs system.

3. Neuro-fuzzy controller

The fuzzy logic based controller was designed using ANFIS to find the nonlinear map that best fits the expected response of the control system. The neuro-fuzzy controller was developed based on the numerical results of the LQG controller whose response is used to define the training data set for the neuro-fuzzy optimization procedure with ANFIS. Floor accelerations and the displacement across the MR damper are the responses of the controlled system used by the LQG controller to determine the desired control force. The control signal is determined from the predicted control force using an inverse Bingham model of the MR damper. The system responses and the desired control signal were recorded and then used to train the neuro-fuzzy controller.

The data sets for training and validation were obtained exposing the LQG controlled system to a set of amplitude-scaled versions of the El Centro NS earthquake excitation (i.e., 100 gal, 200 gal, 335 gal and 503 gal seismic accelerations). The LQG controller combines a LQR algorithm with a Kalman filter estimator. Identically distributed Gaussian white noise is used to simulate acceleration noise measurements. Regarding the LQR controller, the state gain matrix K is tuned through the weighting matrices Q and r. In the present example different configurations of these parameters were evaluated by measuring the effect of each combination in the system response. The following weighting parameters provided best performance in reducing in the structural response

$$Q = \begin{bmatrix} K & 0 \\ 0 & 0 \end{bmatrix}; \quad R = r = 5 \times 10^{-7} \tag{9}$$

The observer gain L must be adjusted to achieve the required performance. A high gain allows the filter to follow the observations more closely while a low gain follows the predictions more closely. This is accomplished by setting

$$Q_w = q_w I_e, \quad R_v = r_v I_m \tag{10}$$

where I_e and I_m are identity matrices related with the number of excitation inputs and measurement signals, respectively. A common approach is to set one of the tuning parameters and adjust the other parameter until the result is satisfying. In this case $I_e = 1$ ($\ddot{x}g$) and $I_m = I_{4\times 4}$ (x, $\ddot{x}_1$, $\ddot{x}_2$, $\ddot{x}_3$).

The recorded velocity data and the control signal from the LQG controller were used to define the training data for the fuzzy controller. The first and third floor velocities are the FIS inputs while the command current represents the fuzzy outcome. An initial, increasing and decreasing step sizes of 0.12, 1.20 and 0.8, respectively during 200 epochs are the parameters involved in the ANFIS optimization procedure. The optimal number of membership functions (MFs) was defined through a trial-and-error process. In this case, six bell-shaped MFs were used to model each input variable (first and third floor velocities). The resultant fuzzy surface is shown in Figure 5.
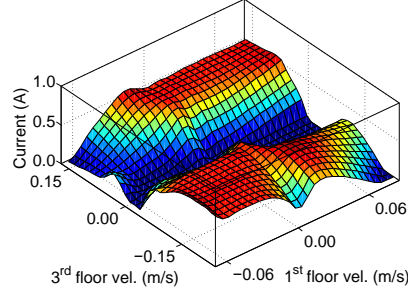
Figure 5. Fuzzy surface of the neuro-fuzzy controller.

When the first and third floor velocities are large and have the same signs, the required control signal is also large. When both velocities are large but have opposite signs, the fuzzy controller delivers the lowest control signal. Besides, the minimum damping force requirement is located around the central zone comprising small floor velocities.

4.   Numerical analysis

A set of numerical simulations was carried out to obtain the response of the three DOF structure using the MR damper in a passive OFF mode (zero voltage/current input), passive ON mode (maximum value of the operating voltage/current) and semi-active control mode. A Simulink model of the semi-active control system is shown in Figure 6.
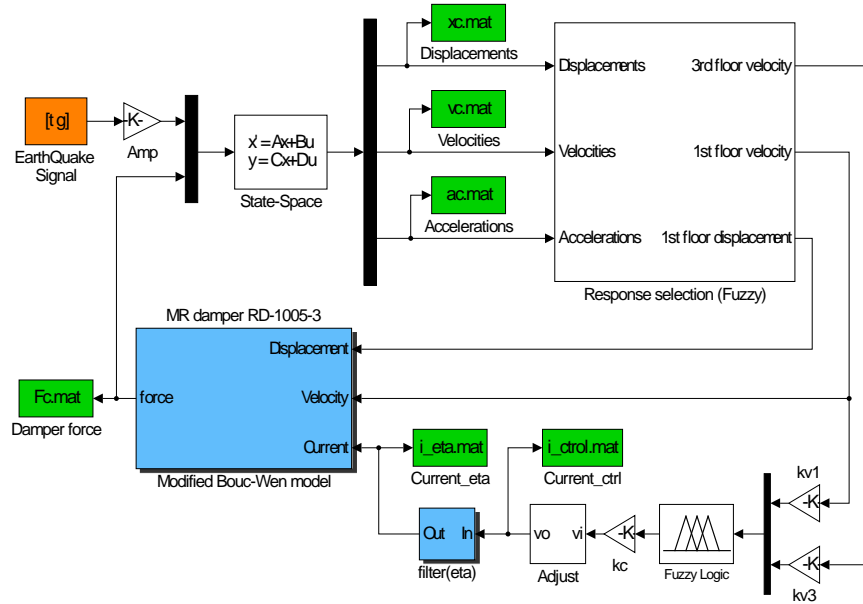
Figure 6. Simulink model of the semi-active control system.

Figure 7 displays the structural response of each floor obtained with the proposed fuzzy based control system along with the uncontrolled response of the third floor during the numerical simulation. As can be seen, the proposed semi-active control system achieves a good performance in reducing the structural responses using only floor velocities as the reference (input) signals to compute the control action. In fact, the main advantage of this fuzzy logic based control system is that only the first and third floor velocities of the structure are required to determine the desired control signal. This means that the damping force generated during the control process does not need to be monitored, as happens in other controllers such as the clipped-optimal algorithm.
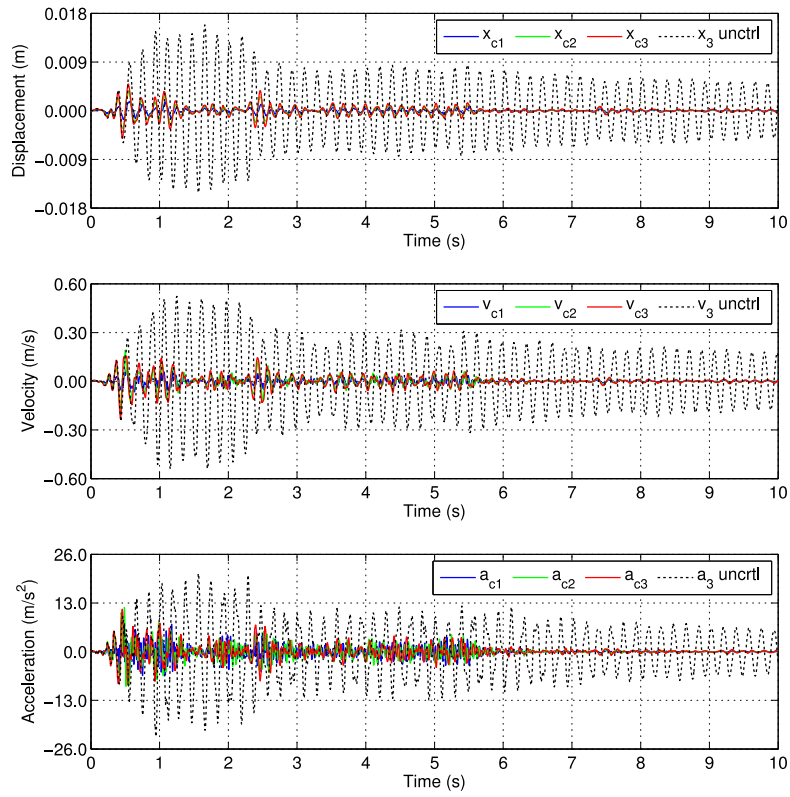
Figure 7. Structural response with the fuzzy logic controller (FLC).

The damper force and the control signal of the semi-active control system are shown in Figure 8. As can be seen, the proposed fuzzy controller provides intermediate levels of control current instead of the bi-state control signal used in many semi-active controllers allowing intermediate damping states over the full range of operation of the device. Generally, the results show that the proposed fuzzy logic controller is capable to determine with sufficient reliability the required control action to reduce the response of the 3DOFs system.

103
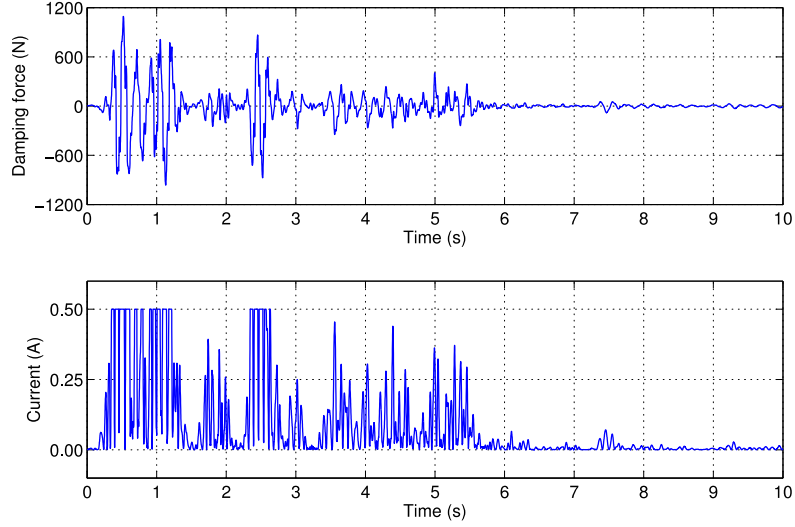
Figure 8. Damper force and corresponding operating current (Semi-active control – FLC).

The hysteretic behavior of the MR damper during the numerical simulation is also characterized in Figure 9. As can be seen the proposed fuzzy based controller explores the operating range of the actuator and globally, the hysteretic loops are in line with those found with the other controllers although in this case presenting a more irregular shape.
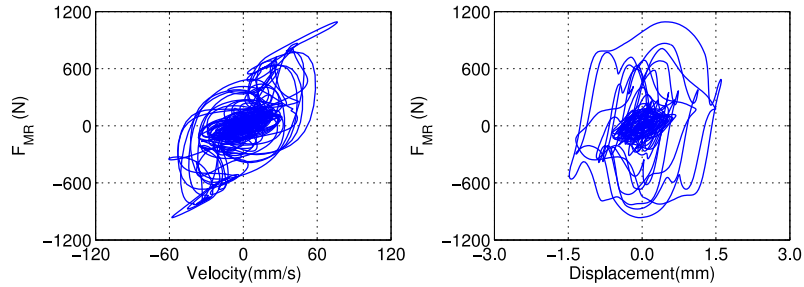
Figure 9. RD-1005-03 MR damper control force (Semi-active control – FLC).

The main drawback of designing fuzzy controllers is related with the definition of the membership function parameters and the inference rules that relate the inputs with the desired control output. Structural systems usually include several sources of non-linearities and/or uncertainties that hinder the development of simple control rules based on human knowledge about the system behavior. In these cases, soft computing techniques such as ANFIS or genetic algorithms (GAs) are most appropriate to find the best set of fuzzy rules or adjustment of a set of fuzzy parameters in accordance with a given training data for a desired control action.

104

The evaluation criteria are based on a comparison of the peak responses of each controlled system to those of the uncontrolled system and passive modes. The results of this analysis are summarized in Table 2. The results show the effectiveness of the proposed fuzzy based controller in reducing the response of the structure. In this case the fuzzy controller outperforms the passive control modes in almost all peak responses (with exception of the 1st floor acceleration, although with a significant reduction compared with the uncontrolled case). The results also show that using the MR damper in a semi-active control mode results in lower peak drifts compared with the passive ON configuration namely in the two upper floors.

Table 2. Peak responses under the time-scaled El-Centro NS earthquake (0.2t).

Control strategy		$x\,(\mathrm{cm})$	$\dot{x}\,(\mathrm{cm/s})$	$\ddot{x}\,(\mathrm{cm/s^2})$	$drift\,(\mathrm{cm})$	$f(\mathrm{N})$
Uncontrolled		0.695 1.251 1.587	27.09 45.78 54.02	1305 1736 2272	0.695 0.581 0.371	----
Passive OFF	Modified Bouc-Wen	0.518 0.907 1.191	20.02 34.51 42.79	999 1358 1791	0.518 0.443 0.292	166.4
Passive ON	**Modified Bouc-Wen**	**0.171** **0.423** **0.560**	**7.77** **19.36** **25.58**	**613** **1066** **1366**	**0.171** **0.253** **0.208**	**1048.9**
Fuzzy logic control (ANFIS)		0.164 (-4%) 0.410 (-3%) 0.529 (-6%)	7.07 (-9%) 17.59 (-9%) 23.64 (-8%)	739 (0.21) 963 (-0.10) 1285 (-0.06)	0.164 0.247 0.194	909.8

Note: Values under parenthesis are the percentage of reduction with respect to the passive ON case. Negative numbers indicate a response reduction. Passive OFF represents zero current input and passive ON represents the maximum operating current.

5. Conclusions

As can be verified, both passive and semi-active control systems are effective in reducing the system response. In this case the semi-active controller allows a more efficient management of the control forces with a better performance in reducing the structural response. It can be concluded that the proposed semi-active strategy is an efficient control approach outperforming the passive control modes. This study reveals the patent advantage of a semi-active fuzzy based control system over a fully passive system in increasing the level of seismic protection through the reduction of structural responses, at least in this non-collocated control system in which one MR damper is being used to control the lateral motion of the upper floors.

References

[1] Jang, J.R. ANFIS: Adaptive-network-based fuzzy inference system. *IEEE Transactions on Systems, Man and Cybernetics*, 23(3), 1993, 665-685.

[2] Sadeghian, A.R. Nonlinear Neuro-Fuzzy Prediction: Methodology, Design and Applications Fuzzy Systems. *The 10th IEEE International Conference on Fuzzy Systems*, (2), 2001, 1022-1026.

[3] Dyke, S.J., and Spencer, B.F. A comparison of semi-active control strategies for the MR damper. *Proceedings of the IASTED International Conference, Intelligent information Systems*, 1997, 580-584.

[4] Jansen, L.M., and Dyke, S.J. Semi-active control strategies for MR dampers: comparative study. *Journal of Engineering Mechanics*, Vol. 125, No. 8, 2000, 795-803.

[5] Braz-Cesar, M., and Barros, R. Experimental and numerical analysis of MR dampers, *COMPDYN 2013 – 4th International Conference on Computational Methods in Structural Dynamics & Earthquake Engineering*, 2013.

Manuel Braz César, Assistant Professor: Department of Applied Mechanics of the Polytechnic Institute of Bragança, Quinta de Santa Apolónia, 5300-253 Bragança, Portugal (*brazcesar@ipb.pt*). The author gave a presentation of this paper during one of the conference sessions.

Rui Barros, Associate Professor: Department of Civil Engineering of the Faculty of Engineering of the University of Porto, Rua Dr. Roberto Frias s/n, 4200-465 Porto, Portugal (*rcb@fe.up.pt*).

Vibration control of asymmetric structures using MR dampers (CON252-15)

Manuel Braz-César, Rui Barros

Abstract: This paper is devoted to study the effectiveness of semi-active control systems with MR dampers to reduce lateral-torsional responses of irregular structures, in particular plan asymmetric building structures. Basic concepts and the analytical formulation of asymmetric structural systems are initially provided. Then, several numerical simulations comprising a two-story, one bay building structure excited by an earthquake ground motion will be used to demonstrate the effectiveness of a non-collocated passive and semi-active control systems in mitigating seismic-induced vibrations. The passive configurations are accomplished using the MR damper as passive energy dissipation devices while the semi-active configurations make use of the controllable nature of this type of actuators. The numerical results achieved with uncontrolled and passive configurations are compared with those of several semi-active controllers to evaluate the performance of each control scheme in reducing the coupled lateral-torsional response of the plan asymmetric structure due to seismic loading.

1. Introduction

In general, building structures are irregular and complex systems that usually present plan and elevation asymmetries as a result or their stiffness, strength and/or mass distribution. In such cases the control system must be designed to deal with coupled lateral-torsional vibrations produced by wind or earthquake loads. Plan asymmetries generate correlated plan translations and rotations that lead to an uneven deformation distribution demand among resisting planes namely at the building edges. The significantly different deformations of the structural elements increase force and ductility demand leading to different damage levels in these elements, which result in structural systems with asymmetrical distribution of resistant capacity (i.e., large capacity in some load-resisting planes). In this context, it has been shown that supplemental energy dissipation systems represent an effective approach of reducing the magnitude of both plan translations and rotations in irregular building structures [1-6].

In this regard, the variable damping provided by MR dampers constitutes an important feature to develop enhanced control systems specifically designed to reduce the correlation between translation and rotation motions. In fact, several studies had already been conducted to investigate the effectiveness of these semi-active actuators to control lateral-torsional coupled responses of asymmetric building structures [7-9].

The present paper is intended to provide an insight into the seismic response control of irregular building structures in order to complement the research work undertaken in this thesis about semi-active control with MR dampers. Thus, the main objective consists in evaluate the effectiveness of MR dampers to mitigate the response of a seismic-excited asymmetric structures namely asymmetric-plan systems. Initially, basic concepts and the theoretical background about the dynamic behavior of irregular building structures are provided. The operation of a semi-active control system with MR dampers for single and multi-story buildings with asymmetric plan is then presented. A set of numerical simulations is developed to evaluate the effectiveness of MR dampers in mitigating correlated translation and rotation motions of a two-story, one bay building structure with one-way asymmetric structural plan under an unidirectional earthquake ground motion. In this case, two MR dampers installed between the base and the first floor (i.e., in a non-collocated configuration) with a symmetrical distribution with respect to the earthquake loading direction are employed as passive and semi-active control devices. The results of the passive and semi-active configurations are compared with those of the uncontrolled case. Finally, the effectiveness and performance of each control system is analyzed and evaluated emphasizing the main advantages and limitations of each methodology in controlling seismic response of the structure.

2. Numerical model

In order to investigate the effectiveness of semi-active control systems for irregular structures, the following presents a numerical study of a two-story asymmetric structure under unidirectional seismic loading whose response is being controlled through two MR damper located between the base and the first floor. The present numerical example consists of a reduced scale model that represents a two-story three-dimensional building structure subjected to a unidirectional seismic excitation as shown in Figure 1. The floor diaphragm can be considered rigid in its own plane and therefore the dynamic analysis is conducted using a lumped mass model where the whole story mass is lumped at the floor level. The properties of the lumped mass structure are given in Table 1.

Table 1. Parameters of the two-story building structure.

Parameter	Value	Parameter	Value
Aspect ratio of the floor slab (l_y/l_x)	0.75	Damping ratio for the 1st and 4th modes (ζ_i)	2%
Lumped mass of the first floor, m_1	1750 kg	Polar moment of inertia (1st floor), I_1	3646 kg-m^2
Lumped mass of the second floor, m_2	1750 kg	Polar moment of inertia (2nd floor), I_2	3646 kg-m^2
Lateral stiffness of each column (x- direction), k_{xi}	1050 kN/m	Lateral stiffness of each column (y- direction), k_{yi}	355 kN/m
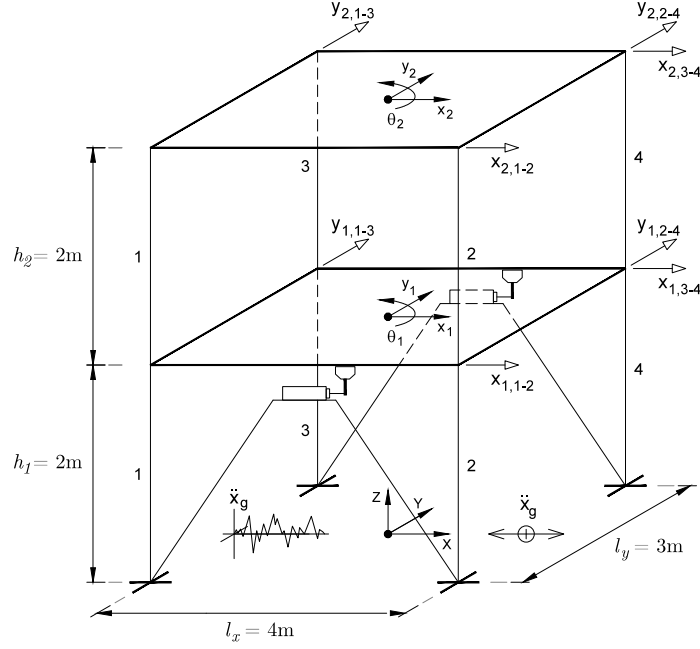
Figure 1. Representation of the two-story building under unidirectional seismic excitation - Passive and semi-active control with two MR dampers at the first floor.

The simulations are conducted using the modified Bouc-Wen model for the MR dampers and a clipped-optimal LQG controller. The performance of the control system is evaluated by comparing the responses due to El Centro earthquake excitation (1940 N-S component) for passive and semi-active configurations with the corresponding uncontrolled response. Note that the mass and stiffness properties were predefined in such a way that the building structure represents a reduced-scale model (1:2). Thus, the seismic signal was scaled in time by a factor of 0.5 to adjust the seismic signal to the magnitude of structural deformations that would be observed in experimental tests (Figure 2).
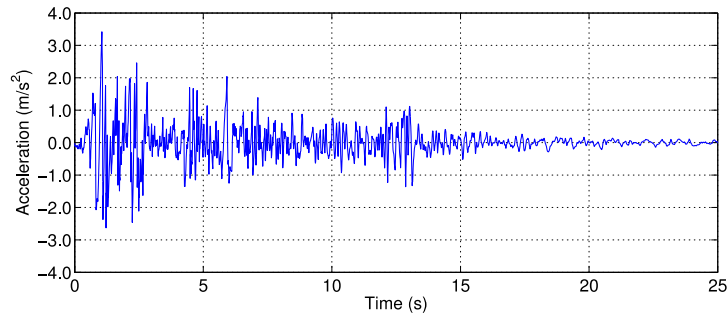
Figure 2. Time-scale El-Centro NS earthquake ground motion (0.5t).

Due to the rigid diaphragm approximation, the response of the structure is described by three DOFs per floor, i.e., two orthogonal translations and a rotation about the vertical axis producing a six DOFs system. Consequently, the displacement vector can be expressed as

$$X(t) = \left\{ x_1(t), y_1(t), \theta_1(t), x_2(t), y_2(t), \theta_2(t) \right\}^T \tag{1}$$

where $x_i(t)$ and $y_i(t)$ denotes the relative displacements of the center of mass of the ith floor in the x- and y- directions, respectively, and $\theta_i(t)$ is the vector of rotations of the ith floor about the vertical axis. The asymmetric configuration of the two-story building structure is achieved by adding an eccentric point mass $m_a = 250$ kg in both floors as shown in Figure 3. The resultant system has a symmetric mass distribution on the y- direction and a non-symmetric distribution with respect to the x- axis, which is characterized by the mass eccentricity e_y depicted in Figure 3.
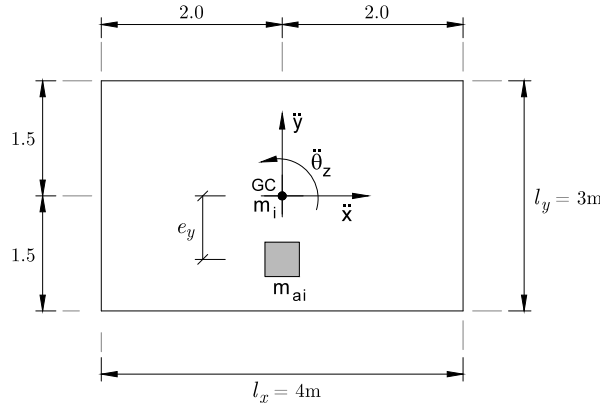
Figure 3. Floor slab with asymmetric mass distribution.

The equation of motion of the two-story building structure ($n= 2$, where n denotes the number of floors) subjected to unidirectional earthquake excitation $\ddot{x}_g$ (x- direction) and comprising two control devices ($m= 2$, where m are the number of control forces) can be expressed as

$$\mathrm{M}\ddot{X}(t) + \mathrm{C}\dot{X}(t) + \mathrm{K}X(t) = -\mathrm{M}\lambda\ddot{x}_g(t) + \Gamma f(t) \tag{2}$$

where M, C and K are the mass, damping and stiffness matrices, respectively. The seismic loading is applied in the structural system using the location vector

$$\lambda = \left\{ 1, 0, 0, 1, 0, 0 \right\}^T \tag{3}$$

The force vector describing the two control forces is given by

$$f(t) = \left\{ f_{c1}(t), f_{c2}(t) \right\}^T \tag{4}$$

and the correspondent location matrix can be expressed as

$$
\Gamma = \begin{bmatrix} 1 & 1 \\ 0 & 0 \\ l_y/2 & -l_y/2 \\ 0 & 0 \\ 0 & 0 \\ 0 & 0 \end{bmatrix}
\tag{5}
$$

Since the slab has a rigid body motion, the mass matrix can be determined defining a lumped system with two masses with mass eccentricities $y_i = e_y$ and $x_i = e_x = 0$. Furthermore, the additional point mass m_a has a negligible rotational inertia and therefore the mass matrix is expressed in accordance with the displacement vector as

$$
M = \begin{bmatrix} m_{1x} + m_{1a} & 0 & -m_{1a}e_y & 0 & 0 & 0 \\ 0 & m_{1y} + m_{1a} & 0 & 0 & 0 & 0 \\ -m_{1a}e_y & 0 & I_1 + m_{1a}e_y^2 & 0 & 0 & 0 \\ 0 & 0 & 0 & m_{2x} + m_{2a} & 0 & -m_{2a}e_y \\ 0 & 0 & 0 & 0 & m_{2y} + m_{2a} & 0 \\ 0 & 0 & 0 & -m_{2a}e_y & 0 & I_2 + m_{2a}e_y^2 \end{bmatrix}
\tag{6}
$$

where m_i and I_i represent the lumped masses and moments of inertia of the ith floor, respectively (with $i = 1, 2$). The stiffness matrix is expressed in accordance with the displacement vector as

$$
K = \begin{bmatrix} K_{x1} + K_{x2} & 0 & 0 & -K_{x2} & 0 & 0 \\ 0 & K_{y1} + K_{y2} & 0 & 0 & -K_{y2} & 0 \\ 0 & 0 & K_{\theta1} + K_{\theta2} & 0 & 0 & -K_{\theta2} \\ -K_{x2} & 0 & 0 & K_{x2} & 0 & 0 \\ 0 & -K_{y2} & 0 & 0 & K_{y2} & 0 \\ 0 & 0 & -K_{\theta2} & 0 & 0 & -K_{\theta2} \end{bmatrix}
\tag{7}
$$

where

$$
K_{xi} = \sum_{i=1}^{2} k_{xi}, \quad K_{yi} = \sum_{i=1}^{2} k_{yi}, \quad K_{\theta i} = \sum_{i=1}^{2} k_{xi}y_i^2 + \sum_{i=1}^{2} k_{yi}x_i^2
\tag{8}
$$

are the stiffness coefficients (the coordinates x_i and y_i can be expressed in terms of the in-plane dimensions of the floor slab l_{ix} and l_{yi} in the x- and y- directions, respectively). The damping matrix can be constructed from the mass and stiffness matrices using the so-called proportional damping (or Rayleigh damping) which can be expressed as

111

$$C = \alpha M + \beta K \tag{9}$$

where α and β are coefficients that can be determined from two vibration modes of the system (in this case, α = 0.476685 and β =0.000671). The state space equation of the controlled structure can be defined as

$$\dot{z}(t) = Az(t) + Bf(t) + E\ddot{x}_g(t) \tag{10}$$

where A is the system matrix, E is the input vector that accounts for the location of the earthquake loading, B is an additional matrix accounting for the position of the control forces in the structure and f is a column vector with the control forces, which are given by

$$A = \begin{bmatrix} 0 & I \\ -M^{-1}K & -M^{-1}C \end{bmatrix}, \quad B = \begin{bmatrix} 0 \\ -M^{-1}\Gamma \end{bmatrix},$$

$$f = \left\{ f_{c1}(t), f_{c2}(t) \right\}^{T}, \quad E = \begin{bmatrix} 0 \\ -\lambda \end{bmatrix} \tag{11}$$

The response of the system can be determined using the state space output vector

$$y(t) = Cz(t) + Df(t) + F\ddot{x}_g(t) \tag{12}$$

where matrices C, D and F are computed as
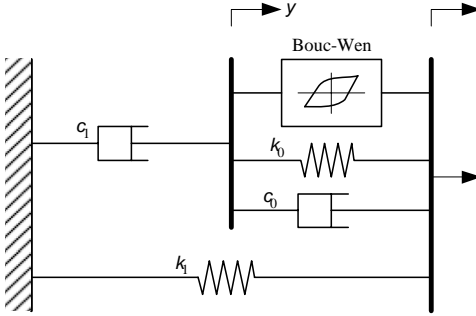
$$C = \begin{bmatrix} I & 0 \\ 0 & I \\ -M^{-1}K & -M^{-1}C \end{bmatrix}, \quad D = \begin{bmatrix} 0 \\ -M^{-1}\Gamma \end{bmatrix}, \quad F = \begin{bmatrix} 0 \\ -\lambda \end{bmatrix} \tag{13}$$

in the case of displacements, velocities and accelerations of each floor/mass are being monitored.

3. Numerical Simulations

Next, a set of numerical simulations is carried out to determine the responses of the two-story asymmetric system. Initially, the response of the uncontrolled structure was obtained from Equation 10 by setting f_c= 0 (i.e., no control forces). The response of the uncontrolled system will be used as the reference signal to evaluate the performance of the passive and semi-active control systems. A new numerical simulation was carried out to obtain the responses of the structure for the passive OFF and passive ON modes with the MR damper. In this case the actuators act on the first floor/mass in a passive control mode (i.e., as passive energy dissipation devices) producing two passive control forces f_{c1} and f_{c1} along the x- direction. The control devices are used to reduce the lateral-torsional response of the structural system. The modified Bouc-Wen model was selected to simulate the behavior of the MR damper (RD-1005-03). The numerical formulation and the corresponding model parameters are presented in Table 2 [10].

Table 2. Modified Bouc-Wen model - Parameters of the RD-1005-3 MR damper.

Modified Bouc-Wen model

$$F(t) = c_1 \dot{y} + k_1(x - x_0)$$

$$\dot{y} = \frac{1}{c_0 + c_1} \left[\alpha z + c_0 \dot{x} + k_0(x - y) \right]$$

$$\dot{z}(t) = -\beta \left| \dot{x}(t) \right| z(t) \left| z(t) \right|^{n-1} - \gamma \dot{x}(t) \left| z(t) \right|^{n} + A \, \dot{x}(t)$$

Current **independent** parameters	A [-]	β [mm^{-1}]	γ [mm^{-1}]	k_0 [N/mm]	f_0 [N]	n
	10.013	3.044	0.103	1.121	40	2
Current **dependent** parameters	$\alpha(I) = -826.67I^3 + 905.14I^2 + 412.52I + 38.24$ [N] $c_0(I) = -11.73I^3 + 10.51I^2 + 11.02I + 0.59$ [N.s/mm] $c_1(I) = -54.40I^3 + 57.03I^2 + 64.57I + 4.73$ [N.s/mm]					

The Clipped-Optimal (CO) algorithm represents a well-known semi-active control strategy for MR dampers. This classical controller has been shown to be very efficient in estimating the control signal allowing it to explore the variable damping force of these semi-active actuators. The basic idea is to append n force feedback loops to induce each device to produce approximately a desired control force [11-14]. In fact, this control strategy combines two controllers:

- A primary controller that includes an optimal control unit which is responsible for determining the optimal or desired control forces of an ideal active control system that should be applied to the structure to reduce the system response;

- A secondary controller or bi-state selector (clipping system). Since only the current/voltage applied to the current driver of the MR damper can be directly controlled, this controller has the function to generate the corresponding control signal in the form of a bi-state control output by clipping the optimal control forces. This accounts for the non-linear nature of MR dampers ensuring that they only produce dissipative forces (i.e., by adapting the ideal control action to the semi-active nature of the actuator).

113

In this case the primary controller uses a Linear Quadratic Gaussian (LQG) regulator to compute the optimal control forces. The LQG controller combines a Linear Quadratic Regulator (LQR) with a Kalman filter or Linear Quadratic Estimator (LQE). The Kalman filter is used to reconstruct the state vector based on a few output measurements of a noisy system and then the LQR component is used to compute the optimal input signal based on the estimated state vector. The observer gain L must be adjusted to achieve the required performance. A high gain allows the filter to follow the observations more closely while a low gain follows the predictions more closely. This is accomplished by setting

$$Q_w = q_w I_e, \quad R_v = r_v I_m \tag{14}$$

where I_e and I_m are identity matrices related with the number of excitation inputs and measurement signals, respectively. Finally, the LQG controller is a combination of a Kalman filter (or a LQE) with a linear quadratic regulator (LQR), i.e.,

$$\dot{\hat{x}} = (A - LC)\hat{x} + Bu + Ly$$
$$u = -K\hat{x} \tag{15}$$

where K and L are the LQR and LQE gain matrices, respectively that need to be adjusted to obtain the desired control action. The solution is based on the separation principle in which the full state feedback controller (i.e., the LQR) and the Kalman filter are designed independently and then combined to form the LQG compensator.

The selection of Q_w and R_v depends on the level of accuracy attributed to the model and the measurements. For an accurate system model measured with poor sensors one should probably select Q_w to be larger than R_v while for a poorly modeled system with accurate measurements one should probably choose R_v to be larger than Q_w. A common approach is to set one of the tuning parameters and adjust the other parameter until the result is satisfying. The key is to have a Kalman filter that removes as much noise as possible without being to slow to adapt to changes.

The secondary controller is used to convert the control forces estimated by the primary controller into a bi-state control signal (bang-bang/on-off controller) to command the MR actuators. The damping forces generated by the MR dampers are dependent on the local responses of the structural system and therefore the devices cannot always produce the desired optimal control forces. Consequently, only the control voltage/current can be directly controlled to change the damper force and a force feedback loop is then incorporated in the control algorithm to make the MR damper to generate approximately the desired optimal control force. To achieve this objective, the following command signal algorithm is applied

$$f_{MR} = \begin{cases} f_c, & f_c \cdot \dot{x} < 0 \\ 0, & \text{otherwise} \end{cases} \tag{16}$$

When the MR damper is delivering the desired optimal force, the operating voltage/current should remain the same. If the magnitude of the damper force is smaller than the magnitude of the desired optimal force and the two forces have the same sign, the voltage applied to the current driver is increased to the maximum level. Otherwise, the commanded voltage is set to zero. The algorithm for selecting the command signal for the ith MR damper can be stated as

$$v_i = V_{\max} H\left[\left(f_{ci} - f_i\right) f_i\right] \tag{17}$$

where $V_{\max}$ is the saturation voltage/current of the MR damper, f_{ci} is the desired optimal control force, f_i is the measured damper force and H is the Heaviside step function.

Hence, the clipped-optimal LQG control algorithm is a semi-active controller that combines a LQG method with a bi-state selection unit. The linear optimal controller is used to compute the desired control force f based on the measured structural responses y and control force vector f applied to the structure through the semi-active device. Next, a secondary controller comprising a clipping unit generates a bi-state control signal based on the optimal force calculated by the first controller so that it can be adapted to the dissipative nature of the MR damper allowing this actuator to generate approximately the desired control force [11-14]. To illustrate the application of the type of control scheme, in the present example it is assumed that acceleration measurements and displacement across the dampers are the only state variables available to design the optimal controller. A probable location of the accelerometers is depicted in Figure 4.
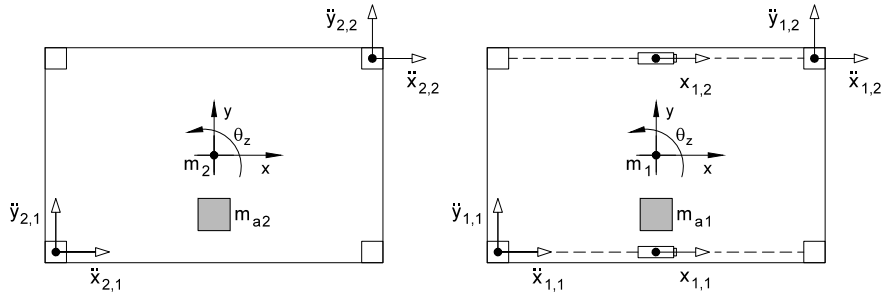
Figure 4. Location of the measurement sensors in each floor (Eight accelerometers and two LVDTs).

The translational and rotational response of the asymmetric structure is described by four accelerometers on each floor, two on the x- direction and two on the y- direction, with a total of eight accelerometers. Additionally, two displacement sensors (e.g., two LVDTs) are used to measure the displacements across the two dampers, which represent the displacement of each corner of the first floor slab in the x- direction. These sensor measurements define the output response vector

$$y = \left\{ x_{1,1}, x_{1,2}, \ddot{x}_{1,1}, \ddot{x}_{1,2}, \ddot{y}_{1,1}, \ddot{y}_{1,2}, \ddot{x}_{2,1}, \ddot{x}_{2,2}, \ddot{y}_{2,1}, \ddot{y}_{2,2} \right\}^T \tag{18}$$

The Kalman gain L is calculating by adjusting Q_w and R_v. It is assumed that each sensor has identically distributed and statistical independent Gaussian white noise and therefore the covariance between the measurement noise and the process noise. Since the measurement noise is equal and independent for all outputs, R_v is a diagonal matrix. Then, Q_w is tuned through q_w until the LQE output is adequate. Likewise, the weighting matrices Q and r of the LQR controller must be adjusted in order to determine the state gain matrix K. In the present example different configurations of the weighting matrix Q and the control parameter r were evaluated by measuring the effect of each combination in the system response. The following weighting parameters provided the best results in reducing the structural responses of the asymmetric system

$$Q = \begin{bmatrix} K & 0 \\ 0 & 0 \end{bmatrix}; \qquad R = r\begin{bmatrix} 1 & 0 \\ 0 & 1 \end{bmatrix}; \qquad r = 2 \times 10^{-5} \tag{19}$$

On this basis, the proposed LQG controller for the two-story building structure has been modeled and simulated in Matlab/Simulink as shown in Figure 5 (the bi-state selector is within the Clipped LQG block). As can be seen, the controller uses the floor accelerations and the displacements across the dampers as the system outputs to compute the control signal. Indeed, a semi-active control strategy based on acceleration feedback seems to be more appropriate for structural control applications instead of full-state feedback or velocity feedback controllers.
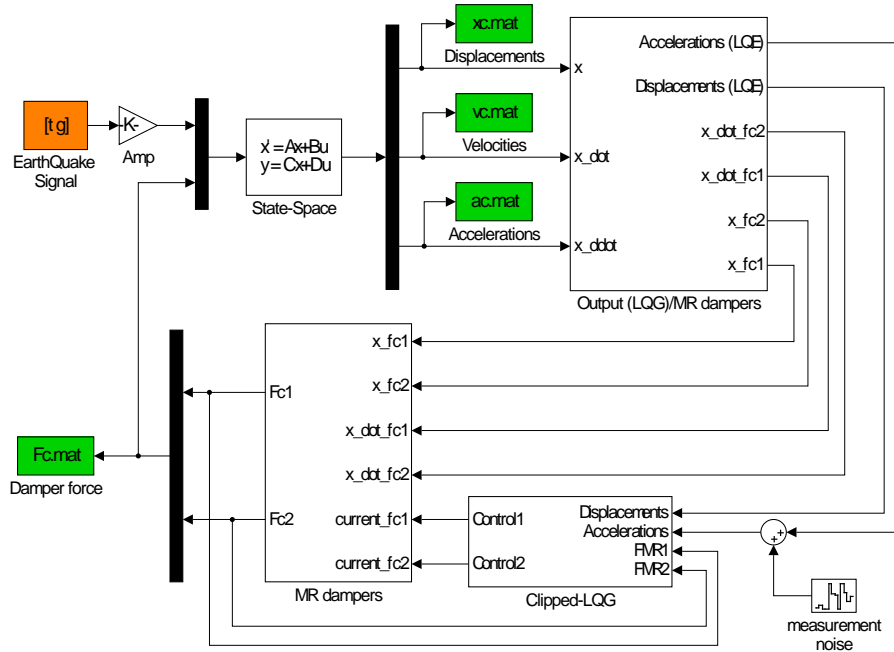
Figure 5. Block diagram of the clipped-optimal LQG controller.

The evaluation criteria are based on a comparison of the peak responses of each controlled system to those of the uncontrolled system and passive modes. The results of this analysis are summarized in Table 3.

Table 3. Peak responses under the time-scaled El-Centro earthquake (0.5*t*).

Control strategy		x (cm)	$\dot{x}$ (cm/s)	$\ddot{x}$ (cm/s²)	q (rad)	$\dot{\theta}$ (rad/s)	$\ddot{\theta}$ (rad/s²)	drift (cm)	$\Delta\theta/h$ (rad)	$f(\mathrm{N})$
Uncontrolled		1.005	28.30	813	8.6e-4	0.028	0.901	1.005	8.6e-4	--
		1.652	42.76	1211	1.4e-3	0.041	1.395	0.658	5.2e-4	--
Passive OFF	Modified Bouc-Wen	0.933	25.61	728	7.6e-4	0.024	0.805	0.933	7.6e-4	213
		1.523	39.40	1100	1.2e-3	0.036	1.227	0.603	4.6e-4	183
Passive ON	Modified Bouc-Wen	**0.540**	**15.03**	**462**	**3.8e-4**	**0.0125**	**0.513**	**0.540**	**3.8e-4**	**1546**
		0.857	**24.43**	**837**	**6.3e-4**	**0.0199**	**0.691**	**0.367**	**2.5e-4**	**1459**
Clipped-Optimal LQG		**0.527**	**13.55**	531	**3.3e-4**	0.0119	0.524	**0.528**	**3.3e-4**	**1421**
		0.819	23.77	**729**	6.0e-4	**0.0191**	0.738	**0.346**	2.7e-4	**1416**

Note: The first and second lines represent the peak responses for the first and second floors, respectively (first and second MR damper in the case of the damper force). Passive OFF represents zero current input and passive ON represents the maximum operating current.

4. Conclusions

Regarding the passive control mode, it can be seen that the passive OFF configuration has almost a reduced effect in the system response (around 10%). The passive ON mode has a major effect in the system response that results in peak responses being significantly reduced, especially the torsional motions (around 55%). As to be expected, the maximum passive control action is achieved by keeping the MR damper permanently switched on, which is clearly observable in the results of the numerical analysis.

Generally, the LQG controller is able to reduce both translational and torsional responses of the asymmetric structure, offering significant performance gains in controlling the torsional motion of the floor decks. Although in some cases the passive configuration performed slightly better than the semi-active system, the latter present overall the best performance. The proposed controller presents a performance improvement in reducing the peak responses exhibiting the best overall performance when compared with the passive configurations. The maximum ratios of the peak responses attained with this controller are generally smaller than that of passive ON configuration, with the significant exception of the angular acceleration of the second floor. Besides, the peak control force achieved by the clipped-optimal LQG algorithm has the lowest value (1416 kN).

References

[1] Jangid, R.S., and Datta, T.K. (1997). Performance of multiple tuned mass dampers system for torsionally coupled system. *Earthquake Engineering and Structural Dynamics* 26, 1997, 307–317.

[2] Goel, R.K. (1998). Effects of supplemental viscous damping on seismic response of asymmetric-plan systems. *Earthquake Eng. and Struct. Dynamics*, 27(2), 1998, 125–141.

[3] Lin, W.H., and Chopra, A. K. Understanding and predicting effects of supplemental damping on seismic response of asymmetric one-storey system. *Earthquake Engineering and Structural Dynamics* 30, 2001, 1475–1494.

[4] Garcıa, M., Llera, J.C., and Almazan, J.L. Torsional balance of plan asymmetric structures with viscoelastic dampers, *Eng. Structures* 29, 2007, 914–932.

[5] Mevada, S.V., and Jangid, R.S. Seismic response of asymmetric systems with linear and non-linear viscous dampers. *International Journal of Advanced Structural Engineering*, 2012.

[6] Joshi, J.H., Mevada, S.V., and Patel, S.B. Response of Two-Way Asymmetric System with Linear & Non Linear Viscous Dampers under Bi-Directional Earthquake. *International Journal of Innovations in Engineering and Technology* 2(2), 2013, 92–102.

[7] Yoshida, O., and Dyke, S.J. Response Control of Full-Scale Irregular Buildings using Magnetorheological Dampers. *Journal of Structural Engineering*, Vol. 131, No. 5, 2005, 734–742.

[8] Yoshida, O., Dyke, S.J., Giacosa, L.M., and Truman, K.Z. Experimental Verification on Torsional Response Control of Asymmetric Buildings Using MR Dampers. *Earthquake Engineering and Structural Dynamics* 32, 2003, 2085–2105.

[9] Bharti, S.D., and Shrimali M.K. (2012). Seismic Response Control of Asymmetric Plan Building with Semiactive MR Damper, *15 WCEE*, Portugal, 2012.

[10] Braz-César, M. *Vibration Control of Building Structures using MR dampers*, Ph.D. thesis, Faculty of Engineering of the University of Porto, 2015, Prof. Rui Barros.

[11] Dyke, S.J., Spencer, B.F., Sain, M.K., and Carlson, J.D. Seismic Response Reduction Using Magnetorheological Dampers. *Proceedings of the IFAC World Congress*, USA, 1996, 145–150.

[12] Dyke, S.J., Spencer, B.F., Sain, M.K., and Carlson, J.D. (1996). Modeling and Control of Magnetorheological Dampers for Seismic Response Reduction, *Smart Materials and Structures* 5, 1996, 565–575.

[13] Dyke, S.J., and Spencer, B.F. A comparison of semi-active control strategies for the MR damper. *IASTED Intl. Conf. on Intelligent Information Systems*. IEEE Computer Society, 1997, 580–584.

[14] Dyke, S.J., Spencer, B.F., Sain, M.K., and Carlson, J.D. Experimental Verification of Semi-Active Structural Control Strategies Using Acceleration Feedback. *Proc. of the 3rd Intl. Conf. on Motion and Vibration Control*, Vol. 3, 1996, 291–296.

Manuel Braz César, Assistant Professor: Department of Applied Mechanics of the Polytechnic Institute of Bragança, Quinta de Santa Apolónia, 5300-253 Bragança, Portugal (*brazcesar@ipb.pt*). The author gave a presentation of this paper during one of the conference sessions.

Rui Barros, Associate Professor: Department of Civil Engineering of the Faculty of Engineering of the University of Porto, Rua Dr. Roberto Frias s/n, 4200-465 Porto, Portugal (*rcb@fe.up.pt*).

Multi-time scale nonlinear interactions of two coupled forced oscillators
(CON138-15)

Simon Charlemagne, Claude-Henri Lamarque, Alireza Ture Savadkoohi, Pierre Abdoulhadi

Abstract: Nonlinear interactions between two coupled oscillators at different scales and states of time are discussed. We study a class of two degrees of freedom coupled nonlinear oscillators. One of them is a linear master system while the other one is a nonlinear energy sink, that is excited by a sinusoidal periodic force. The aim is to control and/or to harvest the vibratory energy of the main oscillator by the slave oscillator that is under external sinusoidal force and possesses very light mass (compared to the first one) and nonlinear potential(s). Fixed points of the system at *fast time scale* provide a three dimensional invariant which depends on the external forcing amplitudes while detected stability borders explain bifurcation(s) of the overall system during energy exchanges between two oscillators. Modulations of the system at *slow time scale* around its invariant at fast time scale lead to predictions of equilibrium and singular points that permit to trace periodic and strongly modulated responses of the system during extreme energy exchanges between two oscillators. Detected invariant, equilibrium and singular points at different scales and states of the time provide useful tools for designing a controller and/or a harvester oscillator.

1. Introduction

Vibratory energy exchanges between coupled oscillators can be endowed for passive control and/or energy harvesting. Energy transfer of main structural systems can be carried out via coupling linear systems, known as Frahm or tuned mass dampers [1], or nonlinear systems such as nonlinear energy sink (NES) devices [2, 14]. The transfer of the vibratory energy of main structures to the NES is carried out via nonlinear vibratory interactions of two systems that is accompanied by bifurcations [13]. Most of past studies are based on the assumption that the NES possess purely smooth nonlinearity, mainely cubic, with no linear part. Some works are carried out which consider nonsmooth nonlinearities for NES systems, such as vibro-impact NES [3, 4, 10] or nonsmooth NES [5–7, 12, 15]. In the current study, we try to enlighten the vibratory energy exchanges between a vertical forced main linear oscillator and a coupled vertical forced NES with nonsmooth potential. Organization of the paper is as it follows: Mathematical model of the considered system and its initial

treatments which include changes of the time domain and system variables, complexification and implementing the Galerkin's method are represented in Sect. 2. The time multi-scale behaviors of the system which allows to detect the invariant manifold, its stable areas and equilibrium and singular points are discussed in Sect. 3. Comparison between analytical results and predictions versus numerical ones are presented in Sect. 4. Finally, the paper is concluded in Sect. 5.

2. Representation of the system and its re-scaling process

The mathematical model of the system under consideration is depicted in Fig. 1. The overall system is under gravity loads, i.e. g. It consists of a main oscillator with the mass, damping and rigidity as M, C and K, respectively which is under external periodic excitation namely $f_{01} \sin(\Omega_1 t)$. The main system is coupled to nonsmooth NES with a very light mass $m \ll M$ that is under external excitation as $f_{02} \sin(\Omega_2 t + \theta)$. The NES possesses a nonsmooth potential, F', which is defined as (see Fig. 2):

$$
F'(y_1 - y_2) = \begin{cases}
k_1'(y_1 - y_2 + \delta_1) \text{ if} & -\Delta_1 \leqslant y_1 - y_2 \leqslant -\delta_1 \\
k_2'(y_1 - y_2 - \delta_2) \text{ if} & \Delta_2 \geqslant y_1 - y_2 \geqslant \delta_2 \\
K_1'(y_1 - y_2 + \Delta_1) \text{ if} & y_1 - y_2 \leqslant -\Delta_1 \\
K_2'(y_1 - y_2 - \Delta_2) \text{ if} & y_1 - y_2 \geqslant \Delta_2 \\
B_0 \text{ if} & -\delta_1 \leqslant y_1 - y_2 \leqslant \delta_2
\end{cases}
\tag{1}
$$
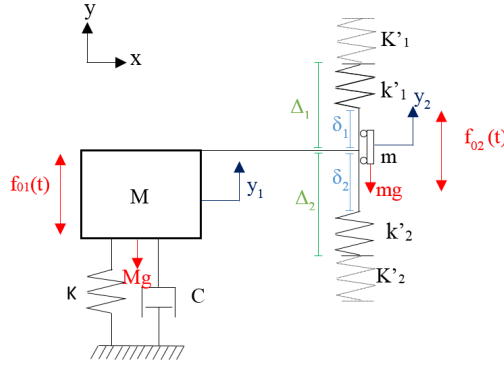
Figure 1. The model of the system: $f_{01}(t) = f_{01} \sin(\Omega_1 t)$, $f_{02}(t) = f_{02} \sin(\Omega_2 t + \theta)$.

The dissipation scenario in the NES depends on its potential. Governing equations of
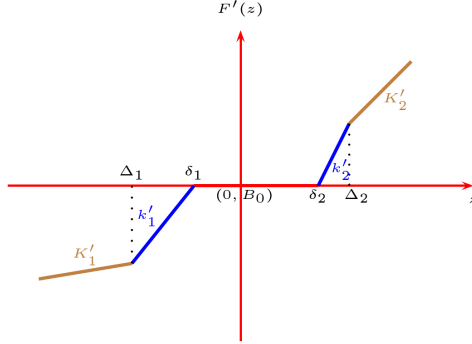
Figure 2. Graphical representation of the potential of the NES.

the systems are summarized as:

$$
\begin{cases}
(M+m)\ddot{y_1} + C\dot{y_1} + c_1(\dot{y_1} - \dot{y_2}) + \tilde{c}_1 \nabla(F'(y_1 - y_2))(\dot{y_1} - \dot{y_2}) + Ky_1 + F'(y_1 - y_2) \\
= f_{01}\sin(\Omega_1 t) + (M+m)g \\
m\ddot{y_2} + c_1(\dot{y_2} - \dot{y_1}) + \tilde{c}_1 \nabla(F'(y_2 - y_1))(\dot{y_2} - \dot{y_1}) + F'(y_2 - y_1) = f_{02}\sin(\Omega_2 t + \theta) + mg
\end{cases}
$$

$$(2)$$

where

$$
\nabla(F'(y_1 - y_2)) =
\begin{cases}
k_1' \text{ if } & -\Delta_1 \leqslant y_1 - y_2 \leqslant -\delta_1 \\
k_2' \text{ if } & \Delta_2 \geqslant y_1 - y_2 \geqslant \delta_2 \\
K_1' \text{ if } & y_1 - y_2 \leqslant -\Delta_1 \\
K_2' \text{ if } & y_1 - y_2 \geqslant \Delta_2 \\
0 \text{ if } & -\delta_1 \leqslant y_1 - y_2 \leqslant \delta_2
\end{cases}
$$

$$(3)$$

We are interested to scale system equations at the new time domain $T = t\sqrt{\dfrac{K}{m+M}}$. The system 2 reads:

$$
\begin{cases}
\ddot{y_1} + a_1\epsilon\dot{y_1} + a_2\epsilon(\dot{y_1} - \dot{y_2}) + a_3\epsilon\nabla(F)(\dot{y_1} - \dot{y_2}) + y_1 + \epsilon F(y_1 - y_2) = \epsilon f_1\sin(\omega_1 T) + \gamma \\
\epsilon\ddot{y_2} + a_2\epsilon(\dot{y_2} - \dot{y_1}) + a_3\epsilon\nabla F(\dot{y_2} - \dot{y_1}) + \epsilon F(y_2 - y_1) = \epsilon f_2\sin(\omega_2 T + \theta) + \epsilon\gamma
\end{cases}
$$

$$(4)$$

where $\epsilon = \dfrac{m}{m+M} \ll 1$, $a_1\epsilon = \dfrac{C}{\sqrt{k(m+M)}}$, $a_2\epsilon = \dfrac{c_1}{\sqrt{k(m+M)}}$, $a_3\epsilon = \dfrac{\tilde{c}_1}{\sqrt{k(m+M)}}$, $\epsilon f_1 = \dfrac{f_{01}}{K}$, $\epsilon f_2 = \dfrac{f_{02}}{K}$, $\omega_1 = \Omega_1\dfrac{M+m}{K}$, $\omega_2 = \Omega_2\dfrac{M+m}{K}$, $k_1 = \dfrac{k_1'}{K}$, $k_2 = \dfrac{k_2'}{K}$, $K_1 = \dfrac{K_1'}{K}$,

$$K_2 = \frac{K_2'}{K}, \; B_o = \frac{B_0}{K}, \; \gamma = \frac{(M+m)g}{K}, \; \omega_1 = \omega + \sigma\epsilon, \; \omega_2 = \omega + \sigma\epsilon \text{ and}$$

$$\epsilon F(y_1 - y_2) = \begin{cases} \frac{k_1'}{K}(y_1 - y_2 + \delta_1) & \text{if} \quad -\Delta_1 \leqslant y_1 - y_2 \leqslant -\delta_1 \\ \frac{k_2'}{K}(y_1 - y_2 - \delta_2) & \text{if} \quad \Delta_2 \geqslant y_1 - y_2 \geqslant \delta_2 \\ \frac{K_1'}{K}(y_1 - y_2 + \Delta_1) & \text{if} \quad y_1 - y_2 \leqslant -\Delta_1 \\ \frac{K_2'}{K}(y_1 - y_2 - \Delta_2) & \text{if} \quad y_1 - y_2 \geqslant \Delta_2 \\ B_0 & \text{if} \quad -\delta_1 \leqslant y_1 - y_2 \leqslant \delta_2 \end{cases} \tag{5}$$

$$\epsilon \nabla F(y_1 - y_2) = \begin{cases} \frac{k_1'}{K} & \text{if} \quad -\Delta_1 \leqslant y_1 - y_2 \leqslant -\delta_1 \\ \frac{k_2'}{K} & \text{if} \quad \Delta_2 \geqslant y_1 - y_2 \geqslant \delta_2 \\ \frac{K_1'}{K} & \text{if} \quad y_1 - y_2 \leqslant -\Delta_1 \\ \frac{K_2'}{K} & \text{if} \quad y_1 - y_2 \geqslant \Delta_2 \\ B_0 & \text{if} \quad -\delta_1 \leqslant y_1 - y_2 \leqslant \delta_2 \end{cases} \tag{6}$$

Let us introduce center of the mass and relative displacement of two oscillators as the new variables of the system equations:

$$\begin{cases} v = y_1 + \epsilon y_2 & \rightarrow \quad y_1 = \frac{v + \epsilon w}{1 + \epsilon} \\ w = y_1 - y_2 & \rightarrow \quad y_2 = \frac{v - w}{1 + \epsilon} \end{cases} \tag{7}$$

The Eqs. 4 will take following form:

$$\begin{cases} \ddot{v} + \frac{a_1\epsilon}{1+\epsilon}(\dot{v} + \epsilon\dot{w}) + \frac{1}{1+\epsilon}(v + \epsilon w) = \epsilon\big(f_1\sin(\omega_1 t) + f_2\sin(\omega_2 T + \theta)\big) + (1+\epsilon)\gamma \\ \ddot{w} + \frac{a_1\epsilon}{1+\epsilon}(\dot{v} + \epsilon\dot{w}) + \frac{1}{1+\epsilon}(v + \epsilon w) + (1+\epsilon)\big(a_2\dot{w} + a_3\nabla F(\dot{w}) + F(w)\big) \\ = \epsilon f_1\sin(\omega_1 t) - f_2\sin(\omega_2 T + \theta) \end{cases} \tag{8}$$

Extended version of complex variables of Manevitch [8] are introduced to the system as it follows $(A_1, A_2 \in \mathbb{R})$ [12, 15]:

$$\begin{cases} \phi_1 e^{i\omega t} + iA_1 = \dot{v} + i\omega v \\ \phi_2 e^{i\omega t} + iA_2 = \dot{w} + i\omega w \end{cases} \tag{9}$$

We endow the Galerkin method using a truncated Fourier series (constant terms and first harmonics). We are interested to analyze the system around a 1 : 1 resonance, so we set: $\omega = 1$, $\omega_1 = \omega + \sigma\epsilon$ and $\omega_2 = \omega + \sigma\epsilon$. The time T is divided to different scales, namely fast $(\tau_0 = T)$ and slow $(\tau_1 = \epsilon\tau_0)$ time scales. A time multi-scale method [9] is used to study system behaviors at each scale (or at each order of ϵ parameter).

3. Time-multi scale behaviors of the system

Constant terms of Fourier series at fast and slow time scales provide $A_1 = \gamma$ and $A_2 = \gamma(2 + \sigma)$. First term of Fourier series at fast time scale provide the invariant manifold of the system which can be represented in general manner as:

$$N_1 = F(N_2, \lambda_2, a_2, a_3, K_1, K_2, k_1, k_2, \Delta_1, \Delta_2, \delta_1, \delta_2, f_2) \tag{10}$$

where $\phi_1 = N_1 e^{i\lambda_1}$ and $\phi_2 = N_2 e^{i\lambda_2}$. It can be seen that the invariant of the system depends on applied external force on the NES, i.e. f_2. The stable zones of the invariant can be detected via perturbation of N_2 and λ_2. A typical invariant for some given system parameters is presented in Fig. 3. At slow time scale, the system equations are analyzed
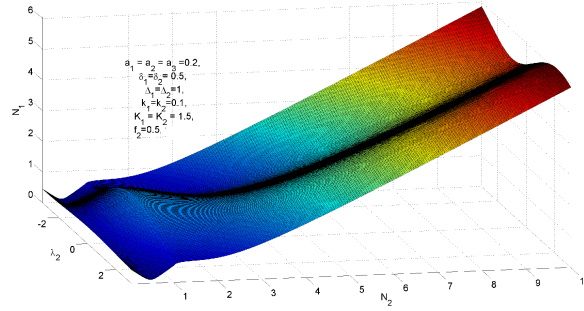
Figure 3. Invariant manifold of system with $f_2 = 0.5$.

around the invariant manifold; this study provides some tools for detection of equilibrium and singular points of the system. Equilibrium points correspond to periodic regimes and singular points are signatures of possible strongly modulated responses (SMR) of the system [11]. The system at fast time scale reads:

$$\begin{cases} \dfrac{\partial N_2}{\partial \tau_1} = \dfrac{h_1(N_2, \lambda_2)}{2N_2^2 g(N_2, \lambda_2)} \\ \dfrac{\partial \lambda_2}{\partial \tau_1} = \dfrac{h_2(N_2, \lambda_2)}{2N_2^2 g(N_2, \lambda_2)} \end{cases} \tag{11}$$

Equilibrium points are those which provide $h_1(N_2, \lambda_2) = h_2(N_2, \lambda_2) = 0$ and $g(N_2, \lambda_2) \neq 0$. Singular points are those which satisfy $h_1(N_2, \lambda_2) = h_2(N_2, \lambda_2) = g(N_2, \lambda_2) = 0$.

4. A numerical example

We set following mathematical examples of numerical data: $a_1 = a_2 = a_3 = 0.2$, $\theta = 0$, $\delta_1 = \delta_2 = 0.5$, $\Delta_1 = \Delta_2 = 1$, $k_1 = k_2 = 0.1$, $K_1 = K_2 = 1.5$, $\sigma = 0.1$, $\epsilon = 10^{-3}$, $f_1 = 1$ and $f_2 = 0.1$. We take the direct numerical integration of the system 4 via the
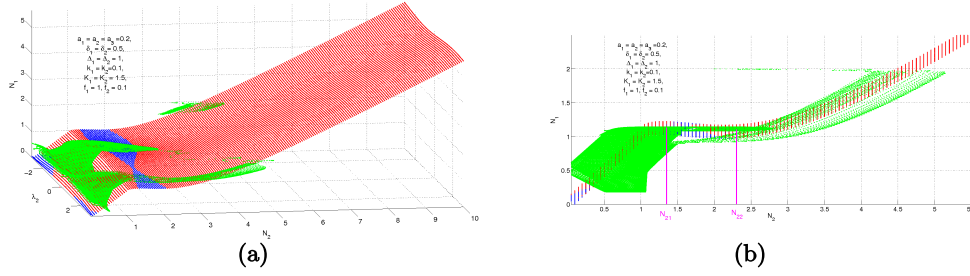
Figure 4. The invariant manifold of system and added numerical results (green line). Unstable zones of the invariant are represented by blue line.: a) 3D view; b) 2D view.
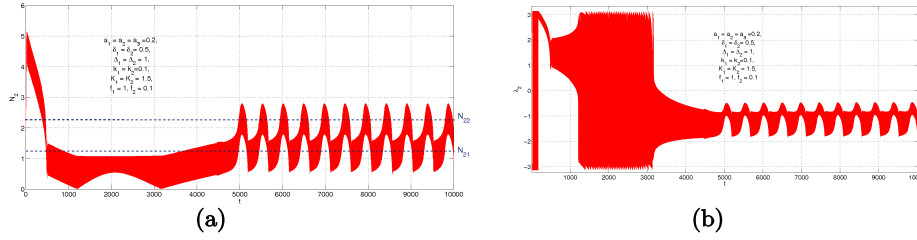
Figure 5. Time histories of N_2 and λ_2: a) N_2; b) λ_2.

*ode*45 function of the Matlab package. Following initial conditions are assumed for the system: $(y_1(0), y_2(0), \dot{y}_1(0), \dot{y}_2(0)) = (2 + y_{10}, y_{20}, 0, 0)$ where y_{10} and y_{20} are the unforced equilibrium states of the main oscillator and the NES due to their weight. Different views of the invariant manifold of the system and obtained numerical results are illustrated in Fig. 4. Time histories of N_2 and λ_2 are depicted in Fig. 5. These figures show that the system faces SMR. This means that it possesses singular points. Positions of equilibrium and singular points of the system are given in Fig. 6. It is seen that the system possesses five singular points namely, points no. 1, 2, 3, 4 and 6 and one equilibrium point namely no. 2 which is in the unstable zone of the invariant. All of singular points are on the border between stable and unstable areas. Looking at time history of N_2 in Fig. 5a we can conclude that the system jumps between points 1 and 3 or 5 and 6.

5. Conclusions

Time multi-scale behavior of two forced vertical oscillators are studied. The main forced oscillator which is supposed to be linear is coupled to a forced nonsmooth nonlinear energy

124
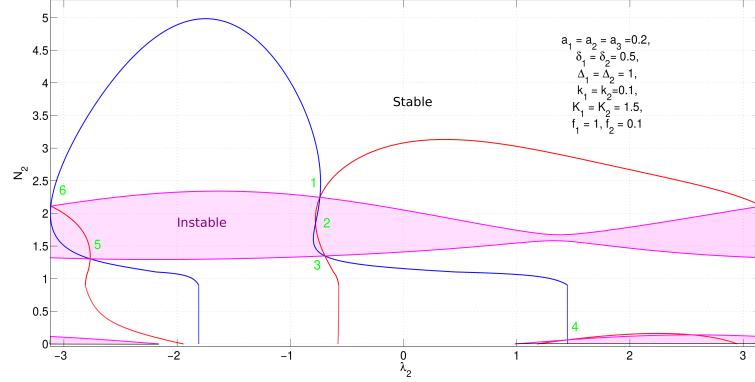
Figure 6. Positions of equilibrium and singular points: $g(N_2, \lambda_2) = 0$ (magenta), $h_1(N_2, \lambda_2) = 0$ (red), $h_2(N_2, \lambda_2) = 0$ (blue)

sink. Studying the system at fast time scale reveals its invariant manifold which in addition to mechanical parameters of the system, depends on the applied force on the nonlinear energy sink. Further studies at slow time scale provide useful information about positions of equilibrium and singular points. The goal of all of these treatments and studies is to tune all equilibrium and singular points (periodic and strongly modulated regimes) which leads to the design of forced nonsmooth nonlinear energy sink for passively controlling main oscillators and/or harvesting their vibratory energy. Potential applications of the developments can be control of vertical oscillations in bridges or vehicles.

References

[1] FRAHM, H. Device for damping vibrations of bodies, Apr. 18 1911. US Patent 989,958.

[2] GENDELMAN, O., MANEVITCH, L. I., VAKAKIS, A. F., AND MCLOSKEY, R. Energy pumping in nonlinear mechanical oscillators: part i - dynamics of the underlying hamiltonian systems. *Journal of Applied Mechanics 68*, 1 (2001), 34–41.

[3] GENDELMAN, O. V. Analytic treatment of a system with a vibro-impact nonlinear energy sink. *Journal of Sound and Vibration 331* (2012), 4599–4608.

[4] GOURC, E., MICHON, G., SEGUY, S., AND BERLIOZ, A. Targeted energy transfer under harmonic forcing with a vibro-impact nonlinear energy sink: analytical and experimental developments. *Journal of Vibration and Acoustics 137*, 3 (2015), 031008.

[5] LAMARQUE, C.-H., GENDELMAN, O., TURE SAVADKOOHI, A., AND ETCHEVERRIA, E. Targeted energy transfer in mechanical systems by means of non-smooth nonlinear energy sink. *Acta Mechanica 221*, 1-2 (2011), 175–200.

[6] LAMARQUE, C.-H., TURE SAVADKOOHI, A., AND DIMITRIJEVIC, Z. Dynamics of a linear system with time-dependent mass and a coupled light mass with non-smooth potential. *Meccanica 49* (2014), 135–145.

[7] LAMARQUE, C.-H., TURE SAVADKOOHI, A., ETCHEVERRIA, E., AND DIMITRIJEVIC, Z. Multi-scales dynamics of two coupled nonsmooth systems. *Internation Journal of Bifucation and Chaos 221* (2012), 1250295.

[8] MANEVITCH, L. I. The description of localized normal modes in a chain of nonlinear coupled oscillators using complex variables. *Nonlinear Dynamics 25* (2001), 95–109.

[9] NAYFEH, A. H., AND MOOK, D. T. *Nonlinear oscillations.* Wiley, New York, 1979.

[10] NUCERA, F., VAKAKIS, A., BERGMAN, A., AND KERSCHEN, G. Targeted energy transfers in vibro-impact oscillators for seismic mitigation. *Nonlinear Dynamics 50* (2007), 651–677.

[11] STAROSVETSKY, Y., AND GENDELMAN, O. V. Strongly modulated response in forced 2dof oscillatory system with essential mass and potential asymmetry. *Physica D 237* (2008), 1719–1733.

[12] TURE SAVADKOOHI, A., LAMARQUE, C.-H., AND DIMITRIJEVIC, Z. Vibratory energy exchange between a linear and a nonsmooth system in the presence of the gravity. *Nonlinear Dynamics 70* (2012), 1473–1483.

[13] VAKAKIS, A., GENDELMAN, O., BERGMAN, L., MCFARLAND, D., KERSCHEN, G., AND LEE, Y. *Nonlinear targeted energy transfer in mechanical and structural systems, I & II.* Springer, Berlin, 2009.

[14] VAKAKIS, A. F. Inducing passive nonlinear energy sinks in vibrating systems. *Journal of Vibration and Acoustics 123*, 3 (2001), 324–332.

[15] WEISS, M., CHENIA, M., TURE SAVADKOOHI, A., LAMARQUE, C.-H., VAURIGAUD, B., AND HAMMOUDA, A. Multi-scale energy exchanges between an elasto-plastic oscillator and a light nonsmooth system with external pre-stress. *Nonlinear Dynamics DOI 10.1007/s11071-015-2314-8* (2015).

Simon Charlemagne, M.Sc. (Ph.D. student): ENTPE, Université de Lyon, LGCB & LTDS UMR CNRS 5513, Rue Maurice Audin, F- 69518 Vaulx-en-Velin Cedex, France
(*simon.charlemagne@entpe.fr*).

Claude-Henri Lamarque, Ph.D.: ENTPE, Université de Lyon, LGCB & LTDS UMR CNRS 5513, Rue Maurice Audin, F- 69518 Vaulx-en-Velin Cedex, France (*lamarque@entpe.fr*).

Alireza Ture Savadkoohi, Ph.D.: ENTPE, Université de Lyon, LGCB & LTDS UMR CNRS 5513, Rue Maurice Audin, F- 69518 Vaulx-en-Velin Cedex, France
(*alireza.turesavadkoohi@entpe.fr*).

Pierre Abdoulhadi, M.Sc.: ENTPE, Université de Lyon, LGCB, Rue Maurice Audin, F- 69518 Vaulx-en-Velin Cedex, France (*pierre.abdoulhadi@entpe.fr*).

Nonlinear elastic waves in a fibre-reinforced composite with an imperfect interface
(ASY148-15)

Vladyslav V. Danishevskyy, Julius D. Kaplunov, Graham A. Rogerson, Nikolai A. Kotov

Abstract: The propagation of nonlinear elastic anti-plane shear waves in a unidirectional fibre-reinforced composite material is studied. A model of structural nonlinearity is considered, for which the nonlinear behaviour of the composite solid is caused by imperfect bonding at the "fibre-matrix" interface. A macroscopic wave equation accounting for the effects of nonlinearity and dispersion is derived using the higher-order asymptotic homogenization method. Explicit analytical solutions for stationary nonlinear strain waves are obtained. This type of nonlinearity has a crucial influence on the wave propagation mode: for soft nonlinearity, localised shock (kink) waves are developed, while for hard nonlinearity localised bell-shaped waves appear. Numerical results are presented and the areas of practical applicability of linear and nonlinear, long- and short-wave approaches discussed.

1. Introduction

Elastic waves propagating in heterogeneous solids can undergo the effects of nonlinearity and dispersion. We study a problem for which the nonlinear behaviour of a composite is associated with imperfect bonding conditions at the interface between constitutive components. This is an example of structural nonlinearity, with the nonlinearity directly related to the presence of a microstructure. Dispersion can be classified as geometrical or structural. Geometrical dispersion is typical for wave-guides and finite-size bodies (e.g., waves in beams and plates). Structural dispersion may be caused by the heterogeneity of a composite solid, with successive reflections and refractions of local waves at the matrix-inclusion interfaces leading to scattering of the overall wave field.

Nonlinearity induces a pumping of energy form the low- to the high-frequency part of the spectrum, with higher-order modes generated and continuous localization of energy occurring, making the wave front steeper. In contrast, dispersion provides scattering of energy and decreases the slope of the wave front. When nonlinearity and dispersion act together, they may balance the influence of each other. In such a case, stationary nonlinear waves of permanent shape and velocity can propagate.

The propagation of nonlinear strain waves in elastic solids has been intensively studied [1–3]. Many authors considered homogeneous systems, with dispersive properties mainly determined by

geometrical factors. At the same time, the effects of structural dispersion, related to the scattering of nonlinear waves by the microstructure, were not studied in great detail.

In this present paper, we apply the asymptotic homogenization method (AHM) to the modelling of anti-plane shear waves propagating in a fibre-reinforced composite material with imperfect interface bonding between the matrix and fibres. The effect of imperfect bonding is predicted by assuming that the displacement jump across the interface is related to the interfacial stress by a certain cohesion function. We specifically study a weakly nonlinear interface, with a cohesion function represented by a power series expansion in terms of non-dimensional displacement jumps.

According to the AHM, physical fields in a spatially periodic heterogeneous medium are represented by a two-scale asymptotic expansion in powers of a small parameter $\eta = l / L$, where l is the size of the unit cell and L is the typical wavelength. This leads to a decomposition of the final solution into global and local components; the latter are evaluated from a recurrent sequence of cell boundary value problems (BVPs). Application of the volume-integral homogenizing operator allows us to obtain a homogenized constitutive equation that describes the macroscopic behaviour of the medium. From its conception, the AHM was intended for the determination of quasi-static properties of heterogeneous media and structures [4]. In the last years, taking into account higher-order terms with respect to η extended the area of applicability of the homogenized models and provided a mechanism to predict the effect of structural dispersion [5, 6].

The paper is organized as follows. In Section 2, an asymptotic model of the imperfect bonding is proposed and the input BVP introduced. In Section 3, the higher-order asymptotic homogenization procedure is developed and the macroscopic nonlinear wave equation is obtained. In Section 4, the analytical solution for stationary nonlinear strain waves is derived in terms of elliptic functions. The interplay between the effects of nonlinearity and dispersion is analysed in Section 5. Section 6 is devoted to the conclusions.

2. Asymptotic model of the imperfect bonding and input BVP problem

Let us consider a unidirectional fibre-reinforced composite consisting of an infinite matrix $\Omega^{(1)}$ and a periodic square array of cylindrical inclusions $\Omega^{(2)}$, see figure 1. It is supposed that geometrical and physical nonlinearity can be neglected, with the nonlinear behaviour of the composite caused by imperfect bonding at the matrix-fibres interface $\partial\Omega$.

We study anti-plane shear waves propagating in the plane $x_1 x_2$. The governing wave equation is as follows:

$$\mu^{(n)} \nabla_x^2 u^{(n)} = \rho^{(n)} \frac{\partial^2 u^{(n)}}{\partial t^2},$$

(1)
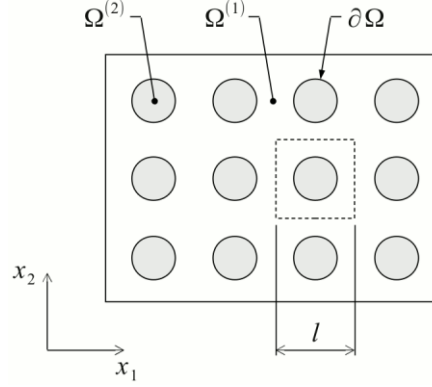
Figure 1. Fibre-reinforce composite structure with a distinguished unit cell.

where $\mu^{(n)}$ is the shear modulus; $\rho^{(n)}$ is the density; $u^{(n)}$ is the displacement in the direction orthogonal to the plane $x_1 x_2$; $\nabla_x = (\partial/\partial x_1)\mathbf{e}_1 + (\partial/\partial x_2)\mathbf{e}_2$; $\mathbf{e}_1$, $\mathbf{e}_2$ are the Cartesian unit vectors. Here, and throughout this paper, the upper index (n) refers to different components of the composite structure, $n = 1,2$.

Let us consider the case of imperfect bonding at the interface $\partial\Omega$. The equilibrium state implies the equality of tangential stresses, thus:

$$\sigma^* = \sigma^{(1)} = \sigma^{(2)} \quad \text{at} \quad \partial\Omega, \tag{2}$$

where $\sigma^{(n)} = \mu^{(n)}\left(\partial u^{(n)}/\partial\mathbf{n}\right)$; $\partial/\partial\mathbf{n}$ is the normal derivative to $\partial\Omega$. Weakening the bonding between the matrix and fibres leads to a jump in the displacement field across the interface. We suppose that the displacement jump $\Delta u^* = u^{(1)} - u^{(2)}$ is related to the interfacial stress σ^* as follows:

$$\sigma^* = f\left(\Delta u^*\right) \quad \text{at} \quad \partial\Omega, \tag{3}$$

where $f\left(\Delta u^*\right)$ is the so-called cohesion function [7, 8]. If the interface exhibits a weakly nonlinear behaviour, the cohesion function can be assumed in the following form:

$$\sigma^* = \mu_1^* \frac{\Delta u^*}{h} + \mu_3^* \left(\frac{\Delta u^*}{h}\right)^3 \quad \text{at} \quad \partial\Omega, \tag{4}$$

where h is the thickness of the interface. From the mathematical point of view, expression (4) can be considered as the first terms of Taylor series expansion of $f\left(\Delta u^*\right)$ in powers of $\Delta u^*/h$. The shear

141

deformation is symmetric, therefore, expansion (4) includes only terms of odd powers. The coefficients μ_1^*, μ_3^* can be interpreted, respectively, as the linear and the nonlinear shear modulus of the interface. We invert series (4), introduce non-dimensional bonding parameters $\alpha = h\mu^{(1)}/(l\mu_1^*)$, $\beta = (\mu_3^*/\mu_1^*)(\mu^{(1)}/\mu_1^*)^2$, and finally let $h \to 0$, $\mu_1^* \to 0$, $\mu_3^* \to 0$. Then expression (4) yields

$$u^{(1)} - u^{(2)} = \alpha l \frac{\sigma^*}{\mu^{(1)}} - \alpha\beta\, l \left(\frac{\sigma^*}{\mu^{(1)}} \right)^3 \quad \text{at} \quad \partial\Omega. \tag{5}$$

The case $\alpha = 0$ corresponds to perfect bonding, $\alpha \to \infty$ – to complete separation of the components. At $\beta = 0$ the interface is purely linear, whilst any increase in $|\beta|$ increases nonlinear effects. The nonlinearity is soft for $\beta < 0$ and hard for $\beta > 0$.

The input BVP includes equations (1), (2), and (5).

3. Higher-order asymptotic homogenization

Let us introduce non-dimensional variables $\bar{u} = u/U$, $\bar{\mathbf{n}} = \mathbf{n}/L$, $\bar{x}_k = x_k/L$, $k = 1,2$, where U is the displacement amplitude and L is the wavelength. The input BVP (1), (2), (5) reads

$$\mu^{(n)} \nabla_{\bar{x}}^2 \bar{u}^{(n)} = \rho^{(n)} L^2 \frac{\partial^2 \bar{u}^{(n)}}{\partial t^2}, \tag{6}$$

$$\mu^{(1)} \frac{\partial \bar{u}^{(1)}}{\partial \bar{\mathbf{n}}} = \mu^{(2)} \frac{\partial \bar{u}^{(2)}}{\partial \bar{\mathbf{n}}} \quad \text{at} \quad \partial\Omega, \tag{7}$$

$$\bar{u}^{(1)} - \bar{u}^{(2)} = \alpha\eta \frac{\partial \bar{u}^{(1)}}{\partial \bar{\mathbf{n}}} - \alpha\eta\delta \left(\frac{\partial \bar{u}^{(1)}}{\partial \bar{\mathbf{n}}} \right)^3 \quad \text{at} \quad \partial\Omega, \tag{8}$$

where $\eta = l/L$, $\delta = \beta\left(U/L\right)^2$, $\nabla_{\bar{x}} = L^{-1} \nabla_x$.

The ratio U/L indicates the magnitude of the elastic strains. We suppose that the size l of the unit cell is smaller than the wavelength L. Hence, the non-dimensional variables η and δ may be considered as natural small parameters characterising, accordingly, the rate of dispersion and the rate of nonlinearity.

Let us introduce so-called *fast* $y_k = \eta^{-1} \bar{x}_k$ and *slow* $\bar{x}_k = \bar{x}_k$ coordinate variables. The spatial derivatives are then given by $\nabla_{\bar{x}} = \nabla_{\bar{x}} + \eta^{-1} \nabla_y$, where $\nabla_y = \left(\partial/\partial y_1\right)\mathbf{e}_1 + \left(\partial/\partial y_2\right)\mathbf{e}_2$. The solution is sought as the asymptotic expansion:

$$\overline{u}^{(n)} = u_0\left(\overline{x}_k\right) + \eta u_1^{(n)}\left(\overline{x}_k, y_k\right) + \eta^2 u_2^{(n)}\left(\overline{x}_k, y_k\right) + \dots.$$

Here the first term u_0 represents the homogenized part of the displacement field; it varies "slowly" on the macrolevel and does not depend on the fast coordinates. The next terms $u_i^{(n)}$, $i = 1,2,3,\dots$, provide order η^i corrections and describe local oscillations of the displacements within each unit cell. Since the composite structure is periodic, the functions $u_i^{(n)}$ satisfy the periodicity condition:

$$u_i^{(n)}\left(\overline{x}_k, y_k\right) = u_i^{(n)}\left(\overline{x}_k, y_k \pm 1\right), \quad i = 1,2,3,\dots \ . \tag{9}$$

Splitting the BVP (6)–(8) with respect to η, we obtain the recurrent sequence of local BVPs:

$$\mu^{(n)}\left(\nabla_{\overline{x}}^2 u_{i-2}^{(n)} + 2\nabla_{\overline{x}} \cdot \nabla_y u_{i-1}^{(n)} + \nabla_y^2 u_i^{(n)}\right) = \rho^{(n)} L^2 \frac{\partial^2 u_{i-2}^{(n)}}{\partial t^2}, \tag{10}$$

$$\mu^{(1)}\left(\frac{\partial u_{i-1}^{(1)}}{\partial \overline{\mathbf{n}}} + \frac{\partial u_i^{(1)}}{\partial \mathbf{m}}\right) = \mu^{(2)}\left(\frac{\partial u_{i-1}^{(2)}}{\partial \overline{\mathbf{n}}} + \frac{\partial u_i^{(2)}}{\partial \mathbf{m}}\right) \quad \text{at} \quad \partial\Omega, \tag{11}$$

$$u_i^{(1)} - u_i^{(2)} = \alpha\left(\frac{\partial u_{i-1}^{(1)}}{\partial \overline{\mathbf{n}}} + \frac{\partial u_i^{(1)}}{\partial \mathbf{m}}\right) - \alpha\delta\left(\frac{\partial u_{i-1}^{(1)}}{\partial \overline{\mathbf{n}}} + \frac{\partial u_i^{(1)}}{\partial \mathbf{m}}\right)^3 \quad \text{at} \quad \partial\Omega, \tag{12}$$

where $i = 1,2,3,\dots$; $u_{-1}^{(n)} = 0$; $\partial/\partial\mathbf{m}$ is the normal derivative to $\partial\Omega$ written in terms of fast variables.

Due to the periodicity condition (9), the local problems (9)–(12) are considered within a distinguished unit cell of the composite structure. Let us replace the outer square contour of the unit cell by a circle of the same area. This simplification is well known in the theory of composites [9]. The accuracy of such an approach is known to be good, when the volume fraction $c^{(2)}$ of the fibres is relatively small. Solutions of the nonlinear local problems (12)–(15) are sought through the asymptotic expansion in powers of δ. The term $u_1^{(n)}$ is evaluated with accuracy $O(\delta)$, the terms $u_2^{(n)}$, $u_3^{(n)}$ – with accuracy $O(\delta^0)$.

Next, we apply to equation (10) at $i = 4$ the homogenizing operator $\iint(\cdot)dy_1 dy_2$ over the unit cell domain. As a result, the macroscopic nonlinear wave equation is obtained. Reverting back to the dimension variables $u = u_0 U$, $x_k = \overline{x}_k L$, the macroscopic wave equation reads

$$\mu_1 \nabla_x^2 u + \frac{1}{3}\beta\mu_2 \nabla_x \cdot \left(\nabla_x u\right)^3 + \eta^2 L^2 \mu_3 \nabla_x^4 u + O\left(\delta^2 + \eta^4\right) = \rho \frac{\partial^2 u}{\partial t^2} \,, \tag{13}$$

where μ_1, μ_2, μ_3 are the effective elastic coefficients. The parameter μ_1 is the linear shear modulus; the parameters μ_2 and μ_3 account, respectively, for nonlinearity and for dispersive properties. For μ_1 and μ_2, explicit analytical formulas are derived, while μ_3 is evaluated by numerical integration over the unit cell. It should be noted that μ_1, μ_2, μ_3 are always positive.

The analysis of numerical examples shows that the obtained solutions for μ_1, μ_2, μ_3 provides a good accuracy at $c^{(2)} < 0.5...0.6$. However, for most real composites materials the volume fraction of the fibres does not exceed $0.4...0.5$.

For the composite structure under consideration, the anti-plane shear problem is transversely isotropic in the long-wave limit, when the wavelength is essentially larger than the size of the microstructure, $l/L \to 0$. If the wavelength decreases, the composite material exhibits anisotropic properties and the parameters of elastic waves become dependant on the direction of propagation [5]. In this paper, the simplification of the geometrical shape of the unit cell implies the axial symmetry of the local problems. Therefore, the derived approximate solution is transversely isotropic and the macroscopic wave equation (13) is invariant to the direction of the wave propagation. A comparison of the obtained results with a solution derived by the Floquet-Bloch method [5] has shown that equation (13) provides a good accuracy at $\eta = l/L < 0.4$.

4. Analytical solution for stationary waves

Let us consider a stationary plane wave propagating with a permanent shape and velocity in the direction of the wave vector $\mathbf{k}$. In such a case the solution meets the following condition: $u(\mathbf{x},t) = u(\xi)$, where ξ is the propagation coordinate, $\xi = \mathbf{e}_k \cdot \mathbf{x} - vt$; v is the phase velocity and $\mathbf{e}_k$ is the unit wave vector. Let us define the strain of the wave profile as follows $f = du/d\xi$ and introduce non-dimensional variables $\bar{f} = f/F$, $\zeta = \xi/L$. Here F is the amplitude of the strain wave and L is the wavelength. After routine transformations, equation (13) reads:

$$\frac{d^2 \bar{f}}{d\zeta^2} + a\bar{f} + b\bar{f}^3 = 0 \,, \tag{14}$$

where $a = \mu_1\left(1 - v^2/v_0^2\right)/\left(\mu_3 \eta^2\right)$, $b = \beta F^2 \mu_2/\left(3\mu_3 \eta^2\right)$, v_0 is the effective phase velocity in the linear long-wave limit, $v_0 = \sqrt{\mu_1/\rho}$.

The type of nonlinearity (soft or hard) has a crucial influence upon the shape and properties of elastic strain waves. For soft nonlinearity ($\beta < 0$), the exact periodical solution of equation (14) is:

$$\bar{f} = \frac{1}{2}\operatorname{sn}(\kappa\zeta, s), \tag{15}$$

where κ is the propagation variable, $\kappa = 4K(s)$, $\operatorname{sn}(\cdot)$ is the elliptic sine, $K(s)$ is the complete elliptic integral of the first kind, s is the modulus of the elliptic functions that is determined form the transcendental equation: $s^2 K(s)^2 = -\beta F^2 \mu_2 / (384\eta^2 \mu_3)$, $0 \le s \le 1$. For the phase velocity v we obtain: $v^2 / v_0^2 = 1 - 16(1 + s^2)K(s)^2 \eta^2 \mu_3 / \mu_1$.

For hard nonlinearity ($\beta > 0$), the solution takes the following form:

$$\bar{f} = \frac{1}{2}\operatorname{cn}(\kappa\zeta, s), \tag{16}$$

where $s^2 K(s)^2 = \beta F^2 \mu_2 / (384\eta^2 \mu_3)$, $v^2 / v_0^2 = 1 - 16(1 - 2s^2)K(s)^2 \eta^2 \mu_3 / \mu_1$.

The magnitude of the modulus s determines the intensity of nonlinear effects. The limit $s = 0$ corresponds to the purely linear case: $\bar{f} = (1/2)\sin(2\pi\zeta)$ at $\beta < 0$; $\bar{f} = (1/2)\cos(2\pi\zeta)$ at $\beta > 0$; $v^2 / v_0^2 = 1 - 4\pi^2 \eta^2 \mu_3 / \mu_1$.

At the opposite limit, $s = 1$, solutions (15) and (16) describe localised solitary waves. In the case of soft nonlinearity, a shock (so-called *kink*) strain wave appears (figure 2, *a*): $\bar{f} = (1/2)\operatorname{th}(\zeta/\Delta)$, $\Delta^2 = -24\mu_3\eta^2 / (F^2 \beta \mu_2)$, $v^2 / v_0^2 = 1 - 2\mu_3\eta^2 / (\mu_1\Delta^2)$. Here the parameter Δ can be treated as the width of the localised wave. The kink wave propagates with a velocity lower than the velocity v_0 associated with the linear long-wave limit: $v < v_0$. This is the so-called *subsonic* mode. The increase in the amplitude F leads to a decrease in the width Δ and the velocity v of the wave.

If nonlinearity is hard, the localised solution takes the form of a bell-shaped wave (figure 2, *b*): $\bar{f} = [2\operatorname{ch}(\zeta/\Delta)]^{-1}$, $\Delta^2 = 24\mu_3\eta^2 / (F^2 \beta \mu_2)$, $v^2 / v_0^2 = 1 + \mu_3\eta^2 / (\mu_1\Delta^2)$. In this case a *supersonic* propagation mode is realised, i.e. $v > v_0$. When the amplitude F grows, the width Δ decreases and the velocity v increases.
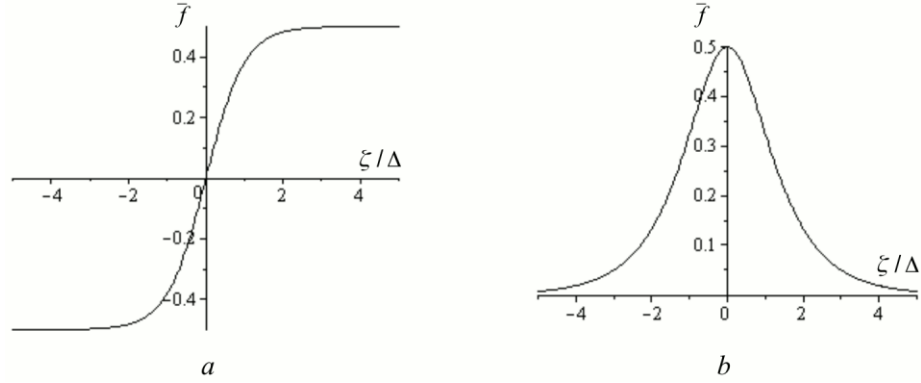
Figure 2. Localised nonlinear elastic strain waves; a – soft nonlinearity, b – hard nonlinearity.

5. Interplay between nonlinearity and dispersion

As an illustrative example, let us consider a composite material consisting of the aluminium matrix ($\mu^{(1)} = 27.9\,\text{GPa}$, $\rho^{(1)} = 2700\,\text{kg/m}^3$) and nickel fibres ($\mu^{(2)} = 75.4\,\text{GPa}$, $\rho^{(2)} = 8940\,\text{kg/m}^3$). The volume fraction of the fibres is $c^{(2)} = 0.4$. The following magnitudes of the bonding parameters are assumed: $\alpha = 0.1$, $|\beta| = 10^5$. Basing on the solutions obtained in Section 3, the effective elastic coefficients are evaluated: $\mu_1 = 33.1\,\text{GPa}$, $\mu_2 = 21.6\,\text{GPa}$, $\mu_3 = 0.119\,\text{GPa}$.

Figure 3 displays the parametric dependence of the modulus s on the amplitude F and the dispersion parameter η. The domain of elastic strains is restricted by $F \leq 10^{-3}$, a regime typical for most engineering materials.

The presented results show how the phenomena of nonlinearity and dispersion compensate the influence of each other. The increase of the amplitude F (at a fixed value of η) leads to the growing of the modulus s and, therefore, the intensity of nonlinear effects increases. In contrary, the decrease of the wavelength and the increase in η (at a fixed F) is followed by the decrease of the modulus s, so the influence of nonlinearity is reduced.

The numerical analysis of the obtained solutions (15), (16) has shown that nonlinearity has a noticeable influence on both the wave shape and velocity if $s > 0.6$. As follows from figure 3, in this case $\eta < 0.2$ and, consequently, the solution can be evaluated utilizing the long-wave approach. On the other hand, the homogenized equation (13) lacks accuracy for $\eta > 0.4$. Then $s < 0.34$, which means that the wave shape and velocity are very close to the linear case and, consequently, an approximate solution may be found utilising the linear theory. This analysis is particularly important, helping to estimate the domain of practical applicability of linear and nonlinear approaches.
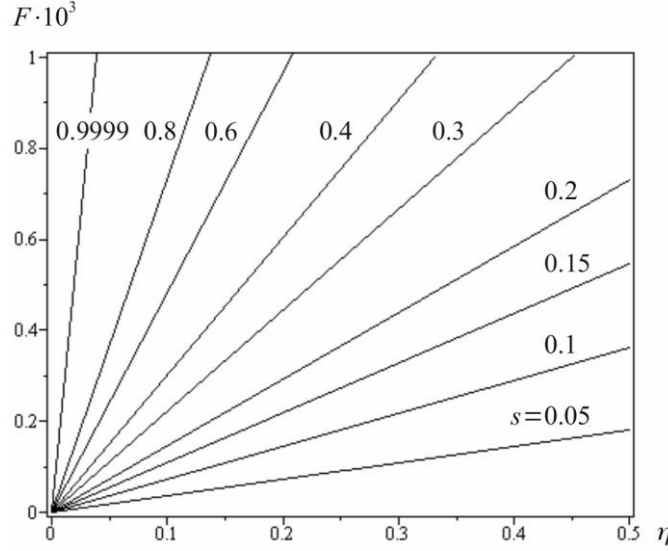
Figure 3. The modulus s characterising the intensity of nonlinear effects.

6. Conclusions

The paper presents analytical solutions that describe the propagation of nonlinear elastic anti-plane shear waves in a unidirectional fibre-reinforced composite material with imperfect bonding between constitutive components. It should be emphasised that this type of nonlinearity has a particularly strong influence upon the propagation mode and the shape of the strain waves. In the case of soft nonlinearity, localised shock (kink) waves appear, while in respect of materials with hard nonlinearity the localised solution takes the form of bell-shaped waves.

The analysis allowed us to estimate the domain of applicability of the different approximate theories used for the modelling of elastic waves in heterogeneous solids. It is shown that nonlinear waves can be adequately described within the long-wave framework (such as the AHM). When dealing with the propagation of short waves, with wave length commensurable with the scale of the microstructure, nonlinear effects become very small. In such a case, an approximate solution may be obtained using the linear Floquet-Bloch theory. This conclusion is true, if the strain amplitude F does not exceed 10^{-3}, which is typical for many solids.

The results presented in the paper can be applied to facilitate the development of new efficient methods of acoustic diagnostic and non-destructive testing in various branches of engineering. Measuring the characteristics of nonlinear waves allows us to receive much more precise information about the internal structure and defects of solids. This is sometimes that may be not possible within a linear framework. We also remark that the propagation of localised nonlinear waves is accompanied

by an essential concentration of mechanical energy. The obtained solutions can help in the development of new criteria for the dynamic failure of heterogeneous materials and structures.

References

[1] Maugin, G.A. *Nonlinear waves in elastic crystals.* Oxford University Press, Oxford, 1999.

[2] Samsonov, A.M. *Strain solitons in solids and how to construct them.* CRC Press, Boca Raton, 2001.

[3] Porubov, A.V. *Amplification of nonlinear strain waves in solids.* World Scientific, Singapore, 2003.

[4] Bakhvalov, N.S., and Panasenko, G.P. *Homogenization: averaging processes in periodic media. Mathematical problems in mechanics of composite materials.* Kluwer, Dordrecht, 1989.

[5] Andrianov, I.V., Bolshakov, V.I., Danishevs'kyy, V.V., and Weichert, D., Higher-order asymptotic homogenization and wave propagation in periodic composite materials. *Proc. R. Soc. A* 464 (2008), 1181–1201.

[6] Craster, R.V., Kaplunov, J., and Pichugin, A.V. High frequency homogenization for periodic media. *Proc. R. Soc. Lond. A* 466 (2010), 2341–2362.

[7] Needleman, A. Micromechanical modelling of interfacial decohesion. *Ultramicroscopy* 40 (1992), 203–214.

[8] Espinosa, H.D., Dwivedi, S.K., and Lu, H-C. Modelling impact induced delamination of woven fibre reinforced composites with contact/cohesive laws. *Comput. Methods Appl. M.* 183 (2000), 259–290.

[9] Christensen, R.M. *Mechanics of composite materials*, 2nd ed. Dover, Mineola, New York, 2005.

Vladyslav V. Danishevskyy, Professor: Keele University, School of Computing and Mathematics, Staffordshire, ST5 5BG, UK (*v.danishevskyy@keele.ac.uk*). The author gave a presentation of this paper during one of the conference sessions.

Julius D. Kaplunov, Professor: Keele University, School of Computing and Mathematics, Staffordshire, ST5 5BG, UK (*j.kaplunov@keele.ac.uk*).

Graham A. Rogerson, Professor: Keele University, School of Computing and Mathematics, Staffordshire, ST5 5BG, UK (*g.a.rogerson@keele.ac.uk*).

Nikolai A. Kotov, PhD: Prydniprovska State Academy of Civil Engineering and Architecture, Chernyshevsky St. 24a, Dnipropetrovsk 49600, Ukraine (*kotokoto@i.ua*)

Analytical predictions of a flexible rotor in journal bearings with adjustable geometry to suppress bearing induced instabilities (STA268-15)

Fadi Dohnal, Bastian Pfau, Athanasios Chasalevris

Abstract: In the past it was shown that a journal bearing with adjustable geometry is capable to improve the vibration behaviour of rotor systems during run-up as well as at steady-state operation. For this purpose, the bearing properties were changed in time by varying the shape and clearance of the bearing periodically. The focus of the present contribution is on exploiting parametric anti-resonances that allow shifting the bearing instability to higher rotor speeds. Stability maps for a simple flexible rotor are computed and compared to analytical predictions resulting from a perturbation calculation. These analytical predictions allow the determination of design parameters that influence the stability of variable geometry bearings.

1. Introduction

The destabilizing effect of journal bearings in rotor systems with flexible shafts can lead to large vibration amplitudes when the so called "oil-whip" phenomenon occurs. Various concepts of fixed geometry journal bearings exist to avoid these vibrations, at least at the operational range of speed, and at their majority incorporate elliptical multi-lobe geometry or tilting pads, [12]. The bearings of fixed elliptical geometry provide better stability characteristics at higher speeds by increasing the effective eccentricity of the journal. In recent past, active and controllable journal bearings have been developed and nowadays are still increasingly found in the literature. The current state of research on controllable oil film bearings can be found in [16]. Many of the existing active and controllable bearing concepts incorporate movable or flexible bearing pads. Other concepts apply external forces on the bearing shell or the journal, for example magnetic in [8, 9] or piezomechanical in [15, 19], without changing the bearing's clearance geometry. Furthermore there are also bearings that utilize an active oil injection as suggested in [16]. In most of the cases, a classical PID controller is used for control.

In this paper, an actively adjustable journal bearing, which is capable to change the fluid film thickness and thus the effective stiffness and damping properties of the bearing, is investigated. Very recently, the concept of passive adjustment of bearing clearance was theoretically investigated [2] and experimentally validated [4]. A journal bearing of variable geometry [2–4]

149

is a plain cylindrical journal bearing separated in two symmetric semi-cylindrical parts, one movable and one fixed. The principle of operation is based on the passive displacement of the movable part as the rotor-bearing system approaches a critical speed. The increment of the journal whirling amplitude leads to the increment of the fluid film dynamic loading, and after exceeding a preloading force, the bearing moving part is displaced mounted on a spring and damper configuration. As the system approaches a critical speed and the bearing moving part is passively displaced, the variation of the effective stiffness and damping characteristics of the fluid film is achieved, leading to variational stiffness and damping properties during resonance and thus the suppression of resonance vibration amplitude [11]; up to 50% amplitude decrement was noticed in both theoretical and experimental studies, with the energy dissipation on the damper mounting the bearing moving part to be much less than this dissipated due to the damping properties of the fluid film.

In the present investigation, the fluid-film thickness is varied under the semi-active displacement of the bearing moving part at a constant frequency and amplitude. These two control parameters are tuned properly in order to achieve a so-called parametric anti-resonance which leads to the suppression of the self-excited vibrations. A parametric anti-resonance is a specific parametric combination resonance which does not lead to a parametric instability but enables an increased dissipation of vibration energy. The beneficial effect of a parametric anti-resonance on self-excited vibration was discovered by TONDL in his pioneering work [18]. This concept was then transferred to general dynamic systems [5], was interpreted physically as an energy transfer between the vibration modes of the original system, and was validated experimentally in simple systems including a flexible rotor. A recent summary on this topic can be found in [6].

A flexible rotor mounted on bearings whose dynamic properties are controlled semi-actively is investigated. Such a concept was proposed for active magnetic bearings in [7] and validated theoretically and experimentally. It allowed the operation of active bearings beyond the stability limit of the implemented PID controller. The very same concept is extended here to fluid-film bearings with adjustable geometry. This allows to operate the rotor well beyond rotor speeds which are associated with the oil-whip instability. This idea was investigated numerically in an initial study in [14].

In the present paper, the journal bearing fluid film properties are varied harmonically in time by changing the clearance of the bearing under the semi-active displacement of the bearing moving part. This control introduces a parametric excitation in the original system. Changing the clearance harmonically results in a periodic change of the dynamic properties which are theoretically expanded into FOURIER series. Corresponding stability charts are generated by employing the FLOQUET method and compared to analytical predictions which

are extracted from a perturbation technique.

2. Adjustable journal bearing

The journal bearing considered here is a lemon-bore bearing in horizontal construction design as shown in figure 1. The sliding surfaces (the segments) can be moved along the vertical direction. This adjustment leads to a change of the bearing clearance and consequently to a change of the preload factor δ which is a measure for the geometrical deviation from a cylindrical bearing. Typical values for lemon-bore bearings are in the region of $\delta = 50\% \ldots 75\%$, see e.g. [10,17]. The effective stiffness and damping properties of the fluid film change due to this geometric adjustment. In this investigations, the preload factor is changed harmonically,

$$\delta(t) = \delta_{\text{mean}} + \Delta\delta \sin(\Omega_P t). \tag{1}$$

Herein, δ_{mean} expresses the setting for the underlying lemon-bore bearing with fixed geometry. For the present study this parameter is fixed to a value of 65%. A more detailed description of the bearing geometry can be found in [14]. The calculation of the bearing
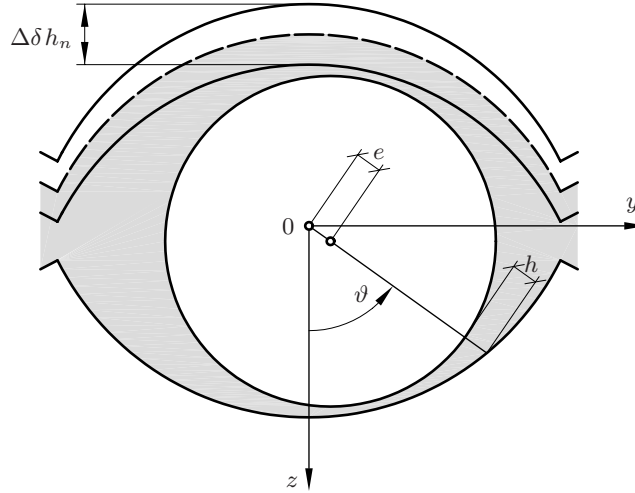
Figure 1. Principle of the adjustable journal bearing; a movement of the upper segment is shown.

forces is performed for both individual segments by numerical integration of the REYNOLDS differential equation of lubricating film theory, see e.g. [12],

$$\frac{1}{R_S^2} \frac{\partial}{\partial \vartheta} \left(h^3 \frac{\partial p}{\partial \vartheta} \right) + \frac{\partial}{\partial x} \left(h^3 \frac{\partial p}{\partial x} \right) = 6\eta_{oil} \left(\Omega \frac{\partial h}{\partial \vartheta} + 2 \frac{\partial h}{\partial t} \right), \tag{2}$$

151

which describes the pressure distribution $p(\vartheta, x)$ in dependency of the segment radius R_S, the bearing width B, the gap function h, the angular speed Ω and the oil viscosity η_{oil}. In general, the fluid-film forces that act on the journal depend on the position and on the velocity of the journal which can be expressed by the nonlinear relationship, $F = F(e, \vartheta, \dot{e}, \dot{\vartheta})$. If an equilibrium position exists, the fluid film force can be linearized which yields

$$
\begin{bmatrix} \Delta F_z \\ \Delta F_y \end{bmatrix} = \begin{bmatrix} b_{zz} & b_{zy} \\ b_{yz} & b_{yy} \end{bmatrix} \begin{bmatrix} \Delta \ddot{w}_L \\ \Delta \dot{v}_L \end{bmatrix} + \begin{bmatrix} k_{zz} & k_{zy} \\ k_{yz} & k_{yy} \end{bmatrix} \begin{bmatrix} \Delta w_L \\ \Delta v_L \end{bmatrix} .
\tag{3}
$$

Equation (3) contains the stiffness coefficients k_{ij} as well as the damping coefficients b_{ij}. Both depend on the preload factor δ and thus depend on the time t. For simplicity, the letter Δ is neglected hereinafter.

3. Rotor model

The dynamic model of the rotor system consists of a JEFFCOTT rotor, see figure 2 for more details. This model represents a simplification of real-world rotors but it is sufficient to show the main physical phenomena. The rotor consists of a flexible, massless shaft (stiffness k) with a centered disc (mass m_S) and two journals (each mass m_Z) mounted at its ends. The bearing forces are acting on the journals and are indicated. All masses are assumed to be balanced. A constant rotor speed Ω is considered. The coordinates are given by w_W and v_W for the disc center and w_L and v_L for the journals in the z- and y-direction. Applying NEWTON's second law together with (3) yields the equation of motion for the linearized system,

$$
\begin{bmatrix} m_S & & & \\ & m_S & & \\ & & 2m_Z & \\ & & & 2m_Z \end{bmatrix} \begin{bmatrix} \ddot{w}_W \\ \ddot{v}_W \\ \ddot{w}_L \\ \ddot{v}_L \end{bmatrix} + \begin{bmatrix} & & & \\ & & & \\ & & 2b_{zz} & 2b_{zy} \\ & & 2b_{yz} & 2b_{yy} \end{bmatrix} \begin{bmatrix} \dot{w}_W \\ \dot{v}_W \\ \dot{w}_L \\ \dot{v}_L \end{bmatrix} +
$$
$$
\begin{bmatrix} k & & -k & \\ & k & & -k \\ -k & & k+2k_{zz} & 2k_{zy} \\ & -k & 2k_{yz} & k+2k_{yy} \end{bmatrix} \begin{bmatrix} w_W \\ v_W \\ w_L \\ v_L \end{bmatrix} = \begin{bmatrix} 0 \\ 0 \\ 0 \\ 0 \end{bmatrix}
\tag{4}
$$

or in matrix notation

$$
M \ddot{q} + B \dot{q} + K q = 0 .
\tag{5}
$$

The physical and geometrical properties of the rotor system are listed in table 1.
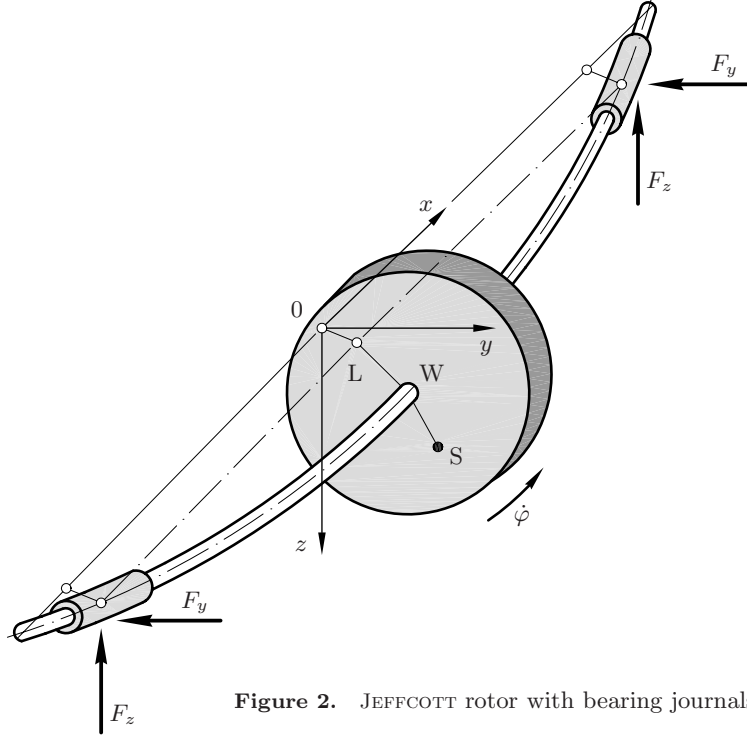
Figure 2. JEFFCOTT rotor with bearing journals.

Note that the matrices $\boldsymbol{B}$ and $\boldsymbol{K}$ are time-dependent and can be split into a constant and a time-periodic part. Furthermore, in the context of fluid-film bearings and rotordynamics, the coefficient matrices for displacements and velocities, $\boldsymbol{B}$ and $\boldsymbol{K}$, are in general not symmetric. However, they can be split into symmetric and skew-symmetric matrices,

$$\boldsymbol{A} = \boldsymbol{A}_0 + \boldsymbol{A}_t = \boldsymbol{A}_0^{\mathrm{sym}} + \boldsymbol{A}_0^{\mathrm{asym}} + \boldsymbol{A}_t^{\mathrm{sym}} + \boldsymbol{A}_t^{\mathrm{asym}}. \tag{6}$$

The index 0 denotes the constant part and the index t the time-dependent part of the corresponding system matrix.

4. Numerical stability analysis

FLOQUET theory is applied for investigating the stability regions of the dynamic system in eq. (5) by numerical means. The stiffness and damping properties are functions of the preload factor δ as well as the SOMMERFELD number So. In the present analysis the movement of the segment is considered to be quasi-static, which means that the coefficients are assumed to be independent from the segment velocity. Although the movement of the upper bearing

153

segment in figure 1 (see also eq. 1) is harmonic, the resulting variation of the effective stiffness and damping coefficients is in general not harmonic, but periodic with period T,

$$\boldsymbol{K}(t) = \boldsymbol{K}(t+T), \qquad \boldsymbol{B}(t) = \boldsymbol{B}(t+T) . \tag{7}$$

A typical variation of a direct stiffness coefficient together with an approximation by a FOURIER series of different orders is shown in figure 3. The visualization shows that a FOURIER series of third order resembles the sample shape sufficiently well.
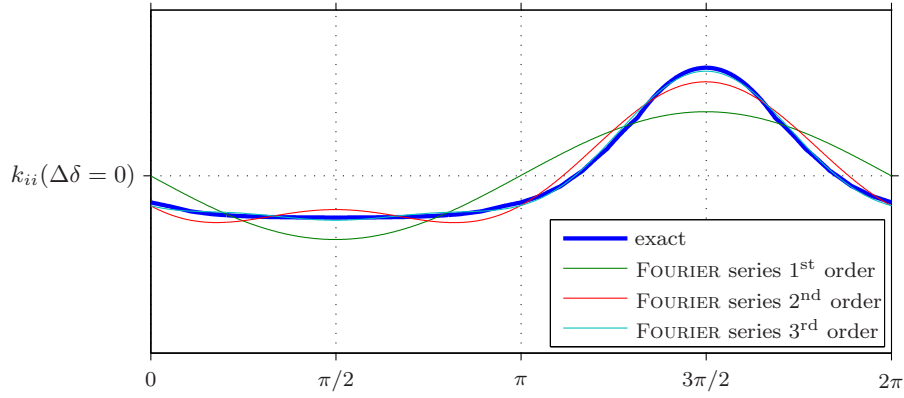
Figure 3. Example periodic variation of a stiffness coefficient due to a harmonic movement of the upper bearing segment in figure 1: exact and approximation by FOURIER series.

Figure 4 shows the stability domains for the exact periodic bearing characteristic as well as for the approximation by a FOURIER series of first order. In comparison to the exact calculation, there is a gap between the stability domain of the underlying system with fixed bearing geometries and the stability domain created by the parametric anti-resonance. Consequently, the stability domain is sensitive at smaller rotor speeds to higher order coefficients. Above the speed of instability of the time-invariant system, which is here at $\Omega/\omega_0 \approx 2$, a large stability domain exists for a certain combination of control frequency and amplitude due to a parametric anti-resonance. The minimum control amplitude strongly depends on the rotor speed. For rotor speeds slightly above the instability speed, a high amplitude has to be chosen in order to achieve a simply connected stability domain at a fixed control amplitude within the full speed range.

The analytical analysis in the following section is focused on the analysis of the system with a truncated FOURIER series of order 1 which is shown in figure 4 on the right hand side.
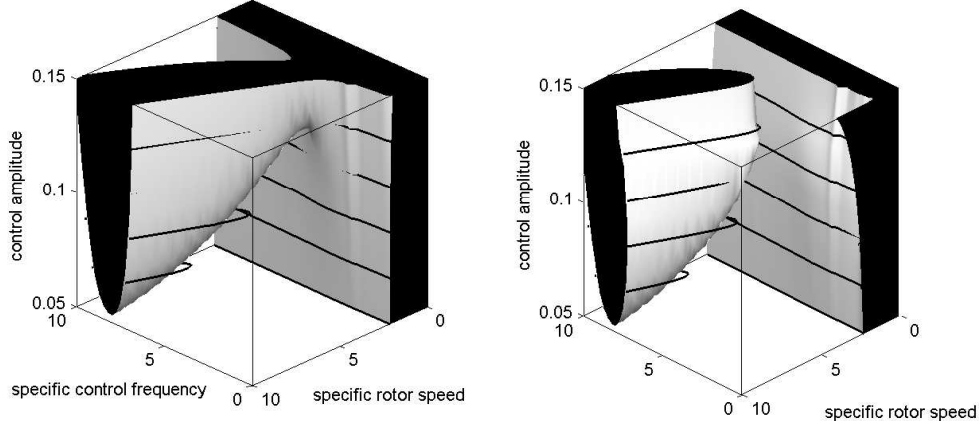
Figure 4. Stability body for (left) full model and (right) for truncated Fourier series of first order (see figure 3). Dark area depicts a stable system.

5. Analytical stability analysis

The analytical approximation of the stability boundary in the parameter space of the trivial solution is outlined in the following. The derived analytical predictions allow the determination of design parameters that influence the stability of variable geometry bearings. The non-conservative system can be rewritten in state space notation as

$$
\begin{bmatrix} \mathbf{I} & \mathbf{0} \\ \mathbf{0} & \mathbf{M} \end{bmatrix} \dot{\mathbf{z}} = \begin{bmatrix} \mathbf{0} & \mathbf{I} \\ -\mathbf{K} - \mathbf{N} & -\mathbf{C} - \mathbf{G} \end{bmatrix} \mathbf{z} \qquad \text{or} \qquad \mathbf{B}\dot{\mathbf{z}} = (\mathbf{A}_0 + \mathbf{A}_t)\mathbf{z} \tag{8}
$$

Consider the corresponding eigenvalue problem and the adjoint eigenvalue problem [13]

$$
\lambda_i \mathbf{B}\mathbf{u}_i = \mathbf{A}_0 \mathbf{u}_i, \qquad \lambda_i \mathbf{B}^T \mathbf{v}_i = \mathbf{A}_0^T \mathbf{v}_i, \qquad i = 1, 2, \ldots, 2 \tag{9}
$$

wherein λ_i are the eigenvalues and $\mathbf{u}_i$, $\mathbf{v}_i$ the right and left eigenvectors of the system in eq. (8). These eigenvectors are biorthogonal and can be normalized to satisfy

$$
v_i^T \mathbf{B} u_j = \delta_{ij}, \qquad v_i^T \mathbf{A}_0 u_j = \lambda_i \delta_{ij} \tag{10}
$$

Since the coefficient matrices in eq. (8) are real, the eigenvalues are real or complex conjugate pairs. For the specific rotor system with variable bearings considered here, the system possesses 3 complex conjugate pairs and 2 real eigenvalues (see figure 5). Two of the complex conjugate pairs are almost identical. Candidates for the parametric anti-resonance are the

155
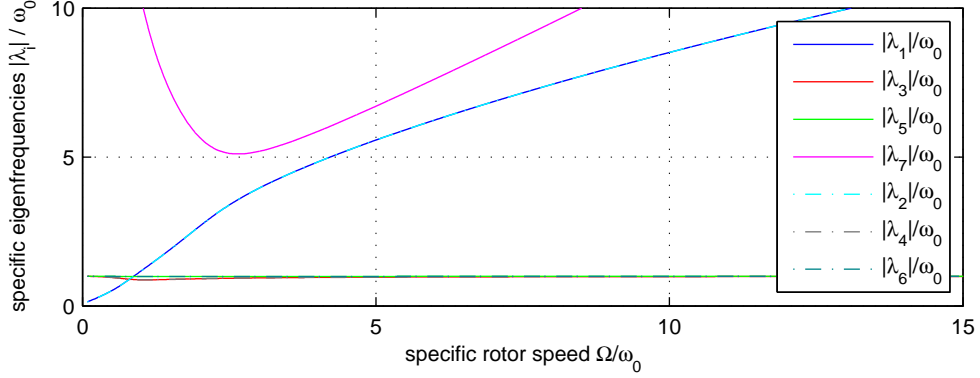
Figure 5. Specific eigenfrequencies of the system listed in table 1.

parametric combination resonance of summation or difference types ($|\omega_i \mp \omega_j|/k$), at least for the dynamic systems considered so far in the literature. For the present system it was found that the region of parametric anti-resonance is approximated best by the stability boundary curve of a parametric resonance frequency ($2\omega_i/k$). This stability boundary curve is derived briefly in the following. The stability boundary curves at parametric combination resonance frequencies will be presented elsewhere.

For one pair of complex conjugate eigenvalues, the complex conjugate eigenvectors $\mathbf{u}_i$, $\mathbf{v}_i$ can translated to real-valued eigenvectors,

$$\widehat{\mathbf{U}} = \left[\Re\{\mathbf{u}_i\}, \; \Im\{\mathbf{u}_i\} \right], \qquad \widehat{\mathbf{V}} = \left[\Re\{\mathbf{v}_i\}, \; -\Im\{\mathbf{v}_i\} \right]. \tag{11}$$

Applying these eigenvectors in the normalization in eq. (10) still diagonalizes the coefficient matrix $\mathbf{B}$ but the coefficient matrix $\mathbf{A}_0$ becomes a block-diagonal matrix of the form

$$\widehat{\mathbf{V}}^T \mathbf{A}_0 \widehat{\mathbf{U}} = \begin{bmatrix} \alpha_i & \beta_i \\ -\beta_i & \alpha_i \end{bmatrix} \tag{12}$$

This matrix can be transformed to an equivalent dynamic system of second order by the similarity transformation

$$\begin{bmatrix} 1 & 0 \\ \alpha_i & \beta_i \end{bmatrix} \begin{bmatrix} \alpha_i & \beta_i \\ -\beta_i & \alpha_i \end{bmatrix} \begin{bmatrix} 1 & 0 \\ -\alpha_i/\beta_i & 1/\beta_i \end{bmatrix} = \begin{bmatrix} 0 & 1 \\ -(\alpha_i^2 + \beta_i^2) & 2\alpha_i \end{bmatrix} \tag{13}$$

and

$$\begin{bmatrix} 1 & 0 \\ \alpha_i & \beta_i \end{bmatrix} \begin{bmatrix} 1 & 0 \\ -\alpha_i/\beta_i & 1/\beta_i \end{bmatrix} = \mathbf{I} \tag{14}$$

156

Note that the relation $\alpha_i^2 + \beta_i^2 = |\lambda_i| = \omega_i$ holds. The similarity transformation allows to express the pair of complex conjugate eigenvalues and eigenvectors by an equivalent dynamic system of second order. The original system in eq. (8) becomes finally of the form (for complex conjugate eigenvalues)

$$\ddot{z}_i + \varepsilon\Theta_{ii}\dot{z}_i + \omega_i^2 z_i = -\varepsilon\left(R_{ij}\dot{z}_j + Q_{ij}z_j\right)\sin\Omega t - \varepsilon\left(S_{ij}\dot{z}_j + P_{ij}z_j\right)\cos\Omega t \tag{15}$$

Herein, the small parameter ε was introduced and the following relations hold:

$$\varepsilon\Theta_{ii} = -2\alpha_i$$
$$\varepsilon Q_{ij}\sin\Omega_P t + \varepsilon P_{ij}\cos\Omega_P t = \widetilde{\mathbf{v}}_i^T(\mathbf{K}_t + \mathbf{N}_t)\widetilde{\mathbf{u}}_j, \tag{16}$$
$$\varepsilon R_{ij}\sin\Omega_P t + \varepsilon S_{ij}\cos\Omega_P t = \widetilde{\mathbf{v}}_i^T(\mathbf{C}_t + \mathbf{G}_t)\widetilde{\mathbf{u}}_j$$

Herein, $\widetilde{\mathbf{u}}_j$, $\widetilde{\mathbf{v}}_j$ are the right and left eigenvectors from eq. (11 that were weighted with coefficient matrices of the similarity transformation in eq. (13). The stability condition for such a general time-harmonic system is derived by applying the averaging method in the quasi-periodic case [20]. In the present discussion a detuning of first order in ε from a parametric resonance frequency is introduced

$$\Omega_P = \frac{2\omega_i}{k} + \varepsilon\sigma_i + \mathcal{O}(\varepsilon^2) \tag{17}$$

which leads to the resonant terms for the coefficients Q_{ii}, P_{ii}, R_{ii}, S_{ii} (see [6] for more details). The analysis at parametric combination frequencies is not presented here. The stability boundary for a parametric excitation in the vicinity of $2\omega_i/k$ is found from the coefficient matrix of the underlying slow dynamics of the perturbed system and employing the ROUTH-HURWITZ conditions [1] which lead to

$$\omega_i S_{ii} + Q_{ii} - 2\omega_i\Theta_{ii} > 0 \tag{18}$$

$$\varepsilon\sigma_i^{\text{crit}} = \mp\frac{1}{2k\omega_i}\sqrt{-4\omega_i^2\Theta_{ii}^2 + (\omega_i S_{ii} + Q_{ii})^2 + (\omega_i R_{ii} - P_{ii})^2} \tag{19}$$

Herein, Θ_{ii} is the modal damping and the coefficients Q_{ii}, P_{ii} and R_{ii}, S_{ii} represent the parametric excitation that is proportional to the displacements and velocities in the modal space. For the specific system parameters listed in Section 3, the coefficients Q_{ii}, P_{ii} are dominant which simplifies eq. (19).

The comparison between the numerical results shown in figure 4 and the analytical prediction in eqs. (19) and (17) is summarized in figure 6. The dashed line shows the natural frequency ω_3 in dependency of the rotor speed. The thin solid line shows the stability boundary $\Theta_{ii} = 0$ of the system with fixed bearings geometry ($\Delta\delta = 0$). The thick solid line shows the analytical prediction of the stable region according to eqs. (19) and (17) for $k = 2$.
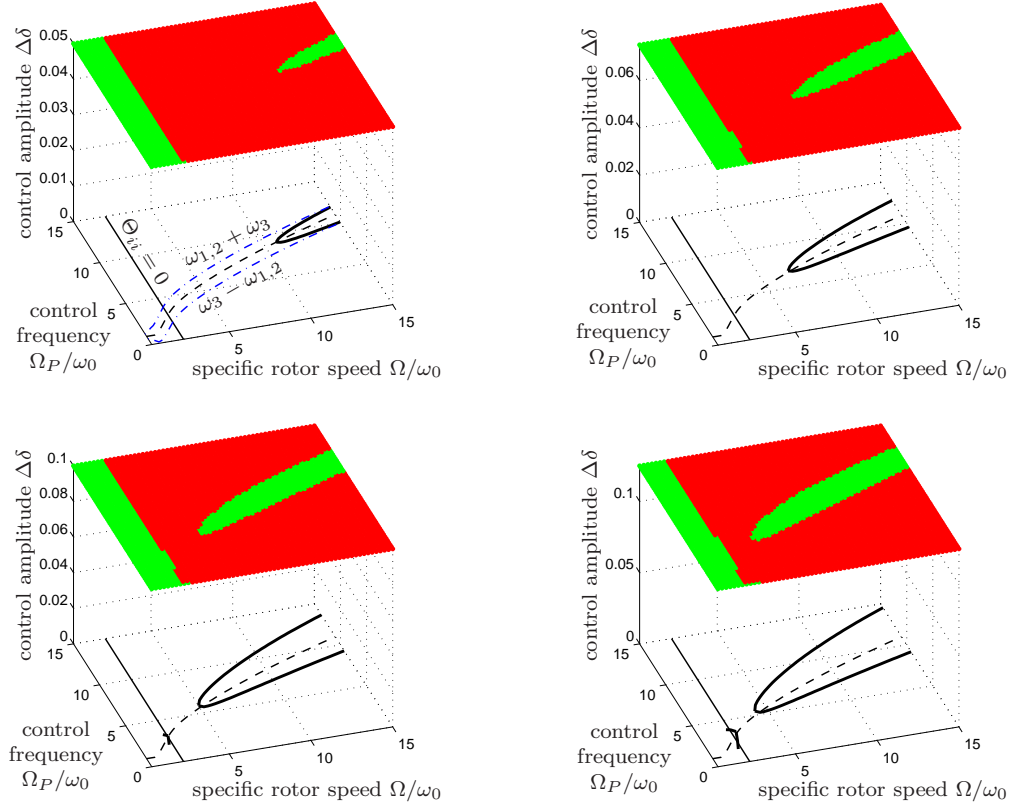
Figure 6. Stability charts for different control amplitudes $\Delta\delta$ extracted from figure 4 for the truncated FOURIER series, overlayed with the analytical prediction according to eqs. (19) and (17) for $k = 2$. The green area depicts a stable system.

6. Conclusions

A simple rotor supported by journal bearings with adjustable geometry is investigated. Due to a harmonic, semi-active adjustment of the bearing clearance, the fluid-film properties alter periodically in time. Tuning the frequency and amplitude of this adjustment, a parametric anti-resonance is achieved at which self-excited vibrations are successfully suppressed. Employing this concept, the rotational speed can be increased far above the stability limit of the originally time-invariant system without becoming unstable. Calculations using FLO-QUET's theorem as well as an analytical prediction confirm the enhanced stability domain. The analytical stability analysis will be extended to higher orders of the FOURIER series. An experimental verification is ongoing.

A. Appendix

Table 1. Physical and geometrical properties of the rotor system.

Mass of the disc	$m_S = 2\,\mathrm{kg}$
Mass of a journal	$m_Z = 0.25\,\mathrm{kg}$
Stiffness parameter	$k = 1.85 \cdot 10^5\,\mathrm{N/m}$
Static load	$F_{stat} = (m_S + 2\,m_Z)\,g = 24.5\,\mathrm{N}$
Bearing width	$B = 27\,\mathrm{mm}$
Radius of the segments	$R_S = 27\,\mathrm{mm}$
Radial clearance (for $\delta = 0$)	$h_n = R_S - R_Z = 132.3 \cdot 10^{-6}\,\mathrm{m}$
Relative gap	$\psi_n = h_n/R_S = 4.9 \cdot 10^{-3}$
Oil viscosity	$\eta_{oil} = 1.3 \cdot 10^{-3}\,\mathrm{N/(m^2 s)}$
Reference angular velocity	$\omega_0^2 = 2\,F_{stat}/(h_n\,m_S) = 92.7 \cdot 10^3\,1/\mathrm{s}^2$
Reference SOMMERFELD-number	$So_0 = F_{stat}\,\psi_n^2/(B\,2R_S\,\eta_{oil}\,\omega_0) = 0.5$
Dimensionless stiffness parameter	$\kappa = 2\,F_{stat}/(h_n\,k) = 1$
Dimensionless mass parameter	$\mu = 2\,m_Z/m_S = 0.25$

References

[1] BILHARZ, H. Bemerkung zu einem Satze von Hurwitz. *ZAMM 24(2)* (1944), 77–82.

[2] CHASALEVRIS, A., AND DOHNAL, F. A journal bearing with variable geometry for the reduction of the maximum amplitude during passage through resonance. *Journal of Vibration and Acoustics 134* (2012), 061005–1–061005–8.

[3] CHASALEVRIS, A., AND DOHNAL, F. Vibration quenching in a large scale rotor-bearing system using journal bearings with variable geometry. *Journal of Sound and Vibration 333* (2014), 2087–2099.

[4] CHASALEVRIS, A., AND DOHNAL, F. A journal bearing with variable geometry for the suppression of vibrations in rotating shafts: Simulation, design, construction and experiment. *Mechanical Systems and Signal Processing 52-53* (2015), 506–528.

[5] DOHNAL, F. Damping by parametric stiffness excitation: resonance and anti-resonance. *Journal of Vibration and Control 14(5)* (2008), 669–688.

[6] DOHNAL, F. *A contribution to the mitigation of transient vibrations, Parametric anti-resonance: theory, experiment and interpretation.* Habilitation thesis, Technische Universität Darmstadt, 2012.

[7] DOHNAL, F., AND MARKERT, R. Enhancement of external damping of a flexible rotor in active magnetic bearings by time-periodic stiffness variation. *Journal of System and Dynamics 5(5)* (2011), 856–865.

[8] EL-SHAFEI, A., AND DIMITRI, A. S. Controlling journal bearing instability using active magnetic bearings. *J. Eng. Gas Turb. Power 132(1)* (2010), 012502–012502–9.

[9] FÜRST, S., AND ULBRICH, H. An active support system for rotors with oil-film bearings. In *Proceedings of the 4th International Conference on Vibrations in Rotating Machinery of the Institution of Mechanical Engineers* (Edinburgh, UK, 1988), pp. 61–68.

[10] GLIENICKE, J. *Feder- und Dämpfungskonstanten von Gleitlagern für Turbomaschinen und deren Einfluß auf das Schwingungsverhalten eines einfachen Rotors (in German).* PhD thesis, Technische Hochschule Karlsruhe, 1966.

[11] ISHIDA, Y., AND LIU, J. Vibration suppression of rotating machinery utilizing discontinuous spring characteristics (stationary and nonstationary vibrations). *Journal of Vibration and Acoustics 130(3)* (2008), 031001/1–7.

[12] LANG, O., AND STEINHILPER, W. *Gleitlager – Berechnung und Konstruktion von Gleitlagern mit konstanter und zeitlich veränderlicher Belastung (Konstruktionsbücher Band 31).* Springer-Verlag, 1978.

[13] MEIROVITCH, L. *Analytical methods in vibrations.* Macmillan Series in Applied Mechanics, 1967.

[14] PFAU, B., RIEKEN, M., AND MARKERT, R. Numerische Untersuchungen eines verstellbaren Gleitlagers zur Unterdrückung von Instabilitäten mittels Parameter-Antiresonanzen. In *First IFToMM D-A-CH Conference 2015* (Dortmund, 2015).

[15] PRZYBYLOWICZ, P. Active stabilisation of a rigid rotor by a piezoelectrically controlled mobile journal bearing system. *Australian J of Mech. Eng. 1(2)* (2004), 123–128.

[16] SANTOS, I. F. On the future of controllable fluid film bearings. *Mécanique & Industries 12* (2011), 275–281.

[17] SOMEYA, T. *Journal-Bearing Databook.* Springer-Verlag, 1989.

[18] TONDL, A. *On the interaction between self-excited and parametric vibrations.* Monographs and Memoranda No. 25, National Research Institute for Machine Design, Běchovice, 1978.

[19] TŮMA, J., ŠIMEK, J., ŠKUTA, J., AND LOS, J. Active vibrations control of journal bearings with the use of piezoactuators. *Mechanical Systems and Signal Processing 36* (2013), 618–629.

[20] VERHULST, F. *Methods and applications of singular perturbations. Boundary layers and multiple timescale dynamics.* Springer-Verlag, 2005.

Fadi Dohnal, Dr. techn. habil.: Alstom Switzerland Ltd., 5401 Baden, SWITZERLAND (*fadi.dohnal@power.alstom.com*). The author gave a presentation of this paper during one of the conference sessions.

Bastian Pfau, M.Sc. (Ph.D. candidate): Technische Universität Darmstadt, 64287 Darmstadt, GERMANY (*pfau@sdy.tu-darmstadt.de*).

Athanasios Chasalevris, Ph.D.: Alstom Renewable UK Ltd., Rugby CV21-2NH, U.K. (*athanasios.chasalevris@power.alstom.com*).

Galvanometer scanning for high-end biomedical and industrial imaging applications
(CON097-15)

Virgil-Florin Duma[1]

Abstract: Galvanometer-based scanners (GSs) are the most utilized devices for high-end applications, such as biomedical imaging – for example in Confocal Microscopy or Optical Coherence Tomography (OCT). We present in this paper our previous and current studies on GSs, regarding several aspects: (i) a comparison of the performances of the most utilized scanning regimes (i.e., triangular, sawtooth, and sinusoidal); (ii) several rules-of-thumb extracted from the experimental studies and from the mathematical modeling concerning the optimal use of GSs in OCT; (iii) optimal custom-made scanning functions to achieve the highest possible duty cycle/time efficiency of the scanning process. Recent progress in our groups regarding the construction of handheld scanning probes using GSs are pointed out. An overview of a range of imaging applications of such devices in OCT - as we have performed in biomedical clinical and industrial environments - concludes the paper.

1. Introduction

Laser scanners are one of the most utilized optomechatronic devices for biomedical imaging (e.g., for Confocal Microscopy (CM) and Optical Coherence Tomography (OCT)), as well as for industrial manufacturing and Non-Destructive Testing (NDT) applications. Although more than forty different configurations of laser scanners were developed since the early 1970s, only five types of such devices are essentially in use nowadays [1, 2]: oscillatory (galvanometer-based or resonant), polygonal, refractive (i.e., with Risley prisms), holographic, electro-, and acousto-optical.

The most utilized – since the early 1990s – are the *galvanometer scanners (GSs)*, while the others have mostly niche applications that are imposed by their different advantages and drawbacks. Thus, *polygon mirror (PM)* scanners [3, 4] provide the highest scanning speeds from all mechanical scanners, therefore they are employed for example in broadband laser sources scanned in frequency for the fastest variant (i.e., Swept Source) of one of the established biomedical imaging techniques: OCT [5-7]. *Risley prisms* are employed in applications that range from satellite positioning to raster scanning in CM [8] or to endoscope scanning probes in OCT – as such devices have high scanning speeds (although with complicated scan patterns [9]) and they can be miniaturized. *Holographic* scanners can also provide a fast scan, but they can only be utilized with the light wavelength with which they have been created, therefore they cannot be used for broadband lasers like those necessary

for low coherence techniques such as OCT. *Acousto- and electro-optical* scanners do not have mechanical inertia therefore they can operate in the MHz region in terms of scan frequency, but their resolution is quite low [2].

In contrast to all the solutions above GSs have good performances for all the scanners characteristics, with no major drawbacks; this actually gives their employability. Thus, GSs have a good positioning position, they provide a good scanning frequency and speed, and are sufficiently compact at reasonable costs per axis. Their technology is mature in most respects, regarding [10]: motors, bearings, mirrors, sensors, control structures, and testing. These advantages have imposed them for example for lateral scan in a multitude of biomedical imaging techniques, including CM, OCT, two photon or multi-photon microscopy [6]. All these techniques gave in return a strong feed-back to further develop and improve not only GSs, but all scanning devices [11].

However, GSs still have issues, especially in the area of their scanning algorithms. This provides an active avenue of research nowadays for the optimization of their parameters and programming. In this respect, the aim of this paper is to present some of our main contributions in this field of work regarding GSs, especially utilized in high-end applications - with a definite focus on OCT. We shall also point out briefly some of these applications on which we have worked on recently, both in the biomedical field (in particular, for dentistry) and in NDT for materials study for industry.

2. Optimization of the most utilized galvoscanning regimes

From a constructive point of view a GS is an electric motor with an oscillatory element (i.e., a moving magnet) which has on its shaft a mirror to deflect a laser beam to a desired position (Fig. 1). The shaft also has spring elements (e.g., flexure bearings) and a damper, as well as a position sensor system which provides its current angular position $\theta(t)$ to a closed-loop control structure.
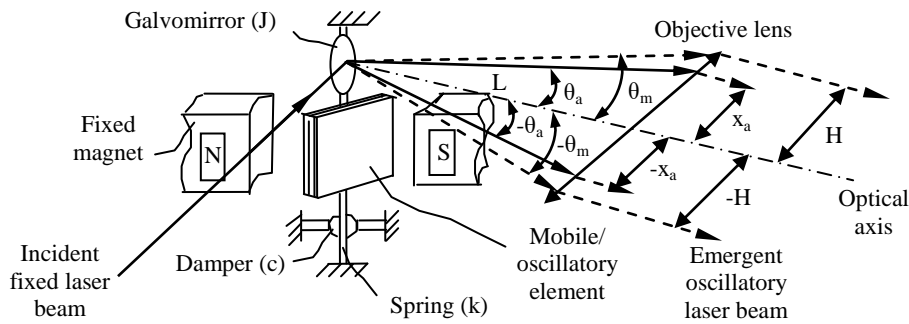
Figure 1. Galvanometer-based Scanner (GS) - principle scheme. Notations: $\theta(t)$, scan angle; θ_a, angular scan amplitude; $x(t)$, position of the scanning spot; x_a, amplitude of the linear scan; H, total scan amplitude; L, distance from the galvomirror axis to the objective lens.

One of the most incorrect assumptions when using GSs in a high-end application is that the output signal (i.e., the current angular position of the galvomirror) will match perfectly the input signal. Actually, this is approximately true only for very low scan/oscillatory frequencies, for which one may consider that the stop-and-turn of the GS shaft (with the mirror attached to it) can be done almost instantaneously. However, as the scan frequency in increased, mechanical inertia begins to play a more significant role and the mobile element of the GS actually needs a certain time to decelerate and stop from a given speed, as well as another finite time interval to accelerate to another value of the scan speed. This is at least the case of two of the most utilized scanning regimes, i.e., *triangular* (Fig. 2a) and *sawtooth* (Fig. 2b). The non-linear portions of the output signal/scanning function that are thus produced become more significant when increasing the scan frequency $f_s=1/T$ (where T is the time period of an oscillation) and/or the scan amplitude θ_m (Fig. 1). We have made a detailed study [12] to characterize these phenomena and to compare the duty cycle of the GS for the three most common scanning regimes which are shown in Fig. 2a-c.

The duty cycle (or *the time efficiency of the scanning process*) is defined as the ratio between the "active" time (i.e., the interval within a time period T for which the scan is performed with a constant speed) and the period T. There is a *theoretical/ideal duty cycle* η_t (of the input signal) equal to 100% for the triangular scan (Fig. 2a) if bi-directional scan is used for the application) and which varies from 50% to 90% for the sawtooth scan (Fig. 2b) - where the former value characterizes a triangular uni-directional scan):

(a) (b) (c)

(d) (e)
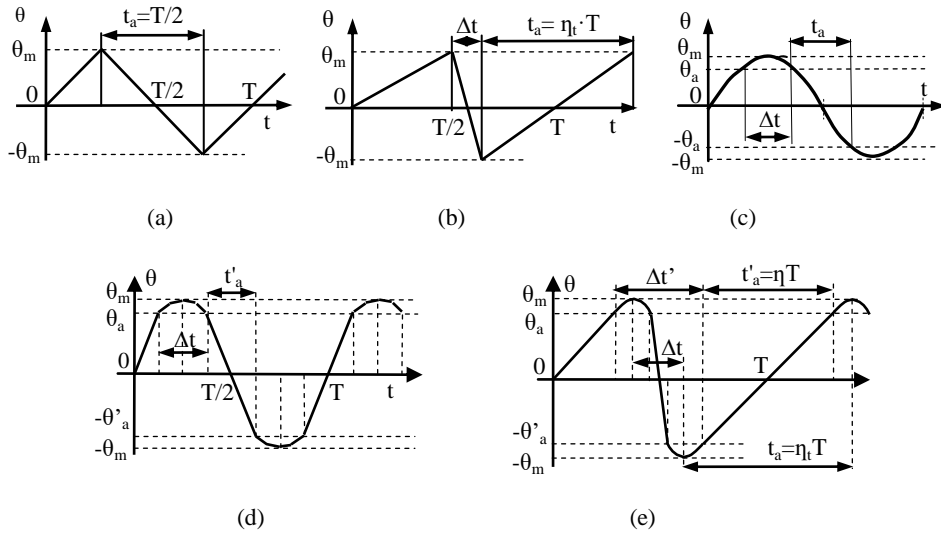
Figure 2. Input and output scanning signals of a GS: (a) triangular, (b) sawtooth, and (c) sinusoidal input signals; (d) triangular and (b) sawtooth output signals.

163

$$\eta_t = 1 - \frac{\Delta t}{T}. \tag{1}$$

The output signal is characterized by an *effective duty cycle η* which takes into account the non-linear portions of the output signal (Fig. 2d, e) produced by mechanical inertia (or directly the non-linearity of the input signal itself when sinusoidal scan is utilized). For the first two scanning regimes:

$$\eta = \frac{4t'_a}{T} = \begin{cases} 1 - \dfrac{4\tau}{T}, & \text{for triangular scan} \\[2mm] 1 - \dfrac{\Delta t'}{T}, & \text{for sawtooth scan} \end{cases} \tag{2}$$

where $\Delta t'$ is the return time of the galvomirror, increased with regard to the Δt return time of the input signal (Fig. 2b) due to the non-linear portions produced by mechanical inertia. For the sawtooth scan, this phenomenon is even more complicated by the fact that the entire output signal (Fig. 2d) "shifts" towards a triangular shape, as we have documented in detail, developing two appropriate mathematical models and deducing the expressions of η in [13].

From the multi-parametric study on η with regard to the scan parameters η_t, f_s, and θ_a, several conclusions can be drawn in order to optimize the scanning regimes, including the following [12, 13]:

(i) Triangular scan is the one that can provide the highest possible effective duty cycle (i.e., the largest time t'_a (Fig. 2d, e) with a constant scanning speed per an oscillatory period T). In OCT imaging, this means that the OCT image is not distorted at reasonable scan frequencies and amplitudes – with limits that we have studied – see for example Fig. 3, as well as Fig. 7 [12].

(ii) However, as a natural tendency of GS users, η_t is increased to have time for an imaging with higher resolution for example in OCT, therefore Δt is decreased for a certain period $T=1/f_s$ of the scanning process. The problem is that, as we have demonstrated [13], this does not produce the desired effect; in fact it produces, for f_s roughly higher than 200 Hz, a saturation of the device from this point of view. Therefore sawtooth scan, although theoretically convenient (it provides theoretically the longest available time with a constant scan speed, i.e., $t_a=\eta_t T$), is in practice strongly affected by the non-linearity of the scanning function, especially since the speed of the return portion (Fig. 2b and e) is significantly higher. In this respect, based on our work in [12], other groups thus obtained corrected OCT images of large scanned samples (e.g., retina) by eliminating the distorted portions of each individual scan [14]. The sawtooth scan is also disadvantageous from a mechanical point of view due to the high stress inflicted on the mobile equipment; this leads on short term to heating of the device (thus affecting its functionality) and on long term to a decrease of its life time.

(iii) Sinusoidal scan is excellent from the mechanical point of view (in contrast to the above sawtooth regime), because the acceleration and then the deceleration are actually continuous (Fig. 2c).

The major consequence is the capability of a certain GS to function only up to a certain maximum scan amplitude θ_{lim} at each scan frequency for sinusoidal, as well as for triangular and sawtooth scan – for each type of GS (fee for example the testing results in Fig. 3); at scan amplitudes higher than θ_{lim} the system looses stability and chaotic vibrations are being recorded. Looking from another angle, one may say that the GS can work at a double limit scan frequency (i.e., 2 kHz for the GS we have tested - Fig. 3) for sinusoidal with regard to triangular scan. The issue is that exactly this aspect affects the optical performance of the device: the non-linearity of the signal produces the smallest η of all three scanning regimes and this results in long distorted portions on the OCT images (Fig. 17, [12]).
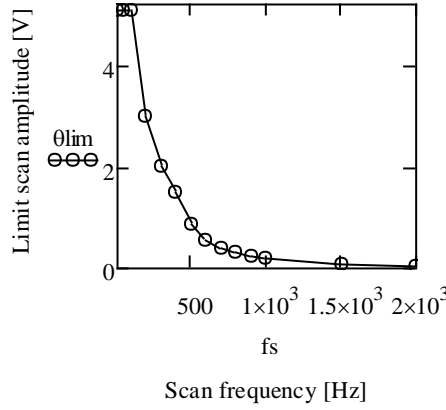
Figure 3. Limit (i.e., maximum achievable) scan amplitudes θ_{lim} that a tested GS [12, 13] is capable to achieve at each scan frequency f_s – example of a testing for sinusoidal input signals.

Distortion is important not only for individual images (i.e., B-scans/transversal sections into the sample for OCT), but also for the case when larger samples have to be imaged, as pointed out above. In this latter case, one must collate individual B-scans to obtain a mosaic image. If the margins of the B-scans are distorted (as it is the case with sinusoidal or sawtooth scan, and even with triangular, for higher f_s frequencies), those portions have to be discarded, and the individual B-scans have to be slightly overlapped; otherwise a grid of lines (which represent wrecked images) will appear on the large, mosaic image. We have studied these aspects in detail in [13], using Gabor Domain Optical Coherence Microscopy (GD-OCM) [15] and produced several mathematical models for the different scanning regimes in order to achieve these goals. OCT images were finally produced (Fig. 6 and 7, [13]), demonstrating the validity of these mathematical models and validating the expressions of the effective duty cycle deduced for the different cases of scanning input signals.

3. Custom-made scanning signals for GSs

A method to increase the duty cycle of the GS is to program in the input signals a non-linearity defined by a certain function [1, 2, 10]. The input signal will therefore be linear (on the constant speed portions) plus polynomials of different orders or sinusoidal-type of different equations. The statement in the literature is that the optimal signal (i.e., the one that produces the highest effective duty cycle η) is the linear plus sinusoidal [10]. As this was contradicting our observations, we have begun to approach this problem in detail [16], starting – for a GS in open loop - from the classical differential equation of the movement of the oscillatory element of the GS:

$$J\ddot{\theta} + c\dot{\theta} + k\theta = T_a(t),$$
(3)

where J is the axial mass inertia moment of the mobile element (including the galvomirror); k is the elastic coefficient; c is the damping coefficient (Fig. 1). Equation (3) can also be written as:

$$\ddot{\theta} + 2\xi\omega_0\dot{\theta} + \omega_0^2\theta = \frac{T_a(t)}{J}$$
(4)

where

$$\omega_0 = \sqrt{\frac{k}{J}} \quad \text{and} \quad \xi = \frac{c}{2\sqrt{Jk}}$$
(5)

are the undamped angular frequency and the damping ratio of the system, respectively.

We have demonstrated [16] that, from the possible equations of the non-linear portions of the GS input signal, the most appropriate ones to provide the maximum effective duty cycle η are the parabolic and the sinusoidal one. In Table 1 we deduced the expressions of η and of the maximum inertia torque of the GS for the two scanning regimes above. Due to the space limitations we do not provide here the details of the mathematical calculus, as they have been discussed in [16].

One may see that if the Eqs. (6) and (7) are compared one may conclude that, as pointed out in the literature [10], the linear plus sinusoidal scanning function is the one that provides the highest η. However, in order to be rigorous one has to complete the analysis with the values of the maximum inertia torque of the GS. Thus, one may see from Eqs. (6) and (7) that, although η_s (for the sinusoidal non-linearity) is slightly higher that η_p (for the parabolic non-linearity) with regard to different values of the parameter $r=\theta_a/\theta_m$, one may see that, for a certain scanner (i.e., characterized by a certain parameter T_i – Eq. (11b)), the values of r that can be reached for each scanning regime are different. Therefore, in order to make a proper comparison one must eliminate the parameter r from the Eqs. (6), (9a), and (11b); in a similar way the parameter r has to be eliminated from the Eqs. (7), (10), and (12b). The final expressions of the effective duty cycle η for the two scanning regimes are therefore

the ones in Eq. (11a) and (12), respectively. In Fig. 4 the two characteristic graphs of these effective duty cycle are presented, as well as the difference between the two values of η for the two scanning regimes – all with regard to the scanning parameter Ti, which includes, as shown by Eqs. (9a), (9b), and (11b), all the different constructive and functional parameters of the GS.

Table 1. Comparison of the two main triangular-type scanning functions $x(t)$ of the GSs analyzed [16] with regard to $r = x_a/H$.

Parameter / Function	Linear plus parabolic (p)	Linear plus sinusoidal (s)
Duty cycle η_t (theoretical)	$1 - \dfrac{4\tau}{T} = \dfrac{r}{2-r}$ (6)	$\dfrac{1}{1 + \dfrac{\sqrt{1-r^2}}{r}\arctan\dfrac{\sqrt{1-r^2}}{r}}$ (7)
Maximum inertia torque $T_{max} = J\ddot{\theta}_{max}$ (8)	$\dfrac{Cv^2}{1-r}$, where (9a) $\quad C = \dfrac{J}{4HL[1+(H/L)^2]}$ (9b)	$Cv^2\dfrac{2}{1-r^2}$ (10)
Duty cycle η (effective)	$\eta_p = \dfrac{T_i - 1}{T_i + 1}$, (11a) where $T_i = T_{max}/Cv^2$ (11b)	$\eta_s = \dfrac{1}{1 + \sqrt{\dfrac{2}{T_i - 2}}\arctan\sqrt{\dfrac{2}{T_i - 2}}}$ (12)
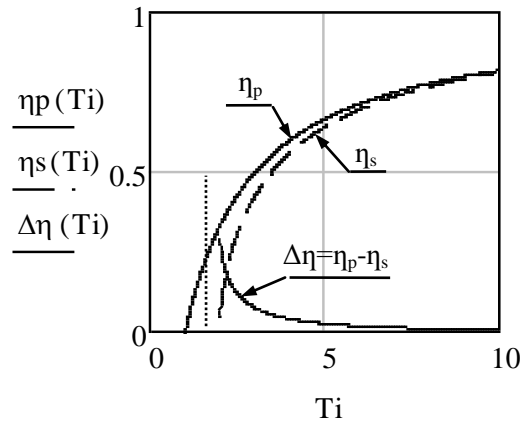
Figure 4. Comparison of the duty cycle for the two main triangular-type (linear plus non-linear) scanning functions: (p) linear plus parabolic; (s) linear plus sinusoidal – conclusion of the study in [16].

The conclusion that can be reached is therefore that the linear plus parabolic scanning function always provides the highest possible η of the GS.

An essential remark is that, while in [16] we have considered this equation from the particular (and somehow less utilized) case of a GS in an open loop, in [17] we have also demonstrated that this equation can be applied approximately for the more common and useful case of a GS with a closed loop, because of the practical values of the parameters of the control structure of the GS. The discussion in [16] can thus also be applied for the most useful case of closed-loop GS structures.

4. Handheld scanning probes with 1D GSs for OCT

In order to move the technology from lab to clinic, mobile OCT units are being made and they have to be equipped with handheld scanning probes with different types of infrared laser scanners [18-22]. We have designed such a family of probes equipped with 1D GSs [21, 22]; thus, they are capable to produce OCT B-scans/transversal images into the sample.

Figure 5 shows one of the variants of the handheld probe developed for OCT. Its main components are: (0) optical fiber; (1) fiber collimator; (2) mount adapter for the fiber collimator; (3) XY mini-translation stage; (4) compact 6-way cage cube; (5) mount of the GS (manufactured in the university workshop), which also has the role of heatsink for the GS; (6) 1-D GS; (7) lens tube (with a 1.5" diameter); (8) lens objective for infrared (9) handle; (10) cover. Details of the Thorlabs^{TM} components we have used in our devices were pointed out in [21], where we included their codes – to allow for their easy reproduction in any photonics lab, as well as a discussion on their weights and costs.

5. Applications in biomedical imaging and in NDT

The initial testing of the handheld probes (in their different variants) was presented in [22], as performed in the lab on different types of materials, as well as on healthy volunteers from the team – in typical OCT investigations of skin and teeth. *Ex vivo* applications in the clinic, for example with investigations of the oral chords, the larynx, and the tympana were presented in [20] as part of the investigations carried on in the Ear-Nose-Throat (ENT) Department of the Northwick Park Hospital (part of London North West Healthcare NHS Trust, London, UK).

Another variant of the same probe is being used, both *ex vivo* and *in vivo,* in the Dental Medicine Department of the Victor Babes Medicine and Pharmacy University of Timisoara. We have presented from these dentistry applications investigations of metalloceramic dental prostheses, for which the hidden defects beneath the surface of the dental construct can be determined, both in position and magnitude [21]. Other *in vivo* investigations are taking place, related to real time investigations of the remaining dentin thickness during the drilling process. B-scans (i.e., transversal sections into the

sample, as provided by the OCT system when employing a 1D scanner are sufficient for such applications: the dentist can thus monitor the drilling process to avoid the penetration of the dentin towards the pulp chamber - as we have recently demonstrated [23]. Also, after the dental procedures, such an inspection using the OCT system coupled with the handheld probe allows for identifying the hidden defects in the interface between the tooth and sealant, as pointed out in the literature [24] and as we have demonstrated *ex vivo* [25].
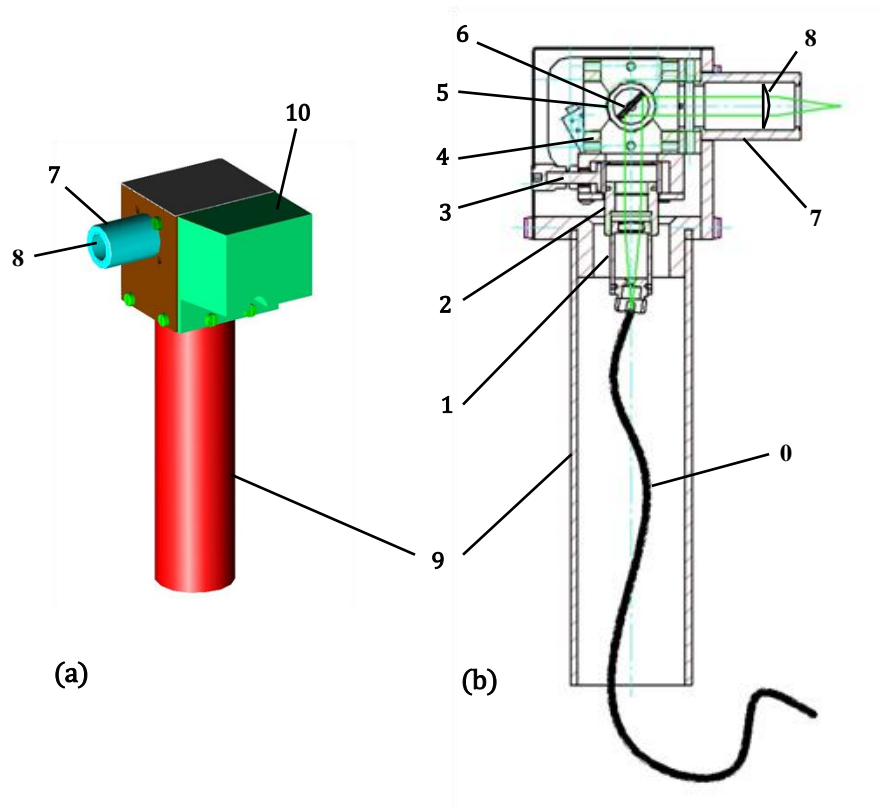
Figure 5. Variant of a handheld scanning probe for OCT with a 1D GS: (a) assembly of the probe; (b) section through the probe with the laser beam emerging the fiber and directed through the collimator (1) on the galvomirror of the GS (6) and through the objective lens (12) towards the sample.

An essential remark is related to the fact that, because our probes are not equipped with 2D scanners like other configurations which have dual axis GSs [18] or MEMS [19], volumetric reconstructions of the probe are not achievable in this way. However, for specific applications as

pointed out above, cross-sectional capabilities into the probe are sufficient for the clinic specialist, who actually provide the third direction of scanning him/herself, by sweeping the sample to inspect the tissue – or, for example, a certain dental work.

The same aspect is valid for numerous industrial applications, for example in NDT. In this domain we have recently demonstrated that 10 μm resolution OCT can successfully replace the 4 nm resolution, costly and time consuming Scanning Electron Microscopy (SEM) for the study of metallic fracture, brittle of ductile [26]. The advantage of OCT in this respect is not only related to costs, but also to the fact that mobile OCT units can be carried out into the field, while for SEM investigations samples have to be collected and carried to the lab.

When handheld probes are being utilized with OCT mobile systems, they also allow for investigations in situ, in real time, around the objects, to investigate all the areas on interest, with results that can be obtained and analyzed on the spot. This direction of work impacts all types of accidents (especially planes), but also incidents like pipe ruptures or turbine failures, for which it is essential to investigate if the materials utilized for the various mechanical parts have been designed properly and if the right materials, with the optimal properties have been used. All these are possible by being able to spot the difference between ductile and brittle fracture, as we have demonstrated possible using OCT [26].

6.   Conclusions

We presented a brief overview of some of our main contributions on GSs optimized from a dynamic point of view with regard to the oscillatory movement of their mobile element (which includes, as the essential element to the scanning process, the galvomirror – Fig. 1). The duty cycle of these laser scanners was maximized for both common and custom-made input signals in order to optimize the effective duty cycle of the GS and to eliminate distortions from the OCT images. Collated mosaic OCT images could also be obtained based on these studies [13].

Handheld scanning probes for OCT were developed, in different configurations, equipped with such optimized 1D GSs. They were applied so far in biomedical imaging in different clinical environments and with different OCT systems [20, 21], thus demonstrating the versatility of our handheld probes, besides the fact that they are simple, easy-to-assemble, light weight, and low cost [21, 22]. Future work with such probes includes both NDT and biomedical applications – the latter especially in dentistry, for both hard [21-23, 25] and soft tissue [27]. Other probes for OCT, with 2D GSs and MEMS are currently under development in our groups, while different, more challenging scanners are being considered for application as well, for example Risley prisms [8, 9].

Another direction of work is related to further improvements of the control structures of GSs, in order to obtain either improved precisions or speeds [17]. This research topic is integrated in our

general direction of work on laser scanners with improved, optimized characteristics applied for high-end applications [11].

Acknowledgments

References

[1] Marshall, G. F. *Handbook of Optical and Laser Scanning.* CRC Press – Taylor & Francis, New York, 2011.

[2] Bass, M. *Handbook of optics.* 3rd Edition, Mc. Graw-Hill Inc., New York, 30.1-30.68, 2009.

[3] Sweeney, M. N. Polygon scanners revisited. Proc. SPIE 3131 (1997), 65-76.

[4] Duma, V.-F., and Podoleanu, A. Gh. Polygon mirror scanners in biomedical imaging: a review. Proc. SPIE 8621 (2013), 8621V.

[5] Huang, D., Swanson, E. A., Lin, C. P., Schuman, J. S., Stinson, W. G., Chang, W., Hee, M. R., Flotte, T., Gregory, K., Puliafito, C. A., and Fujimoto, J. G. Optical coherence tomography. *Science* 254, 5035 (1991), 1178-1181.

[6] Podoleanu, A. Gh., and Rosen, R. B. Combinations of techniques in imaging the retina with high resolution. *Progress in Retinal and Eye Research* 27 (2008), 464– 499.

[7] Drexler, W., Liu, M., Kumar, A., Kamali, T., Unterhuber, A., et al. Optical coherence tomography today: speed, contrast, and multimodality. *J. Biomed. Opt.* 19, 7 (2014), 071412.

[8] Warger II, W. C., and DiMarzio, Ch. A. Dual-wedge scanning confocal reflectance microscope. *Opt. Lett.* 32 (2007), 2140-2142.

[9] Schitea, A., Tuef, M., and Duma, V.-F. Modeling of Risley prisms devices for exact scan patterns. Proc. SPIE 8789 (2013), 8789-40.

[10] Montagu, J. Scanners - galvanometric and resonant, in *Encyclopedia of Optical Engineering*, Driggers, R. G., Hoffman, C., Driggers, R., Eds., 2465-2487, Taylor & Francis, N.Y., 2003.

[11] Duma, V.-F., Rolland, J. P., and Podoleanu, A. Gh. Perspectives of optical scanning in OCT. *Proc. SPIE* 7556 (2010), 7556-10.

[12] Duma, V.-F., Lee, K.-S., Meemon, P., and Rolland, J. P. Experimental investigations of the scanning functions of galvanometer-based scanners with applications in OCT. *Appl. Opt.* 50, 29 (2011), 5735-5749.

[13] Duma, V.-F., Tankam, P., Huang, J., Won, J. J., and Rolland, J. P. Optimization of galvanometer scanning for Optical Coherence Tomography. *Appl. Opt.* 54, 17 (2015), 5495-5507.

[14] Braaf, B., Vermeer, K. A., Vienola, K. V., and de Boer, J. F. Angiography of the retina and the choroid with phase-resolved OCT using interval-optimized backstitched B-scans. *Opt. Express* 20 (2012), 20516-20534.

[15] Tankam, P., Santhanan, A. P., Lee, K., Won, J., Canavesi, C., and Rolland, J. P. Parallelized Multi-Graphics Processing Unit Framework for High-Speed Gabor-Domain Optical Coherence Microscopy. *J. Biomed. Opt.* 19, 7 (2014), 071410.

[16] Duma, V.-F. Optimal scanning function of a galvanometer scanner for an increased duty cycle. *Opt. Eng.* 49, 10 (2010), 103001.

[17] Mnerie, C., and Duma, V.-F. Mathematical model of a galvanometer-based scanner: simulations and experiments. Proc. SPIE. 8789 (2013), 8789-43.

[18] Jung, W., Kim, J., Jeon, M., Chaney, E. J., Stewart, C. N., and Boppart, S. A. Handheld optical coherence tomography scanner for primary care diagnostics. *IEEE Transactions on Biomedical Engineering* 58 (2011), 741-744.

[19] Lu, C. D., Kraus, M. F., Potsaid, B., et al., and Fujimoto, J. Handheld ultrahigh speed swept source optical coherence tomography instrument using a MEMS scanning mirror. *Biomed. Opt. Express* 5 (2014), 293-311.

[20] Cernat, R., Tatla, T. S., Pang, J., et al. Dual instrument for *in vivo* and *ex vivo* OCT imaging in an ENT department. *Biomed. Opt. Express* 3 (2012), 346-3356.

[21] Demian, D., Duma, V.-F., Sinescu, C., Negrutiu, M. L., Cernat, R., Topala, F. I., Hutiu, Gh., Bradu, A., and Podoleanu, A. Gh. Design and testing of prototype handheld scanning probes for optical coherence tomography. *J. of Engineering in Medicine* 228, 8 (2014), 743-753.

[22] Duma, V.-F., Dobre, G., Demian, D., Cernat, R., Sinescu, C., Topala, F. I., Negrutiu, M. L., Hutiu, Gh., Bradu, A., Podoleanu, A. Gh. Handheld scanning probes for optical coherence tomography. *Romanian Reports in Physics* 67, 4 (2015) – in print.

[23] Sinescu, C., Negrutiu, M. L., Bradu, A., Duma, V.-F., and Podoleanu, A. Gh. Noninvasive quantitative evaluation of the dentin layer during dental procedures using Optical Coherence Tomography. *Computational and Mathematical Methods in Medicine*, Paper ID 709076 (2015).

[24] Fried, D., Xie, J., Shafi, S., Featherstone, J. D. B., Breunig, T. M., Le, C. Imaging caries lesions and lesion progression with polarization sensitive optical coherence tomography. *J. Biomed. Opt.* **7,** 4 (2002), 618-627.

[25] Oancea, R., Bradu, A., Sinescu, C., Negru, R. M., Negrutiu, M. L., Antoniac, I., Duma, V.-F., and Podoleanu, A. Gh. Assessment of the sealant/tooth interface using optical coherence tomography. *J. of Adhesion Science and Technology* 29, 1 (2015), 49-58.

[26] Hutiu, Gh., Duma, V.-F., Demian, D., Bradu, A., and Podoleanu, A. Gh. Surface imaging of metallic material fractures using optical coherence tomography. *Appl. Opt.* 53, 26 (2014), 5912-5916.

[27] Canjau, S., Todea, C., Sinescu, C., Negrutiu, M. L., Duma, V.-F., Manescu, A., Topala, F., and Podoleanu, A. Gh. Optical imaging of oral squamous cell carcinoma using optical coherence tomography and micro CT. *Key Engineering Materials* 587 (2014), 331-337.

Virgil-Florin Duma, Professor and Head of the 3OM Optomechatronics Group (http://3om-group-optomechatronics.ro/), "Aurel Vlaicu" University of Arad, 77 Revolutiei Ave., Arad 310130, Romania; Doctoral School, Polytechnics University of Timisoara, 1 Mihai Viteazu Ave., Timisoara 300222, Romania; Faculty of Physics, West University of Timisoara, 4 Vasile Parvan Ave., Timisoara 300223, Romania (duma.virgil@osamember.org).
The author gave a presentation of this paper during one of the conference sessions.

Estimation techniques for uncertain dynamical systems with bilinear and quadratic nonlinearities (CON019-15)

Tatiana F. Filippova, Oxana G. Matviychuk, Elena K. Kostousova

Abstract: The problems of estimating reachable sets of nonlinear control systems with uncertainty in initial states and in the system parameters are studied. The initial states are taken to be unknown but bounded with given bounds. We assume that the nonlinearity in the system may be generated by the presence of nonlinear functions in the right-hand sides of the corresponding differential equations, which are either bilinear (with uncertainty in the elements of related matrices) or quadratic or else a combination of these types. We present two approaches to solving the problems of estimation of reachable sets of uncertain control systems. The first approach is based on the procedures of ellipsoidal state estimation of optimal control theory under uncertainty. The second one develops the polyhedral estimating techniques. We elaborate procedures and numerical schemes for the construction of external and internal estimates of reachable sets of the systems under consideration. Also we present the modification of the above state estimation approaches for the case of nonlinear dynamical systems with impulse controls. The numerical algorithms and examples of constructing the ellipsoidal and polyhedral estimates for studied nonlinear systems are given.

1. Introduction

The paper deals with the estimation problems for uncertain systems in the case when a probabilistic description of noise and errors is not available, but only bounds on them are known $[1, 2, 10$–$12, 14, 15]$. Such models may be found in many applied areas ranged from engineering problems from physics to economics as well as to biological and ecological modeling when it occurs that a stochastic nature of the errors is questionable because of limited data or because of nonlinearity of the model. The solution of many control and estimation problems under uncertainty involves constructing reachable sets and their analogs. For models with linear dynamics under such set-membership uncertainty there are several constructive approaches which allow finding effective estimates of reachable sets. We use here two of the most developed approaches to research in this area. The first one is based on the ellipsoidal calculus $[2$–$5, 10, 11, 13]$ and the second one uses the polyhedral techniques $[8, 9]$ which may be considered as some extension of interval analysis $[6, 7, 15]$.

In this paper the modified state estimation approaches which use the special structure of nonlinearity of studied control system are presented. We assume here that the system

185

nonlinearity is generated by the combination of two types of functions in related differential equations, one of which is bilinear and the other one is quadratic. We find here set-valued estimates of related reachable sets of such nonlinear uncertain control system. The algorithms of constructing the ellipsoidal and polyhedral estimates for studied nonlinear systems and numerical simulation results related to the proposed techniques are given.

2. Uncertain systems with bilinear and quadratic nonlinearities

2.1. Problem formulation

Let us introduce the following basic notation. Let $\mathbb{R}^n$ be the n-dimensional vector space, $\operatorname{comp} \mathbb{R}^n$ be the set of all compact subsets of $\mathbb{R}^n$, $\mathbb{R}^{n \times m}$ stands for the set of all real $n \times m$-matrices, $x'y = (x, y) = \sum_{i=1}^{n} x_i y_i$ be the usual inner product of $x, y \in \mathbb{R}^n$ with prime as a transpose, $\|x\| = \|x\|_2 = (x'x)^{1/2}$, $\|x\|_\infty = \max_{1 \leq i \leq n} |x_i|$ are vector norms for $x \in \mathbb{R}^n$, $I \in \mathbb{R}^{n \times n}$ be the identity matrix, $\operatorname{tr}(A)$ be the trace of $n \times n$-matrix A (the sum of its diagonal elements). We denote by $B(a, r) = \{x \in \mathbb{R}^n : \|x - a\| \leq r\}$ the ball in $\mathbb{R}^n$ with a center $a \in \mathbb{R}^n$ and a radius $r > 0$ and by $E(a, Q) = \{x \in \mathbb{R}^n : (Q^{-1}(x - a), (x - a)) \leq 1\}$ the ellipsoid in $\mathbb{R}^n$ with a center $a \in \mathbb{R}^n$ and with a symmetric positive definite $n \times n$-matrix Q.

Consider the following system

$$\dot{x} = A(t)x + f(x)d + u(t), \quad x_0 \in \mathcal{X}_0, \quad t \in [t_0, T], \tag{1}$$

where $x, d \in \mathbb{R}^n$, $\|x\| \leq K$ ($K > 0$), $f(x)$ is the nonlinear function, which is quadratic in x, $f(x) = x'Bx$, with a given symmetric and positive definite $n \times n$-matrix B. Control functions $u(t)$ in (1) are assumed Lebesgue measurable on $[t_0, T]$ and satisfying the constraint $u(t) \in \mathcal{U}$, for a.e. $t \in [t_0, T]$, (here $\mathcal{U}$ is a given set, $\mathcal{U} \in \operatorname{comp} \mathbb{R}^n$). The $n \times n$-matrix function $A(t)$ in (1) has the form

$$A(t) = A^0 + A^1(t), \tag{2}$$

where the $n \times n$-matrix A^0 is given and the measurable $n \times n$-matrix $A^1(t)$ with elements $\{a_{ij}^{(1)}(t)\}$ ($i, j = 1, \ldots, n$) is unknown but bounded, $A^1(t) \in \mathcal{A}^1$,

$$A(t) \in \mathcal{A} = A^0 + \mathcal{A}^1, \ \mathcal{A}^1 = \big\{A = \{a_{ij}\} \in \mathbb{R}^{n \times n} : |a_{ij}| \leq c_{ij}, \ i, j = 1, \ldots n\big\}, \quad t \in [t_0, T], \tag{3}$$

where $c_{ij} \geq 0$ ($i, j = 1, \ldots n$) are given.

We will assume that $\mathcal{X}_0$ in (1) is an ellipsoid, $\mathcal{X}_0 = E(a_0, Q_0)$, with a symmetric and positive definite matrix Q_0 and with a center a_0.

Let the absolutely continuous function $x(t) = x\big(t; u(\cdot), A(\cdot), x_0\big)$ be a solution to dynamical system (1)–(3) with initial state $x_0 \in \mathcal{X}_0$, with admissible control $u(\cdot)$ and with a matrix

$A(\cdot)$ satisfying (2)–(3). The reachable set $\mathcal{X}(t)$ at time t $(t_0 < t \leq T)$ of system (1)–(3) is defined as the following set

$$\mathcal{X}(t) = \{x \in \mathbb{R}^n : \exists x_0 {\in} \mathcal{X}_0, \ \exists u(\cdot){\in}\mathcal{U}, \ \exists A(\cdot){\in}\mathcal{A}, \quad x = x(t) = x\big(t; u(\cdot), A(\cdot), x_0\big)\}.$$

The main problem here is to find the external ellipsoidal estimate $E(a^+(t), Q^+(t))$ (with respect to the inclusion of sets) of the reachable set $\mathcal{X}(t)$ $(t_0 < t \leq T)$ by using the analysis of a special type of nonlinear control systems with uncertain initial data.

We need further some auxiliary results on the properties of reachable sets for different types of dynamical systems.

2.2. Bilinear systems

Bilinear dynamic systems are a special kind of nonlinear systems representing a variety of important physical processes. A great number of results related to control problems for such systems has been developed over past decades, among them we mention here [3,11,13]. Reachable sets of bilinear systems in general are not convex, but have special properties (for example, may be star-shaped). We, however, consider here the guaranteed state estimation problem and use ellipsoidal calculus for the construction of external estimates of reachable sets of such systems.

Consider the bilinear system

$$\dot{x} = A(t)\,x, \quad t_0 \leq t \leq T, \quad x_0 \in \mathcal{X}_0 = E(a_0, Q_0), \tag{4}$$

where $x, a_0 \in \mathbb{R}^n$, Q_0 is symmetric and positive definite matrix. The unknown matrix function $A(t) \in \mathbb{R}^{n \times n}$ is assumed to be of the form (2) with the assumption (3).

The external ellipsoidal estimate of reachable set $\mathcal{X}(T)$ of the system (4) can be found by applying the following theorem.

Theorem 1 (See [3]). *Let $a^+(t)$ and $Q^+(t)$ be the solutions of the following system of nonlinear differential equations*

$$\dot{a}^+ = A^0 a^+, \quad a^+(t_0) = a_0, \tag{5}$$

$$\dot{Q}^+ = A^0 Q^+ + Q^+ A^{0'} + q Q^+ + q^{-1} G, \quad Q^+(t_0) = Q_0, \quad t_0 \leq t \leq T, \tag{6}$$

$$q = \left(n^{-1}\,\mathrm{tr}\,((Q^+)^{-1} G)\right)^{1/2}, \tag{7}$$

$$G = \mathrm{diag}\left\{(n-v)\big[\sum_{i=1}^{n} c_{ji}|a_i^+| + \big(\max_{\sigma = \{\sigma_{ij}\}} \sum_{p,q=1}^{n} Q_{pq}^+ c_{jp} c_{jq} \sigma_{jp} \sigma_{jq}\big)^{1/2}\big]^2\right\}, \tag{8}$$

the maximum in (8) is taken over all $\sigma_{ij} = \pm 1$, $i,j = 1,\ldots,n$, such that $c_{ij} \neq 0$ and v is a number of such indices i for which we have: $c_{ij} = 0$ for all $j = 1,\ldots,n$. Then the following

external estimate for the reachable set $\mathcal{X}(t)$ of the system (4) *is true*

$$\mathcal{X}(t) \subseteq E(a^+(t), Q^+(t)), \quad t_0 \le t \le T. \tag{9}$$

Corollary 1. *Under conditions of the Theorem 1 the following inclusion holds*

$$\mathcal{X}(t_0 + \sigma) \subseteq (I + \sigma \mathcal{A}) \mathcal{X}_0 + o_1(\sigma) B(0,1) \subseteq E(a^+(t_0 + \sigma), Q^+(t_0 + \sigma)) + o_2(\sigma) B(0,1), \tag{10}$$

where $\sigma^{-1} o_i(\sigma) \to 0$ *for* $\sigma \to +0$ $(i = 1,2)$ *and* $(I + \sigma \mathcal{A}) \mathcal{X}_0 = \bigcup_{x \in \mathcal{X}_0} \bigcup_{A \in \mathcal{A}} \{x + \sigma A x\}.$

2.3. Systems with quadratic nonlinearity

Consider the control system of type (1) but with a known matrix $A = A^0$

$$\dot{x} = A^0 x + f(x) d + u(t), \quad x_0 \in \mathcal{X}_0 = E(a_0, Q_0), \quad t_0 \le t \le T. \tag{11}$$

We assume here that $u(t) \in \mathcal{U} = E(\hat{a}, \hat{Q})$, vectors d, a_0, $\hat{a}$ are given, a scalar function $f(x)$ has a form $f(x) = x' B x$, matrices B, Q_0, $\hat{Q}$ are symmetric and positive definite. Denote the maximal eigenvalue of the matrix $B^{1/2} Q_0 B^{1/2}$ by k^2.

Theorem 2 (See [4]). *The following inclusion is true for any* $t \in [t_0, T]$

$$\mathcal{X}(t) \subseteq E(a^+(t), r^+(t) B^{-1}), \tag{12}$$

where functions $a^+(t)$, $r^+(t)$ *are the solutions of the following system of ordinary differential equations*

$$\dot{a}^+(t) = A^0 a^+(t) + ((a^+(t))' B a^+(t) + r^+(t)) d + \hat{a}, \quad t_0 \le t \le T, \tag{13}$$

$$\dot{r}^+(t) = \max_{\|l\|=1} \left\{ l' \left(2 r^+(t) B^{1/2} (A^0 + 2 d (a^+(t))' B) B^{-1/2} + q^{-1}(r^+(t)) B^{1/2} \hat{Q} B^{1/2}) \right) l \right\}$$

$$+ q(r^+(t)) r^+(t), \quad q(r) = \left((nr)^{-1} \mathrm{tr} \, (B \hat{Q}) \right)^{1/2}, \quad a^+(t_0) = a_0, \quad r^+(t_0) = k^2. \tag{14}$$

Corollary 2. *The following upper estimate holds true*

$$\mathcal{X}(t_0 + \sigma) \subseteq E(a_*^+(\sigma), Q^+(\sigma)) + o(\sigma) B(0,1), \tag{15}$$

where $\sigma^{-1} o(\sigma) \to 0$ *when* $\sigma \to +0$ *and*

$$a_*^+(\sigma) = a(\sigma) + \sigma \hat{a}, \quad a(\sigma) = a_0 + \sigma (A^0 a_0 + a_0' B a_0 d + k^2 d), \tag{16}$$

$$Q^+(\sigma) = (p^{-1} + 1) Q(\sigma) + (p + 1) \sigma^2 \hat{Q}, \quad Q(\sigma) = k^2 (I + \sigma R) B^{-1} (I + \sigma R)', \tag{17}$$

$$R = A^0 + 2 d \cdot a_0' B,$$

and p is the unique positive root of the equation $\sum_{i=1}^{n} \frac{1}{p + \alpha_i} = \frac{n}{p(p+1)}$ with $\alpha_i \geq 0$ ($i = 1, ..., n$) being the roots of the following equation $|Q(\sigma) - \alpha \sigma^2 \hat{Q}| = 0$.

Numerical algorithms basing on Theorem 2 with related examples are given in [4].

2.4. Estimates of reachable sets for bilinear-quadratic control system

Consider the general case (1)–(3) of the system dynamics and here we take $\mathcal{X}_0 = E(a_0, Q_0)$ and $\mathcal{U} = E(\hat{a}, \hat{Q})$ where matrices B, $\hat{Q}$ and Q_0 are symmetric and positive definite.

Theorem 3 . *The following external ellipsoidal estimate holds*

$$\mathcal{X}(t_0 + \sigma) \subseteq E(a^*(t_0 + \sigma), Q^*(t_0 + \sigma)) + o(\sigma)B(0, 1) \tag{18}$$

where $\sigma^{-1}o(\sigma) \to 0$ for $\sigma \to +0$ and where

$$a^*(t_0 + \sigma) = \tilde{a}(t_0 + \sigma) + \sigma(\hat{a} + a_0' B a_0 \cdot d + k^2 d), \tag{19}$$

$$Q^*(t_0 + \sigma) = (p^{-1} + 1)\tilde{Q}(t_0 + \sigma) + (p + 1)\sigma^2 \hat{Q}, \tag{20}$$

with functions $\tilde{a}(t)$, $\tilde{Q}(t)$ calculated as $a^+(t)$, $Q^+(t)$ in Theorem 1 but when we replace matrices Q_0 and A^0 in (5)-(8) by

$$\tilde{Q}_0 = k^2 B^{-1}, \quad \tilde{A}^0 = A^0 + 2d \cdot a_0' B \tag{21}$$

respectively, and p is the unique positive root of the equation $\sum_{i=1}^{n} \frac{1}{p + \alpha_i} = \frac{n}{p(p+1)}$ with $\alpha_i \geq 0$ ($i = 1, ..., n$) being the roots of the following equation $|Q(t_0 + \sigma) - \alpha \sigma^2 \hat{Q}| = 0$.

Proof. Analyzing both results of Theorem 1 and Theorem 2 and of their corollaries and using the general scheme of the proof of Theorem 2 in [4] we obtain the formulas (18)–(21) of the Theorem.

The following iterative algorithm is based on Theorem 3.

Algorithm 1. Subdivide the time segment $[t_0, T]$ into subsegments $[t_i, t_{i+1}]$ where $t_i = t_0 + ih$ ($i = 1, \ldots, m$), $h = (T - t_0)/m$, $t_m = T$.

• Given $\mathcal{X}_0 = E(a_0, Q_0)$, find the smallest $k = k_0 > 0$ such that $E(a_0, Q_0) \subseteq E(a_0, k^2 B^{-1})$ (k^2 is the maximal eigenvalue of the matrix $B^{1/2} Q_0 B^{1/2}$).

• Take $\sigma = h$ and define by Theorem 3 the external ellipsoid $E(a_1, Q_1)$ such that $\mathcal{X}(t_1) \subseteq E(a_1, Q_1) = E(a^*(t_0 + \sigma), Q^*(t_0 + \sigma))$.

• Consider the system on the next subsegment $[t_1, t_2]$ with $E(a_1, Q_1)$ as the initial ellipsoid at instant t_1. Next steps continue iterations 1–3. At the end of the process we will get the external estimate $E(a(t), Q(t))$ of the tube $\mathcal{X}(t)$ with accuracy tending to zero when $m \to \infty$.
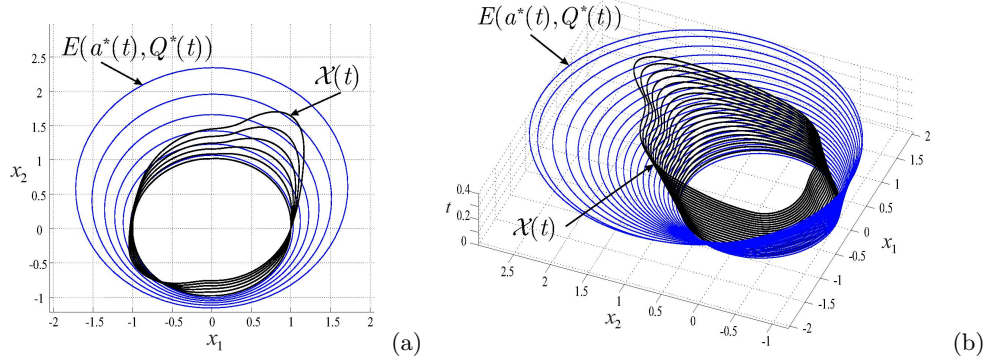
Figure 1. (a) Reachable sets $\mathcal{X}(t)$ and their external estimates $E(a^*(t), Q^*(t))$ for $t = 0.02; 0.08; 0.14; 0.2; 0.26; 0.32$. (b) Trajectory tube $\mathcal{X}(t)$ and its ellipsoidal estimating tube $E(a^*(t), Q^*(t))$ for the bilinear-quadratic control system with uncertain initial states.

Example 1. Consider the following control system

$$\begin{cases} \dot{x}_1 &= x_2 + u_1, \\ \dot{x}_2 &= c(t)x_1 + x_1^2 + x_2^2 + u_2, \end{cases} \qquad x_0 \in \mathcal{X}_0, \qquad t_0 \leq t \leq T. \tag{22}$$

Here we take $t_0 = 0$, $T = 0.4$, $\mathcal{X}_0 = B(0, 1)$ and $\mathcal{U} = B(0, 0.15)$, the uncertain but bounded measurable function $c(t)$ satisfies the inequality $|c(t)| \leq 1$ $(t_0 \leq t \leq T)$. The reachable sets $\mathcal{X}(t)$ and their external ellipsoidal estimates $E(a^*(t), Q^*(t))$ calculated by the Algorithm 1 are given in Figure 1.

3. Impulsive bilinear-quadratic control system

Consider the following control system $(t_0 \leq t \leq T, \ x \in \mathbb{R}^n)$

$$dx(t) = (Ax(t) + x'Bx \cdot d + u(t))dt + Cdv(t), \ A(t) = A^0 + A^1(t), \ A^1(t) \in \mathcal{A}^1, \tag{23}$$

where B is positive definite and symmetric matrix, $A^0 \in \mathbb{R}^{n \times n}$, parameters d, C are n-vectors, $d, C \in \mathbb{R}^n$, the set $\mathcal{A}^1$ is defined in (3). Here the impulsive function $v : [t_0, T] \to \mathbb{R}$ is of bounded variation on $[t_0, T]$, monotonically increasing and right-continuous,

$$\underset{t \in [t_0, T]}{\text{Var}} \ v(t) = \sup\{ \sum_{i=1}^{k} |v(t_i) - v(t_{i-1})| \ \mid \ t_0 \leq t_1 \leq \ldots \leq t_k = T \} \leq \mu,$$

190

We assume also $\mathcal{X}_0 = E(a, k^2 B^{-1})$ $(k \neq 0)$, $u(t) \in \mathcal{U} = E(\hat{a}, \hat{Q})$, and consider the following differential inclusion

$$\frac{d}{d\eta} \begin{pmatrix} z \\ \tau \end{pmatrix} \in H(\tau, z), \ z(t_0) = x_0 \in \mathcal{X}_0, \ \tau(t_0) = t_0, \ t_0 \leq \eta \leq T + \mu, \tag{24}$$

$$H(\tau, z) = \bigcup_{0 \leq \nu \leq 1} \left\{ \nu \begin{pmatrix} C \\ 0 \end{pmatrix} + (1 - \nu) \begin{pmatrix} Az + z'Bz \cdot d + E(\hat{a}, \hat{Q}) \\ 1 \end{pmatrix} \right\}. \tag{25}$$

Denote the reachable set of the system (24) as $\mathcal{W}(t_0 + \sigma) = \mathcal{W}(t_0 + \sigma; t_0, X_0 \times \{t_0\})$.

Theorem 4 . *The following inclusion holds true for $\sigma > 0$:*

$$\mathcal{W}(t_0 + \sigma) \subseteq \bigcup_{0 \leq \nu \leq 1} \mathcal{W}(t_0, \sigma, \nu) + o(\sigma)B(0, 1), \ \mathcal{W}(t_0, \sigma, \nu) = \begin{pmatrix} E\big(a^*(\sigma, \nu), Q^*(\sigma, \nu)\big) \\ t_0 + \sigma(1 - \nu) \end{pmatrix}$$

where $\lim_{\sigma \to +0} \sigma^{-1} o(\sigma) = 0$ and

$$a^*(\sigma, \nu) = \tilde{a}(\sigma, \nu) + \sigma(1 - \nu)(a'Ba \cdot d + k^2 d + \hat{a}) + \sigma\nu C,$$

$$Q^*(\sigma, \nu) = (p^{-1} + 1)\tilde{Q}(\sigma, \nu) + (p + 1)\sigma^2(1 - \nu)^2 \hat{Q},$$

with functions $\tilde{a}(\sigma, \nu)$, $\tilde{Q}(\sigma, \nu)$ calculated as $a^+(t_0 + \sigma)$, $Q^+(t_0 + \sigma)$ in Theorem 1 but when we replace matrices Q_0 and A^0 in (5)–(8) by $\tilde{Q}_0 = k^2 B^{-1}$, $\tilde{A}^0(\nu) = (1 - \nu)(A^0 + 2d \cdot a_0'B)$ respectively. Here $p = p(\sigma, \nu)$ is the unique positive root of the equation $\sum_{i=1}^{n} \dfrac{1}{p + \lambda_i} = \dfrac{n}{p(p + 1)}$ with $\lambda_i = \lambda_i(\sigma, \nu) \geq 0$ $(i = 1, \dots, n)$ satisfying the equation $|\tilde{Q}(\sigma, \nu) - \lambda\sigma^2(1 - \nu)^2 \hat{Q}| = 0$.

Proof. The above generalization is based on a combination of the techniques described above and the results of [5].

The following lemma explains the construction of the auxiliary differential inclusion (24).

Lemma 1 (See [5]). *The reachable set $\mathcal{X}(T)$ is the projection of $\mathcal{W}(T + \mu)$ at the subspace of variable z: $\mathcal{X}(T) = \pi_z \mathcal{W}(T + \mu)$.*

The following algorithm basing on Theorem 4 may be used to produce the external ellipsoidal estimates for the reachable sets of the system (23).

Algorithm 2. Subdivide the time segment $[t_0, T + \mu]$ into subsegments $[t_i, t_{i+1}]$ where $t_i = t_0 + ih$ $(i = 1, \dots, m)$, $h = (T + \mu - t_0)/m$, $t_m = T + \mu$. Subdivide the segment $[0, 1]$ into subsegments $[\nu_j, \nu_{j+1}]$ where $\nu_i = ih_*$, $h_* = 1/m$, $\nu_0 = 0$, $\nu_m = 1$.

• Take $\sigma = h$ and for given $\mathcal{X}_0 = E(a_0, k^2 B^{-1})$ define by Theorem 4 the sets $\mathcal{W}(t_0, \sigma, \nu_i)$ $(i = 0, \dots, m)$.

• Find ellipsoid $E_\varepsilon(w_1(\sigma), O_1(\sigma))$ in $\mathbb{R}^{n+1}$ such that $\mathcal{W}(t_0, \sigma, \nu_i) \subseteq E_\varepsilon(w_1(\sigma), O_1(\sigma))$ $(i = 0, \dots, m)$. At this step we find the ellipsoidal estimate for the union of a finite family of ellipsoids [5].

- Find the projection $E(a_1, Q_1) = \pi_z E_\varepsilon(w_1(\sigma), O_1(\sigma))$ by Lemma 1.

- Find the smallest $k_1 > 0$ such that $E(a_1, Q_1) \subseteq E(a_1, k_1^2 B^{-1})$ (k_1^2 is the maximal eigenvalue of the matrix $B^{1/2} Q_1 B^{1/2}$).

- Consider the system on the next subsegment $[t_1, t_2]$ with $E(a_1, k_1^2 B^{-1})$ as the initial ellipsoid at instant t_1.

- The following steps repeat the previous iteration. At the end of the process we will get the external estimate $E(a^+(T), Q^+(T))$ of the reachable set of the system (23).

Additional discussions of the approach and numerical examples may be found in [5].

4. Polyhedral estimates for dynamical systems with bilinear nonlinearities

Consider the system similar to (1) with $d = 0$

$$\dot{x} = A(t)\, x + u(t), \quad x(t_0) = x_0 \in \mathcal{X}_0, \qquad t \in [t_0, T]. \tag{26}$$

The constraints for controls $u(t)$ and for unknown matrix functions $A(t) \in \mathbb{R}^{n \times n}$ in (26) are defined here as

$$u(t) \in \mathcal{R}(t), \quad t \in [t_0, T], \tag{27}$$

$$A(t) \in \mathcal{A}(t) = \{A \in \mathbb{R}^{n \times n} | \underline{A}(t) \leq A \leq \overline{A}(t)\} = \{A|\, \mathrm{Abs}\,(A - \tilde{A}(t)) \leq \hat{A}(t)\},$$
$$\tilde{A} = (\underline{A} + \overline{A})/2, \quad \hat{A} = (\overline{A} - \underline{A})/2, \quad t \in [t_0, T]. \tag{28}$$

Here $\mathcal{X}_0$, $\mathcal{R}(t)$ are given convex compact sets in $\mathbb{R}^n$, the set-valued map $\mathcal{R}(t)$ is continuous, the matrix functions $\underline{A}(t)$, $\overline{A}(t)$ are continuous. Matrix and vector inequalities ($\leq, <, \geq, >$) are understood componentwise.

We need here and below some additional notations and definitions. Let $\mathrm{e}^i = (0, \ldots, 0, 1, 0, \ldots, 0)'$ be the unit vector oriented along the axis $0x_i$ (the unit stands at i-position), $\mathrm{e} = (1, 1, \ldots, 1)'$. It is more convenient in this section to use the notation with upper and lower indices $A = \{a_i^j\} = \{a^j\}$ for the matrix A with columns a^j. Denote $\mathrm{Abs}\, A = \{|a_i^j|\}$ for a matrix $A = \{a_i^j\}$; $\mathrm{diag}\, \pi$ denotes the diagonal matrix A with $a_i^i = \pi_i$ (π_i are the components of the vector π); $\det A$ is the determinant of $A \in \mathbb{R}^{n \times n}$; $\|A\| = \max_{1 \leq i \leq n} \sum_{j=1}^m |a_i^j|$ is the matrix norm for $A \in \mathbb{R}^{n \times m}$ induced by the vector norm $\|x\|_\infty$.

By a *parallelepiped* $\mathcal{P}(p, P, \pi) \subset \mathbb{R}^n$ we mean a set such that $\mathcal{P} = \mathcal{P}(p, P, \pi) = \{x \in \mathbb{R}^n |\, x = p + \sum_{i=1}^n p^i \pi_i \xi_i,\ \|\xi\|_\infty \leq 1\}$, where $p \in \mathbb{R}^n$; $P = \{p^i\} \in \mathbb{R}^{n \times n}$ is such that $\det P \neq 0$, $\|p^i\|_2 = 1$ (the normality condition $\|p^i\|_2 = 1$ may be omitted to simplify formulas); $\pi \in \mathbb{R}^n$, $\pi \geq 0$. It may be said that p determines the center of the parallelepiped, P is the orientation matrix, p^i are the "directions" and π_i are the values of its "semi-axes".

By a *parallelotope* $\mathcal{P}[p, \bar{P}] \subset \mathbb{R}^n$ we mean a set $\mathcal{P} = \mathcal{P}[p, \bar{P}] = \{x \in \mathbb{R}^n \mid x = p + \bar{P}\zeta,$ $\|\zeta\|_\infty \leq 1\}$, where $p \in \mathbb{R}^n$ and $\bar{P} = \{\bar{p}^i\} \in \mathbb{R}^{n \times m}$, $m \leq n$. We call a parallelotope $\mathcal{P}$ *nondegenerate* if $m=n$ and $\det \bar{P} \neq 0$. Each parallelepiped $\mathcal{P}(p, P, \pi)$ is a parallelotope $\mathcal{P}[p, \bar{P}]$ with $\bar{P} = P \operatorname{diag} \pi$; each nondegenerate parallelotope is a parallelepiped with $P = \bar{P}$, $\pi = \mathrm{e}$.

We call $\mathcal{P}$ an *external (internal) estimate* for $\mathcal{X} \subset \mathbb{R}^n$ if $\mathcal{P} \supseteq \mathcal{X}$ ($\mathcal{P} \subseteq \mathcal{X}$).

Assumption 1. The set $\mathcal{X}_0 = \mathcal{P}_0 = \mathcal{P}[p_0, \bar{P}_0] = \mathcal{P}(p_0, P_0, \pi_0)$ is a parallelepiped, the sets $\mathcal{R}(t) = \mathcal{P}[r(t), \bar{R}(t)]$ are parallelotopes, where $\bar{R}(t) \in \mathbb{R}^{n \times m}$, $m \leq n$; $r(\cdot)$, $\bar{R}(\cdot)$ and $\underline{A}(\cdot)$, $\overline{A}(\cdot)$ are continuous vector and matrix functions.

The main problem of this section is to find some external $\mathcal{P}^+(t) = \mathcal{P}(p^+(t), P^+(t), \pi^+(t))$ and internal $\mathcal{P}^-(t) = \mathcal{P}[p^-(t), \bar{P}^-(t)]$ polyhedral estimates for reachable sets $\mathcal{X}(t)$: $\mathcal{P}^-(t) \subseteq \mathcal{X}(t) \subseteq \mathcal{P}^+(t)$, $t \in [t_0, T]$.

In [8], the following system of ordinary differential equations was obtained for external estimates of $\mathcal{X}(t)$ in the form of parallelepipeds $\mathcal{P}^+(t) = \mathcal{P}(p^+(t), P(t), \pi^+(t))$, where $P(t)$ is a fixed matrix function:

$$\frac{dp^+}{dt} = \dot{P}P^{-1}p^+ + P(\Phi^{(+)} - \Phi^{(-)})/2 + r, \quad p^+(t_0) = p_0, \quad t_0 \leq t \leq T, \tag{29}$$

$$\frac{d\pi^+}{dt} = (\Phi^{(+)} + \Phi^{(-)})/2 + \operatorname{Abs}(P^{-1}\bar{R})\mathrm{e}, \quad \pi^+(t_0) = \operatorname{Abs}(P(t_0)^{-1}P_0)\pi_0,$$
$$\text{where } \Phi_i^{(\pm)} = \max_{\xi \in \boldsymbol{\Xi}_i^\pm}\left(\pm P^{-1}(\tilde{A} - \dot{P}P^{-1})x + \operatorname{Abs}(P^{-1})\hat{A}\operatorname{Abs}x\right)_i, \tag{30}$$
$$x = p^+ + P\operatorname{diag}\pi^+\xi; \ \boldsymbol{\Xi}_i^\pm = \{\xi \mid \xi \in \boldsymbol{E}(\mathcal{P}(t_0, I, \mathrm{e})), \ \xi_i = \pm 1\}, \ i=1,\dots,n,$$

the symbol $\boldsymbol{E}(\mathcal{P})$ denotes the set of all vertices of a parallelepiped $\mathcal{P} = \mathcal{P}(p, P, \pi)$, namely the set of points of the form $x = p + \sum_{j=1}^n p^j \pi_j \zeta_j$, $\zeta_j \in \{-1, 1\}$.

Theorem 5 (See [8]). *Let Assumption 1 be satisfied and $P(t) \in \mathbb{R}^{n \times n}$ be an arbitrary continuously differentiable function such that $\det P(t) \neq 0$, $t \in [t_0, T]$. Then the system (29), (30) has a unique solution $(p^+(\cdot), \pi^+(\cdot))$ on $[t_0, T]$, and the parallelepipeds $\mathcal{P}^+(t) = \mathcal{P}(p^+(t), P(t), \pi^+(t))$ are the external estimates for the reachable sets $\mathcal{X}(t)$ of the system (26), (27), (28): $\mathcal{X}(t) \subseteq \mathcal{P}^+(t)$, $t \in [t_0, T]$.*

The following differential system was obtained in [9] for internal estimates of $\mathcal{X}(t)$:

$$\frac{dp^-}{dt} = \tilde{A}(t)\,p^- + r(t), \quad p^-(t_0) = p_0, \quad t \in [t_0, T], \tag{31}$$

$$\frac{d\bar{P}^-}{dt} = \tilde{A}(t)\,\bar{P}^- + \operatorname{diag}\nu(t, \bar{P}^-; J(t)) \cdot B(\bar{P}^-) + \bar{R}(t)\,\Gamma(t), \quad \bar{P}^-(t_0) = \bar{P}_0,$$
$$\nu_i(t, \bar{P}^-; J) = \hat{a}_i^{j_i}(t) \cdot \eta_{j_i}(t, \bar{P}^-), \quad i = 1, \dots, n,$$
$$\eta(t, \bar{P}^-) = \max\{0, \operatorname{Abs}p^-(t) - (\operatorname{Abs}\bar{P}^-)\mathrm{e}\}, \tag{32}$$
$$B = \operatorname{diag}\beta(\bar{P}^-) \cdot \bar{P}^-, \quad \beta_i(\bar{P}^-) = 1/(\mathrm{e}^{i'}(\operatorname{Abs}\bar{P}^-)\mathrm{e}), \quad i = 1, \dots, n,$$
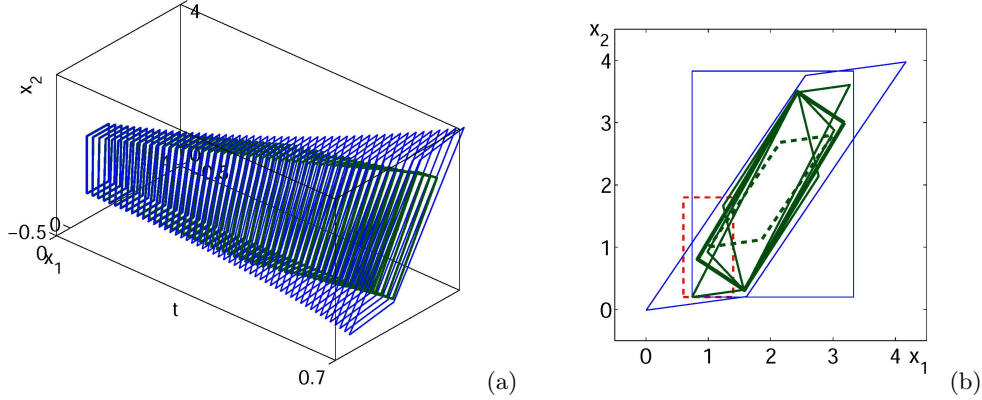
Figure 2. (a) Some external and internal polyhedral estimates for $\mathcal{X}(t)$ in Example 2. (b) The initial set $\mathcal{P}_0$, two external and several internal estimates for $\mathcal{X}(T)$ in Example 2.

(the operation of maximum is understood componentwise). Here $\Gamma(t) \in \mathbb{R}^{m \times n}$ is an arbitrary Lebesgue measurable matrix function satisfying $\|\Gamma(t)\| = \max_{1 \leq i \leq m} \sum_{j=1}^{n} |\gamma_i^j| \leq 1$, a.e. $t \in [t_0, T]$, and $J = \{j_1, \ldots, j_n\}$ is an arbitrary permutation of numbers $\{1, \ldots, n\}$ or even a measurable vector function $J(\cdot)$ with values $J(t)$ being arbitrary permutations of numbers $\{1, \ldots, n\}$. Let $\mathbb{G}$ and $\mathbb{J}$ be the sets of all such functions $\Gamma(\cdot)$ and $J(\cdot)$ respectively.

Theorem 6 (See [9]). *Let Assumption 1 be satisfied, $\mathcal{P}_0$ be a nondegenerate parallelotope ($\det \bar{P}_0 \neq 0$), and $J(\cdot) \in \mathbb{J}$, $\Gamma(\cdot) \in \mathbb{G}$. Then the system (31), (32) has a unique solution $(p^-(\cdot), \bar{P}^-(\cdot))$ at least on some subinterval $[t_0, T_1] \subseteq [t_0, T]$, where $0 < T_1 \leq T$, and we have $\det \bar{P}^-(t) \neq 0$, $t \in [t_0, T_1]$. The corresponding nondegenerate parallelotopes $\mathcal{P}^-(t) = \mathcal{P}[p^-(t), \bar{P}^-(t)]$, $t \in [t_0, T_1]$, are internal estimates for the reachable sets $\mathcal{X}(t)$ of the system (26), (27), (28): $\mathcal{P}^-(t) \subseteq \mathcal{X}(t)$, $t \in [t_0, T_1]$.*

Assumption 2. Either $\mathcal{R}(t)$ are singletons for all $t \in [t_0, T]$ (in this case the function $u(\cdot) \equiv r(\cdot)$ may be assumed to be measurable) or $\Gamma(\cdot) \in \mathbb{G}$ is such that $\bar{R}(t)\Gamma(t) \equiv 0$, $t \in [t_0, T]$.

Corollary 3. *Under conditions of Theorem 6 and additional Assumption 2 the system (31), (32) has a solution on the interval $[t_0, T]$, and we have $\det \bar{P}^-(t) \neq 0$ and $\mathcal{P}^-(t) \subseteq \mathcal{X}(t)$ for any $t \in [t_0, T]$.*

Note that Theorems 5 and 6 describe the whole families of estimates, where $P(\cdot)$, $J(\cdot)$, and $\Gamma(\cdot)$ are parameters.

Example 2. Consider the system (26)-(28) in $\mathbb{R}^2$ with $\tilde{A} \equiv \begin{bmatrix} 0 & 1 \\ 0.2 & 0 \end{bmatrix}$, $\hat{A} \equiv \begin{bmatrix} 0 & 0 \\ 0.2 & 0 \end{bmatrix}$,

$\mathcal{R} \equiv \mathcal{P}((0,1)', I, (0,1)')$, $\mathcal{P}_0 = \mathcal{P}((1,1)', I, (0.4, 0.7)')$, $t_0 = 0$, $T = 0.7$. Fig. 2 presents a series of external and internal polyhedral estimates for reachable sets of the system found using Theorems 5, 6.

Additional details and discussions of the approach and also other numerical examples of polyhedral estimates may be found in [8, 9].

5. Conclusions

The paper deals with the problems of state estimation for uncertain dynamical control systems for which we assume that the initial state is unknown but bounded with given constraints and the matrix in the linear part of state velocities is also unknown but bounded.

We study here the case when the system nonlinearity is generated by the combination of two types of functions in related differential equations, one of which is bilinear and the other one is quadratic. The problem may be reformulated as the problem of describing the motion of set-valued states in the state space under nonlinear dynamics with state velocities having bilinear-quadratic type. We present here procedures and numerical schemes for the construction of external and internal estimates of reachable sets of the systems under consideration.

Acknowledgments

References

[1] BERTSEKAS, D., AND RHODES, I. Recursive state estimation for a set-membership description of uncertainty. *IEEE Transactions on Automatic Control 16* (1971), 117–128.

[2] CHERNOUSKO, F. L. *State Estimation for Dynamic Systems.* CRC Press, Boca Raton, 1994.

[3] CHERNOUSKO, F. L. Ellipsoidal approximation of the reachable sets of linear systems with an indeterminate matrix. *Applied Mathematics and Mechanics 60*, 6 (1996), 940–950.

[4] FILIPPOVA, T. F. Set-valued dynamics in problems of mathematical theory of control processes. *International J. of Modern Physics. Series B (IJMPB) 26*, 25 (2012), 1–8.

[5] FILIPPOVA, T. F., AND MATVIYCHUK, O. G. Algorithms to estimate the reachability sets of the pulse controlled systems with ellipsoidal phase constraints. *Automat. Remote Control 72*, 9 (2011), 1911–1924.

[6] JAULIN, L., KIEFFER, M., DIDRIT, O., AND WALTER, E. *Applied Interval Analysis. With Examples in Parameter and State Estimation, Robust Control and Robotics.* Springer-Verlag, London, 2001.

[7] KORNOUSHENKO, E. K. Interval coordinatewise estimates for the set of accessible states of a linear stationary system. i–iv. *Autom. Remote Control, 41* (1980) 598–606, *41* (1981) 1633–1639, *43* (1983) 1266–1270, *44* (1983) 203–208.

[8] KOSTOUSOVA, E. K. Outer polyhedral estimates for attainability sets of systems with bilinear uncertainty. *J. Appl. Math. Mech. 66*, 4 (2002), 547–558.

[9] KOSTOUSOVA, E. K. State estimation for control systems with a multiplicative uncertainty through polyhedral techniques. *IFIP Advances in Information and Communication Technology (IFIP AICT) 391* (2013), 165–176.

[10] KURZHANSKI, A. B., AND VÁLYI, I. *Ellipsoidal Calculus for Estimation and Control.* Birkhäuser, Boston, 1997.

[11] KURZHANSKI, A. B., AND VARAIYA, P. *Dynamics and Control of Trajectory Tubes. Theory and Computation.* Springer-Verlag, New York, 2014.

[12] MILANESE, M., NORTON, J. P., PIET-LAHANIER, H., AND WALTER, E. E. *Bounding Approaches to System Identification.* Plenum Press, New York, 1996.

[13] POLYAK, B. T., NAZIN, S. A., DURIEU, C., AND WALTER, E. Ellipsoidal parameter or state estimation under model uncertainty. *Automatica 40* (2004), 1171–1179.

[14] SCHWEPPE, F. *Uncertain Dynamic Systems.* Plenum Press, New York, 1973.

[15] WALTER, E., AND PRONZATO, L. *Identification of parametric models from experimental data.* Springer-Verlag, Heidelberg, 1997.

Tatiana F. Filippova, Professor: N.N. Krasovskii Institute of Mathematics and Mechanics of the Ural Branch of the Russian Academy of Sciences and Ural Federal University, 16 S.Kovalevskaya str., Ekaterinburg 620990, Russia (*ftf@imm.uran.ru*).

Oxana G. Matviychuk, Ph.D.: N.N. Krasovskii Institute of Mathematics and Mechanics of the Ural Branch of the Russian Academy of Sciences and Ural Federal University, 16 S.Kovalevskaya str., Ekaterinburg 620990, Russia (*vog@imm.uran.ru*).

Elena K. Kostousova, Professor: N.N. Krasovskii Institute of Mathematics and Mechanics of the Ural Branch of the Russian Academy of Sciences, 16 S.Kovalevskaya str., Ekaterinburg 620990, Russia (*kek@imm.uran.ru*). The author gave a presentation of this paper during one of the conference sessions.

Motion control of unstable mechanical systems
(CON092-15)

A.M. Formalskii

Abstract: The paper is dedicated to the designing control for objects that may have desired working regimes unstable without additional guidance. The control signal is assumed limited in absolute value. The motion equations of a multi-link pendulum mounted on a moving base, on a wheel or a cart, are designed. Under some conditions, mathematical model allows separation of equations that describe only the pendulum motion. The task of stabilizing a single inverted pendulum mounted on a wheel is solved. So called «inertia wheel pendulum» is studied. A control algorithm is proposed and tested experimentally to translate this pendulum from any initial state into the top. Other modes of motion are realized by other proposed algorithms. The double pendulum with stationary suspension joint is considered. The control torque is applied in the inter-link or in the suspension joint. The control algorithms to ensure global stabilization of the inverted pendulum are designed. The problems of optimal swinging and damping are also discussed. A problem of stabilizing of a ball on a straight or curvilinear beam is studied. The goal is to control the voltage applied to the drive so that to stabilize the unstable equilibrium with maximal basin of attraction. The degree of instability of the above considered systems equal to one or two. For maximizing attraction basin of this kind systems, all control resources must be spent on the suppressing the unstable modes. The problem of gyroscopic stabilizing of the upright unstable position of a robot-bicycle is investigated theoretically and practically.

1. Multi-link pendulum on a movable base

Here we consider a plane motion of an *n*-link pendulum that is mounted via a joint on a moving base – a wheel (see Figure 1) or a cart (see Figure 2).

Consider initially an *n*-link pendulum on a wheel. The wheel can roll without slipping over a horizontal plane. The pendulum links can move in the same vertical plane with the wheel. *M* denotes the wheel mass, *R* its radius, ρ its radius of gyration with respect to wheel center (center of mass) *O*. The first link of the pendulum is connected to the wheel by a joint *O* (Figure 1). The links are numbered in sequence, as they are connected to each other further away from point *O*, and the joints are numbered likewise. The movement of wheel center *O* along the horizontal axis is denoted as *x*, and $\dot{x} = -R\dot{\beta}_0$. The mass of the *k*-th link is denoted as m_k , the length of this link – as l_k , the radius of inertia with respect to the *k*-th joint – as r_k . Let the center of mass of each link be located on the segment that connects its ends (joints), and the distance to this center of mass from the *k*-th joint be b_k .

At joint O a control torque L is applied to the first link. If $L>0$, this torque tends to turn this link counter-clockwise. The same (in absolute value) torque, but directed clockwise, is applied to the wheel. All joints are considered ideal (frictionless).
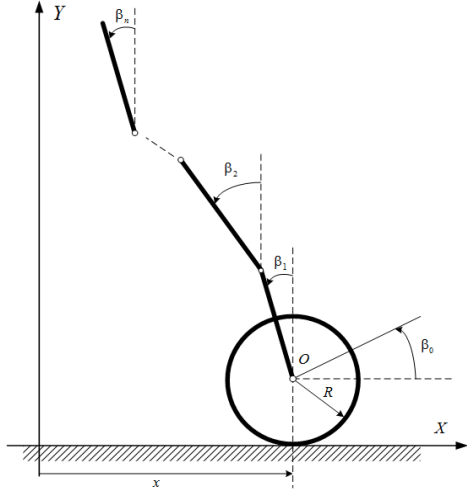
Figure 1. Multi-link pendulum on a wheel.	Figure 2. Multi-link pendulum on a cart.
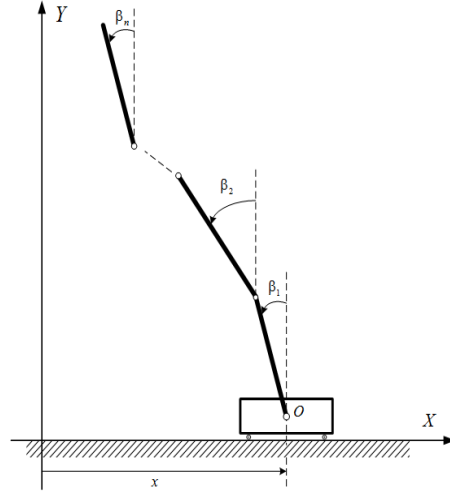
The kinetic energy of the wheel T_0 and of the k-th link T_k can be presented as

$$T_0 = \frac{1}{2}M\left(R^2 + \rho^2\right)\dot{\beta}_0^{\;2} . \tag{1}$$

$$T_k = \frac{1}{2}m_k\left[\left(R\dot{\beta}_0 + \sum_{i=1}^{k-1} l_i\dot{\beta}_i\cos\beta_i\right)^2 + \left(\sum_{i=1}^{k-1} l_i\dot{\beta}_i\sin\beta_i\right)^2 + \right.$$
$$\left. + 2b_k R\dot{\beta}_0\dot{\beta}_k\cos\beta_k + 2\sum_{i=1}^{k-1} l_i b_k\dot{\beta}_i\dot{\beta}_k\cos\left(\beta_k - \beta_i\right) + r_k^2\dot{\beta}_k^2\right]. \tag{2}$$

The potential energy Π and the virtual work δW of torque L are (g is the gravity acceleration)

$$\Pi = \sum_{k=1}^{n} m_k g\left(\sum_{i=1}^{k-1} l_i\cos\beta_i + b_k\cos\beta_k\right), \; \delta W = L\left(\delta\beta_1 - \delta\beta_0\right) . \tag{3}$$

Using relations (1) – (3) to build up the Lagrange's function $\mathcal{L} = T - \Pi$, the $n+1$ equations of motion of the system can be derived. Angle β_0 enters in the equations of motion only as its second derivative $\ddot{\beta}_0$. Let $\mathbf{q} = \left\|\beta_0, \boldsymbol{\beta}^T\right\|^T$ be the vector-column of generalized coordinates of the whole system, $\boldsymbol{\beta} = \left\|\beta_1,...,\beta_n\right\|^T$ – the vector-column of generalized coordinates of the pendulum. Then the motion equations can be written as follows:

$$\mathbf{A}(\boldsymbol{\beta})\ddot{\mathbf{q}} + \mathbf{B}(\boldsymbol{\beta})\|\dot{\mathbf{q}}^2\| - \mathbf{G}\|\sin\boldsymbol{\beta}\| = \mathbf{Q}. \tag{4}$$

Here $\mathbf{A}(\boldsymbol{\beta})$ is the symmetric matrix of kinetic energy, its dimensions are $(n+1)\times(n+1)$:

$$\mathbf{A}(\boldsymbol{\beta}) = \left\|\begin{matrix}
a_{00} & a_{01}\cos\beta_1 & a_{02}\cos\beta_2 & . & a_{0n}\cos\beta_n \\
* & a_{11} & a_{12}\cos(\beta_1-\beta_2) & . & a_{1n}\cos(\beta_1-\beta_n) \\
* & * & a_{22} & . & a_{2n}\cos(\beta_2-\beta_n) \\
. & . & . & . & . \\
* & * & * & . & a_{nn}
\end{matrix}\right\|$$

$$a_{00} = M\left(R^2 + \rho^2\right) + R^2\sum_{i=1}^{n} m_i, \quad a_{0s} = R\left(b_s m_s + l_s\sum_{i=s+1}^{n} m_i\right) \ (s=1,...,n),$$

$$a_{jj} = r_j^2 m_j + l_j^2\sum_{i=j+1}^{n} m_i, \quad a_{js} = l_j\left(b_s m_s + l_s\sum_{i=s+1}^{n} m_i\right) \quad (j,s=1,...,n)$$

$$\mathbf{B}(\boldsymbol{\beta}) = \left\|\begin{matrix}
0 & -a_{01}\sin\beta_1 & -a_{02}\sin\beta_2 & . & -a_{0n}\sin\beta_n \\
0 & 0 & a_{12}\sin(\beta_1-\beta_2) & . & a_{1n}\sin(\beta_1-\beta_n) \\
0 & -a_{12}\sin(\beta_1-\beta_2) & 0 & . & a_{2n}\sin(\beta_2-\beta_n) \\
. & . & . & . & . \\
0 & -a_{1n}\sin(\beta_1-\beta_n) & -a_{2n}\sin(\beta_2-\beta_n) & . & 0
\end{matrix}\right\|,$$

$$\mathbf{G} = \frac{g}{R}\mathrm{diag}(0, a_{01}, ..., a_{0n}), \quad \|\dot{\mathbf{q}}^2\| = \left\|\dot{\beta}_0^2, \quad \dot{\beta}_1^2, \quad ..., \quad \dot{\beta}_n^2\right\|^T,$$

$$\|\sin\boldsymbol{\beta}\| = \|\sin\beta_0, \ \sin\beta_1, \ ..., \ \sin\beta_n\|^T, \quad \mathbf{Q} = \|-L, \quad L, \quad 0, \quad ..., \quad 0\|^T.$$

The first column in matrix $\mathbf{B}(\boldsymbol{\beta})$, as well as in $\mathbf{G}$, is zero. This is natural, since the motion equations do not involve angle β_0 or its velocity $\dot{\beta}_0$. Note that equations (4) include the second powers of generalized velocities $\dot{\beta}_k$ and do not include their products; and the submatrix of the n-th order that is in the right-bottom corner of matrix $\mathbf{B}(\boldsymbol{\beta})$ is skew-symmetric. Relatively simple structure of equations (4) is a result of the choice of generalized coordinates: angles β_k of the link deviation from the vertical were chosen, and not the inter-link angles. Solving equation (4) for the highest order derivatives yields

$$\ddot{\mathbf{q}} = \mathbf{A}(\boldsymbol{\beta})^{-1}\left[\mathbf{Q} - \mathbf{B}(\boldsymbol{\beta})\|\dot{\mathbf{q}}^2\| + \mathbf{G}\|\sin\boldsymbol{\beta}\|\right]. \tag{5}$$

The last n equations in system (5) involve only angles β_k $(k=1,2,\ldots,n)$ with their derivatives. These equations can be separately written as a system

$$\ddot{\boldsymbol{\beta}} = \mathbf{F}(\boldsymbol{\beta},\dot{\boldsymbol{\beta}},L). \tag{6}$$

If torque L applied in joint O does not depend on wheel turn angle β_0 and its angular velocity $\dot{\beta}_0$, system (6) describes *exclusively* the motion of pendulum. System (6) *is different* from the known system of equations used to describe motion of an *n*-link pendulum on a stationary base [1]. In particular, it includes equivalent moment of inertia of the wheel $M\left(R^2+\rho^2\right)$, and with $n=1$ the squared angular velocity of the pendulum $\dot{\beta}_1^2$ (see the next Subsection).

Unlike the wheel-based pendulum, torque L applied in joint O of the pendulum on a cart does not influence *directly* on the cart motion. To derive motion equations of this system, the angular acceleration $\ddot{\beta}_0$ in equations (4) must be replaced with linear acceleration $\ddot{x}$ of the cart using relation $\ddot{\beta}_0 = -\ddot{x}/R$, and the first element $-L$ in column-matrix $\mathbf{Q}$ must be set equal to zero. To make use the expressions for coefficients of matrices $\mathbf{A}(\boldsymbol{\beta})$, $\mathbf{B}(\boldsymbol{\beta})$, the value of R must be set equal to one, and ρ – to zero. Excluding acceleration $\ddot{x}$ from these equations yields a system of n equations like (6).

1.1. Single-link pendulum on a wheel

With $n=1$ the original system consists of a wheel and a single-link pendulum mounted on it (see Figure 3). For simplicity instead of notations β_0 and β_1 we use here φ and β respectively. The device
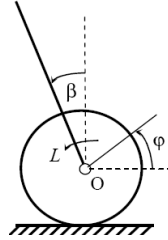
Figure 3. The pendulum with wheel-based pivot.

shown in Figure 3 can be considered as a plane model of "Segway" or "Solowheel" [2] with person on it. This system has two degrees of freedom. Parameters m, r, and b will be respectively mass of the link, its radius of inertia, and distance from point O to its mass center. Introduce non-dimensional time τ and non-dimensional torque μ as $\tau = t\sqrt{gb}/r$, $\mu = L/mgb$. In considered particular case equation (6) becomes scalar equation of second order. This equation involves only angle β. It contains parameters of the pendulum, but *also* parameters of the wheel M, R, and ρ. This scalar equation can be rewritten as the system of second order:

$$\beta' = \omega, \quad \left(1 - d^2\cos^2\beta\right)\omega' + d^2\omega^2\sin\beta\cos\beta - \sin\beta = \left(1 + e^2\cos\beta\right)\mu. \tag{7}$$

Here $d^2 = \dfrac{mb^2}{M(R^2 + \rho^2) + mR^2}\left(\dfrac{R}{r}\right)^2 < 1$, $e^2 = \dfrac{mRb}{M(R^2 + \rho^2) + mR^2}$. Prime mark $'$ represents differentiating with respect to non-dimensional time τ.

If wheel mass $M \to \infty$, then equations (7) *convert* into motion equations of a "regular" pendulum with stationary pivot. System (7) is *different* from these equations.

We assume that the absolute value of control torque L is limited by constant L_0 with $L_0 \le mgb$

$$|L| \le L_0. \quad \left(|\mu| \le \mu_0,\ \mu_0 = L_0/mgb \le 1\right),\tag{8}$$

The set of piecewise-continuous functions $\mu(\tau)$, each of them complying with inequality (8), will further be denoted as W, so $W = \{\mu(\tau):\ |\mu(\tau)| \le \mu_0\}$. With $\mu(\tau) \equiv 0$ system (7) has equilibrium

$$\beta = 0, \quad \omega = 0.\tag{9}$$

Linearization of system (7) about its equilibrium (9) yields the following equations:

$$\beta' = \omega,\ \ a^2\omega' - \beta = c\mu.\tag{10}$$

where $a^2 = 1 - d^2 > 0$, $c = 1 + e^2 > 1$. With $\mu = 0$, one of the eigenvalues of system (10) is positive $(1/a)$, the other one is negative $(-1/a)$. A second order system (10) can be transposed into a system of two first order equations in Jordan form

$$y' = y/a + \mu c/a,\qquad y = \beta + a\beta',\tag{11}$$

$$z' = -z/a - \mu c/a,\qquad z = \beta - a\beta'.\tag{12}$$

Equations (11) and (12) describe the behavior of "unstable" variable y corresponding to positive eigenvalue $(1/a)$ and of "stable" variable z corresponding to negative eigenvalue $(-1/a)$ respectively. When $a = 1$, $c = 1$ equations (10) – (12) lead to equations for the regular pendulum.

1.2. Domain of controllability

Consider a set P of initial states, where for each state there exists an admissible control function $\mu(\tau) \in W$, that moves the system (11), (12), into its equilibrium $y = 0$, $z = 0$ $(\beta = 0,\ \beta' = 0)$. Such set P is called *domain of controllability* [3]. This set is bounded only with respect to the unstable coordinate y [3]. It is described by the following inequality:

$$|y| < c\mu_0,\ \text{ or } \left|\beta + a\beta'\right| < c\mu_0,\ \text{ or } \left|\beta + \sqrt{1 - d^2}\,\omega\right| < \left(1 + e^2\right)\mu_0.\tag{13}$$

Interval (13) of axis y is illustrated in Figure 4. Figure 5 illustrates on the plane of variables β, β' domain of controllability P and domain of controllability Q for the regular pendulum. It is

worth to compare these domains. Stripe P is wider than stripe Q, because $c > 1$ and $0 < a < 1$. However, domain Q does not lie inside domain P.
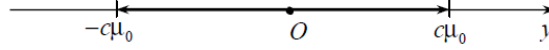
Figure 4. Domain of controllability with respect to variable y.

Remember also, that domains P and Q were built for linear equations, and linearization is valid only for values β and β' that are close enough to zero. And for close-to-zero values of β and (or) β' domain Q lies inside domain P. See that rhomb Π_Q, with four vertices $(\pm\mu_0, 0)$, $(0, \pm\mu_0)$ lies entirely inside rhomb Π_P, with four vertices $(\pm c\mu_0, 0)$, $(0, \pm c\mu_0/a)$ (Figures 5, 6).
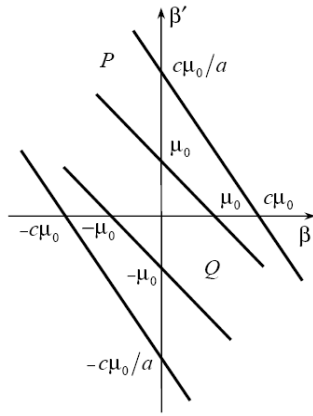
Figure 5. Domains of controllability P for the wheel-based pendulum and Q for regular one.
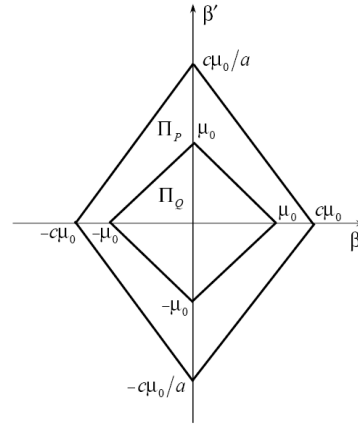
Figure 6. Rhombs Π_P and Π_Q inscribed into controllability domains P and Q.

Thus domain of controllability Q of the regular pendulum is in a sense smaller than domain of controllability of the pendulum on a wheel. Thus, the wheel-based pendulum is easier to stabilize. This is reasonable, since in the latter case the torque generated by the motor actuates not only the body of the pendulum, but also the wheel, accelerating the pivot (the wheel center O) and contributing even more to system stabilization. Rhombs Π_Q and Π_P are drawn to illustrate (symbolically), that in the neighborhood of the origin $\beta = \beta' = 0$ domain Q lies inside domain P. Inequality (13) can be written in terms of original parameters of the device. Using this inequality, it is possible to evaluate the influence of various parameters on the controllability domain. These evaluations are helpful, for example, when constructing a transportation device like Segway, Solowheel.

202

1.3. Maximizing domain of attraction

The unstable motion mode of system (11), (12) can be "suppressed" by means of control function that is effectively a linear feedback with saturation, that is nonlinear feedback:

$$\mu = \mu(y) = \begin{cases} -\mu_0 & \text{when} \quad \gamma y \leq -\mu_0, \\ \gamma y & \text{when} \quad |\gamma y| \leq \mu_0, \\ \mu_0 & \text{when} \quad \gamma y \geq \mu_0 . \end{cases} \qquad \gamma < -1/c . \qquad (14)$$

Under all initial conditions $-c\mu_0 < y(0) < c\mu_0$ the solution to system (11), (14) $y(\tau) \to 0$ as $\tau \to \infty$. Then, in accordance with relation (14), $\mu(\tau) \to 0$. And then solution $z(\tau)$ to equation (12) for *any* initial value $z(0)$ converges to zero. Thus, the trivial solution $y(\tau) = z(t) = 0$ to system (11), (12), (14) is asymptotically stable under initial conditions $-c\mu_0 < y(0) < c\mu_0$, regardless of initial condition $z(0)$. As $\tau \to \infty$, function $|y(\tau)| \to \infty$, if $|y(0)| > c\mu_0$. If $y(0) = \pm c\mu_0$ then $y(\tau) \equiv \pm c\mu_0$. Hence the domain (basin) of attraction B of the coordinates origin $y = 0$, $z = 0$ for control function (14) coincides with domain of controllability P: $B = P$. As usual, domain of attraction is understood as a set of initial coordinate pairs $y(0)$, $z(0)$, from which a controllable system converges asymptotically to a desired state.

To summarize, for maximizing domain of attraction B for system (11), (12), *all resources* of control must be spent on suppressing the *unstable* mode. And it is possible to maximize the domain of attraction using *linear with saturation* feedback.

1.4. Domain of controllability for nonlinear system and time-optimal control

Expressions (13) describe the set P of initial states from which *linear* system (10) can be translated to the origin $\beta = 0$, $\omega = 0$. Now the task is to build in stripe $-\pi \leq \beta \leq \pi$ of the phase plane (β, ω) a set D of states from which *nonlinear* system (7) can be translated to equilibrium $\beta = 0$, $\omega = 0$ *without oscillations* about position $\beta = \pi$. The task of finding such a domain is important for investigation of motion of a device like "Segway", because when a passenger is stabilized on such a device, any large angular deviations from vertical are unacceptable. And, of course, angular deviations greater than $\pi/2$ are impossible. The sought domain of controllability D is apparently symmetric with respect to point $\beta = 0$, $\omega = 0$. Figures 7 and 8 illustrate domain of controllability D for non-linear system (7). Domain D is built numerically with parameters $d = 0.8$, $e = 0.5$, $\mu_0 = 0.5$. Curve lines are the borders of controllability domain D, straight lines in Figure 7 are the borders of controllability domain P (13) of linear system (10). The borders of domain D are build using first integrals of system (7) with $\mu = \pm\mu_0$. At Figure 7 one can see that domain P (13) in the neighborhood of the desired

equilibrium (9) encloses a "considerable" part of exact domain D. Figure 8 illustrates the controlled time-optimal motion inside domain D of the system. Switch curve is noted as K.
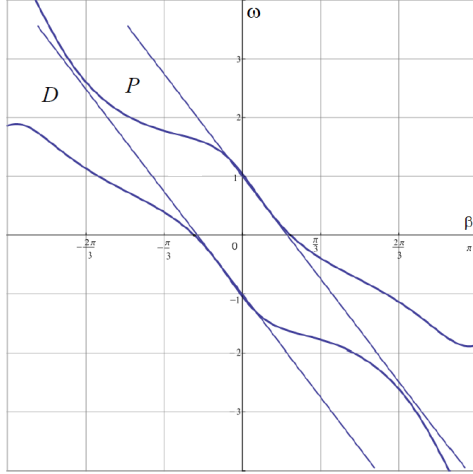
Figure 7. Controllability domain D of the nonlinear model and P of the linear one.
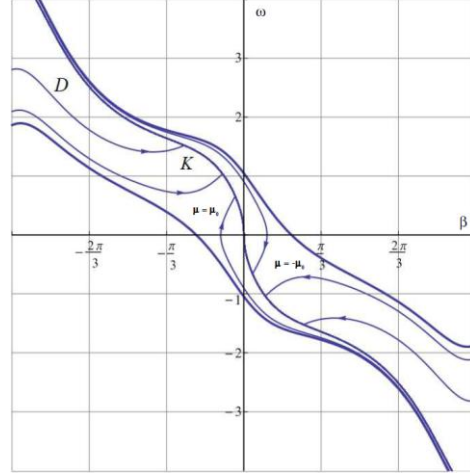
Figure 8. Time-optimal motion trajectories of a wheel-based pendulum.

2. Pendulums with stationary pivot

Here we consider several systems, which contain single- or double-link pendulum on the motionless base. Control algorithms are suggested for relocating the pendulum from its bottom stable equilibrium, into the top unstable one.

2.1. Pendulum with a flywheel

Figure 9 illustrates the pendulum designed in Institute of Mechanics of MSU by head of Mechatronics Lab Anatolii Lenskii. The pendulum can rotate in vertical plane. The data used in the control system includes angles and angular velocities of the link rotation and of the flywheel rotation with respect to the link. Figure 10 illustrates the structure of the pendulum. Link OC is connected to the stationary support at point O. The axis of the joint is perpendicular to the pendulum movement plane (that is the drawing plane). Such device with a flywheel is often referred to as «inertia wheel pendulum» [4].

Applying Lagrange's approach of the second kind, one can derive the motion equations of the pendulum. Angle φ of the flywheel rotation is a *cyclic* variable, because the center of mass of the flywheel together with motor is located at the end of the pendulum link, at point C. Thus, equations of motion contain only the angular velocity of the flywheel $\dot{\varphi}$ with respect to the pendulum link OC. The value of angle φ is of no interest for the problem of controlling pendulum oscillations. The equation that describes only the oscillations of the pendulum can be separated from the mathematical

model of the pendulum with flywheel. It should be noted, however, that this equation *does* contain the parameters of the flywheel. This is similar to the problem of controlling a wheel-based pendulum.
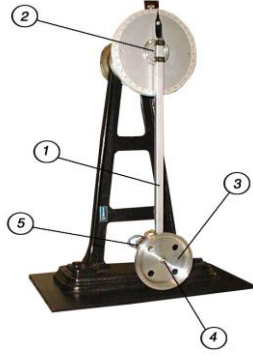
Figure 9. Photo of the pendulum:
1 – pendulum link, *2* – pendulum axle, *3* – flywheel, *4* – flywheel axle, *5* – electric DC motor.
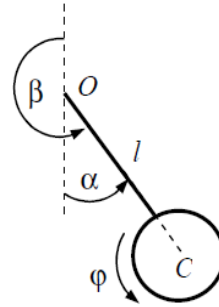
Figure 10. Diagram of the pendulum with flywheel: *O* – pendulum support joint, *C* – flywheel center, $l = OC$.

2.2. Local stabilization of the pendulum in the top equilibrium with maximal domain of attraction

The equations of the motion have only one nonlinear component – $\sin\beta$. Angle β is assumed close to zero during the process of local stabilization. Then substituting for function $\sin\beta$ its argument β transposes these equations into approximate linear equations. This linear model (of third order) has one positive and two negative eigenvalues. If the voltage supplied to the motor is limited then the domain of controllability of the top equilibrium is bounded. Using similar procedure as for the wheel-based single-link pendulum, we extract from the motion equations "unstable" Jordan variable. Using linear *saturated* feedback of kind (14) it is possible to obtain (in linear approximation) maximal domain of attraction. The more the domain of attraction at a local stabilization, the easier it is to build control, providing a global stabilization. Rotating the flywheel to stabilize the pendulum in the top position is similar to swinging arms by a person trying to keep from falling backwards or forwards.

2.3. Translating the pendulum from the bottom equilibrium into the top one

To move the pendulum from its bottom stable position to the top unstable equilibrium it must first be given a swing, and then when it reaches the topmost position, it must be "caught" and stabilized. Switching control law with voltage μ applied to the motor as

$$\mu = -\mu_0 \mathrm{sign}\dot\beta \tag{15}$$

makes the pendulum swing. The swinging stops as energy E of the pendulum reaches value E_0 – its potential energy in the top equilibrium. After the desired energy level is reached, it is kept by pumping under control $\mu = k\left(E - E_0\right)\operatorname{sign}\dot\beta$ (until pendulum gets into the domain of attraction). Then control like (14) stabilizes pendulum. Figures 11 and 12 show numerical and practical experiments.
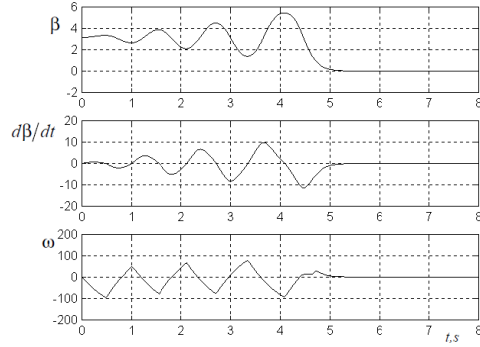
Figure 11. Numerical experiment.	**Figure 12.** Practical experiment.
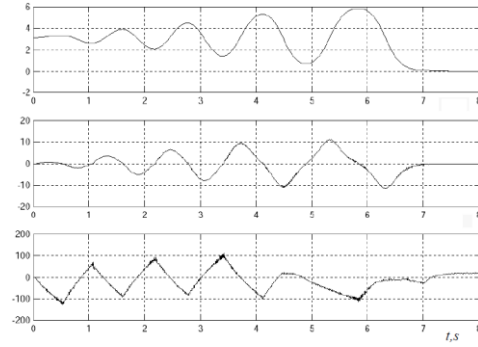
In both Figures, angle β is shown in radians, angular velocity $d\beta/dt$ – in radians per second, flywheel angular velocity ω – in rotations per second. In the numerical experiment pendulum reaches the top equilibrium at 5 s, but in practical experiment – at 7 s.

2.4. Double-link pendulum with limited torque applied in elbow

Plane double-link pendulum is shown in Figure 13. Control torque L is applied in inter-link joint D. Initially we consider the inter-link joint angle α as a limited in absolute value control parameter. Behavior of this parameter is found in order to translate pendulum from the lower stable equilibrium to the top unstable one. The control torque acts like a *servo system* to track the designed angle α. The difference between the designed angle α and the real one is used in the feedback (PD-controller).
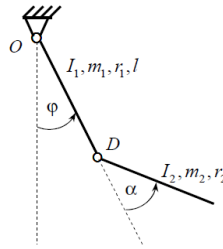
Figure 13. Double pendulum.

To design the control law stabilizing the top unstable position we linearize the motion equations of the pendulum near this position. Two eigenvalues of linearized system are positive and two – negative. The system of equations is reduced to Jordan form. Two motion equations corresponding to

unstable modes are separated from the system. The control law is designed to suppress the unstable motion modes. By this way we achieve maximal as possible domain of attraction (in linear approximation). The designed control contains the unstable Jordan variables only. This feedback is linear one with saturation. Figure 14 illustrates the process of translating the pendulum from its stable lower equilibrium into unstable top one. The top plot shows the time dynamics of angle φ, the next one – dynamics of angle α, the third one – torque L, the bottom plot – full energy E of the system.
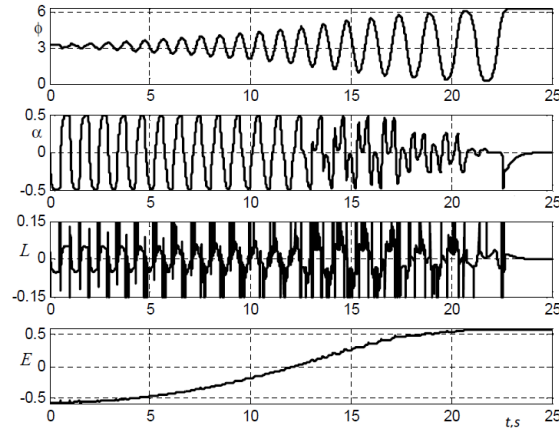
Figure 14. Translating the double pendulum from the bottom equilibrium to the top one.

3. Ball on the beam

The problem of stabilization of the so-called "beam-and-ball system" is considered. The ball can roll without slipping on a beam. The beam may turn about its pivot point that is located below it. Thus the beam is similar to an inverted pendulum. A torque is applied in its pivot. In equilibrium the beam is located horizontally, and the ball is in the middle of the beam, just above its pivot point. Without control this position is unstable. The system has two degrees of freedom, and it is controlled by only a single torque. It is required to build a feedback in such a way that the basin of attraction of the unstable equilibrium would be maximal possible. We consider the curvilinear beam. More exactly, it is a part of a circle. If the radius of this circle is large enough, that is, the curvature is small, the linearized model has one unstable motion mode. If the radius of this circle is small enough, there are two unstable modes. In this latter case, the system is more difficult to stabilize than in the first case. Problem of stabilization with large basin of attraction is solved in both cases – with one unstable mode and with two unstable modes. Numerical experiments have been successfully performed.

4. Robots-bicycles with system of gyroscopic stabilization

Figures 15 and 16 show two bicycles designed in Institute of Mechanics of MSU by A.V. Lenskii.

207

The control torque is applied to the gyrostabilizer to support the unstable upright position of the
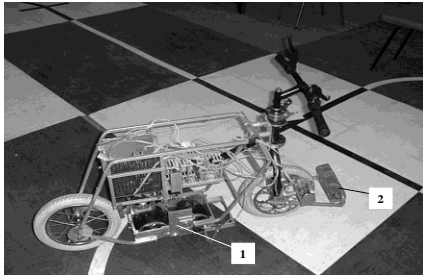
Figure 15. Bicycle with one steering wheel:
1 – gyrostabilizer, 2 – light detector array.
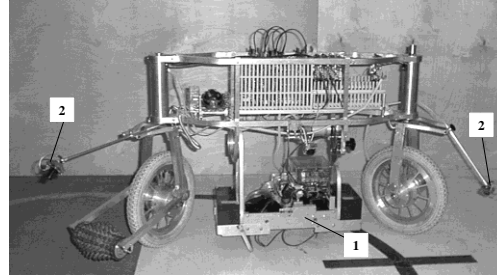
Figure 16. Bicycle with two steering wheels:
1 – gyroscopic stabilizer, 2 – video cameras.

bicycle. We have designed the control torque as a function of bicycle tilt angle, front wheel velocity, steering angle, precession angle, precession angular velocity. Numerical and practical experiments have been successfully performed using this control law.

5. Conclusions

Different concrete systems containing unstable object are analyzed. The control input signal is assumed restricted. Maximal basin of attraction of the desired operating regime is achieved by using all available resources of control to suppress the unstable modes of motion. The control algorithms are developed, discussed, tested numerically and in some cases experimentally.

Acknowledgments

References

[1] Lam, S., Davison, E.J. The real stabilizability radius of the multi-link inverted pendulum. USA, Minneapolis, Minnesota, *Proc. of American Control Conference* 2006, 1814-1819.

[2] www.segway.com, www.solowheel.eu

[3] Formalskii, A.M. *Controllability and stability of systems with limited resources.* Publishing House «Nauka», Moscow, 1974. In Russian.

[4] Block D, Astrom K, Spong M. The reaction wheel pendulum. Princeton NJ, *Synthesis Lectures on Control and Mechatronics.* Morgan & Claypool Publishers, 2007.

Alexander Moiseevich Formalskii, Professor: Lomonosov Moscow State University (MSU)/Institute of Mechanics, 1, Mitchurinskii prospect, 119192, Moscow, Russia (formal@imec.msu.ru).

Influence of nonlinearity simplifications in a reference model of a motor vehicle on the automatic control of the vehicle steering system during a lane-change manoeuvre
(CON266-15)

Mirosław Gidlewski, Dariusz Żardecki

Abstract: The automation of lane-change manoeuvre is fundamental to the automation of motor vehicle driving and it is also the subject matter of scientific works. One of the major parts of our project was the synthesis of a controller that would control an active steering system during the lane-change manoeuvre. Theoretical deliberations and simulation examinations have been based on a mathematical model of the vehicle motion and the controller. The model of the object controlled includes a detail description of the dynamics of motion of a two-axle truck, where nonlinearities and three-dimensional nature of the vehicle motion are taken into account. The model of the controller, founded on the Kalman theory of the linear-quadratic systems, has been based on a "highly" simplified linearized reference model of motor vehicle's dynamics. The subject of this paper is an analysis of the influence of nonlinearity simplifications in the reference model of vehicle motion (on which the controller operation is based) on the control quality. The effects of the simplifications are evaluated with the use of sensitivity indicators based on simulated time histories obtained for models with various degrees of simplification. This work may be interesting both for researchers who are engaged in sensitivity analysis of nonlinear models and for specialists working in the field of mechatronic control systems.

1. Introduction

The present-day motor vehicle becomes more and more automated. As regards the tasks related to the active safety, the systems that prevent vehicle wheels from locking up while braking and stabilize the vehicle motion during rapid turns have become mandatory in new vehicles. Various driver assistance systems, facilitating vehicle driving in road traffic conditions or even automating the performance of some vehicle manoeuvres carried out with low speeds, e.g. parking, are increasingly often offered as over-standard equipment. Works on systems that are to automate traffic manoeuvres at high drive speeds, such as e.g. overtaking or obstacle avoidance, are being carried out at many research centres. The manoeuvres of this kind are difficult for being automated, because the automation requires in this case the controlling of an object whose dynamics is unstable and susceptible to changes in many parameters and whose trajectory is subject to strict limitations.

Usually, a traffic manoeuvre constitutes a sequence of elementary lane-change manoeuvres. Therefore, the automation of the process where a motor vehicle moving with a high speed changes the traffic lane is perceived as fundamental for the automation of complex traffic manoeuvres.

The issue of controlling the angle of turning the road wheels during a lane-change manoeuvre is addressed by numerous scientific studies and publications. Usually, they are based on a vehicle steering concept that covers planning the vehicle path and following the predicted course in a tracking process where appropriate sensors and regulating devices are employed [3, 5, 10, 11, 12]. The vehicle path planning is sometimes treated in such cases as a problem of parametric optimization for the heuristically assumed form of the function of shape of the desired vehicle path (sinusoid segment, composition of arcs, line segments, etc.). At the vehicle path optimization of this kind, not only short manoeuvre duration time, smoothness of the path, or reduction of the feeling of jerks, but also the possibilities of good realization of the manoeuvre in a tracking process should be taken into account (the shape of the vehicle path affects the regulation errors). The regulation systems proposed in such publications are based on the structures and algorithms that are known from theory.

Within project No. N N509 568439, work was undertaken on employing an active steering system for automatic driving of a motor vehicle (medium-capacity motor truck provided with a driving stability system and road monitoring systems) in situations of accident hazard caused by an obstacle having suddenly sprung up. In an authorial concept of a system to control the steering wheel turning angle in the line-change manoeuvre [7, 14], a proposal has been made to use simplified linearized reference models describing the dynamics of vehicle motion in the control system. Such models are used for the generation of the desired vehicle path and for the synthesis of regulating devices. Thanks to their simplicity, the models can be effectively used in the algorithms of the real-time controller. The control method having been developed was satisfactorily verified at many simulation tests, during which the controller having been modelled successfully controlled the motion of the vehicle, which was modelled in great detail.

This paper presents formal grounds for the said linearization and its effects for the quality of the control process. In its essence, the problem presented concerns an analysis of the structural sensitivity of the reference model being simplified by linearization.

2. Concept of the control system for the lane-change manoeuvre

The control strategy is based on decomposition of the process into time-related phases (Fig. 1).
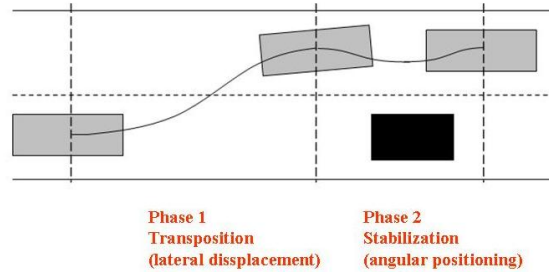
Fig. 1. Concept of decomposition of controlling the lane-change manoeuvre into time-related phases

The control process decomposition as shown above is consistent with the vehicle driving practice followed by experienced drivers. In the first phase of the process, the controlling may be done in a partly-open system ("blindly", "just quickly") by generating an appropriate turn of the steering wheel. The precision of this phase of the manoeuvre should be ensured by the previously identified reference model. During this phase of the control process, corrective controlling will also take place. The steering wheel turning angle is adjusted within this correction on the principle of regulation based on comparing the curve representing the variable that describes the vehicle transposition according to the reference model with the curve representing this variable actually measured. In the second phase, the control process is run in a closed system, on the principle of regulation based on comparing the curves representing the angular position of the vehicle.

According to the concept adopted, the two-phase control process (transposition and angular stabilization) is carried out in one switchable control system (Fig. 2).
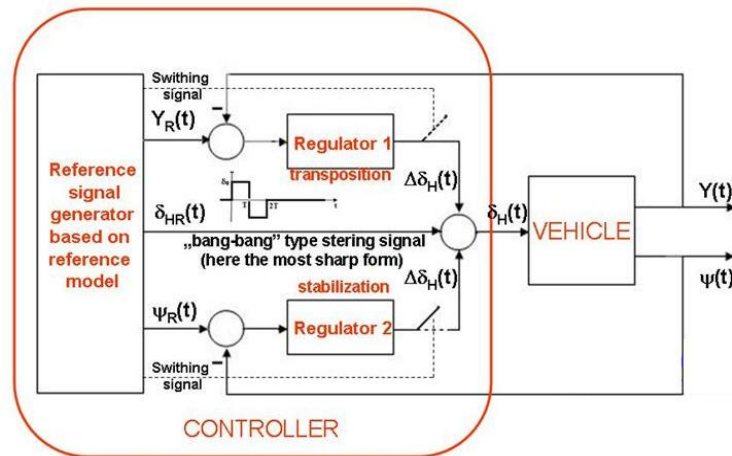
Fig. 2. Block diagram of the automatic control system

The block diagram of the system shows the main system components. Based on the reference model, the generator unit generates reference signals, which represent time histories of $\delta_{HR}(t)$ (steering wheel turning angle), $Y_R(t)$ (lateral vehicle displacement relative to the initial vehicle position), and $\psi_R(t)$ (vehicle yaw angle relative to the road centre line). The signal of primary importance is the "bang-bang" control signal $\delta_{HR}(t)$ [1], applied as an input to the vehicle system and, in its simplest form, being a combination of Heaviside step functions. The response curves $Y_R(t)$ and $\psi_R(t)$ are used as inputs to the regulating systems, correcting the vehicle path.

In the first phase of the control process, the transposition system is on (activated) and the angular stabilization system is off (deactivated); in the second phase, these connections are reversed. The switching over takes place when the centre of vehicle mass reaches a position where the obstacle avoidance is ensured.

The curve representing the reference lateral displacement $Y_R(t)$ is determined by generating a control signal $\delta_{HR}(t)$ whose parameters would be such that the acceleration and velocity values calculated for the reference model could be within their acceptable limits and that the final state could be achieved before the acceptable time limit. In the case that the reference model has the form of a system of linear equations of motion (which is obtained by appropriate linearization of the initial reference model), the control parameters can be determined in a relatively simple way, thanks to the Laplace transformation and properties of the transforms, ensuring the calculation results to be obtained in real time. The reference curve of the vehicle yaw angle is obviously represented by equation $\psi_R(t) = 0$.

The algorithms of the regulating devices (Kalman regulators [2]) are also based on the knowledge of the reference model in its linear version [1, 7, 14].

The algorithms prepared for the controller generating the reference signals and the signals to correct the road wheel turning angles constitute a basis for the controller of an active steering system. In the simplest design, the time history of the steering wheel turning angle $\delta_H(t)$ may be then treated as a scaled curve representing the road wheel turning angle $\delta(t)$. In more sophisticated versions, corrective members may be introduced for the dynamics of the steering system to be taken into account.

The reference model is extremely important for the functioning of the control system. For good results to be obtained by using such a model, it must be not only well matched to the system but also well identified by vehicle equipment. However, the model identification is a separate issue, which is not covered by the scope of this paper.

3. Reference model and its transformations and simplifications

The reference model plays a key role in the synthesis of controlling the process of changing the traffic lane by a moving motor vehicle. For the notation to be simplified, the index R will be omitted and the process will be analysed as if the control input were applied directly to the steered wheels.

To start with, the known "bicycle model" was adopted as the initial reference model [2, 9]. It derives from the Boltzmann-Hamel equations, which describe the dynamics of motion of a nonholonomic system (here: a planar system consisting of a single-mass solid on pneumatic tyres) in "quasi-coordinates", adopted as the linear velocity and angular velocity in moving (local) coordinate system [6, 8].
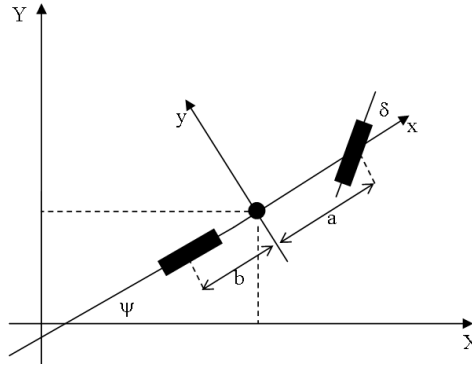
Fig. 3. Idea of the "bicycle model" of a motor vehicle

Symbols adopted to represent the variables and model parameters:

t	– time (t = 0 means the instant when the control system is switched on)
$\delta(t)$	– time history of the front wheels turning angle
$\psi(t)$	– time history of the vehicle yaw angle relative to the road centre line
$\Omega(t)$	– time history of the angular velocity of the vehicle yaw motion ($\Omega(t) = \dot{\psi}(t)$)
U(t)	– time history of the lateral vehicle velocity in the local coordinate system
V	– linear longitudinal vehicle velocity (constant) in the local coordinate system
X(t), Y(t)	– time histories of the global coordinates of the centre of vehicle mass
m	– vehicle mass
J	– vehicle moment of inertia relative to the vertical axis going through the point representing the centre of vehicle mass
a, b	– distances of the front and rear vehicle axles, respectively, from the projection of the point representing the centre of vehicle mass
k_A, k_B	– coefficients of tyre resistance to sideslip for the centres of front and rear wheel axes, respectively

At an assumption that the vehicle moves on a flat road with a constant velocity and the steered wheel turning angles are sufficiently small to assume that the interaction between them and the road surface may be linearly described as an effect of the action of road reactions reduced to the centres of the wheel axes, the equations of motion describing the dynamics of the plane motion of the vehicle body solid in the local coordinate system have the form:

$$m\dot{U}(t) + \frac{k_A + k_B}{V}U(t) + \frac{mV^2 + k_A a - k_B b}{V}\Omega(t) = k_A \delta(t) \tag{1}$$

$$J\dot{\Omega}(t) + \frac{k_A a^2 + k_B b^2}{V}\Omega(t) + \frac{k_A a - k_B b}{V}U(t) = k_A a \delta(t) \tag{2}$$

The following equations transform the velocities from the local moving coordinate system to the global system fixed to the road:

$$\psi(t) = \int_0^t \Omega(\tau)d\tau \tag{3}$$

$$\dot{X}(t) = V\cos(\psi(t)) - U(t)\sin(\psi(t)) \qquad \dot{Y}(t) = V\sin(\psi(t)) + U(t)\cos(\psi(t)) \tag{4, 5}$$

The trajectory of the centre of vehicle mass Y(X) in the global coordinate system is defined by the equations:

$$X(t) = \int_0^t \dot{X}(\tau)d\tau = \int_0^t \left(V\cos(\psi(\tau)) - U(\tau)\sin(\psi(\tau))\right)d\tau \tag{6}$$

$$Y(t) = \int_0^t \dot{Y}(\tau)d\tau = \int_0^t \left(V\sin(\psi(t)) + U(\tau)\cos(\psi(\tau))\right)d\tau \tag{7}$$

From now on, equations (1–7) will be treated here as the "initial reference model".

For small and short-duration disturbances to the motion (and such are the control signals dealt with during an obstacle avoidance manoeuvre), the linearization of the transformation equations may be allowed (such an assumption aimed at simplifying the model will be the main subject of the further sensitivity analyses). At this simplification, the following will hold, according to the expansion into a Taylor series:

$$\cos(\psi(t)) \approx 1 \qquad \sin(\psi(t)) \approx \psi(t) \tag{8, 9}$$

$$U(t)\sin(\psi(t)) \approx 0 \qquad U(t)\cos(\psi(t)) \approx U(t) \tag{10, 11}$$

Hence, based on (4–5):

$$\dot{X}(t) = V \tag{12}$$

$$\dot{Y}(t) = V\psi(t) + U(t) \qquad \ddot{Y}(t) = V\dot{\psi}(t) + \dot{U}(t) \tag{13, 14}$$

as well as:

$$U(t) = \dot{Y}(t) - V\psi(t) \qquad \dot{U}(t) = \ddot{Y}(t) - V\dot{\psi}(t) \tag{15, 16}$$

Having substituted (1–2) to the equations of motion and having simplified the result, we obtain:

$$m\ddot{Y}(t) + \frac{k_A + k_B}{V}\dot{Y}(t) + \frac{k_A a - k_B b}{V}\dot{\psi}(t) - (k_A + k_B)\psi(t) = k_A\delta(t) \tag{17}$$

$$J\ddot{\psi}(t) + \frac{k_A a^2 + k_B b^2}{V}\dot{\psi}(t) - (k_A a - k_B b)\psi(t) + \frac{k_A a - k_B b}{V}\dot{Y}(t) = k_A a\delta(t) \tag{18}$$

The trajectory of the centre of vehicle mass Y(X) may now be defined by the following:

$$X(t) = \int_0^t \dot{X}(\tau)d\tau = \int_0^t V d\tau = Vt \qquad\qquad Y(t) = \int_0^t \dot{Y}(\tau)d\tau \tag{19, 20}$$

Equations (17–20) will now be treated here as the "simplified reference model".

In the initial reference model, equations (1, 2, 3) are linear; therefore, both their sides may be subjected to the Laplace transformation. For zero values of variables U(t) and Ω(t) as the initial conditions, a notation of the reference model partly in a transmittance form, regarding transforms with operational variable "s", will then be obtained.

$$\tilde{U}(s) = G_{U\delta}(s)\tilde{\delta}(s) \qquad \tilde{\Omega}(s) = G_{\Omega\delta}(s)\tilde{\delta}(s) \qquad \tilde{\psi}(s) = \frac{1}{s}\tilde{\Omega}(s) \tag{21, 22, 23}$$

where the transmittances will have standard forms:

$$G_{U\delta}(s) = \frac{G_{U\delta 0}(T_{U\delta}s + 1)}{T_0^2 s^2 + 2\xi_0 T_0 s + 1} \qquad\qquad G_{\Omega\delta}(s) = \frac{G_{\Omega\delta 0}(T_{\Omega\delta}s + 1)}{T_0^2 s^2 + 2\xi_0 T_0 s + 1} \tag{24, 25}$$

and the "transmittance parameters" present there will be described by formulas:

$$T_0 = V\sqrt{\frac{mJ}{k_A k_B(a+b)^2 - MV^2(k_A a - k_B b)}} \qquad \xi_0 = \frac{\left(m(k_A a^2 + k_B b^2) + J(k_A + k_B)\right)}{2\sqrt{mJ\left(k_A k_B(a+b)^2 - mV^2(k_A a - k_B b)\right)}} \tag{26, 27}$$

$$G_{U\delta 0} = \frac{(k_A k_B(a+b)b - mV^2 k_A a)V}{k_A k_B(a+b)^2 - mV^2(k_A a - k_B b)} \qquad T_{U\delta} = \frac{Jk_A V}{k_A k_B(a+b)b - mV^2 k_A a} \tag{28, 29}$$

$$G_{\Omega\delta 0} = \frac{k_A k_B(a+b)V}{k_A k_B(a+b)^2 - mV^2(k_A a - k_B b)} \qquad T_{\Omega\delta} = \frac{maV}{k_B(a+b)} \tag{30, 31}$$

Due to nonlinearities being present in equations (4) and (5), the Laplace transformation and operational calculus are inapplicable to them.

In the simplified reference model, all the equations are linear; therefore, they may be subjected as a whole to the Laplace transformation and appropriate transmittances defining the relationships between transforms of time histories of individual quantities may be determined. For zero values of variables Y(t), U(t), ψ(t), and Ω(t) as the initial conditions, an equivalent notation of the simplified reference model in a transmittance form will then be obtained.

$$\tilde{Y}(s) = G_{Y\delta}(s)\delta(s) \qquad\qquad \tilde{\psi}(s) = G_{\psi\delta}(s)\delta(s) = \frac{G_{\Omega\delta}(s)}{s}\delta(s) \tag{32, 33}$$

where

$$G_{Y\delta}(s) = \frac{G_{\Omega\delta 0}V(T_1^2 s^2 + 2\xi_1 T_1 s + 1)}{s^2(T_0^2 s^2 + 2\xi_0 T_0 s + 1)} \qquad T_1 = \sqrt{\frac{J}{k_B(a+b)}} \qquad \xi_1 = \frac{b}{2V}\sqrt{\frac{k_B(a+b)}{J}} \tag{34, 35, 36}$$

215

The transmittance equations provide a basis for analysing the vehicle behaviour following a rapid turn of the vehicle wheels once to the one side and then to the other side. The analytic form of the input $\delta(t)$, its transform $\tilde{\delta}(s)$, and appropriate transmittances being known, the simple relations known from the operational calculus may be used to analyse the response. Let us consider this for the input signal $\delta(t)$ being a combination of step functions representing a jerk of the steering wheel in both directions, with holding the wheel for a while in the extreme positions (Fig. 4).
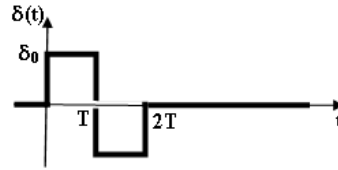
Fig. 4. Time history of the test jerk of the steering wheel in both directions

$$\delta(t) = \delta_0\big(l(t) - 2l(t-T) + l(t-2T)\big) \qquad l(t) - \text{the Heaviside function} \tag{40}$$

In such a case:

$$\tilde{\delta}(s) = \delta_0\left(\frac{1}{s} - 2\frac{1}{s}e^{-sT} + \frac{1}{s}e^{-s2T}\right) = \delta_0\frac{\left(1-e^{-sT}\right)^2}{s} \tag{41}$$

$$\lim_{t\to\infty}Y(t) = \lim_{t\to\infty}(s\tilde{Y}(s)) = \lim_{t\to\infty}(s_{Y\delta0}(s)\tilde{\delta}(s)) = \tag{42}$$

$$= \lim_{s\to0}\left(s\frac{G_{\Omega\delta0}V\left(T_1^2s^2 + 2\xi_1T_1s + 1\right)}{s^2\left(T_0^2s^2 + 2\xi_0T_0s + 1\right)}\delta_0\frac{\left(1-e^{-sT}\right)^2}{s}\right) = T^2G_{\Omega\delta0}V\delta_0 = Y_0$$

$$\lim_{t\to\infty}\psi(t) = \lim_{s\to0}(s\tilde{\psi}(s)) = \lim_{s\to0}\big(sG_{\Omega\delta}(s)\tilde{\delta}(s)\big) = \lim_{s\to0}\left(s\frac{G_{\Omega\delta0}\left(T_{\Omega\delta}s+1\right)}{s\left(T_0^2s^2 + 2\xi_0T_0s + 1\right)}\delta_0\frac{\left(1-e^{-sT}\right)^2}{s}\right) = 0 \tag{43}$$

This confirms the known fact that a jerk of the steering wheel in both directions will cause the vehicle to change its traffic lane. From the vehicle steering concept point of view, it is very important to notice that if the reference model is followed then the vehicle in steady state will move on the changed traffic lane with a zero yaw angle! Obviously, due to random disturbances and model imperfections, the vehicle having achieved the steady state of motion may actually move along a rectilinear path with a non-zero yaw angle, but this is a matter of a next correction.

For the planned lane change Y_0 to be achieved, the control pulse duration time T and amplitude δ_0 should be appropriately chosen, with simultaneously taking into account the values of the amplification parameter $G_{\Omega\delta0}$ and vehicle velocity V. The relations determined on the grounds of the simplified reference model constitute very simple and "quick" calculation tools for the selection of vehicle control parameters.

The reference model proposed may be used for controlling both the trajectory of the centre of vehicle mass (the first phase of the control process) and the vehicle yaw angle (the second phase).

4. Sensitivity analysis of the reference model being linearized

In the classic analysis of structural sensitivity of models of dynamic systems [4, 13], parametric and asymptotic methods are employed. When the initial reference model is linearized, its structure is simplified "abruptly" by disregarding the higher-order members in the model expansion into a Taylor series. Therefore, an analysis of the model sensitivity to linearization is based on a series of simulation experiments, where the simplification effects are evaluated by comparing the output signals of the initial model and the simplified model. For the comparison to be more specific, sensitivity measures are also introduced, including integral indicators, which express the discrepancies between the output signals of the nominal (initial) model and of the model having been changed (linearized) [13] (Fig. 5).
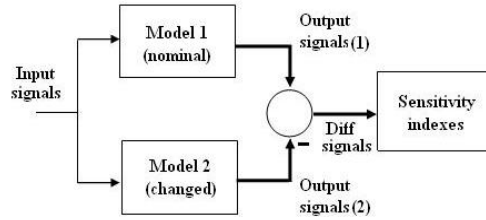
Fig. 5. Schematic diagram of sensitivity analysis. Example index:

$$Wx = 100 \frac{\int_0^\tau (x_1(t) - x_2(t))^2 \, dt}{\int_0^\tau (x_1(t))^2 \, dt} \qquad (44)$$

In the repeated calculations, controller operation having an effect on a real object controlled, i.e. a STAR 1142 motor truck, was simulated. The model of motion of such a vehicle [6] was built with taking into account the multi-mass structure of the moving system, three-dimensionality of the motion, and nonlinearities in the suspension system characteristics and in the processes taking place in the tyre-road contact zone. The model was verified experimentally.
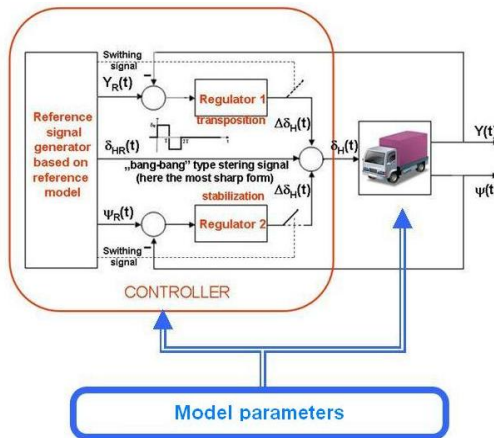
Fig. 6. Block diagram visualizing the simulation tests for the purposes of sensitivity analysis

The calculations were repeated for many different sets of data describing the vehicle and the controller. The example results shown (Figs. 7, 8 and 9) represent the manoeuvre carried out in difficult conditions, i.e. on a slippery road ($\mu = 0.3$) and with a speed of $V = 16.7$ m/s (60 km/h) and $V = 22.2$ m/s (80 km/h). The index values were determined according to equation (44).
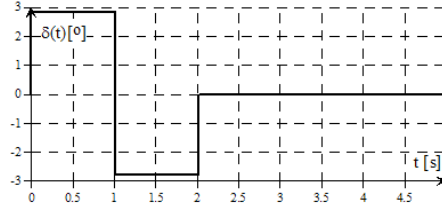
Fig. 7. Set point signal of the front wheels turning angle

$WY_R = 0{,}000498\%$

$W\psi_R = 0{,}000003\%$

$WY = 0{,}000002\%$

$W\psi = 0{,}000039\%$
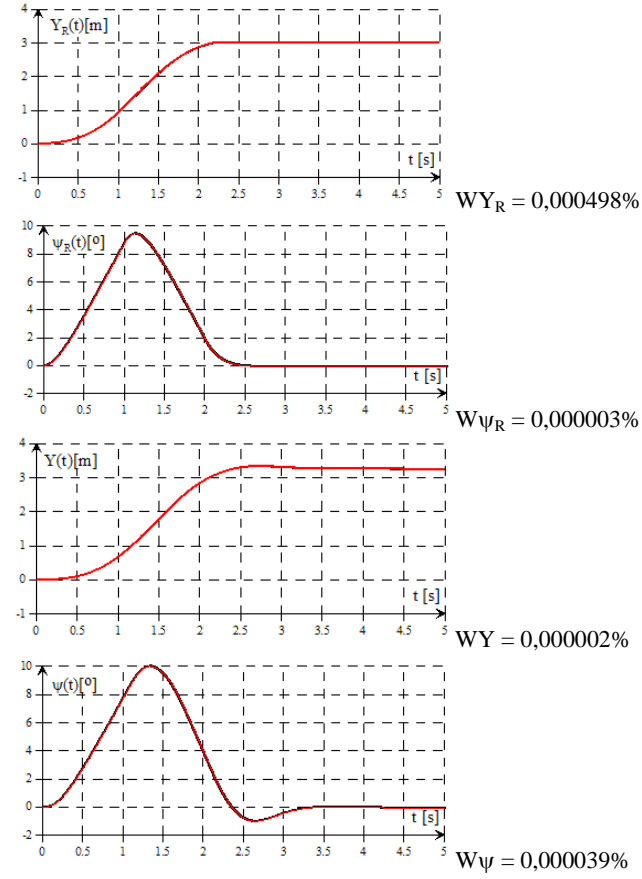
Fig. 8. Results of calculations carried out for the purposes of sensitivity analysis, $V = 60$ km/h
——————— Curves for the initial reference model
——————— Curves for the linearized reference model

218
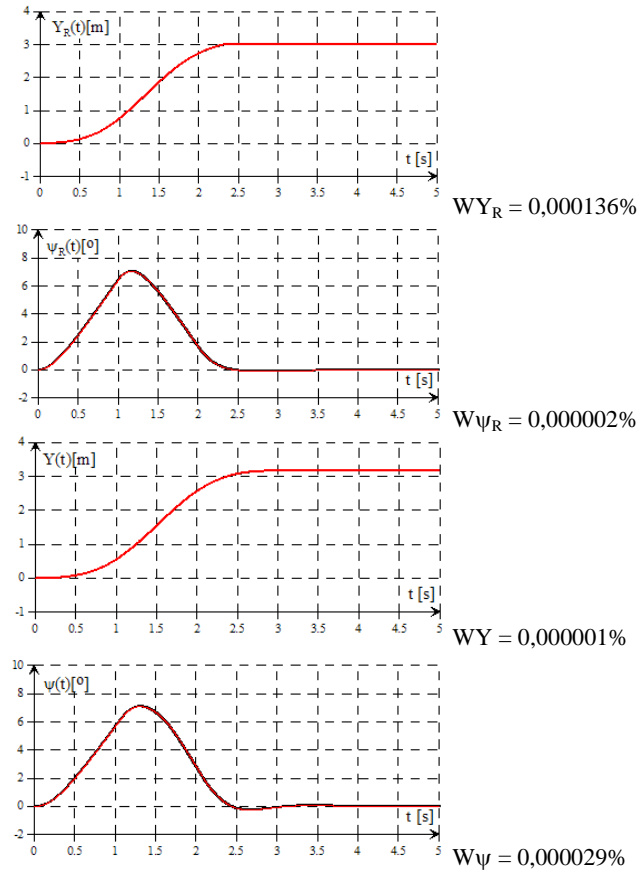
Fig. 9. Results of calculations carried out for the purposes of sensitivity analysis, V = 80 km/h
———————— Curves for the initial reference model
———————— Curves for the linearized reference model

5. Conclusion

The test results collected from many simulation experiments show that the impact of linearization of the reference model on the controller output signals $Y_R(t)$ and $\psi_R(t)$ and on the curves $Y(t)$ and $\psi(t)$ representing the effect of the control process is very small. This means that the parameters defining the signal of the steering wheel turning angle may be quickly and quite well selected on the grounds of simple algebraic equations and similarly, the generation of reference signals may be successfully based on an effective linearized reference model.

The controller sensitivity to changes in the parameters of the object modelled, i.e. its sensitivity to identification imperfections, remains a separate issue, which requires extensive research. The research carried out to date (yet incomplete) show that properly designed regulators can improve the control effect, even if the parameters of the reference model have not been perfectly identified.

Acknowledgements

References

[1] Andrzejewski, R.; Awrejcewicz, J.: *Nonlinear Dynamics of Wheeled Vehicle.* Springer New York, 2003.

[2] Athans, M.; Falb, P. L.: *Optimal control. An Introduction to the Theory and Its Applications.* McGraf-Hill, 1966.

[3] Bevan, G. P.; Gollee, H.; O'Reilly, J: *Trajectory generation for road vehicle obstacle avoidance using convex optimization*. Proceedings of the Institute of Mechanical Engineers Part D – Journal of Automobile Engineering, Vol. 224 (4), 2010.

[4] Frank, P. M.: *Introduction to system sensitivity theory*. Academic Press, 1978.

[5] Gao, Y.; Lin, T.; Borrelli, F.; Tseng, E.; Hrovat, D.: *Predictive control of autonomous ground vehicles with obstacle avoidance on slippery roads.* Dynamic Systems and Control Conference, 2010.

[6] Gidlewski, M.: *Model of a dual axis heavy truck for handling studies in complex road situations*. 11th European Automotive Congress, Budapest 2007.

[7] Gidlewski, M.; Żardecki, D.: *Automatic Control of Steering System During Lane Change.* Proceedings of ESV'2015 Conference in Gothenburg, Sweden, available on the Internet.

[8] Jarzębowska, E.: *Analytic Mechanics*. Oficyna Wydawnicza. Politechniki Warszawskiej (Publishing House of the Warsaw University of Technology), Warszawa 2003 (in Polish).

[9] Kamiński, E.: *Steerability and stability of motor vehicles – Methods and criteria of assessment*. Autotechnika Motoryzacyjna, No. 12, 1985.(in Polish).

[10] Moshchuk, N.; Shih-Ken Chen; Zagorski, C.; Chatterjee A.: *Path planning for collision avoidance maneuver.* Proceedings of the ASME 2013 International Mechanical Engineering Congress and Exposition IMECE2013, San Diego, California, 2013.

[11] Park, J. M.; Kim, D. W.; Yoon, Y. S.; Kim, H. J.; Yi, K. S: *Obstacle avoidance of autonomous vehicles based on model predictive control.* Proceedings of the Institute of Mechanical Engineers Part D – Journal of Automobile Engineering, Vol. 223, 2009.

[12] Shiller, Z.; Sundar, S.: *Optimal Emergency Maneuvers Of Automated Vehicles*. Research Reports California Partners for Advanced Transit and Highways (PATH) – UC Berkeley, 1996.

[13] Żardecki, D.: *The λ-sensitivity analysis and its application in simulation studies of dynamical systems*. Archiwum Automatyki i Telemechaniki: 1980, XXV (3), 335–354 (in Polish).

[14] Żardecki D.: *Control systems for autonomous cars*. (To be published).

Mirosław Gidlewski
University of Technology and Humanities in Radom, Automotive Industry Institute (PIMOT),
miroslaw.gidlewski@gmail.com, miroslaw.gidlewski@uthrad.pl

Dariusz Żardecki
Military University of Technology (WAT), Automotive Industry Institute (PIMOT),
d.zardecki4@upcpoczta.pl, dariusz.zardecki@wat.edu.pl

Dynamics and control of vehicle with vision based navigation system
(CON300-15)

Robert Głębocki, Mariusz Jacewicz

Abstract: Navigation is a major challenge for the operation of an autonomous vehicle. This paper deals with the problem of pose estimation for real-time vision based navigation system. The delays introduced by guidance system into the control system of an unmanned vehicle were tested. Presented method is able to estimate the target pose with high accuracy and does not require any landmark on object. The result of numerical simulation was presented. Experimental results showed that the proposed method of navigation introduced a small delay in the control system. Created system is also robust to occlusions and light variations. The approach will be further evaluated and tested in the continued work.

1. Introduction

The problem of pose estimation of known object is one of the most significant issues in vision navigation. In the last twenty years there were some famous texts about this problem. A lot of modern tracking methods are applicable to pose estimation problem but they are high computational cost. This paper describes the results of analysis, implementation and testing of simulation intended for vision-based guidance, navigation and control applications such as rendezvous and docking of satellites. In this document markerless local features based tracking system has been studied. It was done under the randezvous of satellites on Earth orbit project.

Autonomous randezvous is necessary for space programs. Navigation for proximity operations requires very accurate measurements without human involvement. A servicing satellite is sending to capture target object and perform servicing tasks. There must be a high level of autonomy of system. System focus on all phases of randezvous. It was assumed an image of an object taken by a calibrated camera in each step of time is known, and was assumed a 3D representation of an object model is known. It was proposed a solution for tracking 3D rigid objects that is based on local features and promises better computational performance. Proposed method is more accurate than other methods presented in literature because is more stable and robust on the tracking failures. This is very important issue because of implementation this method on satellite hardware. Projected system is also cheaper than other proposed earlier solutions. Introduced approach has been tested on real images. It was shown that achieved high tracking performance.

2. State of the art

In the literature the problem the relative pose estimation of two objects is well known for a years. First approaches to visual tracking were published in the late 1980s and were based on tracking of the outer contour of a target [1]. Contour-based trackers also gained significant attention upon initial inception, but received slightly less research in the mid-1990s. A lot of existing algorithms for pose estimation and tracking are based on fiducial markers. In some cases, it is worth to add fiducials like LEDs or markers, to the target object to simplify the registration task. It this case it is assumed that one or more fiducials are visible at all times [2]. The 3D positions of the fiducials in the world coordinate system are assumed to be known. This approach [3], [4] in case of satellites is impractical because many existing satellites have not these fiducial markings. Three-dimensional model-based tracking systems have been investigated by several research groups. Pose computation is achieved by minimization the distance between 3D model edges and the corresponding edge features in the image. Achieving model projection in the image has limitations. The most weakness of approach based on 3D model is reliance on high detailed geometric model. There are problems when objects are made with cylindrical, spherical and complex shapes as it is often in case of satellites. This makes the system very fragile. Moreover when the object is complex there are achieved low frame per second rates. First, the system must either be initialized by hand or require the camera to be very close to a specified position. To reject outliers algorithms such as RANSAC (Random Sample Consensus) are implemented to achieve robustness to illumination conditions. Active sensors like LIDAR (Light Detection and Ranging) were used for automatic relative pose estimation. These sensors are expensive. Camera sensors are cheaper and can provide accurate capabilities to obtain relative pose. The use of the interface ring used to attach the satellite to launch vehicle has been proposed for capturing the satellite. This has a disadvantage because it is restricted only for proximity operations where the target satellite is visible from the interface side. Capturing should be performed autonomously because there are communication delays between on-orbit systems and ground. Feature matching computer vision approaches have been developed but they are very computational intensive and cannot be used during whole mission. Critical sensitivity to illumination, relative orientation and occlusions of target had been observed. Learned database is also used on Orbital Express and the algorithms are based on edges in this case. Lepetit suggested for tracking objects in 3D by using corner features with a single camera. This approach was robust to camera displacements and partial occlusion. Drawback of this method was camera should be close enough to one of key frames and there is a real problem when then tracking must be initialized again for example after tracking failure.

Proposed system deals with all three stages of satellite randezvous from far proximity operations to the last stage, contact. Limitation of these methods lies in their long execution time. Moreover, the existing approaches are very computationally expensive. It is much better to rely on naturally present

features, such as edges, corners, or texture. This makes tracking far more difficult: finding and following feature points or edges can be difficult because there are too few of them on many typical objects.

3. Proposed method

In this section the proposed solution was described. The problem of pose estimation is formulated as follow: Given model of the object and a calibrated camera, find the pose of the object with respect to camera.

Presented method of solution is applicable to monocular camera systems. There are given photos of known object which is seen from different camera locations. Unknown are the six parameters that can describe relative pose of two objects: three coordinates x, y, z which describes the linear translation of object in relation to camera and three angles of rotation Φ, Θ, Ψ (roll, pitch, and yaw) which describes the mutual angular orientation of two objects in space.
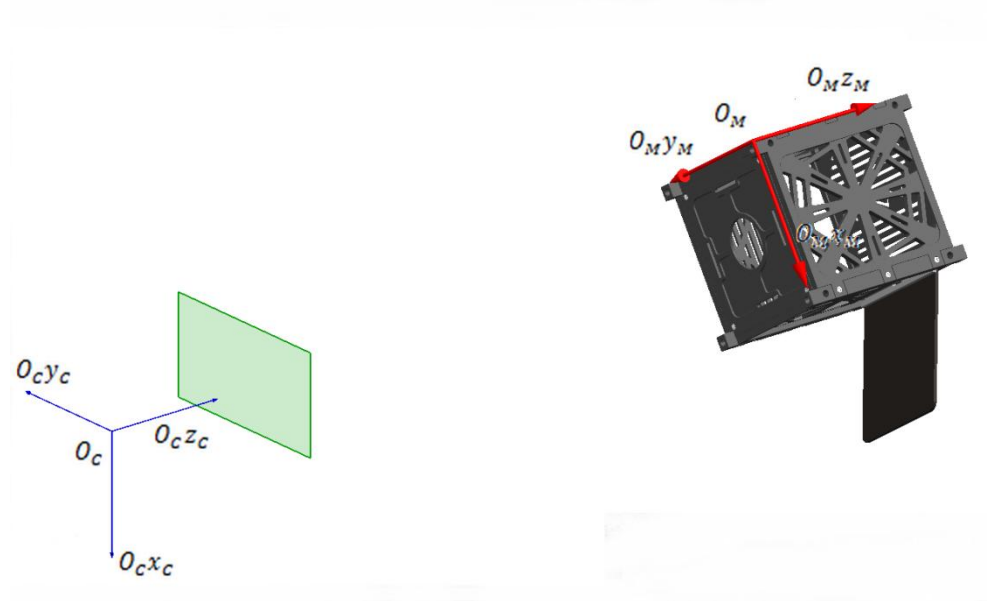
Figure 1. Pose estimation problem [3]

There were defined two main coordinate systems. Both are right hand side (clockwise) oriented Cartesian coordinated systems. The first one is camera coordinate system. The origin O_C of this coordinate system is located in optical center. The $O_C x_C$ axis of this coordinate system is oriented downward, the $O_C y_C$ axes is oriented on right and the $O_C z_C$ axis completes the right handed coordinate system (Figure 1). The position of each pixel on photo is given in camera coordinate system. The second one is model coordinate system. The origin O_M of this coordinate system is

located on the surface of object. $O_M x_M$ axis is oriented in front of the target, the $O_M y_M$ axis on right and the $O_M z_M$ axis completed the coordinated system. Origin of this coordinate system is translated from origin of camera coordinate system by vector $\boldsymbol{t} = \begin{bmatrix} x \\ y \\ z \end{bmatrix}$ in Cartesian coordinates. The down scripts C by coordinates means that coordinates are referred in camera coordinate frame. Down subscripts M means that coordinate are in model coordinate frame. The image plane is parrarel to the $O_C x_C$ and $O_C y_C$ axes of camera coordinate system at distance f from the optical center. Object is rotated and displaced with respect to camera coordinate system.

The equation of mapping 3D points in camera coordinate frame to an image plane in homogenous coordinates is defined as follow:

$$\begin{bmatrix} u \\ v \\ 1 \end{bmatrix} = \begin{bmatrix} \alpha_u & s & u_0 & 0 \\ 0 & \alpha_v & v_0 & 0 \\ 0 & 0 & 1 & 0 \end{bmatrix} \begin{bmatrix} x_C \\ y_C \\ z_C \\ 1 \end{bmatrix} \tag{1}$$

α_u and α_v are the scale factors in the $u-$ and $v-$ coordinate directions. They are proportional to the focal length f of the camera: $\alpha_u = k_u f$ and $\alpha_v = k_v f$, where k_u and k_v are the numbers of pixels per unit distance in the u and v directions [5]. The camera internal parameters are known. This was designated in camera calibration process. In most 3D tracking methods, the internal parameters are assumed to be fixed and known, which means that the camera cannot zoom, because it is difficult to distinguish a change in focal length from a translation along the camera Z-axis. In visual system for servicing satellites it was assumed that there will be two cameras. First camera will be operated when the object is far. Second camera will be operated when the object will be near. For additional details about camera models the interested reader is referred to the photogrammetric literature.

Then small letters u and v describes the coordinates in image plane. Coordinates in image plane and 3D space were described in homogenous coordinates.

The coordinates of points of object are referred in model coordinate frame so before mapping on plane they must be transferred to camera coordinate frame. This is defined as follow:

$$X_C = \begin{bmatrix} R & t \\ 0 & 1 \end{bmatrix} X_M \tag{2}$$

$[\boldsymbol{R}\ \boldsymbol{t}]$ is the 3×4 external parameters matrix, and corresponds to the Euclidean transformation from a world coordinate system to the camera coordinate system. $\boldsymbol{R}$ represents a 3×3 rotation matrix, and $\boldsymbol{t}$ a translation. Unknown are $\boldsymbol{R}$ and $\boldsymbol{t}$, left side and last vector on right are known. A rotation matrix $\boldsymbol{R}$ can always be written as the product of three matrices representing rotations around X, Y, and Z axes. The angular orientation of object was parametrized by using of Euler angles. There is singularity when the coordinate frames are rotated mutual by pitch angle equal $\pi/2$, but is invalid on this developments stage of the system. So in expanded form the equation (2) is defined as follow:

$$
\begin{bmatrix} x_C \\ y_C \\ z_C \\ 1 \end{bmatrix} = \begin{bmatrix} \cos\Theta\cos\Psi & \sin\Phi\sin\Theta\cos\Psi - \cos\Phi\sin\Psi & \cos\Phi\sin\Theta\cos\Psi + \sin\Phi\sin\Psi & x \\ \cos\Theta\sin\Psi & \sin\Phi\sin\Theta\sin\Psi + \cos\Phi\cos\Psi & \cos\Phi\sin\Theta\sin\Psi - \sin\Phi\cos\Psi & y \\ -\sin\Theta & \sin\Phi\cos\Theta & \cos\Phi\cos\Theta & z \\ 0 & 0 & 0 & 1 \end{bmatrix} \begin{bmatrix} x_M \\ y_M \\ z_M \\ 1 \end{bmatrix} \quad (3)
$$

The proposed method work in such manner as described downwards. At first, a photo of real object is taken. Next there are detected local features on this photo. A local feature of object is usually associated with a change of image properties simultaneously, although it is not necessarily localized exactly on this change. To handle as wide as possible a range of viewing conditions, feature point extraction should be insensitive to scale, viewpoint, and illumination changes. The local features of the object are extracted by using of SIFT (Scale Invariant Feature Transform) detector and descriptor proposed by Lowe [6]. Algorithm extracts features and is for object recognition based on local 3D extrema in the scale-space pyramid build with difference-of-Gaussian filters. First the location and scale of the keypoints are determined precisely by interpolating the pyramid of Difference-of-Gaussians used for the detection. The input image is successively smoothed with a Gaussian kernel and sampled. The difference of Gaussian representation is obtained by subtracting two successive smoothed images. The Gaussian kernel and its derivatives are the only possible smoothing kernels for scale space analysis. To achieve image rotation invariance, an orientation is also assigned to the keypoint. It is taken to be the one corresponding to a peak in the histogram of the gradient orientations within a region around the keypoint. All dig levels are constructed by combining smoothing and subsampling. The local 3D extrema in the pyramid representation determine the localization and the scale of the interests points. This method is quite stable under viewpoint changes, and achieves an accuracy of a few degrees. An image is transformed into a group a local features. On the exit of this algorithm there is known the two dimensional vector of coordinates of each feature and the second vector which contains the radius of each feature and the angle of orientation in radians. It represents the left side on equation of mapping (1).

Next, similar to the previous step, the local features of the object from model of target are extracted. During an offline training stage, a database of interest object points was build. Their positions on the object surface are known. Images in which the object has been manually registered were used for this purpose. At runtime, SIFT features are extracted from the current frame, matched against the database, resulting in a set of 2D/3D correspondences.

The next task is the pose estimation of the object. It was assumed earlier a set of point correspondences with model points and image points. The object pose can then be estimated from such correspondences. The unknowns are the translation vector t and rotational vector R. They have been found iteratively by using POSIT algorithm. This algorithm estimates pose uses a scaled

orthographic projection, which resembles the real perspective projection at convergence. Such approximation leads to a linear equation system. This gives the rotation and translation directly and there is no the needs of a starting pose. A scale value is introduced for each correspondence, which is iteratively updated. More details about POSIT algorithm can be found in [7].

Automatic segmentation of vehicle from the background and from other vehicles is assumed to be a priori made. Purpose of this step was to distinguish foreground object from the stationary background.

4. Experiments

This section described experiments which were made. Experiments were tested in Matlab software.

It was used a set of photos of real object. It was presented the tracking results of the real object. Experiments were conducted on various image sequences and show advantages of the chosen approach. The main goal of experiments was to obtain the measurements of position and orientation of object and check how accurate is algorithm. Others goals were to confirm the robustness to varying occluding conditions. Experiments were tested as follow. It was used a plane with example image, which was mounted on mounting stand, which can be precisely translated and rotated due to camera coordinate frame. The object was placed on calibration grid so measured parameters were compared with proposed methods. Typical object was shown on image below. It was used low cost camera. The source of light was fixed. It was provided uniform illumination for all the positions of tested object. There were measured of position and one rotational degree of freedom on ground. Next the result of ground truth measurement was compared with calculated results. It was expected that ground truth measurements should be very close to calculated results. Expected translation error should be below a few millimeters. Similar, rotational error should be less than 4 degrees.
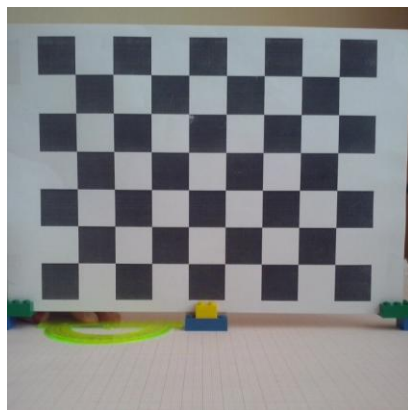
Figure 2.   Exemplary object which had been tested

These internal parameters can be estimated during an offline camera calibration stage. Camera was calibrated the using Caltech calibration method. The motion pattern is visible in the figure. The ground truth error varies around 1mm in space.

The six plots present results for a first chosen example. The camera has a distance of approximately 220 mm to the object. At the beginning the object is not moving. Next the object is moving manually till second 37. The object was constrained and not moved along x and y axes. On the x axes of first three plots there is given time in seconds and on y axes the measured translation in millimeters. On the next plots on x axes there are given, similar as upper figures, time and on y orientation in degrees. Green line shows ground truth and blue line shows the measurements.
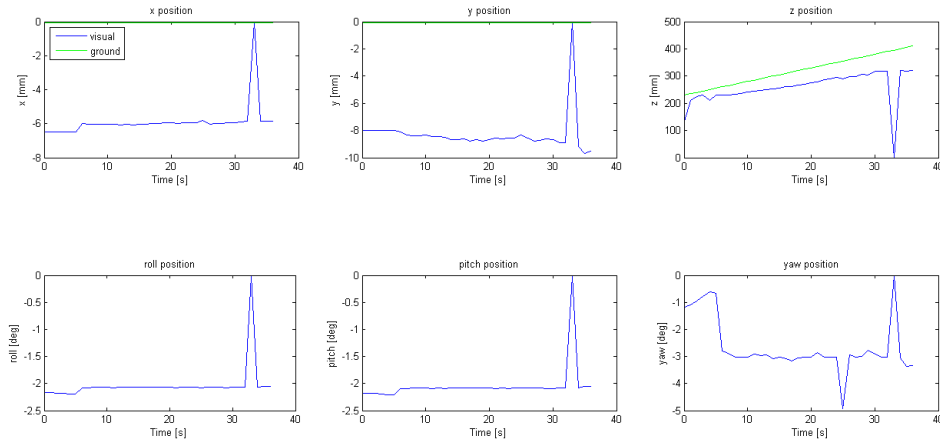
Figure 3. Tests results of the first experiment. Position and orientation of the object.

Ground truth (green line) should be very close to measured results for all degrees of freedom. On the first plot (upper left) there was presented the linear translation of object along x axis of the camera coordinate system. Vision based measurement indices that there was a translation about 6mm. It may be caused by camera mounting. On the second plot there was presented linear translation along y axis. In reality there was no translational motion along y but from vision system measurements one can see that maximum difference for y axis is about 9mm. Possible cause of this errors is nature of presents method. There is possible to try reduce the errors if better correspondence generation algorithm will be obtained. On third plot error for z axis is about 85mm, which is much more than for x and y axis. This is measured in direction perpendicular for image plane and it is distance from camera coordinate system and the object. It was expected that this error should be smaller. Next three plots presents rotations around three axes of object coordinate system. In ground truth measurements there were no

rotation about x and y axes. Four plot presents that there was a rotation about 3deg. On the fifth plot there is small error 3mm between both ground truth rotation and vision based measurement. In the case of rotation around z axis there was quite small error. After 5 second error is three times bigger than at the beginning. The peak at 34 second is caused by software because one frame was lost during simulation.

There results were as expected. It worth nothing that rotational errors were with negative sign. Translational errors were under ten millimeters for x and y axes and bigger for z axis.

Next, there was conducted second experiment. Object was moved but in other manner as in first experiment. The object was moved mainly along z axis, from position far too closer from camera.
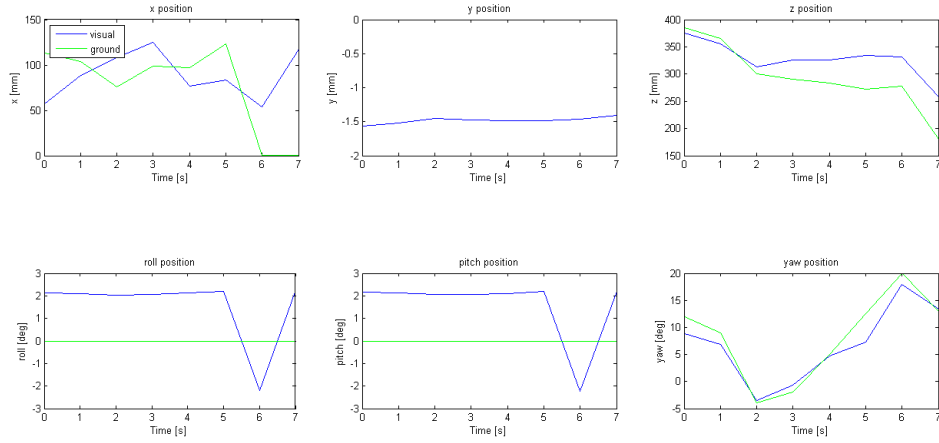
Figure 4. Tests results for second case.

Similar as in the first case there are presented six plots. First three presents linear translations along axes of camera coordinate system and three presents angular orientation of object. First plot presents linear translation along x axis. There is significant error between both measurements. At the end of simulation difference is about 100mm which is very big value. This is caused by mounting of camera. There were small motions caused by imperfectly camera to ground. On the second plot both lines green and blue are very close because object was constrained on y axis and could not pitch and yaw. On the next three plots there are presented measurements for angular orientation of object. For roll motion there is error about 2 degrees. Very similar results were obtained for pitch. For both vision based measurements there is a peak in 6 second. There is no cause of this error. The sixth plot presents yaw. In this case maximum error is about 5 mm.

The experiments take about 13ms per frame on modern CPU. It was shown that introduced method is able to run in real time. The camera bed should be more precisely screwed because it introduced serious problems. There were achieved good results. It is planned to still work on proposed method. Only for planar object results are presented.

5. Conclusions

This paper describes the results of analysis and testing of a pose estimation system intended for vision based navigation for satellites flying in formation. Presented technique of pose estimation is able to run in real-time. The presented method gives a good results and will be developed and implemented in the future research process for satellite flying when the mission need that one satellite approach to another. Offered method is more accuracy than other described methods. The promising results of numerical simulation have been obtained. Approach will be further evaluated and tested in the continued work. In this paper only first step of all system was presented. There is planned to still work on all system.

References

[1] B. Rosenhahn, „Foundations About 2D-3D Pose Estimation Problem".

[2] „Pose Determination and Tracking for Autonomous Satellite Capture," *Proceeding of the 6th International Symposium on Artificial Intelligence and Robotics & Automation in Space.*

[3] „Estimating pose of known target satellite," tom Vol. 36, nr No. 15, 2000.

[4] „Simulation of the Docking Phase for the SMART-OLEV Satellite Servicing Mission," *9th International Symposium on Artificial Intelligence, Robotics and Automation in Space (iSAIRAS).*

[5] P. Vincent, „3D Model-Based Tracking For Space Autonomous Randezvouz".

[6] K. Mikolajczyk, „Scale & Affine Invariant Interest Point Detectors," *International Journal of Computer Vision 60(1),,* pp. 63–86,, 2004.

[7] T. Petersen, „A Comparison of 2D-3D Pose Estimation Methods," Aalborg University , Ballerup, 2008.

The author gave a presentation of this paper during one of the conference sessions.

On the synchronization in power-grid models of Kuramoto-like oscillators
(STA156-15)

J.M.V. Grzybowski, E.E.N. Macau, T. Yoneyama

Abstract: In the context of power-grid models based on Kuramoto-like oscillators, synchronization is defined as the matching of the angular velocities of the oscillators, such that synchronized oscillators evolve most likely out of phase but with equal angular velocities. As such, coherence is usually measured by means of an order parameter in the interval [0,1], which is a function of synchronization quality and persistence over time. In this paper, we present analytical results on the critical coupling in networks of Kuramoto-like oscillators which allow us to evaluate them against an order parameter defined as the normalized sum of absolute values of phase deviations of the oscillators over time. The investigation of frequency synchronization over the subsets of the parameter space of the synchronization problem for power-grid models of Kuramoto-like oscillators is carried out, from which we conclude that the analytical results are rather tight and in good agreement with those observed in the numerical simulations.

1. Introduction

Power grids are large scale distributed dynamical systems whose functional structure resembles that of a living organism in the sense that a great number of subsystems work together and rely on each other to keep in motion a larger system that integrate, interconnect and make sense of them all at once. The coupled generating units have similar functions and are part of large network structures whose stability and robustness are closely related to the individual characteristics of the generators and consumers, to the characteristics of the couplings among them and to the topology of the network through which they are wired together [1][2]. Recent studies show that insights into the topology and dynamics of power-grids can be gained by means of theoretical studies that consider models of electrical generators coupled according to network structures that reproduce the topological and electrical interactions existing in real power-grids [3]-[12]. The transition from a synchronous state to a incoherent state, for example, can be studied from the viewpoint of complex networks of Kuramoto-like oscillators [13] by means of a formal analogy between the paradigm of Kuramoto oscillators and a transmission/distribution grid with generators and consumers. In this context, models that reproduce the dynamical and structural properties of power-grids can enhance and sharpen the identification of unnoticed mechanisms and properties that favor or disfavor stability and robustness characteristics of the in real power-grids.

The object of study here, the Kuramoto-like oscillator, was proposed as a formal analogy between electrical generators/loads and the celebrated Kuramoto model [3]. Since then, a number of studies considered the model to investigate synchronization and stability issues in power-grids [3][6], having concluded that the model retains important characteristics of the real system. It was recognized that the order parameter as formulated to study synchronization in the orignal Kuramoto paradigm is not suitable in the context of power-grid modeling, since in the latter case synchronization is defined somewhat differently, i.e., on the basis of quality and persistence of frequency matching among the oscillators.

In this paper, we consider the generator/machine model proposed in [3] and previous studies on the Kuramoto model [14] to develop analytical expressions for the critical coupling strength in networks of Kuramoto-like oscillators that model power grids. The analytical results are then evaluated against an order parameter based on the ideas on partial synchronization presented by Gómez-Gardeñes et al. [15]. The numerical results obtained by evaluating the order parameter over subsets of the synchronization problem are shown to be rather tight and in good agreement with those obtained from the analytical expressions. The paper is divided as follows: Section 2 presents the Kuramoto-like model with bimodal distribution and the measure of coherence based on those presented in [15]; Section 3 presents the results and Section 4 summarizes the paper and discusses the main points.

2. A model for synchronous electrical generators and loads

Consider a network of N oscillators with dynamics given by the Kuramoto-like model, proposed in [3], such that the equations of the jth oscillator can be written as

$$\dot{\theta}_j = \omega_j$$
$$\dot{\omega}_j = -\alpha\omega_j + P_j + P_{\max}\sum_{k=1}^{N} A_{jk}\sin\left(\theta_k - \theta_j\right) \tag{1}$$

where θ_j and ω_j are functions of time and denote the phase and frequency of the jth oscillator, $j = 1, 2, ..., N$, $\alpha > 0$ is a damping parameter related to the power dissipation by friction, P_j is the power delivered by ($P_j > 0$) or consumed by ($P_j < 0$) the jth node, $P_{\max}$ is the maximum capacity of the transmission line between two nodes and A_{jk} is the entry of the symmetric adjacency matrix A at row j and column k that is equal to one if nodes j and k are linked or to zero, otherwise. As one considers a network of coupled generators ($P_j > 0$ for all j), the synchronous state can be taken as $\omega_1(t) = \omega_2(t) = \cdots = \omega_N(t)$ which means that the frequencies of all the oscillators are matched. Now consider a more general situation in which generators ($P_j > 0$) and loads ($P_j < 0$) are

running counterclockwise and clockwise, respectively. Following [4], consider the condition $\dot{\omega}_j = 0, \omega_j = \omega_s, j = 1,...,N$ for some constant angular velocity ω_s, such that equation (1) becomes

$$0 = -\alpha\omega_s + P_j + P_{\max}\sum_{k=1}^{N} A_{jk}\sin(\Delta_{kj})$$ where $\Delta_{kj} = \theta_k - \theta_j$ is a constant. It was shown in [4] that the summation of N equations in this form for all j yields the synchronous speed $\omega_s = \sum P_j/\varepsilon N$. Note that for perfectly balanced generation/load condition in the power system the equality $\sum P_j = 0$ holds and yields $\omega_s = 0$.

In the context of power-grids, it is relevant to measure synchronization quality and persistence over time since deviations in angular velocities from the nominal value can give rise to instabilities. Further, being synchronization a global phenomenon in an interconnected power-grid the synchronization between any couple of oscillators in the network matters, regardless they are directly linked through a power line or not. Recall that all elements in an electrical circuit are electrically coupled to each other even if they do not belong to the same branch or even to neighboring branches. Finally, recall that, as long as the definition of synchronization given above is concerned, the synchronous angular frequency is not required to be constant, as to allow for time-varying generation/consumption $P_j(t)$. This allows the interconnected grid to slightly adjust is speed according to the generation/load balance condition to which it is subjected at any given time. This fact breaches an assumption commonly made in this kind of study.

It was shown in [4] that the lower bound to the existence of a synchronous manifold to coupled Kuramoto-like oscillators is given by $P_{\max}^* = \max_j\left\{\left|\alpha\omega_s - P_j\right|/d_j\right\}$ where $d_j = \sum_k A_{jk}$, $k = 1,...,N$, is the degree of node j. This indicates that the variance in the distribution of P_j has to be compensated with stronger coupling or increased connectivity. This can be also seen as one looks for the coupling strength c at the onset of synchronization for a fully connected network. Consider the deviation equations $\ddot{\theta}_i - \ddot{\theta}_j$ given by

$$\dot{\omega}_i - \dot{\omega}_j = -\alpha(\omega_i - \omega_j) + (P_i - P_j) + P_{\max}\left\{2\sin(\theta_j - \theta_i) + \sum_{k=1,k\neq i,j}^{N}\left(\sin(\theta_k - \theta_i) + \sin(\theta_j - \theta_k)\right)\right\} \quad (2)$$

and, following [14], calculate the maximum of equation

$$E = 2\sin(\theta_j - \theta_i) + \sum_{k=1,k\neq i,j}^{N}\left(\sin(\theta_k - \theta_i) + \sin(\theta_j - \theta_k)\right) \quad (3)$$

with respect to the phase angles $\theta_i, \theta_j, \theta_k$, then either $\theta_i = \theta_j$ or $2\theta_k = \theta_i + \theta_j$. In case $\theta_i = \theta_j$, there is power flow, and this case is not of interest. For $2\theta_k = \theta_i + \theta_j$ the function E given by equation (3) reaches a maximum and, following [14], the optimal solution $\left(\theta_j - \theta_i\right)_{opt}$ gives the maximum of E and allows the coupling P_{max} to be minimum reads

$$\left(\theta_j - \theta_i\right)_{opt} = 2\arccos\left(\frac{-(N-2)+\sqrt{(N-2)^2+32}}{8}\right) \tag{4}$$

such that

$$E_{max} = 2\sin\left(\theta_j - \theta_i\right)_{opt} + 2(N-2)\sin\left(\theta_j - \theta_i\right)_{opt} \tag{5}$$

The behavior of E_{max} as a function of the number of oscillators is depicted in Figure 1. Note that $E_{max} \to 8$ and $\left(\theta_j - \theta_i\right) \to \pi$ as $N \to \infty$. Regarding the numerical order parameter largely applied to evaluate the quality and persistence of coherent behavior, note that, a constant value of $\Delta\theta_{jk}(t) = c$ indicates that the phase difference between two oscillators is constant, which means that the frequencies are matched. In this case, the parameter equals one.

On its turn, time-varying $\Delta\theta_{jk}(t)$ indicates that frequencies are not matched, thus resulting in a non-negative value less than unity. As the phase differences $\Delta\theta(t)$ are computed for every pair of oscillators over the network in a matrix with entries $\Delta\theta_{jk}(t)$, the mean value can be regarded as a measure of the overall state of network synchronization and it gives the overall quality and persistence of synchronization. It follows that the level of coherence in the power-grid model can be accessed by means of an parameter r_f given as

$$r_f = \frac{1}{N(N-1)}\sum_{k=1}^{N}\sum_{\substack{j=1 \\ j\neq k}}^{N}\left(\left\|\lim_{\Delta t \to +\infty}\frac{1}{\Delta t}\int_{t_r}^{t_r+\Delta t}e^{i\left(\theta_j-\theta_k\right)}dt\right\|\right) \tag{6}$$

where $r_f \in [0,1]$, $r_f = 0$ for totally incoherent or intermittent states, $r_f = 1$ for perfectly matched angular velocities over time while intermediate values $r_f \in (0,1)$ depict levels of intermittent or partial synchronization. The order parameter (6) can be calculated within subsets of the plane coupling strength *vs.* variance and presented in the form of coherence maps in the parameter space, from which the behavior of synchronization in diverse network structures and parameter subsets can be studied.
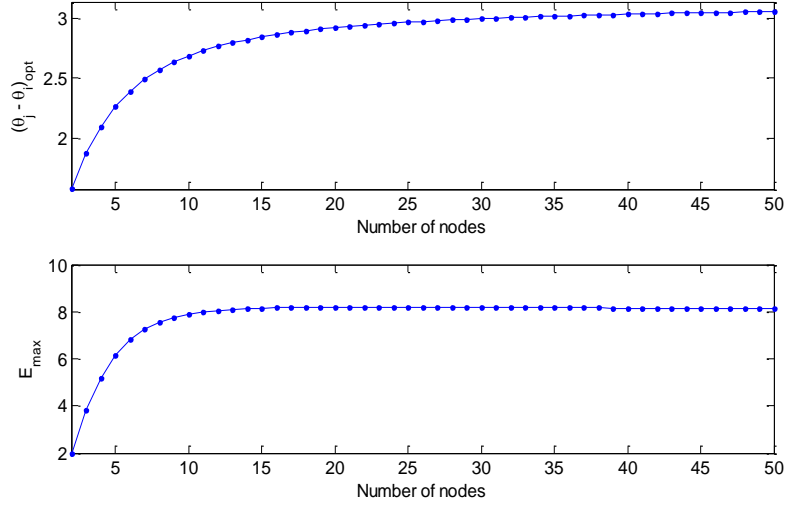
Figure 1. Evolution of the optimal phase difference $\left(\theta_j - \theta_i\right)_{opt}$ and of the term E_{max} as a function of the number of nodes N for a fully connected network. Note that $E_{max} \to 8$ and $\left(\theta_j - \theta_i\right) \to \pi$ as $N \to \infty$.
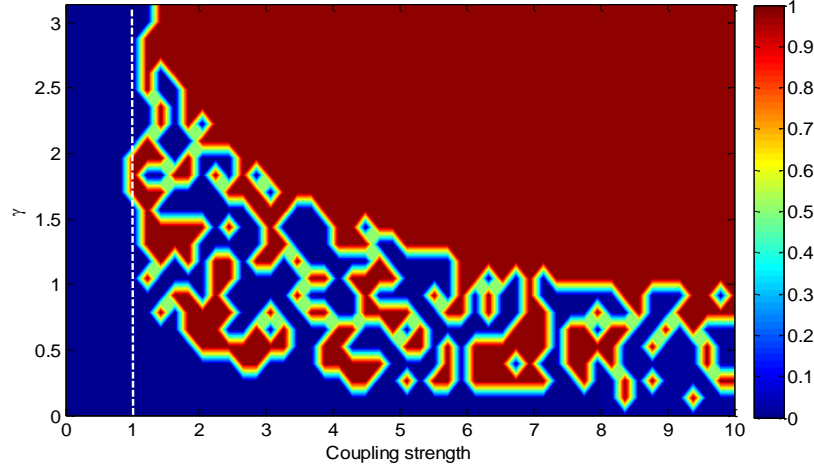
Figure 2. Density diagram for the order parameter as a function of coupling strength P_{max} and the arc length γ for a couple of mutually coupled Kuramoto-like oscillators with $P_1 = 1, P_2 = -1$ and initial conditions $\omega_1(0) = \omega_2(0) = 0$.
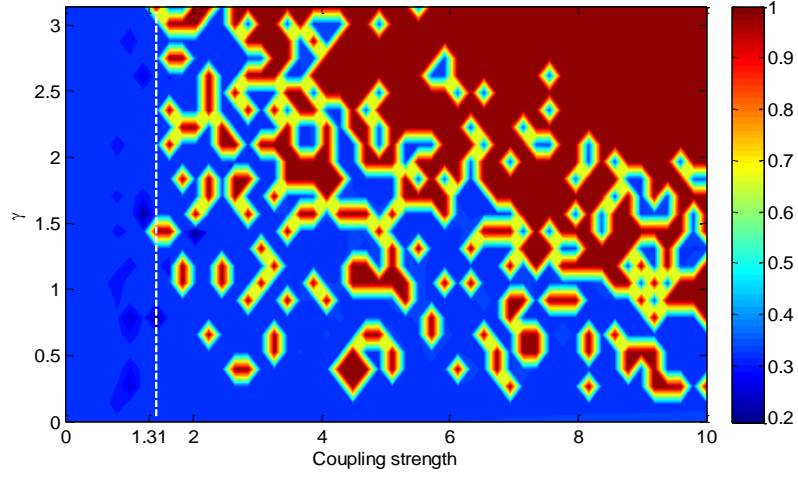
Figure 3. Density diagram for the order parameter as a function of coupling strength $P_{\max}$ and the arc length γ for three Kuramoto-like oscillators with consumer-generator-consumer coupling and $P_1 = -1, P_2 = 2, P_3 = -1$ for the initial conditions $\omega_1(0) = \omega_2(0) = \omega_3(0) = 0$.
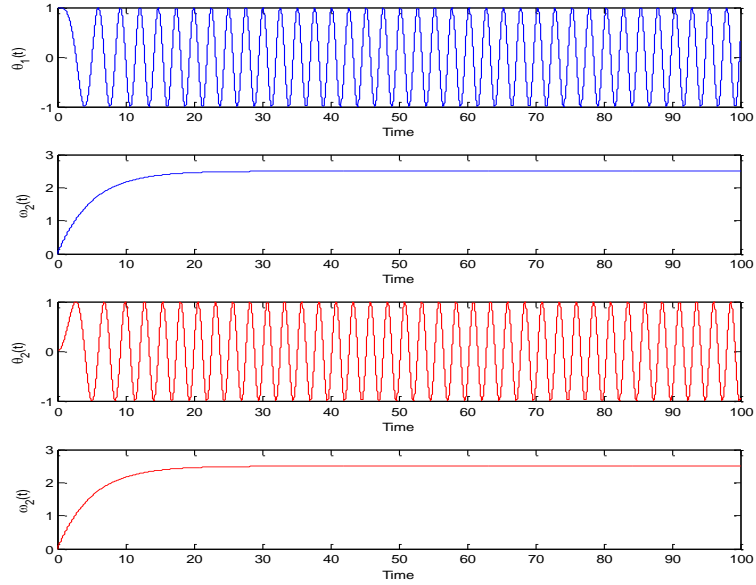
Figure 4. Time evolution of two mutually coupled Kuramoto-like oscillators with $c = 1.5, P_1 = 1, P_2 = -1$. The value of the coupling strength, obtained by means of equation (11), is the minimum for which synchronization between such oscillators can be maintained.

3. Results

As $\left(\theta_j - \theta_i\right) \to \left(\theta_j - \theta_i\right)_{opt}$ then $E \to E_{max}$. Let us consider equation (4) and admit $E = E_{max}$ for the purpose of finding P_{max} for the synchronization onset. Further, let us denote $\omega_i - \omega_j = \Delta\omega_{ij}$ and we obtain the linear ODE $\Delta\dot{\omega}_{ij} + \alpha\Delta\omega_{ij} = \left(P_i - P_j\right) + P_{max}E_{max}$ whose solution is given by

$$\Delta\omega_{ij} = \frac{P_i - P_j}{\alpha} + \frac{P_{max}E_{max}}{\alpha} + \omega_0 e^{-\alpha t} \tag{7}$$

for some arbitrary integration constant ω_0. As $t \to \infty$, the exponential term vanishes and one can rearrange the equation such that

$$P_{max} > \max \frac{\left|\alpha\Delta\omega_{ij} - \left(P_i - P_j\right)\right|}{E_{max}}, i, j = 1,...,N \tag{8}$$

Equation (8) gives a lower bound for the P_{max} required for synchronization. Considering P_i, P_j as constants, then we can approximate the value of P_{max} by evaluating the upper bound of the deviation in angular velocities, $\Delta\omega_{max}$. Consider that the angular velocity for a given oscillator will have a value in the interval $\left[\omega_{min}, \omega_{max}\right]$, where $\omega_{min} = \min\left(\omega_i\right)$, $\omega_{max} = \max\left(\omega_i\right)$, $i = 1,...,N$. Further, one can refine that interval by observing that for weak coupling each oscillator will rotate with angular speed corresponding to its natural frequency as $t \to \infty$, that is, $\omega_i = P_i/\alpha$. On the other hand, for strong coupling and $t \to \infty$, $\omega_i = \omega_s = \sum_i P_i \big/ \alpha N$ such that one obtains

$$\Delta\omega_{max} = \max_i \left|\frac{\sum_i P_i - NP_i}{\alpha N}\right| \tag{9}$$

from which the value of P_{max} from equation (8) can be estimated for a given network of coupled generators/consumers. Note that as ω_i, ω_j eventually evolve to the same value, equation (2) becomes

$$0 = \left(P_i - P_j\right) + c\left\{2\sin\left(\theta_j - \theta_i\right) + \sum_{k=1, k\neq i, j}^{N} \left(\sin\left(\theta_k - \theta_i\right) + \sin\left(\theta_j - \theta_k\right)\right)\right\} \tag{10}$$

and we find $P_{max} > \left|\left(P_i - P_j\right)\right|\big/E_{max}$ which is the value below which synchronization between nodes i and j cannot be maintained. Further, if the injected/consumed power $P_k, k = 1, 2,...,N$ belongs to a compact set [14], then

$$P_{\max} > \frac{P_{\max} - P_{\min}}{E_{\max}} \qquad (11)$$

is the minimum coupling gain that allows synchronization to be maintained. In the following, we compare the results derived in this section to those of numerical simulations. The integration was performed using the 4th order Runge-Kutta algorithm and $h = 5 \times 10^{-4}$ as time step.

In Figure 2 and Figure 3, we explore the behavior of the order parameter as the oscillators are subjected to different initial conditions on the angle. Towards this end, we define γ as the length of the shortest arc in the cycle that covers the geodesic distance between any two initial condition angles of the oscillators. Thus, for example, if $\theta_1(0) = \pi/4, \theta_2(0) = \pi/3, \theta_3(0) = \pi/2$, then the shortest arc lies in a clockwise subtraction, $\gamma = \pi/2 - \pi/4 = \pi/4$. The conditions under which the simulations were performed are informed in the figure captions. The numerical simulation shown in Figure 4 illustrates this result in a network of mutually coupled Kuramoto-like oscillators, for $P_{\max} = 1.5$, $\alpha = 0.2$, $P_1 = 2, P_2 = -1$ and initial conditions corresponding to $\left(\theta_j - \theta_i\right)_{opt}$ and $\omega_k = 0, k = 1, 2, ..., N$. Note that this is the critical coupling value given by equation (11) for the maintenance of synchronization in the case when all the frequencies are matched. As $\Delta\omega(0) = 0$ the reasoning behind equation (11) holds and the oscillators remain synchronized over time, as shown in Figure 4. On the other hand, diverse numerical simulations for $P_{\max}$ below that threshold showed that synchronization is lost as $t \to \infty$, which is also the case when $P_{\max} = 1.5$ and $\Delta\omega \approx 0$. Now, for the same setup, as we consider equation (8) and notice that $P_1/\alpha = 10, P_2/\alpha = -5$, then it follows that $\omega_s = 2.5$ and from (8) and (9) one obtains $P_{\max} > 2.25$. As it can be observed from the numerical simulations in Figure 2 and Figure 3, all the values observed in the numerical simulations are in agreement with those obtained by means of the analytical expressions (8) and (11). As one considers larger networks of oscillators that are not fully-connected (which breaches the assumption made for the calculation of $E_{\max}$, it was observed that the value of the critical $P_{\max}$ increases relatively to the value estimated by the expressions (8) and (11). This case will be further investigated and treated separately somewhere else.

4. Final remarks

This work investigated a couple analytical expressions to determine the critical coupling for networks of Kuramoto-like oscillators. Rather than assuming that the oscillators are currently synchronized in order to derive an expression for the critical coupling, we simply

observe that their angular velocities shall lie within a compact set with known boundaries. The theoretical expressions were evaluated along with an order parameter for synchronization quality and persistence in power-grid models. The parameter follows the general idea of the order parameter from the Kuramoto model, except for it considers some of the specificities of power-grid models such as the existence of two types of nodes, i.e., generators and loads, and a definition of synchronization based on matching the values of angular velocities. The parameter allows the investigation of stability over the parameter space of power-grid models. Further insights can be gained from the exploration of the relations between coherence and the parameters from the model and the coupling network. The numerical simulations were used to validate the theoretical development and it was observed that for small networks the behavior of the critical coupling determined in the analytical expressions closely matches those obtained through numerical simulations for small networks. On the other hand, it was observed in preliminary studies that this matching is not so tight for larger networks. As shown along the reasoning and examples, this approach is a suitable tool for the study of synchronization in power-grid models of Kuramoto-like oscillators and it can hopefully help enhance the comprehension of real features of power-grid dynamics.

References

[1] Rosas-Casals, M., Valverde, S., Sole, R.V. Topological vulnerability of the European power grid under errors and attacks. Int. J. Bifurcation Chaos 17 (2007), 2465-2475.

[2] Arenas, A. et al. Synchronization in complex networks. Phys. Rep. 469 (2008), 93–153.

[3] G. Filatrella, A.H. Nielsen, N.F. Pedersen. Analysis of a power grid using a Kuramoto-like model. Eur. Phys. J. B 61 (2008) 485-491.

[4] R. Carareto, M.S. Baptista, C. Grebogi. Natural synchronization in power-grids with anti-correlated units. Commun. Nonlinear Sci. Numer. Simulat. 18 (2013) 1035-1046.

[5] P. Crucitti, V. Latora, M. Marchiori. A topological analysis of the Italian electric power grid. Physica A 338 (2004) 92-97.

[6] L. Fortuna, M. Frasca, A.S. Fiore. Analysis of the Italian power grid based on Kuramoto-like model. Physcon 2011, León, Spain, September 5-8, 2008.

[7] P. Cruciti, V. Latora, M. Marchiori. Model for cascading failures in complex networks. Phis. Rev. E 69, 045104, 2004.

[8] P. Cruciti, V. Latora, M. Marchiori, A. Rapisarda. Error and attack tolerance of complex networks. Physica A 340, 388-394, 2004.

[9] A.E. Motter, S.A. Myers, M. Anghel, T. Nishikawa. Spontaneous synchrony in power-grid networks. Nature physics, 191-197, 2013.

[10] Rosas-Caldas, M., Cominas-Murtra, B. Assessing European Power grid reliability by means of topological measures. Transactions on Ecology and the Environment, Vol. 121, p. 515-525 (2009) (Energy and Sustainability International Conference, Bolonia, Italy).

[11] Solé, R.V., Rosas-Casals, M., Corominas-Murtra, B., Valverde, S. Robustness of the European power grids under intentional attack. Physical Review E 77 (2008) 026102.

[12] Hines, P., Blumsack, S., Sanchez, E.C., Barrows, C. The topological and electrical structure of power grids. 43rd Hawaii International Conference on System Sciences (HICSS), 5-8 Jan, 2010.

[13] Filatrella, G.; Nielsen, A.H.; Pedersen, N.F. Analysis of a power grid using a Kuramoto-like model. Eur. Phys. J. B 61 (2008) 485-491.

[14] N. Chopra, M.W. Spong. On synchronization of Kuramoto oscillators. Proceedings of the 44th IEEE Conference on Decision and Control and the European Control Conference, Seville, Spain, December 12-15, 2005.

[15] J. Gómez-Gardeñes, Y. Moreno, A. Arenas. Paths to synchronization on complex networks. Physical Review Letters 98, 034101, 2007.

José Mario Vicensi Grzybowski, Ph.D.: Universidade Federal da Fronteira Sul, UFFS, Rodovia RS 135 km 72, Erechim, RS, 99.700-000, Brazil (jose.grzybowski@uffs.edu.br).

Elbert Einstein Nehrer Macau, Ph.D.: National Institute for Space Research, INPE, Av. dos Astronautas, 1758, Jd. Granja, São José dos Campos, SP, 12.227-010, Brazil. (elbert.macau@inpe.br). The author gave a presentation of this paper during one of the conference sessions.

Takashi Yoneyama, Ph.D.: Technological Institute of Aeronautics, ITA, Pca. Marechal Eduardo Gomes, 50, Vila das Acacias, São José dos Campos, SP, 12.228-900, Brazil (takashi@ita.br).

Dynamical load of welds after micro-jet cooling
(STA265-15)

Damian Hadryś

Abstract: Goal of that paper is new welding method on example welding of one grade of steel (ferritic steel). The joining of steel elements by welding is very popular [1-7]. The main reason of paper was investigate about possibilities of achieve a very high plastic properties of welds for particular conditions of maintenance of welded steel constructions. Steel construction needs to present high plastic properties to support dynamic load (impact conditions). A way to improve of plastic properties of welds, especially for impact loads is welding with micro-jet cooling. It is a new method of welding. In this method the microstructure of weld presents the high content of acicular ferrite (AF) in weld metal deposit (WMD). It is a guarantee of high values for the plastic properties [8, 9]. Micro-jet cooling is an innovative method of forced cooling immediately after welding. In this paper the number of micro stream of the cooling gas influence is presented in order to obtain high impact resistance.

1. Introduction

Micro-jet cooling is an innovative method of forced cooling. This method of cooling could be used to cooling of weld area immediately after welding procedure. Micro-jet cooling allows to decrease of heat transfer to material of welded elements. Main goal of this method is fact of obtain high AF amount in WMD. This fact corresponds with high mechanical properties of welds. Welding with micro-jet cooling allows to obtain welds with better mechanical properties in comparison to ordinary welding method [10, 11]. The percentage of AF, and consequently the plastic properties of the weld can be controlled by several variables: type of gas, the number of micro-streams, and distance between device and weld sample, among others.

In standard Metal Inert Gas welding process (MIG) were usually gettable higher amounts of grain boundary ferrite (GBF) and site plate ferrite (SPF) fraction. In welding with micro-jet cooling both structures (GBF and SPF) were not dominant. During cooling of weld time of GBF and SPF formation has been reduced. Because of weld cooling it is too short time to formation great amount of GBF and SPF. This allowed to reduce amount GBF and SPF with increase the amount of ferrite AF in WMD.

A simplified method to analyze the behaviour of welded components under impact load is the coefficient of restitution. This coefficient describes the absorption of impact energy by the structure.

Moreover, it can describe, which part of impact energy is recovered during the return (second phase of impact), i.e. which part of impact energy is transformed to plastic strain or it is returned to elastic strain. Coefficient of restitution R was introduced by Newton. For full plastic impact R=0, and for full elastic impact R=1. During real impact it is obtained an elastic-plastic mixed behaviour, when $0 < R < 1$ [12].

Coefficient of restitution is used to impact analysis. It strongly depends on relative impact velocity. When velocity after impact is smaller than velocity before impact it means that decrease of kinetic energy of system. This variation in kinetic energy is related with irreversible plastic deformation, heat and vibrations [13, 14].

2. Experimental procedure

Coefficient of restitution R, can be determined by different methods. One of ways to restitution coefficient calculation is experimental procedure. During the experimental method, in order to obtain several impact energies four pendulum heights and two different mass are used to calculate the coefficient of restitution (equations 1 to 4).

$$M = \frac{m_2}{m_1} \tag{1}$$

$$\lim_{m_2 \to \infty} M = \lim_{m_2 \to \infty} \frac{m_2}{m_1} = \infty \tag{2}$$

$$R = \frac{1}{M} + \frac{1+M}{M}\sqrt{\frac{h_2}{h_1}} \tag{3}$$

$$\lim_{M \to \infty} R = \lim_{M \to \infty} \frac{1}{M} + \frac{1+M}{M}\sqrt{\frac{h_2}{h_1}} = \sqrt{\frac{h_2}{h_1}} \tag{3}$$

where:

m_1 – mass of pendulum [kg],

m_2 – mass of specimen + mass of test stand + mass of foundation [kg],

h_1 – height of pendulum drop [m],

h_2 – height of pendulum reflect [m].

Test stand (Fig. 1), specimens and impact conditions was selected before the investigation. The test procedure have been carried out on single-blow impact testing machine with modified pendulum. It was used a test stand mass of 700 kg and a pendulum of 20 kg. Test stand has been fixed to the base (foundation), i.e. $m_2 \rightarrow \infty$. For all data two height have been registered: height of pendulum drop (h1) and height of pendulum reflect (h_2).
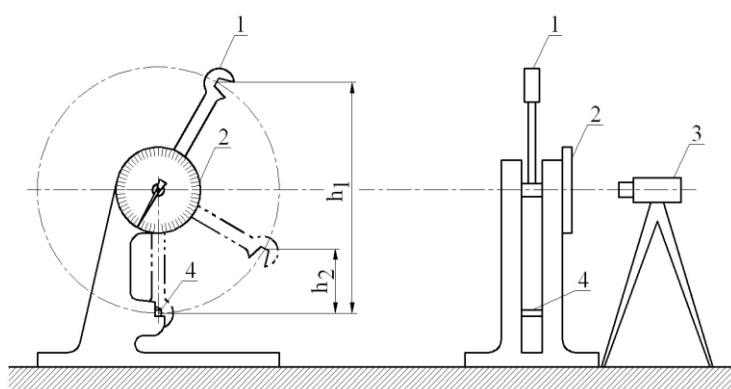
Figure 1.   Detail of experimental procedure:

1 – pendulum, 2 and 3 – registration device, 4 – specimen.

During the test procedure, the pendulum has been dropped from height h_1, and the specimen was deformed due the impact energy, while the pendulum return to height h_2. Impact energy and pendulum velocity values used during tests are presented in table 1. The Figure 2 shows the permanent angle measured in order to evaluate the plastic strain after the impact. During the test, the specimen was supported at the ends, and the impact force was positioned in the middle length of the specimen.

Table 1. Impact conditions during experimental procedure.

Pendulum height h_1 [m]	Impact energy [J]	Impact velocity [m/s]
1.61	315.9	5.6 m/s
1.56	306.1	5.5 m/s
1.41	276.6	5.3 m/s
1.22	239.4	4.9 m/s
0.91	178.5	4.2 m/s
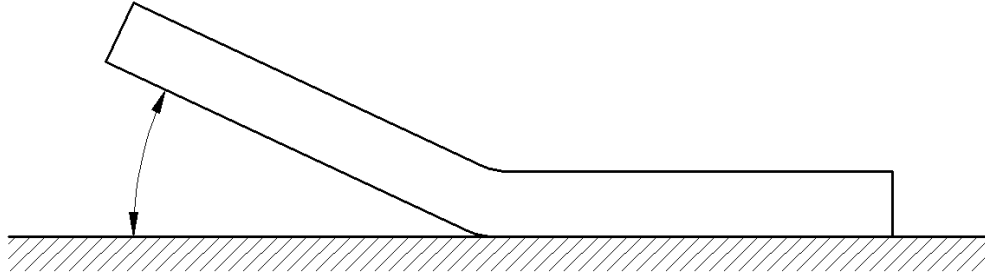
Figure 2. Detail of angle measure to evaluate the plastic deformation.

3. Specimens

Specimens have been made with S235JR steel. This is a grade of steel on steel constructions. It is one of the most popular steel grade. Chemical and mechanical properties of this steel it is presented in next tables (Table 2 and Table 3). Five types of specimens were used in this work:

- specimens without weld,
- specimens welded with traditional MIG method (without micro-jet cooling),
- specimens welded with MIG method, but using micro-jet cooling with one micro stream jet,
- specimens welded with MIG method, but using micro-jet cooling with two micro stream jets,
- specimens welded with MIG method, but using micro-jet cooling with three micro stream jets.

Table 2. Chemical composition of used steel.

Chemical element	Content [%]
C	0.17
S	0.035
P	0.035
Si	0.10 - 0.35
Mn	1.40
Cu	0.55
Ni	0.12

Table 3. Mechanical properties of used steel.

Property	Value
Yield stress	235 MPa
Tensile strength	380 - 520 MPa
Elongation, A_{50}	16 %

Figure 3 shows welded specimens used in investigations and Figure 4 shows arrangement of micro stream jets. Welding of specimens was done with micro-jet cooling, with argon as micro-jet cooling gas. The main data about parameters of welding process were shown in table 4. Apparatus for MIG welding with micro-jet cooling is presented in figure 5.
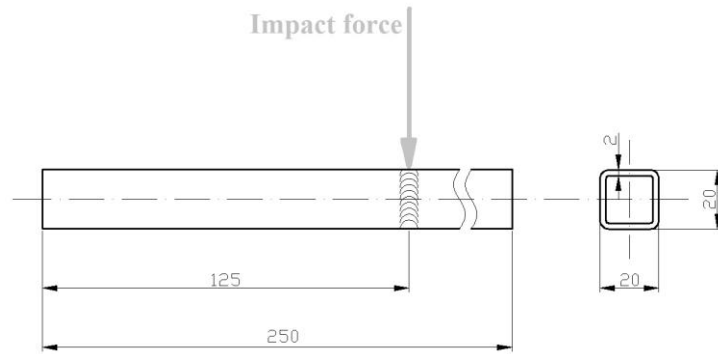
Figure 3. Dimensions of the specimen.
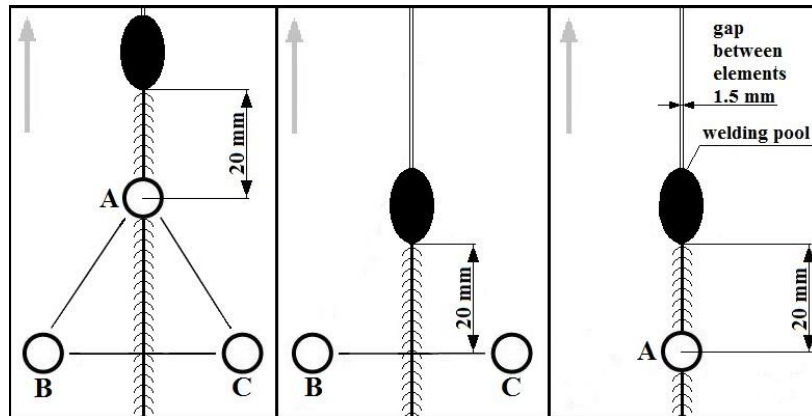
Figure 4. Localization of the micro-jet cooling stream jets (3 cases); the grey arrows indicate the movement direction

245

Table 4. Parameters of welding process

Parameter	Value
Diameter of wire	1.2 mm
Electrode classification	G2Si1 / ER70S-3
Standard current	220 A
Voltage	24 V
Shielding welding gas	Ar
Micro-jet cooling gas	Ar
Micro-jet cooling gas pressure	0.4 MPa
Diameter of micro-jet cooling stream	40 μm
Number of tested micro-jet cooling stream	1 (A) 2 (B + C) 3 (A + B + C) Situated in equilateral triangle with sides 6 mm (Fig. 4).
Weld geometry	butt weld, gap 1.2 mm
Welding position	PA
Number of passes	1
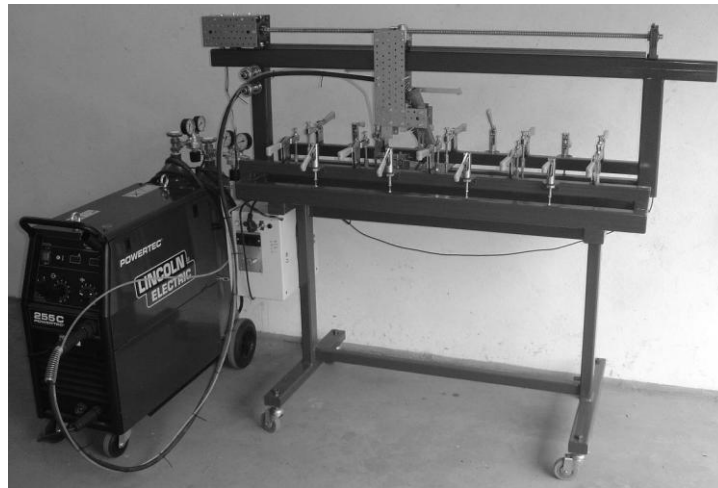
Figure 5. Apparatus for welding with micro-jet injector.

All tested welding processes were chosen with micro-jet cooling conditions which are presented in figure 6. It was possible to get precisely weld cooling conditions especially in range 800-500° C.
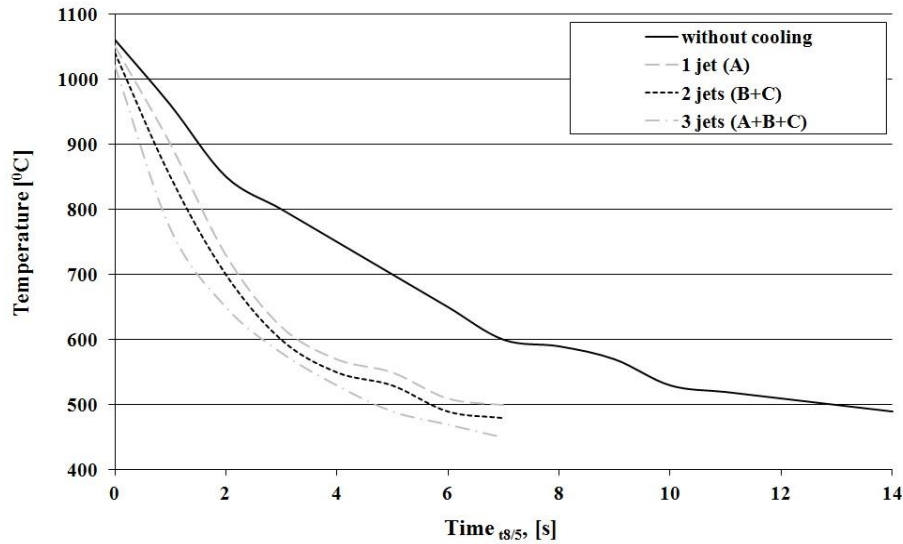
Figure 6. Changes of weld temperature during welding with and without micro-jet cooling.

4. Results and discussion

There were tested and compared various welds were made with ordinary MIG method and with welding with micro-jet cooling. Welding with micro-jet cooling technology were done with different number of micro-jet cooling stream jets. The computations have been carried out with five level impact energy/velocity. The results are the average of five tests.

Figure 7 shows the evaluation of the restitution coefficient in function of the impact energy for five kind of specimens. The value of restitution coefficient has decreased when the impact energy has increased. This results does not depend on the type of specimen. Specimens without weld have had the largest values of restitution coefficient. The smallest value of restitution coefficient has been reached for specimens welded without micro-jet cooling.

Furthermore, it could be observed that the number of micro-jet cooling stream positively influence the results of impact test. Higher number of micro-jet cooling streams allow to obtain a higher value of restitution coefficient. However, this influence is not very significant.

Figure 8 shows the evolution of the plastic strain in function of the impact energy. It was observed that the plastic strain increased when the impact energy is growing. Specimens without weld present the smallest plastic strain. Higher plastic strain has been reached for specimens welded with traditional MIG method (without micro-jet cooling system). Moreover, it was observed that the micro-jet system has positive influence on plastic strain.

247
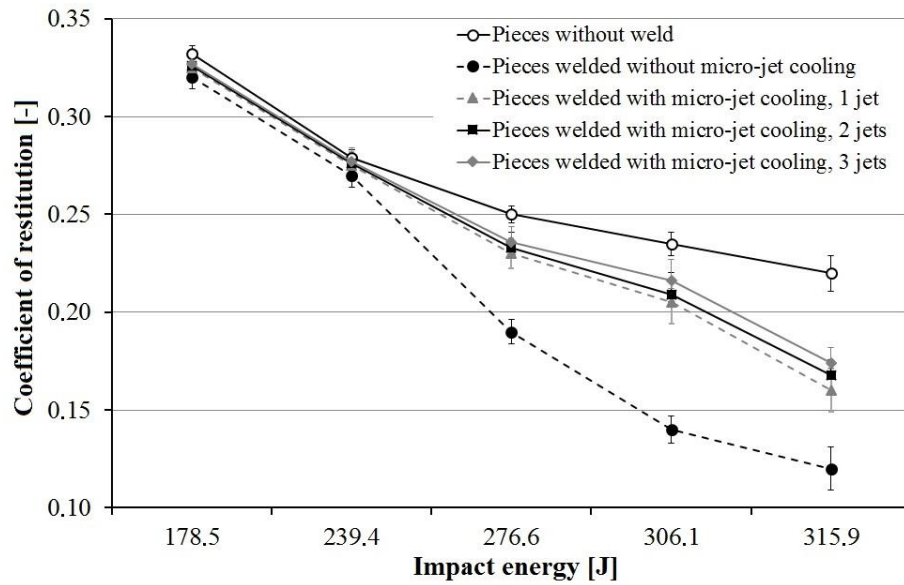
Figure 7. Evaluation of the coefficient of restitution in function of the impact energy.
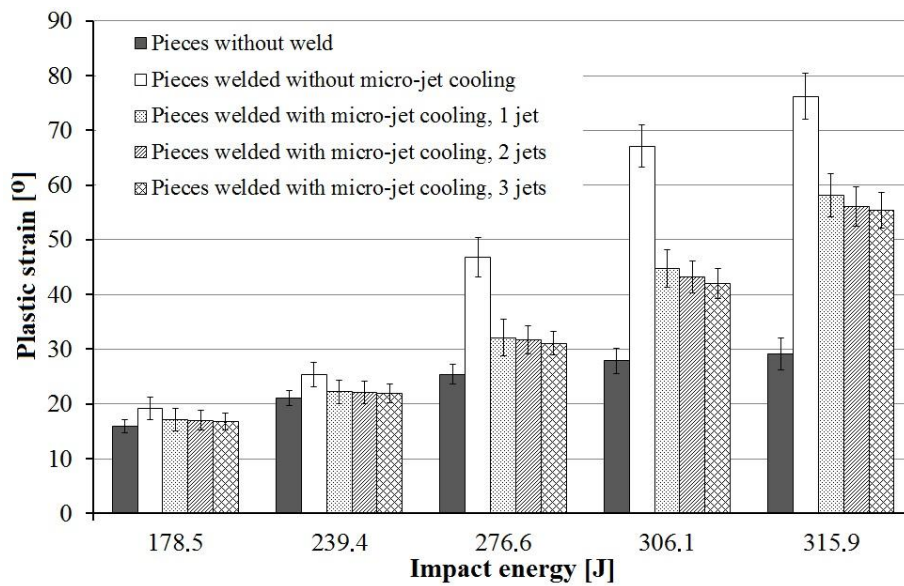
Figure 8. Evaluation of the plastic deformation after impact.

For lower impact energy, 178.5 J and 239.4 J, the results were very similar for all kind of specimens. But for impacts with higher energy, 276.6 J, 306.1 J and 315.9 J, cracks were observed for specimens welded without micro-jet cooling. For specimens welded with micro-jet cooling, were not observed any cracks or fissures. Also the increase of the number of micro-jet cooling stream positively influence the results. Moreover, this effect is positive, but the influence is not significant. Reduction of plastic strain is a desirable property of micro-jet cooling application for welding.

5. Conclusions

Coefficient of restitution for welded specimens with different levels of impact energy were used. It was observed that the value of restitution coefficient decreased when the impact energy increased. Minimum values of restitution coefficient has been reached for specimens welded without micro-jet cooling system.

Poor values of the plastic strain are presented by the specimens without weld. The highest plastic strain has been reached for specimens welded with traditional MIG method, without micro-jet cooling. The presence of the weld has adversely affected the plastic properties of the material element. Plastic properties of the weld in this case are not good. The reason for this is the appearance of the weld and HAZ. It is observed that the use of micro-jet welding influences positively on the plastic strain.

This innovative welding process using the micro-jet cooling and shows good results related with the welding plastic properties. On the basis of this investigation it is possible concluded that:

- micro-jet cooling could be treated as an important element of MIG welding process,
- micro-jet technology in welding could improve plastic properties in the welds,
- argon could be treated as a micro-jet gas in welding process,
- a great number of streams of the micro-jet cooling has positively influence in the welding process, i.e, increasing the number of micro-jet streams promotes the cooling intensity, and consequently it is reduced the plastic strain of the weld.

Further research of welding is needed, especially for other materials, for other elements geometry and others applications (exposure to vibration, impact energy absorption, maintenance of construction at low temperature).

6. References

[1]   Adamiec J., Grabowski A., A. Lisiecki A. *Joining of an Ni-Al alloy by means of laser beam welding,* Proc. SPIE 5229, Laser Technology VII: Applications of Lasers, 2003.

[2]   Lisiecki A. *Welding of titanium alloy by Disk laser*, Proc. of SPIE Vol. 8703, Laser Technology 2012: Applications of Lasers, 2013.

[3]   Lisiecki A. *Diode laser welding of high yield steel*, Proc. of SPIE Vol. 8703, Laser Technology 2012: Applications of Lasers, 2013.

[4]   Hadryś D., Miros M., Węgrzyn T., Pereira da Silva A. *Driver safety in relation to the post-accident vehicle reparation*, Transport Problems, 7(4)/2012.

[5]   Ślązak B., Słania J., Węgrzyn T., Pereira da Silva A. *Process Stability Evaluation of Manual Metal Arc Welding Using Digital Signals*, Materials Science Forum, 2013.

[6]   Węgrzyn T., Hadryś D., Miros M. *Optimization of Operational Properties of Steel Welded Structures*, Maintenance and Reliability, 3/2010.

[7]   Węgrzyn T., Miros M., Hadryś D., Pereira da Silva A. *Truck frame welding reparations by steel covered electrodes with varied amount of Ni and Mo*, Transport Problems, 5(4)/2010.

[8]   Golański G., Słania J. *Effect of different heat treatments on microstructure and mechanical properties of the martensitic GX12CrMoVNbN91 cast steel*, Metallurgy and Materials, 4/2010.

[9]   Węgrzyn T., Mirosławski J., Pereira da Silva A., Pinto D., Miros M. *Oxide inclusions in steel welds of car body*, Materials Science Forum, 2010.

[10] Wegrzyn T., Piwnik J. *Low alloy welding with micro-jet cooling*, Archives of Metallurgy and Materials, 2(57)/2012.

[11] Wegrzyn T., Piwnik J., Baranowski P., Pereira da Silva A., Plata M. *Micro-jet welding for low oxygen process*, ICEUBI 2011, International Conference Innovation and Development, Covilha, Portugal, 2011.

[12] Hadryś D., Miros M. *Coefficient of restitution of model repaired car body parts*, Journal of Achievements in Material and Manufacturing Engineering, 28(1)/2008.

[13] Burdzik R., Konieczny Ł. *Research on structure, propagation and exposure to general vibration in passenger car for different damping parameters*, Journal of Vibroengineering 15 (4)/2013.

[14] Konieczny Ł., Burdzik R., Łazarz B. *Application of the vibration test in the evaluation of the technical condition of shock absorbers built into the vehicle*, Journal of Vibroengineering 15 (4)/2013.

Damian Hadryś, Ph.D. Eng.: Higher School of Labour Safety Management in Katowice, Department of Technical Sciences, 8 Bankowa Street, 40-007 Katowice, Poland (*dhadrys@wszop.edu.pl*). The author will prepare poster.

Vibro-impact dynamics of two rolling heavy disks along rotate circle with constant angular velocity
(BIF125-15)

Katica R. (Stevanović) Hedrih

Abstract: Under the authors' use Petrović's elements of mathematical phenomenology, especially mathematical analogy between kinetic parameters of central collision of two bodies in translator motions and central collision of two rolling different disks, new original expressions of two outgoing angular velocities for each of rolling disks after collision are defined in author previous papers. Using this new and original result of vibro-impact dynamics of two rolling heavy different disks on the rotating circle trace in vertical plane in period of series of collisions is investigated. Use series of the elliptic integrals, new nonlinear equations for obtaining angles of disks positions at positions of collisions are defined. Phase trajectories of the disks in vibro-impact dynamics are theoretically presented. Two cases of vibro-impact dynamics when phase portraits contain trigger of coupled singularities and homoclinic orbit in the form of number "eight" as well as in the case without that trigger of coupled singularities are discussed. Phase trajectory branches of both rolling disks in period from initial positions to first collision between rolling disks are presented..

1. Introduction

Non-linear differential equations of non-linear dynamics of a rolling heavy disk along rotate circle, with constant angular velocity, about axis in three different positions are derived and presented in author's Reference [1]. From comparison between these three nonlinear differential equations, some conclusions of nonlinear dynamics of rolling heavy disk along rotate circle with constant angular velocity about different axis in three different positions are pointed out. For two cases, first that axis of the circle rotation is vertical and central and second that axis is vertical and eccentrically, corresponding equations of phase trajectory portraits depending of kinetic parameters of the system, are obtained. Existence of trigger of coupled singularities [2-7] and homoclinic orbit in the form of number "eight" depending on system kinetic parameters and appearance of the bifurcation of relative equilibrium positions are investigated. For the case that axis of the circle rotation is vertical and central, functional dependence between angle of disk relative arbitrary position on rotate circle and duration of time are derived [1]. For obtaining this solution, an elliptic integral [8] is derived. For solving elliptic integral, a transformation is introduced and functions under the elliptic integral are developed in three series along angle of disk relative arbitrary position on rotate circle [1]. By use obtained functional dependence between time of disk rolling and angle of disk relative position,

discussion of different period duration of rolling disk oscillations along rotate circle trace about vertical central axis is done depending of initial conditions and constant angular velocity of the circle rotation.

2. Non-linear differential equation of a rolling heavy disk motion along rotate circle in vertical plane about vertical central axis

In Figure 1, a model of the heavy homogeneous rolling disk, with radius r and mass M, and axial mass inertia moment for centram axis $\mathbf{J}_C = \frac{1}{2}Mr^2$, along rotate a circle trace, with radius R, which rotate with constant angular velocity Ω about central vertical axis, in vertical plane is presented. Taking into account that: $\mathbf{J}_{\mathbf{P},rel} = \frac{3Mr^2}{2}$ is axial mass inertia moment of the disk for the momentary axis of disk relative rotation-rolling along rotate circle, $\omega_{P,rel} = \left(\frac{R-r}{r}\right)^2 \dot{\varphi}^2$ is angular velocity of relative rotation-rolling along rotate circle, then partial non-linear differential equation of the heavy rolling disk along rotate circle with constant angular velocity $\dot{\vartheta} = \Omega = constat$ about central vertical axis is in the following form (for details see Reference [1]):

$$\ddot{\varphi} + \Omega^2 \left\langle \frac{g}{\left(\frac{\mathbf{i}_{C,rel}^2}{r^2}+1\right)(R-r)\Omega^2} - \frac{1}{\left(\frac{\mathbf{i}_{C,rel}^2}{r^2}+1\right)}\cos\varphi \right\rangle \sin\varphi = 0 \tag{1}$$

or $$\ddot{\varphi} + \frac{\Omega^2}{\kappa}\langle \lambda - \cos\varphi \rangle \sin\varphi = 0 \tag{2}$$
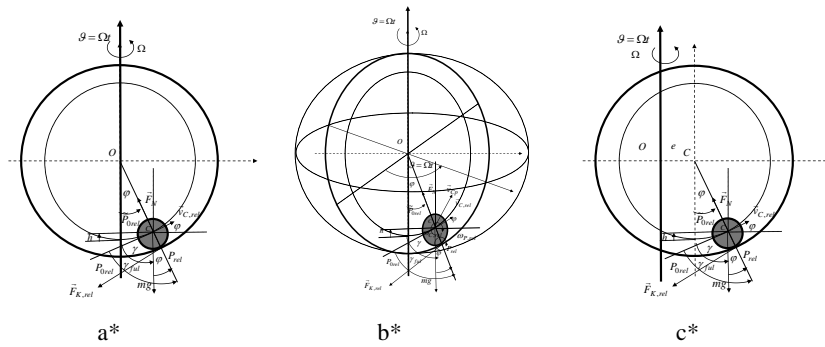
Figure 1. The rolling heavy disk along rotate circle line, with constant angular velocity, in vertical plane: a* and b* Plan of forces and velocities for the central axis of circle rotation; c* Plan of forces and velocities for the eccentrically axis of circle rotation.

where the following denotations are introduced: $\dfrac{\mathbf{J}_{\mathbf{P},rel}}{M} = \mathbf{i}_{\mathbf{P},rel}^2 = \mathbf{i}_{C,rel}^2 + r^2$, $\mathbf{i}_{\mathbf{P},rel}^2 = \dfrac{\mathbf{J}_{\mathbf{P},rel}}{M}$ for radius of axial

mass inertia moment, $\kappa = \left(\dfrac{\mathbf{i}_{C,rel}^2}{r^2} + 1 \right)$ for coefficient of the disk rolling, $\ell_{red} = \left(\dfrac{\mathbf{i}_{C,rel}^2}{r^2} + 1 \right)(R - r)$ for

reduced length of the corresponding rolling pendulum and $\lambda = \dfrac{g}{(R-r)\Omega^2}$. In comparison between

obtained nonlinear differential equation (1) for considered case of rheonomic and relative nonlinear dynamics of a heavy thin rolling disk alog rotate circle with constant angular velocity $\dot{\vartheta} = \Omega = constat$ about central vertical axis and corresponding nonlinear differential equation of a heavy mass particle moving along a rotate circle curvilinear trace in vertical plane about central axis (see References [4, 18]) it is easy to identifies a mathematical analogy (see Reference [20-23]). Analogous kinetic parameters between dynamics of these systems are: for system with disk

$\lambda = \dfrac{g}{(R-r)\Omega^2}$ and for analogous system with mass particle $\lambda = \dfrac{g}{R\Omega^2}$; and for system with disk $\dfrac{\Omega^2}{\kappa}$

and for analogous system with mass particle Ω^2.

As details about singularities and stationary points of nonlinear differential equation (1) or (2) are known from published classical literature [4, 18, 19], then, there these results are listed: 1* for the case that $\lambda > 1$, then, one set of singularities $\varphi_s = s\pi$, $s = 0, \pm 1, \pm 2, \pm 3, ...$ exists, and these singularities are alternatively stable and unstable, starting by stable singular point in zero point $\varphi_0 = 0$, and next $\varphi_{s=2k} = 2k\pi$, $k = \pm 1, \pm 2, \pm 3, ...$ as a type stable center, and next unstable saddle type singular point in $\varphi_1 = \pi$ and next $\varphi_{s=2k+1} = (2k+1)\pi$, $k = \pm 1, \pm 2, \pm 3, ...$; and 2* for the case that $\lambda < 1$, then two sets of singularities exist; first set consists of singular points $\varphi_s = s\pi$, $s = 0, \pm 1, \pm 2, \pm 3, ...$ which are all unstable, saddle type and second set consists of singular points $\varphi_s = \pm \arccos \lambda + 2s\pi$ $s = 0, \pm 1, \pm 2, \pm 3, ...$, all stable, center type. Two singular points of stable centre type, in pair, from second set $\varphi_s = \pm \arccos \lambda + 2s\pi$ $s = 0, \pm 1, \pm 2, \pm 3, ...$ and one unstable saddle type singular point $\varphi_{s=2k} = 2k\pi$, $k = 0, \pm 1, \pm 2, \pm 3, ...$ from first set build series of subsets each of a trigger of coupled singularities .

On the basis of previous results, a conclusiion appeared: coeficinet of rolling of the rolling disk along rotate circle haven't influent to the structural stability of set of system singularities. From the expression of λ it is visible that structural stability of set of system singularities and existence of

trigger of coupled singularities depend of difference $(R-r)$ between radius of rotate circle and radius of the disk, and of angular velocity Ω of circle rotation about vertical central axis.

2.1. Equation of phase trajectory of the non-linear differential equation of a rolling heavy disk motion along rotate circle about vertical central axis

By multiplying corresponding terms of nonlinear differential equation (2) with $2\dot\varphi dt = 2d\varphi$ it is possible to produce integral in the following form:

$$\dot\varphi^2 - \dot\varphi_0^2 + \frac{2\Omega^2}{\kappa}\left\langle \lambda(\cos\varphi_0 - \cos\varphi) - \frac{1}{2}(\cos^2\varphi_0 - \cos^2\varphi)\right\rangle = 0 \tag{3}$$

where φ_0 angle of initial relative position of disk mass centre C on rotate circle, and $\dot\varphi_0$ is initial angular velocity of disk mass centre C relative rotation about rotate circle centre O.

Figure 2. In phase plane $(\dot\varphi, \varphi)$, two phase portraits of nonlinear dynamics of a rolling disk along rotate circle with constant angular velocity around vertical central axis for different kinetic parameters: a* for $\lambda > 1$ without trigger of coupled singularities and b* for $\lambda < 1$ with a trigger of coupled singularities and an homoclinic orbits in the form of number eight.
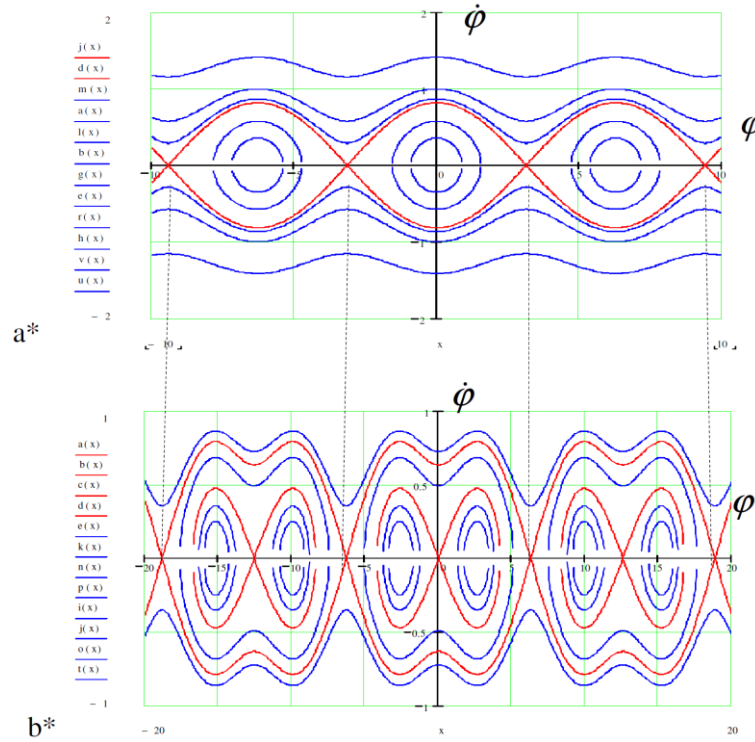
254

In Figure 2, **in** phase plane $(\dot{\varphi}, \varphi)$, two phase portraits of nonlinear dynamics of a rolling disk along rotate circle with constant angular velocity around vertical central axis for different kinetic parameters are presented. In Figure 2.a*, phase portrait is for $\lambda > 1$ without trigger of coupled singularities and in Figure 2.b*, phase portrait is for $\lambda < 1$ with a trigger of coupled singularities and an homoclinic orbits in the form of number eight.

In Figure 3, parametric transformations of homoclinic orbits of phase portrait of a rolling disk nonlinear dynamics on rotate circle with constant angular velocity about central vertical axis are presented. In Figure 3.a* parametric transformation of hmoclinic orbit in the form of number eight is presented, with limit process of the bifurcation one stable point into trigger of coupled singularities I opposite disappearance of trigger of coupled singularities and appear a stable threefold singular point.

In Figure 3. b* and c* layering of homoclinic orbits coursed by parametric variations with two limit cases a separation new homoclinic orbit in the form of number eight from other homoclinic orbit, or appearance homoclinic orbit in the form of number eight from stable singular point centre type by bifurcation and appearance trigger of coupled singularities with a no stable saddle point and two stable centre type singular points.

From equation (3) of phase trajectory of a rolling heavy disk moton along rotate circle with constant angular velocity about vertical central axis is possible to obtain relation betwee time t duration of rolling disk motion from initial position to arrbitrary position on rotate circle determined by angle of relative position φ in the following form (for detail see Reference [1]):

$$t = \int_{\varphi_0}^{\varphi} \frac{d\varphi}{\sqrt{\dot{\varphi}_0^2 - \frac{2\Omega^2}{\kappa} \left\langle \lambda(\cos\varphi_0 - \cos\varphi) - \frac{1}{2}(\cos^2\varphi_0 - \cos^2\varphi) \right\rangle}} \tag{4}$$

Let's introduce the following denotations:

$$\tilde{\omega}_0 = \sqrt{\dot{\varphi}_0^2 - \frac{\Omega^2}{\kappa}(2\lambda os\varphi_0 - \cos^2\varphi_0)}, \quad k^4 = \frac{4\frac{\Omega^2}{\kappa}}{\omega_0^2}$$

$$\omega_0^2 = \tilde{\omega}_0^2 + \frac{\Omega^2}{\kappa}(2\lambda - 1) = \dot{\varphi}_0^2 - \frac{\Omega^2}{\kappa}(2\lambda os\varphi_0 - \cos^2\varphi_0) + \frac{\Omega^2}{\kappa}(2\lambda - 1)$$

$$\tilde{k}^4 = \frac{k^4}{\left\langle 1 + \left(k^2\sqrt{(\lambda-1)}\right)^2 \right\rangle}, \quad k_{\lambda 1} = \frac{1}{\sqrt{\left\langle 1 - \sqrt{(\lambda-1)} \right\rangle}}, \quad k_{\lambda 2} = \frac{1}{\sqrt{\sqrt{(\lambda-1)}}}, \tag{5}$$

$$\omega_{0k,\lambda} = \omega_0 \sqrt{\left\langle 1 + \left(k^2\sqrt{(\lambda-1)}\right)^2 \right\rangle} \sqrt{\left\langle 1 - \sqrt{(\lambda-1)} \right\rangle} \sqrt{\sqrt{(\lambda-1)}}$$

and the integral (4) obtain the following form:

$$t = \frac{2}{\omega_{0k,\lambda}} \int_{u_0 = \sqrt{\left(\sqrt{(\lambda-1)} + \sin^2\frac{\varphi_0}{2}\right)}}^{u = \sqrt{\left(\sqrt{(\lambda-1)} + \sin^2\frac{\varphi}{2}\right)}} \frac{u\,du}{\sqrt{1 - k_{\lambda 1}^2 u^2}\sqrt{1 - k_{\lambda 2}^2 u^2}\sqrt{\left\langle 1 - \tilde{k}^4 u^4 \right\rangle}} \tag{6}$$

Obtained integral is elliptic integral and by use theory of special functions, this integral is possible to solve approximately by developing expressions with roots by series [8] and approximate value of elliptic integral obtain the following form::

$$t = \frac{2}{\omega_0} \int\limits_{u_0=\sqrt{\left(\sqrt{(\lambda-1)}+\sin^2\frac{\varphi_0}{2}\right)}}^{u=\sqrt{\left(\sqrt{(\lambda-1)}+\sin^2\frac{\varphi}{2}\right)}} \left\langle \sum_{n=0}^{\infty}\binom{-\frac{1}{2}}{n}(-1)^n \tilde{k}_1^{4n}u^{4n} \right\rangle \left\langle \sum_{n=0}^{\infty}\binom{-\frac{1}{2}}{n}(-1)^n k_{\lambda 1}^{2n}u^{2n} \right\rangle \left\langle \sum_{n=0}^{\infty}\binom{-\frac{1}{2}}{n}(-1)^n k_{\lambda 2}^{2n}u^{2n}. \right\rangle udu \tag{7}$$

or taking into account only first three terms in each of three series:

$$t \approx \frac{2}{\omega_0} \int\limits_{u_0=\sqrt{\left(\sqrt{(\lambda-1)}+\sin^2\frac{\varphi_0}{2}\right)}}^{u=\sqrt{\left(\sqrt{(\lambda-1)}+\sin^2\frac{\varphi}{2}\right)}} \left\langle 1+\frac{1}{2}\tilde{k}^4u^4+\frac{1\cdot3}{2\cdot4}\tilde{k}^8u^8 \right\rangle\left\langle 1+\frac{1}{2}k_{\lambda 1}^2u^2+\frac{1\cdot3}{2\cdot4}k_{\lambda 1}^4u^4 \right\rangle\left\langle 1+\frac{1}{2}k_{\lambda 2}^2u^2+\frac{1\cdot3}{2\cdot4}k_{\lambda 2}^4u^4 \right\rangle udu \tag{8}$$

3. Collision of two heavy rolling disks along rotate circle trace

3.1. Kinematics of two heavy rolling disks along rotate circle trace

In the case that rolling disks are with different dimensions, and masses and axial mass inertia moment for instantaneous axis of tolling along rotate circle trace, plan of impact pre-central-collision and outgoing post-central-collision relative angular velocities and component relative velocities at impact point T_{12} in collision are presented in Figures 4. See explanation in Reference [24].
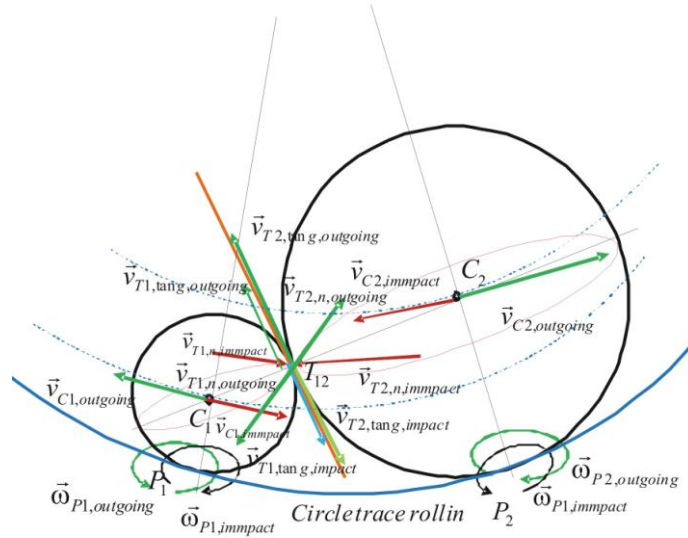

Figure 4. Plan of relative angular velocities and component velocities in pre- and post-central-collision of two rolling heavy rolling disks along rotate circle trace in vertical plane [24]

256

3.2. Dynamics of central collision of two rolling disks along rotate circle trace

Let's start with theory of dynamics of central collision between two rolling disks, with mass m_1 and m_2, and axial mass inertia moments $\mathbf{J}_{P1}$ and $\mathbf{J}_{P2}$ for corresponding momentary axis of rotation in rellative rolling along rotate circle trace with pre-impact (arrival) angular velocities $\vec{\omega}_{P1,impact} = \vec{\omega}_{P1}(t_0)$ and $\vec{\omega}_{P2,impact} = \vec{\omega}_{P2}(t_0)$. Mass ceneters $\mathbf{C}_1$ and $\mathbf{C}_2$ of the dosks move relative transtatory with pre-impact (arrival) velocities $\vec{v}_{C1.impact} = \vec{v}_{C1}(t_0)$ and $\vec{v}_{C2.impact} = \vec{v}_{C2}(t_0)$. Relative angular velocities $\vec{\omega}_{P1,impact} = \vec{\omega}_{P1}(t_0)$ and $\vec{\omega}_{P2,impact} = \vec{\omega}_{P2}(t_0)$ we denote as arrival, or impact or pre-impact relative angular velocietis at the moment t_0 (see Figures 4). At this moment t_0 of the collision start between these relative rolling disks, contact of these two disks is at point $\mathbf{T}_{12}$, in which both disks posses commont tangent plane –plane of contact (touch). In theory of collision, it is proposed that collision takes very shorth period time $(t_0, t_0 + \tau)$, and that τ tend to zeo. After this short period τ bodies-two relative rolling disks in collisoon separate and outgoing by post-impact-outgoing relative angular velocities $\vec{\omega}_{P1,outgoing} = \vec{\omega}_{P1}(t_0 + \tau)$ and $\vec{\omega}_{P2,outgoing} = \vec{\omega}_{P2}(t_0 + \tau)$. Mass ceneters $\mathbf{C}_1$ and $\mathbf{C}_2$ of the disks relative move transtatory with post-impact (autgoing) translatoor velocities $\vec{v}_{C1.outgoing} = \vec{v}_{C1}(t_0 + \tau)$ and $\vec{v}_{C2.outgoing} = \vec{v}_{C2}(t_0 + \tau)$. These relative translator velocities is possible to express each by corresponding relative angular velocity and radius of the corresponding disk [1,24]. Taking into account that translator motion of two bodies in central collision is simpler motion of two bodies, defined by corresponding inertia properties expressed by mass, m_1 and m_2, of each body and also by corresponding translator pre-impact velocity, $\vec{v}_1(t_0)$ and $\vec{v}_2(t_0)$ at the moment before collision and by post-impact-outgoing translator velocities $\vec{v}_1(t_0 + \tau)$ and $\vec{v}_2(t_0 + \tau)$ it is possible to establish a analogy with collision between two rolling balls. Explabation is in following form. Also, rolling balls along horizontal strength trace is simple rotation motion defined only by inertia properties in the axial mass inertia moments $\mathbf{J}_{P1}$ and $\mathbf{J}_{P2}$ for corresponding momentary axis of rotation in rolling along trace with pre-impact (arrival) angular velocities $\vec{\omega}_{P1,impact} = \vec{\omega}_{P1}(t_0)$ and $\vec{\omega}_{P2,impact} = \vec{\omega}_{P2}(t_0)$ and corresponding outgoing post-impact-outgoing angular velocities $\vec{\omega}_{P1,outgoing} = \vec{\omega}_{P1}(t_0 + \tau)$ and $\vec{\omega}_{P2,outgoing} = \vec{\omega}_{P2}(t_0 + \tau)$.

Using Petrović's theory of elements of mathematical phenomenology and phenomenological mappings [20-23] in parts of qualitative and mathematical analogies, in the Reference [20-23] author

indicate a qualitative and mathematical analogy between system translator dynamics and central collision (impact) dynamics of two bodies in translator motion pre-impact and post impact dynamics phenomena and system rolling two disks dynamics and central collision (impact) dynamics of two rolling disks in rolling motion pre-impact and post impact dynamics phenomena. On the basis of this indicated qualitative and mathematical analogies, it is possible list analogous kinetic parameter of these systems. The axial mass inertia moments $\mathbf{J}_{P1}$ and $\mathbf{J}_{P2}$ for corresponding momentary axis of rotation in rolling two disks along circle trace are analogous to the bodies masses m_1 and m_2 of two bodies in ollision in translatory motion. On the basis of Petrović's theory [20-22] and qualitative and mathematical analogies considere in previpus author's Refreneces [24] , post-cebntral-collision ougoing angular velocities of the rolling diss are in the following forms:

$$\omega_{P1}(t_0 + \tau) = \omega_{P1}(t_0) - \frac{1+k}{1 + \dfrac{\mathbf{J}_{P1}}{\mathbf{J}_{P2}}} \left(\omega_{P1}(t_0) - \omega_{P2}(t_0) \right) \tag{9}$$

$$\omega_{P2}(t_0 + \tau) = \omega_{P2}(t_0) + \frac{1+k}{1 + \dfrac{\mathbf{J}_{P2}}{\mathbf{J}_{P1}}} \left(\omega_{P1}(t_0) - \omega_{P2}(t_0) \right) \tag{10}$$

Angular momentum (moment of impulse) of impact dynamics of two relative rolling disks pre-central-collision and post-central-collision relative motion in the the following relation:

$$\mathbf{J}_{P1}\vec{\omega}_{P1}(t_0) + \mathbf{J}_{P2}\vec{\omega}_{P2}(t_0) = \mathbf{J}_{P1}\vec{\omega}_{P1}(t_0 + \tau) + \mathbf{J}_{P2}\vec{\omega}_{P2}(t_0 + \tau) \tag{11}$$

and coefficient of the restitution of rolling disks relative central collision is in the form:

$$k = \frac{\omega_r(t_0 + \tau)}{\omega_r(t_0)} = \frac{\omega_{P2}(t_0 + \tau) - \omega_{P1}(t_0 + \tau)}{\omega_{P1}(t_0) - \omega_{P2}(t_0)} \tag{12}$$

as ratio between difference of relative angular velocities of rolling disks post-collision and pre-collision kinetic states.

3.3. Kinetic parameters of the relative rolling heavy disks along rotate circle trace around vertical central axis

For obtaining posistion of the rilling disks at frst central collision we use expression (9) fr functional dependence between time rolling both disks from vorresponding initial kinetic states to the kinetic state at position of first folliein, taking into accoubt that angles determining diks positions are coupled by geometrical relation: Central angle coordinate of relative position of the disks in state of central collieions are in the following relation: $\varphi_{2,impact,k} = \varphi_{1,impact,k} + \beta$, where angle β depend of geometrical parameters of circle line radius R, and of the both disks radiuses: r_1 and r_2 and is defined by expression in the form: $\beta = \arccos \dfrac{(R-r_1)^2 + (R-r_2)^2 - (r_1+r_2)^2}{2(R-r_1)(R-r_2)} = \arccos \dfrac{\lambda_1(\lambda_1 - \lambda_2 - 1) - \lambda_2}{(\lambda_1 - \lambda_2)(\lambda_1 - 1)}$.

Aproximate nonlinear equation for obtaining angles $\varphi_{1,impact,1}$ and $\varphi_{2,impact,1} = \varphi_{1,impact,1} + \beta$ of relative

positions of two rolling disks at rotate circle trace around vertical central axis with constant angular velocity, taking into account expression (8) for each disk, that is $t_{1,impct,1} = t_{2,impct,1}$ is in the following form:

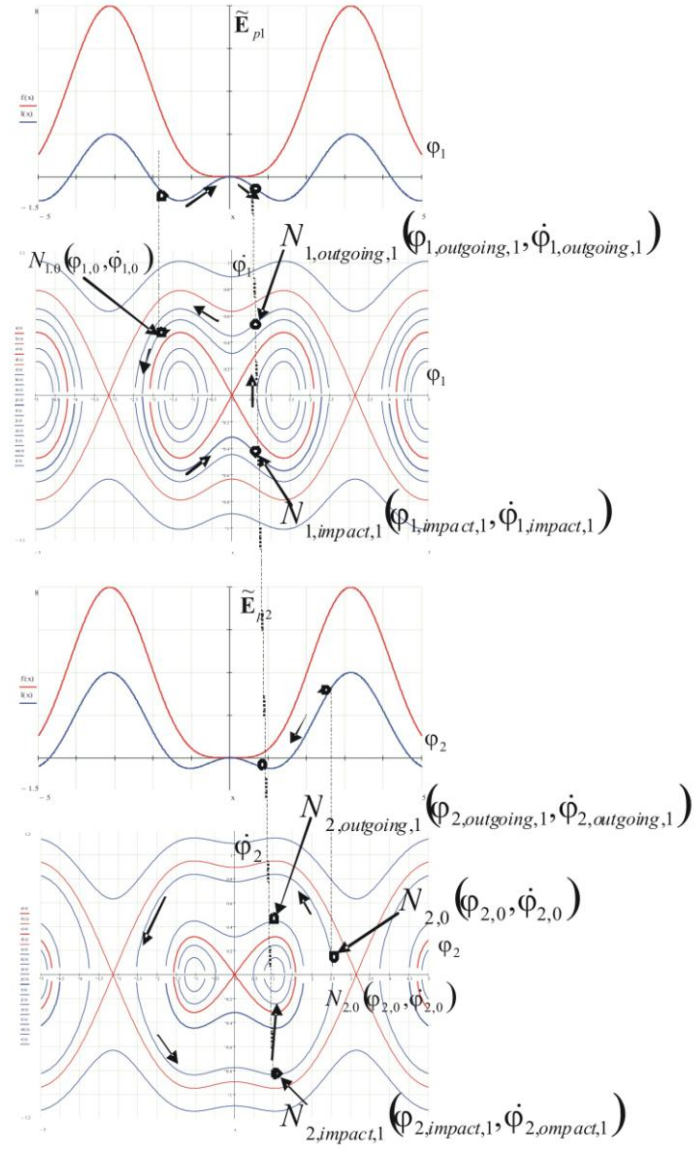
Figure 5. Phase trajectory branches in phase portraits of two rolling disks for relative motion in interval between initial configuration and configurations of pre-first-collision and post-first-collision between two rolling disks

$$\frac{2}{\omega_{0,1}} \int_{u_0=\sqrt{\left(\sqrt{(\lambda-1)}+\sin^2\frac{\varphi_{,20}}{2}\right)}}^{u=\sqrt{\left(\sqrt{(\lambda-1)}+\sin^2\frac{\varphi_{1,impact,1}}{2}\right)}} \left\langle 1+\frac{1}{2}\tilde{k}_2^4 u^4+\frac{1\cdot 3}{2\cdot 4}\tilde{k}_2^8 u^8\right\rangle\left\langle 1+\frac{1}{2}k_{\lambda 1,2}^2 u^2+\frac{1\cdot 3}{2\cdot 4}k_{\lambda 1,2}^4 u^4\right\rangle\left\langle 1+\frac{1}{2}k_{\lambda 2,2}^2 u^2+\frac{1\cdot 3}{2\cdot 4}k_{\lambda 2,2}^4 u^4\right\rangle udu \approx \quad (13)$$

$$\approx\frac{2}{\omega_{0,2}} \int_{u_0=\sqrt{\left(\sqrt{(\lambda-1)}+\sin^2\frac{\varphi_{0,2}}{2}\right)}}^{u=\sqrt{\left(\sqrt{(\lambda-1)}+\sin^2\frac{\varphi_{1,impact,1}+\beta}{2}\right)}} \left\langle 1+\frac{1}{2}\tilde{k}_2^4 u^4+\frac{1\cdot 3}{2\cdot 4}\tilde{k}_2^8 u^8\right\rangle\left\langle 1+\frac{1}{2}k_{\lambda 1,2}^2 u^2+\frac{1\cdot 3}{2\cdot 4}k_{\lambda 1,2}^4 u^4\right\rangle\left\langle 1+\frac{1}{2}k_{\lambda 2,2}^2 u^2+\frac{1\cdot 3}{2\cdot 4}k_{\lambda 2,2}^4 u^4\right\rangle udu$$

where corresponding denotations are used in accordance with expressions (5) for each of the rolling disks.

In Figure 5, phase trajectory branches in phase portraits of two rolling disks for relative motion, in interval between initial condition configuration and configurations of pre-first-collision and post-first-collision between two rolling disks with vibro-impact dynamics [24-26] on rotate circle trace with constant angular velocity around vertical central axis, are presented.

4. Conclusions

In this paper, in short, basic theory and basic kinetic elements of vibro-impact dynamics of collision between two rolling heavy disks, different radii and dimensions, on rotate circle trace are determined. By these kinetic elements and parameters as well as theory of two rolling disks central collision are defined all necessary for research in analysis nonlinear dynamics of all successive impacts of these rolling disks.

Acknowledgments

References

[1] Hedrih (Stevanović) R. K., (2015), *Rolling heavy disk along rotate circle with constant angular velocity*, Invited Lecture, The 8th International Workshop Computer Algebra Systems in Teaching and Research (CASTR'2015), Siedlce, Poland, October 21 – 25, 2015.

[2] Hedrih (Stevanović) R. K., *(2001),Trigger of Coupled Singularities (invited plenary lecture)* , Dynamical Systems-Theory and Applications, Edited By J. Awrejcewicz and all, Lodz 2001, pp. 51-78.

[3] Hedrih (Stevanović) R. K., (2004), *A Trigger of Coupled Singularities*, MECCANICA, Vol.39, No. 3, 2004., pp. 295-314. , DOI: 10.1023/B:MECC.0000022994.81090.5f,

[4] Hedrih (Stevanović) R. K., (2005), *Nonlinear Dynamics of a Heavy Material Particle Along Circle which Rotates and Optimal Control*, Chaotic Dynamics and Control of Systems and Processes in Mechanics (Eds: G.

Rega, and F. Vestroni), p. 37-45. IUTAM Book, in Series *Solid Mechanics and Its Applications, Editerd by G.M.L. Gladwell, Springer*. 2005, XXVI, 504 p., Hardcover ISBN: 1-4020-3267-6.

[5]   Hedrih (Stevanović) R. K., (200), *Nonlinear Dynamics of a Gyro-rotor, and Sensitive Dependence on initial Conditions of a Heav Gyro-rotor Forced Vibration/Rotation Motion*, Semi-Plenary Invited Lecture, Proceedings: COC 2000, Edited by F.L. Chernousko and A.I. Fradkov, IEEE, CSS, IUTAM, SPICS, St. Petersburg, Inst. for Problems of Mech. Eng. of RAS, 2000., Vol. 2 of 3, pp. 259-266.

[6]   Hedrih (Stevanović) R. K., (2008), *The optimal control in nonlinear mechanical systems with trigger of the coupled singularities,* in the book: Advances in Mechanics : Dynamics and Control : Proceedings of the 14th International Workshop on Dynamics and Control / [ed. by F.L. Chernousko, G.V. Kostin, V.V. Saurin] : A.Yu. Ishlinsky Institute for Problems in Mechanics RAS. – Moscow : Nauka, 2008. pp. 174-182, ISBN 978-5-02-036667-1.

[7]   Hedrih (Stevanović) R. K.,   (2008), *Dynamics of coupled systems*, Nonlinear Analysis: Hybrid Systems, Volume 2, Issue 2, June 2008, Pages 310-334.

[8]   Mitrinović D. S., Djoković D. Ž.,   *Special functions (Specijalne gunkcije)* , Gradjevinska knjiga, Beograd, 1964, p. 267..

[9]   Lj. Veljović, *Nelinearne oscilacije giro-rotora (Non-linear oscillations of Gyro-rotors), [in Serbian]*, Doctor's Degree Thesis, Faculty of Mechanical Engineering in Niš, 2011. Supervisor K. Hedrih (Stevanović).

[10] Hedrih (Stevanović) R. K., (1998), *Vectors of the Body Mass Moments*, Monograph paper, Topics from Mathematics and Mechanics, Mathematical institute SANU, Belgrade, Zbornik radova 8(16), 1998, pp. 45-104. published in 1999 .

[11] Hedrih (Stevanović) R. K.,   (2013), *Vector method based on mass moment vectors and vector rotators applied to rigid-body multi-coupled rotations around no intersecting axes*, International Journal of Structural Stability and Dynamics, Vol. 13, No. 7 (2013) 1340007 (20 pages), #.c World Scientific Publishing Company, ISSN: 0219-4554, DOI: 10.1142/S0219455413400075, http://dk.doi.org/10.1142/S0219455413400075

[12] Hedrih (Stevanović) R. K., (2001), *Vector Method of the Heavy Rotor Kinetic Parameter Analysis and Nonlinear Dynamics*, University of Niš 2001, Monograph, p. 252. (in English), YU ISBN 86 7181-046-1.

[13] Hedrih (Stevanović) R. K., (2013), *Vector method based on mass moment vectors and vector rotators applied to rigid-body multi-coupled rotations around no intersecting axes*, International Journal of Structural Stability and Dynamics, Vol. 13, No. 7 (2013) 1340007 (20 pages), #.c World Scientific Publishing Company, ISSN: 0219-4554, DOI: 10.1142/S0219455413400075, http://dk.doi.org/10.1142/S0219455413400075

[14] Hedrih (Stevanović) R. K.,   (2004), *On Rheonomic Systems with Equivalent Holonomic Conservative Systems Applied to the Nonlinear Dynamics of the Watt's Regulator*, Proceedings, Volume 2, The eleventh world congress in Mechanism and machine Sciences, IFToMM, China Machine press, Tianjin, China, April 1-4, 2004, pp. 1475-1479. ISBN 7-111-14073-7/TH-1438. . http://www.iftomm2003.com, Publisher: China Machine press, Tianjin, China

[15] Hedrih (Stevanović) R. K. and Veljovic Lj. , (2011), *Vector Rotators of a Rigid Body Dynamics with Coupled Rotations around Axes without Intersection,* International Journal Mathematical Problems in Engineering, MPE/351269, Hindawi Publishing Corporation, Volume 2011, Article ID 351269.

[16] Hedrih (Stevanović) R. K. and Veljovic Lj. , *New Vector Description of Kinetic Pressures on Shaft Bearings of a Rigid Body Nonlinear Dynamics with Coupled Rotations around No Intersecting Axes*, Acta Polytechnica Hngarica - Journal of Applied Sciences, Special Issue on Applied Mathematics, Guest Editors: Aurél Galántai and Péter T. Nagy, Volume 10, Issue Number 7, 2013, pp. 151-170. ISSN 1785-8860,

[17] Hedrih (Stevanović) R. K., Milosavljević D. and Veljovic Lj. , *Multi-parameter Analysis of a Rigid Body Nonlinear Coupled Rotations around No Intersecting Axes Based on the Vector Method*, Adv. Theor. Appl. Mech., Vol. 6, 2013, no. 2, 49 - 70, HIKARI Ltd, www.m-hikari.com, http://dx.doi.org/10.12988/atam.2013.378.

[18] Andronov A. A., Vitt A. A., Haykin S., (1981), *Teoriya kolebaniy,* Nauka, Moskva., pp. 568.

[19]   Hedrih (Stevanović) R. K., *Models of real system nonlinear dynamics abstractions*, To memory of academicians Yuri Alekseevich Mitropolskiy and Valentin Vitalevich Rumяantsev and   president of IFNA

Professor dr V. Lakšminatham , MATHEMATICS IN ENGINEERING, SCIENCE AND AEROSPACE, MESA - www.journalmesa.com, Vol. 6, No. 3, pp. 1-17, 2015, Ⓒc CSP - Cambridge, UK; I&S - Florida, USA, 2015.

[20] Petrović M., Elementi matematičke fenomenologije (Elements of mathematical phenomenology), Srpska kraljevska akademija, Beograd, 1911. str. 89.

[21] Petrović M., Fenomenološko preslikavanje (Phenomenological mapp), Srpska kraljevska akademija, Beograd, 1933. str. 33.   http://elibrary.matf.bg.ac.rs/handle/123456789/475

[22] Petrović M., Mecanismes communs aux phenomenes disparates, Paris 1921.

[23] Elements of mathematical phenomenology and phenomenological mapping in non-linear dynamics, Edited by Katica R. (Stevanovic) Hedrih, Ivan Kosenko, Pavel Krasilnikov and Pol D. Spanos, Special Issue of International Journal of Non-Linear, Mechanics, Volume 73, Pages 1-128 (July 2015)

[24] Hedrih (Stevanović) R. K., Central collision of two rolling balls: Theory and examples, (manuscript in review process, May 30, 2015).

[25] Hedrih (Stevanović) R. K., *DYNAMICS OF THE ELLIPTIC BILLIARDS AND ROLLING BALL IMPACTS*,.Proceedings, The 5th International Congress of Serbian Society of Mechanics. Arandjelovac, June 15-17, 2015, pp. 98-98. Published by Serbian Society of Mechanics and Faculty of Technical Sciences Novi Sad, ISBN 978-86-7892-715-7,   COBISS.SR-ID 296997639. Plus at USB M2c, pp. 1-4.

[26] Hedrih (Stevanović) K R., Raičević V. and Jović S., Phase Trajectory Portrait of the Vibro-impact Forced Dynamics of Two Heavy Mass Particles Motions along Rough Circle, Communications in Nonlinear Science and Numerical Simulations, 2011 16 (12):4745-4755, DOI 10.1016/j.cnsns.2011.05.027..

Katica R. (Stevanović) Hedrih, University Professor, Doctor of technical Sciences, Department of Mechanics at Mathematical Institute of Serbian Academy of Science and Arts (SANU), Belgrade and Faculty of Mechanical Engineering University of Niš, Serbia, e-mail: khedrih@sbb.rs; Priv. address: 18000- Niš, Serbiam ul. Vojvode Tankosića 3/22.e-mail: khedrih@eunet.rs.

A tracking controller design for a space target interception
(CON071-15)

Elżbieta Jarzębowska, Bartłomiej Pilarczyk

Abstract: Paper presents model-based tracking controller design for a free-floating space robot within scenario of intercepting an object. Such missions are of interest due to growing number of objects needed to be removed from space. Free-floating mode requires spacecraft thrusters to be off and conserved linear (LM) and angular momenta (AM). LM and AM conservation generates respectively holonomic and nonholonomic constraints. Also, free-floating implicates underactuation which is a 2nd order nonholonomic constraint, so the robot is a multi-constraint system. Although there already exist control algorithms of underactuated robots, there are still open issues since control is mission- and robot-specific. Motivation for this research is the potential significance of its results in the future. The growing space exploration results in more space debris and requires sophisticated services. Service tasks and removing debris endangering satellites need to be performed by specialized robots. Paper presents a space robot control oriented dynamics. Mission scenario consists of 3 parts: estimation of target's properties; controller design to track and intercept an object; move to the graveyard orbit. Simulation results of the theoretical control development for a robot intercepting non-tumbling object are shown.

1. Introduction

The paper presents some results on designing *model - based* tracking controllers for a free - floating space robot dedicated to perform maintenance tasks. The focus of this research is on capturing objects, e.g. debris in space. We design a mission scenario for intercepting small debris in space and move it safely to the graveyard orbit or vehicle disposable containers. Such missions are of a significant interest due to a growing number of debris and other space objects needed to be removed from space, as well as due to asteroids which, when captured, may be promising sources of raw materials.

A free - floating operation mode requires spacecraft thrusters to be turned off and the system linear and angular momenta are to be conserved. The condition of linear momentum conservation generates the holonomic constraint on a robot. However, due to the angular momentum conservation space robots are nonholonimic control systems. The free - floating mode implicates that a robot is underactuated. In control setting, the underactuation is treated as a second order nonholonomic constraint, so the free-floating space robot is a multi-constraint control system [1, 2].

Control properties of space robots, as mentioned earlier, and kinds of missions for them make the control design interesting and quite challenging. Although there already exist algorithms which allow controlling underactuated robots and manipulators [4, 5], there are still many open problems and

room for new research in this area, since controls are usually dedicated to specified missions and space robots performing them.

Motivations for taking this research are then the potential significance of its results in the future, in the face of constantly growing interest in conquest and exploration of space. The growing space exploration by a man results in generation of more space debris and requires sophisticated services [3]. The latter ones are often delivered by astronauts, like in *Extra Vehicular Activities* (EVA). Debris moving in space may cause danger for operating satellites and need to be removed successively. Small debris, which are of interest of this paper, can be captured by space robots using the robot hands, leashes or nets, and the bigger ones require removal including docking of the space robot to the debris, flying in formation maneuver and then, bringing the debris, e.g. to Earth.

Both, services in space and debris removal need to be performed by specialized space robots. Also, this research, through a development of new control strategies for space robots may provide a new insight into nonlinear control methods for missions in space.

The paper presents a development of space robot control oriented dynamics. Based upon the dynamics a model based controller is to be developed to serve a debris interception mission. The mission scenario consists of three main steps: (a) estimation of debris motion using long and short range distance cameras, sizing and approximating inertia of the moving target; (b) design of a controller to track and intercept the moving object; (c) safely move to the graveyard orbit.

This research provides a theoretical control development for approaching, capturing and acquisition of an object. The assumptions are that the space robot is supposed to track and capture an object of a relatively small size with respect to that of the robot, and which does not tumble. The theoretic development is illustrated by mission simulation studies.

The research contribution is two–folded. Firstly, intercepting a slowly moving, non-tumbling object, may provide us some insight into the selection of simple and effective control algorithms for this mission. Secondly, a space robot dynamics after an object interception may be monitored. Specifically, the research results may provide a better insight the space robot stable motion due to an object size, weight and kind of motion. Additionally, the results may contribute to a control theoretic basis for future applications in space or for ground manipulators when an extra load in intercepted or one of their actuators fail.

2. Control mission protocol

A mission of capturing a moving target, precisely its very end part, consists of approaching the object, following it, capturing and getting away. The main assumptions and objectives taken into consideration during the control mission protocol design are as follows:

- The space robot dynamics is control oriented, developed w.r.t. The center of the mass of the whole system.
- The space robot is supposed to track and capture an object of a relatively small size with respect to that of the robot, and which does not tumble.
- The debris weight is small comparing to that of the robot. Intercepting an object adds additional mass to the system what may significantly change its dynamics and move it out of its orbit. We assume that the debris weight does not affect the robot motion.
- The debris is assumed to move with relatively low speed.
- The debris inertia can be determined:
    1. The debris motion is monitored and estimated with the help of cameras. It is assumed that image processing algorithms allow obtaining information from the still picture, as well as from a live video feed. Thus, the size of debris can be determined.
    2. The debris mass can be approximated based upon its dimensions, volume, and assuming its density.
    3. A distance from the robot – using stereo vision or a depth camera it is possible to determine the distance and its change with respect to the robot. Based on that, relative motion of the debris can be approximated.
- The motion of the debris can be estimated using cameras so the robot can follow it, track it and grasp by the end effector.
- The research scope as presented does not cover launching of the robot and putting it in the orbit. It is assumed that the robot can reach the debris and it may approach to it at the reachable distance.

The assumptions stated above allow us to distinguish the phases interesting for the research, i.e. approaching, intercepting and moving safely away with the debris to the mission destination. Also, they enable performing the dynamics and control analysis using data delivered by on-board devices.

3. Dynamics model of the space robot

The space robot adapted in this paper is a space manipulator consisting of a base and two arms, see Figure 1.

Although the vehicle is assumed to be three dimensional, certain limitations to its motion are applied. The joints can rotate only around the z – axis. Geometric and inertia robot parameters are provided in the Table 1.
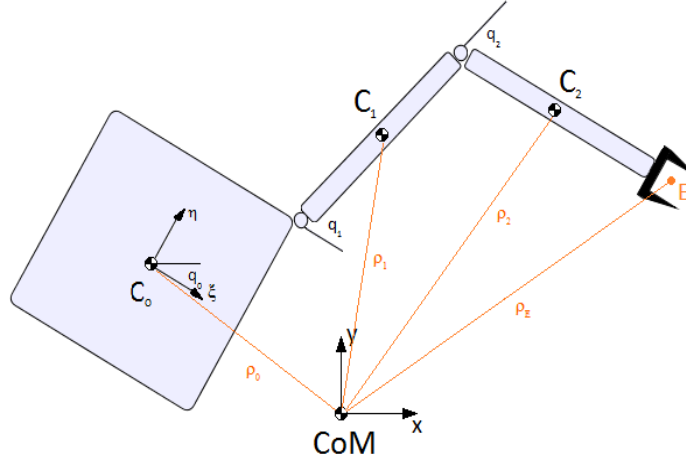
Figure 1. Representation of the space robot model

Table1. Physical parameters of the space robot

Body No.	a_i [m]	l_i [m]	m_i [m]	I_i [kg m^2]
0	1	0.5	40	6.667
1	1	0.5	4	0.333
2	1	0.5	3	0.250

The space robot motion is described by the joint coordinate vector $q = [q_0, q_1, q_2]^T$. The symbols C_0, C_1, C_2 denote centers of mass of each body in the system. Vectors ρ_0, ρ_1, ρ_2 define positions of the centers of masses, where $\rho_i = [\xi, \eta, \zeta]^T$. Also ρ_E is a position vector for end effector of the robot arm. Conservation of the angular momentum for space vehicles results in the non – holonomic constraint. This condition requires the sum of angular momenta of all the bodies in the system to be constant. If the engines are turned off, we may assume this sum to be zero. Taking into account the applied notation, the angular momentum vector depends upon the angular positions q and the angular velocities (dq/dt). Thus, the formula for angular momentum conservation can be written as follows:

$$K = K_0 + K_1 + K_2 = \Phi(q_0, q_1, q_2, \dot{q}_0, \dot{q}_1, \dot{q}_2) \tag{1}$$

Although, the model of the robot is three – dimensional, the motion of the robot is limited, i.e. rotation only around the z – axis is available. Therefore, equation (1) can be written in a simplified form:

$$K_i = \rho_i \times m_i \dot{\rho}_i + I_{i\zeta\zeta} \omega_{iZ} \tag{2}$$

Where $I_{i\zeta\zeta}$ is the inertia tensor of the i-th body and ω_{iZ} is the angular velocity component of the i-th body around the axis perpendicular to the plane in which the motion occurs. Angular velocity of each body can be written as the sum of time derivatives of the rotational angles:

$$\omega_0 = \dot{q}_0, \omega_1 = \dot{q}_0 + \dot{q}_1, \omega_2 = \dot{q}_0 + \dot{q}_1 + \dot{q}_2 \tag{3}$$

Kinetic energy of the space robot has the form:

$$T_i = 0.5[m_i(\dot{x}_i^2 + \dot{y}_i^2) + I_{iCM}\omega_i^2] \tag{4}$$

where x_i, y_i, z_i are the linear velocities of the centres of masses of the robot components. I_{iCM} is the moment of inertia around the centre of mass of the system. Its location is as follows:

$$I_{iCM} = I_i + m_i d_i^2 = I_i + m_i(x_i^2 + y_i^2) \tag{5}$$

Total kinetic energy of the system can be then computed as follows:

$$T = 0.5[m_0(\dot{x}_0^2 + \dot{y}_0^2) + I_{0CM}\omega_0^2 + m_1(\dot{x}_1^2 + \dot{y}_1^2) + I_{1CM}\omega_1^2 + m_2(\dot{x}_2^2 + \dot{y}_2^2) + I_{2CM}\omega_2^2] \tag{6}$$

The motion of the system is described by the Lagrange equations of motion:

$$M(q)\ddot{q} + C(q,\dot{q})\dot{q} = \tau + J_0^T \lambda \tag{7}$$

Matrices M, C and J are derived directly from equation (4). Furthermore, the unknown Lagrange multipliers are decoupled from the control momenta which results in the reduced form of the equations. This procedure is applied to general non – holonomic systems in order to obtain dynamical control models for them. The equations decoupling results in

$$M_{12}(q)\ddot{q}_2 + C_{12}(q,\dot{q}_2)\dot{q}_2 = \tau + J_1^T \lambda \tag{8}$$

$$M_{22}(q)\ddot{q}_2 + C_{22}(q,\dot{q}_2)\dot{q}_2 = \tau; \dot{q}_1 = D(q)\dot{q}_2 \tag{9}$$

Where $q_1 = [q_0]$ and $q_2 = [q_1, q_2]^T$. Equations (8) and (9) state the system's dynamical control model. They are used for computation. Calculations are conducted in MatLAB 2008a. To summarize the variables used in the equations : K_i are the angular momenta of each body, $\Phi(q_i, dq_i)$ is the the known function of joint coordinates and their derivatives with respect to time; T is the system's kinetic energy; Q_i is the vector of generalized forces and λ is the unknown Lagrange multiplier. Generalized forces are equal to the control torques τ_i. In this research only the angles q_1 and q_2 are controlled. Orientation of the base, q_0, is not controlled. Thus, $\tau_0 = 0$ and the only acting torques are τ_1 and τ_2.

4. Results of a space robot simulation

The Wen – Bayard control algorithm is the computed torque type. It requires the complete knowledge of the system dynamics. However, its significant advantage over some of other algorithms, e.g. computed torque, is that the mass matrix does not have to be non – singular.

Throughout this research two experiments have been performed. In the first one, the end effector of the robot followed an object along a circular trajectory. In the second experiment, the end effector followed the object moving on a spiral trajectory. Below, the research results are presented. They were obtained via implementation of the Wen – Bayard algorithm. The error function, $e = e(t)$, is defined in equation (10).

$$e(t) = q(t) - q_d(t) \tag{10}$$

Equation (11) defines the formula for the computed torque:

$$\tau = M_{22}(q)\ddot{q}_{2d} + C_{22}(q_d, \dot{q}_{2d})\dot{q}_{2d} - K_d\dot{e} - K_p e \tag{11}$$
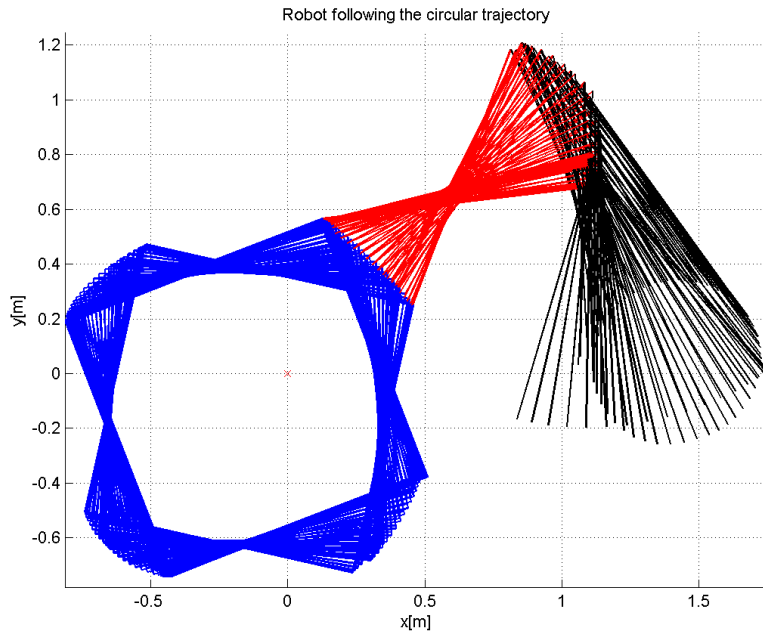
Figure 2. Robot motion tracking a circular trajectory

Figure 2 shows the motion of whole system while tracking the object moving along the circular trajectory.

In the following figure tracking of the circular trajectory is presented in detail. Black line is the desired trajectory to be followed and the crosses show the way of the end effector.
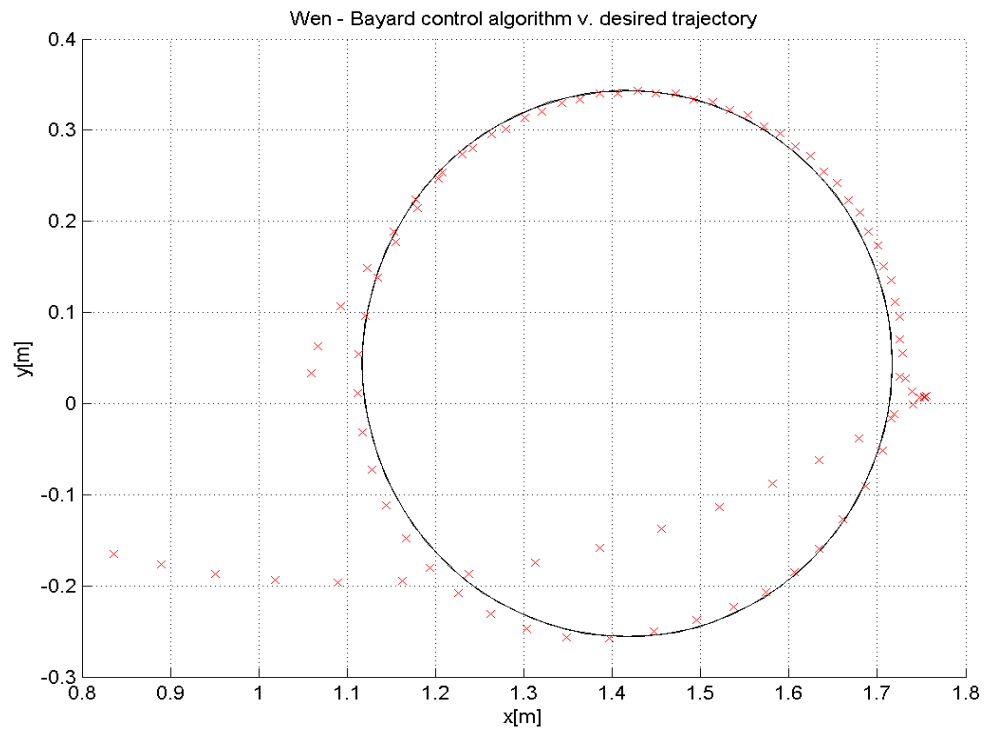
Figure 3. End effector tracking a circular trajectory

Figure 4 shows the motion of whole system while tracking the object moving along the spiral trajectory.
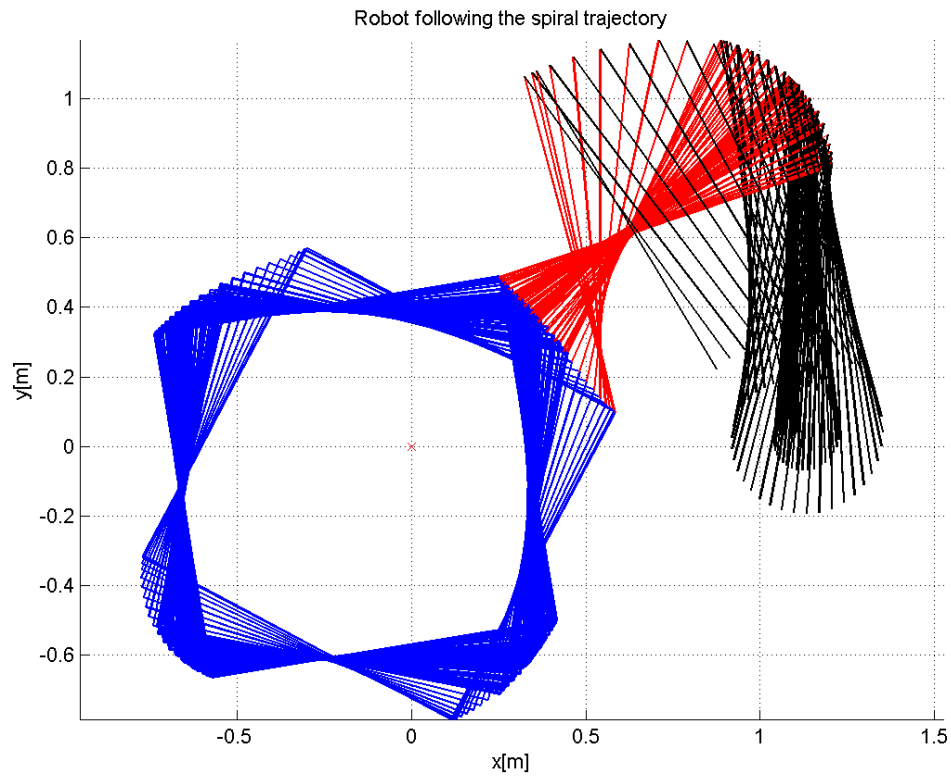
Figure 4. Robot motion tracking a spiral trajectory

In the following figure tracking of the spiral trajectory is presented in detail. Black line is the desired trajectory to be followed and the crosses show the way of the end effector.
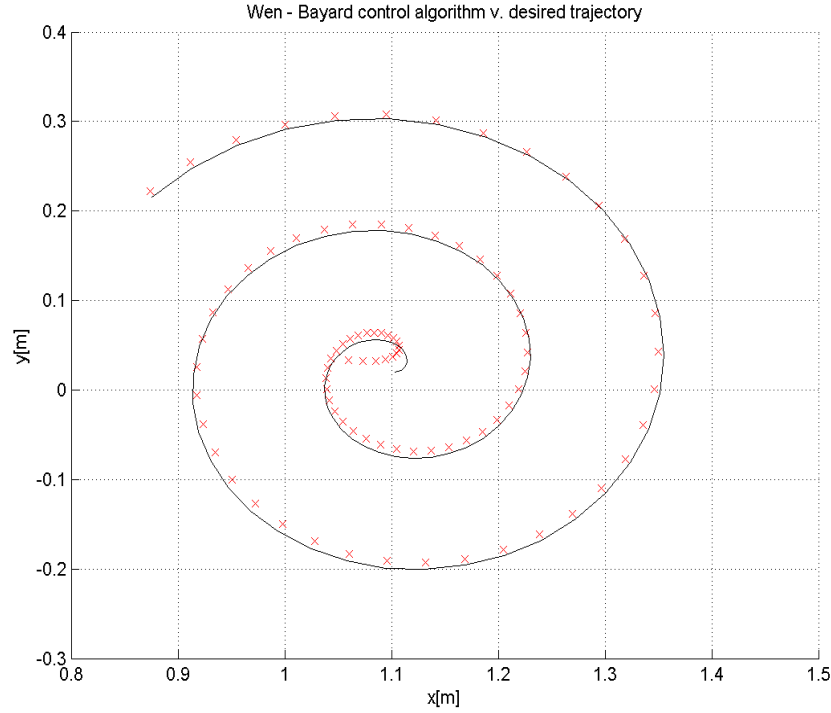
Figure 5. End effector tracking a spiral trajectory

It can be seen that the Wen – Bayard algorithm produces worse tracking performance but its significant advantage is that the inertia matrix does not have to be non-singular. It is of the essential value when capturing debris, since they change inertia properties of a robot-debris system. This is the main reason for applying the Wen – Bayard algorithm for our preliminary capturing mission analysis.

5.   Conclusions

Control design for space robots flying in formation or capturing moving objects, what is in fact formation flying when a robot and an object objects are of comparable masses is a challenging task. Presented research shows the simulation results of controlling the space vehicle capturing the debris. Although, the computations were time consuming, the results are promising. It is also noteworthy, that the control algorithm can applied to track various types of trajectories. Therefore the results obtained in this research are good starting point for further missions and control strategy development for on – line computations.

References

[1] Vafa, Z., Dubowsky, S., The Kinematics and Dynamics of Space Manipulators: The Virtual Manipulator approach, The International Journal of Robotics Research, 1990; 9; 3, DOI 10.1177/027836499000900401.

[2] Vafa, Z. Space manipulator motions with no satellite attitude disturbances, CH2876-1/90/00001770$01.00, 1990 IEEE.

[3] Sagara, S., Taira, Y., Digital control of space robot manipulators with velocity type joint controller using transpose of generalized Jacobian matrix, Artificial Life Robotics (2008) 13:355-358, DOI 10.1007/s10015-008-0584-7.

[4] Nakamura, Y., Mukherjee, R., Nonlinear control for the non-holonomic motion of space robot systems, Advanced Robot Control, Lecture Notes in Control and Information Sciences, Vol. 162, 1991, pp. 83 – 105.

[5] Papadopoulos, E. G., Teleoperation of Free – floating Space Manipulator Systems, Proc. SPIE 1833, Telemanipulator Technology, 122 (March 26, 1993); doi:10.1117/12.142103.

Elżbieta Jarzębowska, Associate Professor: Institute of Aeronautics and Applied Mechanics, Warsaw University of Technology, ul. Nowowiejska 24, 00-665 Warszawa, Poland (*elajarz@meil.pw.edu.pl*)

Bartłomiej Pilarczyk, M.Sc. (Ph.D. student): Institute of Aeronautics and Applied Mechanics, Warsaw University of Technology, ul. Nowowiejska 24, 00-665 Warszawa, Poland (*b.m.pilarczyk@gmail.com*).

Sliding mode control for a class of distributed parameter system with fractional order derivative
(CON131-15)

Jingfei Jiang, Dengqing Cao,Huatao Chen

Abstract: In this paper, the tracking control of the fractional order wave equation subject to persistent external disturbances is studied in Hilbert spaces. First, the second-order sliding control: twisting fractional order sliding mode(2-SM) controller is designed for the infinite dimensional setting and applied for addressing the asymptotic state tracking of the fractional order perturbed wave equation. By introducing the adaptive control law, the unknown bound of the external disturbances is dealt with. Next, based on fractional order extension of Lyapunov direct method, the relative theorem involved in the paper for the proof of the stability is proved. Then, the control algorithms are extended to globally asymptotically stabilize the fractional order uncertain wave equation through choosing the appropriate Lyapunov functional. And the infinite dimensional treatment retains the main robustness features against non-vanishing disturbances similar to those possessed by its finite dimensional counterpart. Finally, numerical simulations are presented to verify the viability and efficiency of the proposed fractional order controller.

1. Introduction

It is well known that many systems and industrial process in practical engineering are governed by functional and partial differential equations or, more general, equations in a Hilbert space, and these systems are often described with a significant degree of uncertainty. Thus, the vibration control of such systems is very important and this leads to a study on the design of the robust controllers for these systems with distributed parameters. With the development of the practical engineering application of viscous-elastic material, much attention has been drawn to the study of fractional order damping. Actually, many of the physical laws are necessary to be described in terms of fractional calculus [1]- [3]. Therefore, the robust control problem of a distributed system with fractional order derivative has attracted the attention of scientists and engineers from many fields such as mathematics, physics and engineering [4]- [5].

The fractional order control of a distributed parameters system is concerned with a control of a fractional order system for which the system dynamics is defined with partial fractional differential equations, or, more general, equations in a Hilbert space. In process

control, a variety of methodologies are emerged that address the control of nonlinear distributed parameters system. Sakthivel et al. [6] considered a class of fractional order neutral control systems governed by abstract nonlinear fractional order neutral differential equations. Feliu-Batlle et al. [7] proposed a new method for controlling main irrigation canals with variable dynamical parameters based on robust fractional order controllers. For the past years, the study of sliding mode control for the distributed parameter systems had been a hot spot topic and the interest involved in the sliding mode control approach had been extended to infinite-dimensional dynamic systems such as distributed parameter systems. Li [8] studied the sliding mode control problem for distributed parameter systems (DPS). YURY [9] addressed the Lyapunov-based design of second-order sliding mode controllers in the domain of distributed parameter systems, Pisano et al. [10] illustrated the generalization to the infinite dimensional setting of the well-known finite-dimensional controllers, namely, the power-fractional controller and two second-order sliding-mode control algorithms. Up to now, there are few achievements involving the control of the distributed parameter system with fractional order derivative via sliding mode approach. Pisano1 et al. [11] developed sliding mode control approaches to stabilize a class of linear uncertain fractional-order dynamics. Guo et al. [12] studied the numerical solutions for fractional partial differential equations. Motivated by the application of viscous-elastic material in engineering and the challenge in the design of control strategies for distributed parameter systems, the main purpose of this paper is focused on the control problem of a class of distributed parameter system with fractional order derivative.

The rest of the paper is outlined as follows. In Section 2, basic definition and preliminaries for the control of the wave process are elaborated. In section 3, the twisting 2-SM control algorithm with the adaptive law is designed for the fractional order wave equation and shows that it guarantees the asymptotic tracking control for the fractional order uncertain wave equation. At last, simulation examples are presented to illustrate the effectiveness of the proposed method.

2. Basic definition and preliminaries

2.1. Definition and notation

There exist many definitions of fractional derivative and fractional integral [2]- [3].
The well-known definition of fractional order integration

$$I_t^q x(t) = \frac{1}{\Gamma(q)} \int_0^t (t-s)^{q-1} x(s) ds, \ 0 < q < 1 \tag{1}$$

and the well-known definition of fractional derivatives

$$\,^{C}_{0}D^{q}_{t}x(t) = \frac{1}{\Gamma(1-q)} \int_{0}^{t} (t-s)^{-q}x'(s)ds, \ 0 < q < 1. \tag{2}$$

The Sobolev space is denoted by $W^{l,2}(a,b) = \{u \in L^2(a,b) : D^\alpha u \in L^2(a,b), \ \forall |\alpha| \le l\}$ and the square integrable functions space denoted by $L_2(a,b) = \{z : ||z(\cdot)||_2 = \sqrt{\int_a^b z^2(\tau)d\tau}\}$ (the detain is listed in [14]). Furthermore, $L_\infty(a,b)$ is a subspace of $L_2(a,b)$ with the norm $||z(\cdot)||_\infty = \max_{a \le t \le b} z(t)$.

A class of uncertain infinite-dimensional systems whose solution (y, y_t) is defined in the Hilbert space $H = L_2(0,1) \times L_2(0,1)$ is governed by a perturbed version of the hyperbolic PDE commonly referred to as the wave equation:

$$\,^{C}D^{\alpha}_{t}y(x,t) = v^2 y_{xx}(x,t) + \theta_1 y(x,t) + u(x,t) + \psi(x,t) \tag{3}$$

where $1 < \alpha \le 2$, $x \in [0,1]$ is the one dimensional space variable, $t > 0$ is the time variable, and $(y, y_t) \in H$, $(t \ge 0)$, is the state vector with the norm $||(y, y_t)||_H = ||y(\cdot,t)||_2 + ||y_t(\cdot,t)||_2$. The coefficient $v^2 \in R$ stands for the elasticity, $u(x,t)$ is the distributed control input and $\psi(x,t) \in L_2(0,\infty)$ represents a distributed uncertain disturbance source term.

The initial conditions (ICs)

$$y(x,0) = \varphi_0(x) \in W^{2,2}(0,1), \ y_t(x,0) = \varphi_1(x) \in W^{2,2}(0,1) \tag{4}$$

are assumed to meet the boundary conditions (BCs) imposed on the system (3).
Consider Dirichlet BCs

$$y(0,t) = y_0(t) \in W^{2,2}(0,\infty), \ y(1,t) = y_1(t) \in W^{2,2}(0,\infty). \tag{5}$$

The solution of the above boundary value problem (3) and (4)-(5) is defined in the mild sense (see Curtain, [14]).

2.2. The control of the wave process

The control task is to make the scalar field $y(x,t)$ follow a given reference $y^r(x,t)$ or make the position $y(x,t)$ and the fractional order velocity $\,^{C}D^{\gamma}_{t}y(x,t)$ to exponentially track a priori given reference signal $y^r(x,t)$ and its fractional order velocity $\,^{C}D^{\gamma}_{t}y^r(x,t)$ in the L_2-space, regardless of whichever admissible disturbance $\psi(x,t)$ affects the system. Furthermore, assume the reference signal is required to be smooth enough and such that $y^r_{tt}(\cdot,t) \in L_2(0,1)$, $y^r_{xx} \in L_2(0,1)$.
The reference $y^r(x,t)$ should be selected in accordance with Dirichlet BCs.

$$y^r(0,t) = y_0(t), \ y^r(1,t) = y_1(t) \tag{6}$$

The deviation variable $e(x, t) = y(x, t) - y^r(x, t)$ is eventually driven to zero in L_2−norm by the designed controller. By the differential manipulations, the dynamics of the error variable is then written as follows:

$$^C D_t^\alpha e(x, t) = v^2 e_{xx}(x, t) + \theta_1 e(x, t) + \theta_1 y^r(x, t) - {}^C D^\alpha{}_t y^r(x, t) + u(x, t)$$
$$+ \psi(x, t) + v^2 y_{xx}^r(x, t) \tag{7}$$

The corresponding ICs is listed in the following:

$$e(x, 0) = \varphi_0(x) - \varphi_0^r(x), \quad e_t(x, 0) = \varphi_1(x) - \varphi_1^r(x) \tag{8}$$

and Dirichlet BCs

$$e(0, t) = 0, \; e(1, t) = 0. \tag{9}$$

Then, the equation (7) can be divided into the following system

$$\begin{cases} ^C D_t^\gamma y_1 = y_2, \\ ^C D_t^\gamma y_2 = v^2 y_{1xx}(x, t) + \theta_1 y_1(x, t) + \theta_1 y^r(x, t) - {}^C D^\alpha{}_t y^r(x, t) + u(x, t) \\ \quad\quad + \psi(x, t) + v^2 y_{xx}^r(x, t) \end{cases} \tag{10}$$

where $\gamma = \alpha/2$ and $y_1(x, t) = e(x, t)$.

The following assumption is about the disturbance.

Assumption 1 The unknown disturbance satisfies the following inequality for the positive constant K_1.

$$||\psi(\cdot, t)||_\infty \leq K_1, \tag{11}$$

Lemma 2.1 *Let $x(t), y(t) \in L_2(0, 1)$ be continuous and derivable functions. Then, for any time instant $t \geq t_0$, the following inequality holds*

$$^C D^\gamma(x(t)y(t)) \leq x(t)^C D^\gamma y(t) + y(t)^C D^\gamma x(t) \tag{12}$$

Proof. Obviously, the following inequalities hold for $0 < \gamma < 1$,

$$\frac{1}{2} {}^C D^\gamma [x(t)]^2 \leq x(t)^C D^\gamma x(t), \; \frac{1}{2} {}^C D^\gamma [y(t)]^2 \leq y(t)^C D^\gamma y(t).$$

$$\frac{1}{2} {}^C D^\gamma [x(t) + y(t)]^2 \leq [x(t) + y(t)]^C D^\gamma [x(t) + y(t)].$$

Thus,

$$^C D^\gamma(x(t)y(t)) \leq x(t)^C D^\gamma y(t) + y(t)^C D^\gamma x(t),$$

which completes the proof.

The stability of the system (10) can be dealt with according to the following theorem.

Theorem 2.2 *Let $x = 0$ be an equilibrium point for the non-autonomous fractional order system* (10)*. Assume that there exists a Lyapunov function $V(t, x)$ satisfying the following conditions:*

1) $V(t, x)$ is positive definite;

2) $^C D^\gamma V(t, x)$ is negative definite;

3) $V(t, x)$ has an infinite upper-bounded;

4) $V(t, x)$ is radially unbounded;

where $\gamma \in (0, 1)$. Then, the system (10) *has global asymptotic stability;*

Proof. According to the definition of class$-K$ functions, we can give new descriptions about the conditions 1), 2) and 3), that is, if $V(t, x)$ is positive definite, then, there exists lass$-K$ function γ_1 such that

$$\gamma_1(||x||) \leq V(t, x).$$

If $^C D^\gamma V(t, x)$ is negative definite, there exists lass$-K$ function γ_3 such that

$$^C D^\gamma V(t, x) \leq -\gamma_3(||x||))$$

and when $V(t, x)$ has an infinite upper-bounded, then, there exists lass$-K$ function γ_2 such that

$$V(t, x) \leq \gamma_2(||x||).$$

By fractional order extension of Lyapunov direct method of the Theorem 6.2 in [15], the system (10) is asymptotically stable. Now, we focus on the global stability.

From the condition 4), the following equality holds

$$\lim_{x \to \infty} \gamma_1(||x||) = \infty$$

which implies the lass$-K$ function γ_1 is radially unbounded, then, there exists a constant R such that $\gamma_2(r) < \gamma_1(R)$ for $\forall r$. In addition, the constant r can be arbitrarily large, thus, the equilibrium point is global asymptotic stability. Then, the proof is completed.

3. The design of adaptive control of the wave equation

Assume that the state vector $(y, {}^C D^\gamma{}_t y)$ is available for measurements. Then, y_1, y_2 are also available for feedback. In order to stability the error dynamics (10), the distributed controller is designed as follows:

$$\begin{cases} u = u_{eq} + u_i, \\ u_{eq} = {}^C D^\alpha{}_t y^r(x, t) - v^2 y^r_{xx}(x, t) - \theta_1 y_1(x, t) - \theta_1 y^r(x, t) - r_1 y_1, \\ u_i = -\lambda_1 sgn(y_1) - \lambda_2 sgn(y_2) - \hat{K}_1 sgn(y_2), \\ {}^C D^\gamma{}_t \hat{K}_1 = \mu_1 ||y_2||_2, \hat{K}_1(0) = K_0. \end{cases} \tag{13}$$

Assume that the positive constant K_1 is unknown and estimated by the adaptive law. μ_1 is a positive constant and $K_0 > 0$ is the initial value of the update parameters $\hat{K}_1$. The controller can be viewed as the sum of two components: a distributed feedback component, and a feedback component consisting of a distributed version of the finite dimensional twisting 2-SM controller [16]. Because of the non-smooth of the controller (13), the precise meaning of the solutions of the uncertain error dynamics (3) and (4)-(5) under the controller (13) can be defined in the generalized sense as a limiting result obtained through a certain regularization procedure [13]. The definitions [10] are listed as follows:

Definition 3.1 *An absolutely continuous function $y^\delta(\cdot, t) \in L_2(0, 1)$, defined on $[0, \tau)$, is said to be an approximate $\delta-$solution of the system(3) and (4)-(5),(13) if it is a strong solution of the corresponding boundary value problem with a continuous approximation $u^\delta(\cdot)$ substituted for the discontinuous control input (13) such that $||u^\delta - u||_2 \le \delta$ for all $y_1, y_2 \in L_2(0, 1)$ subject to $||y_1||_2 \ge \delta$ and $||y_2||_2 \ge \delta$, respectively, where $\delta > 0$.*

Definition 3.2 *An absolutely continuous function $y(\cdot, t) \in L_2(0, 1)$, defined on $[0, \tau)$, is said to be a generalized solution of the system(3) and (4)-(5),(13) if there exists a family of approximate $\delta-$ solutions $y^\delta(\cdot, t)$ of the corresponding boundary value problem such that $\lim_{\delta \to 0} ||y^\delta(\cdot, t) - y(\cdot, t)||_2 = 0$, and $\lim_{\delta \to 0} ||^C D^\gamma y^\delta(\cdot, t) - {}^C D^\gamma y(\cdot, t)||_2 = 0$, uniformly in $t \in [0, \tau)$.*

Lemma 3.3 *Given the nonlinear uncertain system (10) with the control law (13), the gain $\hat{K}_1$ has an upper-bound, i.e. there exists a positive constant K^* such that*

$$\hat{K}_1 \le K^*, \forall t > 0 \tag{14}$$

Proof. Suppose $y_2 \ne 0$, it follows from (13) and ψ is bounded that $\hat{K}_1$ is increasing and there exists a time t_1 such that $\hat{K}_1(t_1) > 0$. As the gain $\hat{K}_1$ is getting large enough for $t \ge t_1$, y_2 is decreasing. Then, there exists a finite time t_2, such that $y_2 = 0$ and $\hat{K}_1(t_2)$ admits a bounded value which implies that there always exists a positive constant K^* such that $\hat{K}_1(t) < K^*$, for all $t \ge 0$. The proof is completed.

Consider the error dynamics (10) along with the BCs and select the following Lyapunov functional:

$$\begin{aligned}
V(t) &= \frac{r_1}{2} \int_0^1 y_1^2 dx + \frac{1}{2} \int_0^1 y_2^2 dx + \frac{1}{2} v^2 \int_0^1 y_{1x}^2 dx + \frac{1}{2\mu} \int_0^1 (\hat{K}_1 - K^*)^2 dx \\
&\quad + \lambda_1 \int_0^1 |y_1| dx
\end{aligned} \tag{15}$$

Taking its derivative with respect to time along the solution of the system (10) under the controller (13) and by the Lemma 2.1, we have

$$
\begin{aligned}
^{C}D_t^{\gamma}V(t) &\le r_1 \int_0^1 y_1 y_2 dx + \int_0^1 y_2\,^{C}D_t^{\gamma} y_2 dx + v^2 \int_0^1 y_{1x}\,^{C}D_t^{\gamma} y_{1x} dx \\
&\quad + \frac{1}{\mu}\int_0^1 (\hat{K}_1 - K^*)D_t^{\gamma}\hat{K}_1 dx + \lambda_1 \int_0^1 y_2 sgn(y_1)dx \\
&= r_1 \int_0^1 y_1 y_2 dx + \int_0^1 y_2[v^2 y_{1xx} + \theta_1 y_1 + \theta_1 y^r + u + \psi + v^2 y_{xx}^r - {}^{C}D^{\alpha}{}_t y^r]dx \\
&\quad + v^2 \int_0^1 y_{1x}\,^{C}D^{\gamma}{}_t y_{1x} dx + \frac{\mu_1}{\mu}\int_0^1 (\hat{K}_1 - K^*)||y_2||_2 dx + \lambda_1 \int_0^1 y_2 sgn(y_1)dx \\
&= r_1 \int_0^1 y_1 y_2 dx + \int_0^1 y_2[v^2 y_{1xx} - r_1 y_1 - \lambda_1 sgn(y_1) - \lambda_2 sgn(y_2) - \hat{K}_1 sgn(y_2) + \\
&\quad \psi]dx + v^2 \int_0^1 y_{1x}\,^{C}D^{\gamma}{}_t y_{1x} dx + \frac{\mu_1}{\mu}\int_0^1 (\hat{K}_1 - K^*)||y_2||_2 dx + \lambda_1 \int_0^1 y_2 sgn(y_1)dx \\
&= v^2 \int_0^1 y_2 y_{1xx} dx - \lambda_1 \int_0^1 y_2 sgn(y_1)dx - \lambda_2 \int_0^1 |y_2|dx + \int_0^1 y_2[-\hat{K}_1 sgn(y_2) + \\
&\quad \psi]dx + v^2 \int_0^1 y_{1x}\,^{C}D^{\gamma}{}_t y_{1x} dx + \frac{\mu_1}{\mu}\int_0^1 (\hat{K}_1 - K^*)||y_2||_2 dx + \lambda_1 \int_0^1 y_2 sgn(y_1)dx \\
&\le -\lambda_2 \int_0^1 |y_2|dx + \int_0^1 |y_2||K_1 + \hat{K}_1|dx - \frac{\mu_1}{\mu}|\hat{K}_1 - K^*|||y_2||_2 \\
&\le -\lambda_2 \int_0^1 |y_2|dx + \int_0^1 |y_2||K_1 + K^*|dx - \int_0^1 |y_2||K^* - \hat{K}_1|dx \\
&\quad - \frac{\mu_1}{\mu}|\hat{K}_1 - K^*|||y_2||_2 \\
&= -(\lambda_2 - |K^* + K_1|)||\sqrt{|y_2|}||_2 - [\frac{\mu_1}{\mu}||y_2||_2 - ||y_2||_2]|K^* - \hat{K}_1|
\end{aligned}
$$

Assumption 2 $\lambda_2 > |K^* + K_1|,\ \mu_1 > \mu$.

According to Assumption 2, $^{C}D_t^{\gamma}V(t) \le 0$ which implies that the error dynamics (10) is stable and the Lyapunov functional $V(t)$ is a non-increasing function of time along error dynamics (10), i,e

$$V(t_2) \le V(t_1), \forall\ t_2 \ge t_1 \ge 0$$

Denote $D_R = \{(y_1, y_2) \in H : V(y_1, y_2) \le R\}$. It is clear that once an arbitrary $R \ge V(0)$ is fixed, the resulting domain D_R is proved to be invariant for the error system trajectories. For the subsequent analysis, we will take into account that the states (y_1, y_2) belong to the domain D_R starting from the initial time $t = 0$ on. Then, it follows from the Lyapunov function $V(t)$ and the definition of D_R, that $||y_2||_2^2 \le \sqrt{2R}||y_2||_2$ and $\int_0^1 y_1 y_2 dx \ge -\frac{1}{2}[||y_1||_2^2 + ||y_2||_2^2]$ hold.

Now consider the augmented functional

$$\bar{V}(t) = V(t) + K \int_0^1 y_1 y_2 dx$$

$$= \frac{r_1}{2} ||y_1||_2^2 + \lambda_1 ||\sqrt{|y_1|}||_2^2 + \frac{1}{2} ||y_2||_2^2 + \frac{v^2}{2} ||y_{1x}||_2^2 + \frac{1}{2\mu} ||\hat{K}_1 - K^*||_2^2 + K \int_0^1 y_1 y_2 dx,$$

where K is a positive constant. Since

$$\bar{V}(t) \geq \frac{r_1}{2} ||y_1||_2^2 + \lambda_1 ||\sqrt{|y_1|}||_2^2 + \frac{1}{2} ||y_2||_2^2 + \frac{v^2}{2} ||y_{1x}||_2^2 + \frac{1}{2\mu} ||\hat{K}_1 - K^*||_2^2$$

$$- \frac{K}{2} [||y_1||_2^2 + ||y_2||_2^2]$$

$$= [\frac{r_1}{2} - \frac{K}{2}] ||y_1||_2^2 + [\frac{1}{2} - \frac{K}{2}] ||y_2||_2^2 + \frac{v^2}{2} ||y_{1x}||_2^2 + \frac{1}{2\mu} ||\hat{K}_1 - K^*||_2^2 + \lambda_1 ||\sqrt{|y_1|}||_2^2$$

Assumption 3 $r_1 > K$, $1 > K$.

According to Assumption 3, the augmented functional $\bar{V}(t)$ is positive definite within the invariant domain D_R and it turns out to be radially unbounded as $R \to \infty$, then $\bar{V}(t)$ can thus be used as a radially unbounded Lyapunov functional to analyze the global asymptotic stability of the error dynamics.

$$^C D_t^\gamma \bar{V}(t) \leq -(\lambda_2 - |K^* + K_1|) ||\sqrt{|y_2|}||_2 - [\frac{\mu_1}{\mu} ||y_2||_2 - ||y_2||_2] |K^* - \hat{K}_1| + K \int_0^1 y_2^2 dx$$

$$+ K \int_0^1 y_1 {}^C D_t^\gamma y_2 dx$$

$$= -(\lambda_2 - |K^* + K_1|) ||\sqrt{|y_2|}||_2 - [\frac{\mu_1}{\mu} ||y_2||_2 - ||y_2||_2] |K^* - \hat{K}_1| + K ||y_2||_2^2$$

$$+ K \int_0^1 y_1 [v^2 y_{1xx} - r_1 y_1 - \lambda_1 sgn(y_1) - \lambda_2 sgn(y_2) - \hat{K}_1 sgn(y_2) + \psi] dx$$

$$= -(\lambda_2 - |K^* + K_1|) ||\sqrt{|y_2|}||_2 - [\frac{\mu_1}{\mu} ||y_2||_2 - ||y_2||_2] |K^* - \hat{K}_1| + K ||y_2||_2^2$$

$$+ K v^2 \int_0^1 y_1 y_{1xx} dx - K r_1 ||y_1||_2^2 - K \lambda_1 \int_0^1 |y_1| dx - K \lambda_2 \int_0^1 y_1 sgn(y_2) dx$$

$$+ K \int_0^1 y_1 [\psi - \hat{K}_1 sgn(y_2)] dx$$

$$\leq -(\lambda_2 - |K^* + K_1|) ||\sqrt{|y_2|}||_2 - [\frac{\mu_1}{\mu} ||y_2||_2 - ||y_2||_2] |K^* - \hat{K}_1| + K ||y_2||_2^2$$

$$+ K v^2 y_1 y_{1x}|_0^1 - K v^2 ||y_{1x}||_2^2 - K r_1 ||y_1||_2^2 - K \lambda_1 \int_0^1 |y_1| dx$$

$$+ K \lambda_2 \int_0^1 |y_1| dx + K |K_1 + \hat{K}_1| \int_0^1 |y_1| dx$$

$$\leq -(\lambda_2 - |K^* + K_1| - \sqrt{2R}K) ||\sqrt{|y_2|}||_2 - K v^2 ||y_{1x}||_2^2 - [K \lambda_1 - K \lambda_2$$

$$- K|K_1 + K^*|]||\sqrt{y_1}||_2 - Kr_1||y_1||_2^2 - [\frac{\mu_1}{\mu}||y_2||_2 - ||y_2||_2]|K^* - \hat{K}_1|$$

Assumption 4 $\lambda_2 > |K^* + K_1| + \sqrt{2R}K$ and $\lambda_1 > \lambda_2 + |K_1 + K^*|$.

According to Assumption 4, $^C D_t^\gamma \bar{V}(t)$ is negative definite. From the Theorem 2.2, it implies that the convergence of $||y_1||_2$ and $||y_2||_2$ to zero as $t \to \infty$. The conclusion is completed.

Theorem 3.4 *Consider the system* (10) *along with the ICs and BCs, and whose parameters and external disturbance satisfy assumption 3 and 4. Then, the distributed control strategy* (13) *guarantees the exponential decay of the* L_2- *norms* $||y_1(\cdot, t)||_2$ *and* $||y_2(\cdot, t)||_2$ *of the solutions* (10)*.*

4. Numerical simulation

In what follows, the Caputo derivative is discretized in terms of the L2 approach [12]. Consider the perturbed equation (7) with $\psi(t, x) = \sin(\pi t)$ and the reference profile $y^r = 0$. For the controller (13), the simulation results are in the following.

Figure 1,2 and 3 show the results for $\alpha = 1.1$, 1.6 and 2, respectively with the value of the
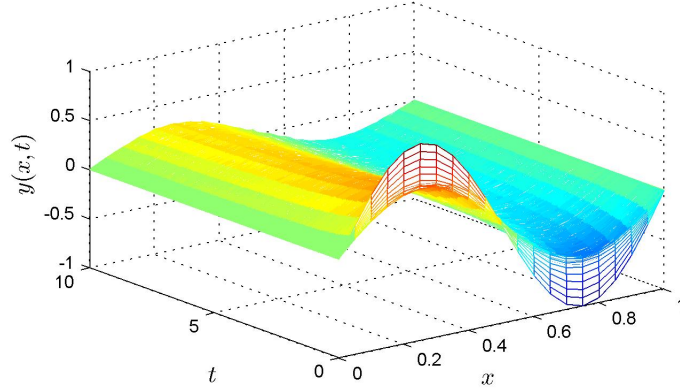
Figure 1. The solution $y(x, t)$ of the controlled wave equation under the controller with $\alpha = 1.1$.

parameters $\alpha = 1.8$, $V = 1, r_1 = 1$, $\lambda_1 = 15$, $\lambda_2 = 6$, $\mu_1 = 0.2$, $\theta = -2$ in controller (13). Comparison of the Figs show that the fractional order derivative $\alpha \to 1$ exhibits diffusion response, while the fractional order derivative $\alpha \to 2$ exhibits wave response. Therefore, when $\alpha = 1.6$, both diffusion and wave response can be observed in Fig.2, which means that the solution of the system (10) continuously depends on the fractional order derivative.

Figure 2. Left plot: the solution $y(x,t)$ of the controlled wave equation under the controller with $\alpha = 1.6$. Right plot: distributed control $u(x,t)$ at the time $t = 0.03$.

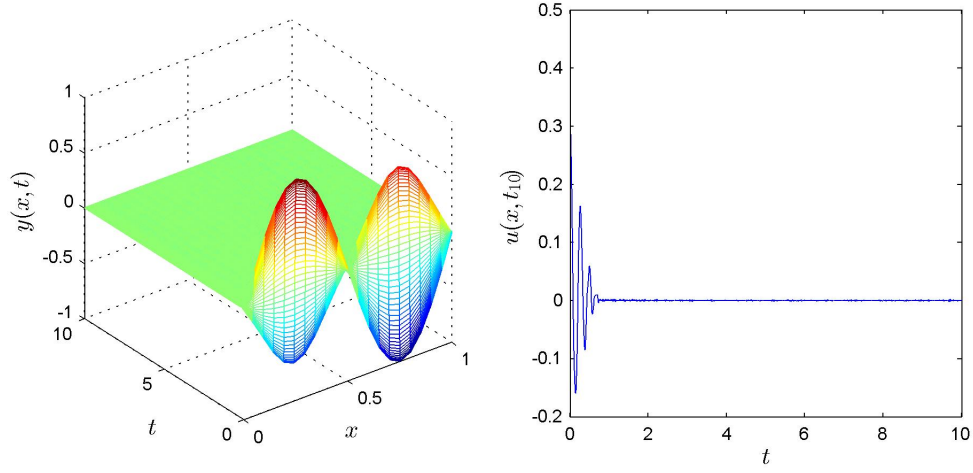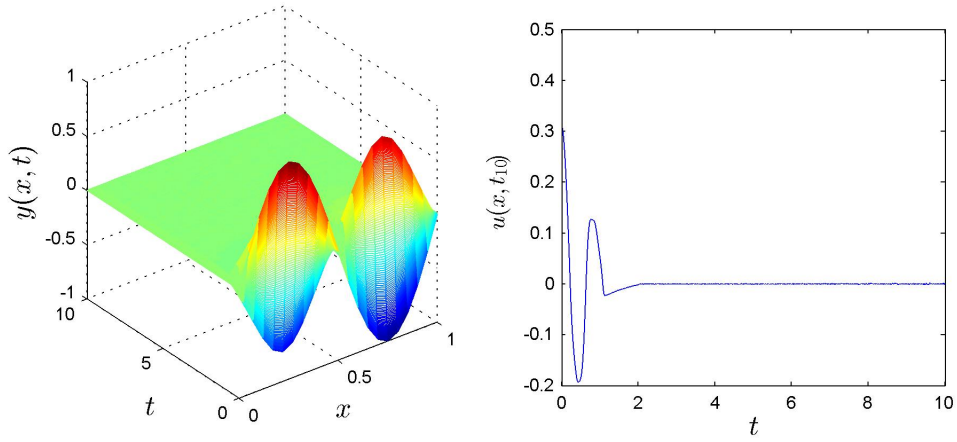**Figure 3.** Left plot: the solution $y(x,t)$ of the controlled wave equation under the controller with $\alpha = 2$. Right plot: distributed control $u(x,t)$ at the time $t = 0.03$.

Figure 2 and 3 illustrate the solution converges to the given reference profile as confirmed in Theorem 3.4. Then, from the figures, we can see that the proposed adaptive sliding mode

control law guarantees the stability of the system (10) and verifies its viability and efficiency.

5. Conclusion

In this paper, the twisting control algorithm has been designed for a fractional order uncertain wave equation. The resulting scheme has been applied to solve the tracking control problem for the fractional order uncertain wave equation subject to persistent external disturbances. The main contributions can be summarized as follows:

(1)The control algorithms are extended to globally asymptotically stabilize the fractional order uncertain wave equation under boundary condition by means of appropriate Lyapunov functionals. And the infinite dimensional treatment retains the main robustness features against non-vanishing disturbances similar to those possessed by its finite dimensional counterpart. The finite time convergence of the proposed algorithms is proved by fractional order extension of Lyapunov direct method.

(2)The adaptive law is introduced into the twisting 2-SM control algorithm for the unknown bound of the uncertain component.

(3)At last, numerical simulation is presented to verify the efficiency of the proposed fractional controller.

References

[1] BAGLEY R L, TORVIK P J. On the fractional calculus model of viscoelastic behavior. *Journal of Rheology*, 30 (1986), 133–155.

[2] I. PODLUBNY. *Fractional Differential Equations*. Academic Press, San Diego, 1999.

[3] A.A. KILBAS, H.M. SRIVASTAVA, J.J. TRUJILLO. *Theory and Applications of Fractional Differential Equations*. Elsevier Science B.V., Amsterdam, 2006.

[4] JESUS S I, MACHADO J A T, RAMIRO S B. On the fractional order control of heat systemsIntelligent Engineering Systems and Computational Cybernetics. *Springer Netherlands*, (2009), 375–385.

[5] ROSSIKHIN Y A, SHITIKOVA M V. New approach for the analysis of damped vibrations of fractional oscillators. *Shock and Vibration*, 16 (2009), 365–387.

[6] SAKTHIVEL R, MAHMUDOV N I, NIETO J J. Controllability for a class of fractional-order neutral evolution control systems. *Applied Mathematics and Computation*, 218 (2012), 10334–10340.

[7] Feliu-Batlle V, Perez R R, Rodriguez L S. Fractional robust control of main irrigation canals with variable dynamic parameters. *Control Engineering Practice*, 15 (2007), 673–686.

[8] Li K C, Leung T P, Hu Y M. Sliding mode control of distributed parameter systems. *Automatica*, 30(1994), 1961–1966.

[9] Orlov Y, Pisano A, Scodina S, et al. On the Lyapunov-based second-order SMC design for some classes of distributed parameter systems. *Journal of Mathematical Control and Information*, IMA , 2012: dns003.

[10] Pisano A, Orlov Y, Usai E. Tracking control of the uncertain heat and wave equation via power-fractional and sliding-mode techniques. *Journal on Control and Optimization*, 49 (2011), 363–382.

[11] Pisano A, Rapaic M R, Jelicic Z D, et al. Sliding mode control approaches to the robust regulation of linear multivariable fractional order dynamics. *International Journal of Robust and Nonlinear Control*, 20 (2010), 2045–2056.

[12] Guo B L, Pu X K, Huang F H. *Fractional Partial Differential Equations and Their Numerical Solutions.* Science Press, Beijing, China, 2011.

[13] Orlov Y V. *Discontinuous systems: Lyapunov analysis and robust synthesis under uncertainty conditions.* Springer Science, Business Media, 2008.

[14] Curtain R F, Zwart H. *An introduction to infinite-dimensional linear systems theory* Springer Science Business Media, 2012.

[15] Li Y, Chen Y Q, Podlubny I. Stability of fractional-order nonlinear dynamic systems: Lyapunov direct method and generalized MittagCLeffler stability. *Computers Mathematics with Applications*, 59 (2010), 1810–1821.

[16] Levant A. Sliding order and sliding accuracy in sliding mode control. *International journal of control*, 58(1993), 1247–1263.

Jingfei Jiang, M.Sc. (Ph.D. student): Harbin Institute of Technology/School of Astronautics/Division of Dynamics and Control, Harbin Institute of Technology, West Dazhi Street No.92, Nangang District, Harbin 150001, China. (*jjf860623@yeah.net*). The author gave a presentation of this paper during one of the conference sessions.

Dengqing Cao, Ph.D.: Harbin Institute of Technology/School of Astronautics/Division of Dynamics and Control, Harbin Institute of Technology, West Dazhi Street No.92, Nangang District, Harbin 150001, China. (*dqcao@hit.edu.cn*).

Huatao Chen, M.Sc. (Ph.D. student): Harbin Institute of Technology/School of Astronautics/Division of Dynamics and Control, Harbin Institute of Technology, West Dazhi Street No.92, Nangang District, Harbin 150001, China. (*htchencn@aliyun.com*).

Non-linear dynamics of a vibration harvest-absorber system (BIF084-15)

Krzysztof Kecik and Andrzej Mitura

Abstract: Energy harvesting (also called power harvesting or energy scavenging) is the process of transforming ambient energy (kinetic energy, vibrations, radial energy etc.) into useful electrical energy. This paper proposes a novel concept of the harvest-absorber device. The system consisting of three main parts: main system (modelled as simply oscillator), a pendulum (absorber) and an electromagnetic harvester device. This conception allows energy recovery, when the pendulum swinging or stay in equilibrium. This paper analyzes the concept of using a vibration absorber for possible energy harvesting. The primary goal is to vibration absorption and the secondary goal is to harvest energy out of the dynamic vibration absorber at the same time.

1. Introduction

The undesirable vibration exists in many engineering constructions. In practice it is very difficult to avoid vibration. It usually occurs because of the dynamic effects or construction problems i.e. manufacturing tolerances, rubbing, rolling, etc. The vibration control in mechanical systems is a crucial problem, by means of which vibrations are suppressed or at least attenuated. However, in some examples the mechanical vibration can be useful. For example, we generate vibration in different aspects: ultrasonic machining (drilling or milling), ultrasonic cleaning baths, rock drills and pile drivers, energy harvesting. The two main aspects of vibrations are: their reduction and their use in practice. In this work we present dynamical vibration absorber which is dedicated to vibration reduction and energy recovery at the same time. Both effects are described by the proposed a new quality indicators.

1.1. Vibration absorbers

The vibration of a mechanical system can be reduced by an additional flexible part (secondary system) tuned to the proper frequency. The system is often called Dynamical Vibration Absorber (DVA) or Mass Damper (MD). The physical phenomenon governing the vibration attenuation involves the energy transfer from the primary system to the vibration absorbers.

The history of the DVA starts with the absorber mass created by a volume of water in the hull of the HMS Inflexible (British ship) in 1883 [1]. The secondary mass the sloshing of the water in the hull acted to cancel the forces from the waves, resulting in the stabilization of the ship's deck so that the guns were able to track targets more effectively. The DVA based on mass-spring structures (without damper) was introduced in 1909 and formally patented by Fraham in 1911 as *"Device for*

Damping Vibration in Bodies" [2]. Since their invention by Frahm, the DVA have been extensively used to mitigate vibrations in various types of mechanical systems. A very well-known practical application is the so-called *Stockbridge damper* [3], widely used to reduce wind-induced vibrations in overhead power transmission lines. In a remarkable engineering application, a 400-ton absorber has been designed for *Citicorp Center* [4], a 274-m high office building in New York City, for suppressing primarily the contribution of the first vibration mode in wind induced oscillations.

Despite of efficacy of the linear vibration absorber its effectiveness is limited to the close neighborhood of a vibration mode, and its inability to damp out several modes of a multi-degree-of-freedom system (MDOF) primary structure and its incapacity to mitigate the vibrations of a nonlinear primary structure [5]. These frequency limitations developments of nonlinear vibration absorbers (NLVAs) which are effective in a larger frequency range due to the frequency-energy dependence of nonlinear oscillations. One of the most popular pendulum vibration absorbers (PVAs) including the autoparametric vibration absorber (AVA) [6], which is probably the earliest passive device that makes use of a purely nonlinear response for vibration suppression [7]. The conception of AVA based on attaching the absorber to the primary system in such a manner that it experiences a parametric base excitation, and therefore, the absorber frequency is tuned around one-half of the troublesome frequency value [8].

In this paper we propose an autoparametric pendulum absorbers with added electromagnetic mounted in the absorber. Such conception allows simultaneously vibration reduction and energy recovery.

1.2. Energy harvesting

Energy Harvesting (EH) is the process by which energy is scavenged from ambient sources and transformed into an utilizable form. The EH is a not new conception. One of the earlier systems used the motion of water in the waterwheel or wind in a windmill as a way of generating useful power (Wright, 2006). Nowadays EH view is the process of extracting small amounts of energy/power from the environment to power small autonomous devices like sensor networks and mobile electronics.

According to their specific harvesting mechanism, vibratory energy harvesters can be classified into the four main categories: Electromagnetic Energy Harvesting (EEH), Magnetostrictive Energy Harvesting (MEH), Capacitive Energy Harvesting (CEH) and Piezoelectric Energy Harvesting (PEH). The EEH harvester based on the magnetic induction generating power through relative motion between a coil of wire and a magnet. Generally, the magnitude of energy harvested depending on the size of harvester system. The PEH harvester builds up a voltage differential across their ends when they are subjected to mechanical deformation. The CEH harvester based on the changing capacitance of vibration-dependent capacitors. The MEH based on magnetostrictive materials, which are a class

of materials which deform physically or strain due to a change in the magnetization state of the material.

Other categories based on achieve relative velocity between the coil and the magnet. Linear harvesters feature the magnet moving along a straight line relative to the coil. Rotational harvesters use magnets mounted on a spinning rotor with stationary coils mounted around the rotor. A pendulum harvesters feature the magnet on a pendulum moving relative to a stationary coil. Beam-based harvesters attach either a magnet or a coil to an elastic beam.

2. Model and problem formulation

2.1. Mechanical model of a vibration absorber

In this section the model of harvest-absorber system is presented. This model has three main elements: the main system (I) which vibration should be eliminate, the absorber-pendulum (II), and electromagnetic harvester device (III). The main system is modelled as simply oscillator composed of mass m_1, a viscous damper (c_1) and a linear spring (k_1). The oscillator is excited in kinematic way by linear spring (k_2) which end is harmonically moved according a periodic function x_0. Scheme of harvest-absorber system in Fig. 1 is shown.
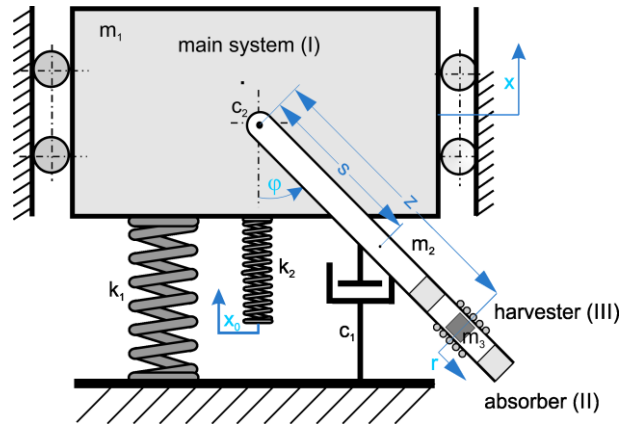
Figure 1. Physical model of harvest-absorber system.

The pendulum (mass m_2 and length l) is attached to the oscillator and can perform swings, rotation and stay in equilibrium. The damping coefficient of the pendulum is denoted as c_2. Such system (the oscillator witch added the pendulum) is called an autoparametric system [9]. It characterized by very complex dynamics including chaotic behavior [10].

To energy recovery the third system is proposed. Inside the pendulum the movable magnet (m_3) is applied. This moving magnet is "suspended" due to magnetic levitation. Detailed description of

magnet in next section is presented. The displacement of magnet denoted as r, the oscillator's displacement assumed as x, and the angular pendulum's displacement φ. The position of magnet according of the pendulum suspension point is z.

2.2. Electromagnetic harvester device

Electromagnetic harvesting operates using Faradays Law of induction; a changing magnetic flux will induce a voltage in a closed loop of conductor. In practice, this is usually accomplished by moving a magnet and a coil relative to each other to produce an AC voltage in the coil. The scheme of electromagnetic harvester device in Fig. 2a is presented. It consists of four main parts: a one fixed magnet, a one adjustable magnet which position can be set, a movable magnet which is suspended in magnetic field by levitation phenomenon and a coil which is wrapped out of the pendulum.
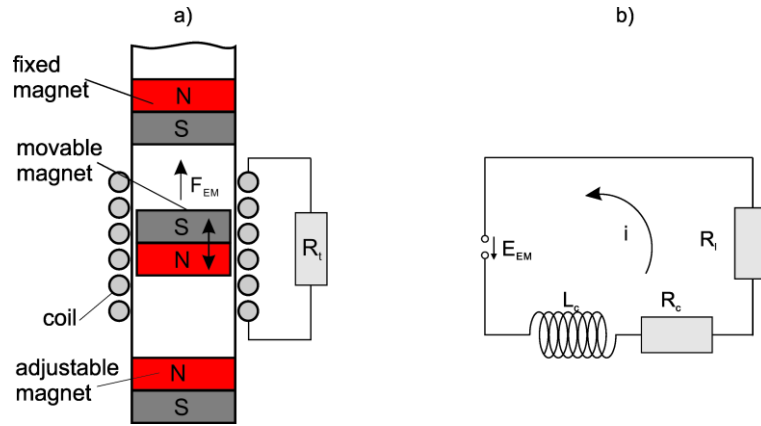
Figure 2. Scheme of the harvester mounted in the pendulum (a) and equivalent electrical circuit (b).

The electrical part is presented as a circuit (Fig. 2b), where E_{EM} is electro-motive force. The electrical part coil is modelled as a series connection of inductance L_c and resistance R_c. The electrical circuit is completed by a load resistor R_l.

Creating a mathematical model we take into account mechanical and electrical parts. Moving magnets induces electromotive force E_{EM} which produces current in the coil. As a result of the interaction current and magnetic field, an electro-dynamic force (Lorentz force) F_{ME} acting on moving elements is generated. The fundamental relations describing electro dynamic force F_{ME} and electromotive force E_M are described by equivalent equations [11]

$$F_{ME} \equiv E_{EM} = \alpha \cdot i = \alpha \cdot \dot{r}, \tag{1}$$

where α is coupling coefficient. The magnetic levitation of moving magnet is replaced by nonlinear spring (k_3). This modification is based on the literature [12], [13], where it is suggested to use an equivalent linear (for small displacement) or nonlinear spring (for larger displacement).

2.3. Equations of motion of a harvest-absorber system

The mathematical model of harvest-absorber system was obtained using classical Lagrange's equations of the second kind and introduced in [14]. The total kinetic energy T of mechanical systems equal

$$T = \frac{1}{2}m_1\dot{x}^2 + \frac{1}{2}m_2\dot{x}^2 + \frac{1}{2}I_0\dot{\varphi}^2 + m_2\dot{\varphi}\dot{x}s\sin\varphi + \frac{1}{2}m_3\dot{r}^2 + \frac{1}{2}m_3\dot{x}^2 + \frac{1}{2}m_3\dot{\varphi}^2(z+r)^2 - \\ -m_3\dot{r}\dot{x}\cos\varphi + m_3\dot{\varphi}(z+r)\dot{x}\sin\varphi, \tag{2}$$

where I_0 means the mass inertial moment. The total potential energy V equal

$$V = m_1gx + m_2g(x+s-s\cos\varphi) + m_3g(x+z-(z+r)\cos\varphi) + \frac{1}{2}k_1x^2 + \frac{1}{2}k_2(x-x_0)^2 + \\ +\frac{1}{2}k_3r^2 + F_{ME}r. \tag{3}$$

The dissipation function is defined as

$$D = \frac{1}{2}c_1\dot{x}^2 + \frac{1}{2}c_2\dot{\varphi}^2. \tag{4}$$

The final equations of motion are obtained in the form:

$$(m_1 + m_2 + m_3)\ddot{x} + (\ddot{\varphi}\sin\varphi + \dot{\varphi}^2\cos\varphi)[m_2s + m_3(z+r)] + m_3(2\dot{r}\dot{\varphi}\sin\varphi - \ddot{r}\cos\varphi) + k_1x + c_1\dot{x} = k_2x_0, \tag{5}$$

$$(I_0 + m_3(z+r)^2)\ddot{\varphi} + (\ddot{x}+g)[m_2s + m_3(z+r)]\sin\varphi + 2m_3\dot{\varphi}\dot{r}(z+r) + c_2\dot{\varphi} = 0, \tag{6}$$

$$m_3\ddot{r} - m_3\ddot{x}\cos\varphi - m_3\dot{\varphi}^2(R+r) + k_3r - m_3g\cos\varphi + \alpha i = 0. \tag{7}$$

The gravity force in equation (5) is not included, because this force is balanced by static preload in springs. The excitation function x_0 (kinetic excitation of the main system) assumed as harmonic, based on laboratory rig

$$x_0 = Q/k_2 \sin\omega t, \tag{8}$$

where ω is the frequency, Q is the amplitude of force excitation.

The equation describing the electrical system can be written in standard form

$$L_c\dot{i} + (R_l + R_c)i = \alpha\dot{r}, \tag{9}$$

where i denotes the generated current. The total resistance denoted as R_t, which is a sum of R_t and R_c. The harvest-absorber system has four degree of freedom: three mechanical and one electrical. To numerical calculation all equation (5)-(9) are investigated.

3. Numerical study

3.1. Bifurcation analysis

The numerical calculations have been done in Matlab software 2015a. The simulation data of mechanical's system has been taken from a laboratory rig [8], [9]: $m_1=0.65kg$, $m_2=0.265kg$, $s=0.0425m$, $k_1=1600N/m$, $k_2=1100N/m$, $c_1=10Ns/m$, $c_2=0.01Nms/rad$, $I_0=0.000496kgm^2$. The electrical device parameters have been adopted from the literature [1, 7]: $m_3=0.02kg$, $z=0.0375m$, $k_3=2000N/m$, $L_c=0.001H$, $R_t=1200\Omega$, $\alpha=3.5N/A$ (or $3.5Vs/m$). The initial conditions are fixed as: $\varphi(0)=\pi/2, \dot{\varphi}(0)=x(0)=\dot{x}(0)=r(0)=\dot{r}(0)=0$. The all numerical simulations have been done nearly the main resonance region ($\omega=41rad/s$).

The bifurcation analysis give us an overview of system dynamics and form of motion. The recovered energy depends on velocity of the magnet. However, the motion of the magnet is coupled with the pendulum and the oscillator motion.
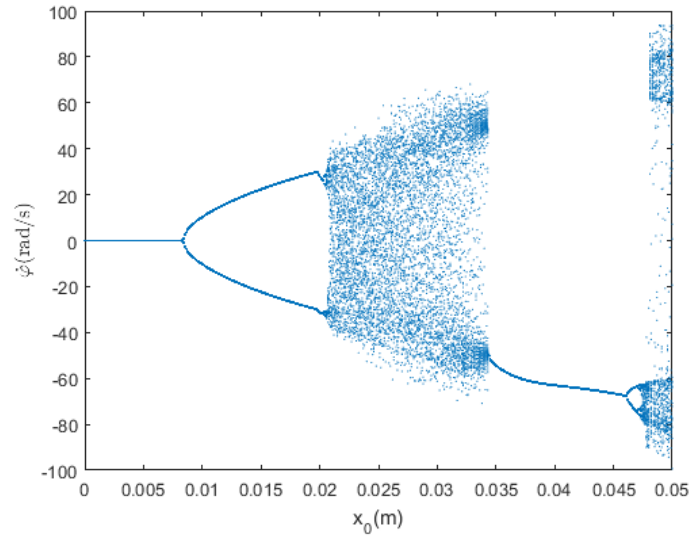
Figure 3. Bifurcation diagram for the absorber (pendulum), for ω=41rad/s.
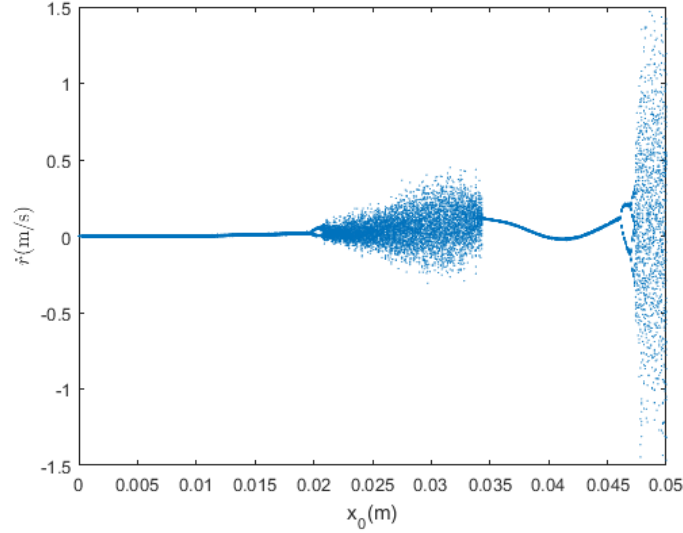
Figure 4. Bifurcation diagram for the harvester (magnet), for ω=41rad/s.

The influence of xo on the pendulum and the magnet behavior are shown in Fig.3 and Fig. 4, respectively. The increase of the kinetic excitation can change solution form: swinging into chaotic behavior, chaos into rotations, and rotation into chaos. Analyzing the results in both diagrams, we can conclude that occur two chaotic regions located for x_o ≈*0.0206m-0.0344m* and x_o ≈*0.0478m-0.05m*. In these regions, velocity of the magnet (and energy harvesting) is higher. After crossing the value of x_o ≈*0.0345*m we observe, that pendulum perform full rotations up to *xo*≈*0.0477m*. It should be highlighted that the pendulum swinging for x_o from *0.0081m to 0.0205m*. Note, that rotation frequency of the pendulum is equals to magnet's frequency. Analysing the obtained results in both diagrams, we can conclude that the dynamics of the system strongly depend on the values of kinetic excitation.

3.2. Vibration absorption and energy harvesting description

To describe electiveness of vibrations absorption and energy recovery two coefficients are proposed. The first is *vibration reduction index* ξ_I, defined as the maximal displacement of the main system with ($\varphi_0 = \pi/2$) and without ($\varphi_0 = 0$) activation of the nonlinear absorber (the pendulum stopped)

$$\xi_1 = abs\left(x_{max}/x_{max}'\right),\tag{10}$$

where x_{max} and x_{max}' mean maximal displacement of the oscillator with and without activation of the absorber, respectively. If the absorber doesn't work, then it poses additional mass of the main system. The smaller value of ξ_1 means higher level of vibration reduction.

The second ξ_2, called the *current gain index*, defines level of recovered energy

$$\xi_2 = abs\ i_{max}\ /\ i_{max}'\ , \tag{11}$$

where i_{max} and i_{max}' describe maximal recovered current for the system with and without activation of the absorber, respectively. Its higher value means greater energy harvesting.

The two parameter analysis ξ_1 (blue line) and ξ_2 (orange line) versus x_o is shown in Fig.5. The smaller value of ξ_1 is observed for nearly entry and exit in the first chaotic zones. This means, that the swinging and rotation regions are most appropriate to the dynamic vibration elimination. The maximal reduction of vibration by the absorber equals about 40 percentages. The most dangerous region for vibration reduction is chaos.
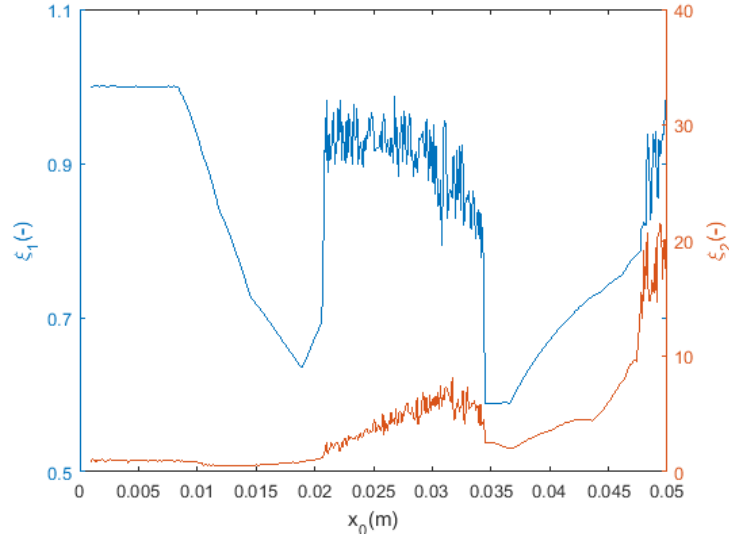
Figure 5. Influence of x_0 on the vibration absorption effect (blue line) and energy harvesting (orange line), for $\omega=41$rad/s.

For ξ_2, we observe, that the most promising regions from energy harvesting point of view are chaotic zones (especially the second chaotic zones) and rotation area. In these regions, the value of current gain index is a several times higher. Please note, that the pendulum swings (x_o from *0.0081m* to *0.0205m*) cases a slight decrease of ξ_2, compared to semi-trivial solution (region where the pendulum stopped x_o from *0* to *0.008*). This is due by appearing force reaction between the magnet and the pendulum.
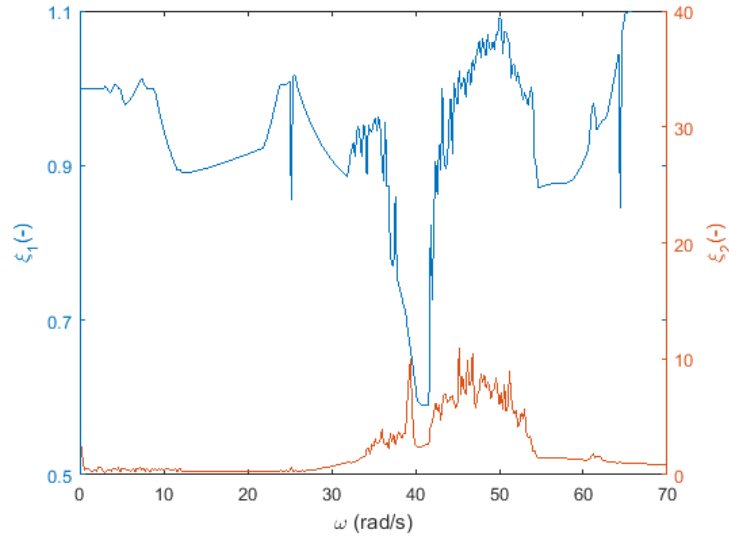
Figure 6. Influence of ω on the on vibration absorption effect (blue line) and energy harvesting (orange line), for $x_o=0.035m$.

The influence of the frequency of excitation (ω) on vibration absorption (blue line) and energy recovery (orange line) is shown in Fig. 6. The high energy harvesting level is observed nearly resonance region ω≈30-55rad/s. Note, that in this region the vibration absorption is observed, too. However, in resonance region increase of vibration level (ξ_1) can apper.

4. Conclusions

This work comprises of problem vibration reduction and energy recovery at the same time. We propose the harvest-absorber model, based on classical oscillator-pendulum system with added harvester device. The harvester causes that system is much more complicated and has a four degree of freedom.

The obtained results shows, that chaotic region is most promising for energy harvesting. Especially, the second chaotic region looks promising for EH. In this region, angular velocity of the pendulum is about two times higher compared to the first chaotic region (Fig.3), but current gain index is four time higher (Fig.5). However, in such region the vibration absorption is poor.
Seeking a compromise between EH and DVA can be note, that in the small part of rotation region (x_o≈0.034-0.037) occurs satisfactory vibrations elimination and inconsiderably increase of EH.

The next step of the investigations is experimental verification and optimization to find compromise between DVA and EH.

Acknowledgments

References

[1] Hunt, J.B. *Dynamic Vibration Absorbers*. Mechanic Engineering Publications LTD, London, 1979.

[2] Fraham, H. *Device for Damping Vibration in Bodies*. United States, 1911.

[3] Barbieri N., Barbieri R. Dynamic Analysis of Stockbridge Damper. *Advances in Acoustics and Vibration*, vol. 2012, Article ID 659398, 2012.

[4] Steffen V.Jr. and Rade D.A. Dynamic vibration absorber. *Encyclopedia of Vibration*, 9–26, Academic Press, 2001.

[5] Regis V. Tuning *Methodology of Nonlinear Vibration Absorbers Coupled to Nonlinear Mechanical Systems*. Ph.D. thesis, University of Liège, 2010, Gaëtan Kerschen.

[6] Haxton R.S. and Barr A.D.S., The autoparametric vibration absorber, *ASME Journal of Engineering for Industry* 94, 1972, 119–125.

[7] Shaw S.W. and Balachandran B. A review of nonlinear dynamics of mechanical systems in year 2008. *Journal of System Design and Dynamics* 2, 2008, 611–640.

[8] Kecik K. Dynamics and control of an autoparametric system. *International Journal of Non-linear Mechanics*, 70, 2015, 63-72.

[9] Warminski J., Kecik K. Instabilities in the main parametric resonance area of mechanical system with a pendulum. *Journal of Sound Vibration* 332, 2009, 612-628.

[10] Kecik K., Mitura A., Sado D., J. Warminski. Magnetorheological damping and semi-active control of an autoparametric vibration absorber. *Meccanica* 49(8), 2014, 1887-1900.

[11] Owens B.A.M., Mann B.P. Linear and nonlinear electromagnetic coupling models in vibration-based energy harvesting. *Journal of Sound and Vibration* 331(4) , 2012, 922-937.

[12] Foisal A.R., Hong C., Chung G.S. Multi-frequency electromagnetic energy harvester using a magnetic spring cantilever. *Sensor and Actuators A: Physical* 182, 2012, 106-113.

[13] Mann B.P,, Sims N.D. Energy harvesting from the nonlinear oscillations of magnetic levitation. *Journal of Sound and Vibration* 319(1-2) , 2009, 515-530.

[14] Mitura A., Kecik K., Warminski J., Jarzyna W., Lenci S. A numerical study of an autoparametric system with electromagnetic energy harvester. *Proceedings of the ECCOMAS Thematic Conference on Multibody Dynamics* 2015, 609-615.

Krzysztof Kecik, PhD: Lublin University Of Technology, Department of Applied Mechanics, Nadbystrzycka 36, 20-618 Lublin, Poland (*k.kecik@pollub.pl*). The author gave a presentation of this paper during one of the conference sessions.

Andrzej Mitura, PhD: Lublin University Of Technology, Department of Applied Mechanics, Nadbystrzycka 36, 20-618 Lublin, Poland (*a.mitura@pollub.pl*).

Dynamics of a double-wing aerodynamic pendulum in a flow (STA128-15)

Liubov Klimina, Anna Masterova, Vladislav Bekmemetyev, Boris Lokshin,
Andrey Holub, Ching-Huei Lin

Abstract: A problem of motion of a double-link aerodynamic pendulum is considered. Each link is connected with a wing that interacts with a flow. A dynamic model of the system is built. Dependences of equilibrium positions on the system parameters such as wing pitch angles and a ratio of areas of the wings are obtained. The problem of stability of equilibrium positions of the system is studied. In some special cases the regions of stability of equilibrium positions in the parameter space are described. It is shown that all equilibrium positions are unstable in a certain range of parameter values. Undamped oscillations arise that can be used for converting medium flow energy into electrical energy. Numerical and analytical study of undamped oscillations behavior is conducted depending on the ratio of the wing areas.

1. Introduction

One of urgent tasks of wind-power and hydro-power engineering is the development of new types of power plants that convert the energy of the flow into mechanical one, while in comparison with the existing power plants, it is desirable to solve the following engineering tasks: to develop a mechanism that does not require to be aligned with the flow direction, as well as to develop a device using the oscillatory motion of blades.

Specifically, the first property is possessed by, for example, the Darrieus-type wind turbine; the development of the plants possessing the second property had been recently begun by the Institute of Mechanics of MSU [1].

This work represents the next stage of the examination of the system, which can later become a prototype of the power plant, which possesses both of the said properties.

System of a similar type was previously considered in [2]. Also a prototype was constructed and tested in the wind tunnel of the Institute of Mechanics of MSU. The test results, as well as analytical conclusions [2], showed the possibility of using such system as wind-receiving device.

The main differences between the system discussed in this paper and in [2] are the presence of an additional wing and the possibility of varying the setting angles of both wings.

Analogously to [3], the presence of additional wings can be used in such system to increase the aerodynamic torque at the stage of spin-up of a wind-receiving element.

2. Statement of the problem

We consider a wind-receiving device representing a double pendulum with two blades in a steady horizontal air flow.

2.1. Reference frame, kinematics, inertia characteristics

We consider the motion of a pendulum with two links in the horizontal plane Oxy (Fig. 1). The pendulum is a system of two solid bodies, each of which consists of a holder OO_1 (O_1O_2) and a rigidly attached wing of a mass m_1 (m_2), respectively, at a setting angle θ_1 (θ_2). The first link of the pendulum rotates about a fixed axis O, the second link is connected to the first one in the point O_1 by the joint. The wings are symmetrical flat plates interacting with the medium flow. The flow velocity is constant. Let J_O be a moment of inertia of the first body relative to the axis of rotation, J_G - moment of inertia of the second body relative to its center of mass G. Assume that the aerodynamic load can be reduced to forces directed through the centers of pressure of plates (C_1 and C_2, respectively).
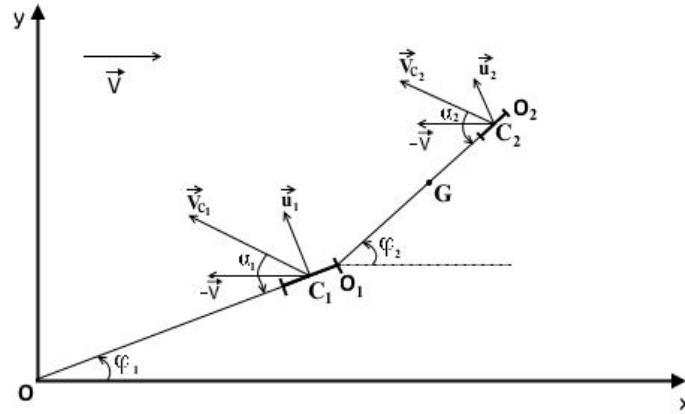
Figure 1. The case $\theta_1 = 0$, $\theta_2 = 0$.

Let $OO_1 = l$, $O_1G = l_G$, $OC_1 = l_{C1}$, $O_1C_2 = l_{C2}$.

Orientation of the pendulum is described by two angles: φ_1, the angle between the axis Ox and the first link, φ_2, the angle between the axis Ox and the second link. To account for the influence of the medium, introduce the following angles that are called angles of attack: α_1 - angle between the velocity $\vec{V}_{C_1}$ of the point C_1 relative to the flow and the first plate, α_2 - angle between the velocity

$\vec{V}_{C_2}$ of the point C_2 relative to the flow and the second plate. The introduced variables satisfy the following kinematic relations:

$$\begin{cases} V_{C_1}\cos(\alpha_1 - \theta_1) = V\cos\varphi_1 \\ V_{C_1}\sin(\alpha_1 - \theta_1) = V\sin\varphi_1 + l_{C_1}\dot{\varphi}_1 \\ V_{C_2}\cos(\alpha_2 - \theta_2) = V\cos\varphi_2 + l\dot{\varphi}_1\sin(\varphi_1 - \varphi_2) \\ V_{C_2}\sin(\alpha_2 - \theta_2) = V\sin\varphi_2 + l_{C_1}\dot{\varphi}_1\cos(\varphi_1 - \varphi_2) + l_{C_2}\dot{\varphi}_2 \end{cases}$$ (1)

2.2. Description of external forces

During the movement of the pendulum we consider only the aerodynamic forces, neglecting the influence of friction. We represent the aerodynamic force applied to the plates at their centers of pressure C_1, C_2, as the sum of resistance force $\vec{D}$ and lift force $\vec{L}$. According to the quasi-static model of aerodynamic effect ([4, 5]), these forces are defined by the following relations:

$$\begin{cases} \vec{D}_1 = -C_D(\alpha_1)\dfrac{\rho V_{C_1}S_1}{2}\vec{V}_{C_1}; \\ \vec{L}_1 = C_L(\alpha_1)\dfrac{\rho V_{C_1}S_1}{2}\left[\vec{e}_z, \vec{V}_{C_1}\right]; \end{cases} \qquad \begin{cases} \vec{D}_2 = -C_D(\alpha_2)\dfrac{\rho V_{C_2}S_2}{2}\vec{V}_{C_2}; \\ \vec{L}_2 = C_L(\alpha_2)\dfrac{\rho V_{C_2}S_2}{2}\left[\vec{e}_z, \vec{V}_{C_2}\right]. \end{cases}$$ (2)

Where ρ – density of the medium, S_1 (S_2) – characteristic area of the first (second) plate, $\vec{e}_z$ – unit vector rising vertically. In the analytical calculations for small angles of attack we assume $C_D(\alpha) = C_{D0} + \underline{O}(\alpha^2)$, $C_L(\alpha) = C_{L1}\alpha + \underline{O}(\alpha^3)$ – coefficients of the corresponding forces. Note that for any kind of an airfoil the following inequalities are satisfied: $C_{D0} > 0$, $C_{L1} > 0$.

2.3. Dynamic equations of the system

We use angles φ_1 and φ_2 as generalized coordinates; than, $\dot{\varphi}_1$ и $\dot{\varphi}_2$ - corresponding generalized velocities. We designate by dash the derivative with respect to the non-dimentional time $\tau = Vtl^{-1}$. We write down the equations of motion of the system in the form of Lagrange equations of the second kind:

$$\begin{cases} \varphi_1'' + b_1\left[\varphi_2''\cos\ \varphi_2 - \varphi_1\ - (\varphi_2')^2\sin\ \varphi_2 - \varphi_1\ \right] = \\ = -\chi_1\ C_D(\alpha_1)\sigma v_1\left[a_1\varphi_1' + \sin\varphi_1\right] + C_L(\alpha_1)\sigma v_1\cos\varphi_1 + \\ + C_D(\alpha_2)v_2\left[\varphi_1' + a_2\varphi_2'\cos(\varphi_2 - \varphi_1) + \sin\varphi_1\right] + \\ + C_L(\alpha_2)v_2\left[a_2\varphi_2'\sin(\varphi_2 - \varphi_1) + \cos\varphi_1\right]\ ; \\ \varphi_2'' + b_2\left[\varphi_1''\cos\ \varphi_2 - \varphi_1\ + (\varphi_1')^2\sin\ \varphi_2 - \varphi_1\ \right] = \\ = -\chi_2 v_2\ C_D(\alpha_2)\left[a_2\varphi_2' + \varphi_1'\cos(\varphi_2 - \varphi_1) + \sin\varphi_2\right] + \\ + C_L(\alpha_2)\left[\cos\varphi_2 - \varphi_1'\sin(\varphi_2 - \varphi_1)\right] \end{cases} \tag{3}$$

Here we introduced the following notations:

$$a_1 = l^{-1}l_{C_1}\ ,\ a_2 = l^{-1}l_{C_2}\ ,\ k = l_{C_2}^{-1}l_G\ ,\ \sigma = a_1 S_1 S_2^{-1}\ ;$$

$$\chi_1 = \frac{l^3\rho S_2}{J_O + m_2 l^2}\ ,\ \chi_2 = \frac{l^3 a_2\rho S_2}{J_G + m_2 l^2 a_2^2 k^2}\ ,\ b_1 = \frac{m_2 k a_2 l^2}{J_O + m_2 l^2}\ ,\ b_2 = \frac{m_2 k a_2 l^2}{J_G + m_2 l^2 a_2^2 k^2}\ ;$$

$$v_1 = \left\|(-a_1\varphi_1'\sin\varphi_1 - 1, a_1\varphi_1'\cos\varphi_1)\right\|,\ v_2 = \left\|(-\varphi_1'\sin\varphi_1 - a_2\varphi_2'\sin\varphi_2 - 1, \varphi_1'\cos\varphi_1 + a_2\varphi_2'\cos\varphi_2)\right\|.$$

The kinematic relations (1) in non-dimensional variables take the following form:

$$\begin{cases} \left\| -a_1\varphi_1'\sin\varphi_1 - 1, a_1\varphi_1'\cos\varphi_1\ \right\|\cos(\alpha_1 - \theta_1) = \cos\varphi_1 \\ \left\| -a_1\varphi_1'\sin\varphi_1 - 1, a_1\varphi_1'\cos\varphi_1\ \right\|\sin(\alpha_1 - \theta_1) = \sin\varphi_1 + a_1\varphi_1' \\ \left\| -\varphi_1'\sin\varphi_1 - a_2\varphi_2'\sin\varphi_2 - 1, \varphi_1'\cos\varphi_1 + a_2\varphi_2'\cos\varphi_2\ \right\|\cos(\alpha_2 - \theta_2) = \\ = \cos\varphi_2 + \varphi_1'\sin(\varphi_1 - \varphi_2) \\ \left\| (-\varphi_1'\sin\varphi_1 - a_2\varphi_2'\sin\varphi_2 - 1, \varphi_1'\cos\varphi_1 + a_2\varphi_2'\cos\varphi_2\ \right\|\sin(\alpha_2 - \theta_2) = \\ = \sin\varphi_2 + a_1\varphi_1'\cos(\varphi_1 - \varphi_2) + a_2\varphi_2' \end{cases} \tag{4}$$

Equations (3) combined with (4) form a closed system.

3. Equilibrium conditions

We write down the equations of balance for the obtained system (3):

$$\sigma\ C_D(\alpha_1)\sin\varphi_1 + C_L(\alpha_1)\cos\varphi_1\ + C_D(\alpha_2)\sin\varphi_1 + C_L(\alpha_2)\cos\varphi_1 = 0\ , \tag{5}$$

$$C_D(\alpha_2)\sin\varphi_2 + C_L(\alpha_2)\cos\varphi_2 = 0\ . \tag{6}$$

Note that in equilibrium positions the formulae of angles of attack will take a relatively simple form: $\alpha_1 = \varphi_1 + \theta_1\ ,\ \alpha_2 = \varphi_2 + \theta_2\ .$

Fig. 2,3 show the curves that represent numerical solutions of the equations (5) and (6) in some special cases. The intersection of curves, where both conditions of equilibrium are satisfied corresponds to the stationary solutions of the system.
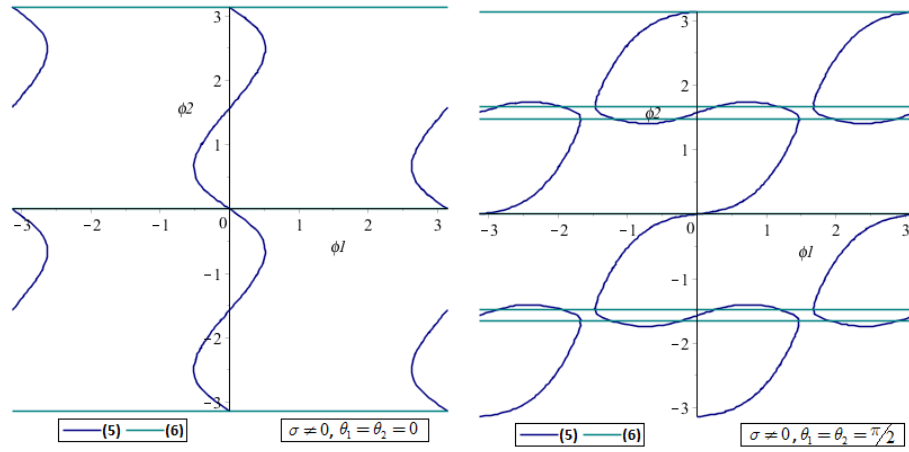
Figure 2. Geometric interpretation of the conditions of equilibrium.

3.1. The case of one wing

Let's examine the case $\sigma = 0$, which corresponds to the absence of wing located closer to the axis Oz.
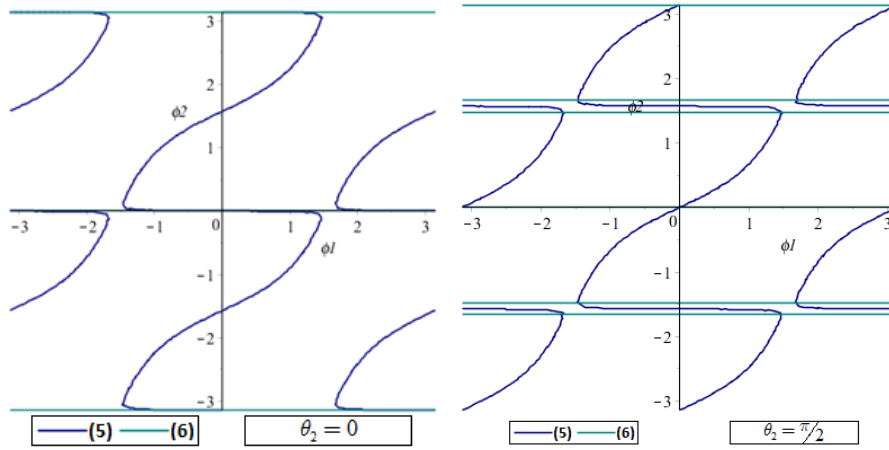
Figure 3. Geometric interpretation of the conditions of equilibrium in the case of $\sigma = 0$.

In the case of $\sigma = 0$ the relationship between steady values of angles φ_1^*, φ_2^* and parameter θ_2 (the only constructive parameter remaining in the conditions of equilibrium) can be analytically obtained from equations (5) and (6) (Fig. 4):

$$\varphi_1^* = \begin{vmatrix} -\arctan\left(\dfrac{C_L(\alpha_2)}{C_D(\alpha_2)}\right) \\ \pi - \arctan\left(\dfrac{C_L(\alpha_2)}{C_D(\alpha_2)}\right) \end{vmatrix}; \qquad \varphi_2^* = \varphi_1^* + n\pi, \quad n \in \mathbb{Z}; \tag{7}$$

$$\theta_2 = \alpha_2 + \arctan\left(\dfrac{C_L(\alpha_2)}{C_D(\alpha_2)}\right). \tag{8}$$

In the expressions (7), (8) the instantaneous angle of attack can take any value from $-\pi$ to π and represents a variable parametrizing the relation between the pitch angle of the single wing and steady-state values of the angles of the pendulum links.
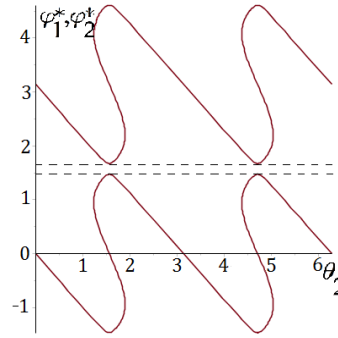
Figure 4. Relation between the steady-state values of the angles of links from the pitch angle θ_2 in the case of absence of the first wing (i.e. when $\sigma = 0$).

Thus, when $\sigma = 0$ angles φ_1^* and φ_2^* are either equal or differ by π. It means that the pendulum in a steady position is either fully extended or folded, and the resultant aerodynamic force is directed along the holders of the pendulum. Specifically, when $\theta_2 = 0$ we receive $\varphi_1^*, \varphi_2^* \in (0,0), (0,\pi), (\pi,0), (\pi,\pi)$.

There is a range of values φ_1^*, φ_2^* (Fig. 4), that do not become positions of equilibrium under any given θ_2. It is a certain range of angles in the vicinity of $\pm\pi/2$, where the lift force can become equal to zero. The uncompensated resistance force pushes the pendulum out of such positions.

3.2. The case of two wings

Let $\sigma \neq 0$. Direct substitution displays that when $\theta_1 = \theta_2$ steady-state values $\varphi_1^*, \varphi_2^* \in (0,0),(0,\pi),(\pi,0),(\pi,\pi)$ are preserved. When $\theta_1 = \theta_2 = 0$ no other positions of equilibrium appear (we don't consider case of $\sigma < 0$). In a range of setting angles $\theta_1 = \theta_2 \neq 0$ presence of additional positions of equilibrium is possible, as illustrated, for example, in Fig. 2b.

4. Investigation of the stability of equilibrium in the case of $\theta_1 = \theta_2 = 0$

Let's examine the case of $\theta_1 = \theta_2 = 0$.

We investigate the character of stability of solutions $\varphi_1^*, \varphi_2^* \in (0,0),(0,\pi),(\pi,0),(\pi,\pi)$ in the first approximation. Using Hurwitz criterion, we see that the equilibrium positions $\varphi_1^*, \varphi_2^* \in (0,\pi),(\pi,0),(\pi,\pi)$ are unstable for any admissible values of the parameters, and the necessary and sufficient conditions for the asymptotic stability of the equilibrium $\varphi_1^*, \varphi_2^* = 0,0$ have that form:

$$\begin{cases} p_2 = \left(C_{D0} + C_{L1} \right)^2 \sigma a_1 a_2 \chi_1 \chi_2 + \left(C_{D0} + C_{L1} \right) \left(\sigma \chi_1 + \chi_2 \right) + \left(C_{D0} - b_2 C_{L1} \right) \chi_1 > 0; \\ \Delta_3 = p_1(p_2 p_3 - p_1 p_4) - p_0 p_3^2 > 0. \end{cases} \tag{9}$$

Here, the following designations are used:

$$p_0 = 1 - b_1 b_2;$$
$$p_1 = (C_{D0} + C_{L1})(\chi_1 a_1 \sigma + \chi_1 + a_2 \chi_2 - b_1 \chi_2 - a_2 b_2 \chi_1);$$
$$p_3 = \chi_1 \chi_2 \left[\sigma \left(a_1 + a_2 \right) \left(C_{D0} + C_{L1} \right)^2 + C_{L1} \left(C_{D0} + C_{L1} \right) \left(a_2 + 1 \right) \right];$$
$$p_4 = \chi_1 \chi_2 \left[\sigma \left(C_{D0} + C_{L1} \right)^2 + C_{D0} \left(C_{D0} + C_{L1} \right) \right].$$

The character of stability of the equilibrium $\varphi_1^*, \varphi_2^* = 0,0$ depends on the constructive parameters, but does not depend on the value of the wind speed (see (9)).

If at least one of the coefficients p_2 and Δ_3 is negative, than equilibrium $\varphi_1^*, \varphi_2^* = 0,0$ is unstable.

Coefficients p_0, p_1, p_3, p_4 are positive with all the possible values of parameters of the model. Coefficient p_2 can be both positive and negative depending on the values of parameters of the model. Specifically, when value of the coefficient b_2 is sufficiently large, coefficient p_2 will be negative, and

therefore all four existing equilibriums will be unstable. In the case of instability of all the possible equilibrium positions the undamped motions appear in the system (regardless of the direction of the wind speed). Such oscillations of two-link pendulum can be used to convert the flow energy into mechanical or electrical energy.

We conduct a more detailed numerical study of the conditions (9), depending on the parameters σ and k for fixed values of the other parameters: $S_2 = 0.02m^2$, $l = 0.4m$, $a_1 = 1$, $a_2 = 1.8$, $\rho = 1.2kg/m^3$, $m_2 = 0.2kg$, $J_O = 0.01kgm^2$, $J_G = 0.005kgm^2$, $C_{D0} = 0.01$, $C_{L1} = 5$, $\theta_1 = \theta_2 = 0$ (fig. 5).
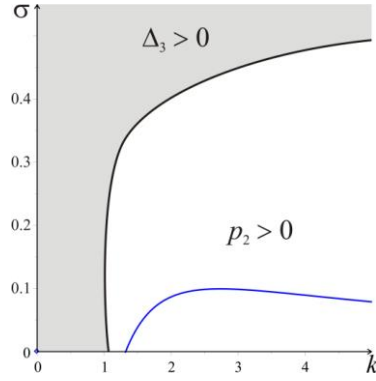
Figure 5. The domain (grey color) of asymptotic stability of the equilibrium (0,0).

From Fig. 5 we see that for any value of the parameter σ there exists sufficiently large k, with which the equilibrium position $\varphi_1^*, \varphi_2^* = 0,0$ becomes unstable.

5. Numerical integration of equations of motion

The results of numerical integration allowed us to confirm the obtained analytical results. Fig. 6 shows an example of numerical integration of the trajectory of the system for the set of parameters that corresponds to the point $k, \sigma = 2, 0.004$ of the Fig. 5 (all equilibriums are unstable, so undamped oscillations should present) with $V = 3m/s$ and with following initial phase speeds: $\varphi_1' = 0.2$ и $\varphi_2' = 0.1$. In numerical calculations for simplicity we use the following formulae: $C_D(\alpha) = \sin^2 \alpha + 0.01$, $C_L(\alpha) = \sin 2\alpha$.
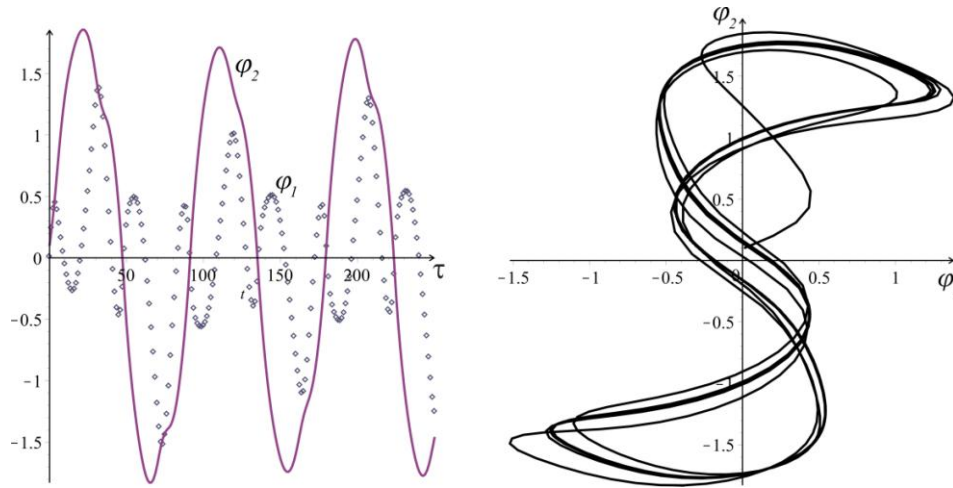
Figure 6. An example of numerical integration of equations of motion.

Numerical integration confirms the possibility of presence of undamped oscillations in the system. It is shown that deflection angles of both holders from the flow direction can vary in a limited range, which indicates of a possibility of using this two-link pendulum as a wind-receiving element of a power plant of nonrotational type. The advantage of such systems is a possibility of additional isolation of working parts from the influence of environment.

6. Conclusions

The paper considers the problem of motion of two-link aerodynamic pendulum, each link of which contains a wing attached to it.

A mathematical model that describes dynamics of such pendulum is built. The equations of motion are devised. The relation between equilibrium positions of the system and the parameters such as pitch angles of the wings and wing area ratio is described. The problems of stability of stationary modes of the system are examined. Regions of stability of the obtained steady-state solutions in a parameter space are described in some special cases. That led to the conclusion that it is possible to select the parameters in such a way that all the equilibrium positions of the system are unstable. Thus, the undamped oscillations are possible in the system which can be used to convert the energy of the wind flow into electrical energy. The numerical integration of the system was conducted, which revealed some specific features of its behavior.

Acknowledgments

References

[1] Patent RU 2 447 320 C2. (Device for renewable energy conversion) Proprietor: Institute of Mechanics of Lomonosov Moscow State University. 5p. 2012.

[2] Dosaev, M., Seliutsky, Yu. On dynamics of double pendulum in airflow. *Proceedings of International conference ENOC-2008, Saint Petersburg, Russia*. 2008. 6 p.

[3] Masterova, A.A., Samsonov, V.A. On the question of optimization of the blade shape for a small-scale wind turbine. *Method of Lyapunov funtions and its applications MFL-2014. Abstracts of International conference*. 2014. p.59.

[4] Dosaev, M.Z., Kobrin, A.I., Lokshin, B.Ya, Samsonov, V.A., Seliutsky, Yu.D. *Constructive theory of small-scale wind power generators. Parts I-II.* Moscow University Press, Moscow, 2007.

[5] Lokshin, B.Ya, Samsonov, V.A. *The problem of motion of a body in a resisting medium. Qualitative analysis.* Moscow University Press, Moscow, 2012.

Liubov Klimina, PhD: Lomonosov Moscow State University, Institute of Mechanics, Michurinsky prosp.,1, 119192, Moscow, Russia (*klimina@imec.msu.ru*).

Anna Masterova, B.A. (M.Sc. student): Lomonosov Moscow State University, Institute of Mechanics, Michurinsky prosp.,1, 119192, Moscow, Russia (*masterovaanya@yandex.ru*).

Vladislav Bekmemetyev, B.A.: Lomonosov Moscow State University, Institute of Mechanics, Michurinsky prosp.,1, 119192, Moscow, Russia (*winter.in.head@gmail.com*). The author gave a presentation of this paper during one of the conference sessions.

Boris Lokshin, Associate Professor: Lomonosov Moscow State University, Institute of Mechanics, Michurinsky prosp.,1, 119192, Moscow, Russia (*blokshin@imec.msu.ru*).

Andrey Holub, M.Sc. (Ph.D. student): Lomonosov Moscow State University, Institute of Mechanics, Michurinsky prosp.,1, 119192, Moscow, Russia (*andrey_90_gektor@mail.ru*).

Ching-Huei Lin, Associate Professor: Chien Hsin University of Science and Technology, No.229, Jianxing Rd., Zhongli Dist., Taoyuan City 32097, TAIWAN (*chlin@gapps.uch.edu.tw*). The author gave a presentation of this paper during one of the conference sessions.

Research on dynamics of car suspension system in MSC.Adams software
(CON276-15)

Łukasz Konieczny, Rafał Burdzik, Jan Warczek

Abstract: The paper presents results of investigation on dynamics of car suspension system. The research was conducted in MSC.Adams software. The Adams/Car module enables designing of subsystems and simulation research of individual elements of suspension system. The paper presents result of investigation on the impact of vibration damping on vehicle dynamic in an Adams Car Ride module. The Multi Body System (MBS) of Fiat Seicento was designed. The examined system of the complete vehicle consists of 49 kinematic degrees of freedom. There are 42 gruebler count, 40 moving parts, 6 cylindrical joint, 9 revolute joint, 4 spherical joints, 5 translational joint, 2 convey joint, 8 fixed joint, 4 hook joint, 1 inline primitive joint, 1 inplane primitive joint, 5 perpendicular primitive joint, 10 motions and 2 couplers. Simulation research in Adams/Car/Ride module allows testing vehicle dynamics forcing by excitation of the plate of test stand. Virtual model of the vehicle was set on four servo-motors exciters. It allows using different combination of excitation of individual actuators. In the previous research the damping characteristics of the front shock absorbers were determined on special test stand. Thus the simulations was conducted for shock absorbers in different technical conditions (for new one and shock absorber with 50% loss of oil). As the results vertical, lateral and angular vibrations were determined. The results of preliminary tests were targeted at describing precise estimates of the technical condition of the shock absorber built in the vehicle.

1. Introduction

The ADAMS software (MSC.Software) is a commercial software for building a multibody structural models. Modular design allows using of applications with different focuses, such as rail, aviation and motor vehicles. Models with a large number of freedom degrees of the components are built with mass concentrated on the assumption that the system is composed of a rigid (or deformable) bodies combined in a specific way (spherical, sliding, rotary connection), moving under the action of the forces and moments of different types (concentrated or distributed forces, the contact forces). Complex multibody systems are automatically generated by the Lagrange equations of motion of the second kind in absolute coordinates. Integral procedures used to solve differential-algebraic equations include multistep algorithms with variable row and a variable-and fixed-step and one-step algorithms. The first one comprises multi-step algorithms of variable order as well as those of variable and

317

constant step. The second group comprises one-step algorithms, and among them the ADAMS software applies the Runge-Kutta-Fehleberga (RFK45) method. The Adams/Car module enables building and simulation-based examination of individual car subsystems such as, for instance, the suspension, steering or driving system as well as their combinations forming a complete car. The program contains an extensive library of structural solutions applied in cars. The geometry and relationship data of individual components stored in libraries, and software operation on a standard user level can be brought down to defining positions of constraints in space. The software is compatible with various CAD programs, thus enabling import of elements created in other applications. Professional software allows to develop complex models with a high degree of complexity and solve various problems (dynamic, thermal, etc.). These models require an appropriate definition of the necessary parameters (mass, stiffness, damping) as well as material parameters .The simulation tests significantly accelerate and reduce the cost for solving complex set of issues associated with the vibration diagnostics of machines and devices [2,9,10-12,16-19,22].

2. Full car model

The study was conducted for the vehicle model of Fiat Seicento. The front suspension subsystem model consist of: 19 moving parts (not included ground), 3 cylindrical joints, 4 revolute joints, 4 spherical joints, 2 convel joints, 8 fixed joints, 2 hooke joint, 1 inplane primitive joint, 5 perpendicular primitive joint, 10 motions and 2 couplers. The view of McPherson front suspension system is presented in Fig.1
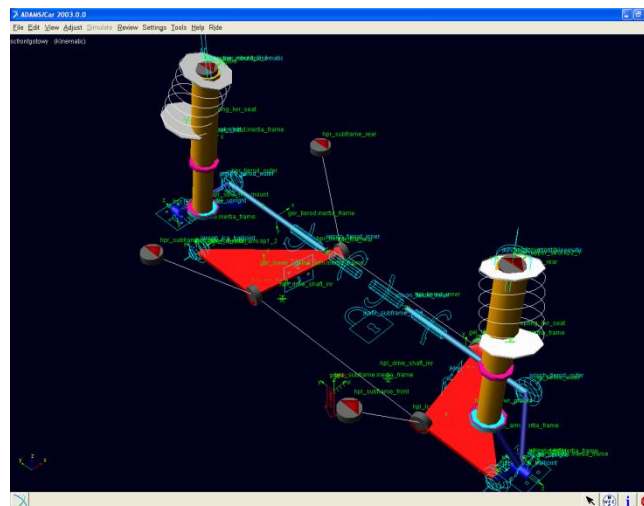
Figure 1. View of McPherson front suspension

Suspension subsystem model of was placed on the plates forcing displacement of the specified range. Examples of the changes in angles (camber, caster and kingpin inclination) as a function of plate displacement are presented in Fig.2. The values obtained during the simulation are consistent with the technical data of the vehicle which confirms the correct kinematic parameters of the model.
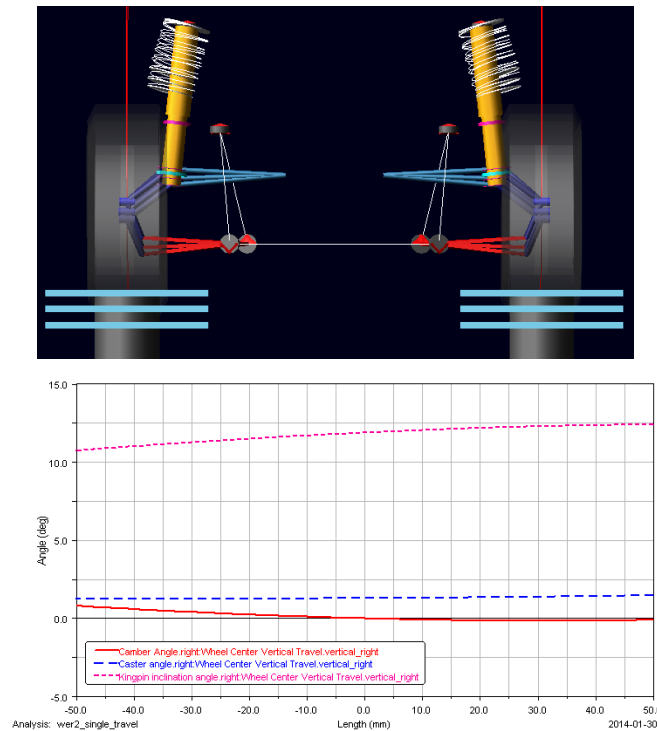
Figure 2. Subsystem on a test stand and sample angle changes (camber, caster and kingpin inclination) as a function of plate displacement.

Adams/Car /Ride module used in simulation allows to test vehicle dynamics forcing the position of the plate of the test stand. Virtual model of the vehicle was set on four servo-motors. They can control any combination of excitation of individual actuators (displacement and amplitude, phase between extortion, etc.) and determine all kinds of vibration (vertical, lateral, angular). The study was conducted for selected parameters of the test rig. The model has been identified. View of full car model on rig test stand and real car on test platform is presented on Fig. 3. The results obtained during the test of kinematic harmonic extortion on the wheels of the vehicle and the simulation model are shown in Figures 4 and 5.
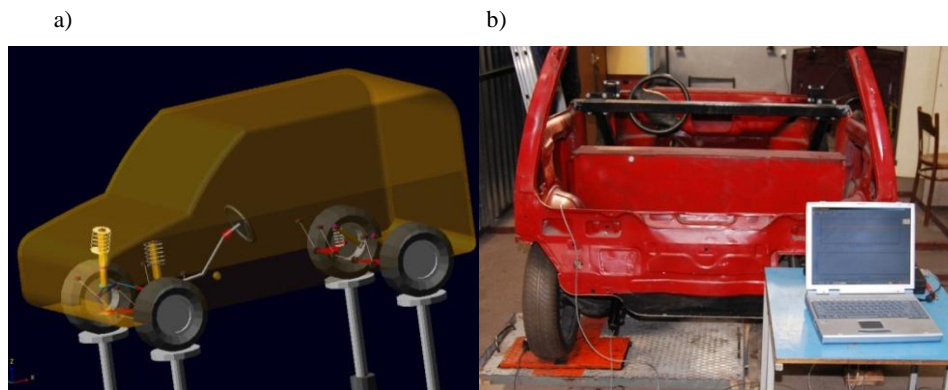
Figure 3. Fiat SC on test stand a) model, b) real car

a)   b)
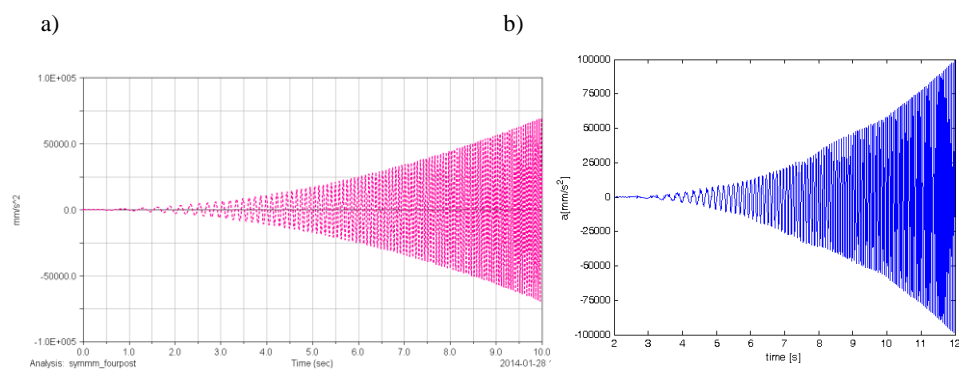
Figure 4. Acceleration on the plate: a) the simulation research (b) - the measurement of the test stand

a)   b)
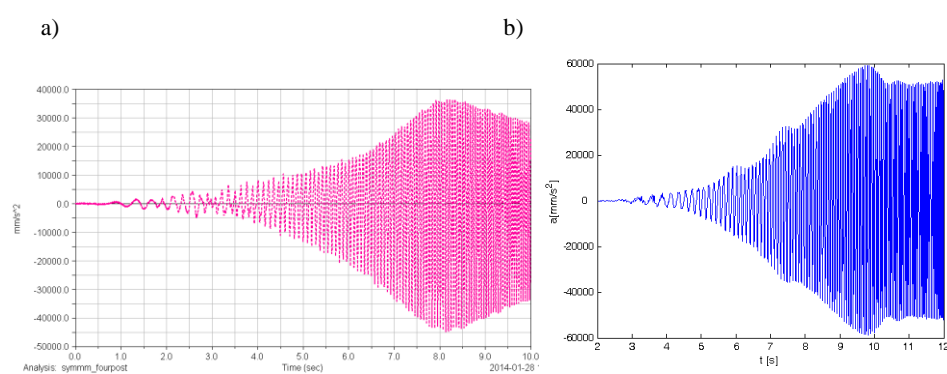
Figure 5. Acceleration on the wheel a) the simulation research (b) - the measurement of the test stand

The qualitative comparison of the received acceleration time charts of simulation model of the vehicle in the Adams / Car (Fig.4a and Fig. 5a) and the time charts of accelerations obtained from experimental studies on the test stand (Fig. 4b and Fig. 5b) confirms the correct identification of the model. The small quantitative differences (differences in the amplitudes of acceleration) may result from the adoption of the theoretical values for some parameters (moments of inertia of the wheels and whole vehicle, location of the center of gravity of the body).

3. Results of research

The technical condition of the shock can be examined on indicator shock absorber test stand. Such an examination can plot the work graph of the shock absorber (force versus displacement) as well as the velocity graph (force versus linear velocity) and determine damping characteristics (Fig.6).

Determination of the damping characteristics can be achieved in two ways. In the first one, the basis of designated force-displacement diagram at a constant stroke and variable angular velocity. In the second approach, the angular velocity is constant and the value of the stroke is changed [1,3-8,13-15, 20,21,23].
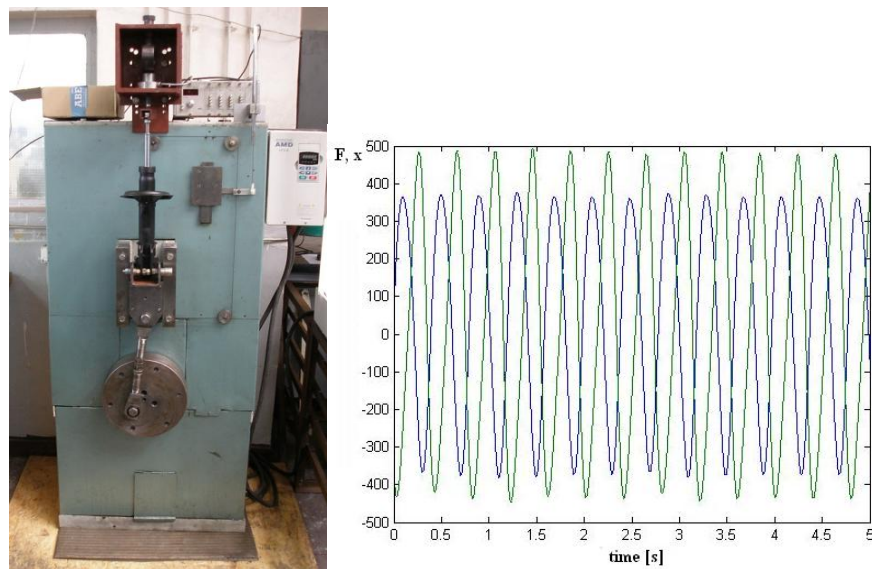
Figure 6. Indicator test stand and time realization of recorded force and displacement signals.

The damping characteristic is determined assuming a value for the maximum damping piston velocity (separately compression and decompression). Determination of the damping characteristics is based on the average value of force in the point of maximum velocity. Last step of determining damping characteristic is joining the points determined for different linear velocity (average line for close loop). Damping characteristic is presented of Fig 7.
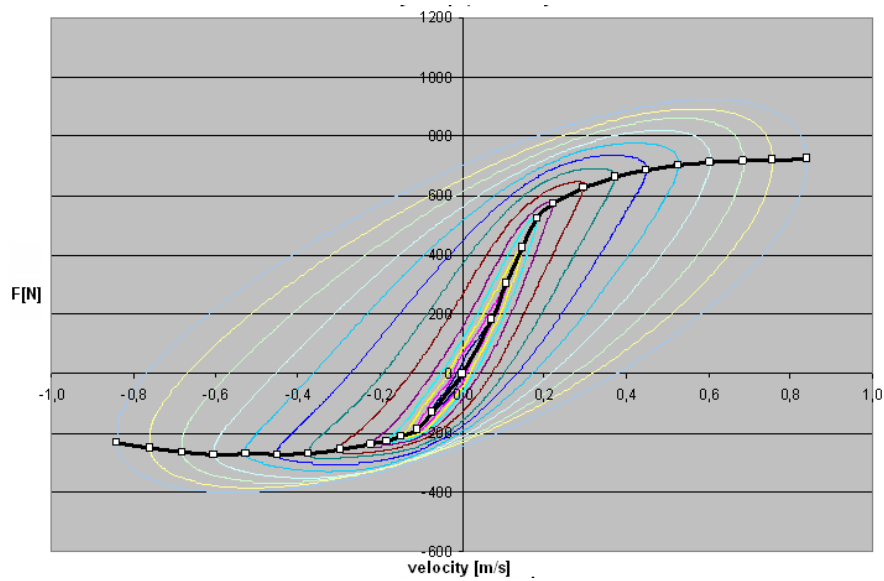
Figure 7. Force vs. velocity diagram and damping characteristic (black line)

Effect of damping were obtained by changing the damping characteristics of the shock absorber. Designated damping characteristics of the front shock absorbers were determined on presented test stand. The damping characteristic of effective new front shock absorber is marked in blue color, and the red color is front shock absorber characteristics of the 50% loss of oil (Fig.8). Similarly, the rear shock absorber characteristics in varying condition was determined.
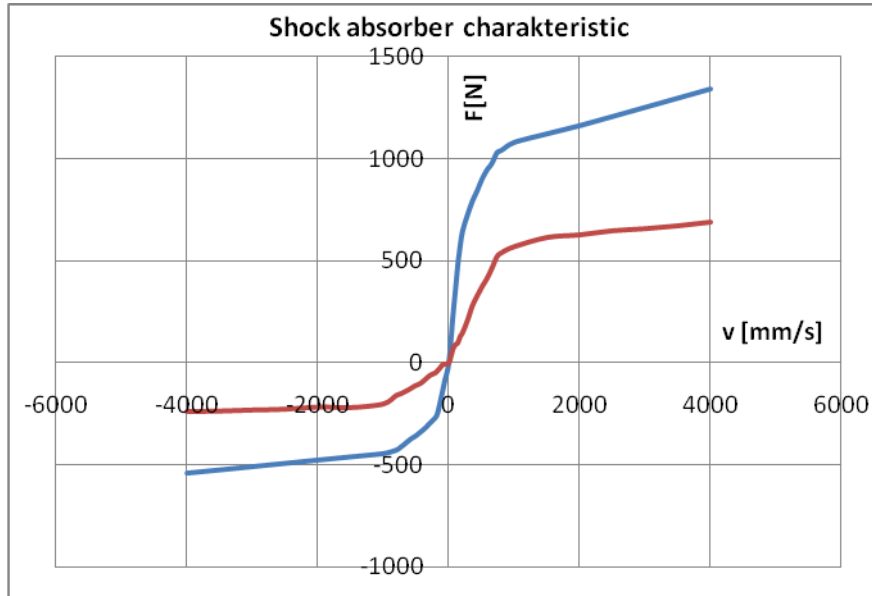
Figure 8. Damping characteristic: blue- new shock absorber, red – shock absorber with 50% loss of oil.

Adams/Car /Ride module allows to test vehicle dynamics forcing the position of the plate of test stand. Virtual model of the vehicle was set on four servo-motors. They can be control any combination of excitation of individual actuators (displacement and amplitude, phase between extortion, etc.) and determine all kinds of vibration (vertical, lateral, angular).

The simulation research was conducted with excitation forces on each wheel in front and rear suspension (Fig. 3a). Test time was 10 [s], the amplitude of displacement 6 [mm], the frequency was increased in the range 0.1-20 [Hz]. The results presented in Fig.9. refer to comparisons of vibration displacements at excitation wheel for new shock absorber and for shock absorber with 50% loss of oil.

a)
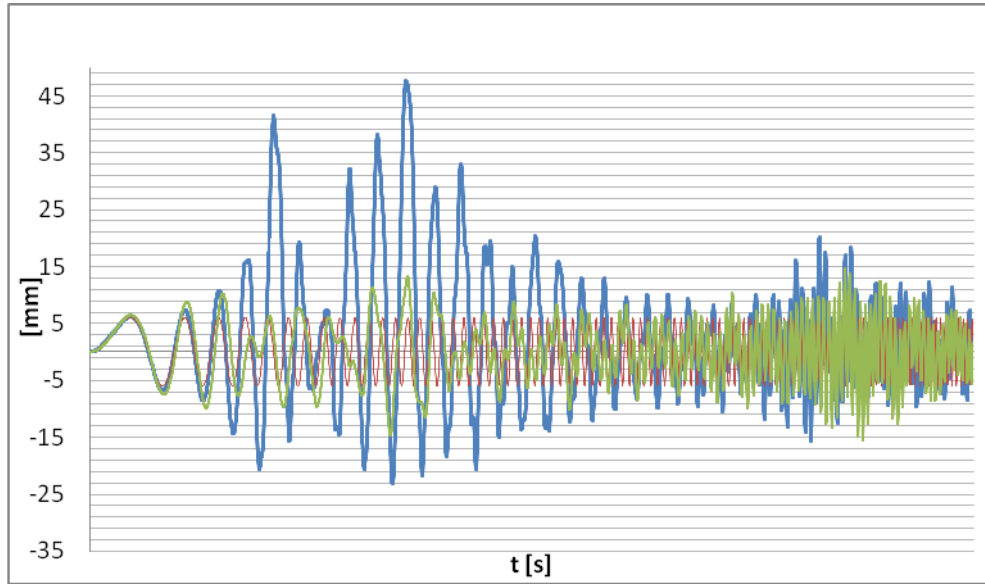
b)
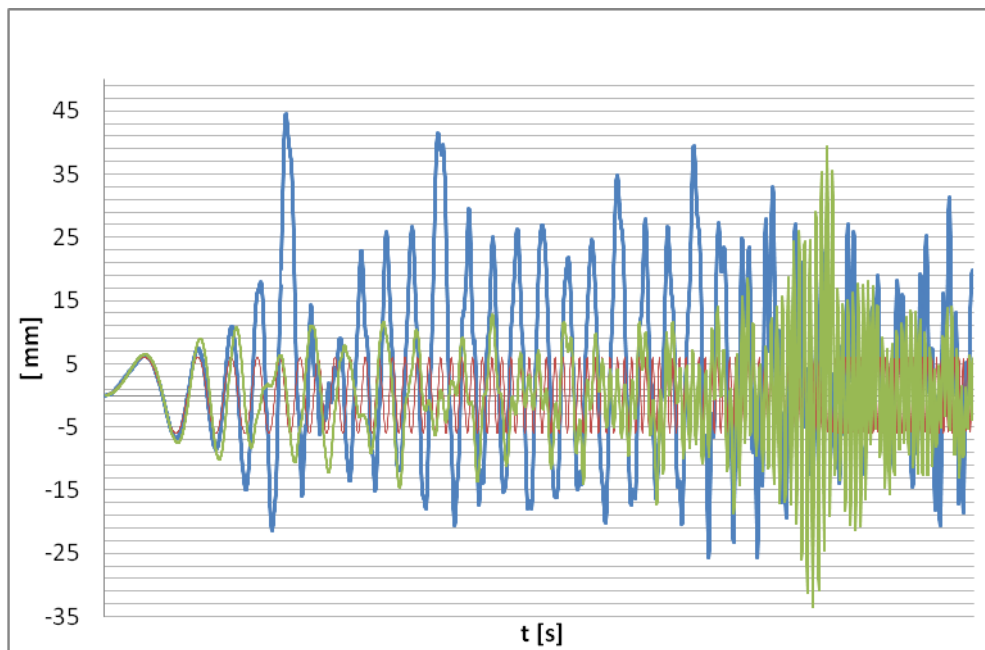
Figure 9. Vibration displacements at excitation wheel for new shock absorber (a) and for shock
absorber with 50% loss of oil (b): red color –displacement of plate, blue color –
displacement of front wheel, green color – displacement of rear wheel

4. Conclusions

The result of the investigation presents that for a new and damaged shock absorber vibration displacements in the low-frequency excitation do not show major differences. It is associated mainly with a small value of the amplitude of excitation (6 mm). When excitation frequency are increasing vibration amplitudes for shock absorber with oil loss are also increasing. This is particularly visible for the suspension with damaged shock absorber in area of resonance frequency of unsprung masses. The results of preliminary tests are targeted at describing precise estimates of the technical condition of the shock absorber built in the vehicle. This applies to the configuration possibilities of individual actuators and excitation to obtain additional information (eg phase angle) in the evaluation of the technical condition of the shock absorber.

References

[1] Benaziz M. and Nacivet S. and Thouverez F. A shock absorber model for structure-borne noise analyses *Journal of Sound and Vibration*, Volume 349, 4 August 2015, Pages 177-194

[2] Blundell. M. and Harty D. *Multibody systems approach to vehicle dynamics.* Elsevier Butterworth –Heineman, Linacre House , Jordan Hill, Oxford, 2004

[3] Burdzik, R. and Konieczny, Ł. and Adamczyk, B. Automatic control systems and control of vibrations in vehicles car. Telematics - support for transport. *TST 2014, Communications in Computer and Information Science ;* vol. 471 Berlin : Springer, 2014, pp1865-0929

[4] Burdzik, R. Monitoring system of vibration propagation in vehicles and method of analysing vibration modes. J. Mikulski (ed.): *TST 2012, CCIS 329, Springer,* Heidelberg, 2012, pp. 406-413

[5] Czop, P. and Sławik, D. and Śliwa, P. and Wszołek, G. Simplified and advanced models of a valve system used in shock absorbers. Journal *of Achievements in Materials and Manufacturing Engineering* 33/2, 2009, pp.173-180.

[6] Czop P. and Sławik D. A high-frequency first-principle model of a shock absorber and servo-hydraulic tester Original Research Article Mechanical Systems and Signal Processing, Volume 25, Issue 6, August 2011, Pages 1937-1955

[7] Dixon J.C. *The Shock Absorber Handbook*. Society of Automotive Engineers Inc., Warrendale, PA, 1999.

[8] Gillespie T. D.: *Fundamentals of vehicle dynamics*. SAE International 1992.

[9] Konieczny, Ł. and Burdzik, R. and Łazarz B. Analysis of properties of automotive vehicle suspension arm depending on different materials used in the MSC.Adams environment, *Archives of Materials Science and Engineering* AMSE 58/2, 2012, pp. 171-176.

[10] Konieczny, Ł. Badania symulacyjne układu zawieszenia pojazdu samochodowego w środowisku ADAMS/CAR *Zeszyty Naukowe Politechnika Śląska seria Transport* nr 1878 z.77,2012, pp 49-54

[11] Konieczny, Ł.: Wykorzystanie oprogramowania ADAMS/CAR RIDE w badaniach komponentów zawieszenia pojazdu samochodowego Z*eszyty Naukowe Politechnika Ślaska seria Transport* nr 1878 z.77, 2012, pp. 55-60

[12] Konieczny, Ł. The statistical analysis of damping parameters of hydraulic shock absorbers. *Diagnostyka* 2014 vol. 15 no. 2, pp. 49-52,

[13] Konieczny, Ł. and Burdzik, R. and Warczek, J. Determinations of shock absorber damping characteristics taking stroke value into consideration account. *Diagnostyka* 2010 nr 3, pp. 51-54

[14] Konieczny, Ł. and Burdzik, R. and Warczek, J. The uncertainty of determining shock absorber damping characteristic on indicator test stand. *Diagnostyka* 2013 Vol.14 no 2, pp. 63-66.

[15] Konieczny, Ł. Damping characteristics of hydropneumatic suspension strut in function of car static load. *Journal of Vibroengineering,* 2015, vol. 17 no. 1, pp. 71-81,

[16] Konieczny, Ł. and Burdzik, R. and Figlus, T. Use of MBS (ADAMS / CAR) software in simulations of vehicle suspension systems. -*Transport Problems* , 2014 vol. 9 iss. 1, pp. 111-118,

[17] Konieczny, Ł. and Burdzik, R. and Folęga, P. Multibody system software used for research of car suspension system dynamics. *ModTech 2014, Advanced Materials Research* ; vol. 1036 pp1662-8985.

[18] Ning, X. and Zhao, C. and Shen, J.: Dynamic analysis of car suspension using ADAMS/Car for development of a software interface for optimization. In: International Workshop on Automobile, Power and Energy Engineering, International workshop on automobile, *Power and energy engineering* Book Series: Procedia Engineering .Volume: 16 Published: 2011.

[19] Tang, A. Modeling and Validation of MBS using Joint Force Actuator in ADAMS CarIn: 3rd International Conference on Manufacturing Science and Engineering (ICMSE 2012) Location: Xiamen, PEOPLES R CHINA Date: MAR 27-29, 2012 *ADVANCED COMPOSITE MATERIALS, PTS 1-3* Book Series: Advanced Materials Research   Volume: 482-484   Pages: 2257-2260 Published: 2012.

[20] Wang S. and Wang J. and Xie W. and Zhao J. Development of hydraulically driven shaking table for damping experiments on shock absorbers *Mechatronics,* Volume 24, Issue 8, December 2014, Pages 1132-1143

[21] Warczek J. and Burdzik R. and Peruń G.: The method for identification of damping coefficient of the trucks suspension , Key Engineering Materials Vol. 588 (2014) p 281-289.

[22] Wojtyra, M. and Frączek, J. *Metoda układów wieloczłonowych w dynamice mechanizmów. Ćwiczenia z zastosowaniem programu ADAMS.* Oficyna Wydawnicza Politechniki Warszawskiej, Warszawa 2007

[23] Xu T. and Liang M. and Li C. and Yang S. Design and analysis of a shock absorber with variable momentof inertia for passive vehicle suspensions. *Journal of Sound and Vibration* 355 (2015) 66–85

Łukasz Konieczny, Ph.D.: Silesian University of Technology, Faculty of Transport, Krasińskiego 8, 40-019 Katowice, POLAND (lukasz.konieczny@polsl.pl), the author presented this work at the conference.

Rafał Burdzik, Ph.D. D.Sc. (Assistant Professor): Silesian University of Technology, Faculty of Transport, Krasińskiego 8, 40-019 Katowice, POLAND (rafal.burdzik@polsl.pl).

Jan Warczek, Ph.D.: Silesian University of Technology, Faculty of Transport, Krasińskiego 8, 40-019 Katowice, POLAND (jan.warczek@polsl.pl).

Dynamics of two coupled 4-DOF mechanical linear sliding systems with dry friction
(BIF304-15)

Angelika Kosińska, Dariusz Grzelczyk, Jan Awrejcewicz

Abstract: The paper introduces a model of two identical coupled 4-DOF mechanical linear sliding systems with dry friction coupled with each other by a linear torsional spring. The appropriate components (bodies) of the coupled systems are riding on two separated driving belts, which are driven at constant velocities, and stick-slip vibrations can be observed. In this case the physical interpretation of the considered model could be two rows of carriages laying on the guideways and coupled by an elastic shaft, which are moving at constant velocity with respect to the guideways as a foundation. From a mathematical point of view the analyzed problem is governed by eight nonlinear ordinary second order differential equations of motion yielded by the second kind Lagrange equations. Numerical analysis is performed in Mathematica software using the qualitative and quantitative theories of differential equations. Some interesting non-linear system dynamics are detected and reported using the phase portraits and the Poincaré maps. Next, power spectra obtained by the FFT technique are reported. The presented results show periodic, quasi-periodic, chaotic and hyper-chaotic orbits. Moreover, synchronization effects between the coupled systems are also detected and studied.

1. Introduction

The question of stick-slip vibrations caused by dry friction is still opened. The fundamental laws of stick-slip phenomena based on dry friction dynamics have been promulgated in the pioneering experiments of Rabinovicz and in the works of Baumberger et al [7]. Firstly, a concept of nonlinear dry friction should be explained. The force, which is required to start the movement of an object, is called the static friction force, but the kinetic force is essential to maintain a constant velocity during the movement of the body. A sufficient condition for stick-slip is that the static coefficient of friction is higher than the kinetic coefficient of friction [10]. Stick-slip phenomena are expected during contact interaction at low-velocity friction. The considered stick-slip phenomenon depends on frequency of vibrations, a relative humidity and load. Stick-slip phenomena occur in everyday life, for instance, from earthquakes, through brake systems (when car is started to move from stationary state) [11], to nano-devices showing up in the scale above several microns. Examples of scientific literature devoted to sticks-slip vibrations in system can be found in the references [1, 3, 5, 6, 8, 9].

Different models in micro- and macro-scale are used for description of stick- slip phenomena. In this work an 8 degree-of-freedom model is used. The body consists of two identical subsystems coupled

by torsion spring. Every subsystem rides on two separated belts which are driven at constant velocity. Bearing in mind principles of relativity one can say that the bodies are moving because of immovable belts. In this case the real interpretation of model may take place in a mine, where two rows of carriages fixed to guideways are moving at constant velocity. As a nonlinear (in stick–slip regime) system, the spring–slider model is very sensitive to weak external impacts, which on a large scale manifests itself in phenomena of induced seismicity, triggering and synchronization effects [2]. The considered in this work mechanical system can be treated as an extension of the mechanical model presented in the paper [4].

2. Mechanical Model

The considered 8-DOF model (two coupled by torsional spring 4-DOF mechanical linear sliding systems with dry friction) is shown in Fig. 1.

Figure 1. The 8-DOF model with dry friction.

The presented system can be considered as a planar system in the Cartesian coordinate system (in the Earth's gravitational field with the gravity coefficient g) with horizontal axis x and vertical axis y. Dynamics of the considered system can be described by the following variables: x_{I1}, $v_{I1} = \dot{x}_{I1}$, y_{I1}, $z_{I1} = \dot{y}_{I1}$, φ_I, $\omega_I = \dot{\varphi}_I$, x_{I2}, $v_{I2} = \dot{x}_{I2}$, x_{II1}, $v_{II1} = \dot{x}_{II1}$, y_{II1}, $z_{II1} = \dot{y}_{II1}$, φ_{II}, $\omega_{II} = \dot{\varphi}_{II}$, x_{II2}, $v_{II2} = \dot{x}_{II2}$. The masses m_{I1}, m_{II1} can rotate about the pivot axes S (moments of inertia about the pivot point S of the mentioned masses are I_I, I_{II}). The entire system is characterized by lengths l_{Ii}, l_{IIi} ($i = 1,2,...,6$) and springs with stiffness coefficients k_{Iix}, k_{IIix}, k_{Ijy}, k_{IIjy} ($i = 1,2,4,5,6$; $j = 3,4,5,6$). Moreover, two additional masses m_{I2}, m_{II2} are laying on the appropriate belts as a foundation, which are moving with a constant velocities v_{I0} and v_{II0}, respectively. Between the mentioned masses m_{I2}, m_{II2} and appropriate belts dry friction forces occur as a functions of the relative sliding velocities $v_{I0} - \dot{x}_{I2}$, $v_{II0} - \dot{x}_{II2}$, respectively.

Equations of motion of the considered system have been derived using the Lagrangian method (the second kind Lagrange equations) [4] and they are as follows

$$\frac{d}{dt}\left(\frac{\partial T}{\partial \dot{q}}\right) - \frac{\partial T}{\partial q} + \frac{\partial V}{\partial q} = Q_n, \tag{1}$$

where: q - vector of generalized coordinates, Q_n - vector of generalized non-conservative force acting in the system, T - total kinetic energy of the system, V - total potential energy of the system, t - time.

In this case dot means differentiation with respect to time t. For presented previously 8-DOF model with dry friction, vector q is reads:

$$q = [x_{I1}, \quad y_{I1}, \quad \varphi_I, \quad x_{I2}, \quad x_{II1}, \quad y_{II1}, \quad \varphi_{II}, \quad x_{II2}]^T. \tag{2}$$

Simultaneously, Q_n can be described by the following vector

$$Q_n = [0, \quad 0, \quad 0, \quad F_{frI}, \quad 0, \quad 0, \quad 0, \quad F_{frII}]^T. \tag{3}$$

The friction forces F_{frI} and F_{frII} are equal to the product of nonlinear kinetic friction coefficients $\mu_k(v_{I0} - \dot{x}_{I2})$, $\mu_k(v_{II0} - \dot{x}_{I2})$ (associated with relative velocities of every subsystems) and the normal forces $N_I = m_{I2}g - (k_{I3y}y_{I1} - k_{I3y}l_{I3}\varphi_I)$, $N_{II} = m_{II2}g - (k_{II3y}y_{II1} - k_{II3y}l_{II3}\varphi_{II})$, which press the masses m_{I2} and m_{II2} to the first belt and to the second one, respectively. It should also be noted that in numerical calculations the values of the normal forces N_I and N_{II} can be less

than zero, greater than zero or equal to zero. In the case of $N_I, N_{II} > 0$, the friction contact between masses m_{I2}, m_{II2} and the appropriate belts moving with velocities v_{I0}, v_{II0} occur. In turn, the case $N_I, N_{II} \leq 0$ means a loss of friction contact between the masses m_{I2}, m_{II2} and the appropriate belts. This is why in our mathematical model we use a discontinuous step functions describing these phenomena, and defined as follow

$$I(N_I) = \begin{cases} 1 & \text{for} \quad N_I > 0, \\ 0 & \text{for} \quad N_I \leq 0. \end{cases}, \quad I(N_{II}) = \begin{cases} 1 & \text{for} \quad N_{II} > 0, \\ 0 & \text{for} \quad N_{II} \leq 0. \end{cases} \tag{4}$$

Finally, forces F_{frI} and F_{frII} have the following form

$$F_{frI}(v_{I0} - \dot{x}_{I2}, y_{I1}, \varphi_I) =$$
$$= \mu_{Ik}(v_{I0} - \dot{x}_{I2}) \cdot [m_{I2}g - (k_{I3y}y_{I1} - k_{I3y}l_{I3}\varphi_I)] \cdot I(m_{I2}g - (k_{I3y}y_{I1} - k_{I3y}l_{I3}\varphi_I)), \tag{5}$$

$$F_{frII}(v_{II0} - \dot{x}_{II2}, y_{II1}, \varphi_{II}) =$$
$$= \mu_{IIk}(v_{II0} - \dot{x}_{II2}) \cdot [m_{II2}g - (k_{II3y}y_{II1} - k_{II3y}l_{II3}\varphi_{II})] \cdot I(m_{II2}g - (k_{II3y}y_{II1} - k_{II3y}l_{II3}\varphi_{II})). \tag{6}$$

Total kinetic energy T of studied model has the following form:

$$T = \frac{1}{2}m_{I1}(\dot{x}_{I1}^2 + \dot{y}_{I1}^2) + \frac{1}{2}I_I\dot{\varphi}_I^2 + \frac{1}{2}m_{I2}\dot{x}_{I2}^2 + \frac{1}{2}m_{II1}(\dot{x}_{II1}^2 + \dot{y}_{II1}^2) + \frac{1}{2}I_{II}\dot{\varphi}_{II}^2 + \frac{1}{2}m_{II2}\dot{x}_{II2}^2. \tag{7}$$

Since small values of angles φ_I and φ_{II} are taken into consideration, the total potential energy V has the following form

$$V = \frac{1}{2}k_{I1x}(x_{I1} + l_{I1}\varphi_I - x_{I2})^2 + \frac{1}{2}k_{I2x}(x_{I1} + l_{I1}\varphi_I - x_{I2})^2 +$$
$$+ \frac{1}{2}k_{I3y}(y_{I1} - l_{I3}\varphi_I)^2 + \frac{1}{2}k_{I4x}(x_{I1} - l_{I2}\varphi_I)^2 + \frac{1}{2}k_{I4y}(y_{I1} - l_{I4}\varphi_I)^2 +$$
$$+ \frac{1}{2}k_{I5x}(x_{I1} + l_{I5}\varphi_I)^2 + \frac{1}{2}k_{I5y}(y_{I1} - l_{I6}\varphi_I)^2 + \frac{1}{2}k_{I6x}(x_{I1} - l_{I2}\varphi_I)^2 +$$
$$+ \frac{1}{2}k_{I6y}(y_{I1} + l_{I7}\varphi_I)^2 + m_{I1}gy_{I1} +$$
$$+ \frac{1}{2}k_{II1x}(x_{II1} + l_{II1}\varphi_I - x_{II2})^2 + \frac{1}{2}k_{II2x}(x_{II1} + l_{II1}\varphi_{II} - x_{II2})^2 +$$
$$+ \frac{1}{2}k_{II3y}(y_{II1} - l_{II3}\varphi_{II})^2 + \frac{1}{2}k_{II4x}(x_{II1} - l_{II2}\varphi_{II})^2 + \frac{1}{2}k_{II4y}(y_{II1} - l_{II4}\varphi_{II})^2 +$$
$$+ \frac{1}{2}k_{II5x}(x_{II1} + l_{II5}\varphi_{II})^2 + \frac{1}{2}k_{II5y}(y_{II1} - l_{II6}\varphi_{II})^2 + \frac{1}{2}k_{II6x}(x_{II1} - l_{II2}\varphi_{II})^2 +$$
$$+ \frac{1}{2}k_{II6y}(y_{II1} + l_{II7}\varphi_{II})^2 + m_{II1}gy_{II1} + \frac{1}{2}k_s(\varphi_I - \varphi_{II})^2. \tag{8}$$

Computing the partial derivatives $\dfrac{d}{dt}\left(\dfrac{\partial T}{\partial \dot{\boldsymbol{q}}}\right), \dfrac{\partial T}{\partial \boldsymbol{q}}, \dfrac{\partial V}{\partial \dot{\boldsymbol{q}}}$, based on (1), we obtain

$$
\begin{cases}
m_{I1}\ddot{x}_{I1} + (k_{I1x} + k_{I2x} + k_{I4x} + k_{I5x} + k_{I6x})x_{I1} + \\
+ (k_{I1x}l_{I1} + k_{I2x}l_{I1} - k_{I4x}l_{I2} + k_{I5x}l_{I5} - k_{I6x}l_{I2})\varphi_I - (k_{I1x} + k_{I2x})x_{I2} = 0, \\
m_{I1}\ddot{y}_{I1} + (k_{I3y} + k_{I4y} + k_{I5y} + k_{I6y})y_{I1} + \\
+ (-k_{I3y}l_{I3} - k_{I4y}l_{I4} - k_{I5y}l_{I6} + k_{I6y}l_{I7})\varphi_I + m_{I1}g = 0, \\
I_I\ddot{\varphi}_I + (k_{I1x}l_{I1} + k_{I2x}l_{I1} - k_{I4x}l_{I2} + k_{I5x}l_{I5} - k_{I6x}l_{I2})x_{I1} + \\
+ (-k_{I3y}l_{I3} - k_{I4y}l_{I4} - k_{I5y}l_{I6} + k_{I6y}l_{I7})y_{I1} + \\
+ (k_{I1x}l_{I1}^2 + k_{I2x}l_{I1}^2 + k_{I3y}l_{I3}^2 + k_{I4x}l_{I2}^2 + k_{I4y}l_{I4}^2 + k_{I5x}l_{I5}^2 + k_{I5y}l_{I6}^2 + k_{I6x}l_{I2}^2 + k_{I6y}l_{I7}^2)\varphi_I + \\
- (k_{I1x} + k_{I2x})l_{I1}x_{I2} + k_s(\varphi_I - \varphi_{II}) = 0, \\
m_{I2}\ddot{x}_{I2} - (k_{I1x} + k_{I2x})x_{I1} - (k_{I1x} + k_{I2x})l_{I1}\varphi_I + (k_{I1x} + k_{I2x})x_{I2} = \\
= \mu_k(v_{I0} - \dot{x}_{I2})\cdot[m_{I2}g - (k_{I3y}y_{I1} - k_{I3y}l_{I3}\varphi_I)]\cdot\boldsymbol{1}(m_{I2}g - (k_{I3y}y_{I1} - k_{I3y}l_{I3}\varphi_I)), \\
m_{II1}\ddot{x}_{II1} + (k_{II1x} + k_{II2x} + k_{II4x} + k_{II5x} + k_{II6x})x_{II1} + \\
+ (k_{II1x}l_{II1} + k_{II2x}l_{II1} - k_{II4x}l_{II2} + k_{II5x}l_{II5} - k_{II6x}l_{II2})\varphi_{II} - (k_{II1x} + k_{II2x})x_{II2} = 0, \\
m_{II1}\ddot{y}_{II1} + (k_{II3y} + k_{II4y} + k_{II5y} + k_{II6y})y_{II1} + \\
+ (-k_{II3y}l_{II3} - k_{II4y}l_{II4} - k_{II5y}l_{II6} + k_{II6y}l_{II7})\varphi_{II} + m_{II1}g = 0, \\
I_{II}\ddot{\varphi}_{II} + (k_{II1x}l_{II1} + k_{II2x}l_{II1} - k_{II4x}l_{II2} + k_{II5x}l_{II5} - k_{II6x}l_{II2})x_{II1} + \\
+ (-k_{II3y}l_{II3} - k_{II4y}l_{II4} - k_{II5y}l_{II6} + k_{II6y}l_{II7})y_{II1} + \\
+ (k_{II1x}l_{II1}^2 + k_{II2x}l_{II1}^2 + k_{II3y}l_{II3}^2 + k_{II4x}l_{II2}^2 + k_{II4y}l_{II4}^2 + k_{II5x}l_{II5}^2 + k_{II5y}l_{II6}^2)\varphi_{II} + \\
+ k_{II6x}l_{II2}^2 + k_{II6y}l_{II7}^2)\varphi_{II} - (k_{II1x} + k_{II2x})l_{II1}x_{II2} + k_s(\varphi_{II} - \varphi_I) = 0, \\
m_{II2}\ddot{x}_{II2} - (k_{II1x} + k_{II2x})x_{II1} - (k_{II1x} + k_{II2x})l_{II1}\varphi_{II} + (k_{II1x} + k_{II2x})x_{II2} = \\
= \mu_k(v_{II0} - \dot{x}_{II2})\cdot[m_{II2}g - (k_{II3y}y_{II1} - k_{II3y}l_{II3}\varphi_{II})]\cdot\boldsymbol{1}(m_{II2}g - (k_{II3y}y_{II1} - k_{II3y}l_{II3}\varphi_{II})).
\end{cases}
\tag{9}
$$

3. Non-dimensional form

We introduce non-dimensional time $\tau = t\big/\sqrt{m_{I2}/(k_{I1x} + k_{I2x})}$, non-dimensional coordinates $X_{I1} = x_{I1}/l_{I1}$, $Y_{I1} = y_{I1}/l_{I1}$, $X_{I2} = x_{I2}/l_{I1}$, $X_{II1} = x_{II1}/l_{I1}$, $Y_{II1} = y_{II1}/l_{I1}$, $X_{II2} = x_{II2}/l_{I1}$ and the following non-dimensional parameters:

$$
a_{I1} = \frac{m_{I2}}{m_{I1}}\left(\frac{k_{I1x} + k_{I2x} + k_{I4x} + k_{I5x} + k_{I6x}}{k_{I1x} + k_{I2x}}\right),
\tag{10}
$$

$$
a_{II1} = \frac{m_{I2}}{m_{II1}}\left(\frac{k_{II1x} + k_{II2x} + k_{II4x} + k_{II5x} + k_{II6x}}{k_{I1x} + k_{I2x}}\right),
\tag{11}
$$

$$
a_{I2} = \frac{m_{I2}}{m_{I1}}\left(\frac{k_{I1x}l_{I1} + k_{I2x}l_{I1} - k_{I4x}l_{I2} + k_{I5x}l_{I5} - k_{I6x}l_{I2}}{(k_{I1x} + k_{I2x})l_{I1}}\right),
\tag{12}
$$

$$a_{II2} = \frac{m_{I2}}{m_{II1}} \left(\frac{k_{II1x}l_{II1} + k_{II2x}l_{II1} - k_{II4x}l_{I2} + k_{II5x}l_{II5} - k_{II6x}l_{II2}}{(k_{I1x} + k_{I2x})l_{I1}} \right), \tag{13}$$

$$a_{I3} = \frac{m_{I2}}{m_{I1}}, \quad a_{II3} = \frac{m_{I2}}{m_{II1}} \left(\frac{k_{II1x} + k_{II2x}}{k_{I1x} + k_{I2x}} \right), \tag{14}$$

$$b_{I1} = \frac{m_{I2}}{m_{I1}} \left(\frac{k_{I3y} + k_{I4y} + k_{I5y} + k_{I6y}}{k_{I1x} + k_{I2x}} \right), \quad b_{II1} = \frac{m_{I2}}{m_{II1}} \left(\frac{k_{II3y} + k_{II4y} + k_{II5y} + k_{II6y}}{k_{I1x} + k_{I2x}} \right), \tag{15}$$

$$b_{I2} = \frac{m_{I2}}{m_{I1}} \left(\frac{k_{I3y}l_{I3} + k_{I4y}l_{I4} + k_{I5y}l_{I6} - k_{I6y}l_{I7}}{(k_{I1x} + k_{I2x})l_{I1}} \right), \tag{16}$$

$$b_{II2} = \frac{m_{I2}}{m_{II1}} \left(\frac{k_{II3y}l_{II3} + k_{II4y}l_{II4} + k_{II5y}l_{II6} - k_{II6y}l_{II7}}{(k_{I1x} + k_{I2x})l_{I1}} \right), \tag{17}$$

$$f_g = \frac{m_{I2}g}{(k_{I1x} + k_{I2x})l_{I1}}, \tag{18}$$

$$c_{I1} = \frac{m_{I2}l_{I1}(k_{I1x}l_{I1} + k_{I2x}l_{I1} - k_{I4x}l_{I2} + k_{I5x}l_{I5} - k_{I6x}l_{I2})}{(k_{I1x} + k_{I2x})I_I}, \tag{19}$$

$$c_{II1} = \frac{m_{I2}l_{I1}(k_{II1x}l_{II1} + k_{II2x}l_{II1} - k_{II4x}l_{II2} + k_{II5x}l_{II5} - k_{II6x}l_{II2})}{(k_{I1x} + k_{I2x})I_{II}}, \tag{20}$$

$$c_{I2} = \frac{m_{I2}l_{I1}(k_{I3y}l_{I3} + k_{I4y}l_{I4} + k_{I5y}l_{I6} - k_{I6y}l_{I7})}{(k_{I1x} + k_{I2x})I_I}, \tag{21}$$

$$c_{II2} = \frac{m_{I2}l_{I1}(k_{II3y}l_{II3} + k_{II4y}l_{II4} + k_{II5y}l_{II6} - k_{II6y}l_{II7})}{(k_{I1x} + k_{I2x})I_{II}}, \tag{22}$$

$$c_{I3} = \frac{m_{I2}(k_{I1x}l_{I1}^2 + k_{I2x}l_{I1}^2 + k_{I3y}l_{I3}^2 + k_{I4x}l_{I2}^2 + k_{I4y}l_{I4}^2 + k_{I5x}l_{I5}^2 + k_{I5y}l_{I6}^2 + k_{I6x}l_{I2}^2 + k_{I6y}l_{I7}^2)}{(k_{I1x} + k_{I2x})I_I} \tag{23}$$

$$c_{II3} = \frac{m_{I2}(k_{II1x}l_{II1}^2 + k_{II2x}l_{II1}^2 + k_{II3y}l_{II3}^2 + k_{II4x}l_{II2}^2 + k_{II4y}l_{II4}^2 + k_{II5x}l_{II5}^2 + k_{II5y}l_{II6}^2 + k_{II6x}l_{II2}^2 + k_{II6y}l_{II7}^2)}{(k_{I1x} + k_{I2x})I_{II}} \tag{24}$$

$$c_{I4} = \frac{m_{I2}l_{I1}^2}{I_I}, \quad c_{II4} = \frac{m_{I2}l_{I1}l_{II1}(k_{II1x} + k_{II2x})}{(k_{I1x} + k_{I2x})I_{II}}, \tag{25}$$

$$d_{II1} = \frac{m_{I2}(k_{II1x} + k_{II2x})}{m_{II2}(k_{I1x} + k_{I2x})} , \quad d_{II2} = \frac{m_{I2}l_{II1}(k_{II1x} + k_{II2x})}{m_{II2}l_{I1}(k_{I1x} + k_{I2x})} , \tag{26}$$

$$k_I = \frac{m_{I2}k_s}{(k_{I1x} + k_{I2x})I_I} , \quad k_{II} = \frac{m_{I2}k_s}{(k_{I1x} + k_{I2x})I_{II}} , \tag{27}$$

$$e_{I1} = \frac{k_{I3y}}{(k_{I1x} + k_{I2x})} , \quad e_{II1} = \frac{m_{I2}k_{II3y}}{m_{II2}(k_{I1x} + k_{I2x})} , \tag{28}$$

$$e_{I2} = \frac{l_{I3}}{l_{I1}}\frac{k_{I3y}}{(k_{I1x} + k_{I2x})} , \quad e_{II2} = \frac{l_{II3}}{l_{I1}}\frac{m_{I2}k_{II3y}}{m_{II2}(k_{I1x} + k_{I2x})} , \tag{29}$$

and the following non-dimensional functions

$$\mu_{Ik}\left(\frac{l_{I1}}{\sqrt{m_{I2}/(k_{I1x} + k_{I2x})}}V_{I0} - \frac{l_{I1}}{\sqrt{m_{I2}/(k_{I1x} + k_{I2x})}}\dot{X}_{I2}\right) = f_{Ik}(V_{I0} - \dot{X}_{I2}) , \tag{30}$$

$$\mu_{IIk}\left(\frac{l_{I1}}{\sqrt{m_{I2}/(k_{I1x} + k_{I2x})}}V_{II0} - \frac{l_{I1}}{\sqrt{m_{I2}/(k_{I1x} + k_{I2x})}}\dot{X}_{II2}\right) = f_{IIk}(V_{II0} - \dot{X}_{II2}) , \tag{31}$$

$$\mathbf{1}(m_{I2}g - (k_{I3y}y_{I1} - k_{I3y}l_{I3}\varphi_I)) = \mathbf{1}(f_g - (e_{I1}Y_{I1} - e_{I2}\varphi_I)) , \tag{32}$$

$$\mathbf{1}(m_{II2}g - (k_{II3y}y_{II1} - k_{II3y}l_{II3}\varphi_{II})) = \mathbf{1}(f_g - (e_{II1}Y_{II1} - e_{II2}\varphi_{II})) . \tag{33}$$

In result, equations of motion in the counter part non-dimensional form are as follows

$$\begin{cases}
\ddot{X}_{I1} + a_{I1}X_{I1} + a_{I2}\varphi_I - a_{I3}X_{I2} = 0, \\
\ddot{Y}_{I1} + b_{I1}Y_{I1} - b_{I2}\varphi_I + f_g = 0, \\
\ddot{\varphi}_I + c_{I1}X_{I1} - c_{I2}Y_{I1} + c_{I3}\varphi_I - c_{I4}X_{I2} + k_I(\varphi_I - \varphi_{II}) = 0, \\
\ddot{X}_{I2} - X_{I1} - \varphi_I + X_{I2} = f_{Ik}(V_{I0} - \dot{X}_{I2})\cdot[f_g - (e_{I1}Y_{I1} - e_{I2}\varphi_I)]\cdot\mathbf{1}(f_g - (e_{I1}Y_{I1} - e_{I2}\varphi_I)) \\
\ddot{X}_{II1} + a_{II1}X_{II1} + a_{II2}\varphi_{II} - a_{II3}X_{II2} = 0, \\
\ddot{Y}_{II1} + b_{II1}Y_{II1} - b_{II2}\varphi_{II} + f_g = 0, \\
\ddot{\varphi}_{II} + c_{II1}X_{II1} - c_{II2}Y_{II1} + c_{II3}\varphi_{II} - c_{II4}X_{II2} + k_{II}(\varphi_{II} - \varphi_I) = 0, \\
\ddot{X}_{II2} - d_{II1}X_{II1} - d_{II2}\varphi_{II} + d_{II1}X_{II2} = \\
\quad = f_{IIk}(V_{II0} - \dot{X}_{II2})\cdot[f_g - (e_{II1}Y_{II1} - e_{II2}\varphi_{II})]\cdot\mathbf{1}(f_g - (e_{II1}Y_{II1} - e_{II2}\varphi_{II})).
\end{cases} \tag{34}$$

4. Numerical computations

Our numerical computations have been performed via the fourth order Runge-Kutta method with constant time step $h = 0.001$ and zero initial conditions. We consider symmetric system with the

values of non-dimensional parameters and non-dimensional functions taken from the previous paper [4], namely:

$$a_{I1} = a_{II1} = a_1 = 0{,}07836 \,, \quad a_{I2} = a_{II2} = a_2 = 0{,}03344 \,, \quad a_{I3} = a_{II3} = a_3 = 0{,}04058 \,,$$

$$b_{I1} = b_{II1} = b_1 = 0{,}09375 \,, \quad b_{I2} = b_{II2} = b_2 = 0{,}03314 \,, \quad c_{I1} = c_{II1} = c_1 = 0{,}02689 \,,$$

$$c_{I2} = c_{II2} = c_2 = 0{,}02666 \,, \quad c_{I3} = c_{II3} = c_3 = 0{,}06181 \,, \quad c_{I4} = c_{II4} = c_3 = 0{,}03264 \,,$$

$$d_{II1} = d_{II2} = 1 \,, \quad f_g = 0{,}00529 \,, \quad e_{I1} = e_{II1} = e_1 = 1{,}37931 \,, \quad e_{I2} = e_{II2} = e_2 = 0{,}47237 \,.$$

Kinetic friction functions $f_{Ik}(V_{I0} - \dot{X}_{I2})$ and $f_{IIk}(V_{II0} - \dot{X}_{II2})$ in our model are described by the Stribeck functions. Because classical signum function is discontinuous, we decide to approximate the mentioned functions by hyperbolic function with numerical control parameter ε and $V_{I0} = V_{II0} = V_0$ in the form

$$f_{Ik}(V_0 - \dot{X}_{I2}) = \mu_0 \tanh\left(\frac{V_0 - \dot{X}_{I2}}{\varepsilon}\right) - \alpha(V_0 - \dot{X}_{I2}) + \beta(V_0 - \dot{X}_{I2})^3 \,, \tag{35}$$

$$f_{IIk}(V_0 - \dot{X}_{II2}) = \mu_0 \tanh\left(\frac{V_0 - \dot{X}_{II2}}{\varepsilon}\right) - \alpha(V_0 - \dot{X}_{II2}) + \beta(V_0 - \dot{X}_{II2})^3 \,, \tag{36}$$

with fixed $\mu_0 = 0{,}8$, $\alpha = 15{,}59$, $\beta = 4252{,}12$ and $\varepsilon = 0{,}0001$.

Moreover, because functions $\boldsymbol{I}(f_g - (e_1 Y_{I1} - e_2 \varphi_I))$, $\boldsymbol{I}(f_g - (e_1 Y_{II1} - e_2 \varphi_{II}))$ are also discontinuous, in our computations we use the following approximations

$$f_{In}(f_g - (e_1 Y_{I1} - e_2 \varphi_I)) = \tanh^3\left(\frac{f_g - (e_1 Y_{I1} - e_2 \varphi_I)}{\varepsilon}\right) \cdot \boldsymbol{I}(f_g - (e_1 Y_{I1} - e_2 \varphi_I)) \,, \tag{37}$$

$$f_{IIn}(f_g - (e_1 Y_{II1} - e_2 \varphi_{II})) = \tanh^3\left(\frac{f_g - (e_1 Y_{II1} - e_2 \varphi_{II})}{\varepsilon}\right) \cdot \boldsymbol{I}(f_g - (e_1 Y_{II1} - e_2 \varphi_{II})) \,. \tag{38}$$

In result, in our numerical simulation we consider the following equations of motion

$$\begin{cases} \ddot{X}_{I1} + a_1 X_{I1} + a_2 \varphi_I - a_3 X_{I2} = 0, \\ \ddot{Y}_{I1} + b_1 Y_{I1} - b_2 \varphi_I + f_g = 0, \\ \ddot{\varphi}_I + c_1 X_{I1} - c_2 Y_{I1} + c_3 \varphi_I - c_4 X_{I2} + k(\varphi_I - \varphi_{II}) = 0, \\ \ddot{X}_{I2} - X_{I1} - \varphi_I + X_{I2} = f_{Ik}(V_0 - \dot{X}_{I2}) \cdot [f_g - (e_1 Y_{I1} - e_2 \varphi_I)] \cdot \boldsymbol{1}(f_g - (e_1 Y_{I1} - e_2 \varphi_I)), \\ \ddot{X}_{II1} + a_1 X_{II1} + a_2 \varphi_{II} - a_3 X_{II2} = 0, \\ \ddot{Y}_{II1} + b_1 Y_{II1} - b_2 \varphi_{II} + f_g = 0, \\ \ddot{\varphi}_{II} + c_1 X_{II1} - c_2 Y_{II1} + c_3 \varphi_{II} - c_4 X_{II2} + k(\varphi_{II} - \varphi_I) = 0, \\ \ddot{X}_{II2} - X_{II1} - \varphi_{II} + X_{II2} = f_{IIk}(V_0 - \dot{X}_{II2}) \cdot [f_g - (e_1 Y_{II1} - e_2 \varphi_{II})] \cdot \boldsymbol{1}(f_g - (e_1 Y_{II1} - e_2 \varphi_{II})). \end{cases} \quad (39)$$

5. Numerical results

Fig. 2 shows the phase trajecories of the system for the velocity of driving belt $V_0 = 0.002$ and zero initial conditions in time interval $\tau \in [10000,12000]$. The time interval was chosen to avoid the transition state.

Obtained results and detect an irregular dynamics of the considered 8 –DOF system. The phase trajectories, Poincaré maps (Fig. 3) as well as power spectral densities (Fig.4) indicate that the character of motion is chaotic. If we increase the value of V_0 then the character of motion changes. This situation is presented in the Fig. 5, Fig.6 and Fig.7. When the dimensionless velocity of driving belts reaches the value of 0.05, the motion exhibit a periodic character.
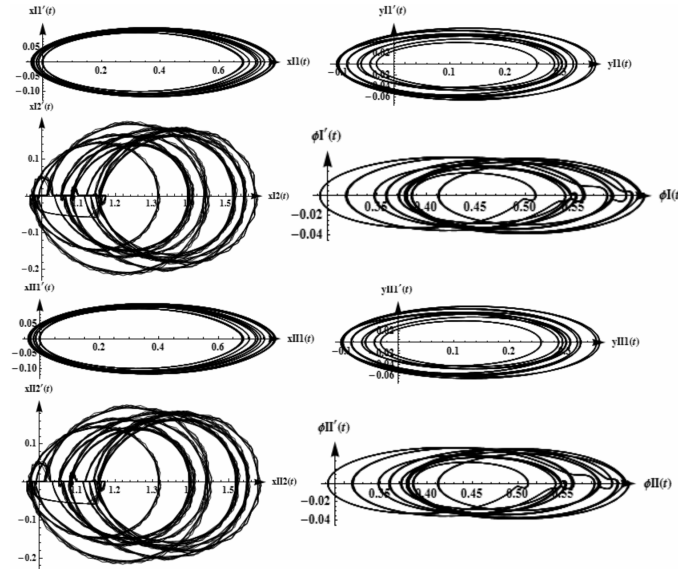
Figure 2. Phase trajectories of the system for $V_0 = 0.002$ in the time interval $\tau \in [10000,12000]$.
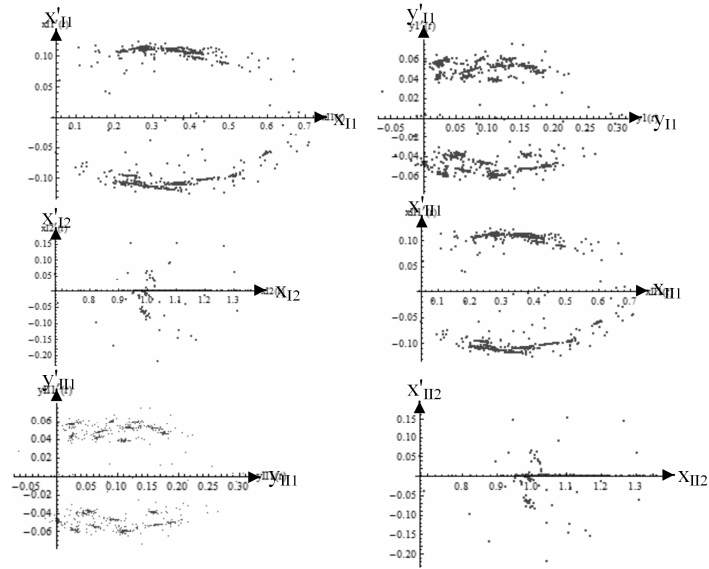
Figure 3. Poincaré map of the system for $V_0 = 0.002$ in the time interval $\tau \in [10000, 12000]$.
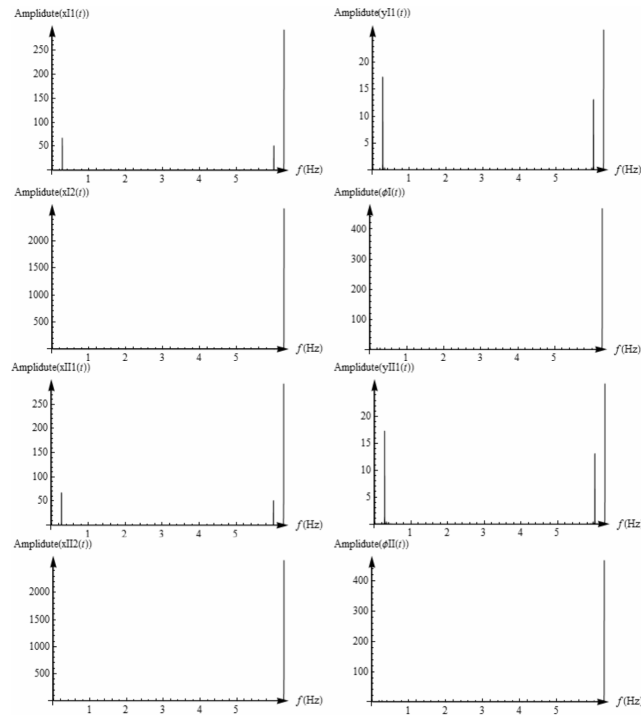
Figure 4. Power spectral of the system for $V_0 = 0.002$ in the time interval $\tau \in [10000, 12000]$.
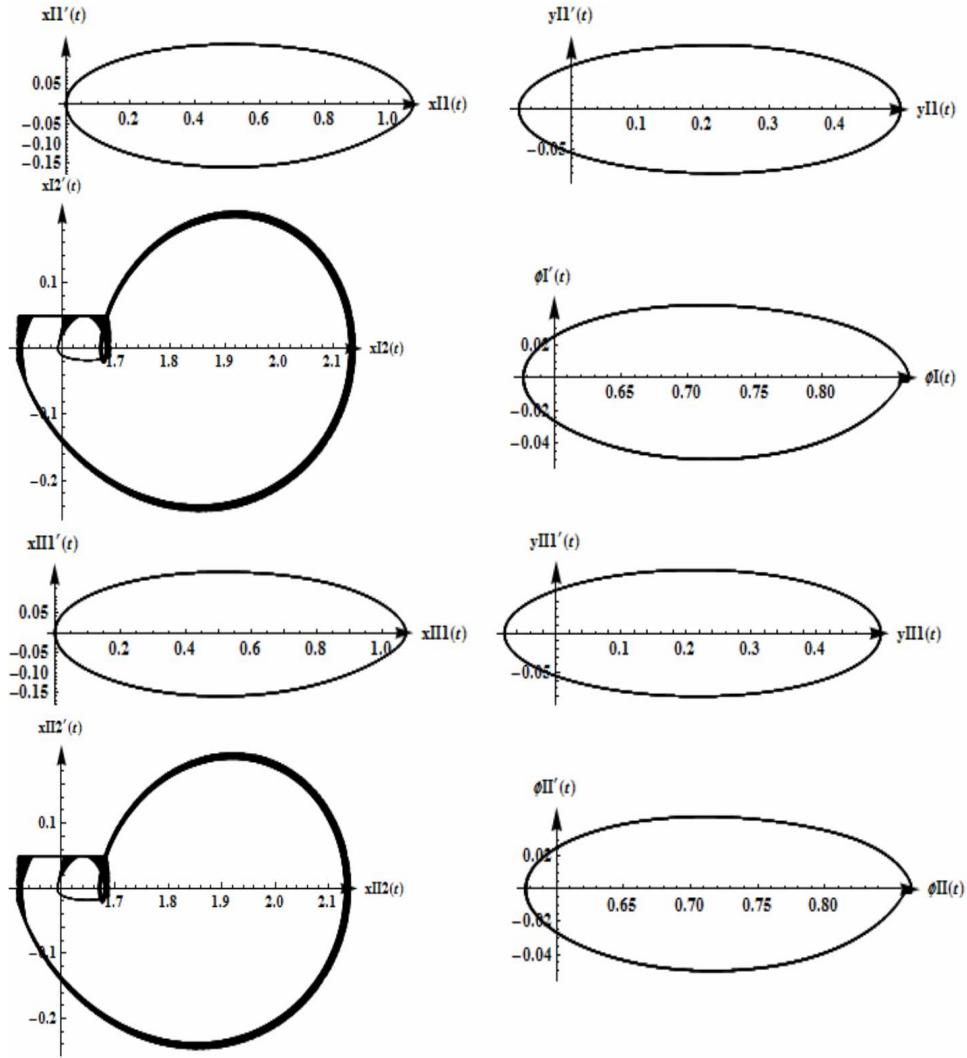
Figure 5. Phase trajectories of the system for $V_0 = 0.05$ in the time interval $\tau \in [10000, 12000]$.
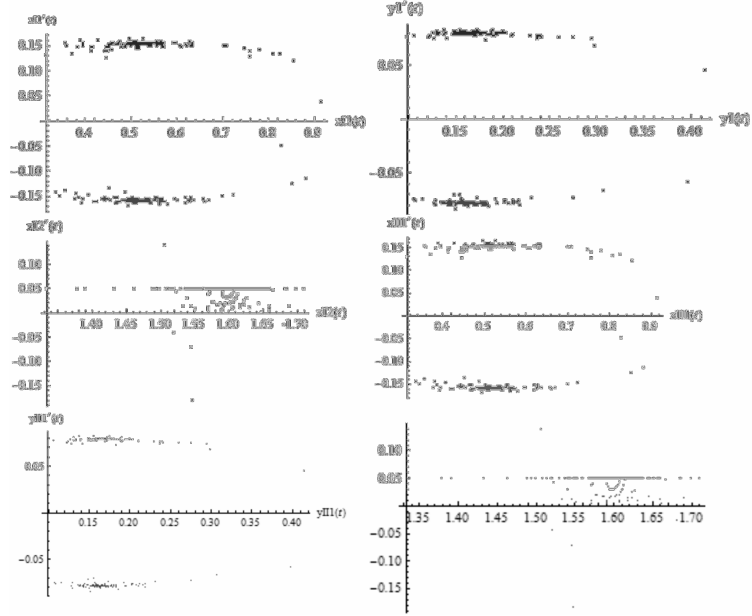
Figure 6. Poincaré map of the system for $V_0 = 0.002$ in the time interval $\tau \in [10000, 12000]$.

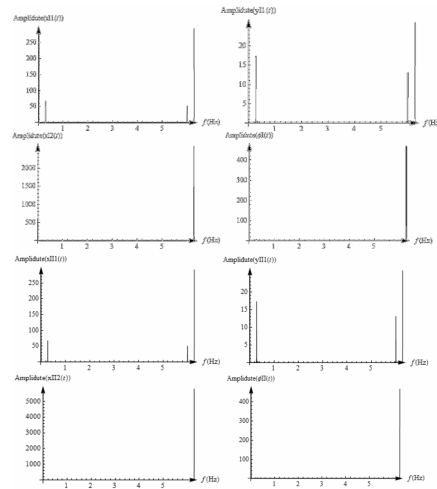**Figure 7.** Power spectral of the system for $V_0 = 0.05$ in the time interval $\tau \in [10000, 12000]$

6. Conclusions

In the paper mathematical model of two coupled 4-DOF mechanical linear sliding systems with dry friction is considered. The considered system can be treated as a system of two identical 4-DOF systems presented earlier in [4] and coupled by torsional spring. In this case the physical

338

interpretation of the considered model could be two rows of carriages laying on the guideways and coupled by an elastic shaft, which moves at constant velocity with respect to the guideways as a foundation. From a mathematical viewpoint the mentioned system is presented as a nonlinear equations of motion, which are obtained using second kind Lagrange's equations. Dynamics of the analyzed system is carried out for one set of system parameters and various non-dimensional V_0.

Interesting dynamics behaviors of the considered system are reported using time series and phase trajectories. The obtained results indicate, that the analyzed system possesses periodic, quasi-periodic or chaotic orbits, as well as fixed points. Moreover, the mentioned results show that synchronization effects between the coupled systems are possible.

Acknowledgments

References

[1] Abdo, J., Tahat, M., Abouelsoud, A., and Danish, M. The effect of frequency of vibration and humidity on the stick–slip amplitude. *International Journal of Mechanics and Materials in Design* 6 (2010), 45–51.

[2] Chelidze, T., Lursmanashvili, O., Matcharashvili, T., Varamashvili, N., Zhukova, N., and Mepharidze, E. High-order synchronization of stick–slip process: experiments on spring–slider system. *Nonlinear Dynamics* 50 (2010), 259–275.

[3] Fan, Q., Xu, C., Niu, J., Jiang, G., and Liu, Y. Stability analyses and numerical simulations of the single degree of freedom spring-slider system obeying the revised rate- and state-dependent friction law. *Journal of Seismology* 18 (2014), 637–649.

[4] Grzelczyk, D., Awrejcewicz, J., Kudra, G. Dynamics of Mechanical Sliding System with Dry Friction. *Machine Dynamics Research* 38(3), (2014), 61-70.

[5] Meurk, A. . Microscopic stick–slip in friction force microscopy. *Tribology Letters* 8 (2000), 161–169.

[6] Motchongom-Tingue, M., Kenmoe, G.D., and Kofane, T. C. Stick–Slip Motion and Static Friction in a Nonlinear Deformable Substrate Potential. *Tribology Letters* 43 (2011), 65–72.

[7] Perfilyev, V., Moshkovich, A., Lapsker, I., Laikhtman, A., and Rapoport. L. Dislocation Structure and Stick–Slip Phenomenon. *Tribology Letters* (2014), 295-301.

[8] Vellinga, W.P., and Hendriks, C.P. Sliding friction dynamics of hard single asperities on soft surfaces. *Tribology Letters* 9 (2000), 119–124.

[9] Zhang, J., and Meng, Y. Stick–Slip Friction of Stainless Steel in Sodium Dodecyl Sulfate Aqueous Solution in the Boundary Lubrication Regime. *Tribology Letters* 56 (2014), 543–552.

[10] Zhang, S.L., and Valentin, J.M. Stick–slip and temperature effect in the scratching of materials. *Tribology Letters* 12, 4 (2002), 195-202.

[11] Zhang, J., Zhang, N., and Crowther, A.R.. Analytical study of brake groan through a coupled 2DOF brake model. *Japan Journal of Industrial and Applied Mathematic* (2011), 205-222.

Jan Awrejcewicz, Professor: Department of Automation, Biomechanics and Mechatronics, Lodz University of Technology, 1/15 Stefanowski Str., 90-924 Lodz, Poland *(jan.awrejcewicz@p.lodz.pl)*.

Angelika Kosińska, M.Sc. (Ph.D. student): Department of Automation, Biomechanics and Mechatronics, Lodz University of Technology, 90-924 Łódź, Poland *(angelica.kosinska@dokt.p.lodz.pl)*. The author gave a presentation of this paper during one of the conference sessions.

Dariusz Grzelczyk, Ph.D.: Department of Automation, Biomechanics and Mechatronics, Lodz University of Technology , 90-924 Łódź, Poland *(dariusz.grzelczyk@p.lodz.pl)*

The dynamic and flutter properties of the new airfoil model NACA0015
(STA228-15)

Jan Kozanek, Vaclav Vlcek, Igor Zolotarev, Martin Stepan

Abstract: The new airfoil model NACA0015 (with a chord length of 59mm, thickness 8.85mm and width of 76.6mm) was traditionally proposed as the dynamic system with two near eigenfrequencies 13.3 Hz and 17.1 Hz corresponding rotation and transversal movability. This design allows the generation of self-excited motion of the airfoil in subsonic air flow with Mach numbers M = 0.2 – 0.4. Inside of the airfoil are placed angle sensor and four semiconductor pressure sensors. For time registration of the transversal movement of the profile rotation centre, the contactless magnetic linear sensor is used. In the paper, the identified eigenvalues and eigenmodes for zero flow will be compared with flutter properties (frequency, modes, time evolutions) of the airfoil situated in the aerodynamic tunnel of the Institute of Thermomechanics AS. The evaluated sensor data serve for the correction of classical interferometric measurements supposing isentropic flow.

1. Introduction

The new airfoil model NACA0015 was constructed with the idea of generation self-excited vibrations in subsonic air flow. For these aerodynamic experiments the suction type aerodynamic tunnel of the Institute of Thermomechanics AS – Fig. 1, was used. This research belongs to the broader field of investigation of complex questions regarding the stability of aerodynamic systems. For this purpose, the fluttering profile is supported as a two-degree of freedom dynamic system, one for rotation (pitch) and the second for translation (shift) motion with mutually near and adjustable eigenfrequencies. Compared with older constructions [1, 2], the translation springs were not changed, but the rotational support was realized using a new coil spring with high elasticity. The corresponding eigenfrequency can be changed by the spring length and by a different diameter of the spring wire. The eigenfrequency of the transversal mode is influenced by using the grub screws – [3].

Figure 1. Measured profile situated in the test section of the wind tunnel.

The new airfoil model with a chord length of 59 mm, thickness 8.85 mm and width of 76.6 mm was divided into five parts - see in Fig. 2. Two miniature ball bearings enable the profile to rotate, the axis of profile rotation is situated in 1/3 of the chord. The weight of the profile is about 38 grams.
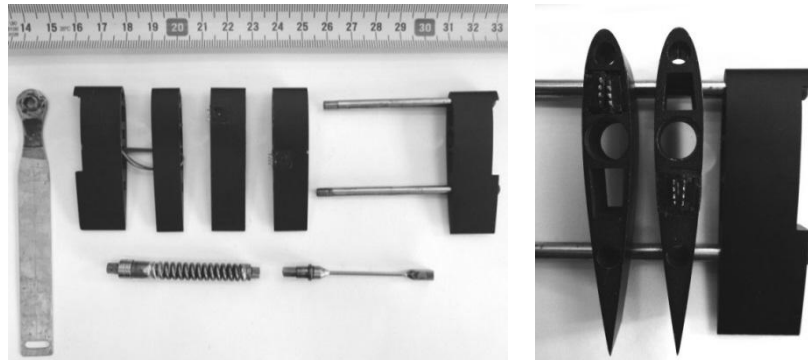
Figure 2. The new airfoil model NACA0015 with two modifications of rotational springs.

Arrangement of the aerodynamic experiment

The schema of the measured profile support and experimental equipment are shown in Fig. 3.
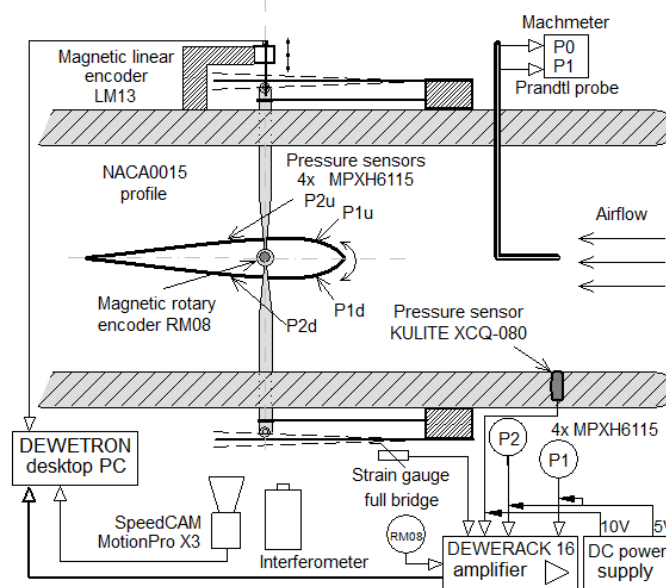
Figure 3. Airfoil rotational and transversal support and the experimental equipment.

Pitch angle of the profile was recorded with the magnetic rotary encoder type RM08. The translation of the frame with fluttering profile was measured with the magnetic non-contact linear encoder LM13TCD40CB10A05. The measurement of the translation is doubled by using a calibrated

strain gauge with full bridge placed on the flat spring. Pressure on the surface of the profile was measured with four semiconductor pressure sensors MPXH6115A6U - FREESCALE SEMICONDUCTOR. Transducers were coupled in pairs on both profile surfaces.

Signals were processed with DEWETRON desktop PC using Dewesoft 7 software. The optical measurements were performed by using a high-speed camera MotionPro X3 at 1000 frames per second. Velocity of the flow field was measured by a Machmeter associated with the wind tunnel. The interferometer is constructed for visualization in an area with a diameter of 160 mm. The flutter was initialized by a 1.7 mm initial deviation of the frame.

2. Eigenvalues and eigenvectors of the system for zero air flow velocity

The modal analysis was carried out in the laboratory Dynamics and Vibration of the Institute of Thermomechanics AS CR. The excitation was realized by pulse-hammer with the force sensor 4519-002 B&K and the measurements were performed with the acceleration pick-up DeltaTron 4519-002. The discretized time signals were registered and evaluated by the PULSE B&K measurement system with card 7537A. Two (marked 1, 2) excited and measured points in the centre of rotation and on the trailing edge are depicted in Fig. 4.

The measured complex frequency transfer functions $v_{j,k}(f)$ as the function of excitation frequency f (see Fig. 6), were evaluated by the fitting identification method – [5]:

$$v_{j,k}(f) = \sum_{v=1}^{2} \frac{a_{v,j,k}}{i\,f - s_v} + h(f) \,, \tag{1}$$
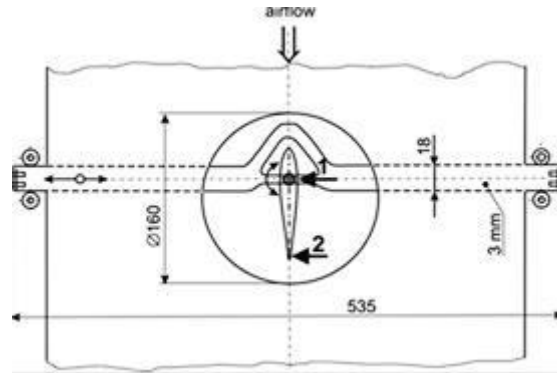
Figure 4. The configuration of the dynamic experiment with the two excited and measured points.

where $v_{j,k}(f)$ is the frequency transfer function (excitation in k-point and pick-up in j-point), s_v is the complex eigenvalue and $a_{v,j,k}$ is the corresponding complex modal contribution and $h(f)$ is the influence of the other modes and experimental perturbations.

Initial pre-tensioning of the transversal springs

Two flat strip springs allow vertical displacements of the profile and their rigidities can be changed by using grub screws. The three positions of the grub screws correspond to the three positions of the grub p1, p2, p3 and define three geometrical deformations of the flat strip springs (see Table 1).

Table 1. Initial tensioning corresponding to the different grub screw positions p1, p2, p3.

p	p1	p2	p3
d [mm]	0.233	0.583	0.933

a)

b)

c)

d)
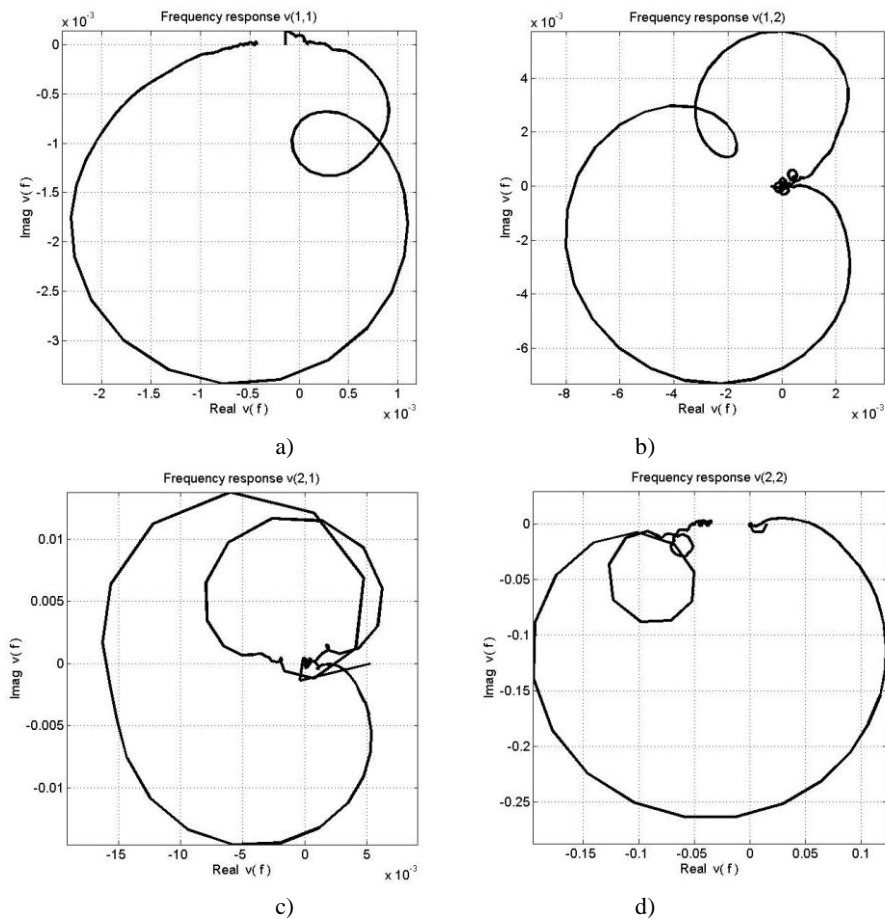
Figure 5. The example of the complex frequency responses v(f) in measured configurations (pick-up,excitation) - a)-(1,1), b)-(1,2), c)-(2,1) and d)-(2,2) - initial tensioning p2.

The identified complex eigenvalues and eigenmodes for three dynamic systems distinguished by their initial tensioning of the transversal springs are summarized in Tables 2, 3, 4, 5, 6, 7 and 8. One of the rotational eigenmodes has very small amplitude and therefore it was neglected.

Table 2. Identified modal parameters $a_{\nu,j,k}$ and eigenvalues s_ν for the initial tensioning p1.

(pick-up,excitation)	(1,1)	(1,2)	(2,1)	(2,2)
$a_{\nu,j,k}$	-0.0002 - 0.003i 0.0003 - 0.005i	-0.003 - 0.017i 0.003 + 0.005i 0.001 + 0.009i	0.003 - 0.005i 0.002 + 0.003i	0.019 - 0.24i 0.030 + 0.015i
s_ν [Hz]	-1.09 +14.26i -0.65 +17.13i	-0.50 +13.37i -0.22 +14.78i -0.27 +17.25i	-0.53 +13.53i -0.91 +17.99i	-0.61 +13.29i -0.24 +14.45i

Table 3. Normalized eigenvectors v_1^T and v_2^T corresponding to rotational and transversal eigenmodes for the initial tensioning p1.

v_1^T	$[a_{1,2,1}\,,a_{1,2,2}]/a_{1,2,2}$	$[0.0197 - 0.0141i, 1]$
v_2^T	$[a_{2,1,1}\,,a_{2,1,2}]/a_{2,1,1}$	$[1, -1.7816 + 0.3069i]$

Table 4. Identified modal parameters $a_{\nu,j,k}$ and eigenvalues s_ν for the initial tensioning p2.

(pick-up,excitation)	(1,1)	(1,2)	(2,1)	(2,2)
$a_{\nu,j,k}$	-0.0000 - 0.001i 0.0002 - 0.002i	-0.0002 - 0.009i 0.001 + 0.004i -0.0002 + 0.004i	-0.003 - 0.0045i 0.001 + 0.003i	0.030 - 0.23i 0.010 + 0.032i
s_ν [Hz]	-0.94 +14.40i -0.67 +17.56i	-0.53 +13.71i -0.25 +14.91i -0.30 +17.66i	-0.58 +13.64i -0.68 +18.19i	-0.80 +13.36i -0.28 +14.44i

Table 5. Normalized eigenvectors v_1^T and v_2^T corresponding to rotational and transversal eigenmodes for the initial tensioning p2.

v_1^T	$[a_{1,2,1}\,,a_{1,2,2}]/a_{1,2,2}$	$[0.0176 - 0.0153i, 1]$
v_2^T	$[a_{2,1,1}\,,a_{2,1,2}]/a_{2,1,1}$	$[1, -1.9901 + 0.0990i]$

Table 6. Identified modal parameters $a_{v,j,k}$ and eigenvalues s_v for the initial tensioning p3.

(pick-up,excitation)	(1,1)	(1,2)	(2,1)	(2,2)
$a_{v,j,k}$	-0.0003 - 0.001i 0.0004 - 0.002i	-0.0004 - 0.008i 0.0016 + 0.004i -0.0002 + 0.004i	-0.004 - 0.003i -0.0002 + 0.002i	0.085 - 0.23i -0.053 + 0.024i
s_v [Hz]	-1.01 +14.56i -0.91 +17.630i	-0.58 +13.69i -0.27 +14.96i -0.59 +17.76i	-0.63 +13.83i -0.82 +18.28i	-0.94 +13.33i -0.41 +14.29i

Table 7. Normalized eigenvectors v_1^T and v_2^T corresponding to rotational and transversal eigenmodes for the initial tensioning p3.

v_1^T	$[a_{1,2,1}, a_{1,2,2}]/a_{1,2,2}$	$[0.0058 - 0.0195i, 1]$
v_2^T	$[a_{2,1,1}, a_{2,1,2}]/a_{2,1,1}$	$[1, -1.9423 + 0.2885i]$

Table 8. Complex eigenvalue s_v corresponding to the largest amplitude - the tensioning of the transversal springs is marked as p1, p2, p3.

s_v [Hz]	Rotational eigenmode	Transversal eigenmode
p1	-0.61+13.29i	-0.65+17.13i
p2	-0.80+13.36l	-0.67+17.56i
p3	-0.94+13.33i	-0.91+17.63i

3. Aerodynamic experiments with airfoil profile NACA0015

Aerodynamic experiments were realized in the Laboratory of the Institute of Thermomechanics AS near Novy Knin for subsonic air flow with Mach numbers M = 0.2-0.4 and Reynolds numbers (2.63-2.83)·10^5. The results, involving flutter regime, with M = 0.21and Re = 2.76 10^5, will be presented as an example in this paper. The measured parameters were shift [mm] of the rotation centre and pitch angle [deg] as a function of time. The frequency spectrum was evaluated for rotational vibration in different time moments. Profile kinematics added the following information for the profile motion. Pressure of the fluid flow on the profile surface was measured in 4 surface points.

3.1 Shift of the centre of rotation in flutter regime

The shift of the centre of rotation in the starting period of the flutter for Mach number M = 0.21 is depicted in Fig. 6 (data No. 2911-21). The initial deviation of the frame for flutter starting was 1.7 mm,

346
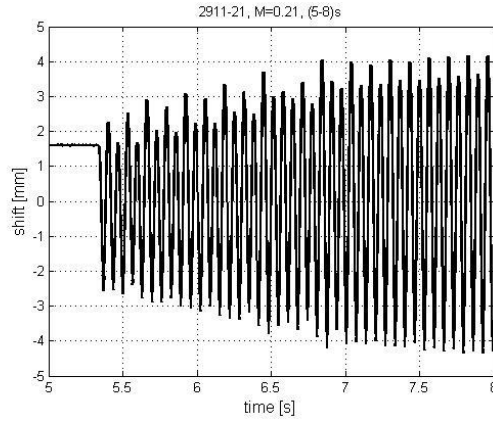
Figure 6. Shift in the starting period of the flutter.

the flutter frequency was 15.2 Hz. About 1.5 s after the flutter initialization, the steady state vibration was registered. The shift response on the interruption of the fluid flow we can see in Fig. 7.
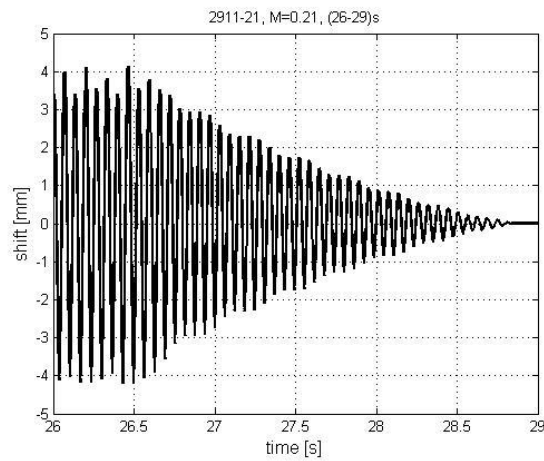
Figure 7. The shift response on the interruption of the fluid flow

Periodic beat vibration, visible on the record, is probably connected with the eigenfrequency of the profile for zero fluid flow (see Tab. 8) and the above-mentioned flutter frequency.

3.2 Pitch angle analysis

The behavior of the pitch angle time records was more complicated compared to the shift of centre of rotation. This also concerns the starting period of flutter and the steady state period of shift motion. The time record of the pitch angle corresponding to the time period from Fig. 6 is depicted in Fig. 8.

347
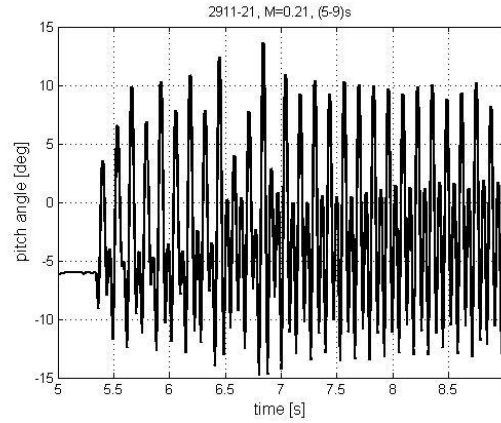
Figure 8. Time record of the pitch angle correspondig to the start of flutter in Fig. 6.

The initial deviation of the frame for the start of flutter caused a pitch angle of about -9 [deg]. Time record (the amplitude increase and steady state part) in Fig. 8 is similar to Fig. 6, but in Fig. 8 we can see significant polyharmonic vibration (7.8 Hz and 15.1 Hz), verified by spectral analysis in the time period (7 – 9) s – see Fig. 9. The vibration with the frequency 15.1 Hz during the start of flutter corresponds to the mutual approach of different rotational (13.3 Hz) and transversal (17.6 Hz) eigenfrequencies in the case of zero air flow velocity. This is caused by the interaction of the fluid flow with the vibrating airfoil. On the other hand, a new generated frequency 7.8 Hz with smaller amplitude corresponds to some subharmonic vibration with half frequency.
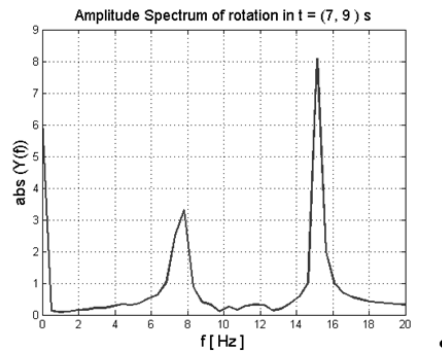
Fig. 9. Spectral analysis of the pitch angle record in the time period (7 – 9) s.

When the tunnel was suddenly closed, the fluid flow influence decreased and the airfoil polyharmonic vibration with frequencies 12.9 Hz and 16.1 Hz approached the case of zero air flow velocity – see Fig. 10.
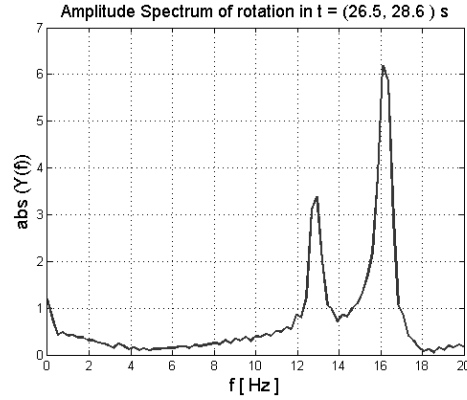
Fig. 10. Spectral analysis of the pitch angle record in the time period (26.5 – 28.6) s – after the interruption of the fluid flow.

3.3 Profile kinematics

The previous paragraphs studied the time records – shift and the pitch angle of the vibrating airfoil. Another possibility of this presentation is to describe their motion simultaneously in the same graph with new axes (pitch angle, shift), where the time becomes the parameter of the curve. For example the short time interval (17 – 17.1) s of the steady state vibration (Data No. 2911) is depicted in Fig. 11, the two parts of the incomplete loops are visible. For this case of our flutter experiments with the airfoil model, which has lower rotational eigenfrequency than transversal, these two incomplete loops are typical.
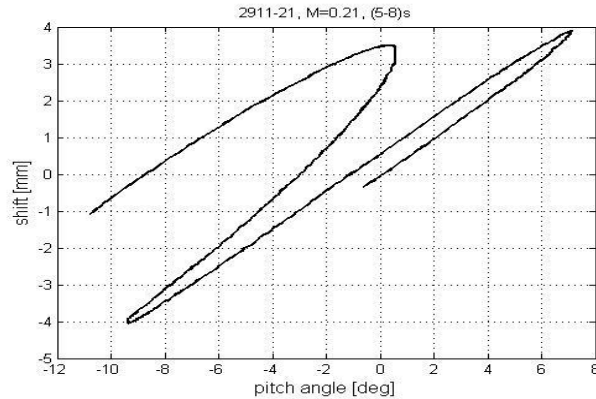
Figure 11. Airfoil motion in (pitch angle, shift) axis with two incomplete loops, data No. 2911-21.

4. Conclusions

The experimental device for the aerodynamic research of the behavior of the airfoil model NACA0015 in the air flow was reconstructed and its operation was verified. The principal aim is to

generate self-excited motion of the airfoil in subsonic air flow in an aerodynamic tunnel. The measuring and data registration system have been extended and improved. The spectral and modal properties of the new airfoil support were identified for different configurations of the flat strip springs. As an example, the experimental results describing the appearance of the flutter vibration for the air flow velocity with Mach number M = 0.21, the steady state vibration and the response to the interruption of the air flow were presented and analyzed. The profile kinematics showed double loop vibration in comparison with the results obtained in the earlier measurements [4].

Acknowledgments

References

[1] Vlcek, V., Kozanek, J. Preliminary interferometry measurements of flow field around fluttering NACA0015 profile, *Acta Technica*, 56, 2011, pp. 379–387.

[2] Kozanek, J., Vlcek, V., Zolotarev, I. Vibrating Profile in the Aerodynamic Tunnel — Identification of the Start of Flutter, Journal of Applied Nonlinear Dynamics 3(4), 2014, pp. 317–323.

[3] Vlcek, V., Stepan, M., Zolotarev, I., Kozanek,J. Experimental Investigation of the Flutter Incidence Range for Subsonic Flow Mach Numbers, Proc. of the 21-st International Conference ENGINEERING MECHANICS 2015, Svratka, Czech Republic, 2015, pp. 350-351.

[4] Zolotarev, I., Vlcek, V., Kozanek, J. Experimental results of a fluttering profile in the wind tunnel. Flow-induced Vibration, School of Engineering Trinity College, Dublin, (eds. Meskell, C., Bennett, G.), 2012, pp. 677-680.

[5] He, J. and Fu, Z.-F. *Modal Analysis*, Butterworth Heinemann, Oxford, 2004.

Jan Kozanek, Ph.D.: Institute of Thermomechanics AS CR, Department of Dynamics and Vibrations, Dolejskova 5, 18200 Prague 8, Czech Republic (kozanek@it.cas.cz). The author gave a presentation of this paper during one of the conference sessions.

Vaclav Vlcek, Ph.D.: Institute of Thermomechanics AS CR, Department of Fluid Dynamics, Dolejskova 5, 18200 Prague 8, Czech Republic (vlcek@it.cas.cz).

Igor Zolotarev, Ph.D.: Institute of Thermomechanics AS CR, Department of Dynamics and Vibrations, Dolejskova 5, 18200 Prague 8, Czech Republic (igor@it.cas.cz).

Martin Stepan, M.Sc.: Technical University of Liberec, Faculty of Mechatronics, Informatics and Interdisciplinary Studies, Liberec, Studentska 1402, 64001 Liberec, Czech Republic (martin.stepan@tul.cz).

Comparative analysis of the methods of controlling the gyroscope-stabilized platform for searching and observing air targets
(CON003-15)

Izabela Krzysztofik, Jakub Takosoglu, Zbigniew Koruba

Abstract: At present, remotely controlled weapon modules are becoming the basic equipment of modern army. The platform for searching and observing air targets is one of the most significant elements of a weapon module. The effectiveness of conducting combat tasks by anti-aircraft defence units also depends on the precision of operation of the said platform. The platform constitutes a stable basis, independent of angular movements of the base on which it is located, for a TV/thermal imaging camera and the coordinator used for searching and observing the detected target. The paper presents the algorithm of control of the platform for searching and observing the manoeuvring air target placed on the deck of a combat vehicle. The optimized, classic PD controller and fuzzy controller PD type were designed. Numerical research of the dynamics of the controlled platform were conducted as well as a comparative analysis of the proposed methods of control. The results of research are presented in a graphical form.

1. Introduction

A self-propelled rocket missile ensures anti-aircraft protection to military units increasing at the same time their mobility. A quick change of a current location is an inseparable element of a strategy indispensable on a contemporary battlefield. Searching, identifying and tracking the detected air target during the movement of a vehicle are important elements of the operation of the missile. At present, more and more countries equip their armies with self-propelled missiles having remotely controlled weapon modules. The platform for searching and observing air targets is one of the most significant elements of a weapon module. The platform constitutes a stable basis, independent of angular movements of the base on which it is located, for a TV/thermal imaging camera and the coordinator used for searching and observing the detected target. Also the effectiveness of the combat tasks conducted by anti-aircraft defence units depends on the precision of operation of the platform [1,2].

The concept of the platform that is possible to be used on the deck of a combat vehicle is shown in figure 1. The gyroscope-stabilized platform is the basis of the structure [3,4]. Inside the platform, there is a TV and a thermal imaging camera and two mechanically-controlled gyroscopes. Step

engines are the elements performing the control of programmed and stabilisation movements. Each engine controls one platform axis. Also a central control unit is mounted in the basis of the device whose function is to control the device operation. The device may perform movements in altitude and in azimuth in the full angular range.
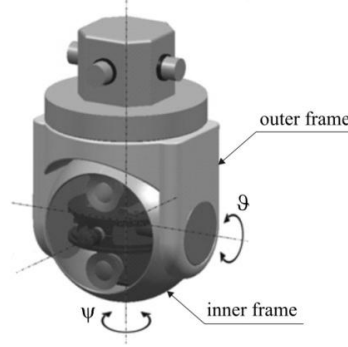
Figure 1. The general view of the platform for searching and observing air targets [5].

When searching for a target, the device axis scans the air space on the set path, i.e. it follows the strictly defined lines in space. Then, the optical system may intersect the thermal radiation emitted by the air target. After detecting the target, the device automatically passes to the automatic tracking of the target, i.e. from that moment its axis overlaps with the line of sight. Thanks to the use of the proposed gyroscope-stabilized platform, the image of the target is stable and the movements of cameras are independent of vibrations and angular movements of the combat vehicle.

The rule of operation and the full mathematical model of one-, two- and three-axis gyroscope-stabilized platform are discussed in detail in paper [5]. In the present paper, a one-axis gyroscope-stabilized platform was considered. Moreover, an assumption was adopted that the device centre of mass overlaps with the centre of its rotations and the moments of inertia of its frames are omitted. Then, the linearized equations of movement of the devices are as follows:

$$J_k\left(\ddot{\vartheta}+\dot{\omega}_y\right)-J_o n\left(\dot{\psi}+\omega_z\right)+\eta_w\dot{\vartheta}=M_w, \tag{1}$$

$$J_k\left(\ddot{\psi}+\dot{\omega}_z\right)+J_o n\left(\dot{\vartheta}+\omega_y\right)+\eta_z\dot{\psi}=M_z, \tag{2}$$

where:

ϑ, ψ – angles of location of the device axis in space;

ω_y, ω_z – angular velocities of tilt and declination of the vehicle deck, respectively;

J_o, J_k – longitudinal and transverse moment of inertia of the device, respectively;

M_w, M_z – moments of controlling forces having an impact on the inner and outer frame, respectively;

η_w, η_z – friction coefficients in suspension bearings of the inner and outer frame, respectively.

2. The algorithm of control of the gyroscope-stabilized platform for searching and observing air targets

The use of the considered platform allows for quick searching of a target in space, stable maintaining of the detected target in the field of view of optical system and attacking the target during the movement of the vehicle. It increases the effectiveness and mobility of the self-propelled rocket missile. The algorithm of operation of the platform when searching the air space and tracking the detected air target is shown in figure 2.
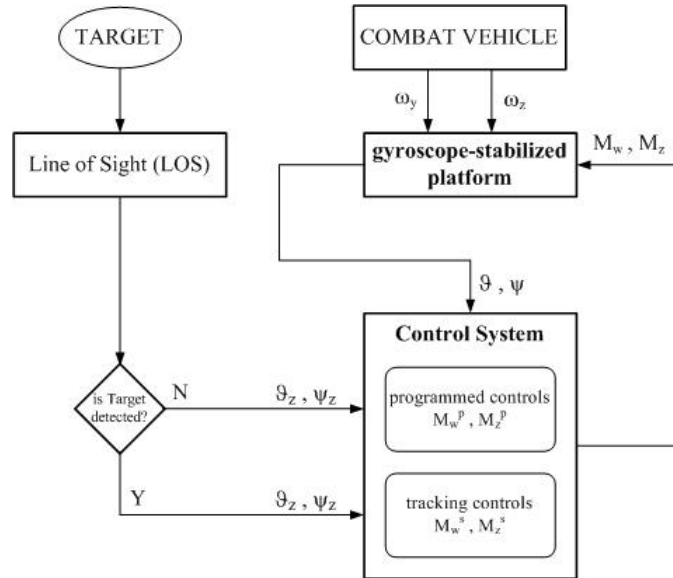
Figure 2. The algorithm of operation of the platform mounted on the deck of a combat vehicle.

The platform is influenced by the disruptions coming from the vehicle. Regardless of the disruptions, the device axis should perform programmed movements (when searching for a target) and tracking movements (when tracking the detected target). Hence, the control moments should be used which have the following form [2,5]:

$$M_w = \mathbf{\Pi}(t_o, t_w) \cdot M_w^p(t) + \mathbf{\Pi}(t_s, t_k) \cdot M_w^s(t), \tag{3}$$

$$M_z = \Pi(t_o, t_w) \cdot M_z^p(t) + \Pi(t_s, t_k) \cdot M_z^s(t), \tag{4}$$

where:

M_w^p, M_z^p –programmed control moments; M_w^s, M_z^s – tracking control moments;

$\Pi(t_o, t_w), \Pi(t_s, t_k)$ – functions of a rectangular impulse; t_0 – moment of starting to scan the space;

t_w – moment of detecting the target; t_s – moment of starting to track the target; t_k – moment of completing the self-guidance process.

The control moments, both programmed and tracking, are generated directly from the platform control system.

2.1. The control system with the PD controller

For controlling the platform and tracking air targets a control system with the PD controller was designed [6].

Then, the control moments have the following form [5]:

$$M_w = k_b(\vartheta_z - \vartheta) - k_c(\psi_z - \psi) + h_g(\dot{\vartheta}_z - \dot{\vartheta}),\tag{5}$$

$$M_z = k_c(\vartheta_z - \vartheta) + k_b(\psi_z - \psi) + h_g(\dot{\psi}_z - \dot{\psi}).\tag{6}$$

The controller coefficients k_b, k_c, h_g were selected in the optimum way due to the minimum deviation between the fulfilled and set path described in detail in paper [5].

It was assumed that the device axis moves with programmed movement on the n-leaved rosette. Then, the set angles of location of its axis are determined from the following dependences:

$$\vartheta_z(t) = \alpha \cdot \sin(\omega_2 \cdot t) \cdot \cos(\omega_1 \cdot t),\tag{7}$$

$$\psi_z(t) = \alpha \cdot \sin(\omega_2 \cdot t) \cdot \sin(\omega_1 \cdot t),\tag{8}$$

where: $\alpha = 0.75\,\text{rad}$, $\omega_1 = 1.25\,\text{rad/s}$, $\omega_2 = 29\,\text{rad/s}$.

When tracking a target, the set angles of location of the device axis are determined from the equations of movement LOS:

$$\frac{d\xi}{dt} = V_c[\cos\chi_c \cos\psi_z \cos(\vartheta_z - \gamma_c) + \sin\chi_c \sin\psi_z] + \\ - V_n[\cos\chi_n \cos\psi_z \cos(\vartheta_z - \gamma_n) + \sin\chi_n \sin\psi_z],\tag{9}$$

$$\frac{d\vartheta_z}{dt} = \frac{1}{\xi\cos\psi_z}[-V_c \cos\chi_c \sin(\vartheta_z - \gamma_c) + V_n \cos\chi_n \sin(\vartheta_z - \gamma_n)],\tag{10}$$

$$\frac{d\psi_z}{dt} = -\frac{1}{\xi}\{V_c[\cos\chi_c \sin\psi_z \cos(\vartheta_z - \gamma_c) - \sin\chi_c \cos\psi_z] + \\ - V_n[\cos\chi_n \sin\psi_z \cos(\vartheta_z - \gamma_n) - \sin\chi_n \cos\psi_z]\}.\tag{11}$$

The diagram of the classic PD controller is shown in figure 3.
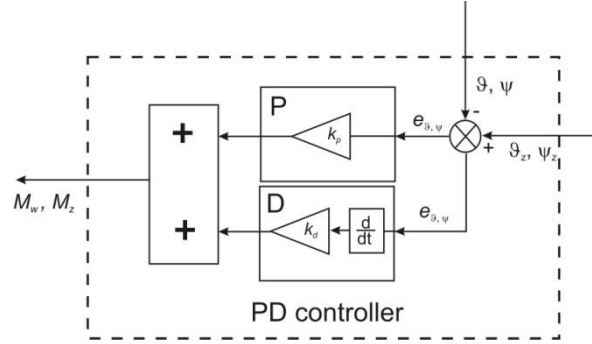
Figure 3. A schematic diagram of PD controller.

2.2. The control system with a fuzzy controller

Classic controllers are successfully used in the analysed dynamic systems. The authors made an attempt to use an alternative algorithm of control using the methods of artificial intelligence, namely the fuzzy controller. Fuzzy controllers are used in household goods and appliances, the automotive industry, as autopilots of ships and planes, as well as auto-tune systems, e.g. autofocus. For both controllers, the controlling signals are the control moments M_z and M_w generated directly from the control system. Controllers input signals are the actual angles of inclination ϑ and declination ψ of the device axis and the set angles of inclination ϑ_z and declination ψ_z of that axis. Based on those input signals, adjustment deviation $e_{\vartheta,\psi}$ is determined. The diagram of the fuzzy controller is shown in figure 4 [7,8]. The designed controller belongs to a class of systems MIMO type because it has four inputs and two outputs. The basis of a fuzzy controller comprises 25 rules of Mac Vicaa-Whelen which constitute the surface of processing shown in figure 5 [9,10].
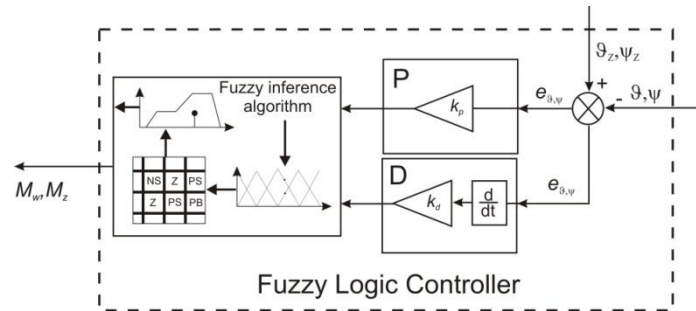
Figure 4. A schematic diagram of the fuzzy logic controller.
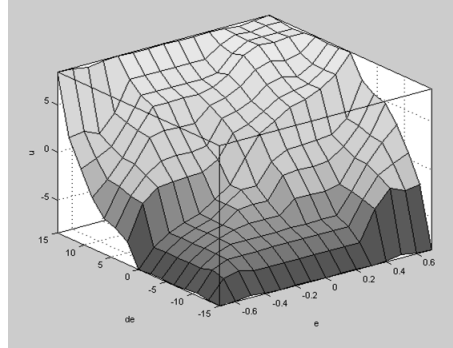
Figure 5. A surface of control.

2.3. Results of numerical research

The results of the conducted numerical research are shown in figures 6-10.

During the process of fuzzy inference, the level of ignition was determined using the MIN operator, the fuzzy implication with the MIN operator, and individual outlets of all rules were aggregated with the use of the MAX operator. In the process of defuzzification, the method of centre of gravity (COG) was applied [11,12].

The conditions of conducting the simulation were as follows:

a) platform parameters

$$J_o = 5 \cdot 10^{-4} \, \text{kgm}^2, \ J_k = 2.5 \cdot 10^{-4} \, \text{kgm}^2, \ n = 600 \, \text{rad/s}, \ \eta_w = \eta_z = 0.05 \ \text{Nms},$$

b) initial parameters for the vehicle and the target

$$X_n = 0 \, \text{m}, \ Y_n = 0 \, \text{m}, \ Z_n = 0 \, \text{m}, \ V_n = 10 \, \text{m/s},$$

$$X_c = 2000 \, \text{m}, \ Y_c = 1000 \, \text{m}, \ Z_c = 2000 \, \text{m}, \ V_c = 200 \, \text{m/s}, \ \gamma_c = 0 \, \text{rad}, \ \chi_c = -0.25 \, \text{rad}.$$

The kinematic forces working on the platform from the side of the vehicle were adopted in the harmonic form:

$$\omega_y = \omega_{yo} \sin(\nu_n t), \ \omega_z = \omega_{zo} \cos(\nu_n t),$$

where: $\omega_{yo} = \omega_{zo} = 2.5 \, \text{rad/s}$, $\nu_n = 10 \, \text{rad/s}$.

a)

b)
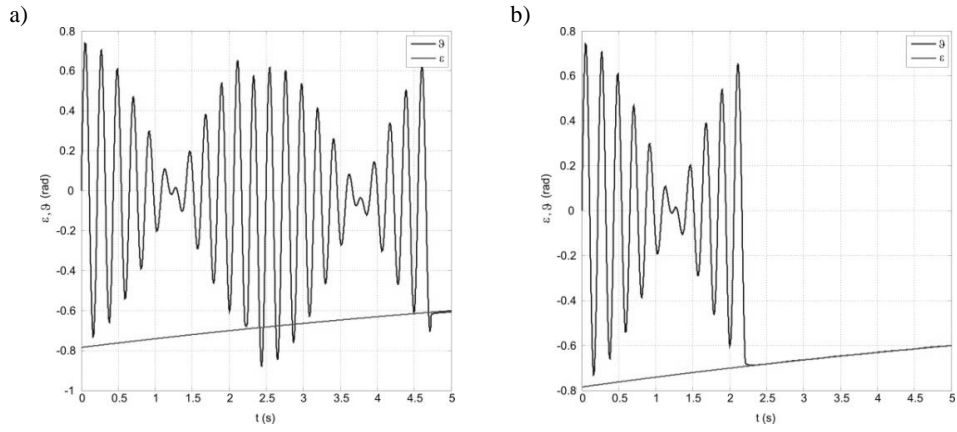
Figure 6. The angles of inclination of platform axis and LOS: a) PD controller; b) fuzzy controller.

a)

b)
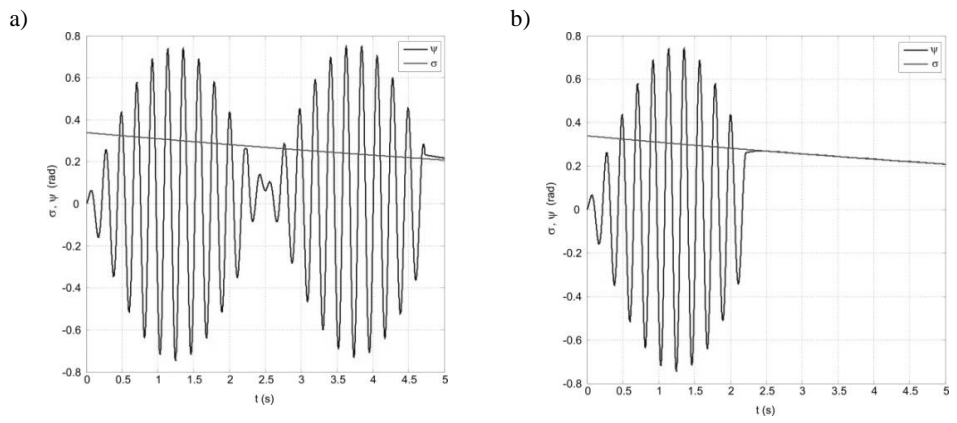
Figure 7. The angles of declination of platform axis and LOS: a) PD controller; b) fuzzy controller.

a)

b)
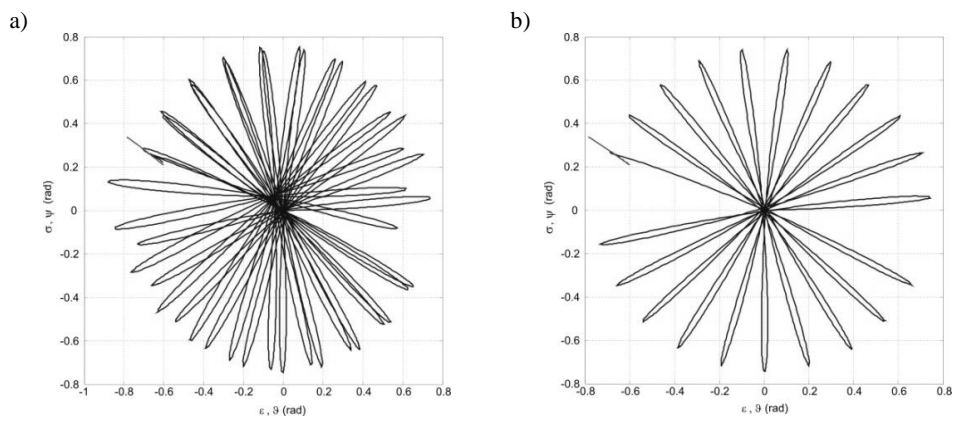
Figure 8. The paths of platform axis and LOS: a) PD controller; b) fuzzy controller.
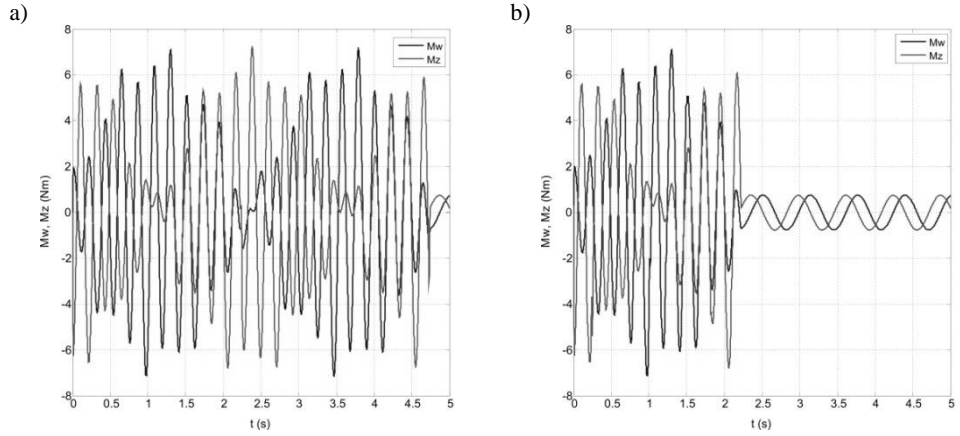
Figure 9. Control moments: a) PD controller; b) fuzzy controller.
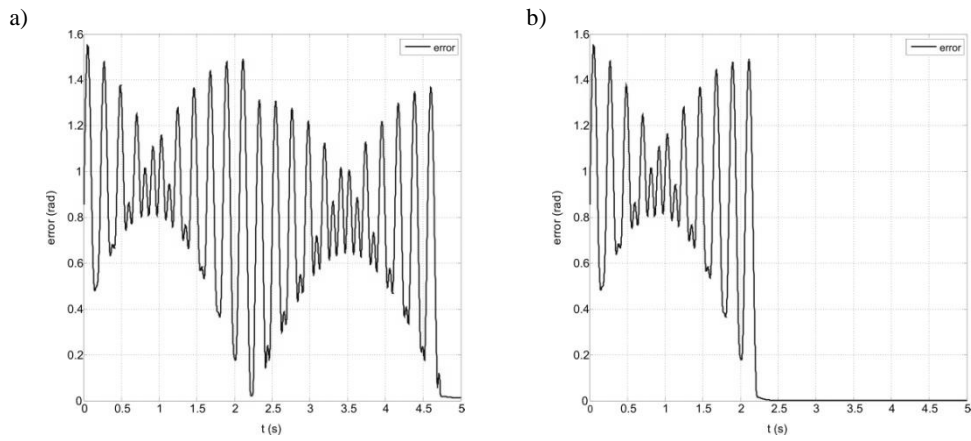
Figure 10. Control errors: a) PD controller; b) fuzzy controller.

4. Comparative analysis of the methods of control

Two types of controllers were used to control the gyroscope-stabilized platform for comparative purposes. The first is the classic PD controller and the second is the fuzzy controller PD type. The quality of the control of the gyroscopes platform was verified by means of standard performance indices including (Table 1) [13]:

Table 1. Performance indices

Indices	Formula	Description
settling time	t_R	With the assumed over-adjustment, it is demanded that the adjustment time was short as possible.
steady-state error	$e_{st} = \lim\limits_{t \to \infty} |e(t)|$	Adjustment error e_{st} appears in the system either after the change of the set value or after the

		change of one of the disruptions, which can potentially affect the system, or simultaneously due to the two above mentioned reasons.
IAE (Integral of Absolute Error)	$$IAE = \int_0^\infty |e(t)|dt$$	The modified Sartorius' criterion indicates all errors in the adjustment system resulting from over-adjustment and under-adjustment.
ISE (Integral of Squared Error)	$$ISE = \int_0^\infty e^2(t)dt$$	The criterion in which the significance of small errors is decreased, and the significance of large errors is emphasized, because of that the ISE criterion gives a more objective image of reality. The control system optimized with the use of ISE may indicate a small, slowly disappearing error of adjustment.
ITSE (Integral of the Time-weighted Squared Error)	$$ITSE = \int_0^\infty te^2(t)dt$$	Optimization with the use of that criterion is used to achieve a control system in which the disappearance of the error is faster.
ISC (Integral of Control)	$$ISC = \int_0^\infty u^2(t)dt$$	Criterion indicating the costs of control
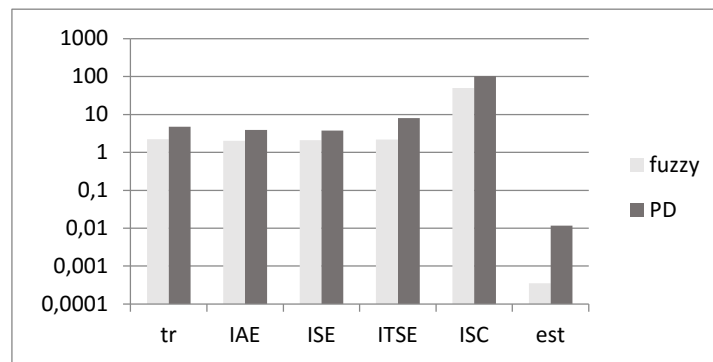
Figure 11. Comparison of performance indices of the classic and fuzzy controller

(logarithmic scale).

5. Concluding remarks

The comparative analysis of the methods of controlling the gyroscope-stabilized platform for searching and observing air targets was conducted in the paper. Two types of controllers were designed: a classic PD controller with optimum parameters and a fuzzy controller with MIMO structure. In order to verify the quality of the control, the synthesis of controllers was made and six selected indices of quality of the control were determined. The use of the fuzzy controller significantly shortened the time of searching the space and detecting a target. The time of detecting a target for a classic controller amounts to 4.7 s, while for the fuzzy controller only 2.2 s. All of the analysed performance indices indicate smaller values in the case of a fuzzy controller. Additionally, a

significantly smaller cost of control (by more than 50%) was stated which was examined with the ISC index in relation to the classic controller.

References

[1] Krzysztofik I. The dynamics of the controlled observation and tracking head located on a moving vehicle. *Solid State Phenomena*, 180, (2012), 313-322.

[2] Krzysztofik I. and Koruba Z. Model of Dynamics and Control of Tracking-Searching Head, Placed on a Moving Object. *Journal of Automation and Information Sciences*, 44(5), (2012), 38-47.

[3] Koruba Z., Dziopa, Z. and Krzysztofik I. Dynamics and control of a gyroscope-stabilized platform in a self-propelled anti-aircraft system. *Journal of Theoretical and Applied Mechanics*, 48(1), (2010), 5-26.

[4] Ogonowski K. and Adamski M. The model of a guided air bomb navigation system using controlled gyroscopic platform. *Scientific Journal of The Polish Air Force Academy*, 1(22), 57 – 66.

[5] Koruba Z. *The elements of the theory and applications of the controlled gyroscope*. Monographs, Studies, Dissertations M7, Kielce University of Technology, Kielce, 2008 (in Polish).

[6] Kaczorek T., Dzieliński A., Dąbrowski W. and Łopatka R. *Fundamentals of control theory*. WNT, Warsaw, 2013 (in Polish).

[7] Sivanandam S. N., Sumathi S. and Deepa S. N. *Introduction to Fuzzy Logic using MATLAB*. Springer-Verlag, Berlin, 2007.

[8] Szymak P. *Selection of Methods for Underwater Robot Control*. *Solid State Phenomena*, 164, (2010), 149-154.

[9] Driankov D., Hellendoorn, H. and Reinfrank M. *Introduction to fuzzy control*. WNT, Warsaw, 1996.

[10] Yager R. R. and Filev D. P. *Fundamentals of fuzzy modelling and control*. WNT, Warsaw, 1995.

[11] Piegat A. *Fuzzy modelling and control*. EXIT, Warsaw, 2003.

[12] Takosoglu J. E., Łaski P. A. and Błasiak S. A fuzzy controller for the positioning control of an electro-pneumatic servo-drive. *Proceedings of the Institution of Mechanical Engineers Part I-Journal of Systems and Control Engineering*, 226(10), (2012), 1335-1343.

[13] Nuruzzaman M. *Control System Analysis & Design in MATLAB and SIMULINK*, Lulu.com, USA, 2015.

Izabela Krzysztofik, Ph.D.: Kielce University of Technology, Department of Applied Computer Science and Armament Engineering, 7 Al. Tysiąclecia PP St., 25-314 Kielce, Poland (*pssik@tu.kielce.pl*). The author gave a presentation of this paper during one of the conference sessions.

Jakub Takosoglu, Ph.D.: Kielce University of Technology, Department of Manufacturing Engineering and Metrology, 7 Al. Tysiąclecia PP St., 25-314 Kielce, Poland (*qba@tu.kielce.pl*).

Zbigniew Koruba, Professor: Kielce University of Technology, Department of Applied Computer Science and Armament Engineering, 7 Al. Tysiąclecia PP St., 25-314 Kielce, Poland, (*ksmzko@tu.kielce.pl*).

Modelling and numerical simulations of a pendulum elastically suspended and driven by frictional contact with rotating disk (BIF204-15)

Grzegorz Kudra, Jan Awrejcewicz

Abstract: The work concerns modelling and numerical simulations of a special kind of physical pendulum frictionally driven. The pendulum's joint is suspended elastically in the plane of the motion resulting in the full plane motion of the pendulum and in tree degrees of freedom of the analysed mechanical system. The pendulum is driven by frictional contact with a disk with a constant angular velocity. Examples of self-excited oscillations and bifurcation dynamics of the pendulum are presented. Majority of the work focuses on efficient approximate modelling of the resultant friction force and moment occurring on the contact surface.

1. Introduction

There are plenty of examples of mechanical systems, where friction plays a crucial role in their dynamical properties and behavior. Friction can be a desirable phenomenon or not, but in both cases its appropriate and efficient mathematical modelling is an important part of analysis and synthesis of mechanical systems with frictional contacts. The classically understood friction model is a relation between single component of friction force and one-dimensional relative displacement of the contacting bodies. This relation can possess different levels of complexity, beginning with the classical Coulomb friction law and ending with advanced relations, where often additional state variables are defined. These kinds of models can be applied directly during mathematical description and analysis of dynamical systems with frictional contacts, where at each element of the contact the same relative motion of the contacting surfaces occurs. But in real life one can encounter many examples of mechanical systems, where the above assumption cannot lead to correct results. One can give such examples like dynamics of rolling bearings, billiard balls, different kinds of tops, the wobblestone, polishing machine, disk clutches and many others. Exact and correct results can be always obtained by detailed physical modelling and space discretization in vicinity of the contact. But this approach leads to computation cost increase and is not appropriate in fast numerical simulations. This is the reason of the interest of many researchers in looking for simple approximate models of contact forces, which would be suitable for fast and realistic simulations of the certain classes of mechanical systems with frictional contacts.

Contensou [1] noticed that if the product of the normal component of the relative angular velocity of the contacting bodies and size of the contact is sufficiently large then one should take into account the coupling between the friction force and moment. He proposed an integral model of the resultant friction forces under assumption of fully developed sliding and Coulomb friction law valid on each element of the circular contact. The results of Contensou were then significantly developed by Zhuravlev [2], who presented exact analytical solution to the Contensou's integral model and also proposed the corresponding approximant models based on the Padé expansions. Further developments and generalizations of the approximant models of the contact forces, including rolling resistance, assuming elliptical contact area, are proposed in the work [3]. Special regularizations of these models can be found in [4, 5], which allow to avoid singularities for vanishing relative motion as well as take into account the different values of the static and kinetic friction coefficients.

Stamm and Fidlin [6] proposed a regularized two-dimensional model of friction forces appearing on finite plane area based on elasto-visco-plastic theory, but requiring discretization of the contact area. They applied their model in modelling and analysis of a disk-on-a-disk system being to certain extent a counterpart of a disk clutch, where alternating sliding and sticking solutions can occur [7]. In the work [8] there are presented results of analytical studies of the similar system, where the approximations based on Taylor's expansion of the friction force and moment for fully developed sliding are used.

In the present work the authors apply their earlier developed models of the resultant friction force and moment in modelling and numerical simulations of the mechanical system being a certain modification of the disk-on-a-disk system analyzed in the works [7, 8].

2. Modelling of friction forces

Let us consider a circular contact area of dimensionless form exhibited in figure 1, where one assumed: i) the fully developed sliding; ii) Classical Coulomb friction law valid on each element of the contact; iii) constant friction coefficient; iv) that the relative motion of the contacting surfaces is a plane motion of rigid bodies. There are also assumed the following relations between real and non-dimensional quantities describing the contact: $\widehat{\mathbf{T}}_s = \mu \widehat{N} \mathbf{T}_s$, $\widehat{\mathbf{M}}_s = \mu \widehat{N} \hat{a} \mathbf{M}_s$, $\hat{\sigma}(x, y) = (\widehat{N}/\hat{a}^2) \sigma(x, y)$, $\widehat{\mathbf{v}}_s = \hat{a} \mathbf{v}_s$ and $\widehat{\boldsymbol{\omega}}_s = \boldsymbol{\omega}_s$, where $\widehat{\mathbf{T}}_s$ and $\widehat{\mathbf{M}}_s$ are the real resultant friction force and moment loading the contact and reduced to the center A of the contact F, $\mathbf{T}_s$ and $\mathbf{M}_s$ – the corresponding non-dimensional resultant friction force and moment, μ – friction coefficient, $\widehat{N}$ – real normal loading of the contact, $\hat{a}$ – characteristic dimension of the contact (in this case real radius of the contact F), $\hat{\sigma}$ and σ – real and dimensionless contact pressure, $\widehat{\mathbf{v}}_s$ and $\mathbf{v}_s$ – relative real and dimensionless relative linear velocity at the point A, $\widehat{\boldsymbol{\omega}}_s = \boldsymbol{\omega}_s$ – relative angular velocity in the plane of the contact. Note that time in all the introduced quantities is real.
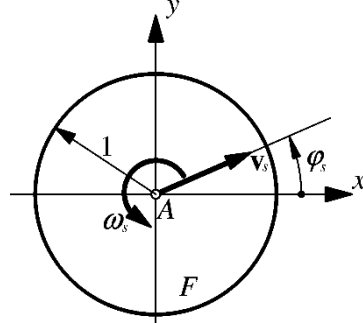
Figure 1. The contact area.

Assuming that $\mathbf{T}_s = -T_{sx}\mathbf{e}_x - T_{sy}\mathbf{e}_y$, $\mathbf{M}_s = -M_s\mathbf{e}_z$, $\mathbf{v}_s = v_{sx}\mathbf{e}_x + v_{sy}\mathbf{e}_y$ and $\boldsymbol{\omega}_s = \omega_s\mathbf{e}_z$, where $\mathbf{e}_\xi$ is the unit vector along the axis ξ, one can find the following integral expressions:

$$T_{sx} = \iint_{dF} n(x,y)\,(v_{sx} - \omega_s y)\,dxdy\,,$$

$$T_{sy} = \iint_{dF} n(x,y)\,(v_{sy} + \omega_s x)\,dxdy\,, \tag{1}$$

$$M_s = \iint_{dF} n(x,y)\,\left(\omega_s(x^2 + y^2) + v_{sy}x - v_{sx}y\right)dxdy\,,$$

where

$$n(x,y) = \sigma(x,y)\left((v_{sx} - \omega_s y)^2 + \left(v_{sy} + \omega_s x\right)^2\right)^{-1/2}.$$

Since the model (1) requires integration over the contact area at each time step, it is not suitable tool for fast and reliable numerical simulations. Based on the results presented in the previous works of the authors [3] and assuming the constant dimensionless contact pressure distribution on circular contact area $\sigma(x,y) = 1/\pi$, one can derive the following two sets of approximations of the integral model (1)

$$T_{sx}^{(I_{0,0})} = \frac{v_{sx}}{\left(\left(v_{sx}^2 + v_{sy}^2\right)^{\frac{m}{2}} + b^m|\omega_s|^m\right)^{\frac{1}{m}}}\,,$$

$$T_{sy}^{(I_{0,0})} = \frac{v_{sy}}{\left(\left(v_{sx}^2 + v_{sy}^2\right)^{\frac{m}{2}} + b^m|\omega_s|^m\right)^{\frac{1}{m}}}\,, \tag{2}$$

$$M_s^{(I_{0,0})} = \frac{\frac{2}{3}b\,\omega_s}{\left(\left(v_{sx}^2 + v_{sy}^2\right)^{\frac{m}{2}} + b^m|\omega_s|^m\right)^{\frac{1}{m}}}\,.$$

and

363

$$T_{sx}^{(I_{1,1})} = \frac{(v_{sx}^2 + v_{sy}^2 + b\omega_s^2)v_{sx}}{\left((v_{sx}^2 + v_{sy}^2)^{\frac{3m}{2}} + b^m |\omega_s|^{3m}\right)^{\frac{1}{m}}},$$

$$T_{sy}^{(I_{1,1})} = \frac{(v_{sx}^2 + v_{sy}^2 + b\omega_s^2)v_{sy}}{\left((v_{sx}^2 + v_{sy}^2)^{\frac{3m}{2}} + b^m |\omega_s|^{3m}\right)^{\frac{1}{m}}}, \qquad (3)$$

$$M_s^{(I_{1,1})} = \frac{\frac{2}{3} b\,\omega_s^3 + \frac{1}{4}\,\omega_s(v_{sx}^2 + v_{sy}^2)}{\left((v_{sx}^2 + v_{sy}^2)^{\frac{3m}{2}} + b^m |\omega_s|^{3m}\right)^{\frac{1}{m}}}.$$

The approximations (2-3), after the replacements $v_{sx} = v_s \cos\varphi_s$ and $v_{sy} = v_s \sin\varphi_s$, fulfil the following properties of the integral model (1)

$$\left.\frac{\partial^i f^{(I_{n1,n2})}}{\partial v_s^i}\right|_{v_s=0} = \left.\frac{\partial^i f}{\partial v_s^i}\right|_{v_s=0}, \qquad i = 1, \dots, n_1\,,$$

$$\left.\frac{\partial^j f^{(I_{n1,n2})}}{\partial \omega_s^j}\right|_{\omega_s=0} = \left.\frac{\partial^j f}{\partial \omega_s^j}\right|_{\omega_s=0}, \qquad j = 1, \dots, n_2\,, \qquad (4)$$

where $f = T_{sx}, T_{sy}, M_s$, while m and b are arbitrary constants. Note that the above approximations possess the same denominators, which is not necessary in general (see [3]), but allows for application of the later presented special form of regularization.

In order to make easier the comparison of the functions (1-3), one introduces the spherical coordinates

$$v_{sx} = \lambda_s \cos\theta_s \cos\varphi_s, \quad v_{sy} = \lambda_s \cos\theta_s \sin\varphi_s, \quad \omega_s = \lambda_s \sin\theta_s. \qquad (5)$$

The parameters m and b are optimized by searching for the best fitting of the corresponding functions on the representative (in the case of circularly symmetric contact pressure distribution) field $\theta_s \in [0, \pi/2]$ and $\varphi_s = 0$. For the functions (2) one found $b = 1.744$ and $m = 0.674$, while for the approximations (3) one obtained $b = 0.765$ and $m = 0.452$. The corresponding plots are exhibited in figure 2. In the further modelling process the approximations (3) will be used.

In the works [4, 5] a special kind of regularization of the models of the type (2-3) was proposed, allowing to avoid singularity for vanishing relative motion of the contacting surfaces, but also to model the situation where the static friction coefficient is greater than the kinetic one. Applying that approach to the components (3) one gets
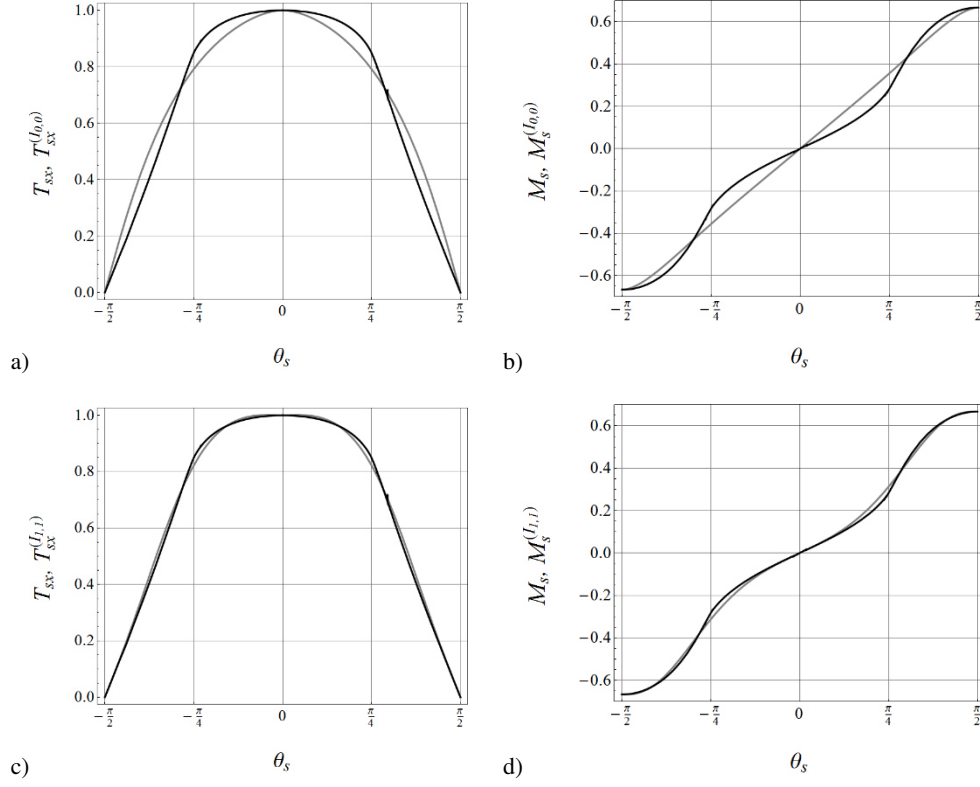
Figure 2. Comparison of the approximate components $T_{sx}^{(I_{0,0})}$ (a), $M_s^{(I_{0,0})}$ (b), $T_{sx}^{(I_{1,1})}$ (c), $M_s^{(I_{1,1})}$ (d) of the friction model (grey lines) with the corresponding full integral components T_{sx} and M_s (black lines), for $\varphi_s = 0$.

$$T_{sx\varepsilon}^{(I_{1,1})} = \left(v_{sx}^2 + v_{sy}^2 + b\omega_s^2\right)v_{sx}\lambda_{sb\varepsilon} \ ,$$

$$T_{sy\varepsilon}^{(I_{1,1})} = \left(v_{sx}^2 + v_{sy}^2 + b\omega_s^2\right)v_{sy}\lambda_{sb\varepsilon} \ , \tag{6}$$

$$M_{s\varepsilon}^{(I_{1,1})} = \left(\frac{2}{3} b \omega_s^3 + \frac{1}{4} \omega_s\left(v_{sx}^2 + v_{sy}^2\right)\right)\lambda_{sb\varepsilon} \ ,$$

where

$$\lambda_{sb\varepsilon} = \frac{1}{\sqrt{\left(\left(v_{sx}^2+v_{sy}^2\right)^{\frac{3m}{2}}+b^m|\omega_s|^{3m}\right)^{\frac{2}{m}}+\varepsilon^6}} + \eta'(\eta)\frac{\varepsilon^9}{\left(\left(\left(v_{sx}^2+v_{sy}^2\right)^{\frac{3m}{2}}+b^m|\omega_s|^{3m}\right)^{\frac{2}{m}}+\varepsilon^6\right)^2},$$

and where ε is a small numerical parameter. The coefficient η' is a function of the parameter η equal to the maximum magnitude of the resultant dimensionless friction force (or $\eta = \mu_0/\mu$, where μ_0 is the

static friction coefficient). This function can be approximated as $\eta'(\eta) \approx -13.607 + 30.893\eta - 22.01\eta^2 + 5.878\,\eta^3$ for $\eta \in [1, 1.3]$ and $\eta'(\eta) \approx -2.41 + 3.985\eta - 0.3581\eta^2 + 0.0493\,\eta^3$ for $\eta \in [1.3, 2.7]$, with the error $|\Delta\eta| < 0.001$ (see [5]). Figure 3 exhibits exemplary plots of the model (6) near zero relative motion, for $\theta_s = \pi/4$, $\varphi_s = 0$, $\eta = 2$ and $\varepsilon = 10^{-3}$.
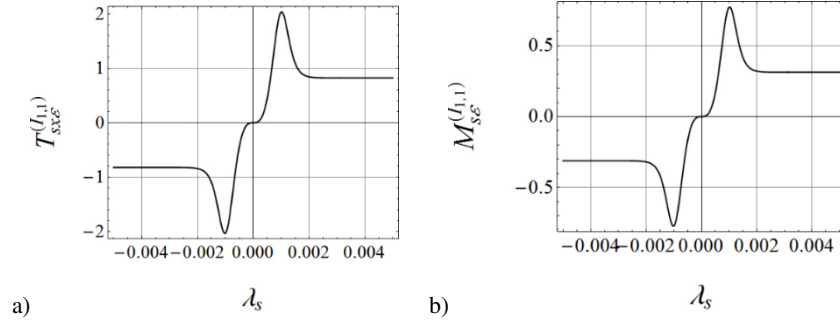
Figure 3. Approximations $T_{sx\varepsilon}^{(I_{1,1})}$ (a), $M_{s\varepsilon}^{(I_{1,1})}$ (b) near zero relative motion - for $\theta_s = \pi/4$, $\varphi_s = 0$, $\eta'(2) = 4.479$ and $\varepsilon = 10^{-3}$.

3. Mathematical model of the pendulum

In figure 4 there is presented a physical conception of the special mechanical system, being a certain modification of the disk-on-a-disk system analyzed in the works [7, 8]. A physical pendulum of mass M and moment of inertia B with respect to the mass center C is rotationally connected, by the use of the joint A, a light platform. The platform is mounted on the support by the use of elasto-damping elements in such a way, that it cannot rotate. The origin O of the introduced coordinate system OXY is defined as a position of the point A of the pendulum in its equilibrium position in the case of no friction forces acting on the mechanical system. The pendulum is equipped with a flat disk of radius R centered in the point A. This disk is in contact with a larger rotating rigid body performing pure rotational motion with constant angular velocity ω_0 about the center S. It assumed a constant contact pressure distribution and Coulomb friction law on each element of the circular contact between the bodies.

The governing equations of the presented mechanical system read

$$M(\ddot{X}_A - e\ddot{\varphi}\sin\varphi - e\dot{\varphi}^2\cos\varphi) + k_X X_A + c_X \dot{X}_A + \mu\widehat{N}T_{sx\varepsilon}^{(I_{1,1})} = 0\,,$$

$$M(\ddot{Y}_A + e\ddot{\varphi}\cos\varphi - e\dot{\varphi}^2\sin\varphi) + k_Y Y_A + c_Y \dot{Y}_A + \mu\widehat{N}T_{sy\varepsilon}^{(I_{1,1})} = 0\,,$$

$$B\ddot{\varphi} + e\left(Mg + k_X X_A + c_X \dot{X}_A + \mu\widehat{N}T_{sx\varepsilon}^{(I_{1,1})}\right)\sin\varphi + \tag{7}$$

$$-e\left(k_Y Y_A + c_Y \dot{Y}_A + \mu\widehat{N}T_{sy\varepsilon}^{(I_{1,1})}\right)\cos\varphi + c_\varphi\dot{\varphi} + \mu\widehat{N}RM_{s\varepsilon}^{(I_{1,1})} = 0\,,$$

where X_A and Y_A are the coordinates of the point A; φ – angular position of the pendulum; $e = AC$ – position of the mass center C; k_X and k_Y – stiffness coefficients of the elements supporting the rotational joint A; c_X and c_Y – the corresponding damping coefficients; c_φ – the coefficient of damping in the rotational joint A; μ - kinetic friction coefficient; $\widehat{N}$ – normal loading of the contact; X_S and Y_S – the coordinates of the point S; g – gravitational acceleration. As a model of the resultant friction force and moment the relations (6) are applied.
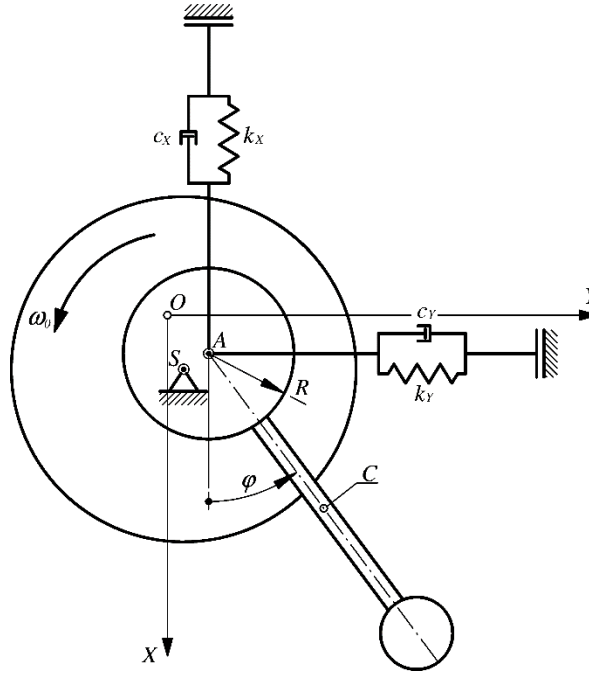
Figure 4. The physical concept of the mechanical system.

The kinematic arguments of the functions (6) read

$$\omega_s = \dot{\varphi} - \omega_0 \,,$$

$$v_{sx} = \frac{\dot{X}_A + \omega_0(Y_A - Y_S)}{R} \,, \tag{8}$$

$$v_{sy} = \frac{\dot{Y}_A - \omega_0(X_A - X_S)}{R} \,.$$

4.   Numerical simulations

In all the presented in this section numerical simulations the following parameters are fixed: $g = 9.81 \text{ m/s}^2$, $b = 0.452$, $m = 0.765$ and $\varepsilon = 10^{-3}$.
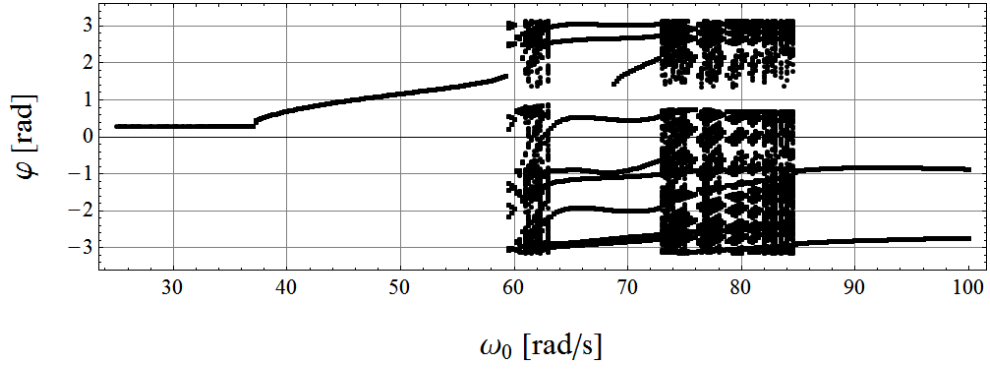
Figure 5. Bifurcation diagram with angular frequency ω_0 as a control parameter.

a)

b)
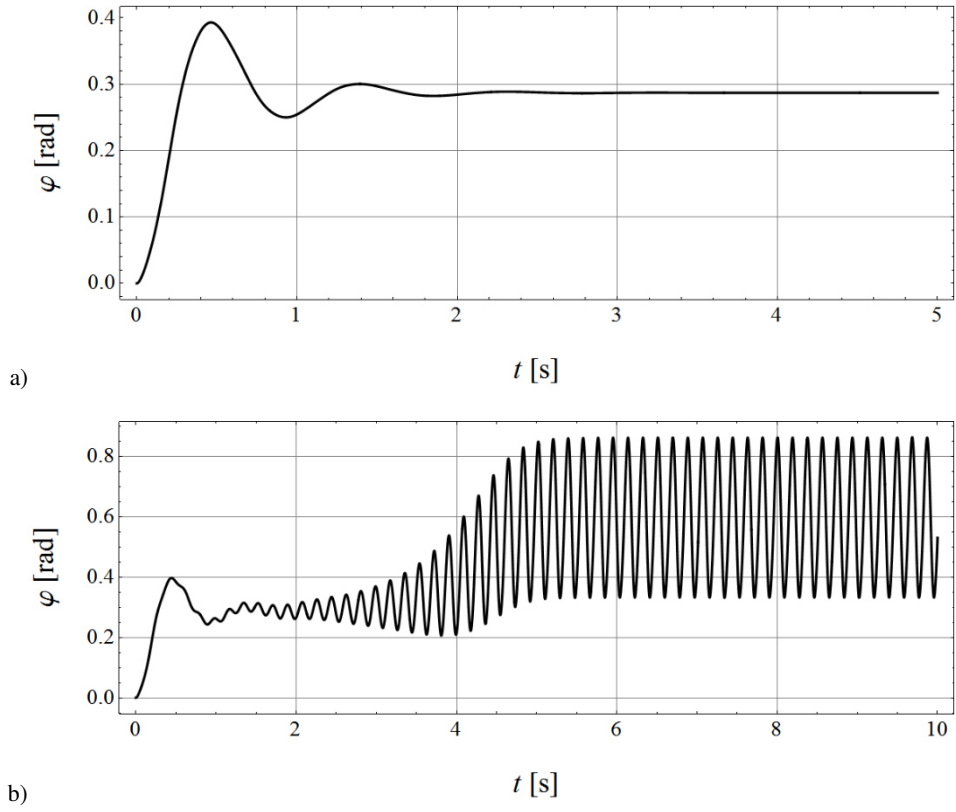
Figure 6. Examples of the system's behavior corresponding to the bifurcation diagram presented in figure 5, for $\omega_0 = 30$ rad/s (a), $\omega_0 = 40$ rad/s (b).

In figure 5 there is presented a bifurcation diagram of the system exhibited in figure 4 with the angular velocity ω_0 playing a role of a bifurcational parameter. The remaining system parameters read: $M = 1.2$ kg, $B = 0.01$ kg m^2, $e = 0.1$ m, $k_X = k_Y = 1000$ N/m, $c_X = c_Y = 0.1$N s/m, $c_\varphi = 0.1$ N·m·s, $X_s = 0$ m, $Y_s = 0$ m, $R = 0.02$ m, $\hat{N} = 25$ N, $\mu = 1$ and $\eta = 1$ (the static friction coefficient is equal to the kinetic one). For low angular velocities one observe a stable equilibrium position – see figure 6(a), where for $\omega_0 = 30$ rad/s the corresponding time history of the angle φ is presented. For the greater values of ω_0 a stable periodic attractor appears - see figure 6(b). Further increase of ω_0 leads to rich bifurcational and irregular dynamics, with full rotations of the pendulum – see figure 7.
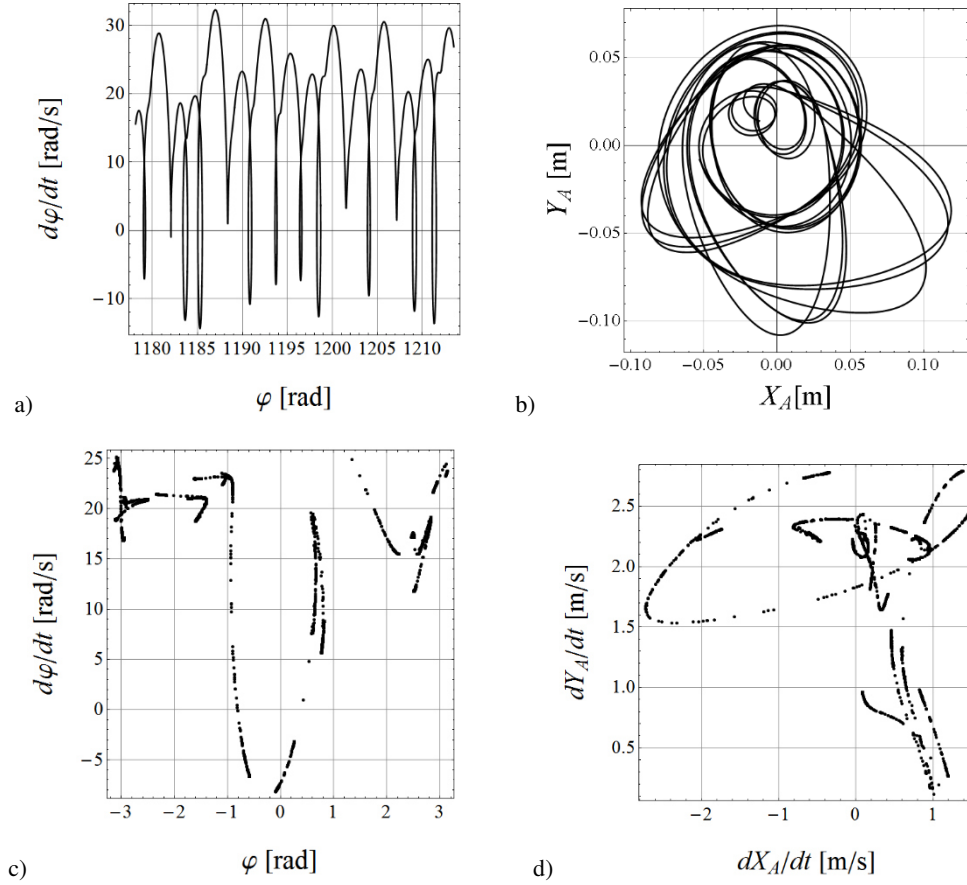
Figure 7. Trajectory of the system (a-b) and Poincaré section (c-d) corresponding to the bifurcation diagram presented in figure 5 for $\omega_0 = 61.5$ rad/s.
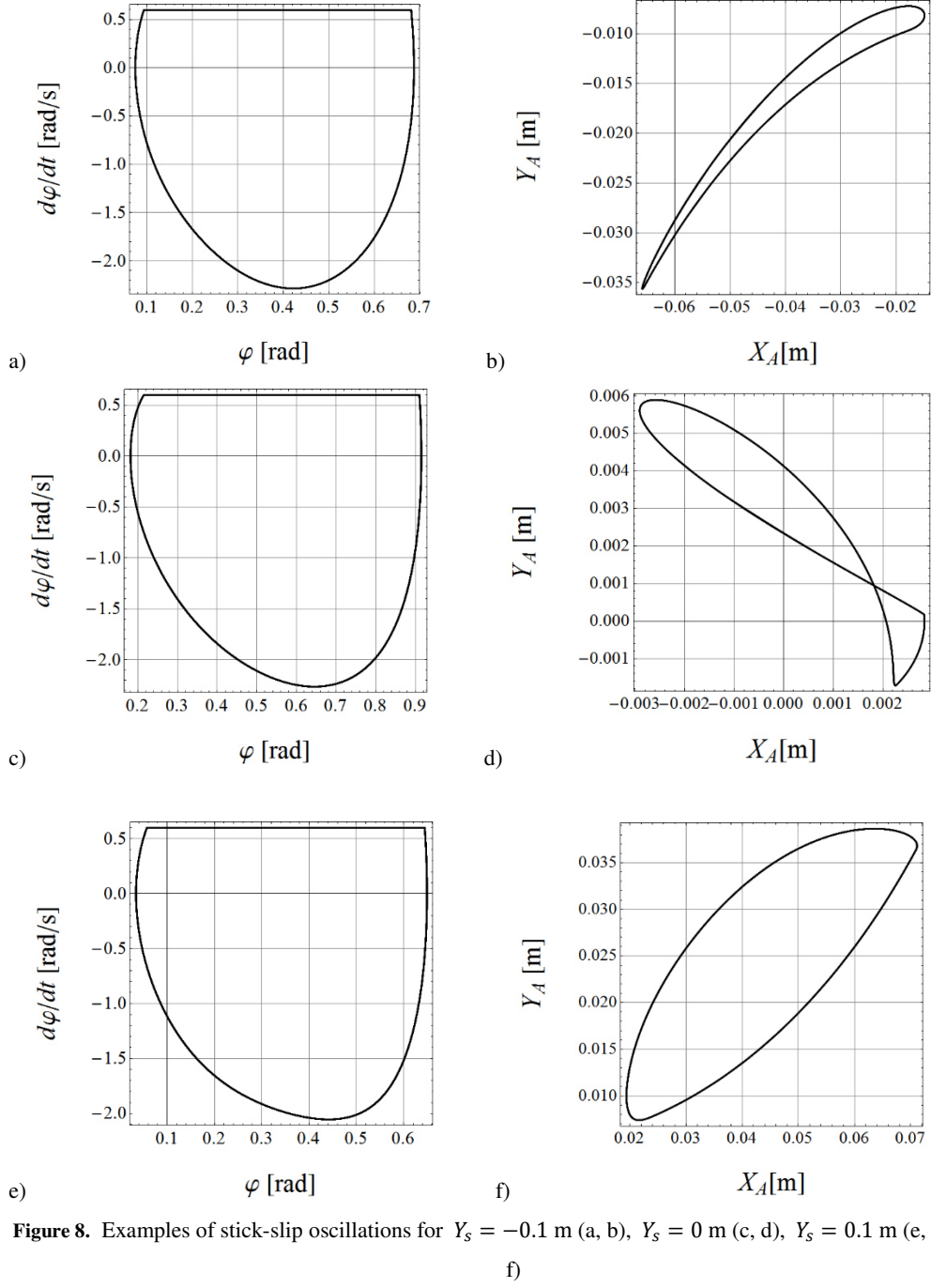
Figure 8. Examples of stick-slip oscillations for $Y_s = -0.1$ m (a, b), $Y_s = 0$ m (c, d), $Y_s = 0.1$ m (e, f)

In figure 8 there are presented examples of periodic stick-slip oscillations of the investigated mechanical system, where the following parameters are assumed: $M = 1.2$ kg, $B = 0.01$ kg$\cdot$m^2, $e = 0.1$ m, $k_X = k_Y = 100$ N/m, $c_X = c_Y = 0.1$N$\cdot$s/m, $c_\varphi = 0.1$ N$\cdot$m$\cdot$s, $X_s = 0$ m, $\omega_0 = 0.6$ rad/s, $R = 0.1$ m, $N = 6$ N, $\mu = 1$ and $\eta = 2.5$. The position of the joint S along the axis X is different for each of the presented solutions: $Y_s = -0.1$ m (a, b), $Y_s = 0$ m (c, d), $Y_s = 0.1$ m (e, f).

5. Conclusions

In the work there have been presented examples of models of the resultant friction force and moment based on the previous works of the authors. They are simple functions, which can be an effective substitute for the exact integral model, suitable for fast and realistic computer simulations of a certain class of mechanical systems with frictional contacts.

These models in their primary form concern the case of a fully developed sliding on the contact area and possess singularity for the case of lack of the relative motion. The applied regularization occurred to be an effective method to avoid that problem and take into account different values of static and kinetic friction coefficients. The drawbacks are the stiff differential equations and the change of physical properties of the system near the stick mode.

In order to test the developed models of friction forces, a mathematical model of a special mechanical system is built, which is some modification of the disk-on-a-disk system analyzed in the works [7, 8], being a strongly simplified disk clutch. It is expected that the proposed model can exhibit much richer bifurcational dynamics, allowing for testing different aspects of friction models. In should be noted that the presented work is in progress and only preliminary results are reported. It is also considered the construction of the corresponding experimental rig in the future.

Acknowledgments

References

[1] Contensou, P. Couplage entre frottement de glissement et de pivotement dans la téorie de la toupe. In: Ziegler H. (Ed.), *Kreiselprobleme Gyrodynamic*, *IUTAM Symposium Celerina*, Springer-Verlag, Berlin, 1962, 201-216.

[2] Zhuravlev, V.P. The model of dry friction in the problem of the rolling of rigid bodies. *Journal of Applied Mathematics and Mechanics* 6, 5 (1998), 705-710.

[3] Kudra, G., Awrejcewicz, J. Approximate modelling of resulting dry friction forces and rolling resistance for elliptic contact shape. *European Journal of Mechanics A/Solids 42* (2013), 358-375.

[4] Kudra G., Awrejcewicz J. Regularized model of coupled friction force and torque for circularly-symmetric contact pressure distribution. *Proceedings of the 11th Conference on Dynamical Systems - Theory and Applications*, Lodz, 2011, 353-358.

[5] Kudra, G., Awrejcewicz, J. A smooth model of the resultant friction force on a plane contact area. *Journal of Theoretical and Applied Mechanics* (2015), to appear.

[6] Stamm, W., Fidlin, A. Regularization of 2D frictional contacts for rigid body dynamics, *IUTAM Symposium on Multiscale Problems in Multibody System Contacts*, Springer, Dordrecht, 2007, 291–300.

[7] Stamm, W., Fidlin, A. Radial dynamics of rigid friction disks with alternating sticking and sliding. *Proceedings of the 6th EUROMECH Nonlinear Dynamics Conference*, Sankt Petersburg, 2008.

[8] Fidlin, A. Stamm, W. On the radial dynamics of friction disks. *European Journal of Mechanics A/Solids* 28, 3 (2009), 526-534.

Grzegorz Kudra, Ph.D., D.Sc.: Lodz University of Technology, Department of Automation, Biomechanics and Mechatronics, Stefanowski St. 1/15, 90-924 Lodz, Poland (*grzegorz.kudra@p.lodz.pl*). The author gave a presentation of this paper during one of the conference sessions.

Jan Awrejcewicz, Professor: Lodz University of Technology, Department of Automation, Biomechanics and Mechatronics, Stefanowski St. 1/15, 90-924 Lodz, Poland (*jan.awrejcewicz@p.lodz.pl*).

Axially excited spatial double pendulum nonlinear dynamics (BIF306-15)

Michał Ludwicki, Grzegorz Kudra, Jan Awrejcewicz

Abstract: Analysis of a 3D spatial double physical pendulum system, coupled by two universal joints is performed. External excitation of the mechanism is realized by axial periodic rotations of the first joint of the pendulum. System of ODEs is solved numerically and obtained data are analyzed by a standard approach, including time series, phase plots and Poincaré sections. Additionally, FFT (Fast Fourier Transform and the wavelet transformation algorithms have been applied. Various wavelet basic functions have been compared to find the best fit, e.g. Morlet, Mexican Hat and Gabor wavelets. The so far obtained results allowed for detection of a number of non-linear effects, including chaos, quasi-periodic and periodic dynamics, as well the numerous and different bifurcations. Scenarios of transition from regular to chaotic dynamics have been also illustrated and studied.

1. Introduction

This paper presents the model and its numerical simulations of a simple 3D double physical pendulums, under variable axial excitations. The periodic torque in axial direction is the only external force considered and realized as a variable angular velocity of the pivot point of first pendulum. Damping force in each joint is modeled by introduction of linear damping characteristic.

Following the subject of current scientific publications related to the multiple physical pendulum use and analysis one can say that it deals mainly with simplified constructions having specific configurations. When searching for the available papers with regard to the pendulum model presented here, we have not detected those considering a double pendulum as a system of rigid bodies, where the only excitation source has been associated with axial vibrations.

Many papers aimed on investigations of the spatial pendulums mostly deal with the single spherical pendulum and its variants, e.g. using a single rigid body cylinder model [1–3] or using simple mathematical pendulum in space ([4], [5]).

More complex spatial pendulum configurations are studied as an objects of nonlinear analysis, but rather to test or develop a control and stabilization techniques, e.g. general model of inverted multiple mathematical pendulum control using single torque [6] or a moving cart [7] or inverted

double rigid body pendulum being the most similar to the construction presented in our paper but controlled by four external torques [8].

Another wide area of application of the pendulum models deals with damping and stabilization phenomena. However here also one can found no spatial multibody pendulums, but rather simplified mathematical pendulums, like a double mathematic pendulum model [9].

Lastly, multiple physical pendulums, often very complex, are sometimes used for modeling biological systems, especially human limbs. One can see the natural similarity of these two (bio-) mechanical systems. Unfortunately, in this scientific research pendulums are mainly used to map real body movements, so the main goal is to develop a proper control algorithm, e.g. inverted pendulum models of human gait [10] or to model some body characteristic by similar configuration of pendulums, like kicking power calculated by a similar model of a double physical pendulum [11].

Some additional vibration analysis techniques, like *Continuous Wavelets Analysis* are also presented in our paper. This investigation method is widely used in mechanical vibration analysis, including chaotic dynamics of beams [12], gears and bearings fault detection methods ([13], [14]), carrying out stability analysis during earth-quakes [15] or even brain oscillations effects using EEG and wavelets [16].

This paper presents the results of numerical computations of a complex mechanical system using both classical and non-classical (wavelets) techniques. A lot of nonlinear behavior effects of the system is observed and discussed, using multiple graphical interpretation.

1.1. The Pendulum Model

Presented mechanical system consists of two simple physical pendulums connected by two universal joints O_1 and O_2 (see Figure 1). Each single pendulum is treated as a rigid body having a mass m_i and moment of inertia approximated by an axially symmetric cylinder. Its length L_i and the position of center of masses e_i are also known. The suspension joint of first pendulum can oscillate in two directions (φ_1 and θ_1) and additionally it rotates around vertical axis with variable in time angular velocity.

The model takes into account a simple viscous damping characteristics in each joint described by the following equations:

$$\mathbf{M}_d = \left[M_{d\theta_1} - M_{d\theta_2}, M_{d\varphi_1} - M_{d\varphi_2}, M_{d\theta_2} - M_{d\varphi_2} \right]^T, \tag{1}$$

where $\mathbf{M}_i$ are corresponding damping torques proportional to the angular velocities.
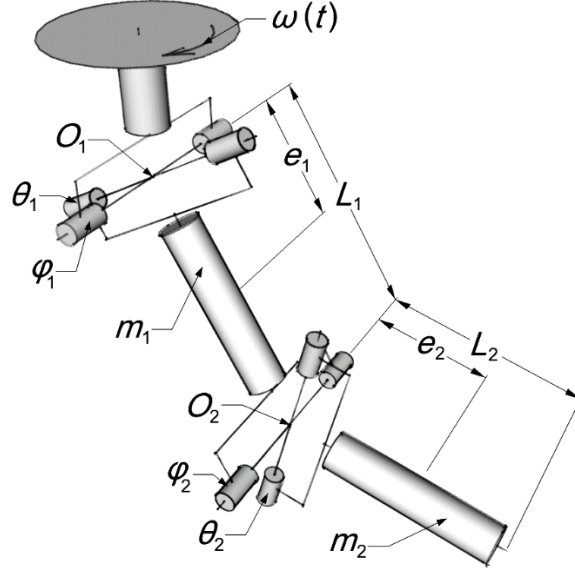
Figure 1. Coupled pendulums.

Air resistance forces have been neglected owing to their small values comparing to the mass and inertia forces occurring in the system. External source of exciting torque is applied to the point of suspension of the pendulum as a variable angular velocity function

$$\omega(t) = \omega_0 + q \sin(\Omega\, t), \tag{2}$$

where ω_0 is a constant part of velocity [rad/s], q states for the amplitude [N·m] and Ω stands for frequency [rad/s].

Finding potential and kinetic energy of the system and using the Langrange equations of the second kind, the govering equations of motion have been derived in an analytical way. After performing several transformations to simplify their form, a set of four ODEs can be written as follows

$$\mathbf{M(q)} \cdot \begin{bmatrix} \ddot{\theta}_1 \\ \ddot{\varphi}_1 \\ \ddot{\theta}_2 \\ \ddot{\varphi}_2 \end{bmatrix} + \mathbf{A}\begin{pmatrix} \theta_1 \\ \varphi_1 \\ \theta_2 \\ \varphi_2 \end{pmatrix} \cdot \mathbf{a} + \mathbf{B}\begin{pmatrix} \theta_1 \\ \varphi_1 \\ \theta_2 \\ \varphi_2 \end{pmatrix} \cdot \begin{bmatrix} \dot{\theta}_1 \\ \dot{\varphi}_1 \\ \dot{\theta}_2 \\ \dot{\varphi}_2 \end{bmatrix} + \mathbf{R}\begin{pmatrix} \theta_1 \\ \varphi_1 \\ \theta_2 \\ \varphi_2 \end{pmatrix} = 0, \tag{3}$$

where $\mathbf{a} = \left[\dot{\theta}_1^2, \dot{\varphi}_1^2, \dot{\theta}_2^2, \dot{\varphi}_2^2,\ \dot{\theta}_1\dot{\varphi}_1, \dot{\theta}_1\dot{\varphi}_2, \dot{\theta}_2\dot{\varphi}_1, \dot{\theta}_2\dot{\varphi}_2,\ \dot{\varphi}_1\dot{\varphi}_2, \dot{\theta}_1\dot{\theta}_2\right]^T$ and $\mathbf{M}$, $\mathbf{A}$, $\mathbf{B}$, $\mathbf{R}$ denote matrices and vectors, here not defined explicitly (see Appendix).

387

2. Numerical computations

Results of the numerical computations presented in this paper concern the following fixed parameters (see Fig. 1) listed in Table 1.

Table 1 Numerical computation parameters.

	simulation example	
	first joint	second joint
weight of the pendulums [kg]	$m_1 = 0.5$	$m_2 = 0.5$
length [m]	$L_1 = 0.2$	$L_2 = 0.2$
position of the mass center [m]	$e_1 = 0.1$	$e_2 = 0.1$
moments of inertia [kg·m]	$I_{x1} = 0.002$ $I_{y1} = 0.002$ $I_{z1} = 0.0001$	$I_{x2} = 0.002$ $I_{y2} = 0.002$ $I_{z2} = 0.0001$
viscous damping coefficient [N·s/m]	$c_1 = 0.1$	$c_2 = 0.1$

The ODEs solving algorithm (named `NDSolve[]` in *Wolfram Mathematica*® package) is based on higher order *Runge-Kutta* methods including automatic step control technique and other computation performance improvements. Numerical results are automatically interpolated to any chosen time step.

During numerical calculations, every first 400 s time steps were ignored as transient motions and next 400 or more (if needed) were used as significant for the further analysis.

2.1. The Wavelet Analysis

Numerically computed results have been studied by a standard approach, including time series, phase plots and Poincaré sections. Additionally, FFT (Fast Fourier Transform) and the wavelet transformation algorithms have been used.

Various wavelet basic functions have been compared to find the best fit, e.g. Morlet, Mexican Hat and Gabor wavelets. Detailed comparison showed that non-orthogonal Morlet wavelets [17] (see equation (4)) are the most convenient for analysis of the studied mechanical system. The *Continuous Wavelet Transformation* performed for this wavelets produces smooth wavelet scalograms with clearly exhibited frequency variations keeping relatively fast numerical calculations. This transformation is based on the following formula

$$\psi(t) = 1/\sqrt[4]{\pi} \cos\left(t\,\pi\sqrt{2/log(2)}\right) \exp\left(-\frac{t^2}{2}\right) \tag{4}$$

3. Results

Here, a few representative results of classical nonlinear dynamics analysis combined with FFT and wavelet continuous transformation are presented. All plots and diagrams have been generated using *Mathematica*[®] package. It is important to mention, that there are three possible control parameters that control a value of angular velocity function (see eq. (2)) – a constant part of angular velocity ω_0 [rad/s], the amplitude q [N·m] and the excitation angular velocity frequency Ω [rad/s]. The periods number maps have been calculated for a constant q and variable ω_0 and Ω while bifurcation diagrams for variable control parameter Ω and constant q and ω_0 are constructed.

3.1. Classical analysis vs. Continuous Wavelets Transformation

For $\omega_0 = 6.5$ rad/s, $q = 3$ N·m, $\Omega = 6$ rad/s and very small initial deflection of the first pendulum ($\theta_1 = 0.001$ rad) the dynamical system finally tends to a stable quasi-periodic solution. The quasi-periodic pulsation can be seen clearly in the phase plot shown in Figure 2b. For this case of non-stationary nonlinear behavior, one can see an obvious advantage of the wavelet analysis, since the resulting scalograms show a structure of scale variable of wavelet basic function corresponding to frequency vs. time.

The dark horizontal line in the wavelet scalogram (Figure 2d) on scale level 5 represents the quasi-periodic solution (after $t \approx 300$ s), while the dark regions in higher scales (before $t \approx 300$ s) correspond to the transient behavior. In general, in wavelet analysis, the higher the scale value is a lower frequency is represented. Similar observation holds for a 3D representation of this scalogram reported in Figure 2e.

For higher amplitude of excitation $q = 12$ N·m, keeping constant $\omega_0 = 0$ rad/s and $\Omega = 5.49$ rad/s our dynamical system exhibits chaotic behavior. It can be seen in the Poincaré sections in Figure 3a and the in the phase plots in Figure 3b. The FFT analysis distinguishes one outstanding frequency which is also seen in the wavelet scalogram marked by one darker horizontal region on scale level 3.
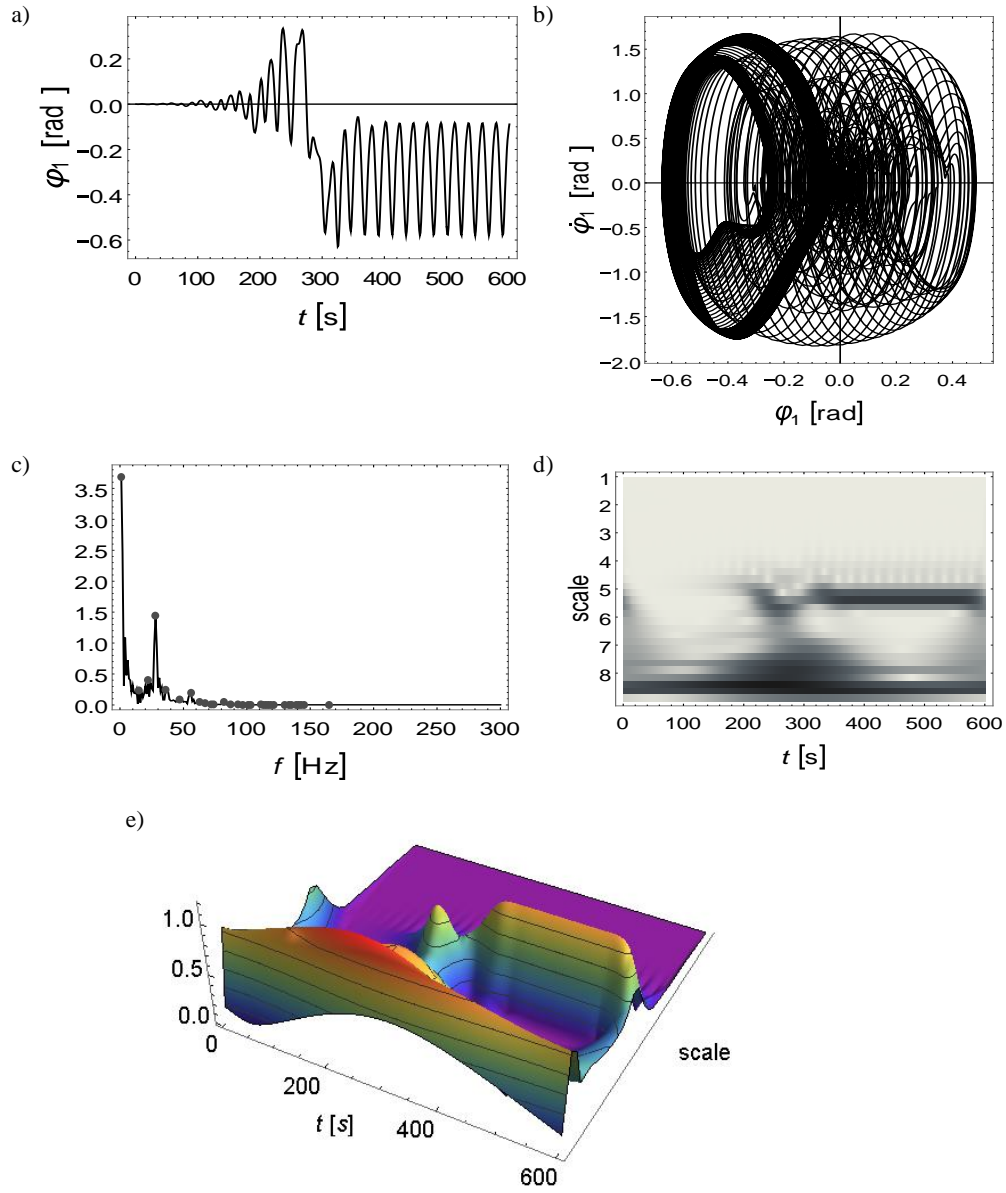
Figure 2. Time series (a), phase plots (b), FFT analysis (c), wavelets scalogram (d) and the same scalogram in 3D (e) for $\omega_0 = 6.5$ rad/s, $q = 3$ N·m, $\Omega = 6$ rad/s.
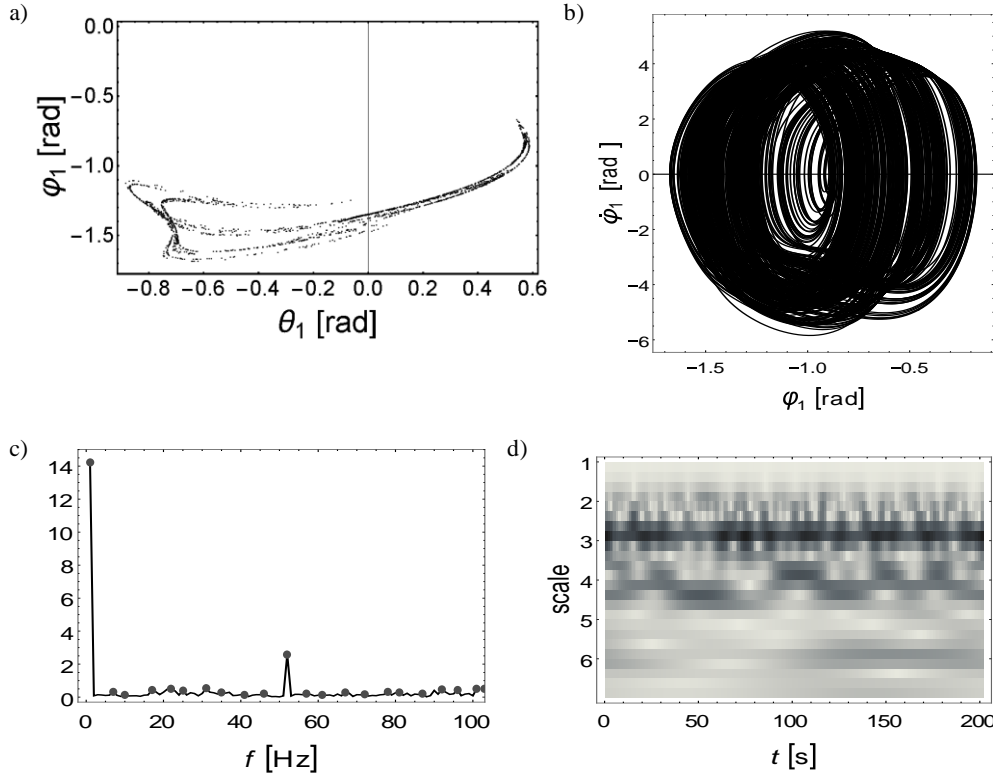
Figure 3. Poincaré section for 2000 s (a), phase plots (b), FFT analysis (c) and wavelets scalogram (d) for 200 s ($\omega_0 = 0$ rad/s, $q = 12$ N·m, $\Omega = 5.49$ rad/s).

Last set of the presented results (see Figure 4) contains maps showing a number of periods, which are combined with bifurcational diagrams for three different amplitudes of excitation. The white horizontal line in the maps shows the path of control parameter changes in corresponding bifurcational diagrams. The gray background of the maps represents one period vibrations, while the dark regions, a maximum counted periods, which corresponds to chaos or a high-order quasi-periodicity.

a) $q = 3.0$ N·m

b) $q = 3.0$ N·m

c) $q = 5.0$ N·m

d) $q = 5.0$ N·m

e) $q = 7.0$ N·m

f) $q = 7.0$ N·m
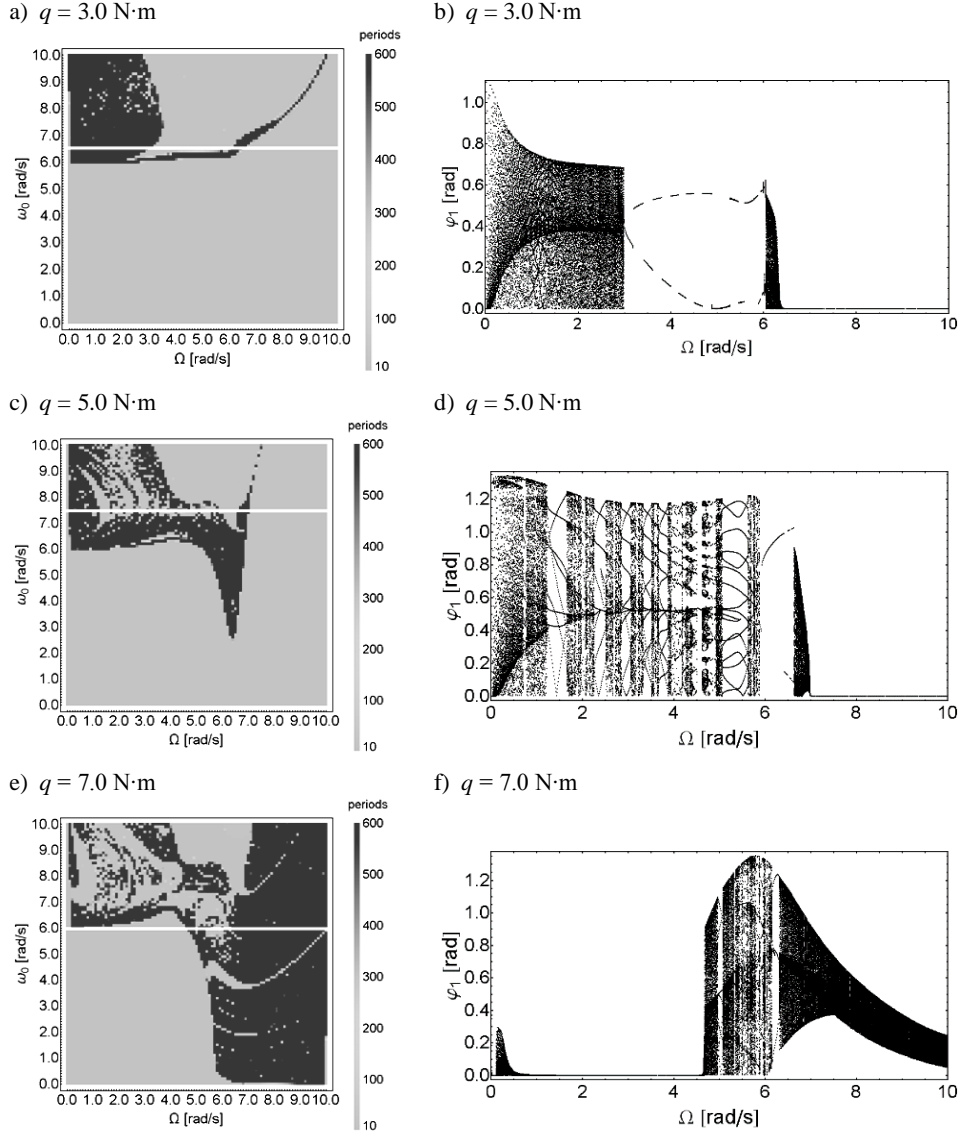
Figure 4. Periods number in the plane (ω_0, Ω) for constant amplitude q, after 400 s of transient oscillations and bifurcation diagrams for φ_1 with variable Ω and constant value of ω_0 marked by white horizontal line on the maps. (a)-(b) for $q = 3$ N·m, (c)-(d) for $q = 5$ N·m and (e)-(f) for $q = 7$ N·m.

Observe that both charts presented in pairs in Figure 4, are complementary. The knowledge of the number of periods provides a general information of the nature of system dynamical behaiour, while bifurcational diagrams supply more complex data, but for a particular range of the control

parameter. In Figure 4a one can see that the system shows no irregular vibrations over a large range of low frequencies of excitation. Over $\omega_0 \approx 6$ N·m, a clear line appears above which the system transits to chaotic behavior. Presented bifurcational diagram (see Figure 4b) shows that in spite of the quasi-periodic and chaotic dynamics, the wide window of period 2 oscillations occurs for $\Omega \in \langle 3,6 \rangle$.

Similar observations can be made on the remaining pairs of images representing the results of calculations for higher values of excitation amplitude q. Among others, for $q = 5$ N·m system passes through a number of states of the multiple period, quasi-periodic and chaotic regions.

4. Conclusions

The present paper is an extension of the work published in reference [18], where a basic nonlinear dynamic analysis and the announcement of the experimental rig has been introduced. In comparison to the previous paper, here we have applied novel techniques for monitoring of the system dynamics by studying nonlinear behaviour maps (number of periods maps), as well as the application of the wavelets transformation techniques, which have been adapted and compared with the standard FFT methods.

The application of Continuous Wavelet Analysis to the investigation of chaotic vibrations of the pendulums is a helpful tool to show and analyse systems behaviour vs. time including a bifurcation diagrams vs. control parameter. The most important role in this type of investigation plays the choice of the proper wavelet base function. The carried out tests and validation approves indicated a Morlet wavelet as the best choice, which is confirmed by research devoted to ([12], [15], [19], [20]).

In conclusion, it was noticed that the double system of physical pendulums despite the small initial deflections (about 0.001 rad) shows an irregular behaviour at relatively low angular velocities. In that conditions, we have been recorded numerous ranges of control parameters for which the vibration character was periodic or quasi-periodic. These test conditions are important from the experimental point of view. Chaotic behaviour obtained from the simulation on a real system is dangerous, since test stand exhibiting chaos can be quickly damaged due to large amplitudes of vibrations.

The developed model brought a good tool for analysis and prediction of nonlinear dynamics of the presented in the previous work real pendulum. That will be the subject of a separate paper.

Appendix

Full form of matrices and vectors **M**, **A**, **B**, **R** from equation (3) in *Wolfram Mathematica* notation.

M = {

{½ Cos[$\varphi_1(t)$]² (2 I_{11} + I_{21} + I_{23} + 2 $e_1$² m_1 + $e_2$² m_2 + 2 $L_1$² m_2 + 4 e_2 L_1 m_2 Cos[$\theta_2(t)$] Cos[$\varphi_2(t)$] + I_a Cos[2 $\varphi_2(t)$]) - e_2 L_1 m_2 Sin[2 $\varphi_1(t)$] Sin[$\varphi_2(t)$] + Sin[$\varphi_1(t)$]² (I_{13} + I_b Sin[$\theta_2(t)$]² + Cos[$\theta_2(t)$]² (I_{23} Cos[$\varphi_2(t)$]² + I_c Sin[$\varphi_2(t)$]²)) - I_a Cos[$\theta_2(t)$] Cos[$\varphi_1(t)$] Sin[$\varphi_1(t)$] Sin[2 $\varphi_2(t)$],

Sin[$\theta_2[t]$] (½ Cos[$\theta_2(t)$] (-I_{21} + 2 I_{22} - I_{23} + $e_2$² m_2 + I_a Cos[2 $\varphi_2(t)$]) Sin[$\varphi_1(t)$] + Cos[$\varphi_2[t]$] (e_2 L_1 m_2 Sin[$\varphi_1(t)$] + I_a Cos[$\varphi_1(t)$] Sin[$\varphi_2(t)$])),

Cos[$\theta_2(t)$] Cos[$\varphi_2(t)$] (e_2 L_1 m_2 Cos[$\varphi_1(t)$] - I_a Sin[$\varphi_1(t)$] Sin[$\varphi_2(t)$]) + Cos[$\varphi_1(t)$] (I_c Cos[$\varphi_2(t)$]² + I_{23} Sin[$\varphi_2(t)$]²),Sin[$\theta_2(t)$] (I_b Sin[$\varphi_1(t)$] - e_2 L_1 m_2 Cos[$\varphi_1(t)$] Sin[$\varphi_2(t)$])},

{Sin[$\theta_2(t)$] (½ Cos[$\theta_2(t)$] (-I_{21} + 2 I_{22} - I_{23} + $e_2$² m_2 + I_a Cos[2 $\varphi_2(t)$]) Sin[$\varphi_1(t)$] + Cos[$\varphi_2(t)$] (e_2 L_1 m_2 Sin[$\varphi_1(t)$] + I_a Cos[$\varphi_1(t)$] Sin[$\varphi_2(t)$])),

I_{12} + $e_1$² m_1 + I_b Cos[$\theta_2(t)$]² + 2 e_2 L_1 m_2 Cos[$\theta_2(t)$] Cos[$\varphi_2(t)$] + Cos[$\varphi_2(t)$]² ($L_1$² m_2 + I_{23} Sin[$\theta_2(t)$]²) + ($L_1$² m_2 + I_c Sin[$\theta_2(t)$]²) Sin[$\varphi_2(t)$]²,I_a Cos[$\varphi_2(t)$] Sin[$\theta_2(t)$] Sin[$\varphi_2(t)$],

I_b Cos[$\theta_2(t)$] + e_2 L_1 m_2 Cos[$\varphi_2(t)$]},{Cos[$\theta_2(t)$] Cos[$\varphi_2(t)$] (e_2 L_1 m_2 Cos[$\varphi_1(t)$] - I_a Sin[$\varphi_1(t)$] Sin[$\varphi_2(t)$]) + Cos[$\varphi_1(t)$] (I_c Cos[$\varphi_2(t)$]² + I_{23} Sin[$\varphi_2(t)$]²),

I_a Cos[$\varphi_2(t)$] Sin[$\theta_2(t)$] Sin[$\varphi_2(t)$],

I_c Cos[$\varphi_2(t)$]² + I_{23} Sin[$\varphi_2(t)$]²,0},{Sin[$\theta_2(t)$] (I_b Sin[$\varphi_1(t)$] - e_2 L_1 m_2 Cos[$\varphi_1(t)$] Sin[$\varphi_2(t)$]),I_b Cos[$\theta_2(t)$] + e_2 L_1 m_2 Cos[$\varphi_2(t)$],0,I_b}

};

A = {

{0,

Sin[$\theta_2(t)$] (½ Cos[$\theta_2(t)$] Cos[$\varphi_1(t)$] (-I_{21} + 2 I_{22} - I_{23} + $e_2$² m_2 + I_a Cos[2 $\varphi_2(t)$]) + Cos[$\varphi_2(t)$] (e_2 L_1 m_2 Cos[$\varphi_1(t)$] - I_a Sin[$\varphi_1(t)$] Sin[$\varphi_2(t)$])),

Cos[$\varphi_2(t)$] Sin[$\theta_2(t)$] (-e_2 L_1 m_2 Cos[$\varphi_1(t)$] + I_a Sin[$\varphi_1(t)$] Sin[$\varphi_2(t)$]),

-e_2 L_1 m_2 Cos[$\varphi_1(t)$] Cos[$\varphi_2(t)$] Sin[$\theta_2(t)$],

-2 (Cos[$\varphi_1(t)$]² (e_2 L_1 m_2 + I_a Cos[$\theta_2(t)$] Cos[$\varphi_2(t)$]) Sin[$\varphi_2(t)$] - e_2 L_1 m_2 Cos[$\theta_2(t)$]² Sin[$\varphi_1(t)$]² Sin[$\varphi_2(t)$] - e_2 L_1 m_2 Sin[$\theta_2(t)$]² Sin[$\varphi_1(t)$]² Sin[$\varphi_2(t)$] + Cos[$\theta_2(t)$] Cos[$\varphi_2(t)$] (e_2 L_1 m_2 Sin[2 $\varphi_1(t)$] - I_a Sin[$\varphi_1(t)$]² Sin[$\varphi_2(t)$]) + ½ Cos[$\varphi_1(t)$] Sin[$\varphi_1(t)$] (2 I_{11} - 2 I_{13} + I_{21} - I_{22} + I_{23} + 2 $e_1$² m_1 + $L_1$² m_2 + (I_{22} + ($e_2$² - $L_1$²) m_2) Cos[2 $\theta_2(t)$] + I_{21} Cos[2 $\varphi_2(t)$] - I_{23} Cos[2 $\varphi_2(t)$] + $e_2$² m_2 Cos[2 $\varphi_2(t)$] + 2 Cos[$\theta_2(t)$]² ($L_1$² m_2 - I_{23} Cos[$\varphi_2(t)$]² - I_c Sin[$\varphi_2(t)$]²))),

2 Sin[$\theta_2(t)$] (½ Cos[$\theta_2(t)$] (-I_{21} + 2 I_{22} - I_{23} + $e_2$² m_2 + I_a Cos[2 $\varphi_2(t)$]) Sin[$\varphi_1(t)$]² + Cos[$\varphi_1(t)$] Cos[$\varphi_2(t)$] (-e_2 L_1 m_2 Cos[$\varphi_1(t)$] + I_a Sin[$\varphi_1(t)$] Sin[$\varphi_2(t)$])),

2 (-Cos[$\varphi_1(t)$] Cos[$\varphi_2(t)$] (e_2 L_1 m_2 Sin[$\theta_2(t)$]² Sin[$\varphi_1(t)$] + I_a Cos[$\varphi_1(t)$] Sin[$\varphi_2(t)$]) +Cos[$\theta_2(t)$]² Cos[$\varphi_2(t)$] Sin[$\varphi_1(t)$] (-e_2 L_1 m_2 Cos[$\varphi_1(t)$] + I_a Sin[$\varphi_1(t)$] Sin[$\varphi_2(t)$]) - Cos[$\theta_2(t)$] Cos[$\varphi_1(t)$] (I_a Cos[$\varphi_2(t)$]² Sin[$\varphi_1(t)$] + Sin[$\varphi_2(t)$] (e_2 L_1 m_2 Cos[$\varphi_1(t)$] - I_a Sin[$\varphi_1(t)$] Sin[$\varphi_2(t)$])))),

Sin[$\varphi_1(t)$] (-I_{22} Sin[$\theta_2(t)$]² - $e_2$² m_2 Sin[$\theta_2(t)$]² - Cos[$\varphi_2(t)$]² (I_c - I_{23} Sin[$\theta_2(t)$]²) - I_{23} Sin[$\varphi_2(t)$]² + I_{21} Sin[$\theta_2(t)$]² Sin[$\varphi_2(t)$]² + $e_2$² m_2 Sin[$\theta_2(t)$]² Sin[$\varphi_2(t)$]² + Cos[$\theta_2(t)$]² (I_b - I_{23} Cos[$\varphi_2(t)$]² - I_c Sin[$\varphi_2(t)$]²)),

Sin[$\theta_2[t]$] (Cos[$\varphi_1(t)$] (I_b + I_a Cos[2 $\varphi_2(t)$]) - I_a Cos[$\theta_2(t)$] Sin[$\varphi_1(t)$] Sin[2 $\varphi_2(t)$]),

$\text{Cos}[\theta_2[t]]$ $((I_b - I_a \, \text{Cos}[2 \, \varphi_2(t)]) \, \text{Sin}[\varphi_1(t)] - 2 \, e_2 \, L_1 \, m_2 \, \text{Cos}[\varphi_1(t)] \, \text{Sin}[\varphi_2(t)]) - I_a \, \text{Cos}[\varphi_1(t)] \, \text{Sin}[2 \, \varphi_2(t)]\}$,

$\{\text{Cos}[\varphi_1(t)]^2 \, (e_2 \, L_1 \, m_2 + I_a \, \text{Cos}[\theta_2(t)] \, \text{Cos}[\varphi_2(t)]) \, \text{Sin}[\varphi_2(t)] \, -e_2 \, L_1 \, m_2 \, \text{Cos}[\theta_2(t)]^2 \, \text{Sin}[\varphi_1(t)]^2 \, \text{Sin}[\varphi_2(t)] - e_2 \, L_1 \, m_2$
$\text{Sin}[\theta_2(t)]^2 \, \text{Sin}[\varphi_1(t)]^2 \, \text{Sin}[\varphi_2(t)] + \text{Cos}[\theta_2(t)] \, \text{Cos}[\varphi_2(t)] \, (e_2 \, L_1 \, m_2 \, \text{Sin}[2 \, \varphi_1(t)] - I_a \, \text{Sin}[\varphi_1(t)]^2 \, \text{Sin}[\varphi_2(t)]) + ½$
$\text{Cos}[\varphi_1(t)] \, \text{Sin}[\varphi_1(t)] \, (2 \, I_{11} - 2 \, I_{13} + I_{21} - I_{22} + I_{23} + 2 \, e_1{}^2 \, m_1 + L_1{}^2 \, m_2 + (I_{22} + (e_2{}^2 - L_1{}^2) \, m_2) \, \text{Cos}[2 \, \theta_2(t)] + I_{21}$
$\text{Cos}[2 \, \varphi_2(t)] - I_{23} \, \text{Cos}[2 \, \varphi_2(t)] + e_2{}^2 \, m_2 \, \text{Cos}[2 \, \varphi_2(t)] + 2 \, \text{Cos}[\theta_2(t)]^2 \, (L_1{}^2 \, m_2 - I_{23} \, \text{Cos}[\varphi_2(t)]^2 - I_c \, \text{Sin}[\varphi_2(t)]^2))$,

0,

$I_a \, \text{Cos}[\theta_2(t)] \, \text{Cos}[\varphi_2(t)] \, \text{Sin}[\varphi_2(t)]$,

$-e_2 \, L_1 \, m_2 \, \text{Sin}[\varphi_2(t)]$,

0,

½ $\text{Cos}[\theta_2(t)]^2 \, (-I_{21} + 2 \, I_{22} - I_{23} + e_2{}^2 \, m_2 + I_a \, \text{Cos}[2 \, \varphi_2(t)]) \, \text{Sin}[\varphi_1(t)] + \text{Sin}[\varphi_1(t)] \, (\text{Cos}[\varphi_2(t)]^2 \, (I_c + I_{23} \, \text{Sin}[\theta_2(t)]^2) +$
$I_{23} \, \text{Sin}[\varphi_2(t)]^2 + \text{Sin}[\theta_2(t)]^2 \, (-I_{22} - e_2{}^2 \, m_2 + I_c \, \text{Sin}[\varphi_2(t)]^2)) + \text{Cos}[\theta_2[t]] \, (2 \, e_2 \, L_1 \, m_2 \, \text{Cos}[\varphi_2(t)] \, \text{Sin}[\varphi_1(t)] + I_a$
$\text{Cos}[\varphi_1(t)] \, \text{Sin}[2 \, \varphi_2(t)])$,

$-\text{Sin}[\theta_2(t)] \, (\text{Cos}[\varphi_1(t)] \, (I_b - I_a \, \text{Cos}[2 \, \varphi_2(t)]) + \text{Sin}[\varphi_1(t)] \, (2 \, e_2 \, L_1 \, m_2 \, \text{Sin}[\varphi_2(t)] + I_a \, \text{Cos}[\theta_2(t)] \, \text{Sin}[2 \, \varphi_2(t)]))$,

$2 \, \text{Sin}[\theta_2(t)] \, (-e_2 \, L_1 \, m_2 \, \text{Cos}[\varphi_2(t)] + \text{Cos}[\theta_2(t)] \, (-I_{22} - e_2{}^2 \, m_2 + I_{23} \, \text{Cos}[\varphi_2(t)]^2 + I_c \, \text{Sin}[\varphi_2(t)]^2))$,

$2 \, (-e_2 \, L_1 \, m_2 \, \text{Cos}[\theta_2(t)] + I_a \, \text{Cos}[\varphi_2(t)] \, \text{Sin}[\theta_2(t)]^2) \, \text{Sin}[\varphi_2(t)]$,

$-(I_b - I_a \, \text{Cos}[2 \, \varphi_2(t)]) \, \text{Sin}[\theta_2(t)]\}$,

$\{\text{Sin}[\theta_2(t)] \, (-(½) \, \text{Cos}[\theta_2(t)] \, (-I_{21} + 2 \, I_{22} - I_{23} + e_2{}^2 \, m_2 + I_a \, \text{Cos}[2 \, \varphi_2(t)]) \, \text{Sin}[\varphi_1(t)]^2 + \text{Cos}[\varphi_1(t)] \, \text{Cos}[\varphi_2(t)] \, (e_2 \, L_1 \, m_2$
$\text{Cos}[\varphi_1(t)] - I_a \, \text{Sin}[\varphi_1(t)] \, \text{Sin}[\varphi_2(t)]))$,

$\text{Sin}[\theta_2(t)] \, (e_2 \, L_1 \, m_2 \, \text{Cos}[\varphi_2(t)] + \text{Cos}[\theta_2(t)] \, (I_b - I_{23} \, \text{Cos}[\varphi_2(t)]^2 - I_c \, \text{Sin}[\varphi_2(t)]^2))$,

0,0,

$-(½) \, \text{Cos}[\theta_2(t)]^2 \, (-I_{21} + 2 \, I_{22} - I_{23} + e_2{}^2 \, m_2 + I_a \, \text{Cos}[2 \, \varphi_2(t)]) \, \text{Sin}[\varphi_1(t)] - \text{Sin}[\varphi_1(t)] \, (\text{Cos}[\varphi_2(t)]^2 \, (I_c + I_{23} \, \text{Sin}[\theta_2(t)]^2)$
$+ I_{23} \, \text{Sin}[\varphi_2(t)]^2 + \text{Sin}[\theta_2(t)]^2 \, (-I_{22} - e_2{}^2 \, m_2 + I_c \, \text{Sin}[\varphi_2(t)]^2)) - \text{Cos}[\theta_2[t]] \, (2 \, e_2 \, L_1 \, m_2 \, \text{Cos}[\varphi_2(t)] \, \text{Sin}[\varphi_1(t)] + I_a$
$\text{Cos}[\varphi_1(t)] \, \text{Sin}[2 \, \varphi_2(t)])$,

0,

$-\text{Cos}[\theta_2(t)] \, (I_b + I_a \, \text{Cos}[2 \, \varphi_2(t)]) \, \text{Sin}[\varphi_1(t)] - I_a \, \text{Cos}[\varphi_1(t)] \, \text{Sin}[2 \, \varphi_2(t)]$,

0,

$(I_b + I_a \, \text{Cos}[2 \, \varphi_2(t)]) \, \text{Sin}[\theta_2(t)]$,

$-I_a \, \text{Sin}[2 \, \varphi_2(t)]\}$,

$\{\text{Cos}[\varphi_1(t)] \, \text{Cos}[\varphi_2[t]] \, (e_2 \, L_1 \, m_2 \, \text{Sin}[\theta_2(t)]^2 \, \text{Sin}[\varphi_1(t)] + I_a \, \text{Cos}[\varphi_1(t)] \, \text{Sin}[\varphi_2(t)]) + \text{Cos}[\theta_2(t)]^2 \, \text{Cos}[\varphi_2(t)] \, \text{Sin}[\varphi_1(t)]$
$(e_2 \, L_1 \, m_2 \, \text{Cos}[\varphi_1(t)] - I_a \, \text{Sin}[\varphi_1(t)] \, \text{Sin}[\varphi_2(t)]) + \text{Cos}[\theta_2(t)] \, \text{Cos}[\varphi_1(t)] \, (I_a \, \text{Cos}[\varphi_2(t)]^2 \, \text{Sin}[\varphi_1(t)] + \text{Sin}[\varphi_2(t)] \, (e_2 \, L_1$
$m_2 \, \text{Cos}[\varphi_1(t)] - I_a \, \text{Sin}[\varphi_1(t)] \, \text{Sin}[\varphi_2(t)]))$,

$(e_2 \, L_1 \, m_2 \, \text{Cos}[\theta_2(t)] - I_a \, \text{Cos}[\varphi_2(t)] \, \text{Sin}[\theta_2(t)]^2) \, \text{Sin}[\varphi_2(t)]$,

$I_a \, \text{Cos}[\varphi_2(t)] \, \text{Sin}[\varphi_2(t)]$,

0,

$\text{Sin}[\theta_2[t]] \, (\text{Cos}[\varphi_1(t)] \, (I_b - I_a \, \text{Cos}[2 \, \varphi_2(t)]) + \text{Sin}[\varphi_1(t)] \, (2 \, e_2 \, L_1 \, m_2 \, \text{Sin}[\varphi_2(t)] + I_a \, \text{Cos}[\theta_2(t)] \, \text{Sin}[2 \, \varphi_2(t)]))$,

$\text{Cos}[\theta_2(t)] \, (I_b + I_a \, \text{Cos}[2 \, \varphi_2(t)]) \, \text{Sin}[\varphi_1(t)] + I_a \, \text{Cos}[\varphi_1(t)] \, \text{Sin}[2 \, \varphi_2(t)]$,

0,

$-(I_b + I_a \, \text{Cos}[2 \, \varphi_2(t)]) \, \text{Sin}[\theta_2(t)]$,

0,

0}};

I = {

{0,

-ω (Sin[$\theta_1(t)$] (Cos[$\varphi_1(t)$] (-2 e_2 L_1 m_2 Cos[$\varphi_2(t)$] Sin[$\theta_2(t)$] + I_{23} Cos[$\varphi_2(t)$]² Sin[2 $\theta_2(t)$] + Sin[2 $\theta_2(t)$] (-I_{22} - e_2^2 m_2 + I_c Sin[$\varphi_2(t)$]²)) + I_a Sin[$\theta_2(t)$] Sin[$\varphi_1(t)$] Sin[2 $\varphi_2(t)$]) + ½ Cos[$\theta_1[t]$] (Cos[$\varphi_1(t)$]² (2 I_{11} - 2 I_{13} + I_{21} - I_{22} + I_{23} + 2 e_1^2 m_1 + L_1^2 m_2 + (I_{22} + (e_2^2 - L_1^2) m_2) Cos[2 $\theta_2(t)$] + I_a Cos[2 $\varphi_2(t)$]) + 2 Cos[$\theta_2(t)$]² (I_b - 2 e_2 L_1 m_2 Sin[2 $\varphi_1(t)$] Sin[$\varphi_2(t)$] + Cos[$\varphi_1(t)$]² (L_1^2 m_2 - I_{23} Cos[$\varphi_2(t)$]² - I_c Sin[$\varphi_2(t)$]²) + Sin[$\varphi_1(t)$]² (-L_1^2 m_2 + I_{23} Cos[$\varphi_2(t)$]² + I_c Sin[$\varphi_2(t)$]²)) + 2 (I_{12} + e_1^2 m_1 - Cos[$\varphi_2(t)$]² (-L_1^2 m_2 + I_c Sin[$\varphi_1(t)$]² + Sin[$\theta_2(t)$]² (-I_{23} + L_1^2 m_2 Sin[$\varphi_1(t)$]²)) - 2 e_2 L_1 m_2 Sin[$\theta_2(t)$]² Sin[2 $\varphi_1(t)$] Sin[$\varphi_2(t)$] + L_1^2 m_2 Sin[$\varphi_2(t)$]² + I_{21} Sin[$\theta_2(t)$]² Sin[$\varphi_2(t)$]² + e_2^2 m_2 Sin[$\theta_2(t)$]² Sin[$\varphi_2(t)$]² - Sin[$\varphi_1(t)$]² (I_{11} - I_{13} + e_1^2 m_1 + I_{23} Sin[$\varphi_2(t)$]² - Sin[$\theta_2(t)$]² (I_b - L_1^2 m_2 Sin[$\varphi_2(t)$]²))) - 2 Cos[$\theta_2[t]$] (-4 e_2 L_1 m_2 Cos[$\varphi_1(t)$]² Cos[$\varphi_2(t)$] + I_a Sin[2 $\varphi_1(t)$] Sin[2 $\varphi_2(t)$])))),

½ ω (-(½) (2 I_{21} + 2 I_{23} + 2 e_2^2 m_2 + 2 (I_{21} - 2 I_{22} + I_{23} - e_2^2 m_2) Cos[2 $\theta_2(t)$] - I_a Cos[2 ($\theta_2(t)$ - $\varphi_2(t)$)] + 2 I_{21} Cos[2 $\varphi_2(t)$] - 2 I_{23} Cos[2 $\varphi_2(t)$] + 2 e_2^2 m_2 Cos[2 $\varphi_2(t)$] - I_{21} Cos[2 ($\theta_2(t)$ + $\varphi_2(t)$)] + I_{23} Cos[2 ($\theta_2(t)$ + $\varphi_2(t)$)] - e_2^2 m_2 Cos[2 ($\theta_2(t)$ + $\varphi_2(t)$)]) Sin[$\theta_1(t)$] Sin[$\varphi_1(t)$] + Cos[$\theta_1(t)$] Sin[$\theta_2(t)$] (Cos[$\theta_2(t)$] (-I_{21} + 2 I_{22} - I_{23} + e_2^2 m_2 + I_a Cos[2 $\varphi_2(t)$]) Sin[2 $\varphi_1(t)$] + 4 Cos[$\varphi_2(t)$] Sin[$\varphi_1(t)$] (e_2 L_1 m_2 Cos[$\varphi_1(t)$] - I_a Sin[$\varphi_1(t)$] Sin[$\varphi_2(t)$]))),

ω (Sin[$\theta_1(t)$] Sin[$\theta_2(t)$] (Cos[$\varphi_1(t)$] (I_b + I_a Cos[2 $\varphi_2(t)$]) - I_a Cos[$\theta_2(t)$] Sin[$\varphi_1(t)$] Sin[2 $\varphi_2(t)$]) + 1/4 Cos[$\theta_1[t]$] (-2 Cos[$\theta_2(t)$] (2 I_{22} + 2 e_2^2 m_2 + I_a Cos[2 ($\varphi_1(t)$ - $\varphi_2(t)$)] - e_2 L_1 m_2 Cos[2 $\varphi_1(t)$ - $\varphi_2(t)$)] + I_{21} Cos[2 ($\varphi_1(t)$ + $\varphi_2(t)$)] - I_{23} Cos[2 ($\varphi_1(t)$ + $\varphi_2(t)$)] + e_2^2 m_2 Cos[2 ($\varphi_1(t)$ + $\varphi_2(t)$)] + e_2 L_1 m_2 Cos[2 $\varphi_1(t)$ + $\varphi_2(t)$)]) + Cos[$\varphi_2(t)$] (-8 e_2 L_1 m_2 Cos[$\varphi_1(t)$]² + I_a (5 + Cos[2 $\theta_2(t)$]) Sin[2 $\varphi_1(t)$] Sin[$\varphi_2(t)$]) + I_a Cos[$\theta_2(t)$]² Sin[2 $\varphi_1(t)$] Sin[2 $\varphi_2(t)$]))},

{ω (Sin[$\theta_1(t)$] (Cos[$\varphi_1(t)$] (-2 e_2 L_1 m_2 Cos[$\varphi_2(t)$] Sin[$\theta_2(t)$] + I_{23} Cos[$\varphi_2(t)$]² Sin[2 $\theta_2(t)$] + Sin[2 $\theta_2(t)$] (-I_{22} - e_2^2 m_2 + I_c Sin[$\varphi_2(t)$]²)) + I_a Sin[$\theta_2(t)$] Sin[$\varphi_1(t)$] Sin[2 $\varphi_2(t)$]) + ½ Cos[$\theta_1[t]$] (Cos[$\varphi_1(t)$]² (2 I_{11} - 2 I_{13} + I_{21} - I_{22} + I_{23} + 2 e_1^2 m_1 + L_1^2 m_2 + (I_{22} + (e_2^2 - L_1^2) m_2) Cos[2 $\theta_2(t)$] + I_a Cos[2 $\varphi_2(t)$]) + 2 Cos[$\theta_2(t)$]² (I_b - 2 e_2 L_1 m_2 Sin[2 $\varphi_1(t)$] Sin[$\varphi_2(t)$] + Cos[$\varphi_1(t)$]² (L_1^2 m_2 - I_{23} Cos[$\varphi_2(t)$]² - I_c Sin[$\varphi_2(t)$]²) + Sin[$\varphi_1(t)$]² (-L_1^2 m_2 + I_{23} Cos[$\varphi_2(t)$]² + I_c Sin[$\varphi_2(t)$]²)) + 2 (I_{12} + e_1^2 m_1 - Cos[$\varphi_2(t)$]² (-L_1^2 m_2 + I_c Sin[$\varphi_1(t)$]² + Sin[$\theta_2(t)$]² (-I_{23} + L_1^2 m_2 Sin[$\varphi_1(t)$]²)) - 2 e_2 L_1 m_2 Sin[$\theta_2(t)$]² Sin[2 $\varphi_1(t)$] Sin[$\varphi_2(t)$] + L_1^2 m_2 Sin[$\varphi_2(t)$]² + I_{21} Sin[$\theta_2(t)$]² Sin[$\varphi_2(t)$]² + e_2^2 m_2 Sin[$\theta_2(t)$]² Sin[$\varphi_2(t)$]² - Sin[$\varphi_1(t)$]² (I_{11} - I_{13} + e_1^2 m_1 + I_{23} Sin[$\varphi_2(t)$]² - Sin[$\theta_2(t)$]² (I_b - L_1^2 m_2 Sin[$\varphi_2(t)$]²))) - 2 Cos[$\theta_2[t]$] (-4 e_2 L_1 m_2 Cos[$\varphi_1(t)$]² Cos[$\varphi_2(t)$] + I_a Sin[2 $\varphi_1(t)$] Sin[2 $\varphi_2(t)$])))),

0,

1/4 ω (-2 (-2 (I_{21} - 2 I_{22} + I_{23} - e_2^2 m_2) Cos[$\theta_2(t)$] + I_a Cos[$\theta_2(t)$ - 2 $\varphi_2(t)$] + 4 e_2 L_1 m_2 Cos[$\varphi_2(t)$] + I_{21} Cos[$\theta_2(t)$ + 2 $\varphi_2(t)$] - I_{23} Cos[$\theta_2(t)$ + 2 $\varphi_2(t)$] + e_2^2 m_2 Cos[$\theta_2(t)$ + 2 $\varphi_2(t)$]) Sin[$\theta_1(t)$] Sin[$\theta_2(t)$] + Cos[$\theta_1[t]$] (Cos[$\varphi_1(t)$] (2 I_{21} + 2 I_{23} + 2 e_2^2 m_2 - 2 (I_{21} - 2 I_{22} + I_{23} - e_2^2 m_2) Cos[2 $\theta_2(t)$] + 4 e_2 L_1 m_2 Cos[$\theta_2(t)$ - $\varphi_2(t)$] + I_{21} Cos[2 ($\theta_2(t)$ - $\varphi_2(t)$)] - I_{23} Cos[2 ($\theta_2(t)$ - $\varphi_2(t)$)] + e_2^2 m_2 Cos[2 ($\theta_2(t)$ - $\varphi_2(t)$)] + 2 I_{21} Cos[2 $\varphi_2(t)$] - 2 I_{23} Cos[2 $\varphi_2(t)$] + 2 e_2^2 m_2 Cos[2 $\varphi_2(t)$] + 4 e_2 L_1 m_2 Cos[$\theta_2(t)$ + $\varphi_2(t)$] + I_{21} Cos[2 ($\theta_2(t)$ + $\varphi_2(t)$)] - I_{23} Cos[2 ($\theta_2(t)$ + $\varphi_2(t)$)] + e_2^2 m_2 Cos[2 ($\theta_2(t)$ + $\varphi_2(t)$)]) - 4 I_a Cos[$\theta_2(t)$] Sin[$\varphi_1(t)$] Sin[2 $\varphi_2(t)$])),

ω (-(½) (4 e_2 L_1 m_2 Cos[$\theta_2(t)$] + 2 I_a Cos[$\theta_2(t)$]² Cos[$\varphi_2(t)$] + I_a (-3 + Cos[2 $\theta_2(t)$]) Cos[$\varphi_2(t)$]) Sin[$\theta_1(t)$] Sin[$\theta_2(t)$] + Cos[$\theta_1(t)$] Sin[$\theta_2(t)$] ((I_b - I_a Cos[2 $\varphi_2(t)$]) Sin[$\varphi_1(t)$] - Cos[$\varphi_1(t)$] (2 e_2 L_1 m_2 Sin[$\varphi_2(t)$] + I_a Cos[$\theta_2(t)$] Sin[2 $\varphi_2(t)$]))))},

{1/2 ω (½ (2 I_{21} + 2 I_{23} + 2 e_2^2 m_2 + 2 (I_{21} - 2 I_{22} + I_{23} - e_2^2 m_2) Cos[2 $\theta_2(t)$] - I_a Cos[2 ($\theta_2(t)$ - $\varphi_2(t)$)] + 2 I_{21} Cos[2 $\varphi_2(t)$] - 2 I_{23} Cos[2 $\varphi_2(t)$] + 2 e_2^2 m_2 Cos[2 $\varphi_2(t)$] - I_{21} Cos[2 ($\theta_2(t)$ + $\varphi_2(t)$)] + I_{23} Cos[2 ($\theta_2(t)$ + $\varphi_2(t)$)] - e_2^2 m_2 Cos[2 ($\theta_2(t)$ + $\varphi_2(t)$))]) Sin[$\theta_1(t)$] Sin[$\varphi_1(t)$] + Cos[$\theta_1(t)$] Sin[$\theta_2(t)$] (-Cos[$\theta_2(t)$] (-I_{21} + 2 I_{22} - I_{23} + e_2^2 m_2 + I_a Cos[2 $\varphi_2(t)$]) Sin[2 $\varphi_1(t)$] + 4 Cos[$\varphi_2(t)$] Sin[$\varphi_1(t)$] (-e_2 L_1 m_2 Cos[$\varphi_1(t)$] + I_a Sin[$\varphi_1(t)$] Sin[$\varphi_2(t)$]))),

396

$-(1/4)\,\omega\,(-2\,(-2\,(I_{21} - 2\,I_{22} + I_{23} - e_2^2\,m_2)\,\mathrm{Cos}[\theta_2(t)] + I_a\,\mathrm{Cos}[\theta_2(t) - 2\,\varphi_2(t)] + 4\,e_2\,L_1\,m_2\,\mathrm{Cos}[\varphi_2(t)] + I_{21}\,\mathrm{Cos}[\theta_2(t)$
$+ 2\,\varphi_2(t)] - I_{23}\,\mathrm{Cos}[\theta_2(t) + 2\,\varphi_2(t)] + e_2^2\,m_2\,\mathrm{Cos}[\theta_2(t) + 2\,\varphi_2(t)])\,\mathrm{Sin}[\theta_1(t)]\,\mathrm{Sin}[\theta_2(t)] + \mathrm{Cos}[\theta_1[t]]\,(\mathrm{Cos}[\varphi_1(t)]\,(2$
$I_{21} + 2\,I_{23} + 2\,e_2^2\,m_2 - 2\,(I_{21} - 2\,I_{22} + I_{23} - e_2^2\,m_2)\,\mathrm{Cos}[2\,\theta_2(t)] + 4\,e_2\,L_1\,m_2\,\mathrm{Cos}[\theta_2(t) - \varphi_2(t)] + I_{21}\,\mathrm{Cos}[2\,(\theta_2(t) -$
$\varphi_2(t))] - I_{23}\,\mathrm{Cos}[2\,(\theta_2(t) - \varphi_2(t))] + e_2^2\,m_2\,\mathrm{Cos}[2\,(\theta_2(t) - \varphi_2(t))] + 2\,I_{21}\,\mathrm{Cos}[2\,\varphi_2(t)] - 2\,I_{23}\,\mathrm{Cos}[2\,\varphi_2(t)] + 2\,e_2^2\,m_2$
$\mathrm{Cos}[2\,\varphi_2(t)] + 4\,e_2\,L_1\,m_2\,\mathrm{Cos}[\theta_2(t) + \varphi_2(t)] + I_{21}\,\mathrm{Cos}[2\,(\theta_2(t) + \varphi_2(t))] - I_{23}\,\mathrm{Cos}[2\,(\theta_2(t) + \varphi_2(t))] + e_2^2\,m_2\,\mathrm{Cos}[2$
$(\theta_2(t) + \varphi_2(t))]) - 4\,I_a\,\mathrm{Cos}[\theta_2(t)]\,\mathrm{Sin}[\varphi_1(t)]\,\mathrm{Sin}[2\,\varphi_2(t)])),$

$0,$

$\omega\,((I_b + I_a\,\mathrm{Cos}[2\,\varphi_2(t)])\,\mathrm{Sin}[\theta_1(t)]\,\mathrm{Sin}[\theta_2(t)] - \mathrm{Cos}[\theta_1[t]]\,(\mathrm{Cos}[\theta_2(t)]\,\mathrm{Cos}[\varphi_1(t)]\,(I_b + I_a\,\mathrm{Cos}[2\,\varphi_2(t)]) - I_a\,\mathrm{Sin}[\varphi_1(t)]$
$\mathrm{Sin}[2\,\varphi_2(t)]))\},$

$\{\omega\,(-\mathrm{Sin}[\theta_1(t)]\,\mathrm{Sin}[\theta_2(t)]\,(\mathrm{Cos}[\varphi_1(t)]\,(I_b + I_a\,\mathrm{Cos}[2\,\varphi_2(t)]) - I_a\,\mathrm{Cos}[\theta_2(t)]\,\mathrm{Sin}[\varphi_1(t)]\,\mathrm{Sin}[2\,\varphi_2(t)]) + 1/4\,\mathrm{Cos}[\theta_1[t]]$
$(2\,\mathrm{Cos}[\theta_2(t)]\,(2\,I_{22} + 2\,e_2^2\,m_2 + I_a\,\mathrm{Cos}[2\,(\varphi_1(t) - \varphi_2(t))] - e_2\,L_1\,m_2\,\mathrm{Cos}[2\,\varphi_1(t) - \varphi_2(t)] + I_{21}\,\mathrm{Cos}[2\,(\varphi_1(t) + \varphi_2(t))]$
$- I_{23}\,\mathrm{Cos}[2\,(\varphi_1(t) + \varphi_2(t))] + e_2^2\,m_2\,\mathrm{Cos}[2\,(\varphi_1(t) + \varphi_2(t))] + e_2\,L_1\,m_2\,\mathrm{Cos}[2\,\varphi_1(t) + \varphi_2(t)]) - \mathrm{Cos}[\theta_2(t)]\,(-8\,e_2\,L_1\,m_2$
$\mathrm{Cos}[\varphi_1(t)]^2 + I_a\,(5 + \mathrm{Cos}[2\,\theta_2(t)])\,\mathrm{Sin}[2\,\varphi_1(t)]\,\mathrm{Sin}[\varphi_2(t)]) - I_a\,\mathrm{Cos}[\theta_2(t)]^2\,\mathrm{Sin}[2\,\varphi_1(t)]\,\mathrm{Sin}[2\,\varphi_2(t)])),$

$-\omega\,(-(1/2)\,(4\,e_2\,L_1\,m_2\,\mathrm{Cos}[\theta_2(t)] + 2\,I_a\,\mathrm{Cos}[\theta_2(t)]^2\,\mathrm{Cos}[\varphi_2(t)] + I_a\,(-3 + \mathrm{Cos}[2\,\theta_2(t)])\,\mathrm{Cos}[\varphi_2(t)])\,\mathrm{Sin}[\theta_1(t)]$
$\mathrm{Sin}[\varphi_2(t)] + \mathrm{Cos}[\theta_1(t)]\,\mathrm{Sin}[\theta_2(t)]\,((I_b - I_a\,\mathrm{Cos}[2\,\varphi_2(t)])\,\mathrm{Sin}[\varphi_1(t)] - \mathrm{Cos}[\varphi_1(t)]\,(2\,e_2\,L_1\,m_2\,\mathrm{Sin}[\varphi_2(t)] + I_a$
$\mathrm{Cos}[\theta_2(t)]\,\mathrm{Sin}[2\,\varphi_2(t)]))),$

$\omega\,(-(I_b + I_a\,\mathrm{Cos}[2\,\varphi_2(t)])\,\mathrm{Sin}[\theta_1(t)]\,\mathrm{Sin}[\theta_2(t)] + \mathrm{Cos}[\theta_1[t]]\,(\mathrm{Cos}[\theta_2(t)]\,\mathrm{Cos}[\varphi_1(t)]\,(I_b + I_a\,\mathrm{Cos}[2\,\varphi_2(t)]) - I_a$
$\mathrm{Sin}[\varphi_1(t)]\,\mathrm{Sin}[2\,\varphi_2(t)])),$

$0\}$

$\};$

R = {

$1/8\,(2\,I_{11}\,\omega^2\,\mathrm{Sin}[2\,\theta_1(t)] - 4\,I_{12}\,\omega^2\,\mathrm{Sin}[2\,\theta_1(t)] + 2\,I_{13}\,\omega^2\,\mathrm{Sin}[2\,\theta_1(t)] - I_{22}\,\omega^2\,\mathrm{Sin}[2\,\theta_1(t)] - 2\,e_1^2\,m_1\,\omega^2\,\mathrm{Sin}[2\,\theta_1(t)] -$
$2\,L_1^2\,m_2\,\omega^2\,\mathrm{Sin}[2\,\theta_1(t)] - 3\,I_{22}\,\omega^2\,\mathrm{Cos}[\theta_2(t)]^2\,\mathrm{Sin}[2\,\theta_1(t)] - 4\,e_2\,L_1\,m_2\,\omega^2\,\mathrm{Cos}[\theta_2(t)]\,\mathrm{Cos}[\varphi_2(t)]\,\mathrm{Sin}[2\,\theta_1(t)] + 3\,I_{22}$
$\omega^2\,\mathrm{Sin}[2\,\theta_1(t)]\,\mathrm{Sin}[\theta_2(t)]^2 + 1/4\,\mathrm{Cos}[\theta_1[t]]\,(-\omega^2\,(-4\,I_{21} - 4\,I_{23} + 4\,e_2^2\,m_2 - 12\,(I_{21} + I_{23} - e_2^2\,m_2)\,\mathrm{Cos}[2\,\theta_2(t)] - 2$
$(I_{21} + I_{23} - e_2^2\,m_2)\,\mathrm{Cos}[2\,(\theta_2(t) - \varphi_1(t))] + 4\,I_{21}\,\mathrm{Cos}[2\,\varphi_1(t)] + 4\,I_{23}\,\mathrm{Cos}[2\,\varphi_1(t)] - 4\,e_2^2\,m_2\,\mathrm{Cos}[2\,\varphi_1(t)] - 2\,I_{21}$
$\mathrm{Cos}[2\,(\theta_2(t) + \varphi_1(t))] - 2\,I_{23}\,\mathrm{Cos}[2\,(\theta_2(t) + \varphi_1(t))] + 2\,e_2^2\,m_2\,\mathrm{Cos}[2\,(\theta_2(t) + \varphi_1(t))] + 6\,I_{21}\,\mathrm{Cos}[2\,(\theta_2(t) - \varphi_2(t))] -$
$6\,I_{23}\,\mathrm{Cos}[2\,(\theta_2(t) - \varphi_2(t))] + 6\,e_2^2\,m_2\,\mathrm{Cos}[2\,(\theta_2(t) - \varphi_2(t))] + I_{21}\,\mathrm{Cos}[2\,(\theta_2(t) - \varphi_1(t) - \varphi_2(t))] - I_{23}\,\mathrm{Cos}[2\,(\theta_2(t) -$
$\varphi_1(t) - \varphi_2(t))] + e_2^2\,m_2\,\mathrm{Cos}[2\,(\theta_2(t) - \varphi_1(t) - \varphi_2(t))] + 6\,I_{21}\,\mathrm{Cos}[2\,(\varphi_1(t) - \varphi_2(t))] - 6\,I_{23}\,\mathrm{Cos}[2\,(\varphi_1(t) - \varphi_2(t))] + 6$
$e_2^2\,m_2\,\mathrm{Cos}[2\,(\varphi_1(t) - \varphi_2(t))] + I_{21}\,\mathrm{Cos}[2\,(\theta_2(t) + \varphi_1(t) - \varphi_2(t))] - I_{23}\,\mathrm{Cos}[2\,(\theta_2(t) + \varphi_1(t) - \varphi_2(t))] + e_2^2\,m_2\,\mathrm{Cos}[2$
$(\theta_2(t) + \varphi_1(t) - \varphi_2(t))] - 12\,I_{21}\,\mathrm{Cos}[2\,\varphi_2(t)] + 12\,I_{23}\,\mathrm{Cos}[2\,\varphi_2(t)] - 12\,e_2^2\,m_2\,\mathrm{Cos}[2\,\varphi_2(t)] + 6\,I_{21}\,\mathrm{Cos}[2\,(\theta_2(t) +$
$\varphi_2(t))] - 6\,I_{23}\,\mathrm{Cos}[2\,(\theta_2(t) + \varphi_2(t))] + 6\,e_2^2\,m_2\,\mathrm{Cos}[2\,(\theta_2(t) + \varphi_2(t))] + I_{21}\,\mathrm{Cos}[2\,(\theta_2(t) - \varphi_1(t) + \varphi_2(t))] - I_{23}\,\mathrm{Cos}[2$
$(\theta_2(t) - \varphi_1(t) + \varphi_2(t))] + e_2^2\,m_2\,\mathrm{Cos}[2\,(\theta_2(t) - \varphi_1(t) + \varphi_2(t))] + 6\,I_{21}\,\mathrm{Cos}[2\,(\varphi_1(t) + \varphi_2(t))] - 6\,I_{23}\,\mathrm{Cos}[2\,(\varphi_1(t) +$
$\varphi_2(t))] + 6\,e_2^2\,m_2\,\mathrm{Cos}[2\,(\varphi_1(t) + \varphi_2(t))] + I_{21}\,\mathrm{Cos}[2\,(\theta_2(t) + \varphi_1(t) + \varphi_2(t))] - I_{23}\,\mathrm{Cos}[2\,(\theta_2(t) + \varphi_1(t) + \varphi_2(t))] + e_2^2$
$m_2\,\mathrm{Cos}[2\,(\theta_2(t) + \varphi_1(t) + \varphi_2(t))])\,\mathrm{Sin}[\theta_1(t)] + 32\,e_2\,g\,m_2\,\mathrm{Cos}[\varphi_2(t)]\,\mathrm{Sin}[\theta_2(t)]) - \omega^2\,\mathrm{Cos}[\varphi_1(t)]^2\,\mathrm{Sin}[2\,\theta_1(t)]\,(2\,I_{11}$
$- 2\,I_{13} - I_{22} + 2\,e_1^2\,m_1 + 2\,L_1^2\,m_2 + I_{22}\,\mathrm{Cos}[\theta_2(t)]^2 + 4\,e_2\,L_1\,m_2\,\mathrm{Cos}[\theta_2(t)]\,\mathrm{Cos}[\varphi_2(t)] - I_{22}\,\mathrm{Sin}[\theta_2(t)]^2) + 2\,I_{11}\,\omega^2$
$\mathrm{Sin}[2\,\theta_1(t)]\,\mathrm{Sin}[\varphi_1(t)]^2 - 2\,I_{13}\,\omega^2\,\mathrm{Sin}[2\,\theta_1(t)]\,\mathrm{Sin}[\varphi_1(t)]^2 - I_{22}\,\omega^2\,\mathrm{Sin}[2\,\theta_1(t)]\,\mathrm{Sin}[\varphi_1(t)]^2 + 2\,e_1^2\,m_1\,\omega^2\,\mathrm{Sin}[2\,\theta_1(t)]$
$\mathrm{Sin}[\varphi_1(t)]^2 + 2\,L_1^2\,m_2\,\omega^2\,\mathrm{Sin}[2\,\theta_1(t)]\,\mathrm{Sin}[\varphi_1(t)]^2 + I_{22}\,\omega^2\,\mathrm{Cos}[\theta_2(t)]^2\,\mathrm{Sin}[2\,\theta_1(t)]\,\mathrm{Sin}[\varphi_1(t)]^2 + 4\,e_2\,L_1\,m_2\,\omega^2$
$\mathrm{Cos}[\theta_2(t)]\,\mathrm{Cos}[\varphi_2(t)]\,\mathrm{Sin}[2\,\theta_1(t)]\,\mathrm{Sin}[\varphi_1(t)]^2 - I_{22}\,\omega^2\,\mathrm{Sin}[2\,\theta_1(t)]\,\mathrm{Sin}[\theta_2(t)]^2\,\mathrm{Sin}[\varphi_1(t)]^2 - 8\,e_2\,g\,m_2\,\mathrm{Sin}[\theta_1(t)]$
$\mathrm{Sin}[\varphi_1(t)]\,\mathrm{Sin}[\varphi_2(t)] + 4\,e_2\,L_1\,m_2\,\omega^2\,\mathrm{Sin}[2\,\theta_1(t)]\,\mathrm{Sin}[2\,\varphi_1(t)]\,\mathrm{Sin}[\varphi_2(t)] + 2\,\mathrm{Cos}[\varphi_1(t)]\,\mathrm{Sin}[\theta_1(t)]\,(4\,e_1\,g\,m_1 + 4\,g$
$L_1\,m_2 + 4\,e_2\,g\,m_2\,\mathrm{Cos}[\theta_2(t)]\,\mathrm{Cos}[\varphi_2(t)] + 4\,e_2\,L_1\,m_2\,\omega^2\,\mathrm{Cos}[\varphi_2(t)]\,\mathrm{Sin}[\theta_1(t)]\,\mathrm{Sin}[\theta_2(t)] - I_{21}\,\omega^2\,\mathrm{Sin}[\theta_1(t)]\,\mathrm{Sin}[2$
$\theta_2(t)] + 2\,I_{22}\,\omega^2\,\mathrm{Sin}[\theta_1(t)]\,\mathrm{Sin}[2\,\theta_2(t)] - I_{23}\,\omega^2\,\mathrm{Sin}[\theta_1(t)]\,\mathrm{Sin}[2\,\theta_2(t)] + e_2^2\,m_2\,\omega^2\,\mathrm{Sin}[\theta_1(t)]\,\mathrm{Sin}[2\,\theta_2(t)] + I_a\,\omega^2$
$\mathrm{Cos}[\varphi_2(t)]^2\,\mathrm{Sin}[\theta_1(t)]\,\mathrm{Sin}[2\,\theta_2(t)] - I_{21}\,\omega^2\,\mathrm{Sin}[\theta_1(t)]\,\mathrm{Sin}[2\,\theta_2(t)]\,\mathrm{Sin}[\varphi_2(t)]^2 + I_{23}\,\omega^2\,\mathrm{Sin}[\theta_1(t)]\,\mathrm{Sin}[2\,\theta_2(t)]$
$\mathrm{Sin}[\varphi_2(t)]^2 - e_2^2\,m_2\,\omega^2\,\mathrm{Sin}[\theta_1(t)]\,\mathrm{Sin}[2\,\theta_2(t)]\,\mathrm{Sin}[\varphi_2(t)]^2) - 4\,I_{21}\,\omega^2\,\mathrm{Sin}[\theta_1(t)]^2\,\mathrm{Sin}[\theta_2(t)]\,\mathrm{Sin}[\varphi_1(t)]\,\mathrm{Sin}[2\,\varphi_2(t)] +$
$4\,I_{23}\,\omega^2\,\mathrm{Sin}[\theta_1(t)]^2\,\mathrm{Sin}[\theta_2(t)]\,\mathrm{Sin}[\varphi_1(t)]\,\mathrm{Sin}[2\,\varphi_2(t)] - 4\,e_2^2\,m_2\,\omega^2\,\mathrm{Sin}[\theta_1(t)]^2\,\mathrm{Sin}[\theta_2(t)]\,\mathrm{Sin}[\varphi_1(t)]\,\mathrm{Sin}[2\,\varphi_2(t)] + 2$

I_{21} ω² Cos[$\theta_2(t)$] Sin[2 $\theta_1(t)$] Sin[2 $\varphi_1(t)$] Sin[2 $\varphi_2(t)$] - 2 I_{23} ω² Cos[$\theta_2(t)$] Sin[2 $\theta_1(t)$] Sin[2 $\varphi_1(t)$] Sin[2 $\varphi_2(t)$] + 2 e_2^2 m_2 ω² Cos[$\theta_2(t)$] Sin[2 $\theta_1(t)$] Sin[2 $\varphi_1(t)$] Sin[2 $\varphi_2(t)$] - 4 ω² Cos[$\theta_1(t)$]² Sin[$\theta_2(t)$] (Cos[$\varphi_1(t)$] (2 e_2 L_1 m_2 Cos[$\varphi_2(t)$] + Cos[$\theta_2(t)$] (-I_{21} + 2 I_{22} - I_{23} + e_2^2 m_2 + I_a Cos[2 $\varphi_2(t)$])) - I_a Sin[$\varphi_1(t)$] Sin[2 $\varphi_2(t)$])),

1/8 (8 g Cos[$\theta_1(t)$] ((e_1 m_1 + L_1 m_2 + e_2 m_2 Cos[$\theta_2(t)$] Cos[$\varphi_2(t)$]) Sin[$\varphi_1(t)$] + e_2 m_2 Cos[$\varphi_1(t)$] Sin[$\varphi_2(t)$]) - 1/4 ω² Cos[$\theta_1(t)$]² ((8 I_{11} - 8 I_{13} + 2 I_{21} - 4 I_{22} + 2 I_{23} + 8 e_1^2 m_1 - 2 e_2^2 m_2 + 8 L_1^2 m_2 + 4 I_{22} Cos[$\theta_2(t)$]² - 2 (I_{21} + I_{23} - e_2^2 m_2) Cos[2 $\theta_2(t)$] + I_{21} Cos[2 ($\theta_2(t)$ - $\varphi_2(t)$)] - I_{23} Cos[2 ($\theta_2(t)$ - $\varphi_2(t)$)] + e_2^2 m_2 Cos[2 ($\theta_2(t)$ - $\varphi_2(t)$)] + 16 e_2 L_1 m_2 Cos[$\theta_2(t)$] Cos[$\varphi_2(t)$] + 6 I_{21} Cos[2 $\varphi_2(t)$] - 6 I_{23} Cos[2 $\varphi_2(t)$] + 6 e_2^2 m_2 Cos[2 $\varphi_2(t)$] + I_{21} Cos[2 ($\theta_2(t)$ + $\varphi_2(t)$)] - I_{23} Cos[2 ($\theta_2(t)$ + $\varphi_2(t)$)] + e_2^2 m_2 Cos[2 ($\theta_2(t)$ + $\varphi_2(t)$)] - 4 I_{22} Sin[$\theta_2(t)$]²) Sin[2 $\varphi_1(t)$] + 8 Cos[2 $\varphi_1[t]$] (2 e_2 L_1 m_2 Sin[$\varphi_2(t)$] + I_a Cos[$\theta_2(t)$] Sin[2 $\varphi_2(t)$])) - ½ ω² (Cos[$\theta_1(t)$]² (I_a Cos[2 $\theta_2(t)$] Cos[2 $\varphi_2(t)$] Sin[2 $\varphi_1(t)$] + (I_{21} + I_{23} - e_2^2 m_2 - (I_{21} + I_{23} - e_2^2 m_2) Cos[2 $\theta_2(t)$] + 3 I_a Cos[2 $\varphi_2(t)$]) Sin[2 $\varphi_1(t)$] + 4 Cos[$\varphi_1[t]$]² (2 e_2 L_1 m_2 Sin[$\varphi_2(t)$] + I_a Cos[$\theta_2(t)$] Sin[2 $\varphi_2(t)$])) - 2 (I_a Cos[$\varphi_2(t)$]² Sin[2 $\theta_1(t)$] Sin[2 $\theta_2(t)$] Sin[$\varphi_1(t)$] + 4 e_2 L_1 m_2 Cos[$\varphi_2(t)$] (Sin[2 $\theta_1(t)$] Sin[$\theta_2(t)$] Sin[$\varphi_1(t)$] - Cos[$\theta_1(t)$]² Cos[$\theta_2(t)$] Sin[2 $\varphi_1(t)$])) + ½ Sin[2 $\varphi_1[t]$] ((-3 I_{21} + 4 I_{22} - I_{23} + e_2^2 m_2 + I_a Cos[2 $\varphi_2(t)$]) Sin[2 $\theta_2(t)$] Sin[$\varphi_1(t)$] + 4 I_a Cos[$\varphi_1(t)$] Sin[$\theta_2(t)$] Sin[2 $\varphi_2(t)$]) - Cos[$\theta_1[t]$]² ((2 I_{11} - 2 I_{13} - I_{22} + 2 e_1^2 m_1 + 2 L_1^2 m_2 + I_{22} Cos[2 $\theta_2(t)$]) Sin[2 $\varphi_1(t)$] - 2 Sin[$\varphi_1[t]$]² (2 e_2 L_1 m_2 Sin[$\varphi_2(t)$] + I_a Cos[$\theta_2(t)$] Sin[2 $\varphi_2(t)$]))))),

1/8 (-2 ω² Cos[$\theta_2(t)$]² Cos[$\varphi_1(t)$] (-I_{21} + 2 I_{22} - I_{23} + e_2^2 m_2 + I_a Cos[2 $\varphi_2(t)$]) Sin[2 $\theta_1(t)$] - e_2 m_2 (-6 L_1 ω² + 2 L_1 ω² Cos[2 $\theta_1(t)$] - 4 g Cos[$\theta_1(t)$ - $\varphi_1(t)$] + L_1 ω² Cos[2 ($\theta_1(t)$ - $\varphi_1(t)$)] + 2 L_1 ω² Cos[2 $\varphi_1(t)$] - 4 g Cos[$\theta_1(t)$ + $\varphi_1(t)$] + L_1 ω² Cos[2 ($\theta_1(t)$ + $\varphi_1(t)$)]) Cos[$\varphi_2(t)$] Sin[$\theta_1(t)$] + 2 I_a ω² Cos[$\varphi_1(t)$] Cos[$\varphi_2(t)$]² Sin[2 $\theta_1(t)$] Sin[$\theta_2(t)$]² + ω² (Cos[$\varphi_1(t)$] (-3 I_{21} + 4 I_{22} - I_{23} + e_2^2 m_2 + I_a Cos[2 $\varphi_2(t)$]) Sin[2 $\theta_1(t)$] Sin[$\theta_2(t)$]² - 2 I_{22} Cos[$\theta_1(t)$]² Cos[$\varphi_1(t)$]² Sin[2 $\theta_2(t)$] - 1/4 I_{22} (-6 + 10 Cos[2 $\theta_1(t)$] + Cos[2 ($\theta_1(t)$ - $\varphi_1(t)$)] + 2 Cos[2 $\varphi_1(t)$] + Cos[2 ($\theta_1(t)$ + $\varphi_1(t)$)]) Sin[2 $\theta_2(t)$] + 2 I_a Cos[$\theta_1(t)$]² Sin[$\theta_2(t)$] Sin[2 $\varphi_1(t)$] Sin[2 $\varphi_2(t)$]) + Cos[$\theta_2[t]$] (4 e_2 m_2 Cos[$\varphi_2(t)$] (2 g Sin[$\theta_1(t)$] - L_1 ω² Cos[$\varphi_1(t)$] Sin[2 $\theta_1(t)$]) - ½ I_a ω² (-2 + 6 Cos[2 $\theta_1(t)$] + Cos[2 ($\theta_1(t)$ - $\varphi_1(t)$)] + 2 Cos[2 $\varphi_1(t)$] + Cos[2 ($\theta_1(t)$ + $\varphi_1(t)$)]) Cos[$\varphi_2(t)$]² Sin[$\theta_2(t)$] + ω² (-(1/4) (-2 + 6 Cos[2 $\theta_1(t)$] + Cos[2 ($\theta_1(t)$ - $\varphi_1(t)$)] + 2 Cos[2 $\varphi_1(t)$] + Cos[2 ($\theta_1(t)$ + $\varphi_1(t)$)]) (-3 I_a + I_a Cos[2 $\varphi_2(t)$]) Sin[$\theta_2(t)$] + 2 I_a Sin[2 $\theta_1(t)$] Sin[$\varphi_1(t)$] Sin[2 $\varphi_2(t)$]))),

1/8 (-4 I_a ω² Cos[$\theta_1(t)$] Cos[$\varphi_2(t)$]² (Cos[$\theta_1(t)$] Cos[$\theta_2(t)$] Cos[$\varphi_1(t)$] - 2 Sin[$\theta_1(t)$] Sin[$\theta_2(t)$]) Sin[$\varphi_1(t)$] + 8 e_2 g m_2 Cos[$\theta_1(t)$] (Cos[$\varphi_2(t)$] Sin[$\varphi_1(t)$] + Cos[$\theta_2(t)$] Cos[$\varphi_1(t)$] Sin[$\varphi_2(t)$]) + ω² Cos[$\varphi_2(t)$] (-2 e_2 L_1 m_2 Cos[$\theta_1(t)$]² Sin[2 $\varphi_1(t)$] - 1/8 I_a (20 - 12 Cos[2 $\theta_1(t)$] + 6 Cos[2 ($\theta_1(t)$ - $\theta_2(t)$)] - 20 Cos[2 $\theta_2(t)$] + 6 Cos[2 ($\theta_1(t)$ + $\theta_2(t)$)] + 6 Cos[2 ($\theta_1(t)$ - $\varphi_1(t)$)] + Cos[2 ($\theta_1(t)$ - $\theta_2(t)$ - $\varphi_1(t)$)] + 2 Cos[2 ($\theta_2(t)$ - $\varphi_1(t)$)] + Cos[2 ($\theta_1(t)$ + $\theta_2(t)$ - $\varphi_1(t)$)] + 12 Cos[2 $\varphi_1(t)$] + 6 Cos[2 ($\theta_1(t)$ + $\varphi_1(t)$)] + Cos[2 ($\theta_1(t)$ - $\theta_2(t)$ + $\varphi_1(t)$)] + 2 Cos[2 ($\theta_2(t)$ + $\varphi_1(t)$)] + Cos[2 ($\theta_1(t)$ + $\theta_2(t)$ + $\varphi_1(t)$)]) Sin[$\varphi_2(t)$]) + ω² Cos[$\theta_1[t]$]² (-2 I_a Cos[$\theta_2(t)$] Cos[$\varphi_2(t)$]² Sin[2 $\varphi_1(t)$] + Cos[$\varphi_2(t)$] (-2 e_2 L_1 m_2 Sin[2 $\varphi_1(t)$] - ½ I_a (-6 + 6 Cos[2 $\theta_2(t)$] + Cos[2 ($\theta_2(t)$ - $\varphi_1(t)$)] + 6 Cos[2 $\varphi_1(t)$] + Cos[2 ($\theta_2(t)$ + $\varphi_1(t)$)]) Sin[$\varphi_2(t)$]) + 4 Cos[$\theta_2(t)$] Cos[$\varphi_1(t)$] Sin[$\varphi_2(t)$] (-e_2 L_1 m_2 Cos[$\varphi_1(t)$] + I_a Sin[$\varphi_1(t)$] Sin[$\varphi_2(t)$])) - 2 (4 e_2 g m_2 Sin[$\theta_1(t)$] Sin[$\theta_2(t)$] Sin[$\varphi_2(t)$] + ω² Cos[$\theta_2(t)$] Sin[$\varphi_2(t)$] (-3 e_2 L_1 m_2 + e_2 L_1 m_2 Cos[$\theta_1(t)$]² Cos[$\varphi_1(t)$]² - e_2 L_1 m_2 Sin[$\varphi_1(t)$]² - I_{21} Sin[2 $\varphi_1(t)$] Sin[$\varphi_2(t)$] + I_{23} Sin[2 $\varphi_1(t)$] Sin[$\varphi_2(t)$] - e_2^2 m_2 Sin[2 $\varphi_1(t)$] Sin[$\varphi_2(t)$] + Sin[$\theta_1(t)$]² (-e_2 L_1 m_2 + e_2 L_1 m_2 Sin[$\varphi_1(t)$]² + I_a Sin[2 $\varphi_1(t)$] Sin[$\varphi_2(t)$])) - ω² Sin[2 $\theta_1[t]$] (-2 I_a Sin[$\theta_2(t)$] Sin[$\varphi_1(t)$] Sin[$\varphi_2(t)$]² + Cos[$\varphi_1[t]$] (2 e_2 L_1 m_2 Sin[$\theta_2(t)$] Sin[$\varphi_2(t)$] + I_a Sin[2 $\theta_2(t)$] Sin[2 $\varphi_2(t)$])))) },

where

$$I_a = I_{21} - I_{23} + e_2^2\, m_2,$$

$$I_b = I_{22} + e_2^2\, m_2,$$

$$I_c = I_{21} + e_2^2\, m_2.$$

References

1. J. Shen, A. K. Sanyal, N. A. Chaturvedi, D. Bernstein, H. McClamroch. Dynamics and control of a 3D pendulum. *43rd IEEE Conference on Decision and Control, 2004. CDC* 1 (2004), 323–328.
2. N. A. Chaturvedi, N. H. McClamroch. Asymptotic stabilization of the hanging equilibrium manifold of the 3D pendulum. *International Journal of Robust and Nonlinear Control* 17, 16 (2007), 1435–1454.
3. N. A. Chaturvedi, T. Lee, M. Leok, N. H. McClamroch. Nonlinear Dynamics of the 3D Pendulum. *Journal of Nonlinear Science* 21, 1 (2010), 3–32.
4. J. Náprstek,C. Fischer. Types and stability of quasi-periodic response of a spherical pendulum. *Computers & Structures* 124 (2013), 74–87.
5. L. Consolini, M. Tosques. On the exact tracking of the spherical inverted pendulum via an homotopy method. *Systems & Control Letters* 58, 1 (2009), 1–6.
6. I. M. Anan'evskii, N. V. Anokhin. Control of the spatial motion of a multilink inverted pendulum using a torque applied to the first link. *Journal of Applied Mathematics and Mechanics* 78, 6 (2014), 543–550.
7. T. Lee, M. Leok, and N. H. Mcclamroch, Dynamics and Control of a Chain Pendulum on a Cart. *Proc. of the IEEE Conference on Decision and Control*, (2012), 2502–2508.
8. Xinjilefu, V. Hayward, H. Michalska. Hybrid Stabilizing Control for the Spatial Double Inverted Pendulum. *Brain, Body and Machine*, Springer Berlin Heidelberg, (2010), 201–215.
9. P. Egger and L. Caracoglia. Analytical and experimental investigation on a multiple-mass-element pendulum impact damper for vibration mitigation. *Journal of Sound and Vibration* 353, (2015), 38–57.
10. M. McGrath, D. Howard, R. Baker. The strengths and weaknesses of inverted pendulum models of human walking. *Gait & Posture* 41, 2 (2015), 389–394.
11. H. Ozaki, K. Ohta, and T. Jinji. Multi-body power analysis of kicking motion based on a double pendulum. *Procedia Engineering* 34 (2012), 218–223.
12. J. Awrejcewicz, A. V. Krysko, N. A. Zagniboroda, V. V. Dobriyan, V. A. Krysko. On the general theory of chaotic dynamics of flexible curvilinear Euler–Bernoulli beams. *Nonlinear Dynamics* 79, 1 (2014), 11–29.
13. K. Vernekar, H. Kumar, K. V. Gangadharan. Gear Fault Detection Using Vibration Analysis and Continuous Wavelet Transform. *Procedia Materials Science* 5, (2014), 1846–1852.
14. N. G. Nikolaou, I. A. Antoniadis. Demodulation of vibration signals generated by defects in rolling element bearings using complex shifted Morlet wavelets. *Mechanical Systems and Signal Processing* 16, 4 (2002), 677–694.
15. H. Li, T. Yi, M. Gu, L. Huo. Evaluation of earthquake-induced structural damages by wavelet transform. *Progress in Natural Science* 19, 4 (2009), 461–470.
16. J. Gross. Analytical methods and experimental approaches for electrophysiological studies of brain oscillations. *Journal of Neuroscience Methods* 228, (2014), 57–66.
17. R. Büssow. An algorithm for the continuous Morlet wavelet transform. *Mechanical Systems and Signal Processing* 21, 8 (2007), 2970–2979.
18. M. Ludwicki, J. Awrejcewicz, G. Kudra. Spatial double physical pendulum with axial excitation: computer simulation and experimental set-up. *International Journal of Dynamics and Control* 3, 1 (2014), 1–8.

19. J. Awrejcewicz, A. V. Krysko et al. Analysis of chaotic vibrations of flexible plates using fast Fourier transforms and wavelets. *International Journal of Structural Stability and Dynamics* 13, 7 (2013), 1340005.
20. J. Awrejcewicz et al. Analysis of chaotic vibrations of flexible plates using Fast Fourier Transforms and wavelets. *International Journal of Structural Stability and Dynamics* 13, 7 (2013), 1340005-1 - 1340004-12.

Michał Ludwicki, Ph.D.: Lodz University of Technology, Department of Automation, Biomechanics and Mechatronics, 1/15 Stefanowski St., 90-924 Lodz, Poland (*michal.ludwicki@p.lodz.pl*). The author gave a presentation of this paper during one of the conference sessions.

Jan Awrejcewicz, Professor: Lodz University of Technology, Department of Automation, Biomechanics and Mechatronics, 1/15 Stefanowski St., 90-924 Lodz, Poland (*jan.awrejcewicz@p.lodz.pl*).

Grzegorz Kudra, Ph.D.: Lodz University of Technology, Department of Automation, Biomechanics and Mechatronics, 1/15 Stefanowski St., 90-924 Lodz, Poland (*grzegorz.kudra@p.lodz.pl*).

Influence of intermediate foil on air-foil bearings performance and exploitation properties
(STA162-15)

Jakub Łagodziński, Kacper Miazga

Abstract: Air-foil technology is an interesting alternative for classic rolling or oil bearings in turbomachinery. It ensures low power losses, do not require external lubrication or pressurization and is capable of working with high rotational speeds. Numerous studies brought significant improvement in materials and design solutions for the aerodynamic shaft support system. The paper presents effects of modification performed by adding intermediate foil to typical structure of air-foil bearing. The main aim of the investigation was focused on analyze of its influence on characteristic parameters and exploitation properties of operating bearing, i.e. bearing load capacity and bearing resistance to thermal runaway phenomenon [4]. The thermal runaway is also known as foil bearing thermal instability. The tests confirmed proper behavior of the modified device and brought new knowledge in air-foil technology field.

1. Introduction

The last decades brought remarkable progress in the field of high speed turbomachinery. New kinds of air cycle devices are designed with consideration of decreasing their dimensions and ability to work with high rotational frequencies. Moreover great attention is paid to limitation of power losses and assurance of reliability.

In order to meet such demands new kinds of rotor support systems had to be developed. One of the proposed solutions is an idea of Oil-Free technology, in which air-foil bearings have great potential.

1.1. Air-foil Technology

Air-Foil bearings are self-acting aerodynamic bearings that use ambient gas as their working fluid. The main idea of their design is based on two foils placed between shaft and sleeve: bump and top (see figure 1). As the shaft starts rotating, the ambient gas (e.g. air) is pushed between top foil and journal due to its viscosity that creates thin gas film. After reaching characteristic rotational speed called lift-off speed the air gap is continuous and there is no contact between the shaft and the top foil. In this solution the bump foil is considered to be an elastic support for top foil.
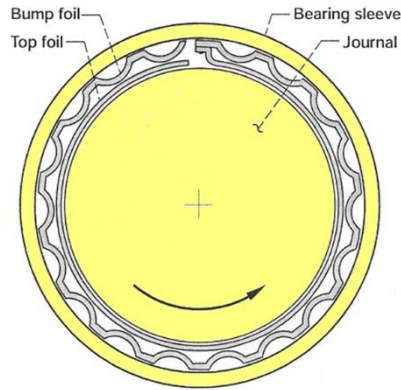
Figure 1. A basic schematic of the air-foil bearing

Air-foil bearings are mainly considered as shaft support system for high rotational speeds cycle machines of low and medium power, usually up to 100kW. They were firstly applied in Air Cycle Machines and Environmental Control Machines mainly in military aircrafts [1], confirming their high performance abilities. With growing demands and advances in technology the field of use was expanded to many other devices such as blowers, turbojet engines, ORC generators, compressors, turboexpanders etc.

1.2. Air-foil bearings features and design

There are many advantages considered with the air-foil bearings. First to be mentioned they are self-acting, aerodynamic supports, therefore, unlike aerostatic bearings, there is no need for external pressurization. It leads to elimination of additional pressure supply systems and simplifying the construction of the machine. Moreover, using ambient gas as working medium air-foil technology is free from oil lubrication, which ensures total cleanliness of working medium. It is significant especially for systems where seals are problematic and any contamination of cycle gas is inadmissible. Furthermore, power losses in machines with air-foil bearings applied are strongly reduced due to their non-contact operation with high rotational speeds.

Despite many advantages, air-foil bearings have significant limitations that have to be considered. First of all there is dry friction phenomenon that occurs during start up and shut down of the machine. Before the thin gas film is formed, the surfaces of the top foil and the shaft have contact with each other. The frictional contact limits the lifetime of the bearing due to surface degradation and leads to destruction of these parts. Solution of this problem lies in application of special coating materials that reduce dry friction and protect foil and shaft from wear. Moreover, such materials should ensure chemical stability, especially where air is not working fluid, good adhesion to the base and solid lubrication possibly. The investigations of coatings brought many different solutions, such

as ceramics, polymers, metallic materials and composites suitable for wear protection, considering various temperature ranges of operation [2, 3]. They can strongly improve the performance of the bearing, ensuring sufficient number of start-stop cycles without undesirable wear.

Another important issue of the air-foil bearings is limited load capacity. With thin self-acting gas film and elastic bump foil as the only support for the journal, the mass of rotating system is limited. If the rotor is too heavy, it can break the continuous gas gap and cause an ineffective operation of the bearing, including damage due to friction.

Under a heavy load, a foil bearing thermal runaway phenomenon may appear. This phenomenon, known also as foil bearing thermal instability, results from too tight fitting in the bearing. This causes positive feedback loop between the frictional torque and journal thermal expansion. The thermal runaway develops very quickly and can cause severe damage to the bearing.

The numerous studies of the air-foil bearing construction brought various concepts for the structure of the device. Main differences lies in the slot-like locks, which are responsible for fixing foils in the sleeve (see figure 2) and elastic support for top foil. The classic bump foil was usually modified by circumferential splits and variable pitch bumps. Another idea was based on substituting bump foil by elastic metal mesh [5]. Numerous different structural variants of air-foil bearings were developed and tested considering multipad, hydresil or multilayer bearings with additional intermediate foil [1].

Figure 2. Different types of retaining slots

2. Intermediate foil in air-foil bearings

The basic structure of air foil bearing consists of flat top foil and corrugated bump foil which acts as a spring. Most common modifications leading to improvement of the bearing performance were made to bump foils, distinguishing them in three main generations [4][6]. Another interesting adjustment

was made by introducing intermediate foil into the bearing, which was placed between bump and top foils. This additional element improves damping of the foils structure. Moreover with intermediate foil, the top foil has additional support that decreases a phenomenon of sagging (see figure 3). It occurs in collapsing of the top foil between pitches of the bump foil when thin gas film is formed under operation of the bearing [7].
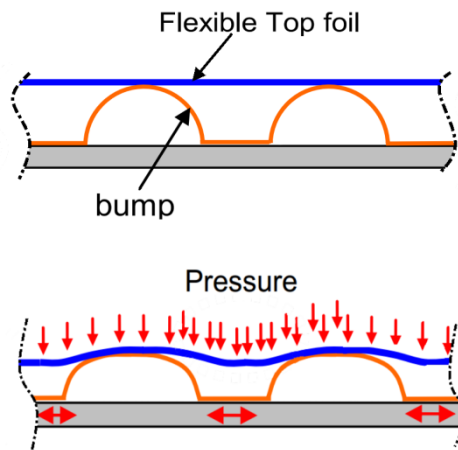

Figure 3. The effect of sagging

During initial tests the intermediate foil occurred to have positive influence on bearing performance. Comparing to basic air-foil bearing construction, the torque at the start-up was reduced. Moreover wear of top foils working in modified bearings was noticeable lower, resulting in increase of the bearing lifetime. These observations brought an idea of tests that could precisely describe influence of intermediate foil in air-foil bearings.

2.1. The test rig for air foil bearing with intermediate foil.

The idea of checking the results of intermediate foil implementation was based on comparing a performance of the same bearing with and without this element. The sleeve was prepared to work with three segments of bump foil with circumferential splits, intermediate foil and top foil coated with wear resistant polymer AS20. The shafts coating consisted of chromium oxide ceramic material. The bearing was transformed into classic type by removing intermediate foil and placing three pieces of flat foils with the same thickness as the intermediate between bearings sleeve and bump foil segments. This way it was possible to test two variants of the bearing with the same initial preload, which usually is adjusted by inner diameter of the sleeve [8].
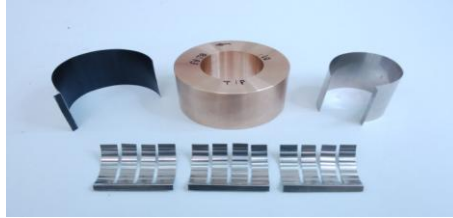
Figure 4. Elements of the air-foil bearing with the intermediate foil.

The test rig was based on electrical spindle controlled by frequency converter. The measured values were rotational speed of the shaft, provided by an optical sensor and bearing torque measured with force gauge attached to its sleeve. The idea of the experiment was to compare a behavior of both variants of bearings working under variable static load. The design of test rig allowed adjustment of static load by suspending a weight on bearings sleeve. In order to eliminate an influence of the weights on force sensor measurement, an externally pressurized aerostatic bearing was placed on the investigated air-foil bearing to provide pendulous attachment of mass.
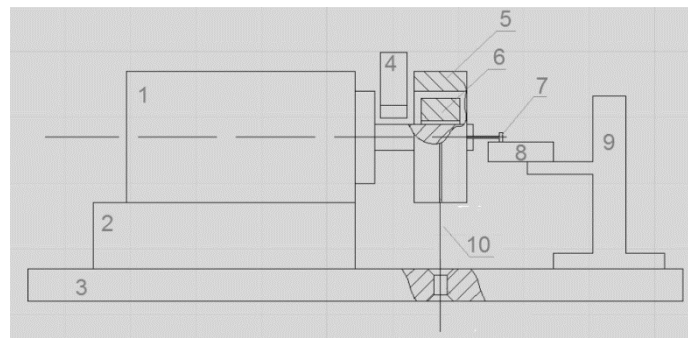
Figure 5. The test rig schematic (1 - electric spindle, 2 – pedestal, 3 – table, 4 – optical sensor, 5 – aerostatic bearing, 6 – investigated aerodynamic air-foil bearing, 7 – torque lever, 8 – force sensor, 9 – force sensor rack, 10 – suspension of static load).

2.2. Load capacity of air-foil bearings.

The air-foil bearings, as self-acting rotor support system without external pressure supply, are usually used in low and medium power applications, with limited mass of shaft and rotor. The design of the machine needs to consider a specific nature of their performance.

The analysis of air-foil bearings capacity is a strongly complicated issue. Comparing to other types of bearings, the behavior of elastic structure of foils is difficult to describe with equations. Moreover, there has to be considered dependency between thin gas film of working medium and solid structural foils. Another important phenomenon comes from friction between bump and top foils that

slightly shift their relative position during bearing operation. Considering the complexity of phenomenon that occurs in the air-foil bearings numerical models that can entirely describe their behavior are difficult to create.

Load capacity of the air foil bearing is strongly related to its construction. The experimental data brought a simple method of its estimation. It was shown, that load capacity is linearly related to dimensions of the bearing projected area and surface velocity [9].

Nevertheless, experimental investigations are significant in determining behavior of air-foil bearings in different working conditions. Test performed with variable static load can be used for creating performance map, which is a characteristic based on surface plot that describes power loss in bearing depending on the rotational speed and applied load [10]. With the map, optimal operational points and safety margins can be found.

3.   Experimental results and discussion.

The experimental tests were performed in two series, beginning with classic type of air-foil bearing, then with the bearing with the intermediate foil. Both devices were loaded with the same static loads forces from 6.3N to 113.5N (the values considered mass of air-foil and aerostatic bearings sleeves). For each value of load the force on air-foil bearing sleeve was measured and then recalculated to torque and power loss at rotational frequencies from 200Hz to 400Hz with step of 50Hz.

3.1.   Results of measurements.

With collected data the following plots were created, which present operating parameters of both bearings. The characteristics on the Figure 6 present the performance maps of both bearings.
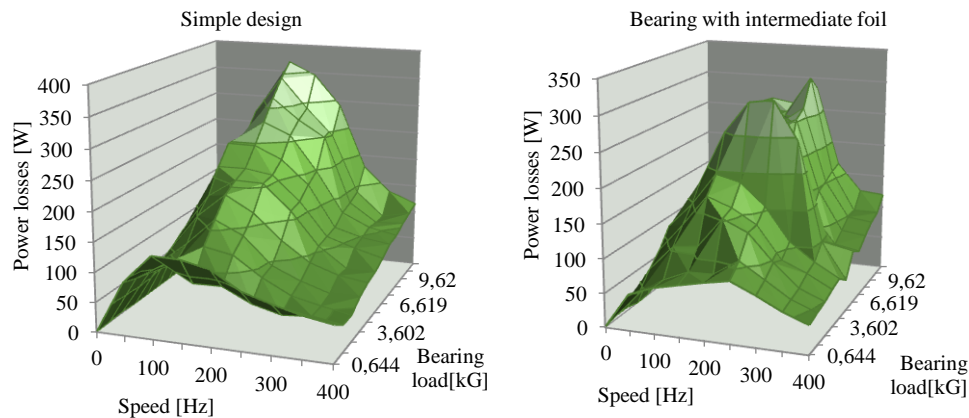

Figure 6. Performance maps.

In order to get a clear comparison of operation parameters of air-foil bearings with and without the intermediate foil the relation of torque value to suspended static load for specific rotational frequencies of the shaft were plotted.
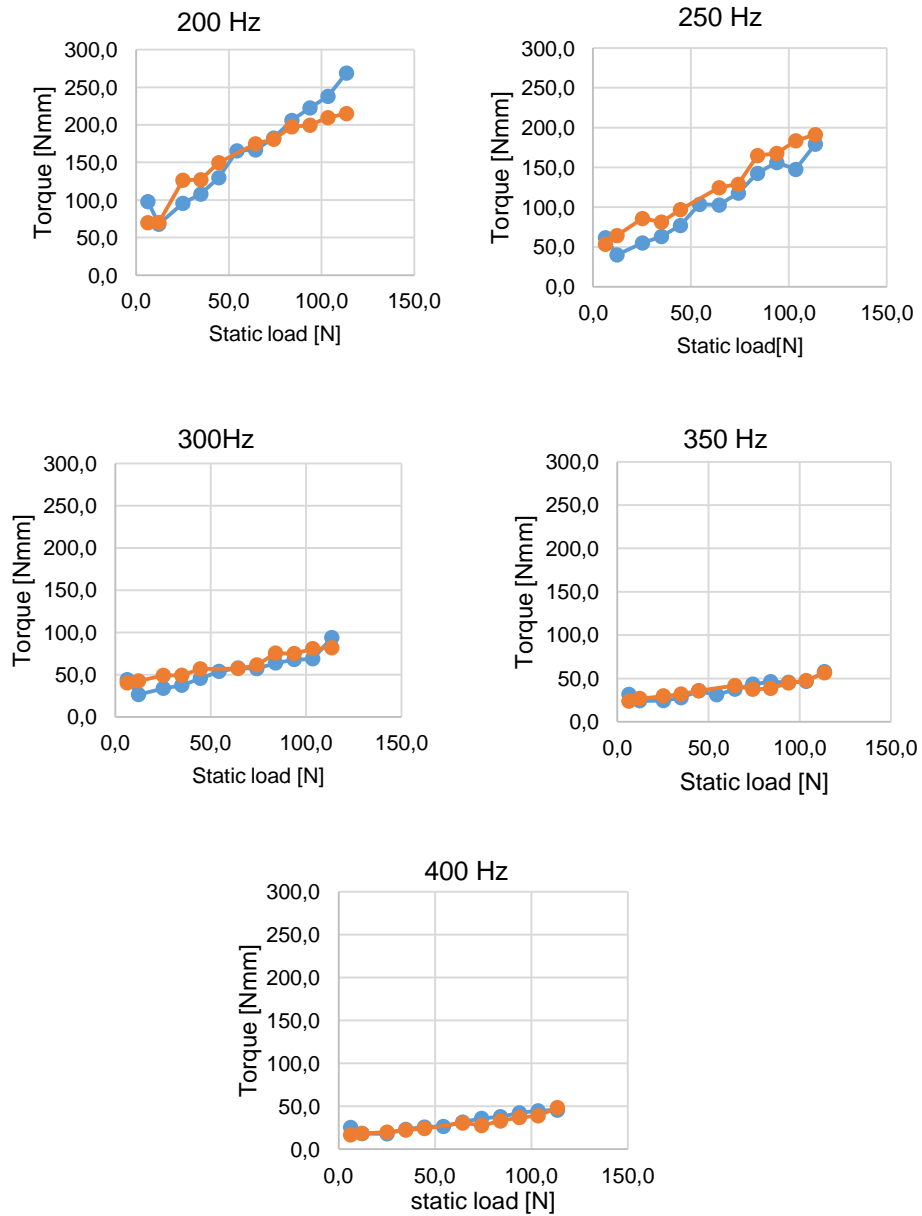

Figure 7. Measured values of torque for specific rotational frequencies of the journal. Note: vertical scales are the same.

An additional analysis was done to the measured peak values of the torque at the start-up of the bearing for each value of static load, as it is critical moment in operation of the device when dry friction occurs.
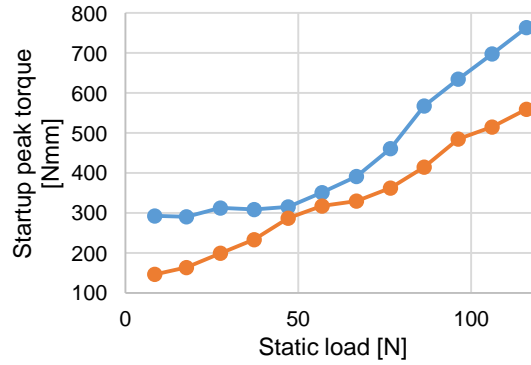
Figure 8. Peak values of measured torque at the star-up of the bearing.

3.2. Discussion.

The analysis of the results shows very strong influence of static load on operating parameters of the air-foil bearings. According to former predictions, the measured torque increases with the increase of mass loaded on the bearing sleeve in entire range of rotational speeds of the shaft. In case of implementation of this rotor support system in a machine it would result in growth of power losses with increase of rotating systems mass.

If we take into consideration the power losses dissipated in the bearing (see performance maps in Figure 6), it is clearly visible that applying the intermediate foil can cause a reduction of power losses by ~ 25%. One can observe, that with simple design, the bearing power losses performance map reaches a peak value of almost 400 Watts, but the bearing with intermediate foil, for the same operating conditions, has a maximum power loss value at only 300 Watts. This means less heat generated during operation, less journal thermal expansion and wider bearing thermal stability margin.

In the Figure 7, were the ranges of all torque axes are the same for all plots, it is found, that static load has bigger influence on measured torque with lower rotational speeds of the shaft. With the increase of rotation frequencies, the lower change of bearings torque is observed with defined increment of static load.

The Figure 7 brings also a comparison of operating parameter of the air-foil bearing with and without intermediate foil. Eventually, there was no significant difference found in performance of both tested variants. The values of measured torque for all rotational speeds and static loads were very

near. In this case, there cannot be seen any significant influence of the intermediate foil on operation of the air-foil bearing.

The different situation can be observed in plot of measured torque at the star-up of the bearing (see Figure 8). It is a critical moment of the bearings operation where dry friction occurs before formation of the continuous gas film and cause wear of top foils and journals surfaces. In this case the implementation of the intermediate foil causes visible decrease of measured torque. It is translated into reduction of frictional force between the top foil and the journal at the start-up.

The analysis of the results was also based on visual inspection of the top-foils of both bearing variants after tests were performed. It brought an information about level of wear of the coating materials.
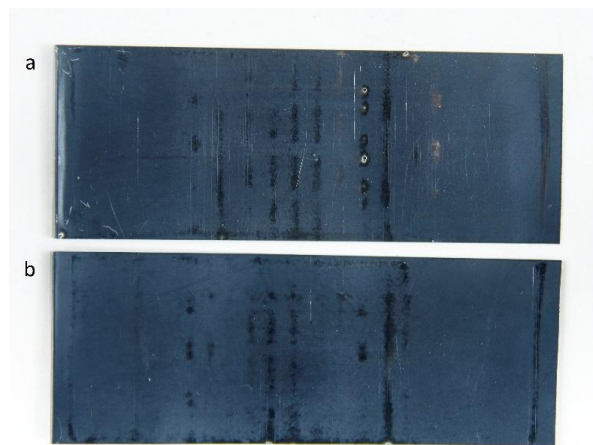

Figure 9. Top foils after test: a – basic type of the bearing, b – bearing with the intermediate foil.

The top-foils worked in very similar conditions, being subjected to approximately the same number of start-up and shut-down cycles. The visual inspection showed lower level of wear in AS20 polymer on the top foil which worked in the bearing with implemented intermediate foil. The top-foil from the basic type of the bearing had more degraded surface, even with local complete loss of coating material.

4. Conclusions.

The purpose of the experimental tests presented in the paper was to investigate the influence of intermediate foil implemented in the aerodynamic air-foil bearing on operating and exploitation properties of this rotor support system. The evaluation of this variation was based on comparison of the performance of basic and modified bearings working under variable static load.

The analysis of the test results showed that intermediate foil have a significant influence on power losses in air-foil bearing under operation with continuous gas gap formed. The values of measured torque for both bearings working with the same rotational speeds and suspended static loads varied very slightly. The significant difference was found in measurements of torque at the start-up of the bearings. The application of the intermediate foil caused reduction of measured torque in this critical moment.This indicates decrease in the friction force between the top foil and the journal. The positive effect was also confirmed by visual inspection, which showed lower wear of the top foil that worked in the modified bearing.

The intermediate foil is an interesting modification for aerodynamic air-foil bearings. It improves mutual operation of foils resulting in advances of exploitation properties of the bearing and increases damping by introduction of additional friction between foils and reduces the effect of sagging.

References

[1] Agrawal, G.L. Foil air/gas bearings technology – an overview. *ASME Publication* 97-GT-347.

[2] Miazga, K., Tkacz, E., Kozanecki, Z., and Łagodziński, J. Investigation of coating materials for air-foil bearings. *Cieplne maszyny przepływowe. Turbomachinery* 140, 2011, 149-156.

[3] Hashmat, H., Hryniewicz, P., Walton, J.F., Willis, J.P., Jahanmir, S., and DellaCorte, C. Low-friction wear-resistant coatings for high-temperature foil bearings. *Tribology International* 38, 2005, 1059-1075.

[4] DellaCorte, C., Radil, K.C., Bruckner, R.J., and Howard, S.A. Design, Fabrication and performance of open source generation I and II compliant hydrodynamic gas foil bearings. NASA/TM-2007-214691

[5] San Andres, L., and Chirathadam, T., Performance Characteristics of Metal Mesh Foil Bearings: Predictions vs. Measurements. *ASME Journal of Engineering for Gas Turbines Power*. 135,2013, 1-8.

[6] Nalepa, K., Pietkiewicz, P., and Zywica, G., Developement of the foil bearing technology. Technical Sciences. 12, 2009, 229-240.

[7] San Andres, L., and Kim, T.H., Analysis of gas foil bearings integrating FE top foil models. *Tribology International*, 42, 2009, 111-120.

[8] Radil, K.C., Howard, S.A., and Dykas, B., The role of radial clearance on the performance of foil air bearing, *Tribology Transactions*. 45, 2002, 485-490.

[9] DellaCorte, C., and Valco, M.J., Load capacity estimation of foil air journal bearings for oil-free turbomachinery applications. *Tribology Transactions*. 43, 2000, 795-801.

[10] Radil, K.c., and DellaCorte, C., A three dimensional foil bearing performance map applied to oil free turbomachinery. *Tribology Transactions*. 53, 2010, 771-778.

Jakub Łagodziński, Ph.D.: Lodz University of Technology, Institute of Turbomachinery. 219/223 Wolczanska St, 90-924 Lodz, Poland. (*jakub.lagodzinski@p.lodz.pl*). The author gave a presentation of this paper during one of the conference sessions.

Kacper Miazga, M.Sc. (Ph.D. student): Lodz University of Technology, Institute of Turbomachinery. 219/223 Wolczanska St, 90-924 Lodz, Poland. (kacper.miazga@p.lodz.pl)

Remote monitoring of the train driver along with the locomotive motion dynamics in the course of shunting using mobile devices (CON273-15)

Jakub Młyńczak, Rafał Burdzik, Ireneusz Celiński

Abstract: A train in operation may be considered as a dynamic system. Many interesting dynamic train properties may be observed while it is performing the shunting activity. Therefore, the first stage of the experiments conducted was devoted to development of a remote monitoring system using mobile devices for monitoring of the train driver's actions and the locomotive motion dynamics. The paper describes implementation of the method for the sake of application of remote monitoring in the course of shunting of the SM42 locomotive. For this purpose the research was conducted at a test station. The shunting locomotive was equipped with a recording unit with a proprietary mobile application installed. The application developed by the authors uses the accelerometer system to measure linear accelerations and velocity of the locomotive. For establishing the geographical position within the test station area the GPS system was used. This system makes it possible to monitor physical parameters of the shunting activity. Along with simultaneous measurement of positions of shunting locomotives, it allows for assessment of the driver's actions to be assessed from the perspective of their legitimacy and conformity with the relevant work regulations. For the sake of prospective application in measurements, locomotive traffic data may be transferred to a signal box by means of the SMS protocol for purposes of the shunting management.

1. Introduction

Problems of dynamics of rail vehicles are addressed in a vast number of scientific studies on account of the extensive impact of dynamic phenomena on such aspects as safety, technical reliability, efficiency of processes and comfort. The obstacles one encounters while modelling and observing dynamic phenomena in rail vehicles are due to limitations of accessibility, external conditions and dimensions. Therefore, the research assumption adopted was the observation of dynamics of a locomotive in the course of shunting. One of the most important aspects of operation of a railway station comprises shunting activity. Principal goals of such activity are mainly marshalling and setting of train sets. In the course of shunting, there is often a necessity of changing the number of cars or cars are being reset and admitted at different technical points of a station (for cargo handling). Such a large range of activities enables observation of multiple dynamic phenomena under relatively advantageous conditions. Moreover, when properly performed, shunting activity is a prerequisite of efficient railway traffic management. Besides general regulations typical of the given railway line,

shunting activity is performed in accordance with shunting rules and regulations established for the given technical point [7,8]. While conducting this type of activity, what proves decisive of its characteristics is often the type of the means of transport being marshalled and the cargo being transported.

Figure 1. Shunting runs studied, plotted against a plan of the Chabówka (Poland) station. Source: OSM/JSOM [1,2,3]

The authors of the article have discussed both a concept and application of a simple method of remote supervision of shunting runs using mobile devices enabling observation and recording of chosen dynamic parameters of a rail vehicle. In the course of the studies, an SM42 series diesel locomotive was used, being one of the most popular means of cargo transport. Figure 1 is a site plan of the railway station with the blue line designating the GPS trace of the locomotive studied while performing shunting activity [1-5].

Figure 2. Interior of the test locomotive driver's cab. Source: authors' own materials.

2. Methodology

Assumptions of the method proposed are as follows: mobility, simplicity of operation, short time of installation of measuring apparatus, synchronisation of time and location (positioning). For the sake of these assumptions, an application was developed for mobile phones to replace standard measuring devices. A mobile phone is attached to the driver's cab floor in such a manner that its top part indicates the driving direction while the locomotive is moving ahead. The phone's vertical axis is perpendicular to the track substructure plane. The mobile phone features an application created by the authors, dedicated to the Android platform, which uses the accelerometer system to record linear accelerations occurring in the course of the shunting locomotive's operation.

What is also recorded is the shunting locomotive running speed and, by means of the mobile phone's GPS unit, its physical position in space. Also a number of other parameters are recorded, including speed, locomotive altitude above sea level etc. Such a simple measuring system allows for monitoring of basic physical parameters of shunting operations performed by the shunting locomotive driver. In combination with simultaneous measurement of the shunting locomotive position, it enables verification of legitimacy of the manoeuvres performed by the driver and their parameters as well as the degree to which the driver adheres to specific legal regulations and standards. In the course of the measurement, basic data related to the locomotive's running characteristics may be sent to the shunting signal box using the SMS protocol. Depending on the data transmission technique applied, the data transferred only concern mean values of the characteristics examined (SMS) of aggregated

data (GPRS). In this manner, an additional reverse channel is created while conducting shunting activity (supplementary to the channels used in accordance with the applicable legal regulations, i.e. the visual and the radio one), which accurately enables supervision of the work performed by the shunting locomotive driver based on the characteristics being measured [6,7]. In the aftermath of the research in question, the authors are planning to use transmission channels to remotely control the driver's work by means of the WiFi and BT protocols. The graphical material provided in the article has been developed based on the data recorded while studying the locomotive running along the trace plotted on the test station site plan (Figure 1).
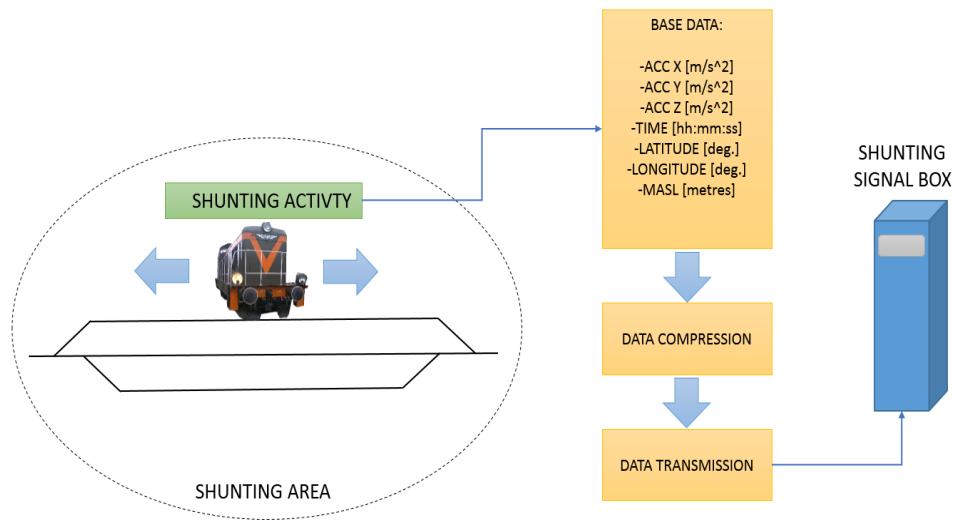
Figure 3. Concept of the research methodology. Source: authors' own materials.

Figure 3 is a diagram illustrating the research methodology applied in the scope of remote control of shunting activity using a locomotive. Based on the characteristics acquired by means of a mobile device, data of the locomotive's linear acceleration and positioning (as well as a number of other characteristics, such as speed, altitude above sea level) are processed. The data in question are aggregated and/or compressed, and then, using the chosen transmission channel (SMS, GPRS), sent to the shunting signal box. This enables the shunting signal box personnel to acquire accurate knowledge on the locomotive parameters, and owing to the station's radio communication system, they can monitor changes in these parameters.

3. Train marshalling process

In accordance with Instruction Ir-1 (R-1) on "train traffic management", shunting operations are defined as intended movements of railway vehicles. The foregoing also applies to other activities related to the said movements, as they are performed on tracks of shunting stations [7]. The operations excluded from those activities are the train entry, exit and passing. Shunting is performed with motor-driven railway vehicles, among others.

The method described in the article mainly applies to this kind of shunting activity, although, on account of its simplicity, it may also be used for the sake of marshalling conducted by means of rail and road tractors or special machinery [7]. The shunting activity is performed in a place referred to as a shunting area. It is a pre-defined (delimited) section of a railway station territory forming an independent set of tracks and machines used for shunting activity by one shunting manager by means of one shunting locomotive. A division into shunting areas and districts (two or more shunting areas) has been introduced in order to enable efficient and safe performance of shunting activity.

One of major parameters of shunting activity is the shunting speed, as specified in Instruction Ir-9 (R34) [6]. Shunting operations are often performed in tracks occupied by rolling stock. It is for that reason that individual shunting operations should be performed with care, maintaining safe running speed, as defined in Instruction Ir-9 [6]. Shunting speeds have been precisely specified in the instruction with reference to different cases of technological activities and incidents. Safety of shunting activity is not only the matter of the rolling stock, but it also concerns the goods transported by rail, and primarily people. Permissible running speed ranges for shunting activity are defined in Instruction Ir-9. While performing shunting operations, the running speed must not exceed 25 km/h, however, depending on the technology used for shunting and the infrastructure elements involved, the permissible speeds range considerably from 3 km/h up to 40 km/h. For instance, a self-propelled railway vehicle running in the "idle" mode, in certain cases and at selected points of the shunting area, may run with the permissible speed as high as 40 km/h. In an extremely restrictive case, while a shunting locomotive is driving up to the rolling stock, this speed must not exceed 3 km/h. In accordance with the methodology proposed in the article, the shunting signal box receives real-time information on the shunting locomotive position and its actual speed. This enables remote monitoring of correctness of the shunting activity to be performed by shunting brigades, even those operating within particularly vast shunting areas and under diversified weather conditions. Not only is it important from the perspective of shunting safety, but also regarding potential claims of owners/insurers of the goods transported. The method in question allows for documenting the course of shunting activity using highly accurate parameters by way of verifiable measurement. In such a case, each shunting activity is digitised and stored at the appropriate shunting signal box or centrally archived. Moreover, working characteristics of individual shunting brigades may be compared

between one another, e.g. in order to calculate bonuses for individual members of brigades in recognition of their effort.

Information on the shunting activity is transferred in real time to the shunting signal box which enables the activity to be adjusted using reverse communication channels from the signal box (mainly radio communications, but video and audio signals as well).

What matters while performing shunting activity is the precise information on locations of shunting vehicles and members of shunting brigades. In accordance with the applicable regulations, vehicles must be equipped with an active bottom headlight whose position corresponds to the driver's station arrangement (left side, right side). This piece of information is particularly is important for shunting brigades. Knowing it, one may determine the side on which the driver is seated as well as the direction in which the shunting locomotive is moving. Assuming that members of shunting brigades have been equipped with appropriate terminals enabling them to acquire information on the locomotive position, the methodology proposed may additionally increase safety of shunting activity. For instance, as the shunting locomotive is approaching, a brigade member may be warned with vibrations or an audible signal [12-14]. Such safeguards are fundamental to shunting activity conducted at large marshalling yards of high throughput as well as when working under difficult atmospheric conditions (fog, heavy rain etc.). Unfavourable station layout, i.e. considerable slopes or longitudinal profiles with large curvature, should also be considered as a factor imposing implementation of such safety procedures.

4. Analysis

The methodology proposed is mainly based on indications of an accelerometer installed inside the locomotive driver's cab as well those provided by a GPS receiver. Such a simple system enables monitoring of the locomotive position and parameters of its motion as it performs shunting activity.
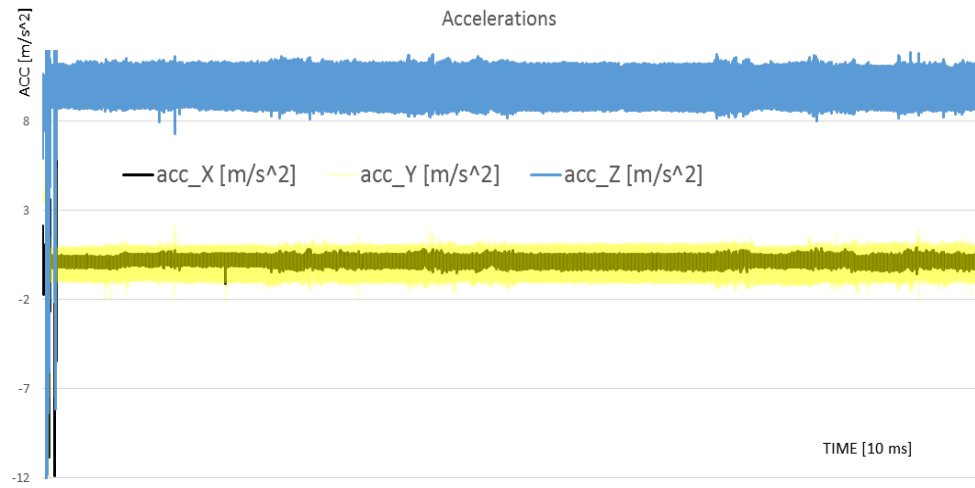
Figure 4. Accelerations measured within an hour of shunting activity. Source: authors' own materials.

Figure 4 illustrates linear accelerations measured inside the cabin of the SM42 diesel locomotive performing shunting activity. The colour blue in Figure 4 marks vertical accelerations (ACC_Z). Yellow corresponds to accelerations in the longitudinal axis of the locomotive's motion (ACC_Y), and black (in the background of characteristic ACC_Y) – in the axis transverse to the direction of the locomotive's movement (ACC_X), i.e. lateral accelerations.
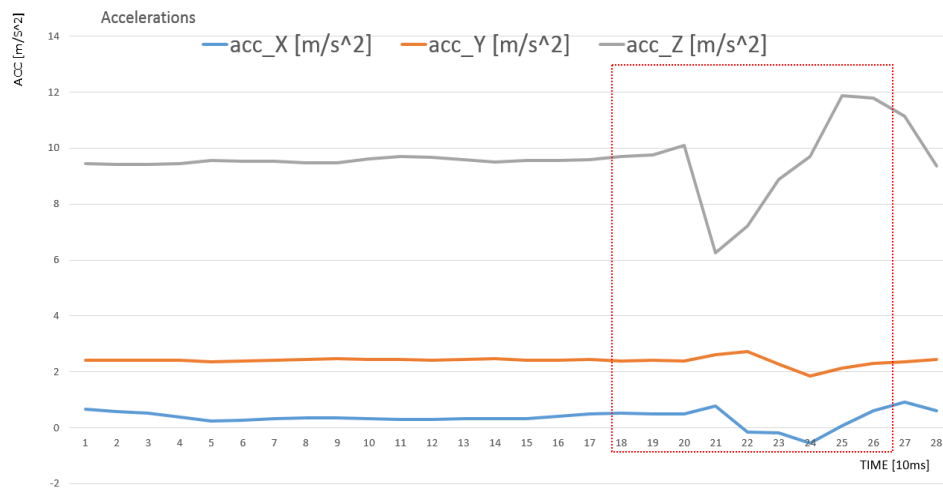
Figure 5. Zoomed-in section of acceleration characteristics. Source: authors' own materials.

Figure 5 shows only a section of the graph illustrating the shunting activity parameters measured, selected from within the entire period of the measurement in question. It demonstrates temporary changes to linear accelerations in individual axes of the freedom of movement. 28 intervals have been provided for the duration time of 10 ms, which corresponds to the observation time of 0.3 of a second. In Figure 4, marked with a red frame, one can notice abrupt changes to the vertical (ACC_Z), longitudinal (ACC_Y) and transverse (ACC_X) acceleration. Such changes are correlated with the physical location of the locomotive in the physical space of a shunting station (Figure 1). Each of the characteristics (ACC_X, ACC_Y and ACC_Z) stems directly from the type and parameters of the actions undertaken by the driver, which may prove variable within a certain range, as well as from the physical position of the locomotive over specific elements of the track infrastructure. To a considerable degree, it also results from the condition of the rolling stock performing the shunting operations and technical characteristics of the locomotive itself. What also affects these characteristics, yet to a lesser extent, is the weather conditions and other random factors, such as e.g. physical condition of the driver performing shunting operations.
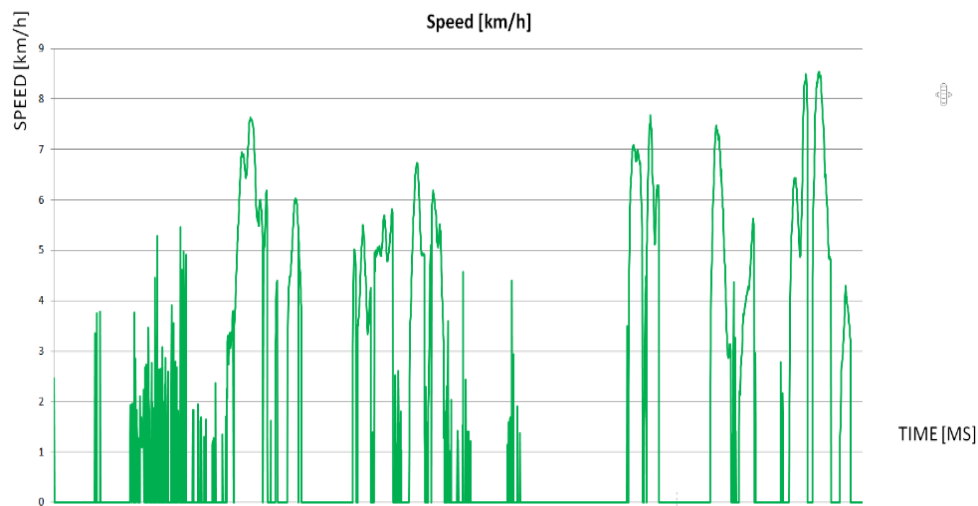

Figure 6. Shunting locomotive speed profile. Source: authors' own materials.

Figure 6 illustrates the shunting locomotive speed during the test. Apart of standard assessment of the speed adjustment to the shunting operations performed (in correlation with the locomotive location on the station plan), such a graph also makes it possible to assess the efficiency of utilising the shunting locomotive working time. Furthermore, the graph provided in Figure 6 enables estimation of fuel consumption in the course of the shunting activity being conducted. Since changes to the running speed illustrated in the graph in Figure 6 are considerably dynamic, it may also be

considered as a premise for optimisation of a schedule of shunting operations for the sake of fuel saving etc.
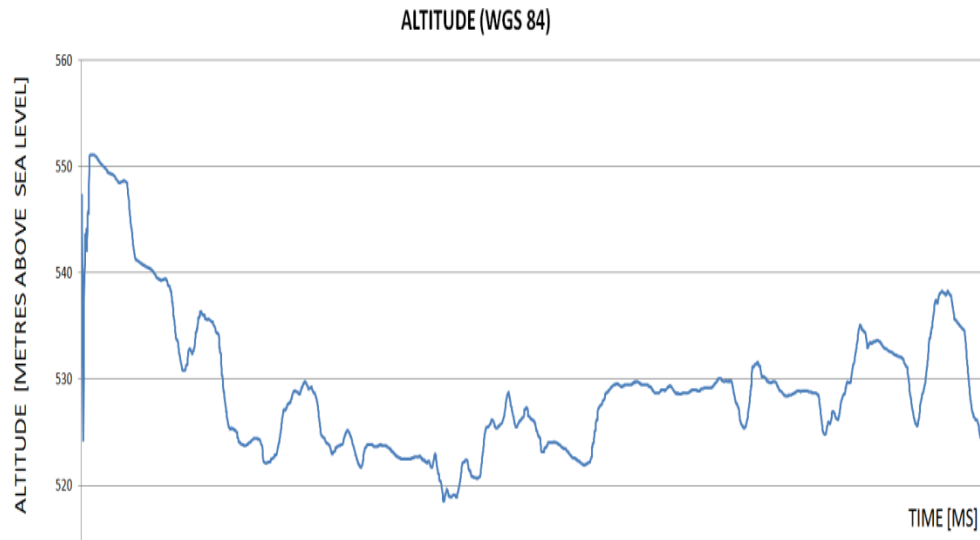

ALTITUDE (WGS 84)

Figure 7. Profile of the locomotive altitude above sea level. Source: authors' own materials.

The shunting locomotive altitude profile provided in Figure 7 with reference to the sea level proves particularly helpful for purposes of the running speed control. The track slope exerts a major impact on the locomotive running speeds (particularly at mountain stations, ramp-type shunting stations and those featuring a gravity yard hump). In correlation with the locomotive's traction characteristics as well as its position on the station plan, it enables calibration of the shunting locomotive speed (this subject will not be discussed in detail in this article).

According to the method proposed, the remote monitoring of shunting activity is ensured by using the SMS and GPR transmission channels. There are numerous restrictions to the first option, namely those of technical and economic nature. The maximum SMS length is 140 8-bit characters (900 characters owing to the CSMS technology) [9]. The foregoing means that a single SMS may only be used to send information about ca. 3 data sets (each in the minimum composition: three values of linear acceleration, value of longitude and latitude) at three pre-defined locations of the shunting station. Therefore, this technology only enables data to be sent in an aggregated form, and only for certain sections of long tracks. In practice, it virtually precludes ongoing supervision of a shunting rail vehicle. What seems prospective for the method proposed is the use of communication channels based on the WiFi and BT technologies [10,11]. Nevertheless, when considering the latter

case, one should bear in mind the technical (length related) constraints of this method, since not all track systems will allow for this technology to be deployed.

5. Conclusions

The research method, the mobile application and the procedures for analysing the locomotive's shunting activity at a marshalling yard, all discussed in this article, enable assessment whether the locomotive driver's duties are pursued in a correct manner. Within the given shunting area, one can monitor the shunting activity by application of the method in question. Prospectively, such an information channel combined with a reverse channel (radio communications) enables the driver's operations to be corrected. As regards further prospects of application, it may also enable completely automated shunting activity (once the relevant legal regulations are amended in this respect).

The method proposed offers interesting new opportunities for performance of shunting activity at large marshalling yards, especially in cases when the given shunting run extends on neighbouring switching circuits. Knowing the shunting locomotive position enables the personnel to efficiently set the travelling route between individual circuits.

The method proposed also proves useful while switching passenger cars with people inside, when specific instructions must be followed and special precautions maintained. One should bear in mind that, in cases of railway accidents with casualties, investigation procedures are particularly lengthy and liquidation of damages – costly. The same applies to hazardous and valuable goods. The method presented provides analytical tools supporting investigation procedures as well as acquisition of non-personal evidence material for purposes of investigations conducted by law enforcement bodies and of potential lawsuits. In this respect, it should be noted that, unlike with dedicated on-board recording devices of rail vehicles, owing to simplicity and practically non-existent investment expenditures related to the method implementation, not only all vehicles participating in shunting operations may be furnished with the devices in question, but also all members of shunting brigades. In extreme cases (hazardous substances, cargo of very high market value), also the rolling stock being switched may be equipped with recording devices of this type.

With regard to providing members of shunting brigades with mobile phones with the application installed, there is a problem of how to appropriately mount the phone. It is meant to potentially allow for establishing the manner in which the given worker moves (linear accelerations made) and the GPS-based positioning method does not change.

A separate issue is the identification of technical condition of the track and its substructure at shunting stations. Elements of railway infrastructure at shunting stations are usually more complex in terms of structure than other technical operating facilities for railway. Firstly, there are far more

turnouts at these stations. Additionally, these elements are more exploited in operation (multiple changes of travelling routes, several times more frequent than in other sections of railway infrastructure). In light of the foregoing, one should keep in mind that not only does the method proposed enable control over characteristics of the shunting locomotive operating condition, but also rough assessment of technical condition of the shunting station infrastructure. For these purposes, one must record and archive parameters of linear accelerations of shunting locomotives. A single shunting area is typically handled by one locomotive. Therefore, by comparing its linear accelerations in the course of operation in a long-term horizon, this is how one may indirectly examine the service wear of track infrastructure elements. This type of wear may be statistically observable through comparisons of linear acceleration characteristics of the same shunting locomotive, assuming that no significant changes of traction parameters have been introduced within the period analysed.

By reversing the foregoing assumptions, i.e. assuming invariability of track substructure characteristics in a certain time horizon, one may attempt to apply the methodology discussed for rail vehicle diagnostics. Any anomalies detected in linear accelerations, after collating them with databases used to record typical ranges of rail vehicle responses at individual infrastructure elements, should provide grounds for undertaking specific repair or maintenance actions towards the given vehicle. It is a complex problem which requires further detailed research.

This article has provided several illustrations to solutions enabling the data in question to be analysed. The authors have also proposed other options for monitoring parameters of shunting activity as well as technical condition of both facilities and means of transport taking part in shunting. This subject is very multi-faceted and requires considerable technical and financial resources to be involved.

References

[1] Web-based data filtering tool for Open Street :Map (OSM): http://overpass-turbo.eu/ (10-08-2015)

[2] OpenStreetMap: http://www.openstreetmap.org/#map=17/50.16707/18.91026 (10-08-2015)

[3] JOSM Extensible editor for OpenStreetMap: https://josm.openstreetmap.de/ (10-08-2015)

[4] Parkinson, B.W. *Global Positioning Systems*. American Institute of Aeronautics and Astronautics. 1996

[5] Mendizabal, R. and Berenguer, R. and Melendez, J. *GPS and Galileo, GPS & Galileo: Dual RF Front-end Receiver and Design, Fabrication, and Test*. McGraw Hill 2009.

[6] Ir-9 (R-34), *Instruction on manoeuvres technique*. PKP Polskie Linie Kolejowe S.A., Warszawa 2012.

[7] Ir-1 (R-1), *Instruction about the conduct of train traffic*. PKP Polskie Linie Kolejowe S.A, Warszawa 2008.

[8] Ir-9, *Instruction on manoeuvres technique execution*, PKP Polskie Linie Kolejowe S.A, Warszawa 2012.

[9] http://www.clockworksms.com/blog/concatenated-sms/ (10-08-2015)

[10] Ross, J. *The book of wirelees..*, No starch press, CA, 2008.

[11] http://people.csail.mit.edu/rudolph/Teaching/Articles/BTBook.pdf (10-08-2015)

[12] Burdzik, R. *Identification of sources, propagation and structure of vibrations affecting men in means of transport based on the example of automotive vehicles*. JVE International Ltd., Kaunas, 2014.

[13] Burdzik, R. Identification of structure and directional distribution of vibration transferred to car-body from road roughness. *Journal of Vibroengineering,* 16(1) (2014) 324-333.

[14] Dabrowski, Z. and Zawisza, M. Investigations of the Vibroacoustic Signals Sensitivity to Mechanical Defects not Recognised by the OBD System in Diesel Engines. *Solid State Phenomena,* 180 (2012) 194-199.

1) Jakub Młyńczak, Ph.D. assistant Professor: Silesian University of Technology, Faculty of Transport, Department of Transport Systems and Traffic Engineering, Krasinskiego 8, 40-019 Katowice, Poland (*jakub.mlynczak@polsl.pl*).

2) Rafał Burdzik, Ph.D. D.Sc. Assistant Professor: Silesian University of Technology, Faculty of Transport, Krasińskiego 8, 40-019 Katowice, Poland (rafal.burdzik@polsl.pl), the author presented this work at the conference.

3) Ireneusz Celiński, M. Sc.: Silesian University of Technology, Faculty of Transport, Department of Transport Systems and Traffic Engineering, Krasinskiego 8, 40-019 Katowice, Poland (*ireneusz.celiński@polsl.pl).*

Advanced control structures for galvanometer scanners for improved parameters in biomedical imaging
(CON166-15)

Corina Mnerie, Stefan Preitl, Virgil-Florin Duma

Abstract: Galvanometer-based scanners (GSs) are optomechatronic systems utilized in a wide range of applications, from commercial and industrial to high-end, the latter for example in biomedical imaging. A GS consists of an oscillatory element (shaft, magnet, and galvomirror) in a motor structure equipped with a positioning servo-system built usually in a closed-loop structure and controlled by different algorithms. The development of a high-performance control solution for such a device is based in this study on a closed-loop GS which consists of a proportional-derivative (PD-L1) controller and a servomotor. The mathematical model (MM) and the parameters of the basic construction are identified using a theoretical approach followed by an experimental identification. With the indentified model, an extended control solution is proposed, with an additional controller of proportional-integrator-derivative (PID-L1) type, which will ensure a better speed response and a good immunity to constant disturbances which can affect the servo system. A good match was found between the theory, the simulations, and the testing for different types of input signals, such as triangular, sinusoidal, and sawtooth – the latter with different duty cycles. The paper finally presents a Model based Predictive Control (MPC) solution for the mobile element of a GS. The control solutions proposed are supported by simulations carried out in Matlab/Simulink.

1.   Introduction

From the numerous types of laser scanning systems that exist [1], the galvanometer-based scanners are the most utilized nowadays [2], in a range of applications that range from commercial and industrial to high-end, the latter mostly in biomedical imaging, for example for Optical Coherence Tomography [3, 4], Confocal Microscopy, or combinations of different techniques [5]. Although the main use is to produce the lateral scan of the samples in such applications, there are also other objectives, such as: generating the sampling function simultaneous to the probe scan in Time Domain OCT [6] or scanning delay line Fourier Domain OCT [7].

GSs are advantageous because of their mature technology [8], their good positioning capabilities, and the satisfactory scan frequencies for the above applications. However, they do have issues, especially regarding their scanning functions and control structures. We have approached these two aspects in several works, and demonstrated the best type of custom scanning function to obtain the

highest possible duty cycle [9], and rules of-thumb to obtain the most distortion-free images with different OCT techniques [10, 11].

The aim of this paper is to carry on the researches on the optimization control structures and algorithms for which we have completed a series of studies in [12-16], in order to obtain a trade-off between speed and precision for this type of scanning devices.

1.1. A mathematical model of a uni-dimensional (1D) GS.

GSs are optomechatronic oscillatory devices utilized as scanning systems for laser spot positioning or for raster scanning. The performances achieved by a GS depend upon the choice of the main constructive elements: DC motor, detector, mirror, and servo amplifier [1]. The most utilized GSs have a moving magnet motor, usually build in the Brushless DC motor (BLDC) technology, with a high performance optic or capacitive detector embedded on the motor shaft; this design is in a closed-loop configuration with an appropriate control algorithm. The galvomirror is rigid mounted, coaxial with the motor shaft. The speed and accuracy of the entire scanning system depend upon the positioning control algorithms required by the application.

The GS utilized in this study consists of a moving magnet servomotor and a Proportional-Derivative with first order Lag controller (PD-L1). The mathematical model (MM) and the parameters of the basic construction were identified in [12] using a theoretical approach followed by an experimental identification. The angular position of the mirror is considered equal to the angular position of the rotor due to the high torsion rigidity of the scanner [1].

The equivalent MM in transfer function form is [12]:

$$H_{GS}(s) = \frac{k_{GS}}{1 + 2s\varsigma T + s^2 T^2} ,$$

(1)

where k_{GS} is the global gain (it includes the gain of the servomotor and the gain of the PD-L1 controller), ξ is the damping factor, and T is the time constant of the GS.

1.2. Control structures

The basic control solution of the GS has a classic closed-loop structure [17-18]. The new and improved solutions are designed considering a cascade control structure with a second controller in the extended loop. In such structures the performances achieved in the first loop are improved by the controller placed in the extended loop [17-18]. Figure 1 presents the block diagram of a cascade control structure applied for the GS. Based on the number of the available detectors the extended loop is closed through the same detector or through the second one.

Another control structure used in this paper for the implementation of the new solutions is the Two Degree of Freedom control structure (2-DOF) [19]. The advantage consists in the separation of the two major problems of the control, i.e. the reference tracking and disturbances rejection, with two independent controllers [19]. This structure is used for implementing the predictive control algorithm [20]. Figure 2 presents the general block diagram of a 2-DOF control structure in the RST polynomial form (R, S, T are polynomials in the backward shift operator z^{-1} and Δ is the differencing operator $1-z^{-1}$).
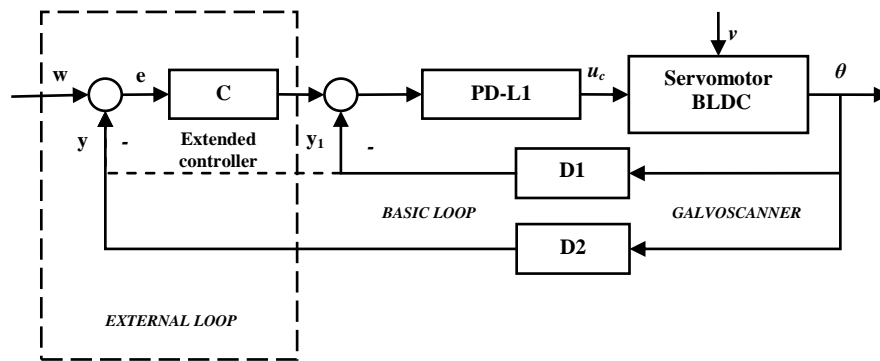

Figure 1. The block diagram of the cascade control structure. Components: C - Extended Controller, PD-L1 – Internal Controller of the GS, D1 – first detector, D2 – second detector.
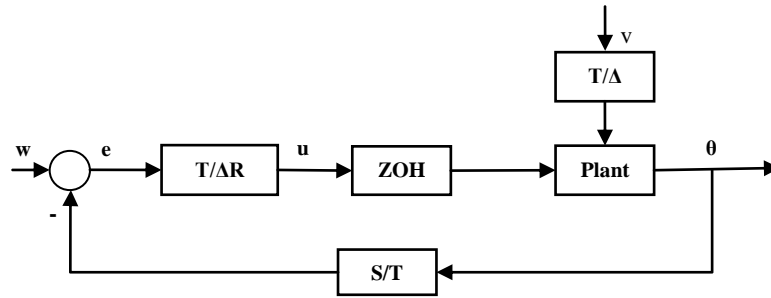

Figure 2. The block diagram of the 2-DOF control structure.

2. Control solutions for improved performance parameters

The main objectives of the control algorithm are the positioning tracking and the good rejection of disturbances. In order to achieve a performance enhancement of the system, different type of control design methods were used; they include classical and advanced methods.

2.1. Classical control solutions

Although the basic control solution has good positioning tracking results, the PD controller does not ensure a proper accuracy in the presence of disturbances. Two classic control solutions proposed in our former work were tested by simulations [16]. First a PI controller was introduced in series with the existing PD-L1 controller, in the angular position feedback loop. The controller was designed using an Extended Symmetrical Optimum method (ESO-m) [21] for different values of the β parameter. The transfer function of the PI controller is:

$$H_{C\text{-}PI}(s) = \frac{k_c}{sT_C}(1+sT_C) .$$ (2)

The controller parameters of the design performed using the ESO-m are:

$$k_c = \frac{1}{k_0\beta^{3/2}T_\Sigma^2}$$ (3)

$$T_c = \beta T_\Sigma ,$$ (4)

where T_Σ is the small time constants sum of the open system, k_0 is the gain of the open system, k_c is the controller gain and T_C is the integrative time of the PI controller.

The second control solution is based on a cascade control structure with the PID-L1 controller in the external loop. The controller is designed based on the Modulus Optimum method given by Kessler [22]. The transfer function of the real PID controller is:

$$H_{C\text{-}PID}(s) = \frac{k_{C1}}{s} \frac{1+2s\xi T+s^2T^2}{1+sT_{f1}} ,$$ (5)

where k_{c1} is the gain of the PID-L1 controller, T is the time constant, ς is the damping factor, and T_{f1} is the filtering time constant.

The new control solutions were tested through simulations on unit step input signal and on standard and specific periodic signals. The simulation results are presented in the next section. Table 1 shows a synthesis of the performances achieved, expressed by the overshoot σ_1, the first settling time t_{r1} and by the settling time of the system t_r.

Table 1. Synthesis of the performances achieved using classical control solutions.

Indicator	Basic solution	Solutions with PI controller			Solution with PID-L1 controller
		$\beta=4$	$\beta=9$	$\beta=16$	
σ_1 [%]	9	50	27	17	7
t_{r1} [ms]	0.33	0.19	0.30	0.46	0.10
t_r [ms]	0.64	1.50	2.00	3.00	0.5

2.2. The Predictive control solutions

For the basic GS a Model based Predictive Control (MPC) solution is presented in the following. The predictive control solutions ensure robustness and good disturbances rejection for the system. The model of the plant (GS) is used to predict the future behavior [20, 23-24]; an objective function is minimized and based on it and the control law is obtained.

The model of the plant can be identified in a CARIMA form:

$$A(z^{-1})y(t) = B(z^{-1})z^{-d}u(t-1) + C(z^{-1})\frac{e(t)}{1-z^{-1}}, \tag{6}$$

where *A, B, C* are polynomials of degree *na, nb nc, d* is the discrete dead time of the system, *e(t)* is the zero mean white noise, *u(t)* is the control signal generated by the predictive controller, and *y(t)* is the output sequence.

The optimization of the objective function ensures good tracking performances by minimizing the error between the future output on the considered horizon and the determined reference signal; it also penalizes the necessary control effort. The general form of the objective function is:

$$J = \sum_{j=N_1}^{N_2} \delta(j) [\hat{y}(t+j|t)\text{-}w(t+j)]^2 + \sum_{j=1}^{N_u} \lambda(j) [\Delta u(t+j\text{-}1)]^2 , \tag{7}$$

where $\hat{y}((t+j|t))$ is the expected value of the output at time *(t+j)* with the available information about the output *y* at time *t*, *w(t+j)* is the future reference signal, N_1 and N_2 are the limits of the predictive horizon, and N_u is the control horizon. The common values for the control weighting sequences are *δ(j)* equal to 1 and *λ(j)* equal to a constant [20].

To obtain the predictive control algorithm the Diophantine equations for the prediction output have to be solved [23]. The entire algorithm is detailed in [20, 23].

$$E_j(z^{-1})A(z^{-1})\Delta + z^{-1}F_j(z^{-1}) = 1 . \tag{8}$$

The value of the optimal prediction output at time *(t+j)* with the information available at the moment *t* is given by:

$$\hat{y}(t+j|t)=G_j\left(z^{-1}\right)\Delta u\left(t+j\text{-}d\text{-}1\right)+F_j\left(z^{-1}\right)y(t) , \tag{9}$$

where the polynomial $G(z^{-1})$ has the expression:

$$E_j(z^{-1})B(z^{-1}) = G_j(z^{-1}). \tag{10}$$

The polynomials E_j, F_j and G_j, have been calculated in a recursive algorithm, starting from the initial values, from the GS mathematical model, with *j* from N_1 to N_2 in the prediction horizon.

Replacing Eq. (10) in (9) the predicted output of the system consists in two components: one related with the future reference trajectory and the other one related with the free response of the plant

($f(t)$). The latter one is computed from the present and from the past values of the output and of the control signals:

$$f(t) = F(z^{-1})y(t) + G'(z^{-1})\Delta u(t-1) \tag{11}$$

$$\Delta u(t) = K(w(t) - f(t)), \tag{12}$$

where G is square matrix, G' is column vector, both computed from the coefficients of the polynomials G_i, F is the column vector of the polynomials $F'(z^{-1})$, and K is the resulting vector from the first line of matrix $(G^T G + \lambda I)^{-1} G^T$ [20].

Based on the incremental form of the control equation (12), the predictive control algorithm was implemented in the 2 DOF structure [19-20, 25], with the incremental control law:

$$\Delta u(t) = \frac{T(z^{-1})}{R(z^{-1})}w(t) - \frac{S(z^{-1})}{R(z^{-1})}y(t) . \tag{13}$$

$R(z^{-1})$, $S(z^{-1})$ and $T(z^{-1})$ are polynomials and their coefficients were obtained from direct identification with Eq. (12).

The predictive control algorithm is based on a discrete form of the GS transfer function from Eq. (1), considering the sample time of 0.03 ms. The numerical form is [13]:

$$H_{GS}(z^{-1}) = z^{-1}\frac{0.0272 + 0.02436z^{-1}}{1 - 1.6670z^{-1} + 0.7185z^{-2}} = \frac{y(t)}{u(t)} . \tag{14}$$

The study covers different values of the control horizon N_u and of the control weighting λ [15]. The best control solution was selected considering simulation results. The performances achieved are presented in Table 2. Based on these performances the selected predictive control solution is for $\lambda=0.8$ and $N_u=10$.

Table 2. Synthesis of the performances achieved using predictive control solutions.

Indicator	Basic solution	Predictive Control solutions					
		$N_u=3$		$N_u=5$		$N_u=10$	
	-	$\lambda=0.1$	$\lambda=0.8$	$\lambda=0.1$	$\lambda=0.8$	$\lambda=0.1$	$\lambda=0.8$
σ_1 [%]	9	50	39	20	21	18	**9**
t_{r1} [ms]	0.33	0.11	0.25	0.12	0.2	0.12	**0.23**
t_r [ms]	0.64	> 2	2	0.8	0.9	0.8	**0.4**

3. Simulation results

The simulations are carried out in Matlab/Simulink. The results of the simulation using the control solutions are presented with respect to the basic structure (i.e., servomotor and PD controller). All proposed solutions were tested on a unit step reference signal in order to evaluate the performances

achieved and on general or specific periodical signals (i.e., sine wave, triangular, and sawtooth) or specific periodic signals [9-10] used in practical applications.

In Figure 3 the response of the basic GS structure is presented for different reference signals. In order to validate the GS model the experimental results were compared with the simulation results obtained in [14].
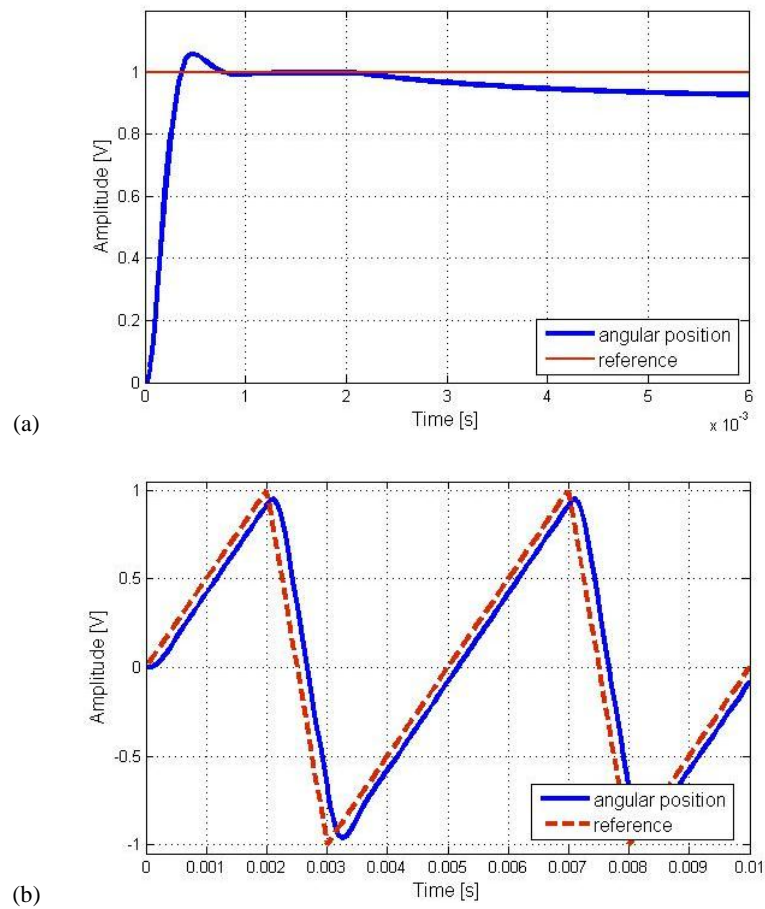

(a)

(b)

Figure 3. The basic GS structure: (a) step response when considering a disturbance; (b) response on a periodic reference sawtooth signal.

The responses of the classic control solution proposed (i.e., the solution with PI controller in the main loop and the solution with the PID-L1 controller in the extended loop) are presented in Fig. 4. To highlight the efficient rejection of the disturbances, a step/limited ramp disturbance was applied in the torque of the servomotor. The solution with PID-L1 controller showed better dynamic performances (see Table 1 and Fig. 4 (c) and (d)).
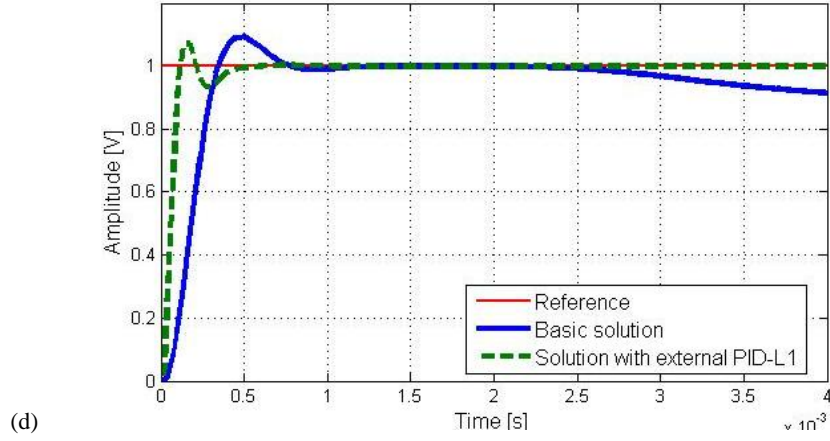
(a)

(b)

(c)

(d)
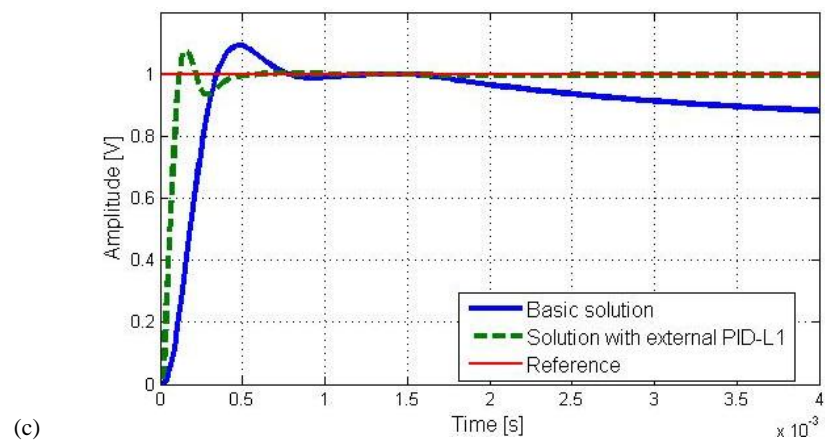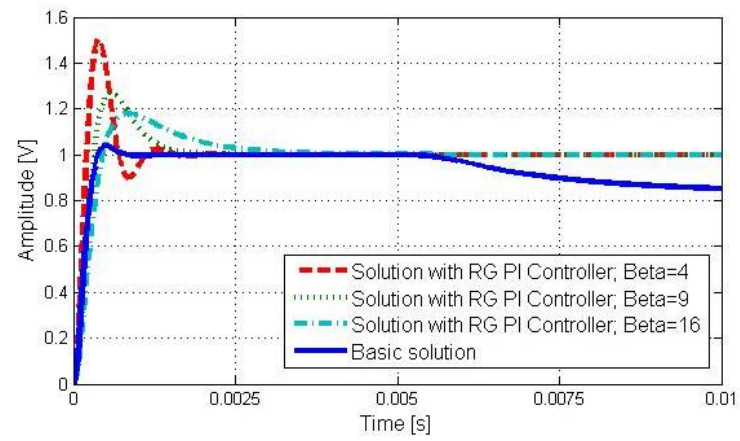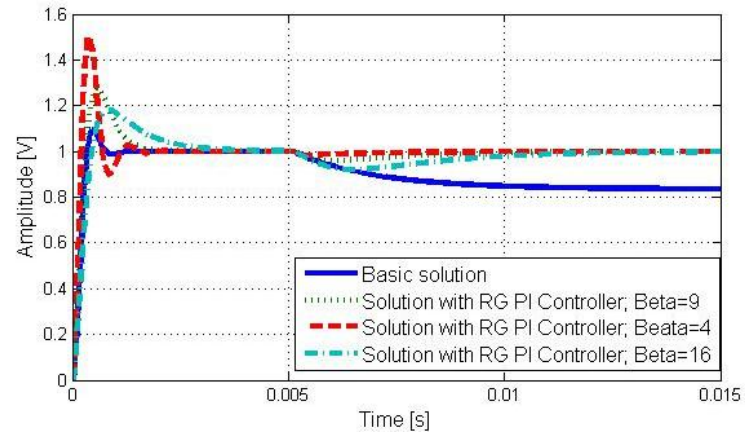
Figure 4. The classical control solutions - system response based on a unit step reference signal: (a) solution with the PI controller, step type disturbance; (b) limited ramp type disturbance; (c) solution with a cascade extended PID-L1 controller, step type disturbance, (d) limited ramp type disturbance.

Selected simulation results for the predictive control solution proposed are presented in Fig. 5. Different cases, for different parameters values, were studied in order to find "the best solution". Based on the analysis of the simulation results, the most attractive predictive control solution can be considered for the control horizon of 10 sampling time and the weighting factor of 0.8. In Fig. 6 a comparison is presented between the basic structure of the GS, the best classical solution (i.e., the one with extended PID-L1 controller), and the selected predictive solution.
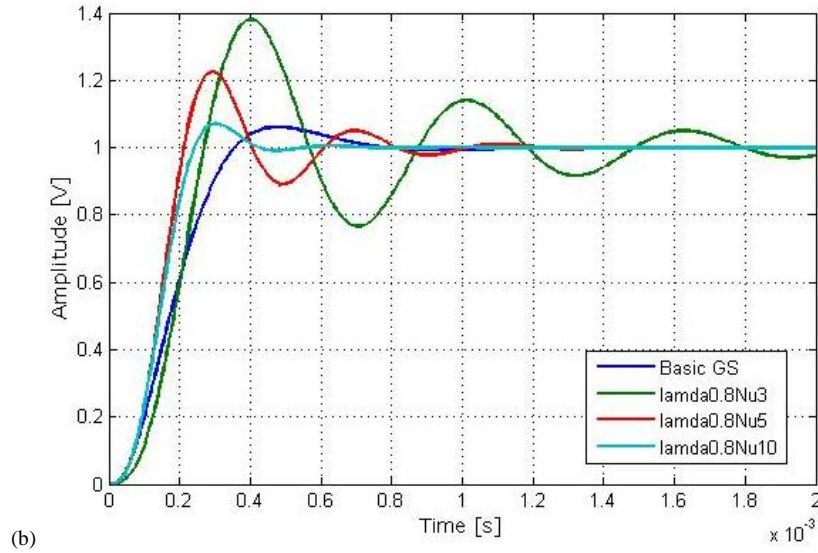

(a)

431

(b)
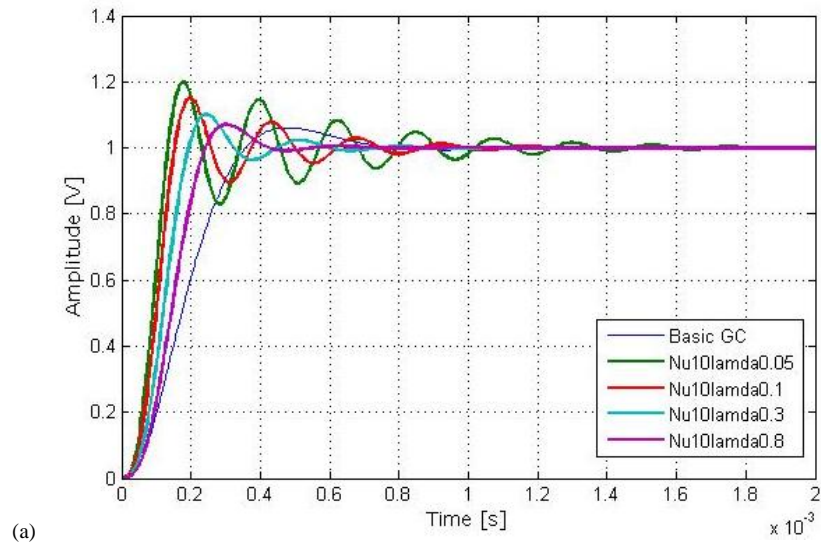
Figure 5. Solution with extended Predictive Controller - system response cases: (a) N_u=10, λ=0.8, 0.3, 0.1, 0.05; (b) λ=0.8, N_u=3, 5, 10.
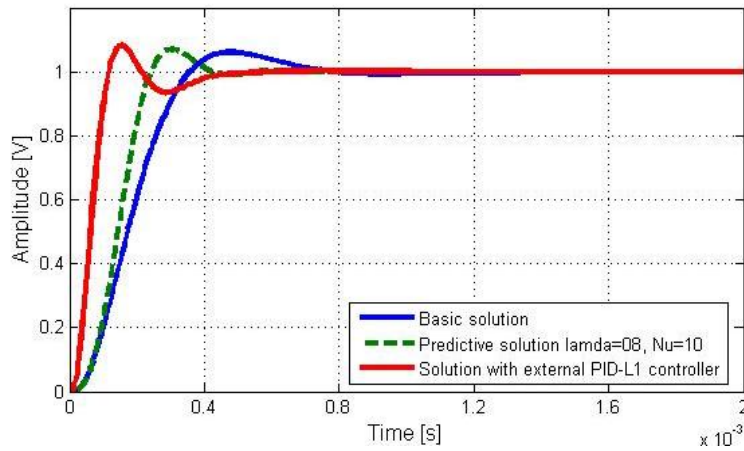

Figure 6. Classic PID-L1control solution versus Predictive control solution for λ=0.8 and N_u=10.

4. Conclusions

In this paper some classic and advance control solutions for 1D GSs were developed and presented. Although the design methods are quite different, the solutions can be compared considering the performances achieved by the scanning system – for which the output signal represents the angular position of the mobile element.

Based on the analysis of the simulation results, both the proposed predictive solution and extended PID-L1 solution provide better dynamical performances then the basic structure of the GS. The global settling times are comparable, while the first settling time is shorter for the PID-L1 structure, and the disturbances rejection is more efficient in the selected predictive case. From the scanning point of view these performances consists in speed and accuracy. The proposed predictive solution was selected based on an extensive study regarding the design parameters of the Model Predictive Control method. All solutions have been validated through numeric simulations.

Current and future work includes the integration of the GSs in complex scanning systems intended for biomedical applications, especially for handheld scanning probes for OCT [26].

Acknowledgments

References

[1] Marshall, G. F. *Handbook of Optical and Laser Scanning.* CRC Press – Taylor & Francis, New York, 2011.

[2] Bass, M. *Handbook of optics.* 3rd Edition, Mc. Graw-Hill Inc., New York, 30.1-30.68, 2009.

[3] Huang, D., Swanson, E. A., Lin, C. P., Schuman, J. S., Stinson, W. G., Chang, W., Hee, M. R., Flotte, T., Gregory, K., Puliafito, C. A., and Fujimoto, J. G. Optical coherence tomography. *Science* 254, 5035 (1991), 1178-1181.

[4] Drexler, W., Liu, M., Kumar, A., Kamali, T., Unterhuber, A., et al. Optical coherence tomography today: speed, contrast, and multimodality. *J. Biomed. Opt.* 19, 7 (2014), 071412.

[5] Podoleanu, A. Gh. and Rosen, R. B. Combinations of techniques in imaging the retina with high resolution. *Progress in Retinal and Eye Research* 27 (2008), 464– 499.

[6] Podoleanu, A. Gh., Dobre, G. M., and Jackson, D. A. *En-face* coherence imaging using galvanometer scanner modulation. *Opt. Letters* 23 (1998), 147-149.

[7] Rosa, C. C., Rogers, J., and Podoleanu, A. Gh. Fast scanning transmissive delay line for optical coherence tomography. *Opt. Letters* 30, (2005), 3263-3265.

[8] Montagu, J. Scanners - galvanometric and resonant, in *Encyclopedia of Optical Engineering*, Driggers, R. G., Hoffman, C., Driggers, R., Eds., 2465-2487, Taylor & Francis, N.Y., 2003.

[9] Duma, V.-F. Optimal scanning function of a galvanometer scanner for an increased duty cycle. *Opt. Eng.* 49, 10 (2010), 103001.

[10] Duma, V.-F., Lee, K.-S., Meemon, P., and Rolland, J. P. Experimental investigations of the scanning functions of galvanometer-based scanners with applications in OCT. *Appl. Opt.* 50, 29 (2011), 5735-5749.

[11] Duma, V.-F., Tankam, P., Huang, J., Won, J. J., and Rolland, J. P. Optimization of galvanometer scanning for Optical Coherence Tomography. *Appl. Opt.* 54, 17 (2015), 5495-5507.

[12] Mnerie, C. A., Preitl, S. and Duma, V.-F., Mathematical model of a galvanometer-based scanner: simulations and experiments, *Proc. SPIE* 8789, (2013) 8789-43.

[13] Mnerie, C. A., Preitl, S. and Duma, V.-F., Classical PID versus predictive control solutions for a galvanometer based scanner, *SACI: 10th IEEE International Symposium on Applied Computational Intelligence and Informatics*, (2015) 349-353.

[14] Mnerie, C. A., Preitl, S. and Duma, V.-F., Mathematical model of a galvanometer-based scanner: simulations and experiments, *Proc. SPIE* 8789, (2013), 8789-43.

[15] Mnerie, C. A. *Control solution for optomechatronic devices used in biomedical aplications.* Ph.D. thesis, Politehnica University of Timisoara (Supervisor Prof. Stefan Preitl), 2015.

[16] Mnerie, C. A., Preitl, S. and Duma, V.-F., Performance enhancement of galvanometer scanners using extended control structures, *SACI: 8th IEEE International Symposium on Applied Computational Intelligence and Informatics*, (2013), 127-130.

[17] Astrom, K. J. and Wittenmark, B. *Computer controlled systems: theory and design*, Prentice-Hall International Inc., 1984.

[18] Kuo, B. C. and Golnaraghi, F. *Automatic Control Systems*, 8th ed. John Wiley, New York, 2003.

[19] Tang, K. K., Wang, Q.-G., Hang, C. C. and Hägglund, T. J. *Advances in PID Control*, Springer Verlag, Berlin, 1999.

[20] Camacho, E. F. and Bordons, C. *Model Predictive Control*, Springer-Verlag, 1998.

[21] Preitl, S. and Precup, R.-E. An extension of tuning relations after symmetrical optimum method for PI and PID controllers, *Automatica* 35, (1999), 1731–1736.

[22] Kessler, Uber die Vorausberechnung Optimal abgestimter Regelkreise, Regelungstechnik, vol. 2 (1954), H12, 274-281.

[23] Clarke, D. W., Mohtadi, C. and Tuffs, P. S. Generalized Predictive Control. Part 1: The Basic Algorithms, *Automatica* 23, 2 (1987), 137-148.

[24] Maciejowski, J.M. *Predictive Control with Constrains*, Prentice Hall, 2002.

[25] Preitl, Zs., Bars, R. and Haber, R. Internal Model Representation for Generalized Predictive Control with Constraint handling, *IEEE 4th International Conference on Intelligent Systems Design and Application*, (2004).

[26] Demian, D., Duma, V.-F., Sinescu, C., Negrutiu, M. L., Cernat, R., Topala, F. I., Hutiu, Gh., Bradu, A., and Podoleanu, A. Gh. Design and testing of prototype handheld scanning probes for optical coherence tomography. *J. of Engineering in Medicine* 228, (2014), 743-753.

Corina Anca Mnerie, Ph.D: 3OM Optomechatronics Group, "Aurel Vlaicu" University of Arad, 77 Revolutiei Ave., Arad 310130, Romania (*corina.mnerie@gmail.com*).

Stefan Preitl, Professor: Polytechnics University of Timisoara, 1 Vasile Parvan Ave., Timisoara 300222, Romania (*stefan.preitl@aut.upt.ro*).

Virgil-Florin Duma, Professor and Head: 3OM Optomechatronics Group, "Aurel Vlaicu" University of Arad, 77 Revolutiei Ave., Arad 310130, Romania; Doctoral School, Polytechnics University of Timisoara, 1 Mihai Viteazu Ave., Timisoara 300222, Romania; Faculty of Physics, West University of Timisoara, 4 Vasile Parvan Ave., Timisoara 300223, Romania (*duma.virgil@osamember.org*).
The author gave a presentation of this paper during one of the conference sessions.

The application of physical models in scale to test of vehicle lateral stability
(STA182-15)

Krzysztof Parczewski, Henryk Wnęk

Abstract: The issue of the article has been dedicated the possibility of using physical models of vehicles in the scale in the research of motion dynamics. In paper discussed the problems of lateral stability of vehicle motion. Particular attention was paid to the danger of rollover, which occurs especially in commercial vehicles of high center of gravity position. Problem concerning the construction of the model, control and selection of research equipment was discussed. During the construction of vehicle model in scale, the research and analysis of the results, was used the theory of similarity of π-Buckingham. Comparative tests were carried for full-size vehicle, having a high center of gravity, and model of the vehicle made in the scale of 1: 5. Described the tests used in the research of vehicle dynamics and especially in terms of roll stability. In the end of the paper was made comparison of the research results of stability motion of full-size firefighting car with vehicle model in scale.

1. Introduction

During constructing means of transport studies are being conducted physical models. In aviation, aircraft scale models are tested in wind tunnels, maritime transport ship models are tested in pools.

The article presents an attempt to use physical models of vehicles made on a smaller scale to test vehicles on the tracks research in the implementation of new vehicles or upgrade existing ones, especially in the case of vehicles manufactured single units, for which testing is impossible or unprofitable. The use of dimensional analysis, theory of similarity and π-Buckingham theorem, allows you to transfer the results of tested vehicles in scale to the full-size vehicles. This results in an increase in road safety and reduce the time and cost of testing.

The study was addressed the lateral stability of vehicles and in particular their resistance to rollover.

2. The definition of stability

The vehicle motion parameters will be result from the driver's actions, and external forces, when the vehicle is moving along a specified track. For this reason, the actual vehicle motion parameters may be different than assumed by the driver. The steerability are called all the properties of system vehicle-driver-environment, which was determining the degree of opportunities to approach the desired and actual motion parameters [12].

In the literature on the concept of vehicle stability and the stability of motion is used interchangeably [1,9,12,22]. The motion stability of vehicles concerns characteristics that describe the traffic conditions of the vehicle and the vehicle itself. The directional stability of the vehicle is understood as the ability for self-maintenance of the trajectory defined by the position of the steerable wheels and the ability to self-return to the previous state of motion after precipitation it from this state, by the outer short-term disturbance [1,2,19,21]. In tests on vehicles using the concept of technical stability relating to phenomena whose duration is limited, called [1] stability in the sense of Bogusz. Definitions of vehicles stability was described by Wicher J. [22], and they are also included in the standard for terminology that is used to assess the movement of vehicles [24,25].

Matters of vehicles motion stability address different aspects of vehicle motion. Andrzejewski R. has identified the following issues related to the stability of the vehicle motion [1]:

- driving or braking of the vehicle during linear motion,

- motion on the road with inclination: longitudinal and / or lateral,

- driving in a curve of the road: with a uniform motion, during acceleration or braking,

- phenomenon of understeer and oversteer,

- the wheel rotation and its impact on the vehicle motion,

- disturbances affecting on the motion of the vehicle, for example: side wind, uneven road surface, weather conditions, etc.

The driver performing certain maneuvers also influences on the vehicle motion. Keeping of a car desired path of movement, despite the presence of interfering forces, it is possible by the features of the vehicle known as directional stability [12,21]. Directional stability of the vehicle depends on many factors relating to the vehicle, such as: location of the vehicles center of gravity, vehicles dimensions, the load size and its distribution, condition and type of the tires, the condition and the type of suspension and also factors relating to vehicles motion parameters such as: steering wheel angle, acceleration, and speed. Litwinow defines the concept of directional stability, in addition to distinguish the concept of overturn stability in lateral and longitudinal direction and slip stability [12].

Dajniak H. and Prochowski L. gave the definition of stability, dividing it into the stability of the longitudinal and lateral [8.19]. A loss of the lateral stability can cause that the vehicle will rollover around a line connecting the outer points of contact between the wheels with the road (one side of the vehicle). This definition refers to issues related to rollover the car. In the literature often can be found, used interchangeably, the terms on transverse stability: rollover propensity (tendency to rollover at the side) and roll stability (stability due to the vehicle to tip over sideways) [10,11,17]. The second of the terms was introduced in 1983 in a report on parametric analysis of the dynamic stability of heavy vehicles (C. Winkler, P. Fancher and C. MacAdam) made for the NHTSA (National Highway Traffic

Safety Administration) [23]. This term had been accepted and is quite widely used, particularly for heavy vehicles and combinations of vehicles as well as for vans and sport utility vehicles.

The loss of longitudinal stability is revealed to deviation from the assumed trajectory of the vehicle, this deviation rapidly growing, and isn't possible to correct by the driver. The loss of lateral stability is revealed to exceeding the permissible roll angle of the vehicle [13].

During testing of vehicles in order to evaluate the stability of the movement, are measured such variables as: the speed of motion of the center of gravity and its deviation from the longitudinal axis (usually measured are the various components of vehicle speed), acceleration acting on the center of gravity, the roll angle and angular velocity of the body roll (measured the center of gravity of the vehicle relative to the longitudinal axis of the vehicle), the pitch angle and pitch angular velocity of longitudinal inclination (as measured relative to the transverse axis of the vehicle, parallel to the plane of the ground) and the yaw angle and yaw rate (measured relative to an axis perpendicular to the road surface passing through the center of gravity of the vehicle).

Loss of motion stability can be caused by exceeding the maximum permissible speed limit on the road curve, an external impulse like: side wind, uneven roads, etc.

The directional stability are particularly important issues, in the case of trucks because the its associated with sudden and uncontrolled change in the motion direction. The loss of transverse stability can lead to vehicle rollover.

3. Use the theory of similarity in the construction of the model, research and analysis of results

The theory of similarity and dimensional analysis is used particularly widely in cases where it is difficult to describe the desired parameters in equations, and variables are known to affect the desired parameter. Applying this theory to the evaluate vehicle roll stability using vehicle made at a scale requires the designation of comparable parameters and variables describing the vehicle motion and define the criteria of similarity.

3.1. Conditions to provide similarity vehicle and a physical model

Some of the basic assumptions of similarity theory and dimensional analysis already appeared in the works of Fourier in the early nineteenth century. Greater its development dates from the end of this century, this applies to works of Rayleigh, Reynolds, Maxwell, Froude, Carvallo, Pascha and others [20]. Similarity theory can be used wherever its use gives reasonable results, decrease costs of studies or in cases where other methods of analysis are difficult to apply [3].

The Buckingham π-theorem is based on dimensional analysis, and the basic idea is to replace the physical quantities on dimensionless quantities [7]. Dimensionless quantities are obtained by referring them to the selected of basic quantities (e.g. weight, length, and time).

Dimensional analysis reduces the number of variables that must be specified to describe an event. If it is assumed that the system can be described by k number of variables, the mathematical description of this system is as follows:

$$u = f(u_1, u_2, u_3, ..., u_k) . \tag{1}$$

The same system can be described using dimensionless quantities, the write will take the form:

$$\pi = f(\pi_1, \pi_2, \pi_3, ..., \pi_{k-r}) . \tag{2}$$

where r - number of selected basic quantities.

From the Backingham's π-theorem we assumed that the description of the system need less variables than in a dimensional analysis. Typically, the basic quantities are: mass, length and time.

From the condition of similarity follows that: two systems are similar if they can be described by the same variables and working under the same conditions.

To be able to compare the dynamics of vehicles, they must be met according to criteria known as the similarities. This dependencies related to both: the vehicle structure, the conditions of its motion and external forces. There are three general similarities criteria:

- geometrical - length scale,
- kinematic - scale speed or acceleration,
- dynamic - the scale of strength.

The fulfillment of these criteria allows the interpretation of the model results studies and relating them to the dynamics of full dimensional vehicle's motion.

3.2. Dimensionless parameters of compared vehicles

The compared dimensionless parameters for vehicles full-dimensional and scaled, have been defined using the Buckingham π-theorem. Characteristic parameters of the test vehicle have been converted into dimensionless system. On their basis were determined required parameters of the scaled vehicle like: the linear dimensions, mass and moments of inertia, stiffness and damping of the suspension and tires stiffness. Below are the parameters π (for a simplified two wheel model supplemented by vehicle rollover model). These are (normalized by weight, length and time): distances to center of gravity from the front and rear axle π_1, π_2, tires cornering stiffness for front and rear axle π_3, π_4, the moment of inertia about the axis Z π_5, center of gravity height π_6, wheelbase π_7, moments of inertia about the axis X and Y π_8, π_9, mass suspended π_{10}, distance from roll centre to the center of gravity π_{11}, angular

stiffness of suspension π_{12}, damping of the inclining by the suspension π_{13}, stiffness of the tires and suspension in the longitudinal and vertical direction (X and Z) $\pi_{14} \div \pi_{19}$. Achieving full compliance of each dimensionless parameter is difficult to realize, hence generally are dealt with partial similarity.

3.3. Errors caused by the use of partial similarity

During the analysis of vehicle motion and its rollover conditions, were compared selected parameters of motion: lateral acceleration, velocity, roll and pitch rate of vehicle body, inclination angles, slip angle, yaw rate and yaw angle wheels slip angles and the vehicles track.

The tests were conducted under real conditions while maintaining the similarity scale factors for the individual parameters. While the analysis is not determined and not taken into consideration the aerodynamics forces and rolling resistance, because their impact on comparable motion parameters was small enough that it could be omitted. Due to the different technology of producing tires the problem of their selection was dealt with in [15]. In our analysis we could not get the full compliance of the dimensionless parameters of tires and suspensions. For this reason, the results were analyzed in terms of their confusion caused by these factors, knowing that the partial similarity may lead to differences in results to describe the behavior of the compared vehicle [3].

4. The scaled vehicle, construction, control system, measuring instrumentation

To verify the methodology of research using physical models, it was built vehicle on a smaller scale, taking into account the requirements arising from the similarity theory. The values of parameters characteristic of the vehicle in scale were determined on the basis of dimensionless parameters of full-size vehicle. Attempts were made to get maximum compliance with dimensionless parameters.

During construction vehicle model were used parts from the radio-controlled vehicle model, equipped with an internal combustion engine with a cylinder capacity 26 cm^3, centrifugal clutch, and gearbox, central and final transmissions, driving the rear axle of the vehicle. The behaviour of similarity in relation to the vehicle real (truck special with a high centre of gravity) resulted in the necessity to take a number of actions which resulted in, the selection and change of appropriate dimensions: track wheels and wheelbase, position of the centre of gravity, changes suspension front and rear axles, selection of tires with appropriate parameters and changes distribution of masses enabling to obtain the required mass moments of inertia. These works have been described in previous publications [14,15,16].

To control the movement of the vehicle was made system consisting of: steering system, the microprocessor controller and control program. This system allows the driver to program the operating settings of servomotors in time: the steering angle and acceleration - braking. The trajectory of the vehicle depends on the saved parameters of vehicle motion in the controller. The disadvantage

of this control system is the inability to respond to the disturbances associated with an increased wheel rolling resistance or a local change in the coefficient of adhesion of the scaled vehicle. Typically, the effect of such disturbances, will change the direction of the vehicle relative to the path assumed (programmed). To avoid this, the test must be carried out on a flat, clean and relatively smooth road surface.

The scaled vehicle control system allows for two modes of operation: steering vehicle using a conventional radio control apparatus and steering with the controller mounted on the vehicle.

The controller has been made based on a microprocessor from ST Microelectronics STM32F103VCT6. It allows you to define and save the settings servo for phases: acceleration, braking, performs specific maneuvers and stops the vehicle, and also to remember the initial settings.
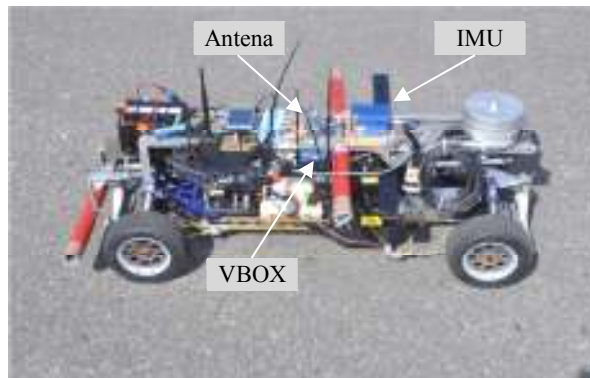

Figure 1. The vehicle in scale ~ 1: 5 with installed measurement equipment

The scaled vehicle is equipped with measuring devices enabling recording of the important parameters of its motion. Was used apparatus Racelogic VBOX with module IMU, using GPS technology, due to its small size and small weight. Recording test results were on a Compact Flash card with a frequency of 100 Hz. Figure 1 shows a scaled vehicle with the mounted measuring devices.

5. Research tests used for the testing of vehicles in scale

For comparisons chosen two tests: driving on a circular path in the steady-state conditions and the maneuver of step input with the linear escalation of rotation angle of the steering wheel [24,25]. The first of the proposed tests is to determine the characteristics of the vehicle during the steady-state vehicle motion and the other in the dynamically changing conditions. The selected attempts not require correction of the steering wheel angle by the driver.

Figure 2 shows the adopted movement path in the test of driving in a circular path with a constant speed and method of a test implementation of the step input with the linear escalation of the steering wheel angle.
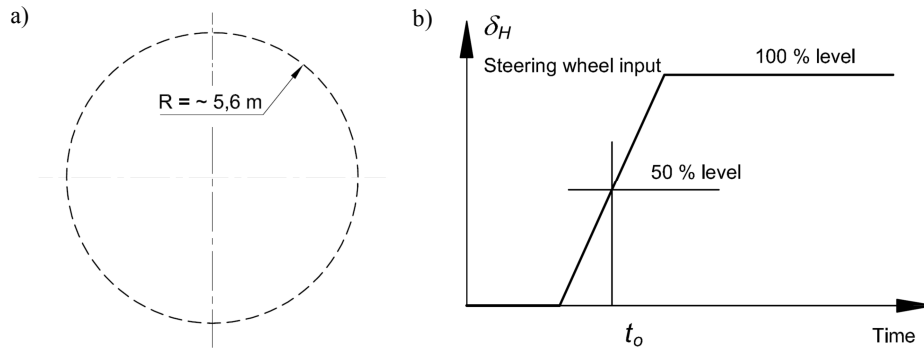

Figure 2. Carried out tests: driving in a circular path at a steady-state condition (a) and step steering input (b).

The test was carried out with the vehicle speed of ~17 km/h, the lateral acceleration of -4,5 m/s2 (equivalent to the actual vehicle speed of ~ 40 km/h moving on a track with a radius of ~ 21,5 m).

During the tests the vehicle was moving at a predetermined speed straight ahead and then at a designated place performed a turn of established angle value. The test was carried out with the vehicle speed of ~17 km/h, initially on straight track and then the vehicle performed a steer maneuver to moving on a circle with a radius of ~5.6 m (which corresponds to the actual vehicle speed of ~40 km/h moving on circle with a radius of ~21,5 m).

6.   Comparison of measurements results of the vehicle motion stability

Full-size vehicle testing were performed on a test track TATRA in Koprivnice (Czech Republic) [4,5,6,18]. Tests of physical model of the vehicle were carried out on the airport board in Kaniow near Czechowice-Dziedzice.

Comparison of the results of measurements of model and actual vehicle required the use of scale factors and conversion of vehicles motion parameters on a dimensionless scale. Due to the fact that the results presented in a dimensionless system are difficult to assess, they was converted to a dimension scale for a full-size vehicle.

6.1. Steady-state circular test

During the test vehicles were moving at a predetermined speed on a circular path. Below were presented the time courses of selected vehicles motion parameters in full-size and scale (figures 3÷6). Actual vehicle was moving at a speed of ~40 km/h and vehicle in a scale of ~20 km/h.

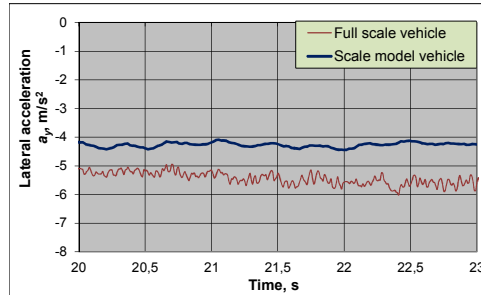**Figure 3.** Comparison of the lateral acceleration achieved by the full-scale vehicle and the scale model vehicle in the steady-state circular test.
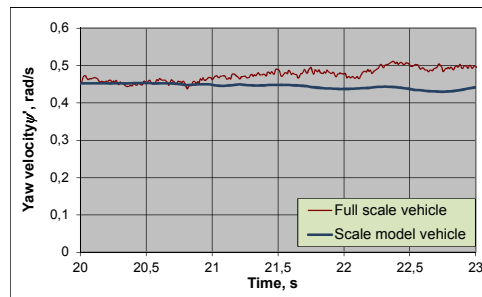

Figure 4. Comparison of the yaw rate achieved by the full-scale vehicle and the scale model vehicle in the steady-state circular test.

During the motion on a circular path there was a certain difference in speed, hence differences of lateral acceleration obtained during tests.
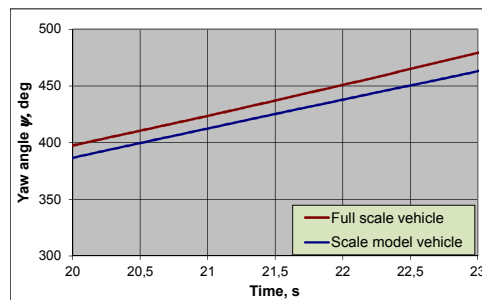

Figure 5. Comparison of the yaw angle achieved by the full-scale vehicle and the scale model vehicle in the steady-state circular test.
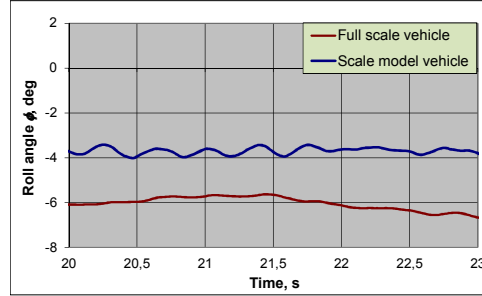
Figure 6. Comparison of the roll angle achieved by the full-scale vehicle and the scale model vehicle in the steady-state circular test.

The differences of yaw rate of vehicles, as well as acceleration, result from differences in speed of the individual vehicles. Increments of yaw angles of vehicles are very similar, indicating similar conditions of performance the tests (after translation into motion of a full-size car).

The physical model of the vehicle shows less heeling angle. Appearing differences are due to differences of the suspension stiffness and may be taken into account while analyzing the results.

6.2. Step steering input test

During the step steering input test the full-size vehicle was moving at a constant velocity of ~40 km/h and the vehicle in scale ~21 km/h, which after conversion corresponds to a similar velocity. The driver performed a turn maneuver by turning the steering wheel by a fixed angle, where the lateral acceleration has reached of ~ 4 m/s^2. In the case of the model the turn wheels angles were setting by adjusting the position of the actuator. Selection the wheels turn angles in the physical model results from the setting of the steering servomotor by a specified number of units.
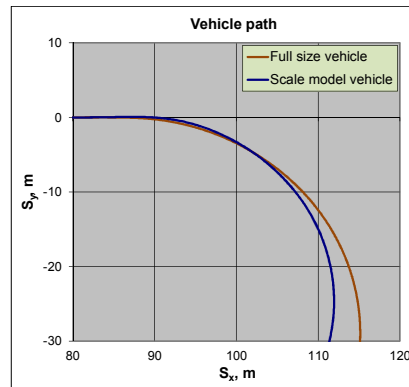

Figure 7. Comparison of the motion trajectory of the full-scale vehicle and the scale model vehicle in step steering input test.

Differences occur in increase speed of the turn. On actual value steer angle influences a variety of factors among others clearances in the steering system or steer resistance. For this reason, there were differences of each waveform of the variables. Figure 7 shows the trajectory of motion of both tested vehicles. During the tests failed to get similar tracks vehicles due to the fact of necessity to convert the track for the model. This resulted in the existence certain differences of the other parameters. The drawings 8÷11 present the waveforms of selected motion parameters of tested vehicles.
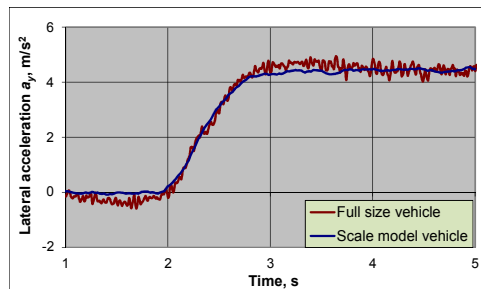

Figure 8. Comparison of the lateral acceleration achieved by the full-scale vehicle and the scale model vehicle in step steering input test.
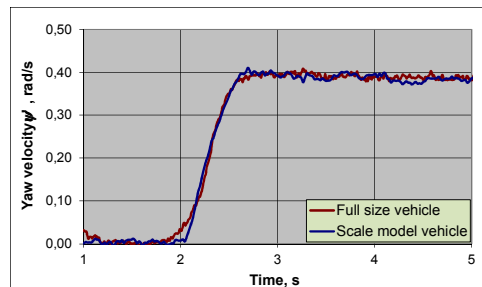

Figure 9. Comparison of yaw rate achieved by the full-scale vehicle and the scale model vehicle in step steering input test.

During the step steering input test the full-size vehicle was moving at a speed of 38 km/h and physical model 39 km/h, after the conversion resulting from the scale of similarity. The differences of the acceleration are from speed of the turning manoeuvres. Vehicle yaw rates in the initial phase were a little different. After achieving the maximum velocity differences are bigger and result from differences of the circle radius and velocity. Due to the angle of the steer extortion are slightly higher the values of yaw rate.

During the step steering input test the yaw angle was greater for the full size vehicle than in the case of the model, what results from driving on circular path of lesser radius. Generated side slip angle of

the gravity centre for the full size vehicle is greater than for mobile model, due mainly to the other characteristics of the tires.

On the basis of the indicators shown in Table 1 it can be concluded that there is a large coincidence of parameters such as: the time to reach 90% of the yaw rate, yaw rate, side slip angle and the dynamic overshoot value of yaw rate. Greater differences are observed for parameters such as lateral acceleration or dynamic overshoot for lateral acceleration of the vehicle.

Table 1. Summary of parameters that define the behavior of the vehicle: the full scale vehicle and scale model vehicle in step steering input test.

Parameter	Symbol	Value		Unit
		Full scale vehicle	**Scale model vehicle°**	
Steady-state yaw rate response gain	$\left(\dfrac{\dot\psi}{\delta}\right)_{ss}$	2.439	2.310	1/s
Steady-state lateral acceleration response gain	$\left(\dfrac{a_y}{\delta}\right)_{ss}$	29.85	31.50	m/s²/rad
Time to 90% of the yaw rate in steady-state motion	$T_{R\dot\psi}$	0.42	0.43	s
Yaw rate peak response time	$T_{\dot\psi max}$	0.63	0.69	s
Yaw rate peak	$\dot\psi_{max}$	0.399	0.405	rad/s
Yaw rate in steady-state condition	$\dot\psi_{ss}$	0.387	0.387	rad/s
Steering wheel angle in steady-state condition	δ_{ss}	9.23	8.75	°
Side slip angle in steady-state condition	β_{ss}	-6.78	-4.00	°
Lateral acceleration peak	a_{ymax}	4.60	4.60	m/s²
Lateral acceleration in steady-state condition	a_{yss}	4.21	4.20	m/s²
Overshoot value of yaw rate	$U_{\dot\psi}$	0.031	0.046	-
Overshoot value of lateral acceleration	U_{a_y}	0.092	0.095	-
Indicator $T_\beta = T_{\dot\psi max} \cdot \beta_{ss}$	T_β	4.27	2.76	°

Reference to parameters related in rotation of the steering wheel was replaced into parameters relative to the average angle of turn the wheels.
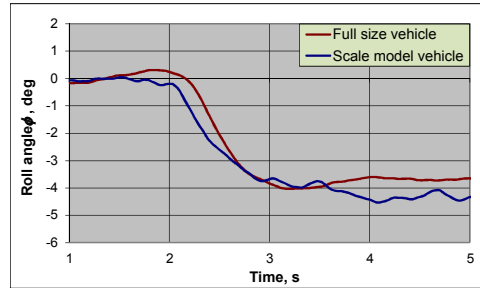
Figure 10. Comparison of roll angle achieved by the full-scale vehicle and the scale model vehicle in step steering input test.
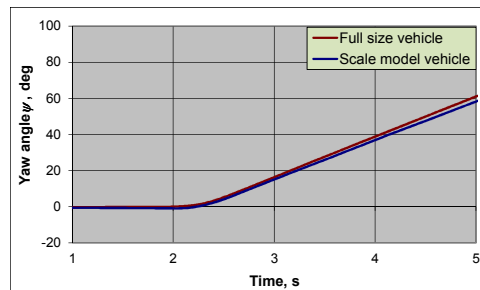

Figure 11. Comparison of the yaw angle achieved by the full-scale vehicle and the scale model vehicle in step steering input test.

7.   Summary and conclusion

The use of physical scale models for vehicles testing is attracting attention of researchers. Conducted research on vehicles models can partly replace and partly to limit the tests of full size vehicles. The study of physical models of vehicles made in scale, are carried out by a number of centers, among others in the US, France, Germany, India and South Korea. Vehicle models are used for motion analysis, both whole vehicles and the operation of selected assemblies (eg. the suspension, steering or brakes). The scope of research focuses on issues of dynamics, aerodynamics, as well as to evaluate the braking maneuver performed on straight and curvilinear section of the track and turning maneuvers. Mobile models are also used for rapid prototyping of the controllers to systems prevent wheel lock during braking, stability control, roll stability, steering or power train systems. The cost of testing the physical vehicle models made in the scale is lower (for a scale of 1:3 by half, for the scale of 1:5 about one-quarter of the cost for one test of the full size vehicle).

Based on the presented comparisons it can be concluded that the physical models in scale may be also used to assess the stability of vehicles manufactured as the low serial production or individually. The proposed research methodology of the vehicles roll stability allows for testing any vehicle using a

physical model made in scale. The research of the model on the test tracks allow for its rapid modifications and determine the rollover risk indicators limits for different possible applications of the vehicle. The carried out tests shows that the vehicle models are particularly useful in the studies, while which can lead to vehicle rollover and also in conditions of simulating abrupt maneuvers in the field of non-linear tire cooperation with the road surface. In such case, even with a possible rollover of the model, there are no health risk drivers and the material losses are relatively small.

It has been found that while maintaining the similarity of the tests:

- The tested traffic parameters of the physical model with a sufficient accuracy correspond to measurement results of the full size vehicle (deviation of the results from 8 to 15% depending on the test).

- The greatest discrepancies exhibit a designated side slip angles of the vehicle centre of gravity (8 to 15%).

- The greatest coincidence of results was reported for the yaw rate (difference of results ~4%).

- The roll angles of the mobile model and the full size vehicle have a good coincidence (the deviation does not exceed 8%).

The carried out comparative studies of the full size vehicle and the physical model, support the conclusion that physical models of vehicles can be used to assess the stability of large-size vehicles at a given confidence level. From analysis of the dimensionless parameters the confidence level for carried out researches was established at 95%. During research on the test tracks, while maintaining the similarity of the performed tests, it was observed discrepancies of compared parameters at ~ 8% to 15%, wherein larger differences were related with those parameters on which were influenced occurring the non-compliances of the dimensionless parameters.

References

[1] Andrzejewski R.: Stabilność ruchu pojazdów kołowych. WNT Warszawa, 1997.

[2] Arczyński St.: Mechanika ruchu samochodu. WNT Warszawa, 1993.

[3] Baker W.E., Eestine P.S., Dodge F.T.: Similarity methods in engineering dynamics Theory and practice of scale modeling. Spartan Books, New Jersey, 1978.

[4] Brennan S., Alleyne A.: The Illinois Roadway Simulator: A Mechatronic Testbed for Vehicle Dynamics and Control. IEEE Transactions on Mechatronics, 5(2000) 4, 349-359.

[5] Brennan S.: Modeling and control issues associated with scaled vehicles. Master's thesis, University of Illinois at Urbana Champaign, 1999.

[6] Brennan S.: On size and control: the use of dimensional analysis in controller design. Doctors's thesis, University of Illinois at Urbana Champaign, 2002.

[7] Buckingham E.: On physically similar systems: Illustration of the use of dimensional equations. Physics Review, 4/1914, 345÷376.

[8] Dajniak H.: Ciągniki. Teoria ruchu i konstruowanie. WKŁ, Warszawa, 1985.

[9]   Gillespie T. D.: Fundamentals of Vehicle Dynamics. SAE, Warrendale, 1992.

[10]   Hac A.: Rollover Stability Index Including Effects of Suspension Design. SAE Technical Paper, 2002-01-0965.

[11]   Lapapong S.: Vehicle rollover prediction for banked surfaces. Pennsylvania State University, 2010.

[12]   Litwinow A.: Kierowalność i stateczność samochodu. WKŁ, Warszawa, 1975.

[13]   Lozia Z.: Ocena odporności pojazdu na przewrócenie na bok – wpływ stopnia skomplikowania modelu na wyniki obliczeń. Zeszyty Naukowe Instytutu Pojazdów, 79 (2010) 3.

[14]   Parczewski K., Wnęk H.: Analiza wpływu parametrów masowych na stateczność ruchu samochodu ciężarowego w oparciu o badania mobilnego modelu pojazdu. Postępy Nauki i Techniki, SIMP; 14 (2012), 208-223.

[15]   Parczewski K., Wnęk H.: The tyre characteristics of physical models used to investigate vehicles lateral stability. Part D: Journal of Automobile Engineering, London, 2015, Vol. 229(10) 1419–1426, DOI: 10.1177/0123456789123456.

[16]   Parczewski K.: Analiza możliwości wykorzystania modelu fizycznego pojazdu do oceny stateczności ruchu pojazdów wielkogabarytowych. Wydawnictwo Akademii Techniczno-Humanistycznej w Bielsku-Białej, Rozprawa naukowa 52/2014.

[17]   Patil C.B.: Antilock Brake System Re-design and Control Prototyping using a One-fifth Scale Vehicle Experimental Test-bed. Master's Thesis, Department of Mechanical Engineering, The University of Texas at Austin, Austin, Texas, 2003.

[18]   Pieniążek W.: Wybrane zagadnienia badania stateczności i kierowalności samochodów. Zeszyty Naukowe Instytutu Pojazdów 79 (2010) 3.

[19]   Prochowski L.: Mechanika ruchu. WKŁ, Warszawa, 2005.

[20]   Schofield B.: Vehicle dynamics control for rollover prevention, Lund University 2006.

[21]   Świder P.: Teoria ruchu samochodów. cz.1, Wydawnictwo Politechniki Krakowskiej, Kraków, 2012.

[22]   Wicher J.: Stabilność układów a stateczność pojazdów drogowych. Zeszyty Naukowe Instytutu Pojazdów 79 (2010) 3.

[23]   Winkler C.: Rollover of Heavy Commercial Vehicles, University of Michigan Transportation Research Institute, Research Review 31 4/2000.

[24]   ISO 4138 (2012): Road Vehicles – Steady State Circular. Test Procedure.

[25]   ISO 7401 (2003): Road Vehicles – Lateral Transient Response. Test Method.

Krzysztof Parczewski, Assistant Professor: University of Bielsko-Biala/Department of Combustion Engines and Vehicles/Division of Vehicles, Willowa 2 street, 43-309 Bielsko-Biala, Poland (kparczewski@ath.bielsko.pl). The author gave a presentation of this paper during one of the conference sessions.

Henryk Wnęk, Ph.D.: University of Bielsko-Biala/Department of Combustion Engines and Vehicles/Division of Vehicles, Willowa 2 street, 43-309 Bielsko-Biala, Poland (hwnek@ath.bielsko.pl).

Comparison of acceleration severity index of vehicle impacting with permanent road equipment support structures (STA193-15)

Mariusz Pawlak

Abstract: The acceleration Severity Index (ASI) is one of three energy absorption types, described in European norm EN12767 (Passive safety of support structures for road equipment, Requirements, classification and test method), and is regarded as the most important rate of impact on occupants. Vehicle models, used in simulation has been developed by the National Crass Analysis Center (NCAC) of The George Washington University. To perform numerical vehicle crash simulation, the finite element models of permanent road equipment support structures, using the available LS Dyna software were developed. Results are presented to study the dynamic response of vehicle after impact with the permanent road equipment support structures. The acceleration severity index curves are calculated and visualized in Matlab.

1. Introduction

Permanent road equipment support structures are columns for traffic signals, information signals, signs and lights used permanently on the streets. During design process of support structures are taken into account conditions described in norm EN-40[4][5]. In 2011 Road and Bridge Research Institute, which has been granted the accreditation of the Polish Centre for Testing and Certification as a certifying unit, decided that from the beginning of 2015 all street light used on roads and located within safety zone should be passively safe, or additional safety barriers should be applied[6][7][8]. More informations are described in literature [28] It means that columns must be also certificated according to norm EN 12767:2007, approved by CEN (Cimité Européen de Normalisation) in 2007. The norm introduce classification of permanent road equipment support structures by velocity, absorption of energy and safety of passenger.

Tab.1. Classification of support structures [3]

Parameters taken into consideration	Alternatives
1. Speed class [km/h]	50, 70 or 100
2. Energy absorption category	HE, LE or NE
3. Occupant safety level	1,2,3 or 4

Information, to which energy absorption category belongs column is received by measuring post-impact speed of a vehicle 12 m after an impact point.

Tab.2. Support structures categories for energy absorption [3]

Impact speed V_i [km/h]	Post-impact speed V_e [km/h] measured 12 m after impact point with support structure		
	HE	LE	NE
50	$V_e = 0$	$0 < V_e \leq 5$	$5 < V_e \leq 50$
70	$0 \leq V_e \leq 5$	$5 < V_e \leq 30$	$30 < V_e \leq 70$
100	$0 \leq V_e \leq 50$	$50 < V_e \leq 70$	$70 < V_e \leq 100$

Finally Occupant safety level is identified by calculation of Acceleration Severity Index (ASI) and Theoretical Head Impact Velocity THIV.

Tab.3. Occupant safety level [3]

Energy absorption category	Occupant safety level	Speed			
		Crash test at a speed of 35 km/h		Crash test at speeds of 50,70 and 100 km/h	
		Maximum values		Maximum values	
		ASI	THIV [km/h]	ASI	THIV [km/h]
HE	3	1.0	27	1.0	27
	2	1.0	27	1.2	33
	1	1.0	27	1.4	44
LE	3	1.0	27	1.0	27
	2	1.0	27	1.2	33
	1	1.0	27	1.4	44
NE	3	0.6	11	0.6	11
	2	1.0	27	1.0	27
	1	1.0	27	1.2	33

One crash test is taken at vehicle speed 35 km/h to check how column works with low velocity, and next one with higher velocity (50, 70 or 100 km/h)

Till now there is still in use many street ligths, which are in "0" class of vehicle passenger safety, what means that risk of injury or death after crash accident is high. Most of them are concrete columns and local authorities are gradually replacing them. Newer columns are aluminum and steel , the newest one are made from composites.

Certification of column is carried out by passive safety tests.. To reduce the number of expensive experiments there are attempts to create numerical simulation of vehicle impact with designed column. However the real tests must be done to make validation of numerical results and must be in accordance with the conditions described in the norm. The numerical model of column and vehicle must be detailed enough to behave in similar way as in reality. Too many simplifications can lead to inadequate conclusion and it can be found when compared with experiments. Software used in

automotive industry for numerical crash tests is LS Dyna, information about explicit methods implemented in this application are described in literature [1][2][11][12].

In numerical simulations three vehicle models were used. Resultant velocities, accelerations and acceleration severity index curves from impact at a speed of 35 km/h will be presented because at low velocity ASI index is more sensitive to vehicle center of mass and column mounting . First model was Toyota Yaris model 2010 sedan, created by The National Crash Analysis Center and The George Washington University. Second was Geo-Metro Finite Element model (GM_R3) developed at Politecnico di Milano and third vehicle model was Geo-Metro Finite Element model developed also by the National Crass Analysis Center (NCAC) of The George Washington University. Detailed geometry of car with suspension, applied initial linear velocity of driving and angular velocities of rotating car wheels has strong advantage, comparing with simple models without suspension, only sliding with assumed velocity.

Acceleration Severity Index is a parameter, sensitive to vehicle model, location of vehicle's mass center and column with fundaments center of mass. Its value depends on material of column, the way of mounting to the ground and soil model. In this article will be presented sample results from numerical crash tests and conclusion.

2. The acceleration Severity Index

Acceleration Severity Index is an indicator of acceleration, it is dimensionless and one of most important parameter calculated for road equipment such as barriers, signal, sign and light columns. According to CEN test procedures ASI is computed by following equation:

$$\boldsymbol{ASI(t)} = \sqrt{\left[\left(\frac{\bar{a}_x}{\hat{a}_x}\right)^2 + \left(\frac{\bar{a}_y}{\hat{a}_y}\right)^2 + \left(\frac{\bar{a}_z}{\hat{a}_z}\right)^2\right]} \tag{1}$$

where:

$\bar{a}_x, \bar{a}_y, \bar{a}_z$ are the 50 ms average component vehicle acceleration along X (longitudinal), Y (transverse) and Z (vertical) axis;

$\hat{a}_x = 12g, \hat{a}_y = 9g, \hat{a}_z = 10g$ are the corresponding limit accelerations of a vehicle along X, Y and Z axis;

This index gives an information how harmful can be motion of a car for passengers sitting close to the reference point during impact. The reference point is constantly in a vehicle, what means that it is assumed, that passengers are keeping contact with the vehicle by seat belts.

The limit accelerations can be interpreted as values, below which risk of passenger injury is very low. As was mentioned before, ASI index is dimensionless scalar function of time and has only positive value. The maximum value of ASI index is assumed as measure of acceleration intensity:

$$ASI = \max[ASI(t)] \tag{2}$$

If i is time in ms, than 50 ms average vehicle acceleration along X, Y and Z axis can be calculated as:

$$\overline{a}(t) = \frac{v_{(t=i+50ms)} - v_{(t=i)}}{50\ ms} \tag{3}$$

Calculation of ASI is based on velocity curves, received for node marked as sensor in vehicle center of gravity.

3. Mathematical model of column, fundament and soil

For numerical crash tests was created sample column 13 m high, assumed to be made from aluminum alloy. The stress-strain curve used in material model was taken from literature about tension of aluminum circular pipes [25] . Model of material used in LS Dyna *MAT_PLASTICITY_WITH_DAMAGE_ORTHO_TITLE, includes erosion criteria, and effective plastic strain is applied as a function of effective plastic stress[24] . Generally aluminum alloy is insensitive to strain rate, but to fully describe dynamic behavior of a column during impact, welds were modeled by elements *CONSTRAINED_GENERALIZED_WELD_FILLET, which have ductile and brittle failure criteria implemented.

After reviewing literature about numerical crash tests of support structures [13] [14][16][17] there is almost no information about influence of fundament and soil on results. Generally ASI index is higher when supporting structure is flange mounted because in ground planted (rooted) center of mass is higher and vehicle during impact decelerate more smoothly. Description of test place with fundament and soil is given in norm [3], and below is presented numerical model of sample column flange mounted.
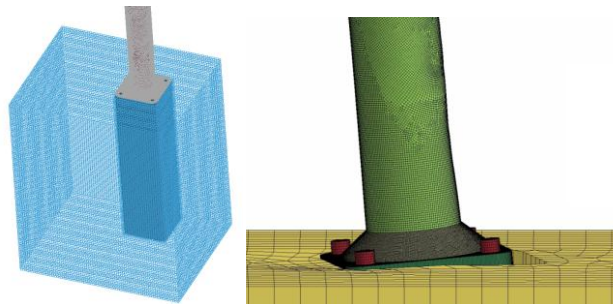

Figure 1.   View of column with fundament and soil numerical model

Fundament is concrete, soil is implemented in LS Dyna as *MAT_SOIL_AND_FOAM [10] , material properties are take as for unwashed Gantry Sand [18][19]. Adding two components to the numerical model increased significantly number of finite elements and time of calculation. But as a result was received visible large displacement of fundament in a soil, appeared gaps and flowing of soil, as it really happens in experimental tests.

4. Results from numerical crash tests at a speed of 35 km/h

As it was mentioned earlier ASI index curve from impact with low velocity is more sensitive to vehicle center of mass and way of column mounting. The most popular vehicle used in crash tests is Suzuki Geo Metro, known in Europe as Swift II, manufactured in 1992-2002. The mass and center of gravity of this car meet the requirements described in norm[3].

But interesting aspect is behave of column during impact with modern car with front crumple zone and higher mass/ kinetic energy. Therefore as a first vehicle was chosen numerical model of Toyota Yaris model 2010 sedan, created and validated by The National Crash Analysis Center and The George Washington University at real crash tests with rigid wall[22].

Time of simulation was assumed 200 ms, finite element method model in LS Dyna consists of 2.6 mln nodes and 2.4 mln of elements.
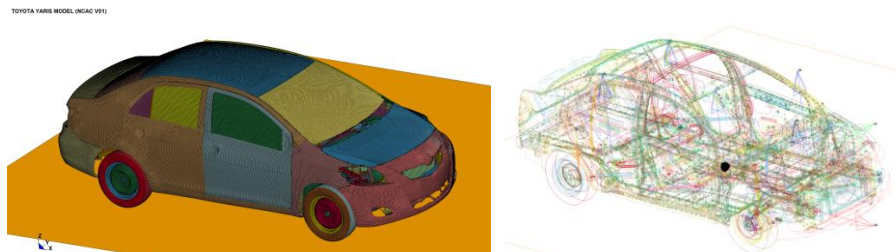

Figure 2.   Model of Toyota Yaris model 2010 sedan with marked sensor at center of gravity[26]

Sensor was located at center of gravity (node 4000406), its position in global coordinate system is 1004 mm in X,
 -4,4 mm in Y and 569 mm in Z axis. The total mass of a vehicle is 1100 kg.

Below are presented results for crash test of model Toyota Yaris sedan 2010 with sample column at a speed of 35 km/s what is ~9.72 m/s
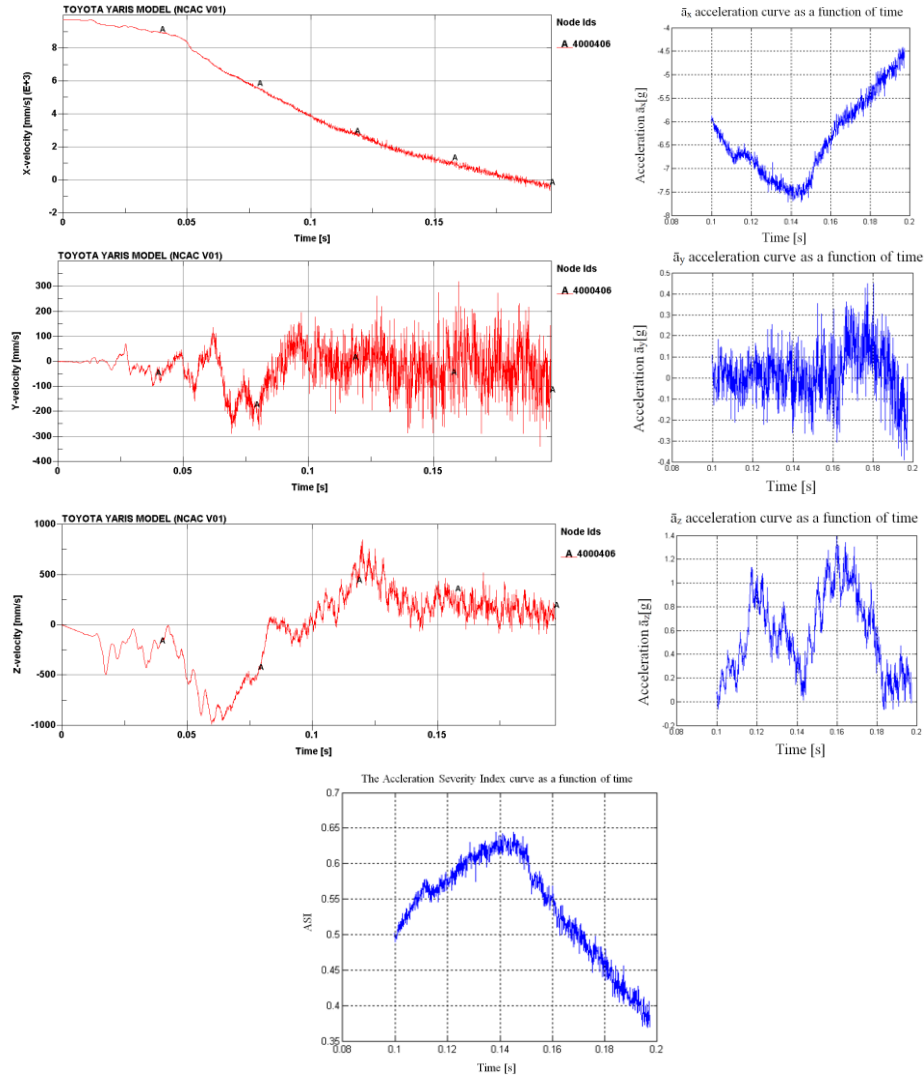
Figure 3.   Toyota Yaris resultant velocities, accelerations and acceleration severity index curves, impact at 35 km/h

The maximum ASI index was 0.63, what is significantly below 1.0. As can be noticed mass of a car is 200 kg more than suggested in norm, what means higher kinetic energy at the first phase of impact (~11 %). During crash can be observed plastic deflection of column and front hood of a car, motion of fundament and a gap in a soil.
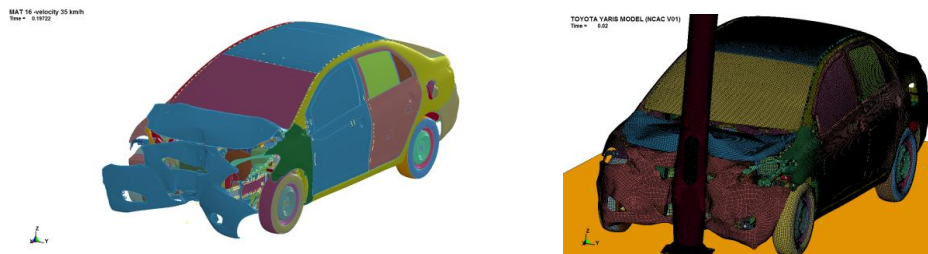
Figure 4. Model of Toyota Yaris model 2010 sedan after crash with sample column

In further numerical crash tests were used models of Suzuki Geo Metro, known in Europe as Swift II, manufactured in 1992-2002. The mass and center of gravity of this car meet the requirements described in norm[3], but during validation of numerical models with results from experiments it turned out that small changing of center of gravity within model has influence on results.

As a second vehicle was used the finite element vehicle model of Geo Metro with full working steering system, front and rear suspensions modified by Department of Aerospace engineering Politecnico di Milano [27]. Was noticed additional mass on wheels comparing with other model [26]

Sensor of acceleration was located at center of gravity (node 700002), center of gravity in global coordinate system is at X -1683mm, Y 30 mm Z 512 mm, mass of vehicle is 880 kg.
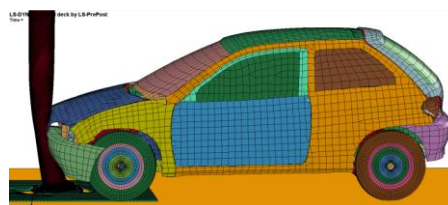

Figure 5. View of sample column impact with Geo-Metro car model (ver. GM_R3)

As a third vehicle was used numerical model of Geo Metro, developed by the National Crass Analysis Center (NCAC) of The George Washington University under a contract with the FHWA and NHTSA of the US DOT, developed and shared for research purposes[26]. The location of center of gravity was modified by additional mass inside cabin of a car in the same manner as is done in experiments, when is no engine in a vehicle.
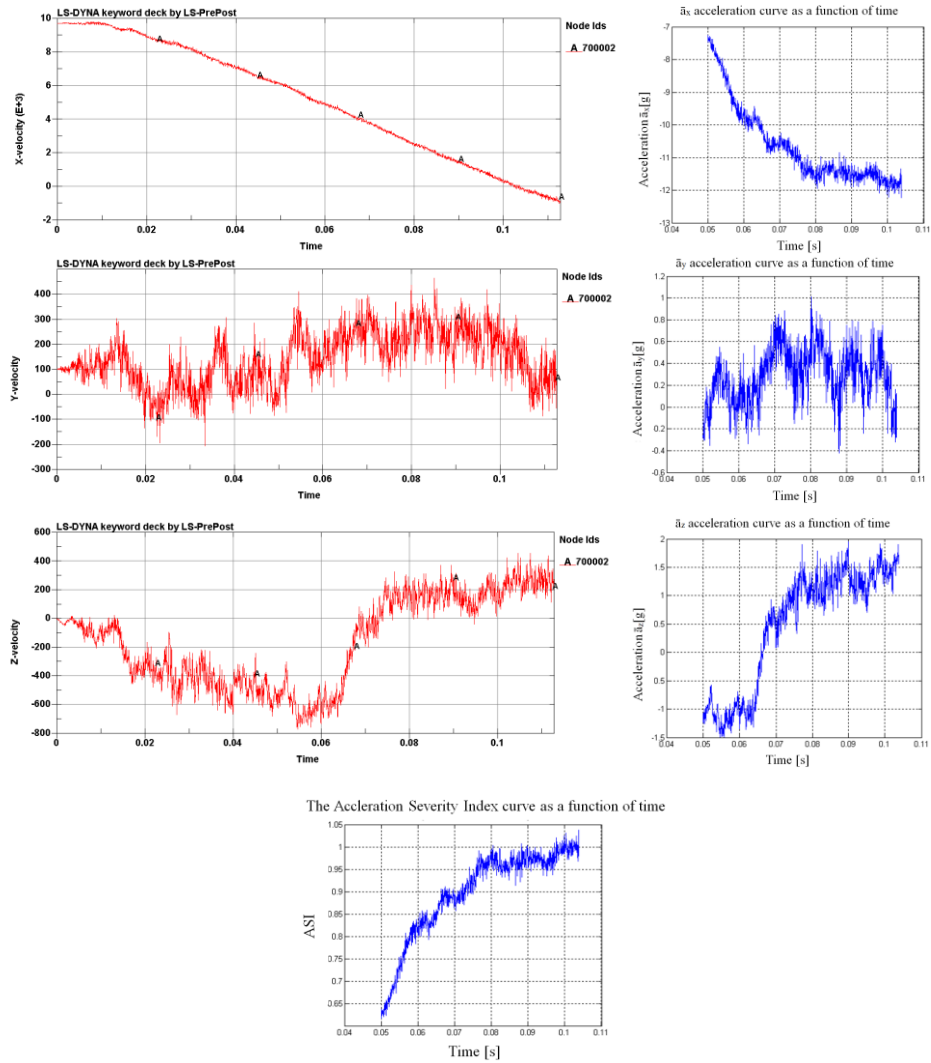
Figure 6.   Geo-Metro car model (Ver. GM_R3) resultant velocities, accelerations and acceleration severity index curves, impact at 35 km/h

Figure 7.   View of Geo-Metro car model (ver. NCAC) with additional mass inside cabin

468

Sensor of acceleration was located at center of gravity (node 700002), center of gravity in global coordinate system is at X -1708 mm, Y -16 mm Z 478 mm, mass of vehicle is 878 kg.

Figure 8. Geo-Metro car model (Ver. NCAC) resultant velocities, accelerations and acceleration severity index curves, impact at 35 km/h

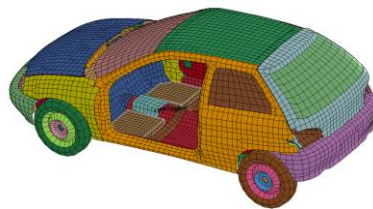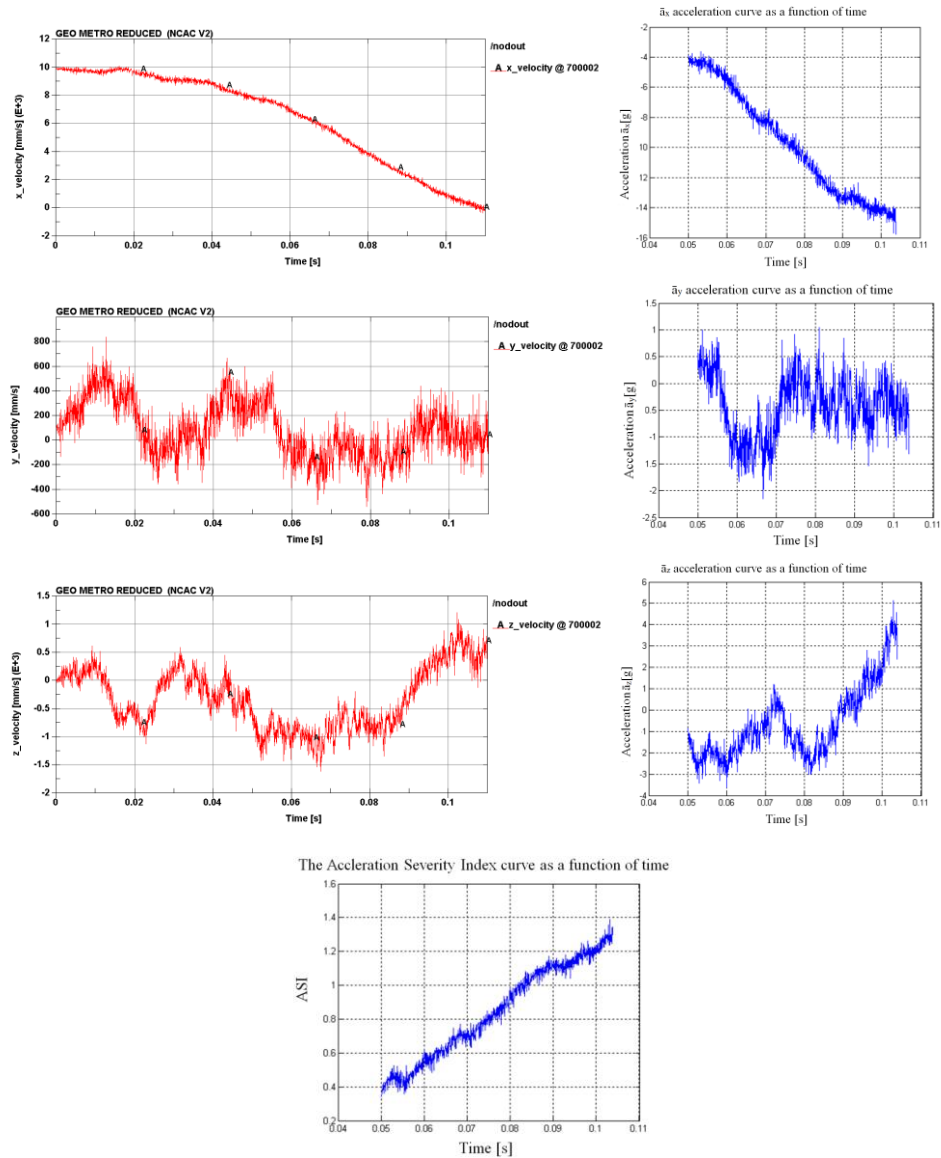As could be seen, Suzuki Geo-Metro car models during impact had different velocities and acceleration curves. It appears that results from NCAC model are more realistic.
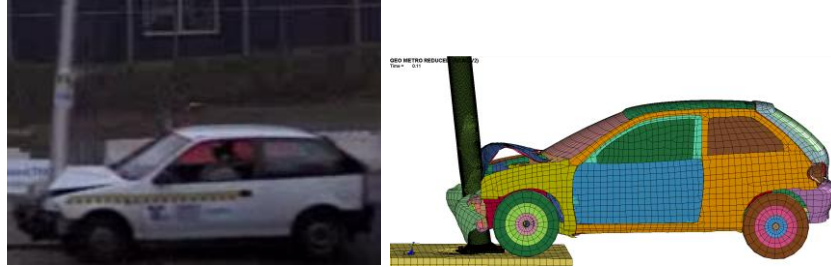
Figure 9. Crash test Sapa Pole Products 100LE3 8 meter column vs Geo-Metro car model (Ver. NCAC) crash test
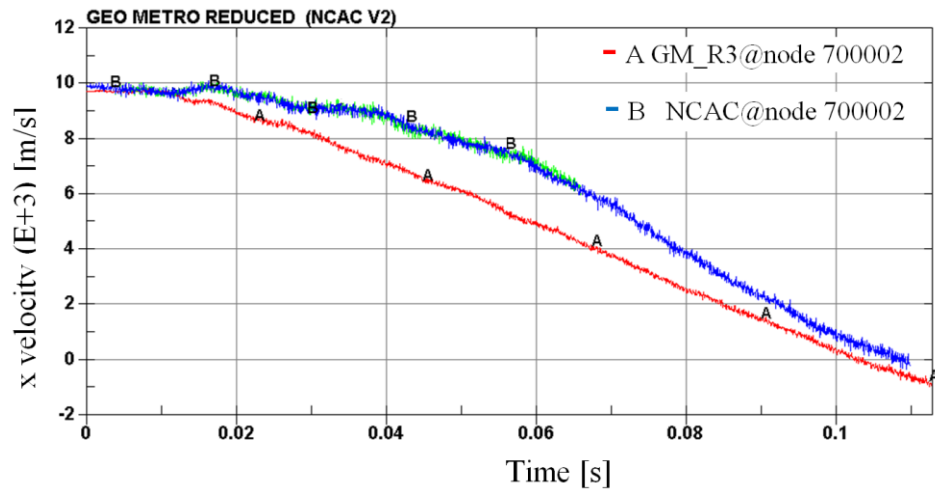
Figure 10. X velocity curves for two Suzuki Geo Metro models

5. Conclusions

Reviewing results of simulations presented here, it is obvious that using newer version of vehicle with front crumple zone, designed to absorb the energy from the impact by controlled deformation, will give lower value of ASI index. Mass of Toyota Yaris is about 1100 kg, unacceptable if crash test have to be made according to the norm, 200 kg more is noticeably in increased kinetic energy.

Location of vehicle's center of gravity has influance on character of impact. Viewing results from Suzuki Geo Metro model with modified suspension system and higher center of gravity in z axis (Ver. GM_R3) , the conclusion is that energy absorbed by column was higher, car almost hit into the column and ground, velocity was lowered more smoothly, regularly from the beginning till the end of impact. This situation had confirmation in lower value of 50 ms average component vehicle accelerations and ASI index.

In case of Suzuki Geo Metro, where center of gravity was lower in z axis (Ver. NCAC) , than the energy absorbed by column during impact was lower comparing to the previous condition. Car was driving partly on a column and start loose velocity more abruptly when column overturn about 10 deg. In this case kinetic energy is slower transferred to internal energy, can be seen rotational motion of a column at the beginning of impact.

When maximum value of ASI index at impact velocity 35 km/h is above 1.0 than modifications should be applied. It is said that stiffening of columns by additional flanges or by increased thickness of column shells should decrease velocity of car more smoothly, absorb more kinetic energy at the beginning of crash and transfer to internal energy (plastic deflection). This phenomenon would occur if the ground was regarded as rigid. But in reality ground is deflectable, soft or hard soil, and in the first phase of crash test take place movement and rotation of a column with fundament. As a result velocity of car in a first phase is higher. At some point, when fundament is not moving anymore, plastic deflection of a column is appearing. Stiffening of columns by additional flanges or by increased thickness of column shells decrease plastic deflection and even more abruptly slowing down a car in second phase. And is received an opposite effect, ASI index is higher.

References

[1] Belytschko T., Liu W. K., Moran B. Nonlinear Finite Elements for Continua and Structures, John Willey&Sons, Inc, New York, 2001.

[2] Hiermaier S. J., A. *Structures Under Crash and Impact, Continuum Mechanics, Discretization and Experimental Characterization.* Springer, 2008.

[3] European Committee for Standardiazation: EN 12767 Passive safety of support structures for road equipment – Requirements and test methods. Draft proposal of revised EN 12767. 2005-06-02. 30 p.

[4] European Committee for Standardization: SFS-EN- 40-3-3 Lighting columns – Part 3-3: Design and Verification – Verification by calculation. Helsinki: Finnish Standards Association, 2004. 73 p. ICS 93.080.40

[5] European Committee for Standardization: SFS-EN 40-3-1 Lighting columns – Part 3-1: Design and Verification – Specification for characteristic loads. Helsinki: Edita Oyj, 2000. 32 p. ICS 91.160.20

[6] European Committee for Standardization: SFS-EN 1317-1 Road restraint systems, Part 1: Terminology and general criteria for test methods. Helsinki: Edita Oyj, 1998. 30 p. ICS 01.040.93; 13.200; 93.080.30

[7] European Committee for Standardization: SFS-EN 1317-2 Road restraint systems, Part 2: Performance classes, mpact test acceptance criteria and test methods for safety barriers. Helsinki: Edita Oyj, 1998. 15 p. ICS 13.200; 93.080.30

[8] European Committee for Standardization: SFS-EN 1317-3 Road restraint systems, Part 3: Performance classes, impact test acceptance criteria and test methods for crash cushions. Helsinki: Edita Oyj, 2001. 19 p. ICS 13.200; 93.080.30

[9] Zukas J. A. High velocity impact dynamics. John Willey&Sons, Inc, New York, 1990.

[10] Hallquist, J. O. LS-DYNA Keyword User's Manual, Version 971, Livermore Software Technology Company, Livermore, CA, August 2006

[11] Hallquist, J. O. LS-DYNA Theory Manual, Version 971, Livermore Software Technology Company, Livermore, CA, August 2006

[12] Hallquist, J. O. Recent developments in LS-DYNA, German LS-DYNA Forum 10/13/2011

[13] Borovkov A., Klyavin O., Michailov A.,Kemppinen M., Kajatsalo M. Finite Element Modeling and Analysis of Crash Safe Composite Lighting Columns, Contact-Impact Problem, 9th International LS-DYNA Users Conference

[14] Mitchell G., Tolnai M., Gokani V., Picon R., Yang S. Klinger R.E., Williamson E.B. *Design of Retrofit Vehicular Barriers Using Mechanical Anchors.* CTR Technical Report October 2006.

[15] Eppinger R., et al., Development of Improved Injury Criteria for the Assessment of Advanced Automotive Restraint Systems – II, NHTSA, Nov 1999

[16] Kosaka I. Improvement of Energy Absorption for the Side Member Using Topography Optimization, 11th International LS-DYNA Users Conference

[17] Kiczko A., Niezgoda T., Nowak J., Dziewulski P. Numerical implementation of car impact into the modified road barrier, Journal of Kones Powertrain and Transport, Vol. 17, No. 3 2010

[18] Fasanella E. L., Jackson K.E., Kellas S. Soft Soil Impact Testing and Simulation of Aerospace Structures, Proceeding of the 10th LS-DYNA Users Conference, Dearborn, MI, June 8-10, 2008.

[19] Fasanella E. L., Jackson K.E. Developing Soil Models for Dynamic Impact Simulations, NASA Langley Research Center, Hampton, VA, United States, NASA Technical Reports Server, May 2009

[20] Kolling S. Haufe A. Material Models of Polymers for Crash Simulation, Dynamore Infotag Impetus, 30.11.2009

[21] Tsuchida T., Yamamoto S., Isomura K. The application of the damage & fracture material model to crashworthiness evaluations for Aluminum cars, 4th European LS-DYNA Users Conference

[22] Report 2010 Toyota Yaris FE Model, The National Cras Analysis Center, The George Washington University from http://www.ncac.gwu.edu/vml/models.html

[23] Mario Mongiardini WP5- Computational Mechanics Geo-Metro Finite Element model (GM_R3): Improvements of Steering System and Suspensions, ROBUST project, ROBUST-05-006-Rev.0

[24] M. Langseth M., Hopperstad O.S., Berstad T.:Crashworthiness of aluminium extrusions: validation of numerical simulation, efect of mass ratio and impact velocity, International Journal of Impact Engineering 22 (1999) p. 829-854

[25] Marre M, Grundlagen der Prozessgestaltung fur das Fugen durch Weiten mit Innenhochdruck, Remscheid, 2009

[26] http://www.ncac.gwu.edu/vml/models.html

[27] http://www.vegvesen.no/s/robust/Computational_mechanics/Vehicle%20models/

[28] http://www.ibdim.edu.pl/images/stories/dokumenty/slupy_oswietleniowe.pdf

Mariusz Pawlak, PhD :Silesian University of Technology, 44-100 Gliwice, Konarskiego 18a, POLAND (mariusz.pawlak@polsl.pl)

"The author gave a presentation of this paper during one of the conference sessions

Epidemiology of HIV with cell-to-cell transmission (STA098-15)

Carla M.A. Pinto, Ana R.M. Carvalho

Abstract: In this paper, we propose a model for the dynamics of HIV infection, that includes two types of transmission: virus-to-cell and cell-to-cell transmission. We compute the basic reproduction number and the stability of the disease free equilibrium. Simulations of the model show the relevant contribution of the two transmission types for the epidemics of HIV.

1. Introduction

AIDS is still a major challenge for public health worldwide. In Europe, focus is put in the control of the epidemics, since there are no clear signs of decline. Countries in the East show increased numbers in new reported cases. On the contrary, in Portugal, the data from 2013 shows a sustainable trend of decline in the number of new reported cases. There is a decrease of 13.7% in this number, when compared to 2012. It has also been observed a decrease in the mortality associated to AIDS.

HIV impairs the immune system and leads eventually, without treatment, to its collapse. The leukocytes with $CD4^+$ receptors, known as $CD4^+$ T cells, are the main targets of HIV [5]. Thus, it is extraordinarily important to understand the mechanisms behind cell-to-cell transmission in the epidemiology of HIV. It is believed that the infectivity of HIV is 10^2 to 10^3 times greater in cell-to-cell transmission than in virus-to-cell transmission [2].

The interest in developing mathematical models that included cell-to-cell transmission started in the 90's. Spouge *et al* [6] compare two models, one for virus-to-cell transmission and one for cell-to-cell transmission. Their numerical results revealed similar behaviors in the two models. Agosto *et al* [1] use current experimental data to show that most ART regimens are effective in blocking cell-to-cell virus transmission and preventing $CD4^+$ T cells depletion. They advocate a deeper knowledge of HIV epidemiology *in vivo* to devise better ART regimens, and ease the burden of HIV infected people.

In this paper, we propose a model for HIV dynamics that includes cell-to-cell and virus-to-cell transmissions and drug-resistance. In Section 2 we describe the model. In Section 3 we compute the reproduction number and the stability of the disease-free equilibrium. In Section 4, we present and discuss the simulations of the model. We conclude our work in the last section.

2. The model

The model describes the dynamics of the populations of the healthy CD4$^+$ T cells (T), the drug-sensitive T cells (T_s), the drug-resistant T cells (T_r), the drug-sensitive virus (V_s), and of the drug-resistant virus (V_r). The first term in the equation of the T cells represents the growth rates of these cells. The second and third terms represent the infection of the T cells by sensitive and resistant virus, V_s and V_r, at rate k_1. The parameter $u_1 \in [0,1]$, with 0 and 1 indicating no treatment and full treatment, respectively, represents the efficacy of reverse-transcriptase inhibitors (RTIs). RTIs inhibit the infection of CD4$^+$ T cells by virus. The drug-resistance indicates the inability of RTIs to inhibit the infection of T cells. The virus resistant strain is less fitted to infect T cells. This fitness factor is incorporated in the equations of the model using parameter ψ. The last two terms of the first equation represents the cell-to-cell transmission, at an infection rate k_2. The drug-sensitive T cells, T_s, can become resistant to drugs with a probability u. They die at a rate δ_2. V_s and V_r particles are produced by the corresponding infected CD4$^+$ populations, with bursting sizes of drug-sensitive strain, N_s, and of drug-resistant strain, N_r. The parameter u_2 represents the efficacy of protease inhibitors (PIs). The later inhibit the production of infectious virus from already infected cells. The constant virus loss due to infection of CD4$^+$ T cells is done with a rate k_3. The virus population is cleared at a rate c. The nonlinear system describing the dynamics of the model is:

$$
\begin{aligned}
\dot{T}(t) &= f(T(t)) - (1-u_1)k_1 V_s(t)T(t) - \psi k_1 V_r(t)T(t) - k_2 T(t)T_s(t) - \psi_1 k_2 T(t)T_r(t) \\[2mm]
\dot{T}_s(t) &= (1-u)(1-u_1)k_1 V_s(t)T(t) + k_2 T(t)T_s(t) - \delta_2 T_s(t) \\[2mm]
\dot{T}_r(t) &= \psi k_1 V_r(t)T(t) + uk_1(1-u_1)V_s(t)T(t) + \psi_1 k_2 T(t)T_r(t) - \delta_2 T_r(t) \\[2mm]
\dot{V}_s(t) &= N_s \delta_2 (1-u_2)T_s(t) - k_3 T(t)V_s(T) - cV_s(t) \\[2mm]
\dot{V}_r(t) &= N_r \delta_2 \psi T_r(t) - k_3 T(t)V_r(t) - cV_r(t)
\end{aligned}
$$

$$(1)$$

We will consider $f(T) = \lambda - dT + rT\left(1 - \frac{T+T_s+T_r}{T_{max}}\right)$, where λ is the source of new cells and d is the mortality rate of the CD4$^+$ T cells. The healthy T cells are assumed to proliferate exponentially at rate r until they reach the carrying capacity T_{max}, in the absence of virus or infected T cells.

3. Reproduction numbers and stability of disease-free equilibria

In this subsection, we compute the reproduction number of model (1), R_0. The basic reproduction number is defined as the number of secondary infections due to a single infection in a completely susceptible population.

We begin by considering two sub-models of model (1). Model (2) is obtained from model (1) by setting the variables concerning the resistance dynamics (T_r and V_r) to zero, and model (5) follows from model (1) by setting the variables concerning the sensitive dynamics (T_s and V_s) to zero. We then compute the reproduction number of system (2), R_s, using the next generation method [3].

$$
\begin{aligned}
\dot{T}(t) &= f(T(t)) - (1 - u_1)k_1 V_s(t)T(t) - k_2 T(t)T_s(t) \\[2mm]
\dot{T}_s(t) &= (1 - u)(1 - u_1)k_1 V_s(t)T(t) + k_2 T(t)T_s(t) - \delta_2 T_s(t) \\[2mm]
\dot{V}_s(t) &= N_s \delta_2 (1 - u_2)T_s(t) - k_3 T(t)V_s(T) - cV_s(t)
\end{aligned}
\tag{2}
$$

The disease-free equilibrium of model (2) is given by:

$$
P_0^1 = (T^0, T_s^0, V_s^0) = \big(f(T^0), 0, 0\big)
\tag{3}
$$

where $T^0 = \dfrac{T_{max}\left[(r-d) + \sqrt{(r-d)^2 + \frac{4r\lambda}{T_{max}}}\right]}{2r}$. Using the notation in [3] on system (2), matrices for the new infection terms, F, and the other terms, V, are given by:

$$
F = \begin{pmatrix} k_2 T^0 & (1-u)(1-u_1)k_1 T^0 \\ 0 & 0 \end{pmatrix}
$$

$$
V = \begin{pmatrix} \delta_2 & 0 \\ -N_s \delta_2 (1-u_2) & k_3 T^0 + c \end{pmatrix}
$$

The associative basic reproduction number is thus:

$$
R_s = \rho(FV^{-1}) = \frac{k_2 T^0}{\delta_2} + \frac{N_s(1-u_2)(1-u)(1-u_1)k_1 T^0}{k_3 T^0 + c}
\tag{4}
$$

where ρ indicates the spectral radius of FV^{-1}. By Theorem 2 [3], we obtain the following lemma.

Lemma 1 *The disease-free equilibrium P_0^1 is locally asymptotically stable if $R_s < 1$ and unstable if $R_s > 1$.*

We proceed with the computation of the reproduction number of model (5) below, R_r.

$$
\begin{aligned}
\dot{T}(t) &= f(T) - \psi k_1 V_r(t)T(t) - \psi_1 k_2 T(t)T_r(t) \\
\dot{T}_r(t) &= \psi k_1 V_r(t)T(t) + \psi_1 k_2 T(t)T_r(t) - \delta_2 T_r(t) \\
\dot{V}_r(t) &= N_r \delta_2 \psi T_r(t) - k_3 T(t)V_r(t) - cV_r(t)
\end{aligned}
\tag{5}
$$

The disease-free equilibrium state P_0^2 of model (5) is given by:

$$
P_0^2 = (T^0, T_r^0, V_r^0) = \big(f(T^0), 0, 0\big)
\tag{6}
$$

The matrices for the new infection terms, F, and the other terms, V, are given by:

$$
F = \begin{pmatrix} \psi_1 k_2 T^0 & \psi k_1 T^0 \\ 0 & 0 \end{pmatrix}
$$

$$
V = \begin{pmatrix} \delta_2 & 0 \\ -N_r \delta_2 \psi & k_3 T^0 + c \end{pmatrix}
$$

The corresponding basic reproduction number is:

$$
R_r = \rho(FV^{-1}) = \frac{\psi_1 k_2 T^0}{\delta_2} + \frac{N_r \psi^2 k_1 T^0}{k_3 T^0 + c}
\tag{7}
$$

where ρ indicates the spectral radius of FV^{-1}. The following lemma follows from By Theorem 2 [3].

Lemma 2 *The disease-free equilibrium P_0^2 is locally asymptotically stable if $R_r < 1$ and unstable if $R_r > 1$.*

We repeat the same procedure for the calculation of the reproduction number of the full model (1), R_0. The disease-free equilibrium state, P_0, of model (1) is given by:

$$
\begin{aligned}
P_0 &= (T^0, T_s^0, T_r^0, V_s^0, V_r^0) \\
&= \big(f(T^0), 0, 0, 0, 0\big)
\end{aligned}
\tag{8}
$$

The corresponding F and V matrices are computed to be:

$$F = \begin{pmatrix} k_2 T^0 & 0 & (1-u)(1-u_1)k_1 T^0 & 0 \\ 0 & \psi_1 k_2 T^0 & u(1-u_1)k_1 T^0 & \psi k_1 T^0 \\ 0 & 0 & 0 & 0 \\ 0 & 0 & 0 & 0 \end{pmatrix}$$

$$V = \begin{pmatrix} \delta_2 & 0 & 0 & 0 \\ 0 & \delta_2 & 0 & 0 \\ -N_s \delta_2 (1-u_2) & 0 & k_3 T^0 + c & 0 \\ 0 & -N_r \delta_2 \psi & 0 & k_3 T^0 + c \end{pmatrix}$$

and the corresponding basic reproduction number is:

$$R_0 = \rho(FV^{-1}) = \max\{R_s, R_r\} \tag{9}$$

where ρ indicates the spectral radius of FV^{-1}. By Theorem 2 [3], we obtain the following lemma.

Lemma 3 *The disease-free equilibrium P_0 is locally asymptotically stable if $R_0 < 1$ and unstable if $R_0 > 1$.*

4. Simulations

We simulate the model (1). The parameters used in the simulations are given in Table 1 and the initial conditions are set to $T(0) = 10^6$, $T_s(0) = 10^3$, and all other variables are set to 10.

In Figure 1, we observe that the model (1) approaches asymptotically the disease-free equilibrium.

In Figure 2, we simulate the dynamics of model (1) for different values of the parameter r, the proliferation rate of healthy T cells. We observe that as r increases, the number of infected (sensitive and resistant) T cells and virus (sensitive and resistant) also increases. This was an expected behaviour since, in the case of the endemic state, a larger number of uninfected cells boosts the virus dynamics (i.e., there are more cells to be infected).

In Figure 3, we depict the dynamics of system (1) for different values of the parameter k_2, the cell-to-cell transmission rate. From the observation of the figures, we note that as k_2 decreases the number of uninfected T cells increases, on the contrary to what is seen in the number of sensitive infected T cells that decreases. This is in agreement with previous works in the literature [8].

Parameter	Value	Units	Reference
λ	10^4	cells mL^{-1} day^{-1}	[2]
d	0.01	day^{-1}	[2]
δ_2	1	day^{-1}	[2]
r	0.03	day^{-1}	[2]
c	23	day^{-1}	[2]
T_{max}	10^6	mL^{-1}	[2]
u_1	0.6		[7]
u_2	0.3		[7]
u	3×10^{-5}		[4]
ψ	0.5		[4]
ψ_1	0.1		[4]
k_1	1.5×10^{-8}	mL day^{-1}	[2]
k_2	2.4×10^{-7}	mL day^{-1}	[8]
k_3	7.79×10^{-9}	mL day^{-1}	[4]
N_s	3000		[7]
N_r	2000		[7]

Table 1. Parameters used in the numerical simulations of model (1).

In Figure 4, we observe the contribution of k_1 and k_2 to R_0. As expected, augmenting k_1 and k_2 is translated in an increase in R_0. In terms of the infection, this means that there is a change in the epidemiology of HIV, from a disease-free equilibrium to an endemic state.

5. Conclusions

We proposed a model for the dynamics of HIV epidemics, considering two types of transmission: cell-to-cell and virus-to-cell, and drug-resistance. Simulations of the model show that both cell-to-cell and virus-to-cell transmission are relevant for the development of the disease. We believe that efforts should be applied in better understanding HIV pathogenesis *in vivo*, in order to develop smarter ART regimens, to reduce the treatment burden of people living with HIV.
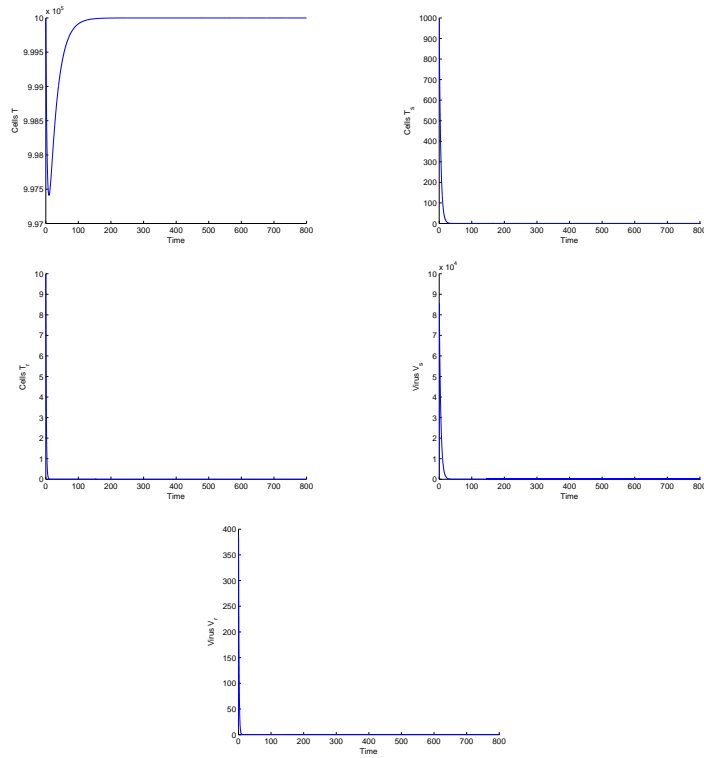
Acknowledgments

Figure 1. Disease-free equilibrium of system (1) for parameter values in Table 1 and given initial conditions.

References

[1] AGOSTO, L., UCHI, P., AND MOTHES, W. Hiv cell-to-cell transmission: effects on pathogenesis and antiretroviral therapy. *Trends in Microbiology*, 5 (2015).

[2] CONWAY, J., AND PERELSON, A. Post-treatment control of hiv infection. *Proceedings of the National Academy of Sciences of the United States of America 112*, 17 (2015), 5467–72.

[3] DRIESSCHE, P., AND WATMOUGH, P. Reproduction numbers and sub-threshold endemic equilibria for compartmental models of disease transmission. *Mathematical Biosciences 180* (2002), 29–48.

[4] HADJIANDREOU, M., CONEJEROS, R., AND WILSON, D. Long-term hiv dynamics subject to continuous therapy and structured treatment interruptions. *Chemical Engineering Science 64* (2009), 1600–1617.
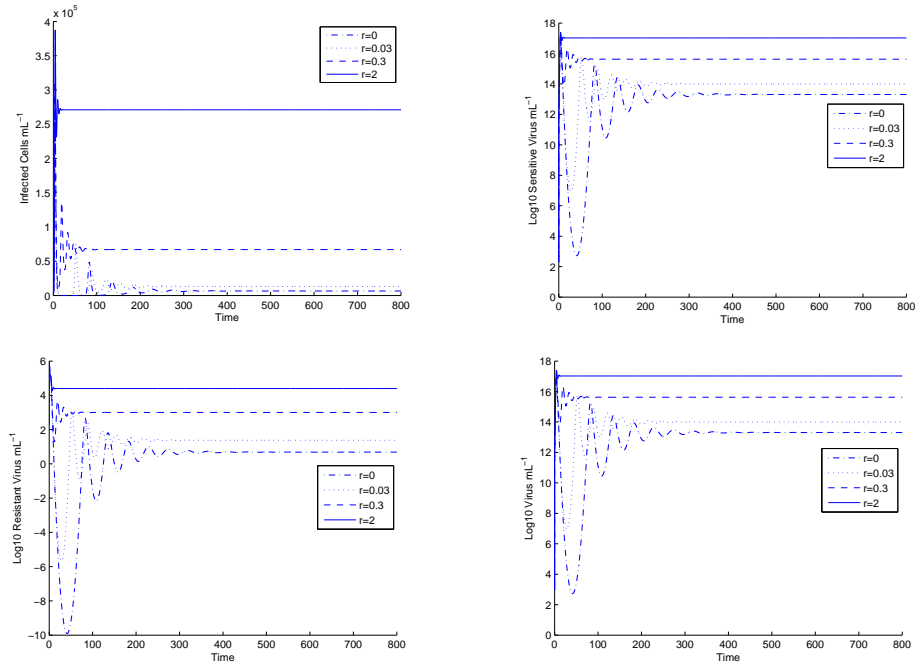
Figure 2. Dynamics of the system (1) for different values of r, the proliferation rate of healthy T cells, for parameter values in Table 1, except $k_2 = 2.4 \times 10^{(-6)}$, and given initial conditions.

[5] KOMAROVA, N., ANGHELINA, D., VOZNESENSKY, I., TRINIT, B., LEVY, D., AND WODARZ, D. Relative contribution of free-virus and synaptic transmission to the spread of hiv-1 through target cell populations. *Biology Letters 9*, 1 (2013), 20121049.

[6] SPOUGE, J., SHRAGER, R., AND DIMITROV, D. Hiv-1 infection kinetics in tissue cultures. *Mathematical Biosciences 138*, 1 (1996), 1–22.

[7] WANG, Y., BRAUER, F., WU, J., AND HEFFERNAN, J. A delay-dependent model with hiv drug resistance during therapy. *Journal of Mathematical Analysis and Applications 414* (2014), 514–531.

[8] WEN, Q., AND LOU, J. The global dynamics of a model about hiv-1 infection in vivo. *Ricerche di Matematica 58* (2009), 77–90.

Carla M.A. Pinto, Ph.D.: School of Engineering, Polytechnic of Porto and Center for Mathematics of the University of Porto, Rua Dr António Bernardino de Almeida 431, 4200-072 Porto, Portugal (*cap@isep.ipp.pt*). The author gave a presentation of this paper during one of the conference sessions.
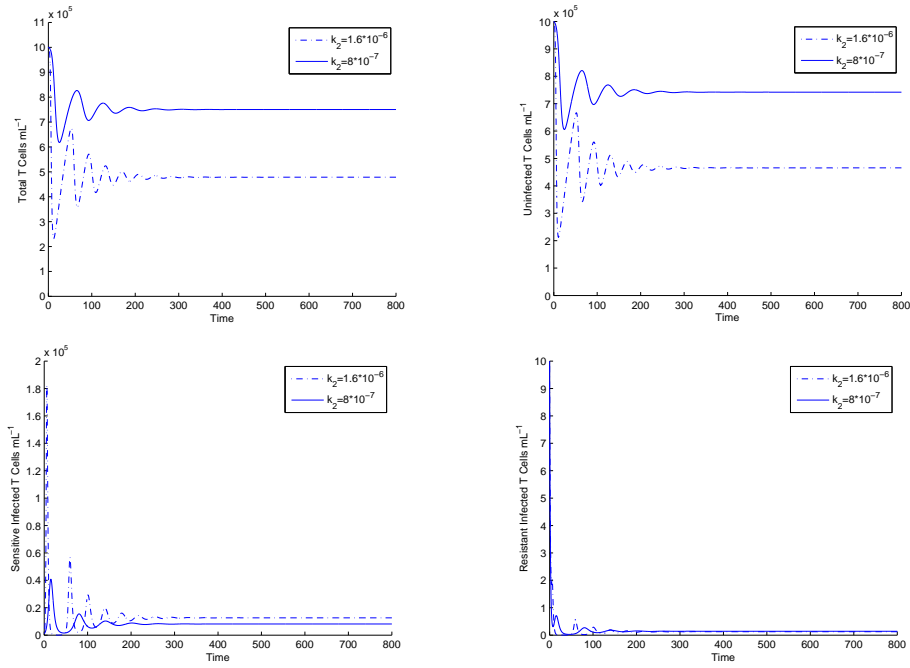
Figure 3. Dynamics of the system (1) for different values of k_2, the cell-to-cell transmission rate, for parameter values in Table 1 and given initial conditions.

Figure 4. Contribution of the virus-to-cell transmission rate k_1 and of the cell-to-cell transmission rate k_2 for the value of the reproduction number R_0.

Ana R.M. Carvalho, M.Sc. (Ph.D. student): Faculty of Sciences, University of Porto, Rua do Campo Alegre s/n, 4169-002 Porto, Portugal (*up080301038@alunos.fc.up.pt*).

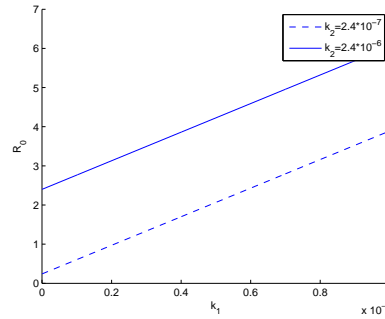# Electromagnetic stabilisation of a slender rotating shaft
(STA197-15)

Piotr M. Przybyłowicz

Abstract: The paper is concerned with the problem of loss of dynamical stability of a slender rotating shaft and the making use of electromagnetic actuators to prevent the rotor from such a situation. It is known that internal friction in the shaft material may destabilise its static equilibrium position during operation. At a certain angular velocity, called the critical speed, the static equilibrium bifurcates into a new oscillatory state manifested by additional precession-like motion having some amplitude and frequency. To avoid this disadvantageous, sometimes even dangerous situation, an active method incorporating electromagnetic actuators is proposed and discussed. The actuators generate an attractive force interacting with the ferromagnetic shaft. At the same time transverse motion of the shaft induces electromotive force in the electric circuit supplying the magnetic cores. This electromagneto-mechanical coupling gives an effect resembling viscous damping, but in fact it is a strongly non-linear phenomenon. Either way, the electromagnetic interaction highly influences dynamics of the shaft and noticeably stabilizes the system. Another problem studied in the paper is the non-linear response of the rotor near the critical point. To this end, mathematical formalism handling Hopf's bifurcation is introduced, an approximation of the bifurcation solution built and its orbital stability checked. Numerical simulations of the thus formulated model clearly show that the introduction of electromagnetic actuators reduces the amplitude post-critical vibrations.

1.   Introduction

Rotating shafts, even perfectly balanced, may exhibit self-excited vibration brought about by the presence of internal friction in the shaft material. Self-excitation occurs while exceeding a certain critical rotation speed (over the first eigenfrequency of the shaft treated as a beam) and manifests itself by a sudden growth of vibration amplitude with small variations in the angular velocity. It is to be emphasized at this point that this is completely different phenomenon than another one related to critical rotation speed, but corresponding to the first resonant speed and the first eigenfrequency of the shaft. The static equilibrium position of the rotor evolves into a qualitatively new state of oscillatory character. Such a situation is known as flutter, i.e. bifurcation of the static equilibrium into dynamical periodic behavior. In terms of mathematical analysis this phenomenon is called Hopf bifurcation [1].

The problem of dynamical loss of stability of rotating shafts has been a subject of thorough research works for the recent decades. Investigations by Dimentberg [2], Tylikowski [3] as well as by

Kurnik [4] deserve here particular mentioning. For an equally long time the problem of how to eliminate such instability or, at least, to shift it away outside the operational regime of rotation speed has been undertaken by many researchers and engineers. At hand have remained structural modifications to the rotors (changing their elasticity and rigidity) but always they were only passive solutions.

In this paper, an active approach towards stabilization of a rotating shaft is proposed and discussed. It is a fully controllable method incorporating electromagnetic actuators into the system. The actuators however are not supports of the shaft (as in systems with magnetic contactless bearings) but additional elements exerting some attractive force on the ferromagnetic shaft. The concept comes from considerations initiated by Kurnik [5] and elaborated on by Dziedzic [6] where such a solution was applied to the rigid rotor supported on hydrodynamical oil bearings. In this contribution, that method has been adapted for stabilization and reduction of vibration of a slender shaft mounted on rolling bearings, where two pairs of electromagnetic actuators have been placed somewhere between the stiff mechanical supports in both perpendicular planes.

2. The analyzed model and governing equations

In the study, an elastic shaft in form of a Euler-Bernoulli beam made of some ferromagnetic material possessing certain energy dissipative properties is assumed. The shaft equipped with a system of two pairs of electromagnetic actuators is shown in Fig. 1. The shaft undergoes lateral displacement in both transverse directions y and z. The total displacement is then $w = \sqrt{y^2 + z^2}$.
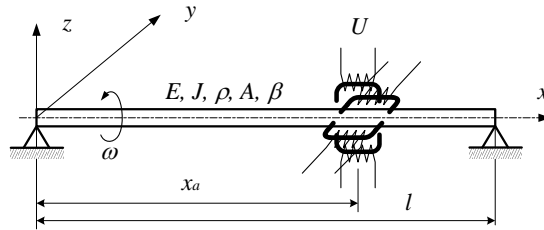

Figure 1. Model of the rotating shaft with electromagnetic actuators

The structural and material parameters assumed in the calculations are the following: length of the shaft $l = 1$ m, diameter $d = 0.01$ m, area of the cross-section $A = 7.85 \times 10^{-5}$ m^2, geometric cross-sectional moment of inertia $J = 4.91 \times 10^{-9}$ m^4, material density $\rho = 7800$ kg/m^3, Yong's modulus $E = 2.1 \times 10^{11}$ Pa, retardation time of the material (Kelvin-Voigt rheological model) $\beta = 0.0001$ s, coefficient of the external damping (surrounding medium) $c = 2.0$ kg/(m^{2}s). The parameters of the electromagnetic stabilization system are: length of the magnetic core $l_c = 0.2$ m, cross-section area of the core $S = 3.14 \times 10^{-4}$ m^2, nominal air gap in the magnetic circuit $\delta = 0.01$ m, number of wire

windings $N = 500$, electric resistance of the supply circuit $R = 8\ \Omega$, relative magnetic permeability of the core $\mu = 5000$.

Detailed derivation of equations of motion of an elastic rotating shaft was laboriously given by Kurnik [5] who examined the class of rotating beams made of a material having damping properties described by the Kelvin-Voigt model according to which the stress in the material is directly proportional to strain (Hooke's law) as well as to strain velocity (viscous effect). These equations are as follows:

$$
\begin{aligned}
&\frac{\partial^2 y}{\partial t^2} + h\frac{\partial y}{\partial t} + a^2\left[\left(1 + \frac{\partial}{\partial t}\right)\frac{\partial^4 y}{\partial x^4} + \beta\,\omega\,\frac{\partial^4 z}{\partial x^4}\right] = q_{my}\,\delta(x - x_a) \\
&\frac{\partial^2 z}{\partial t^2} + h\frac{\partial z}{\partial t} + a^2\left[\left(1 + \frac{\partial}{\partial t}\right)\frac{\partial^4 z}{\partial x^4} - \beta\,\omega\,\frac{\partial^4 y}{\partial x^4}\right] = q_{mz}\,\delta(x - x_a)
\end{aligned}
\tag{1}
$$

where $\delta(x - x_a)$ denotes the Dirac delta function. It describes the presence of the electromagnetic actuators place at $x = x_a$ and are assumed to act as tip-concentrated forces. The quantities F_{my}, F_{mz} are magnetic forces, i.e. $q_{my} = F_{my}/(\rho A)$, $q_{mz} = F_{mz}/(\rho A)$, besides $h = c/(\rho A)$, $a^2 = EJ/(\rho A)$. An explicit form of the magnetic forces q_{my}, q_{mz} is given in (4). They were derived by Kurnik [5].

The analyzed object is a one-dimensional continuous system described by partial differential equations (1). It has an infinite number of degrees of freedom. Keeping in mind the fact that dynamics of the system is mainly governed by first eigenfunctions of the shaft, expressions (1) will be discretized into ordinary differential equations by projecting them onto the subspace ranged over the first eigenmode corresponding to the simply supported beam. This approach would yield a possibly exact and simple at the same time mathematical model of the system enabling analysis of its response within the linear and non-linear domain.

The first eigenform of the simply supported Euler-Bernoulli beam is a sine function $\sin(\pi x/l)$. Accordingly, the first approximation (Fourier method) to equations (1) is:

$$
y(x,t) = Y(t)\sin\frac{\pi x}{l} \quad \text{and} \quad z(x,t) = Z(t)\sin\frac{\pi x}{l}
\tag{2}
$$

Application of Galerkin's unimodal discretization to (1) based on predictions (2) gives:

$$
\begin{aligned}
&\ddot{Y} + h\dot{Y} + k_1^4(Y + \beta\dot{Y} + \beta\omega Z) - \frac{2}{l}q_{my}\sin\frac{\pi x_a}{l} = 0 \\
&\ddot{Z} + h\dot{Z} + k_1^4(Z + \beta\dot{Z} - \beta\omega Y) - \frac{2}{l}q_{mz}\sin\frac{\pi x_a}{l} = 0
\end{aligned}
\tag{3}
$$

where $k_1 = \pi^4/l^4$. The expressions for the electromagnetic forces are:

$$q_{my} = \frac{SN^2\mu_c}{4\rho A}\left\{\frac{i_{y2}^2}{(\Delta - y_a)^2} - \frac{i_{y1}^2}{(\Delta + y_a)^2}\right\}, \quad q_{mz} = \frac{SN^2\mu_c}{4\rho A}\left\{\frac{i_{z2}^2}{(\Delta - z_a)^2} - \frac{i_{z1}^2}{(\Delta + z_a)^2}\right\} \tag{4}$$

where S denotes cross-sectional area of the magnetic core, $\mu_c = \mu_0\mu$ its resultant magnetic permeability ($\mu_0 = 4 \times 10^{-7}$ H/m − magnetic permeability of vacuum), i_{y1}, i_{y2}, i_{z1}, i_{z2} are currents in the electric circuits in both actuators (four independent electric circuits), N − number of wire windings in each electromagnet, Δ − normalized gap in the magnetic circuit $\Delta = \delta + l_c/2\mu_{cr}$, y_a and z_a transverse displacements of the shaft at the point of actuators placement: $y_a = Y\sin\pi x_a/l$, $z_a = Z\sin\pi x_a/l$.

Equations of electrodynamics of the electric circuits supplying every half of the electromagnets are the following:

$$\frac{di_{y2}}{dt} = \frac{2(U - i_{y2}R)(\Delta - y_a)}{N^2S\mu_0} - i_{y2}\frac{\dot{Y}}{\Delta - y_a}, \qquad \frac{di_{y1}}{dt} = \frac{2(U - i_{y1}R)(\Delta + y_a)}{N^2S\mu_0} + i_{y1}\frac{\dot{Y}}{\Delta + y_a}$$

$$\frac{di_{Z2}}{dt} = \frac{2(U - i_{z2}R)(\Delta - z_a)}{N^2S\mu_0} - i_{Z2}\frac{\dot{Z}}{\Delta - z_a}, \qquad \frac{di_{Z1}}{dt} = \frac{2(U - i_{z1}R)(\Delta + z_a)}{N^2S\mu_0} + i_{Z1}\frac{\dot{Z}}{\Delta + z_a} \tag{5}$$

and the explicit form of electro-mechanical coupled equation of motion of the shaft is finally:

$$\ddot{Y} + h\dot{Y} + k_1^4(Y + \beta\dot{Y} + \beta\omega Z) - \frac{SN^2\mu_0}{2\rho Al}\left\{\frac{i_{y2}^2}{(\Delta - y_a)^2} - \frac{i_{y1}^2}{(\Delta + y_a)^2}\right\}\sin\frac{\pi x_a}{l} = 0$$

$$\ddot{Z} + h\dot{Z} + k_1^4(Z + \beta\dot{Z} - \beta\omega Y) - \frac{SN^2\mu_0}{2\rho Al}\left\{\frac{i_{z2}^2}{(\Delta - z_a)^2} - \frac{i_{z1}^2}{(\Delta + z_a)^2}\right\}\sin\frac{\pi x_a}{l} = 0 \tag{6}$$

As a result, we have two ordinary differential equations of the second order and four equations of the first order. To get some more organized and neat mathematical formulation of the above, let us introduce new variables which will transform these expressions all into differential equations of the first order and, additionally, make the equilibrium position of the electro-mechanical system trivial. Normally, mechanical equilibrium is at the zero point ($Y = 0$, $Z = 0$) but the electric currents do not: $i_{y1} = i_{y2} = i_{z1} = i_{z2} = U/R$. To achieve the goal, we introduce:

$$Y = u_1, \quad \dot{Y} = u_2, \quad Z = u_3, \quad \dot{Z} = u_4$$

$$i_{y1} = u_5 + \frac{U}{R}, \quad i_{y2} = u_6 + \frac{U}{R}, \quad i_{z1} = u_7 + \frac{U}{R}, \quad i_{z2} = u_7 + \frac{U}{R} \tag{7}$$

which leads to the system of eight differential equations of the first order:

$$\dot{u}_1 = u_2$$

$$\dot{u}_2 = -hu_2 - k_1^4(u_1 + \beta u_2 + \beta \omega u_3) + \xi_a \sigma \left[\left(\frac{u_6 + \frac{U}{R}}{\Delta - u_1 \xi_a} \right)^2 - \left(\frac{u_5 + \frac{U}{R}}{\Delta + u_1 \xi_a} \right)^2 \right]$$

$$\dot{u}_3 = u_4$$

$$\dot{u}_4 = -hu_4 - k_1^4(u_3 + \beta u_4 - \beta \omega u_1) + \xi_a \sigma \left[\left(\frac{u_8 + \frac{U}{R}}{\Delta - u_3 \xi_a} \right)^2 - \left(\frac{u_7 + \frac{U}{R}}{\Delta + u_3 \xi_a} \right)^2 \right]$$

$$\dot{u}_5 = \frac{-u_5}{\sigma V \rho}(\Delta + u_1 \xi_a) + \frac{\left(u_5 + \frac{U}{R}\right)u_2}{\Delta + u_1 \xi_a} \ , \quad \dot{u}_6 = \frac{-u_6}{\sigma V \rho}(\Delta - u_1 \xi_a) - \frac{\left(u_6 + \frac{U}{R}\right)u_2}{\Delta - u_1 \xi_a} \tag{8}$$

$$\dot{u}_7 = \frac{-u_7}{\sigma V \rho}(\Delta + u_3 \xi_a) + \frac{\left(u_7 + \frac{U}{R}\right)u_4}{\Delta + u_3 \xi_a} \ , \quad \dot{u}_8 = \frac{-u_8}{\sigma V \rho}(\Delta - u_1 \xi_a) - \frac{\left(u_6 + \frac{U}{R}\right)u_4}{\Delta - u_3 \xi_a}$$

where $\xi_a = \sin \frac{\pi x_a}{l}$, $\sigma = \frac{S N^2 \mu_0}{2V}$ and $V = \rho A l$.

The system (8) can be presented in a concise vector formulation:

$$\dot{\mathbf{u}} = \mathbf{f}(\omega, \mathbf{u}) = \mathbf{A}(\omega)\mathbf{u} + \mathbf{N}(\omega, \mathbf{u}) \tag{9}$$

where $\mathbf{f}$ stands for the right-hand side of the system, $\mathbf{A}$ is a matrix of the linear part of (8), $\mathbf{N}$ – the remaining non-linear part.

3. Critical rotation speed

Find now the critical rotation speed, i.e. the angular velocity at which the shaft loses its stability and self-excitation occurs. To this end, eigenvalues of the matrix $\mathbf{A}$ (see eq. 9) around the trivial equilibrium $\mathbf{u} = \mathbf{0}$ should be determined.

$$\mathbf{A}(\omega) = \begin{bmatrix} 0 & 1 & 0 & 0 & 0 & 0 & 0 & 0 \\ -k_1^4 + U_\xi & -h - k_1^4 \beta & -k_1^4 \beta \omega & 0 & -U_\sigma & U_\sigma & 0 & 0 \\ 0 & 0 & 0 & 1 & 0 & 0 & 0 & 0 \\ k_1^4 \beta \omega & 0 & -k_1^4 + U_\xi & -h - k_1^4 \beta & 0 & 0 & -U_\sigma & U_\sigma \\ 0 & U_R & 0 & 0 & -\Delta_\rho & 0 & 0 & 0 \\ 0 & -U_R & 0 & 0 & 0 & -\Delta_\rho & 0 & 0 \\ 0 & 0 & 0 & U_R & 0 & 0 & -\Delta_\rho & 0 \\ 0 & 0 & 0 & -U_R & 0 & 0 & 0 & -\Delta_\rho \end{bmatrix} \tag{10}$$

where the following notations have been introduced:

$$U_\sigma = 2U \frac{\sigma \xi_a}{R\Delta^2} \ , \ U_R = \frac{U}{R\Delta} \ , \ U_\xi = 2U_\sigma U_R \xi_a \ , \ \Delta_\rho = \frac{\Delta}{V\rho\sigma} \tag{11}$$

Thus we look for a solution to the eigenproblem $\det[\mathbf{A}(\omega) - r\mathbf{I}] = 0$, where the matrix $\mathbf{A}$ is explicitly given in (10), r – is the eigenvalue to be found, $\mathbf{I}$ is the identity matrix of the rank 8. The eigenvalue which decides about stability of the system has the greatest real part. Denote it by $r_{dec} = r_1$. By tracking its trajectory on the complex plane $\mathrm{Re}\{r_1\} - \mathrm{Im}\{r_1\}$ one can easily notice the moment at which $\mathrm{Re}\{r_1\}$ reaches zero and intersects the imaginary axis. Positive values of $\mathrm{Re}\{r_1\}$ mean destabilization of the system and the onset of self-excited vibration (flutter).
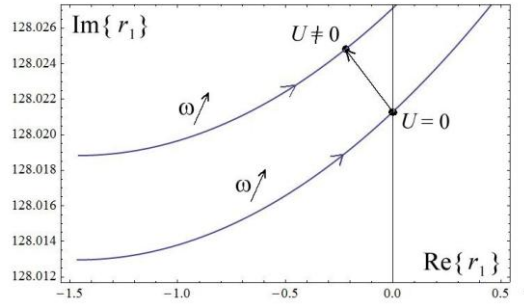

Figure 2. Trajectory of the decisive eigenvalue for the disabled and enabled actuators.

The situation is shown in Fig 2. Initially, at a low angular velocity, the eigenvalue stays on the left half of the complex plane and the system remains stable. Growing ω makes the eigenvalue r_1 move rightwards. At $\omega = \omega_{cr}$ it passes through the ordinate – the stability is lost and ω gains the critical threshold. Activation of the electromagnetic actuators however shifts the trajectory leftwards (as seen in Fig. 2) and stabilizes the shaft which for a certain $U \neq 0$ acquires a new, greater value of the critical speed.

Naturally, an infinite growth of ω_{cr} by application of a larger and larger voltage is not possible because of obvious safety reasons and also due to threat of divergent behavior of the shaft which might attach to one of the electromagnets as a result of too excessive attracting force.

In Fig. 3, the critical velocity ω_{cr} is shown in function of the voltage U supplied to the electric circuits of the actuators. Apparently, relatively small values of U of 20 V lead to an increase in the critical speed by 40 %.
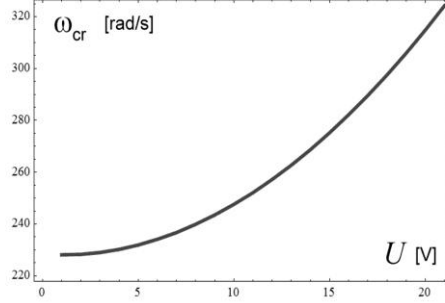
Figure 3. Critical rotation speed vs. voltage applied to the electromagnetic actuators.

4. Non-linear analysis of the system

The newly born situation – the loss of stability and appearance of self-excited vibration requires additional investigation to be made in order to examine the character of such vibrations. The main problem here is to find out whether the newly occurred limit cycle (flutter) is orbitally stable or not. This is of vital importance to the system.

The near-critical nature of self-excited vibration can be analyzed by constructing a bifurcating solution composed of an infinite series of $2\pi i$-periodic functions of the form:

$$\mathbf{u}(\varepsilon,\Omega t) = \sum_{i=1}^{\infty} \frac{\varepsilon^i}{i!} \mathbf{u}^{(i)}(\Omega t) \tag{12}$$

where $\mathbf{u}^{(i)}$ are the sought harmonics of the frequency Ω being itself expressed in terms of the series in the small parameter ε :

$$\Omega = \Omega_0 + \sum_{i=1}^{\infty} \frac{\varepsilon^i}{i!} \Omega_i \tag{13}$$

where Ω_0 denotes the initial frequency of the flutter $\Omega_0 = \text{Im}\{r_1(\omega_{cr})\}$. Analogously, the angular speed is also expanded into the series:

$$\omega = \omega_{cr} + \sum_{i=1}^{\infty} \frac{\varepsilon^i}{i!} \omega_i \tag{14}$$

Now, take into consideration only the first approximation of the bifurcating solution:

$$\mathbf{u}(\varepsilon,\Omega t) = \varepsilon \mathbf{u}^{(1)}(\Omega t)$$
$$\Omega = \Omega_0 + \frac{1}{2}\varepsilon^2 \Omega_2 , \quad \omega = \omega_{cr} + \frac{1}{2}\varepsilon^2 \omega_2 \tag{15}$$

489

since $\Omega_1 = 0$ and $\omega_1 = 0$ are zero (like any other odd terms). The first approximation $\mathbf{u}^{(1)}$ is based on the eigenvector $\mathbf{q}$ corresponding to the eigenproblem $\{\mathbf{A}(\omega_{cr}) - i\Omega_0\}\mathbf{q} = \mathbf{0}$, whereas the parameters ω_2 and Ω_2 are obtained from relationships given by Iooss and Joseph [1]:

$$\omega_2 = -\frac{\text{Re}\{\Psi_2\}}{3\text{Re}\left\{\dfrac{d\,r_1(\omega_{cr})}{d\,\omega}\right\}} \ , \quad \Omega_2 = \omega_2\,\text{Im}\left\{\frac{d\,r_1(\omega_{cr})}{d\,\omega}\right\} + \frac{1}{3}\text{Im}\{\Psi_2\} \tag{16}$$

in which the complex number Ψ_2 is to be found from:

$$\Psi_2 = \frac{3}{2}\sum_{i=1}^{8}\sum_{j=1}^{8}\sum_{k=1}^{8}\frac{\partial^2 f_i(\omega_{cr},\mathbf{0})}{\partial u_j\,\partial u_k}\overline{q}_i^*(q_j K_k + \overline{q}_j L_k) + 3\sum_{i=1}^{8}\sum_{j=1}^{8}\sum_{k=1}^{8}\sum_{l=1}^{8}\frac{\partial^3 f_i(\omega_{cr},\mathbf{0})}{\partial u_j\,\partial u_k\,\partial u_l}\overline{q}_i^*q_j q_k \overline{q}_l \tag{17}$$

where f_i is the i-th component of the right-hand side vector of the governing equations of motion (8), and K_k, L_k are k-th components of vectors found from the following expressions:

$$\mathbf{K} = -2\mathbf{A}^{-1}(\omega_{cr})\sum_{j=1}^{8}\sum_{k=1}^{8}\frac{\partial^2 \mathbf{f}(\omega_{cr},\mathbf{0})}{\partial u_j\,\partial u_k}q_j\overline{q}_k$$
$$\mathbf{L} = -\{\mathbf{A}(\omega_{cr}) - 2i\Omega_0\}^{-1}\sum_{j=1}^{8}\sum_{k=1}^{8}\frac{\partial^2 \mathbf{f}(\omega_{cr},\mathbf{0})}{\partial u_j\,\partial u_k}q_j q_k \tag{18}$$

The vector $\mathbf{q}^*$ standing in (17) is another base vector corresponding to the adjoint eigenproblem $\{\mathbf{A}^{\text{T}}(\omega_{cr}) + i\Omega_0\}\mathbf{q}^* = \mathbf{0}$. Both vectors $\mathbf{q}$ and $\mathbf{q}^*$ can be determined with an accuracy up to a constant. For uniqueness, their orthonormalisation is used:

$$\sum_{i=1}^{8}q_i q_i = 0 \ \text{ and } \ \sum_{i=1}^{8}\overline{q}_i q_i = 1 \tag{19}$$

where the overbar means the complex conjugate. All the above formulas enable numerical calculation of the first bifurcating approximation whose most important characteristic is its amplitude. It is illustrated in Fig. 4.

As can be easily noticed, for $U = 0$ (no actuation) we observe an infinite jump of self-excited vibration. This is because the considered system is fully linear in its mechanical part. The non-linearity comes from electrodynamics only. Application of $U \neq 0$ encloses the bifurcating solution on a limit cycle with a certain amplitude (see Fig. 4). Greater values of U smoothen this amplitude more and more. The effect of reduction of the vibration is easily seen.

What is especially interesting, the observed bifurcation is always supercritical. This means that the amplitude of flutter monotonically grows with an increase in the rotation speed and no sudden

jumps will appear (like in the case of subcritical bifurcation). This has been numerically confirmed by calculating the Floquet exponent given by the equation:

$$\sigma(\varepsilon) = \text{Re}\{\Psi_2\}\varepsilon^2 + O(\varepsilon^4) \tag{20}$$

where $O(\varepsilon^4)$ denotes small terms of higher orders. Since $\varepsilon^2 > 0$, the sign of σ is ruled by the magnitude of $\text{Re}\{\Psi_2\}$, and the analysis proves that it is always negative. And $\sigma < 0$ means that the limit cycle is orbitally stable.
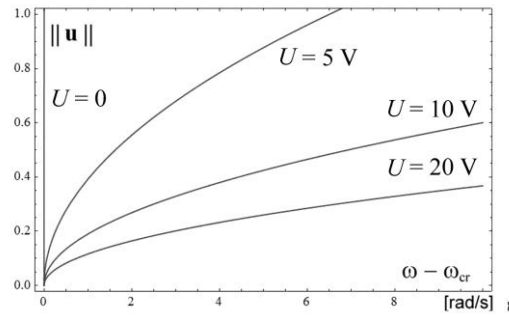

Figure 4. Amplitude of the bifurcating solution around the critical point for some selected voltages in the electromagnetic actuators.

5. Concluding remarks

In this paper, a method of stabilization and reduction of vibration in an elastic rotating shaft by making use of electromagnetic actuators is presented. The electromagnets introduce kind of an additional stiffness and damping to the system by generating an attractive magnetic force proportional to the lateral displacement and velocity of the shaft. The character of this force is strongly non-linear. A very good efficiency of the proposed method has been confirmed. A shaft of length $l = 1$ m and diameter $d = 1$ cm exhibits growth of the critical rotation speed by 40 % for a moderate voltage of 20 V. Another advantageous effect of this stabilization approach is observed in the non-linear scope as well. It has been observed that the loss of stability is always accompanied by smooth and safe supercritical bifurcation.

The analyzed model is yet mechanically linear. Further research is the required to get a complete understanding of the phenomena taking place in the system.

Acknowledgment

References

[1]   Iooss, G., Joseph, D.D., *Elementary stability and bifurcation theory*, Springer-Verlag, New York, 1980.

[2]   Dimentberg, F.M., *Flexural Vibrations of Rotating Shafts*, Butterworths, London, 1961.

[3]   Tylikowski, A., Dynamic Stability of a Rotating Shaft, *Ingenieur Archiv*, 49(1980), 214-221.

[4]   Kurnik, W., Hysteretic Behaviour of a Rotating Shaft with Geometric and Physical Nonlinearities, *Zaitschrift für Angewandte Mathematik und Mechanik*, 72, 4 (1992), T37-T75.

[5]   Kurnik W., Active Magnetic Antiwhirl Control of a Rigid Rotor Supported on Hydrodynamic Bearings, *Machine Dynamics Problems*, 10 (1995), 21-36.

[6]   Dziedzic K., *Dynamics of rotors with active magnetic damping in the bearings* (in Polish), Ph.D. thesis, Warsaw University of Technology, 2005, Supervisor: W. Kurnik.

Piotr M. Przybyłowicz, Ph.D.: Warsaw University of Technology, Institute of Machine Design Fundamentals, ul. Narbutta 84, 02-524 Warszawa, Poland (*piotr.przybylowicz@simr.pw.edu.pl*). The author gave a presentation of this paper during one of the conference sessions.

Using saturation phenomenon to improve energy harvesting in a portal frame platform with passive control by a pendulum (CON004-15)

Rodrigo Tumolin Rocha, José Manoel Balthazar, Ângelo Marcelo Tusset, Vinicius Piccirillo, Reyolando M.L.R. Fonseca Brasil, Jorge L. Palacios Felix

Abstract: A new model of energy harvester based on a simple portal frame structure subjected to saturation phenomenon is presented. Energy is collected via a piezoelectric device whose nonlinearities are considered in the mathematical model. The system is a bi-stable Duffing oscillator presenting chaotic behavior. Optimization of power harvesting and stabilization of chaotic motions to a given periodic orbit is obtained analyzing the average power output and bifurcation diagrams. Control sensitivity to parametric errors in the damping and stiffness parameters of the portal frame is studied. The proposed passive control technique uses a simple pendulum tuned to the vibrations of the structure to improve energy harvesting. The results show that with the implementation of this control strategy it is possible to eliminate the need for active or semi active control, usually more complex. The control also provides a way to regulate the energy captured to a desired operating frequency.

1. Introduction

In recently past years, the research about vibration energy harvesting has been increased substantially. Many of those vibration sources are found in structures that are excited by wind, sea waves, vehicles traffics, i.e., external excitations. One of most promising and studied device as a means of low power energy harvesting is the piezoelectric material.

The research about these materials begun with some experiments, showing itself a nonlinear material [1]. Recently, a big gamma of works introducing the piezoelectric material as a means of energy transduction has been widely studied as we see in [2-6]. Specially, the nonlinearities of the piezoelectric material, which was experimentally found, was analytically proposed as an approximation by [7]. The nonlinearities of vibratory energy harvesting were widely exploited by [8].

The vibratory energy harvesting generally contains the piezoelectric material coupled to a structure. Some kind of structures may present particular configurations that may improve the energy harvesting, even provide periodic behaviour. One of the particular exploited configurations is the internal resonance, such as 2:1, between two modes of vibration, so that the system transfers part of the vibration energy available at a certain coordinate to the another one. This is the saturation

phenomenon described by many authors, for example, among others [9-11]. The implementation of saturation as a control method was proposed and studied by [12-14], among others.

Works involving electro-mechanical systems have been recently studied by many authors. A model of an energy harvester based on a simple portal frame of a single-degree-of-freedom structure was presented in [15]. The system was considered as a non-ideal system (NIS) due to a full interaction of the structure motions, with the energy source, a DC motor with limited power supply. The nonlinear piezoelectric material was considered in the coupling mathematical model. The system was found to be a bi-stable Duffing oscillator presenting chaotic behaviour. The structure was controlled using a pendulum as a passive control and improved the energy harvesting of the system.

The passive control using a pendulum was implemented by [16], showing to be a very useful controller and energy harvesting tune.

In this work, we will explore the passive control using a pendulum coupled in a simple portal frame of two-degree-of-freedom structure, as studied by [17,18]. We will show the control and improvement of energy harvesting of the system setting a control parameter of the pendulum.

2. Energy harvesting modelling

The energy harvesting model studied in this paper, illustrated in Fig. 1, consists in a portal frame of two-degrees-of-freedom with a piezoelectric material coupled to a column and a linear pendulum coupled to the mid span of the beam, i.e., the pendulum will move according to the symmetric mode movement.

The portal frame consists of two columns clamped in their bases with height h and a horizontal beam pinned to the columns at both ends with length L. Both column and beam have flexural stiffness EI. The mass at mid span of the beam is M. The masses of the columns are m. The structure is modelled as a lumped mass system with two-degrees-of-freedom. The coordinate q_1 is related to the horizontal displacement in the sway mode, with natural frequency ω_1, and q_2 to the mid-span vertical displacement of the beam in the symmetric mode, with natural frequency ω_2. The linear stiffness of the columns and the beam can be evaluated by a Rayleigh-Ritz procedure using cubic trial functions. Geometric nonlinearity is introduced by considering the shortening due to bending of the columns and of the beam.

The linear pendulum is coupled to the mass of the mid-span of the beam, consisting of a mass m_3, rotational stiffness k_3, and rotational damping as c_3.

The nonlinear piezoelectric material is coupled to the column as an electric circuit, which is excited by an internal voltage (back-emf) proportional to the mechanical velocity, in order to harvest energy from the vibration of the column. This circuit consists of a resistor R, a produced charge Q and a capacitance C_p of the capacitor. The dimensionless relation of nonlinearity of the piezoceramic is

502

given by $d(q_1) = \theta(1+\Theta|q_1|)$ defined by [7], where θ is the linear piezoelectric coefficient and Θ is the nonlinear piezoelectric coefficient.

The mechanical system is based-excited by a harmonic force which has amplitude F_0 and external frequency ω_n. This external force frequency is set near resonance with the symmetric mode. Frequency ω_2 is also set twice the frequency of the sway mode as $2\omega_1 = \omega_2$. These conditions of resonance are necessary to have modal coupling in the nonlinear adopted model. In these conditions, we have the saturation phenomenon.
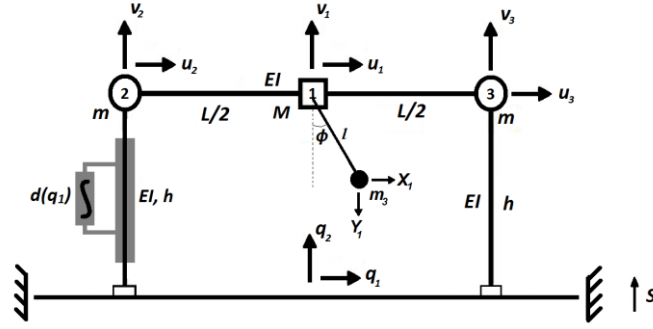

Figure 1. Physical mode of a simple portal frame of two-degree-of-freedom structure

2.1. Modelling of the dynamical system

The modelling of the physical model will be developed by Lagrange`s energy method which uses the Lagrangian function and Euler-Lagrange equation.

Nodal displacements, shown in Fig. 1, are

$$u_1 = q_1 \qquad u_2 = u_1 + \frac{B}{4}v_1^2 \qquad u_3 = u_1 - \frac{B}{4}v_1^2 \qquad X_1 = -u_1 + l\sin\phi$$

$$v_1 = q_2 \qquad v_2 = -\frac{A}{2}u_1^2 \qquad v_3 = -\frac{A}{2}u_1^2 \qquad Y_1 = v_1 + l\cos\phi \tag{1}$$

where $A = 6/5h$ and $B = 24/5L$. The stiffness of the beam and column calculated by the Rayleigh-Ritz method are, respectively, $k_b = 48EI/L^3$ and $k_c = 3EI/h^3$.

The generalized coordinates considered here, are the displacements of the mass at the mid span of the beam M. Using nodal displacements of (1), the kinetic energy is defined in Eq. (2).

$$T = \frac{1}{2}M\left(\dot{u}_1^2 + \dot{v}_1^2\right) + \frac{1}{2}m\left(2\dot{u}_1^2\right) + \frac{1}{2}m_3\left(\dot{X}_1^2 + \dot{Y}_1^2\right) \tag{2}$$

Introducing the generalized coordinates q_1 and q_2, the kinetic energy becomes to Eq. (3).

$$T = \frac{1}{2}M\left(\dot{q}_1^2 + \dot{q}_2^2\right) + \frac{1}{2}m\left(2\dot{q}_1^2\right) + \frac{1}{2}m_3\left(\dot{q}_1^2 + \dot{q}_2^2 + l^2\dot{\phi}^2 + 2l\dot{\phi}\left(\dot{q}_1\cos\phi + \dot{q}_2\sin\phi\right)\right) \tag{3}$$

The potential energy of the system is given by the strain energy of the structure, the stiffness of the pendulum, the work of the weight of the masses of the beam, columns and pendulum, and by electrical potential part of the piezoelectric circuit with the contribution of the piezoelectric and the capacitor, resulting in Eq. (4).

$$U = \frac{1}{2}k_c\left(u_2^2 + u_3^2\right) + \frac{1}{2}k_b\left(v_1 - \frac{v_2+v_3}{2}\right)^2 + mg\left(v_2 + v_3\right) + Mgv_1 + m_3gY_1 + ...$$
$$...\frac{1}{2}k_3\phi^2 - \frac{d(q_1)}{C_p}Q(u_2+v_2) + \frac{1}{2}\frac{Q^2}{C_p} \tag{4}$$

Substituting (1) in (4), in terms of the general coordinates q_1, q_2, ϕ and Q, we have the potential energy in Eq. (5).

$$U = \left(k_c - mgA\right)q_1^2 + \frac{1}{2}k_b\left(q_2^2 + Aq_2q_1^2\right) + Mgq_2 + m_3g\left(-q_2 + l\cos\phi\right) + \frac{1}{2}k_3\phi^2 - ...$$
$$...+ \frac{d(q_1)}{C_p}Q\left(q_1 + \frac{B}{4}q_2^2\right) + \frac{1}{2}\frac{Q^2}{C_p} \tag{5}$$

Now, we consider energy dissipation of the system, comprising the structural and pendulum damping defined by a Rayleigh function and the resistor of the electrical circuit. Then it follows in Eq. (6).

$$D = \frac{1}{2}c_1\dot{q}_1^2 + \frac{1}{2}c_2\dot{q}_2^2 + \frac{1}{2}c_3\dot{\phi}^2 + \frac{1}{2}R\dot{Q}^2 \tag{6}$$

The harmonic excitation force is given by (7).

$$S = F_0\cos(\omega_n t) \tag{7}$$

The Lagrangian function is defined by Eq. (8). Substituting Eqs. (3) and (5) in Eq. (8) we have the Lagrangian of Eq. (9).

$$L(q,\dot{q},t) = T - U \tag{8}$$

$$L = \frac{1}{2}M\left(\dot{q}_1^2 + \dot{q}_2^2\right) + \frac{1}{2}m\left(2\dot{q}_1^2\right) + \frac{1}{2}m_4\dot{q}_4^2 - \begin{bmatrix} \left(k_c - mgA\right)q_1^2 + \frac{1}{2}k_b\left(q_2^2 + Aq_2q_1^2\right) + ... \\ Mgq_2 + m_3g\left(-q_2 + l\cos\phi\right) + \frac{1}{2}k_3\phi^2 - ... \\ \frac{d(q_1)}{C_p}Q\left(q_1 + \frac{B}{4}q_2^2\right) + \frac{1}{2}\frac{Q^2}{C_p} \end{bmatrix} \tag{9}$$

Now, using Euler-Lagrange, Eq. (10), we have the equation of motion of the system that are Eqs. (11), (12), (13) and (14).

$$\frac{d}{dt}\left(\frac{\partial L}{\partial \dot{q}_i}\right) - \frac{\partial L}{\partial q_i} + \frac{\partial D}{\partial \dot{q}_i} = Q_{ext} \qquad i = 1,4 \tag{10}$$

$$(2m + M + m_3)\ddot{q}_1 + 2(k_c - mgA)q_1 + k_b A q_2 q_1 + c_1 \dot{q}_1 = m_3 l(\ddot{\phi}\cos\phi - \dot{\phi}^2 \sin\phi) + \frac{d(q_1)}{C_p}Q \qquad (11)$$

$$(M + m_3)\ddot{q}_2 + k_b q_2 + c_2 \dot{q}_2 + (M + m_3)g + \frac{Ak_b}{2}q_1^2 = F_0 \cos\omega_n t + m_3 l(\ddot{\phi}\sin\phi + \dot{\phi}^2 \cos\phi) + \frac{d(q_1)}{C_p}\frac{B}{2}Qq_2$$
$$(12)$$

$$m_3 l^2 \ddot{\phi} + c_3 \dot{\phi} + k_3 \phi + m_3 l[\ddot{q}_1 \cos\phi + (\ddot{q}_2 - g)\sin\phi] = 0 \qquad (13)$$

$$R\dot{Q} - \frac{d(q_1)}{C_p}\left(q_1 + \frac{B}{4}q_2^2\right) + \frac{Q}{C_p} = 0 \qquad (14)$$

For a better analysis, a dimensionless process is carried out, resulting the dimensionless equations of motion of the system as follows

$$x_1'' + \mu_1 x_1' + x_1 + \alpha_1 x_1 x_2 = \gamma_1 \left(\phi'' \cos\phi - \phi'^2 \sin\phi\right) + \theta(1 + \Theta|x_1|)\delta_1 V \qquad (15)$$

$$x_2'' + \mu_2 x_2' + \omega_2^2 x_2 + \alpha_2 x_1^2 + G_0 = E_0 \cos\Omega\tau + \theta(1 + \Theta|x_1|)\delta_2 V x_2 + \gamma_2 \left(\phi'' \sin\phi + \phi'^2 \cos\phi\right) \qquad (16)$$

$$\phi'' + \mu_3 \phi' + \omega_3^2 \phi + \gamma_3 x_1'' \cos\phi + (\gamma_4 x_2'' - G_3)\sin\phi = 0 \qquad (17)$$

$$V' - \theta(1 + \Theta|x_1|)(\delta_3 x_1 + \delta_4 x_2^2) + \delta_3 V = 0 \qquad (18)$$

where dimensionless parameters are

$$x_1 = \frac{q_1}{h}, \qquad x_2 = \frac{q_2}{L}, \qquad V = \frac{Q}{q_0}, \qquad \tau = \omega_1 t, \qquad \omega_1 = \sqrt{\frac{2(k_c - mgA)}{M_T}}, \qquad \hat{d}(x_1) = \frac{h}{q_0}d(q_1)$$

$$\mu_1 = \frac{c_1}{M_T \omega_1}, \qquad \mu_2 = \frac{c_2}{(M + m_3)\omega_1}, \qquad G_2 = \frac{g}{\omega_1^2 L}, \qquad E_0 = \frac{F_0}{(M + m_3)\omega_1^2 L}, \qquad G_3 = \frac{g}{\omega_1^2 l}, \qquad e = \frac{1}{m_3}$$

$$\omega_2 = \frac{1}{\omega_1}\sqrt{\frac{k_b}{(M + m_3)}}, \qquad \alpha_1 = \frac{Ak_b L}{M_T \omega_1^2}, \qquad \alpha_2 = \frac{Ak_b h^2}{2(M + m_3)\omega_1^2 L}, \qquad \Omega = \frac{\omega_n}{\omega_1}, \qquad \gamma_3 = \frac{h}{L} \qquad (19)$$

$$\delta_1 = \frac{q_0^2}{\omega_1^2 h^2 M_T C_p}, \qquad \delta_2 = \frac{Bq_0^2}{2(M + m_3)\omega_1^2 h C_p}, \qquad \delta_3 = \frac{1}{RC_p \omega_1}, \qquad \delta_4 = \frac{BL^2}{4RC_p \omega_1 h}, \qquad \gamma_4 = \frac{l}{L}$$

$$\omega_3 = \frac{1}{\omega_1}\sqrt{\frac{k_3}{m_3}}, \qquad M_T = (2m + M + m_3), \qquad \mu_3 = \frac{c_3}{m_3 l^2 \omega_1}, \qquad \gamma_1 = \frac{m_3 l}{M_T h}, \qquad \gamma_2 = \frac{m_3 l}{(M + m_3)L}$$

To calculate the harvested power of the system, Eqs. (20) and (21) are given as dimensional and dimensionless harvested power, respectively.

$$P = R\dot{Q}^2 \qquad (20)$$

$$P = R_0 V'^2 \qquad (21)$$

where $R_0 = R(\omega_1 q_0)^2$.

The average power of the system can be calculated by Eq. (22), as in [7,15,17,18].

$$P_{avg} = \frac{1}{T}\int_0^T P(\tau)d\tau \qquad (22)$$

Next, section 3 will discuss numerical simulations with and without the pendulum, considering the nonlinear piezoelectric contribution fixed in $\Theta = 1$.

3. Numerical simulations results and discussions

The numerical simulations realized in this work were performed by MATLAB© software. The parameters considered to the numerical simulations are in Tab. 1. The parameters were adjusted to has saturation phenomenon at the portal frame system, that is, $\omega_2 = 2\omega_1$, and the external force frequency is in resonance with the symmetric mode ($\Omega = \omega_2 + \sigma$), where σ is a detuning factor.

Table 1. Dimensional System Parameters

Parameters	Values	Means	k_3 [Nm/rad]	0.403	Torsional Pendulum Stiffness
g [m/s²]	9.81	Gravity acceleration	L [m]	0.52	Beam Length
M [kg]	2.00	Beam Mass	h [m]	0.36	Column Length
m [kg]	0.50	Column Mass	l [m]	0.16	Pendulum Length
			F_0[N]	40	External Excitation Amplitude
m_3 [kg]	Vary	Pendulum Mass	R [kΩ]	100	Piezoelectric Resistance
c_1[Ns/m]	0.001	Column Damping	C_p[μF]	1	Piezoelectric Capacitance
c_2[Ns/m]	0.002	Beam Damping	ω_n [rad/s]	146.9	External Excitation Frequency
c_3[Ns/rad]	0.061	Pendulum Damping	θ	0.1	Linear Piezoelectric Coefficient
EI [Nm²]	128	Linear Stiffness	Θ	1	Nonlinear Piezoelectric Coefficient

A new control parameter will be considered in order to configure the system with the optimal energy harvesting and behaviour of the system. This new parameter will be defined in eq. (23).

$$e = \frac{1}{m_3} \tag{23}$$

The parameter "e" will be varied with an acceptable ratio that the pendulum mass (m_3) should not overpass the value of the mass of the mid span (M). This interval is $0.5 \leq e \leq 100$.

Next, we will present results of numerical simulations considering and not considering the passive control, and in the end, compare the results each other showing the contribution of the pendulum as a passive controller.

3.1. Dynamical analysis of the portal frame structure

In this section, we will show some analysis of behaviour and energy harvesting of the system without the pendulum coupling to show the saturation phenomenon and its advantage to harvest energy. Using the parameters of Tab. 1, next figures provide results of the analysis.

Figures 2a and 2b show the bifurcation diagrams of the horizontal and vertical movement, respectively, related to the external force frequency. We can see some values of the frequency that the system tends to be chaotic. The interval of the frequency showed in the bifurcation diagrams shows the relation of resonance between the vertical movement and the external excitation.
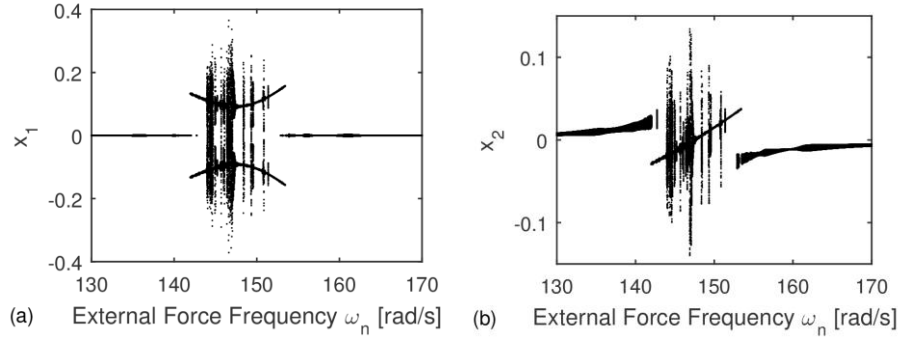

Figure 2. Bifurcation diagrams of (a) Horizontal movement, (b) Vertical movement.

The external force frequency $\omega_n = 146.9$rad/s (the same as Tab. 1) will be analyzed in order to comparison, because it is in the chaotic area of the bifurcation. Therefore, next simulations we will consider the external frequency as $\omega_n = 146.9$rad/s.

Figures 3a and 3b show the Poincaré maps of the horizontal and vertical movement, respectively, in order to analyze the behaviour of the system. We see that the system is chaotic.
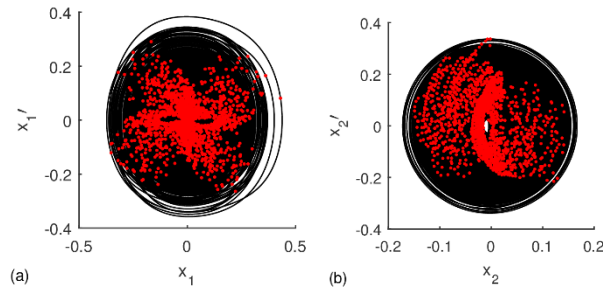

Figure 3. Phase plane (in black) and Poincaré maps (red dots) of; (a) horizontal movement, (b) vertical movement

Finally, we calculated the average harvested power of the chaotic system, and it is 9.169, approximately.

In next section, we will show the influence of the pendulum coupled to the mass "M" of the mid-span of the beam to the behaviour and energy harvesting of the system.

507

3.2. Analysis of the pendulum coupled to the dynamical system

In this section, we will perform some analysis of behaviour and energy harvesting of the system with the pendulum coupled to the portal frame. To the analysis of the control of the chaotic behaviour, we will set a control parameter by "e". This control parameter is the inverse of the mass ($e = 1/m_3$), so we can see the influence of the mass at the behaviour of the system.

To follow the same line as in Sec. 3.1, we will consider the external force frequency as in Tab. 1 to the next simulations.

Firstly, we built a bifurcation diagram related to the control parameter and we can carry some results. Figures 4a, 4b and 4c show the bifurcation diagram of the horizontal, vertical and pendulum movement. Figure 5 shows the average harvested power related to the control parameter. We see some intervals of e that controlled the chaotic behaviour, forcing it to a periodic behaviour. This interval is approximately $25 \leq e \leq 68$ (region 1). The average power at region (1) is approximately 4.80. In region (2), $e < 25$, we see a great improvement of the energy harvesting; a peak of 69.02 amount of power, however, the behaviour is most of time quasiperiodic, sometimes the system presents periodic behaviour. In region (3), $e > 68$, we see the average harvested power increasing slowly from 4.80 to 8.63, approximately, but the behaviour tends to be quasiperiodic all the time. Analyzing the full interval of e, we see no chaotic behaviour.
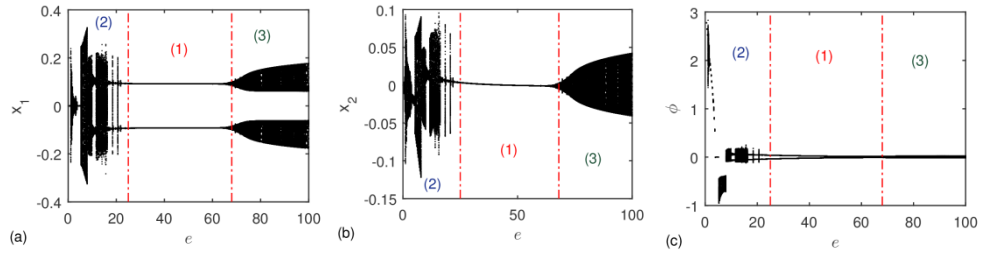

Figure 4. Bifurcation diagram related to the control parameter "e" of (a) horizontal movement, (b) vertical movement and (c) pendulum movement
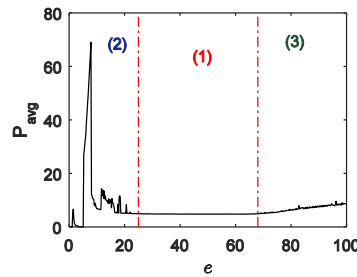

Figure 5. Parametrical analysis of the control parameter "e" related to the average harvested power

4. Conclusions

This work presented the energy harvesting of a simple portal frame of two-degrees-of-freedom structure using a pendulum as a passive control.

The pendulum showed to be very useful as a controller, it eliminated the chaotic behaviour, forcing the system to a periodic and quasiperiodic behaviour, it will depend on the value of the parameter control "*e*".

The energy harvesting could be improved. We see in Fig. 5 that some regions of the parametrical analysis have more or less harvested power. In region (1) the system presented periodic behaviour all the time, while in region (2) and (3) the system presented most of time quasiperiodic behaviour. However, the average power goes from 4.80 to 69.02, approximately. It will depend on the value of "*e*".

The advantage of using a passive control is that, it not necessary any electronic component to control the system, as an active control. Therefore, we can tune the energy harvesting choosing a desired parameter control.

Based on the results obtained in this paper, we should compare the efficiency between the NES [19], which is a small mass-spring-damping system coupled to a degree-of-freedom of the main structure, and the present pendulum approach.

References

[1] Crawley, E. F., and Anderson, E. H. Detailed models of piezoceramic actuation of beams. *Journal of Intelligent Material Systems and Structures*,*1*(1), (1990), 4-25.

[2] Erturk, A., and Inman, D. J. Piezoelectric energy harvesting. John Wiley & Sons, 2011.

[3] Erturk, A., Hoffmann, J., and Inman, D. J. A piezomagnetoelastic structure for broadband vibration energy harvesting. Applied Physics Letters, 94(25), (2009), 254102.

[4] Litak, G., Friswell, M. I., Kwuimy, C. A. K., Adhikari, S., and Borowiec, M. Energy harvesting by two magnetopiezoelastic oscillators with mistuning. Theoretical and Applied Mechanics Letters, 2(4), (2012), 043009.

[5] Stephen, N. G.. On energy harvesting from ambient vibration. Journal of Sound and Vibration, 293(1), (2006), 409-425.

[6] Priya, S., and Inman, D. J. (Eds.). Energy harvesting technologies (Vol. 21). New York: Springer. 2009.

[7] Triplett, A., and Quinn, D. D.. The effect of non-linear piezoelectric coupling on vibration-based energy harvesting. *Journal of Intelligent Material Systems and Structures*, *20*(16), (2009), 1959-1967.

[8] Daqaq, M. F., Masana, R., Erturk, A., & Quinn, D. D.. On the role of nonlinearities in vibratory energy harvesting: a critical review and discussion. *Applied Mechanics Reviews*, *66*(4), (2014), 040801.

[9] Mook, D. T., Plaut, R. H., and HaQuang, N.. The influence of an internal resonance on non-linear structural vibrations under subharmonic resonance conditions. Journal of Sound and Vibration, 102(4), (1985), 473-492.

[10] Nayfeh, A. H., and Mook, D. T.. Nonlinear oscillations. John Wiley & Sons. 2008.

[11] Nayfeh A. H., Nonlinear interactions (Wiley, New York), 2000.

[12] Pai, P. F., Wen, B., Naser, A. S., and Schulz, M. J.. Structural vibration control using PZT patches and non-linear phenomena. Journal of Sound and vibration, 215(2), (1998), 273-296.

[13] Tusset, A. M., Piccirillo, V., Bueno, A. M., Balthazar, J. M., Sado, D., Felix, J. L. P., and da Fonseca, R. M. L. R. Chaos control and sensitivity analysis of a double pendulum arm excited by an RLC circuit based nonlinear shaker. Journal of Vibration and Control, (2015),1077546314564782.

[14] Felix, J. L. P., Balthazar, J. M., and Brasil, R. M. On saturation control of a non-ideal vibrating portal frame foundation type shear-building. Journal of Vibration and Control, 11(1), (2005), 121-136.

[15] Iliuk, I., Balthazar, J. M., Tusset, A. M., Piqueira, J. R. C., de Pontes, B. R., Felix, J. L. P., and Bueno, Á. M. A non-ideal portal frame energy harvester controlled using a pendulum. *The European Physical Journal Special Topics*, *222*(7), (2013), 1575-1586.

[16] Arbex, H. C., Balthazar, J. M., de Pontes Junior, B. R., da Fonseca, R. M. L. R., Felix, J. L. P., Tusset, A. M., and Bueno, Á. M.. On nonlinear dynamics behavior and control of a new model of a magnetically levitated vibrating system, excited by an unbalanced DC motor of limited power supply. *Journal of the Brazilian Society of Mechanical Sciences and Engineering*, (2014), 1-12.

[17] Balthazar, J. M., Rocha, R. T., Brasil, R. M. F. L., Tusset, A. M., de Pontes, B. R., and Silveira, M.. Mode saturation, mode coupling and energy harvesting from ambient vibration in a portal frame structure. In*ASME 2014 International Design Engineering Technical Conferences and Computers and Information in Engineering Conference* (pp. V008T11A044-V008T11A044). American Society of Mechanical Engineers. (2014, August).

[18] Rocha, R. T.; Balthazar, J.M.; Tusset, A. M.; Piccirillo, V.; Felix, J. L. P. and Brasil, R. M. L. R. F.. On energy harvesting of a flexible portal frame support exploiting the saturation phenomenon. In: ASME 2015 International Design Engineering Technical Conferences & Computers and Information in Engineering Conference (IDETC/CIE 2015), 2015, Boston, Massachusetts, USA. Proceedings of ASME-IDETC/CIE 2015. NY, USA: ASME, 2015. v. 2015. p. 1. (Technical review/presented).

[19] Vakakis, A. F.. Nonlinear targeted energy transfer in mechanical and structural systems (Vol. 156). Springer Science and Business Media, 2008.

Rodrigo Tumolin Rocha, M.Sc. (Ph.D. student): São Paulo State University (UNESP), 17033-360, Bauru, SP, Brazil (*digao.rocha@gmail.com*). The author gave a presentation of this paper during one of the conference sessions.

José Manoel Balthazar, Professor: Aeronautics Technological Institute (ITA), 12228-900, São José dos Campos, SP, Brasil, and São Paulo State University (UNESP), 17033-360, Bauru, SP, Brazil (*jmbaltha@gmail.com*).

Angelo Marcelo Tusset, Ph.D: Federal Technological University of Paraná (UTFPR), 83016-210, Ponta Grossa, PR, Brazil (*tusset@utfpr.edu.br*).

Vinicius Piccirillo, Ph.D: Federal Technological University of Paraná (UTFPR), 83016-210, Ponta Grossa, PR, Brazil (viniciuspiccirillo@yahoo.com.br).

Reyolando M.L.R. Fonseca Brasil, Professor: Federal University of ABC (UFABC), 09210-180, Santo André, SP, Brazil. (*reyolando.brasil@ufabc.edu.br*).

Jorge L. Palacios Felix, Ph.D: Federal University of Pampa (UNIPAMPA), 96412-420, Alegrete, RS, Brazil (*Jorge.felix@unipampa.edu.br*).

Passive and semi-active vibroisolation of a horizontal platform (CON164-15)

Stefan Segla, Milan Žmindák, Martin Orecny

Abstract: The paper deals with modelling, control and optimization of a horizontal platform suspension system, which is kinematically excited in two mutually perpendicular directions. The platform is intended to be used as the working machine seat suspension in the machine cabin. Its primary goal is to reduce horizontal vibration of the seat, while the vertical vibration is reduced by the seat itself. Three alternatives of the platform are investigated. The first one is suspended with passive elements, the second one is suspended using idealized semi-active dampers and the third one is equipped with magnetorheological dampers. The skyhook control algorithm is applied to control the idealized semi-active and also magnetorheological dampers. The design parameters of the mechanical and also control parts of the three suspensions are optimized using multi-objective optimization with the objective function expressing minimization of the frequency weighted accelerations and relative displacements. The numerical simulation results show that using idealized semi-active and also magnetorheological platform suspensions gives significant platform vibration reduction compared with the passive platform suspension.

1. Introduction

The operators of various land vehicles and machines are exposed to vibrations due to their operation. Prolonged exposure to vibrations has a significant influence on the operator's fatigue and can even lead to a deteriorating health state. Among human inner organs the vertebra is the most affected. Medical research studies presented by Griffin in [1, 2] showed the need for proper suspension design ensuring desirable comfort of the operator. Another need is related to the controllability of working machines in the fields of the heavy earth-moving machinery and mobile agricultural machinery.

A lot of research has been devoted to the mitigation of the vertical vibrations in various kinds of vehicles. The conventional seat or vehicle suspension involves passive springs (often air-springs) and dampers. Multicriteria optimization techniques are often applied to determine the optimum values of the suspension damping and stiffness parameters leading to optimum dynamic performance of the passive suspensions. Stein et al. [3] studied locomotive driver′s seat vertical suspension with an adjustable damper. The seat model was augmented with the seat cushion dynamic model and a two-parameter optimization was performed. Maciejewski et al. presented in [4] comparison of transmissibility functions for a conventional and modified passive suspension of working machine seats. Vibro-isolation properties of the modified system were improved by a modification of an air-

spring and shock absorber. Segla and Trišović in [5] used 1.5 degree of freedom Zener′s model to model and optimize a working machine seat suspension. The paper also points on the possibility of improving the dynamic characteristics of the seat with the use of a passive dynamic vibration absorber. In [6] the effect of asymmetry on vertical dynamic response of railway vehicles was investigated and in [7] possibilities of multi-objective optimization for selecting dynamic characteristics of seat suspension systems and quarter-car models were presented.

Active suspension system involves replacing the conventional suspension elements with an actuator. It uses the external power supply for generating the active force that is regulated by a control system reacting to system parameters (displacement, velocity and acceleration). This system is still costly, involving a number of precision components, and its energetic demand is high. The most important characteristics of these systems can be found e.g. in [8], [9]. Maciejewski et al. in [10] investigated the dynamic response of an active vibro-isolating pneumatic suspension seat. Active control of the air-spring force used a triple feedback loop control system. Misselhorn et al. [11] presented a testing method in which real-time measurements on physical hardware replace the mathematical model of the vehicle model during simulation.

Semi-active suspensions fill the gap between active and passive systems. The idea of the active system can be modified so that the actuator is only capable of dissipating energy. The semi-active suspension system is characterized by a rapidly adjustable damper parallel with a spring which supports the static load. Hardware requirements are considerably less. Required external energy is in general very small [8]. Magnetorheological (MR) dampers are mostly used semi-active devices in automotive engineering. The key feature of an MR damper is the magnetorheological oil whose rheological properties can be altered by applying a magnetic field. By controlling the field variable damping force can be produced. Overview of semi-active control algorithms (balance, skyhook and groundhook algorithms), MR and friction dampers, vehicle modelling and human body analysis can be found in [9]. Georgiou et al. [7] presented comparison of passive and semi-active suspension systems with a constant horizontal speed over roads involving an isolated or a distributed geometric irregularity. Optimization was based on three performance criteria related to ride comfort, suspension travel and road holding.

2. Dynamic and mathematical models of passive platform suspension

In Fig. 1, the dynamic model of a passive suspension system is presented. It consists of a rectangular plate of mass m, linear springs k and linear dampers c.

Special ball bearings are assumed to be used between the working machine cabin and the horizontal platform. Low friction of the bearings enables neglecting friction forces between the cabin and the platform.
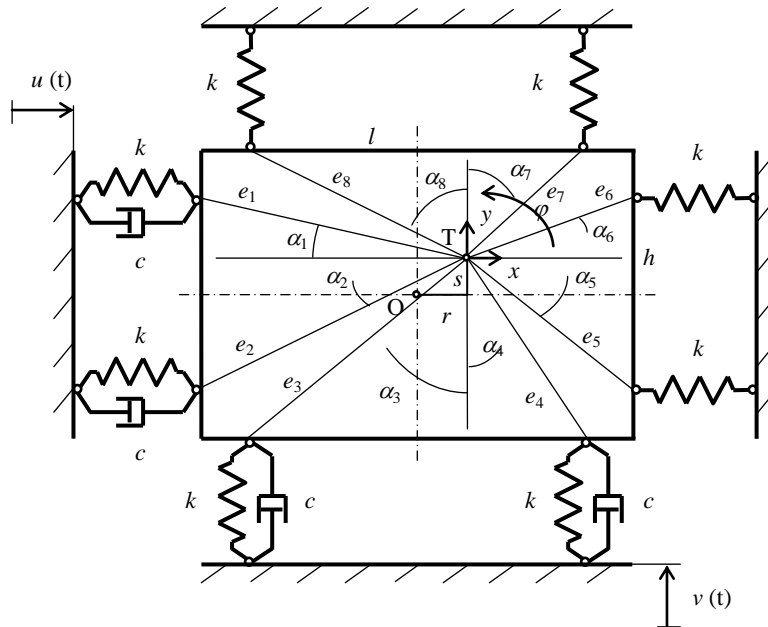
Figure 1. Passive platform suspension.

Time functions u(t) and v(t) represent kinematic excitation of the platform induced by the vibrating cabin. They were obtained experimentally in the cabin of the bucket-wheel excavator Schrs 1320 [12] in a coal strip mine in Bílina (the Czech Republic), Fig. 2. The bucket-wheel excavator is one of the most suitable possibilities of application of the horizontal platform.

Figure 2. Bucket-wheel excavator Schrs 1320.

In the following the equations of small plane motion will be derived for the platform. The absolute linear displacements x and y of the platform center of mass T and the angular displacement φ, Fig. 1, determine an instantaneous position of the platform. Point O is the geometric center of the rectangular plate of dimensions l and h. The points O and T are not identical in order to take into account actual placing of the real seat with an operator sitting on it.

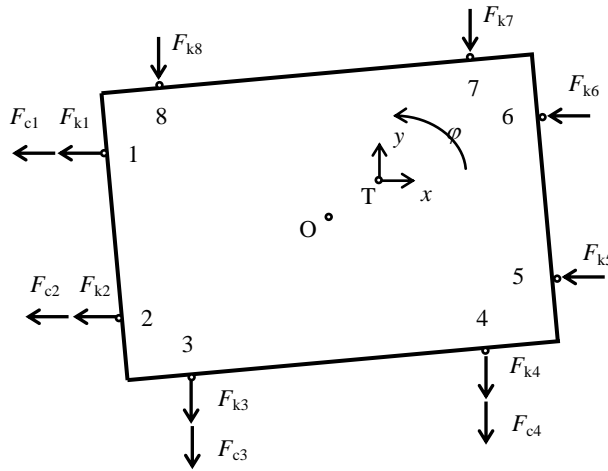Assuming small motions of the platform, the motion equations can be written in the form (see Fig. 3)

Figure 3. Free body diagram.

$$m\,\ddot{x} = -\sum_{i=1,2,5,6} F_{ki} - \sum_{i=1,2} F_{ci}, \tag{1}$$

$$m\,\ddot{y} = -\sum_{i=3,4,7,8} F_{ki} - \sum_{i=3,4} F_{ci}, \tag{2}$$

$$I_T\,\ddot{\varphi} = \sum_{i=1,3,6,8} F_{ki}\,e_i \sin\alpha_i - \sum_{i=2,4,5,7} F_{ki}\,e_i \sin\alpha_i + \sum_{i=1,3} F_{ci}\,e_i \sin\alpha_i - \sum_{i=2,4} F_{ci}\,e_i \sin\alpha_i, \tag{3}$$

where x, y and φ are generalized coordinates – linear displacements x and y of the platform centroid T and angular displacement φ of the platform, m is the platform mass, I_T is the mass moment of inertia of the platform about its center of mass T, l, h and e_i are geometric dimensions of the platform, r and s are geometric lenghts determining position of the platform center of mass T with regard to the geometric center of the platform O, α_i are angels, F_{ki} (i = 1, 2, … , 8) are spring forces acting at points 1, 2, … , 8, F_{ci} (i = 1, 2, … , 4) are damping forces acting at points 1, 2, 3 and 4.

The spring and damping forces acting on the platform can be written e.g. for points 1 and 2 in the form

$$F_{k1} = k \left(x - u - \varphi \, e_1 \sin \alpha_1 \right), \qquad F_{k2} = k \left(x - u + \varphi \, e_2 \sin \alpha_2 \right), \tag{4}$$

$$F_{c1} = k \left(\dot{x} - \dot{u} - \dot{\varphi} \, e_1 \sin \alpha_1 \right), \qquad F_{c2} = k \left(\dot{x} - \dot{u} + \dot{\varphi} \, e_2 \sin \alpha_2 \right), \tag{5}$$

In chapter 6 the optimum values of the chosen design variables k and c will be determined by minimizing the objective function expressing the frequency weighted platform accelerations and relative displacements.

3. Dynamic and mathematical models of idealized semi-active platform suspension

Dynamic model of this suspension differs from the passive suspension, Fig. 1, in using idealized semi-active dampers instead of passive ones.

The control law of the semi-active dampers is based on the sky-hook control. The task of each damper is to generate the same force, with the same direction and magnitude, as the fictitious sky-hook damper (with the damping coefficient c_{sky}) acting on the platform would generate. For example, for point 1, Fig. 4, the fictitious sky-hook damper is placed between points 1 and 1'. The point 1' absolute location in the horizontal direction is fixed. The semi-active damper is capable of generating the damping force of the required direction only if the direction of the absolute velocity $\dot{x}_1$ of point 1 and the relative velocity between the platform and the working machine cabin are of the same direction. It can be expressed by the following inequality
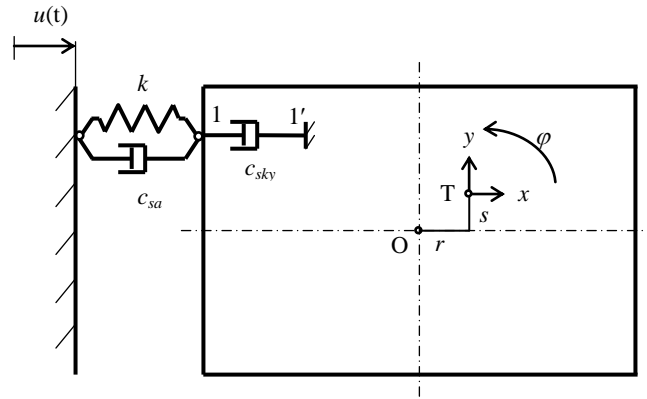

Figure 4. Idealized semi-active platform suspension.

$$\dot{x}_1 \left(\dot{x}_1 - \dot{u} \right) > 0. \tag{6}$$

The following equations hold for the semi-active damping forces at points 1 to 4

$$F_{sa,1} = c_{sky} \left(\dot{x} - \dot{\varphi} \, e_1 \sin \alpha_1 \right) \quad \text{if} \quad \left(\dot{x} - \dot{\varphi} \, e_1 \sin \alpha_1 \right) \left(\dot{x} - \dot{u} - \dot{\varphi} \, e_1 \sin \alpha_1 \right) > 0, \tag{7}$$

$$F_{sa,2} = c_{sky} \left(\dot{x} + \dot{\varphi} \, e_2 \sin \alpha_2 \right) \quad \text{if} \quad \left(\dot{x} + \dot{\varphi} \, e_2 \sin \alpha_2 \right) \left(\dot{x} - \dot{u} + \dot{\varphi} \, e_2 \sin \alpha_2 \right) > 0, \tag{8}$$

$$F_{sa,3} = c_{sky} \left(\dot{y} + \dot{\varphi} \, e_3 \sin \alpha_3 \right) \quad \text{if} \quad \left(\dot{x} + \dot{\varphi} \, e_3 \sin \alpha_3 \right) \left(\dot{x} - \dot{v} + \dot{\varphi} \, e_3 \sin \alpha_3 \right) > 0, \tag{9}$$

$$F_{sa,4} = c_{sky} \left(\dot{y} - \dot{\varphi} \, e_4 \sin \alpha_4 \right) \quad \text{if} \quad \left(\dot{y} - \dot{\varphi} \, e_4 \sin \alpha_4 \right) \left(\dot{y} - \dot{v} - \dot{\varphi} \, e_4 \sin \alpha_4 \right) > 0, \tag{10}$$

If condition (6) is not met then the semi-active damper is not capable of generating the damping force of the required direction and it has to be in the "off" state.

On the magnitude of the semi-active damping force $F_{sa,i}$ an upper limit preventing the damper from generating higher damping forces than a real magnetorheological (MR) damper can do will be applied. In the "off" state of the semi-active damper a zero damping force $F_{sa,i}$ will be applied (unlike to real MR dampers).

In chapter 6 the optimum values of the chosen design variables c_{sky} and k will be determined by the same procedure as described at the end of chapter 2.

4. Dynamic and mathematical models of platform suspension with MR dampers

The dynamic model of this suspension differs from the idealized semi-active suspension in using MR dampers [13] instead of the idealized semi-active ones. In literature a lot of mathematical models of real MR dampers, whose parameters were obtained experimentally, can be found. It is of great importance to choose MR dampers whose parameters are suitable from the point of view of the force range, its magnitude in the "off" state and time delay.

The mathematical model of the MR platform suspension differs from the idealized semi-active platform model in replacing eqs. (7) to (10). The governing equations of the control force produced by the i-th MR damper are expressed in the form

$$F_{MR,i} = \sigma_a z_i + \sigma_0 z_i U_i + \sigma_1 \dot{z}_i + \sigma_2 A_i + \sigma_b A_i U_i, \quad i = 1, 2, ..., 4, \tag{11}$$

$$\dot{z}_i = A_i - a_0 \left| A_i \right| z_i, \tag{12}$$

$$\begin{aligned} A_1 &= \left(\dot{x} - \dot{u} - \dot{\varphi} \, e_1 \sin \alpha_1 \right), \quad A_2 = \left(\dot{x} - \dot{u} + \dot{\varphi} \, e_2 \sin \alpha_2 \right), \\ A_3 &= \left(\dot{y} - \dot{v} + \dot{\varphi} \, e_3 \sin \alpha_3 \right), \quad A_4 = \left(\dot{y} - \dot{v} - \dot{\varphi} \, e_4 \sin \alpha_4 \right). \end{aligned} \tag{13}$$

These equations are modified LuGre dynamic friction model described in [13]. In eqs. (11), (12) z_i denotes an internal state variable related to the MR fluid deformation and U_i is the applied voltage that acts as the control input. $U_{i,max} = 4$ V and the other parameters are defined in [13].

A two-state control strategy based on sky-hook control is used and it is defined by the following equations and conditions

$$U_i = U_{opt}, \quad \text{if} \quad A_i B_i > 0, \quad otherwise \quad U_i = 0, \quad i = 1, 2, ..., 4, \tag{14}$$

$$
\begin{aligned}
B_1 &= (\dot{x} - \dot{\varphi}\, e_1 \sin \alpha_1), & B_2 &= (\dot{x} + \dot{\varphi}\, e_2 \sin \alpha_2), \\
B_3 &= (\dot{y} + \dot{\varphi}\, e_3 \sin \alpha_3), & B_4 &= (\dot{y} - \dot{\varphi}\, e_4 \sin \alpha_4).
\end{aligned}
\tag{15}
$$

The optimum values of the chosen design parameters k and U_{opt} will be determined in chapter 6.

5. Formulation of the optimization problem

Optimization of the platform suspension parameters is necessary because of two opposite requirements

- minimization of the platform accelerations to protect the operator's health (maximization of his comfort),

- minimization of the platform relative displacements to ensure the controllability of the working machine.

Numerical simulations showed that angular displacements φ and also angular accelerations $\ddot{\varphi}$ are negligible compared with the linear displacements x, y and accelerations $\ddot{x}$, $\ddot{y}$. This justifies their neglecting in the objective function.

In order to improve clarity of the optimization results both frequency weighted effective accelerations in the x and y directions will create one function f_1. The same holds for both effective relative displacements in the x and y directions. It is justified by negligible differences of the effective values of these quantities in the x and y directions. The same holds for the kinematic excitations in both directions.

The best compromise between the opposite criteria mentioned above create a nonlinear optimization problem. An appropriate procedure of its solving is by minimizing the objective function

$$f_{op} = w \frac{f_1}{f_{1,nom}} + (w-1) \frac{f_2}{f_{2,nom}}, \tag{16}$$

where w is the weighting coefficient which depends on the significance of the criteria ($w \in \langle 0, 1 \rangle$). Function f_1 is expressing the platform frequency weighted effective accelerations in the x and y directions

$$f_1 = \sqrt{\frac{1}{T} \int_0^T \ddot{x}^2(t)\, d t} + \sqrt{\frac{1}{T} \int_0^T \ddot{y}^2(t)\, d t}, \tag{17}$$

and function f_2 is expressing the platform effective relative displacements in the x and y directions

$$f_2 = \sqrt{\frac{1}{T}\int_0^T (x(t) - u(t))^2 \, dt} + \sqrt{\frac{1}{T}\int_0^T (y(t) - v(t))^2 \, dt}, \tag{18}$$

where T is the time of integration. It must be sufficiently long to capture the dynamics of the system.

Both the effective values f_1 and f_2 in eq. (16) are devided by their nominal values (defined for the mean values of the design variables in their search intervals), because the values are not commensurable.

6. Optimization results and discussion

The specified values of the platform suspension are: mass of the platform $m = 220$ kg, mass moment of inertia of the platform $I_T = 22.5$ kg.m^2, $l = 0.75$ m, $h = 0.65$ m, $r = 0.09$ m, $s = 0.11$ m, $e_1 = 0.5227$ m, $e_2 = 0.6131$ m, $e_3 = 0.6085$ m, $e_4 = 0.4721$ m, $e_5 = 0.4592$ m, $e_6 = 0.3290$ m, $e_7 = 0.3254$ m, $e_8 = 0.5032$ m, $\alpha_1 = 22°$, $\alpha_2 = 37.7°$, $\alpha_3 = 47°$, $\alpha_4 = 28.5°$, $\alpha_5 = 54.7°$, $\alpha_6 = 36.4°$, $\alpha_7 = 43.7°$, $\alpha_8 = 62.2°$ (see Fig. 1). The weighting coefficient is $w = 0.9$ and the time of integration is T = 20 s.

Using the Global Optimization Toolbox of MATLAB [12] the following results of optimization were obtained

– the passive platform suspension: $k = 4600$ N/m, $c = 650$ N.s/m,

– the idealized semi-active platform suspension: $k = 4050$ N/m, $c_{sky} = 8740$ N.s/m,

– the MR semi-active platform suspension: $k = 3000$ N/m, $U_{opt} = 3.02$ V.

The performance of both semi-active suspensions are compared with the passive suspension. Table 1 presents effective relative displacements and also frequency weighted effective accelerations (according to ISO 2631). It can be seen from the table that both semi-active suspensions bring significant improvements compared with the passive suspension.

Table 1. Effective relative displacements and frequency weighted effective accelerations.

Suspension	Direction	Effective relative displacement [m]	Frequency weighted effective acceleration [m.s^{-2}]
Passive	x	0.0023	0.2533
	y	0.0022	0.2455
Idealized semi-active	x	0.00072	0.1855
	y	0.00083	0.2166
MR semi-active	x	0.0015	0.2124
	y	0.0014	0.2043

In Fig. 5 the platform accelerations of the passive versus the idealized semi-active suspension in the *x* direction are presented and in Fig. 6 the platform accelerations of the passive versus the MR semi-active suspension in the *x* direction are shown. The time interval of 20 s was reduced to 10 s to better see the details.
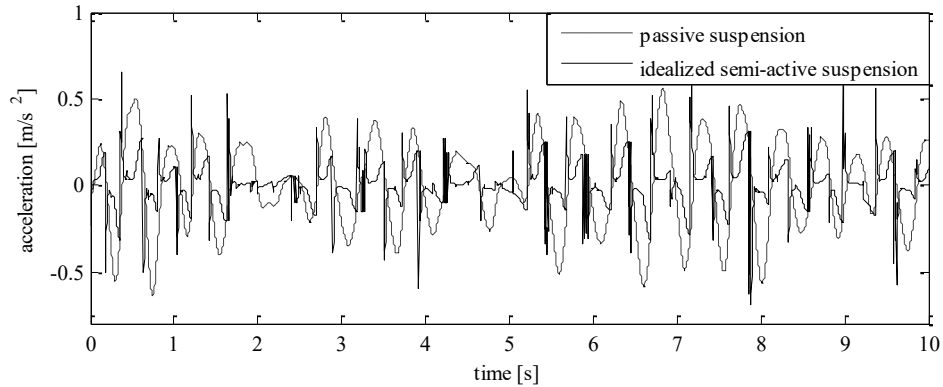

Figure 5. Acceleration in the *x* direction (passive versus idealized semi-active suspension).
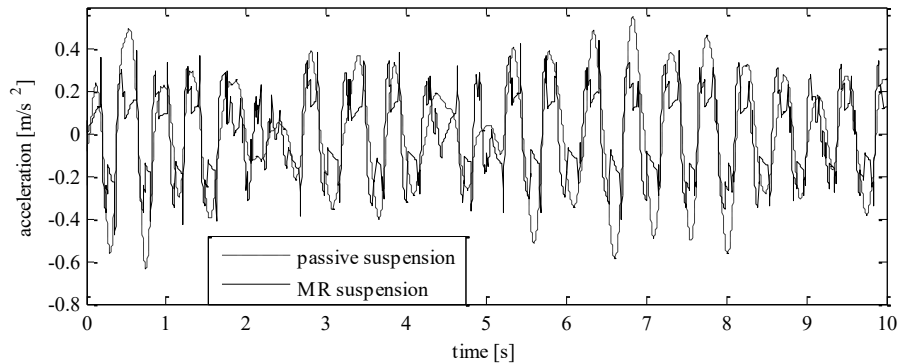

Figure 6. Acceleration in the *x* direction (passive versus MR semi-active suspension).

7. Conclusions

In the paper three different suspensions of a horizontal platform which can be used in the cabin of a working machine are presented. Their parameters were optimized in the time domain. The control algorithms used to control the idealized and MR semi-active dampers are based on sky-hook control (continuous and two-state control). The results of numerical simulations show significant platform vibration reduction of semi-active platform suspensions compared with the passive platform suspension.

Acknowledgments

References

[1] Griffin, M. *Handbook of Human Vibrations.* Academic Press, London, 1994.

[2] Griffin, M. Discomfort from feeling vehicle vibration. *Vehicle System Dynamics*. 45, 7-8 (2007), 679–698.

[3] Stein, G.J., Múčka, P., Gunston, T.P. A study of locomotive driver's seat vertical suspension system with adjustable damper. *Vehicle System Dynamics*. 47, 3 (2009), 363–386.

[4] Maciejewski, I., Meyer, L., Krzyzynski, T. Modelling and multi-criteria optimisation of passive seat suspension vibro-isolating properties. *Journal of Sound and Vibration* 324 (2009), 520–538.

[5] Segla, S., Trišović, N. Modeling and optimization of passive seat suspension. *American Journal of Mechanical Engineering* 1, 7 (2013), 221–225.

[6] Nangolo, F., Soukup, J. The effect of asymmetry on vertical dynamic response of railway vehicles. *Manufacturing Technology*. 14, 3 (2014), 375–380.

[7] Georgiou, G., Verros, G., Natsiavas, S. Multi-objective optimization of quarter-car models with a passive or semi-active suspension system. *Vehicle System Dynamics*. 45, 1 (2007), 77–92.

[8] Venhovens, P.J.Th. *Optimal Control of Vehicle Suspensions*. Delft University of Technology, Delft, 1993.

[9] Guglielmino, E., Sireteanu, T., Stammers, Ch.W., Ghita, G., Giuclea, M. *Semi-active Suspension Control. Improved vehicle Ride and Road Friendliness*. Springer, London, 2008.

[10] Maciejewski, I., Meyer, L., Krzyzynski, T. The vibration damping effectiveness of an active seat suspension system and its robustness to varying mass loading. *Journal of Sound and Vibration* 329 (2010), 3898–3914.

[11] Misselhorn, W.E., Theron, N.J., Els, P.S. Investigation of hardware-in-the-loop for use in suspension development. *Vehicle System Dynamics*. 44, 1 (2006), 65–81.

[12] Orecny, P. Semi-active suspension of a horizontal platform with magnetorheological dampers and dynamic absorbers. Ph.D. thesis, Technical University of Košice, 2015, Segla, S.

[13] Cetin, S. et al. Adaptive control of structures with MR damper. In: 18th IEEE International Conference on Control Applications, Saint Petersburg (Russia), July 8-10, 2009.

[14] *Global Optimization Toolbox User's Guide*. The MathWorks, Inc., Natick, MA, 2015.

Stefan Segla, Professor: Technical University of Košice, Faculty of Mechanical Engineering, Letná 9, 042 00, Slovakia (*stefan.segla@tuke.sk*). The author gave a presentation of this paper during one of the conference sessions.

Milan Zmindak, Professor: University of Žilina, Faculty of Mechanical Engineering, Univerzitná 1, 010 26, Slovakia (*milan.zmindak*@fstroj.uniza.sk)

Martin Orecny, M.Sc. (Ph.D. student): Technical University of Košice, Faculty of Mechanical Engineering, Letná 9, 042 00, Slovakia (*martin.orecny@gmail.com*).

Limit cycles in dynamics of bluff bodies of airflow (STA058-15)

Yury Selyutskiy

Abstract: Motion of elastically supported bluff body under the action of airflow is considered. It is supposed that the body can perform translational motion in the direction perpendicular to the flow. In order to describe unsteady aerodynamic effects, the empirical model is used that was developed earlier for simulation of dynamics of aerodynamic pendulum. Limit cycles appearing in the obtained dynamic system are analyzed. Dependence of their amplitude and frequency upon the flow speed is studied. Influence of model parameters upon the characteristics of the cycles is studied. It is shown that simulation results are in qualitative agreement with available experimental data.

1. Introduction

One of well-known and commonly observed phenomena occurring for structures submerged in flow are vortex induced vibrations. These vibrations are performed in direction transversal to the flow velocity and occur for different types of bluff bodies (like pipes, bridges, transmission lines, suspended cables, etc.) in a certain range of flow speeds and can intensify the fatigue effects or, sometimes, lead to serious damage of the construction. This engineering importance gave rise to great interest to the problem, which resulted in appearance of many papers dedicated to it (e.g., [1-5]).

Experimental investigation of transverse oscillations of bluff bodies in flow is technically very complicated. However, a number of studies of this kind was performed ([6], [7], etc.). These tests revealed hysteresis of the amplitude and the frequency of the oscillations when the flow speed increases and then decreases. This phenomenon is due not to the properties of the elastic mounting of the body, but to the inherent properties of the flow.

In order to perform efficient parametric analysis of body behavior without having to integrate Navier-Stocks equations, a range of phenomenological models (e.g., [2, 5]) were proposed to describe the said vortex-induced oscillations of bluff bodies. Most of them are based on so-called wake oscillator approach, when an additional ordinary differential equation of the second order is added to the original motion equations, and the extra variable represents the unsteady lift force acting upon the body. This equation is usually of the Van-der-Pol type. Such method allows describing some features observed in experiments.

In [8], an attached oscillator approach was proposed to describe the behavior of the aerodynamic pendulum. This model is based on introducing an additional degree of freedom that integrally simulates the internal dynamics of the flow. It was shown that this approach allows obtaining results that are in good agreement with available experimental data.

Comparison of the attached oscillator model and wake oscillator models suggests that a more general phenomenological approach could be developed that would allow simulating characteristic features of behavior of both bluff and streamlined bodies. Such approach would be useful, for instance, to simulate unsteady effects arising for wing-type bodies at large angles of attack.

2. Motion equations

Consider a bluff body (like cylinder, prism, etc.) elastically mounted and immersed in a flow in such a way that it can move in the direction perpendicular to the flow speed (Fig. 1). Position of the body is determined by the ordinate Y of its center of mass C.

Assume that under steady conditions (that is, when no wake takes place) there arises no lift force. Separate the aerodynamic load upon the body into two components: steady one, F_a^s, determined by the drag force directed along the body velocity with respect to the flow; and unsteady one, F_u. In order to describe the latter, we use the attached oscillator model proposed in [8] and allowing simulating unsteady effects in dynamics of airfoils. The coordinate z of the oscillator with respect to the body will be the second degree of freedom.

However, for the case of a bluff body, this model needs some modifications. This is due to the fact that the wake is essentially nonlinear phenomenon, and it is necessary to introduce some nonlinearity into the model. So, we assume that an additional force F_{nl} acts upon the attached oscillator, and this force depends upon $\dot{z}$ in a non-linear way.
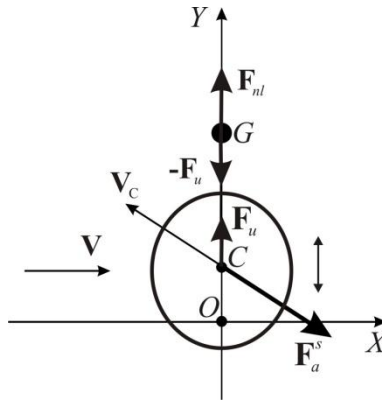

Figure 1. *Body with the attached oscillator*

The steady aerodynamic force (drag) is applied to the body in its center of pressure and directed against the velocity of this point. Assume for simplicity sake that the center of pressure coincides with the center of mass. Then F_a^s can be represented in the following form:

$$F_a^s = -\frac{\rho S}{2} C_d V_C^2 ,$$

where $V_C = \sqrt{V^2 + \dot{Y}^2}$ ρ is the density of the medium, S is the characteristic area of the body, V is the flow speed, C_d is the dimensionless drag coefficient. We suppose that this coefficient remains constant.

Taking into account the above stated, behavior of the system comprising the body and the attached oscillator is described by the following dynamical system:

$$\begin{aligned} \bar{M}\ddot{Y} + \bar{D}\dot{Y} + \bar{K}Y &= F_{ay}^s + F_u \\ \bar{m}\,\ddot{z} + \ddot{Y} &= -F_u + F_{nl} \end{aligned} \qquad (1)$$

Here $\bar{M}$ is the mass of the body, $\bar{K}$ and $\bar{D}$ are stiffness and damping of the elastic mounting, $\bar{m}$ is the mass of the attached oscillator.

Similarly to [8], suppose that the force of interaction between the attached oscillator and the body, F_u, is linear elastic force depending only on relative position and speed of the oscillator with respect to the body:

$$F_u = \bar{k}z + \bar{h}\dot{z}$$

As for F_{nl}, it seems reasonable to assume that this force should non-linearly depend on the oscillator speed:

$$F_{nl} = \bar{h}_1\dot{z} - \bar{h}_3\dot{z}^3$$

Hence, (1) can be rewritten as follows:

$$\begin{aligned} \bar{M}\ddot{Y} + \bar{D}\dot{Y} + \bar{K}Y &= -\frac{\rho S}{2} C_d V\dot{Y} + \bar{k}z + \bar{h}\dot{z} \\ \bar{m}\,\ddot{z} + \ddot{Y} &= -\bar{k}z - (\bar{h} - \bar{h}_1)\dot{z} - \bar{h}_3\dot{z}^3 \end{aligned} \qquad (2)$$

It should be noted that $\bar{h} - \bar{h}_1 < 0$, so that the oscillator would be unstable, and limit cycles would appear.

In order to make the notation clearer, we rewrite (2) in non-dimensional form. For that, introduce the dimensionless time $\tau = t\sqrt{\bar{K}/\bar{M}}$ and the following non-dimensional parameters and variables:

$$y = \frac{Y}{R}, \quad \eta = \frac{z}{R}, \quad \zeta = \frac{\bar{D}}{2\sqrt{\bar{M}\bar{K}}}, \quad u = \frac{V}{R}\sqrt{\frac{\bar{M}}{\bar{K}}}, \quad M = \frac{2\bar{M}}{\rho SR}$$

$$m = \frac{2\bar{m}}{\rho SR}, \quad k = \frac{2\bar{k}R}{\rho SV^2}, \quad h = \frac{2\bar{h}}{\rho SV}, \quad h_1 = \frac{2\bar{h_1}}{\rho SV}, \quad h_3 = \frac{2V\bar{h_3}}{\rho S}$$

Here R is characteristic dimension of the body.

Then equations (2) can be rewritten as follows (dots mean derivatives with respect to τ):

$$\ddot{y} + \left(2\zeta + \frac{C_d u}{M}\right)\dot{y} + y = \frac{1}{M}\ k\eta + h\dot{\eta}$$

$$m\ \ddot{\eta} + \ddot{y}\ + k\eta - (h_1 - h)\dot{\eta} + h_3\dot{\eta}^3 = 0$$

(3)

Evidently, this dynamic system has only one equilibrium position, and it is always unstable.

3.   Limit cycles

In order to obtain some estimation of parameters of limit cycles arising in the system, we search the solution corresponding to the limit cycle in form

$$y = y_0 \sin\ \omega t\ , \quad \eta = \eta_0 \sin\ \omega t + \varphi_0$$

(4)

In what follows, we'll assume that the body is heavy, that is, $M = \varepsilon^{-2} \gg 1$ (ε is a small parameter). Such relation is quite common for solid bodies moving in air. Besides, suppose that the structural damping is small:

$$\zeta = \zeta_0 \varepsilon^2 \ll 1$$

Represent the cycle frequency as $\omega = \omega_0 + \varepsilon^2 \omega_1$. Then, substituting (4) in (3), using the harmonic balance method, and neglecting members of the second order of smallness and higher, we obtain:

$$y_0 \frac{1 - \omega_0^2}{\varepsilon^2} - \eta_0 u\ uk\cos\varphi_0 - h\omega_0\sin\varphi_0\ - 2y_0\omega_1\omega_0 = 0$$

$$-\eta_0 u\ h\omega_0\cos\varphi_0 + uk\sin\varphi_0\ + C_d u + 2\zeta_0\ y_0\omega_0 = 0$$

$$\eta_0\ m\omega_0^2 - u^2 k\ + m\omega_0^2 y_0\cos\varphi_0 = 0$$

$$3\omega_0^2\eta_0^3 h_3 - 4\eta_0\ h_1 - h\ u^2 + 4\omega_0 y_0 mu\sin\varphi_0 = 0$$

(5)

From (5) it immediately follows that $\omega_0 = 1$. The second and the third equations of (5) yield the following relation for the phase φ_0 :

$$C_d u + 2\zeta_0\ \tan^2\varphi_0 + \frac{mku^2}{m - ku^2}\tan\varphi_0 + C_d u + 2\zeta_0 + \frac{mhu}{m - ku^2} = 0$$

The amplitudes are given by the following formulae:

$$\eta_0 = \sqrt{\frac{4u}{3h_3}\left(m - ku^2\right)\tan\varphi_0 + \left(h_1 - h\right)u}\ ,\quad y_0 = \eta_0 u\frac{h\omega_0\cos\varphi_0 + uk\sin\varphi_0}{C_d u + 2\zeta_0} \tag{6}$$

Finally, for ω_1 we have:

$$\omega_1 = -\frac{\eta_0 u\left(uk\cos\varphi_0 - h\sin\varphi_0\right)}{2y_0}$$

Thus, the frequency of the cycle is given by the following formula:

$$\omega = 1 - \frac{\eta_0 u\left(uk\cos\varphi_0 - h\sin\varphi_0\right)}{2y_0 M}$$

Note, however, that the above relations for parameters of cycles are valid only under assumption that both amplitudes are not small: $y_0 \sim 1$, $\eta_0 \sim 1$.

However, this system has yet another cycle. In order to determine its characteristics, we'll search for it under assumption that $y_0 = y_2\varepsilon^2$, $\eta_0 \sim 1$.

Then we obtain the following equations:

$$\begin{aligned}
&y_2\left(1 - \omega^2\right) - \eta_0 u\left(uk\cos\varphi_0 - h\omega\sin\varphi_0\right) = 0 \\
&\eta_0 u\left(h\omega\cos\varphi_0 + uk\sin\varphi_0\right) = 0 \\
&\eta_0\left(m\omega^2 - u^2 k\right) = 0 \\
&3\omega^2\eta_0^3 h_3 - 4\eta_0\left(h_1 - h\right)u^2 = 0
\end{aligned} \tag{7}$$

From the third equation of (7) we obtain that

$$\omega = u\sqrt{\frac{k}{m}}$$

This means that the amplitude of the cycle is proportional to the flow speed, which agrees with the fact that the shedding frequency increases linearly with the flow speed when it is far enough from the resonance with the natural frequency.

For the amplitude of the attached oscillator we have:

$$\eta_0 = \sqrt{\frac{4m}{3k}\frac{h_1 - h}{h_3}}$$

Note that this amplitude does not depend on the flow speed in a first approximation.

For the phase one readily obtains:

$$\tan\varphi_0 = \frac{\sqrt{km}}{h}$$

Finally, (7) yields the following formula for the amplitude of the body:

$$y_0 = \sqrt{\frac{4}{3}\frac{h_1 - h}{h_3}}\, \frac{hu}{|m - u^2 k|}\, \frac{\sqrt{km} - h}{\sqrt{km + h^2}}$$

Evidently, these formulae can be used only in the range of flow speeds where $m - u^2 k$ is not small in absolute value.

Thus, two limit cycles exist in the system, which makes prerequisites for hysteretic behavior.

4. Numerical simulation

Basing on the above mathematical model, numerical simulation was performed in order to study behavior of the body at different flow speeds.

For the dimensionless body mass there was used the following value: $M = 500$. Like in [2], we assume that the total drag coefficient is constant, and $C_d = 2$.
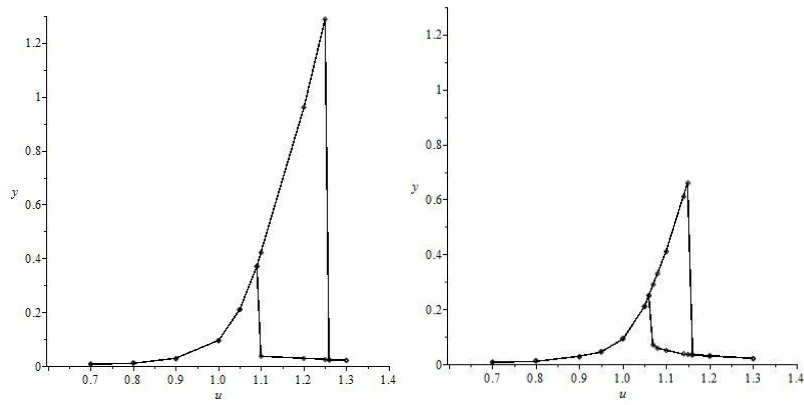
Figure 2. *a)* $\zeta = 0$; *b)* $\zeta = 0.0015$.
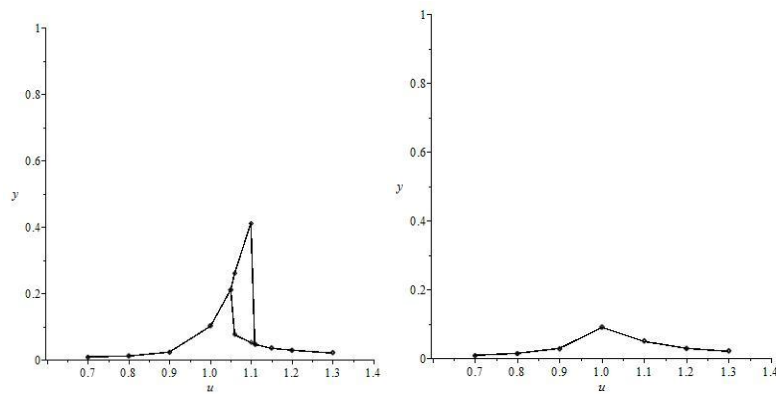
Figure 3. *a)* $\zeta = 0.003$; *b)* $\zeta = 0.01$.

The values of parameters of the attached oscillator parameters should be determined in such a way as to provide reasonable agreement with experimental data. Here, the following values were chosen:

$$m = 1.5, \quad k = 1.6, \quad h = 1.0, \quad h_1 = 2.5, \quad h_3 = 0.5.$$

Dynamic system (3) was integrated numerically for different values of the structural damping ζ and different flow speeds. For each combination of parameters, limit cycles were found, and their characteristics were determined. Some results of computations are presented in Fig. 2, 3, where amplitudes of oscillations of the body are shown as functions of u.

Note that a hysteretic behavior is observed: in the area close to the resonance between the natural frequency of the body with its elastic support and the partial frequency of the attached oscillator, two attracting limit cycles are observed. This phenomenon, as well as the dependence of the limit cycle amplitude on the flow speed, is in qualitative agreement with results of experiments [6].

As the damping increases, the hysteresis zone becomes smaller, and finally disappears. In the same time, the speed corresponding to the maximum amplitude of oscillations decreases. Both these facts were also observed in tests [6].

5. Conclusions

Transverse oscillations of an elastically supported bluff body in airflow are considered, and its unsteady interaction with the flow is simulated using the attached oscillator model. Limit cycles appearing in the obtained dynamic system are analyzed. It is shown that simulation results are in qualitative agreement with available experimental data.

Thus, the attached oscillator model can be used as an element of a phenomenological approach that would allow describing unsteady effects arising both for streamlined and bluff bodies.

Acknowledgments

References

[1] Blevins, R.D. Flow-Induced Vibrations. Van Nostrand Reinhold, New York (1990).

[2] Balasubramanian, S., Skop, R.A. A nonlinear oscillator model for vortex shedding from cylinders and cones in uniform and shear flows. *J. of Fluids and Structures,* 10 (1996), 197–214.

[3] Bearman, P.W. Vortex shedding from oscillating bluff bodies. *Annual Review of Fluid Mechanics 16* (1984)*, 195–222.*

[4] Williamson, C.H.K., Govardhan, R. A brief review of recent results in vortex-induced vibrations. *J. Wind Engineering and Industrial Aerodynamics* 96 (2008), 713–735.

[5] Facchinetti, M.L., de Langre, E., Biolley, F. Coupling of structure and wake oscillators in vortex-induced vibrations. *J. of Fluids and Structures* 19 (2004), 123–140.

[6] Feng, C.C., The measurement of vortex-induced effects in flow past a stationary and oscillating circular and D-section cylinders. University of British Columbia, Vancouver (1968). 174 p.

[7] Khalak, A., Williamson, C.H.K. Motions, forces and mode transitions in vortex-induced vibrations at low mass-damping. *J. of Fluids and Structures* 13 (1999), 813–851.

[8] Selyutskiy, Yu.D., Samsonov, V.A., Andronov, P.R. On oscillations of aerodynamic pendulum. *Int. J. of Structural Stability and Dynamics* 13 (7) (2013), doi:10.1142/S0219455413400105.

Yury Selyutskiy, Ass. Professor: Institute of Mechanics of Lomonosov Moscow State University, Michurinsky prosp. 1, 119192, Moscow, Russia (*seliutski@imec.msu.ru*). The author gave a presentation of this paper during one of the conference sessions.

On rocking of a rigid body on a moving rough plane (STA132-15)

Yury Selyutskiy, Rinaldo Garziera, Luca Collini

Abstract: One of the most destructive effects of earthquakes upon buildings and other constructions is due to horizontal displacement of the ground. This paper proposes a simplified approach to description of behavior of tower-like structures in such conditions. For this aim, a plane-parallel motion of a rigid body over horizontal plane with dry friction is considered. It is assumed that the plane performs harmonic oscillations in horizontal direction. In order to describe collisions between the body and the supporting plane, Routh hypothesis is used. Conditions of overturning of the body are obtained for different values of amplitude and frequency of oscillations of the plane, depending on model parameters, such as body aspect ratio, friction coefficient, coefficient of restitution, etc.

1. Introduction

The behavior of different tall structures, such as monuments, towers, chimneys, oil or water tanks, etc., installed on a shaking foundation has been a problem of technical interest for many years. This is due, in particular, to the fact that such objects are especially vulnerable during earthquakes, and it's necessary to develop methods to prevent their overturning.

Study of dynamics of such bodies is related with the fundamental problem of describing the motion of bodies on a plane with dry friction. The complicated nature of the interaction between the body and the surface and presence of paradoxes (like Painleve paradoxes) and the practical importance of the topic led to appearance of a large number of studies dedicated to this topic. Results obtained in classical works by Routh, Painleve, McMillan, etc., were extended and complemented, for instance, in [1-3].

Another important problem related with rocking of blocks is modeling the collision between the block and the supporting plane in presence of dry friction. Some paradoxes were detected (like increase of mechanical energy after the collision) and ways of their solving were proposed (e.g., [4], [5]).

The first systematic research of rocking of a rigid block on moving horizontal plane was performed in [6]. This pioneering work was followed by a large number of subsequent studies (for example, [7-12]). In these works, an extensive study was performed of behavior of rocking rigid blocks, both free and forced. However, some specific effects due to the presence of dry friction with non-infinite coefficient are still to be investigated.

2. Motion equations

Consider a rigid block on a horizontal rough rigid plane. Suppose that the block can perform plane-parallel motion in vertical plane. Suppose also that the supporting plane can move along a fixed horizontal axis. Let OXY be the moving coordinate frame fixed to the supporting plane, X_G, Y_G be coordinates of the center of mass G of the block, and φ the angle between the block basement and the supporting plane (Fig. 1).
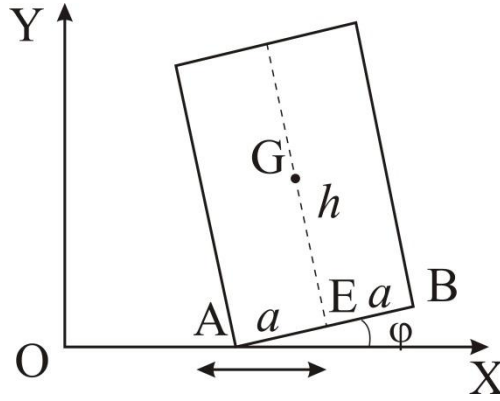

Figure 1. *Block on the moving plane.*

Equations describing the dynamics of the block depend on the state of motion: whether the block contacts the supporting plane or is in free flight; whether the block contacts the supporting plane in one point ($\varphi \neq 0$) or over the whole base ($\varphi = 0$); whether the contact point moves or not.

If the block remains in contact with the plane, and its base makes a non-zero angle with this plane, the following kinematical relations hold:

$$Y_G = h\cos\varphi + a\sin\varphi\,\mathrm{sgn}\,\varphi$$
$$\Delta X = h\sin\varphi - a\cos\varphi\,\mathrm{sgn}\,\varphi \tag{1}$$

Here a is the half-width of the block base, h is the distance from the base to the center of mass, ΔX is the distance between the projection of the center of mass onto the supporting plane and the contact point.

In this situation, motion equations can be written as follows:

$$m\ddot{X}_G = \tilde{F}_f - m\tilde{a}_e$$
$$-m\dot{\varphi}^2 Y_G - m\ddot{\varphi}\Delta X = \tilde{N} - mg \tag{2}$$
$$mr^2\ddot{\varphi} = \tilde{F}_f Y_G + \tilde{N}\Delta x$$

Here r is the radius of inertia of the block, m is the block mass, g is the gravity acceleration, $\tilde{F}_f$ is the friction force, $\tilde{N}$ is the normal reaction, $\tilde{a}_e$ is the acceleration of the supporting plane.

In order to simplify the notation, introduce the dimensionless time $\tau = t\sqrt{g/h}$ and the following non-dimensional parameters:

$$\alpha = \frac{a}{h}, \quad \rho = \frac{r}{h}, \quad F_f = \frac{\tilde{F}_f}{mg}, \quad N = \frac{\tilde{N}}{mg}, \quad a_e = \frac{\tilde{a}_e}{g}, \quad x_G = \frac{X_G}{h}, \quad y_G = \frac{Y_G}{h}, \quad \Delta x = \frac{\Delta X}{h}$$

Then equations (1) can be rewritten in non-dimensional form as follows (dot means the derivative with respect to τ):

$$\begin{aligned}
\ddot{x}_G &= F_f - a_e \\
-\dot{\varphi}^2 y_G - \ddot{\varphi}\Delta x &= N - 1 \\
\rho^2 \ddot{\varphi} &= F_f y_G + N\Delta x
\end{aligned} \tag{3}$$

In what follows, we'll assume that at the initial time the block is at rest in its "nominal" position (i.e., $\varphi = 0$). Besides, we suppose that the block height is much larger than the block width:

$$\alpha \ll 1$$

Under such assumptions, the block motion will be purely translational if the friction coefficient f is small enough (i.e., $f \leq \alpha$). In the same time, if the plane is perfectly rough, the body can perform rocking motion (and, possibly, turn over).

We'll consider an "intermediate" case of sufficiently large friction coefficient:

$$f > \frac{\alpha^2 + \rho^2}{\alpha} \tag{4}$$

One can readily show that in this situation pure translation is impossible.

Consider now different states of motion of the block and corresponding motion equations.

2.1. Motion with $\varphi \neq 0$ and with sliding

In this case, rotation angle is not zero (hence, there is only one contact point), and the contact point velocity v_C is also not zero.

Then from (3) we readily obtain

$$F_f = -fN \operatorname{sgn} v_C, \quad N = \frac{\rho^2\left(1 - y_G\dot{\varphi}^2\right)}{\Delta x^2 + \rho^2 - fy_G\Delta x \operatorname{sgn} v_C} \tag{5}$$

Consider slow enough motions of the body (that is, $\dot{\varphi} = \omega < \sqrt{1/y_G} \leq 1$). Then, for small φ, sliding is only possible if v_C and Δx are of different sign (the block slides on its rear edge); for larger φ, when Δx tends to zero, sliding is possible in both directions.

Note that if v_C and Δx are of the same sign, then there exists such angle φ, for which the denominator of the second relation of (5) vanishes. This situation can be interpreted as "friction impact" that results in instantaneous stop of the contact point.

Acceleration of the center of mass and angular acceleration are given by the following relations:

$$\ddot{x}_G = \frac{fy_G\omega^2\rho^2\,\mathrm{sgn}\,v_C + fy_G a_e\Delta x\,\mathrm{sgn}\,v_C - f\rho^2\,\mathrm{sgn}\,v_C - a_e\Delta x^2 - a_e\rho^2}{\Delta x^2 + \rho^2 - fy_G\Delta x\,\mathrm{sgn}\,v_C}$$

$$\ddot{\varphi} = \frac{fy_G^2\omega^2\,\mathrm{sgn}\,v_C - y_G\Delta x\omega^2 - fy_G\,\mathrm{sgn}\,v_C + \Delta x}{\Delta x^2 + \rho^2 - fy_G\Delta x\,\mathrm{sgn}\,v_C}$$

2.2. Motion with $\varphi \neq 0$ and without sliding

In this case, the contact point velocity is zero. First, determine the friction force and normal force required to maintain zero acceleration of this point:

$$F_f^* = \frac{y_G^2\Delta x\omega^2 + \Delta x^3\omega^2 + \Delta x\omega^2\rho^2 + a_e\Delta x^2 + a_e\rho^2 - y_G\Delta x}{1 + \alpha^2 + \rho^2},$$

$$N^* = -\frac{y_G^3\omega^2 + y_G\Delta x^2\omega^2 + y_G\omega^2\rho^2 + y_G a_e\Delta x - y_G^2 - \rho^2}{1 + \alpha^2 + \rho^2}$$

If $\left|F_f^*\right| \leq fN^*$ then instantaneous acceleration of the contact point is zero, and the block performs pure rocking. Hence:

$$\ddot{x}_G = \frac{y_G^2\Delta x\omega^2 + \Delta x^3\omega^2 + \Delta x\omega^2\rho^2 - a_e y_G^2 - y_G\Delta x}{1 + \alpha^2 + \rho^2},$$

$$\ddot{\varphi} = \frac{a_e y_G + \Delta x}{1 + \alpha^2 + \rho^2}$$

Note, however, that if $\Delta x \neq 0$ (that is, for almost all values of φ) there exist values of a_e, such that $N^* < 0$. This situation can be interpreted as a loss of contact with the supporting plane (bouncing of the block), and requires a more detailed analysis.

If $\left|F_f^*\right| > fN^* \geq 0$, then the instantaneous acceleration of the contact point is not zero, and the following relation holds:

$$F_f = fN\,\mathrm{sgn}\,F_f^*$$

Motion equations can be rewritten as follows:

$$\ddot{x}_G = \frac{-fy_G\omega^2\rho^2\,\mathrm{sgn}\,F_f^* - fy_G a_e\Delta x\,\mathrm{sgn}\,F_f^* + f\rho^2\,\mathrm{sgn}\,F_f^* - a_e\Delta x^2 - a_e\rho^2}{fy_G\Delta x\,\mathrm{sgn}\,F_{f*} + \Delta x^2 + \rho^2}$$

$$\ddot{\varphi} = \frac{-fy_G^2\omega^2\,\mathrm{sgn}\,F_f^* - y_G\Delta x\omega^2 + fy_G\,\mathrm{sgn}\,F_f^* + \Delta x}{fy_G\Delta x\,\mathrm{sgn}\,F_f^* + \Delta x^2 + \rho^2}$$

The normal force is given by the following formula:

$$N = -\frac{\rho^2 \left(y_G \omega^2 - 1\right)}{f y_G \Delta x \operatorname{sgn} F_f^* + \Delta x^2 + \rho^2}$$

If $N < 0$ (which takes place, for example, for large a_e such that $a_e \Delta x > 0$), the block loses contact with the supporting plane.

2.3. Motion with $\varphi = 0$ and zero angular speed

Now discuss the case when the block contacts the supporting plane with its total basement (i.e., $\varphi = 0$), and $\omega = 0$. Then second relation of (1) is not valid, and it is necessary to determine Δx from other considerations.

First, analyze the case of sliding. Then it is natural to assume that $\Delta x = \alpha \operatorname{sgn} v_C$, and we obtain the following relations for friction and normal forces:

$$F_f = -fN \operatorname{sgn} v_C, \quad N = -\frac{\rho^2}{f\alpha - \alpha^2 - \rho^2}.$$

But from (4) it follows that $N < 0$, hence, sliding of the block with the basement contacting the supporting plane is impossible.

Let now $v_C = 0$. One can easily obtain conditions for the block to remain at rest: $F_f = a_e$, $\Delta x = -a_e$. This occurs if $|a_e| \le \alpha$.

For larger values of a_e the angular acceleration can't remain zero. Find the friction and normal forces for which acceleration of the contact point would be zero:

$$F_f^{**} = \frac{a_e \alpha^2 + a_e \rho^2 - \alpha \operatorname{sgn} a_e}{1 + \alpha^2 + \rho^2}, \quad N^{**} = \frac{1 + \rho^2 + |a_e|\alpha}{1 + \alpha^2 + \rho^2} > 0$$

One can readily show that if (4) is satisfied then $\left|F_f^{**}\right| < fN^{**}$ for any a_e. Hence, acceleration of the contact point is zero, and motion equations are as follows:

$$\ddot{x}_G = \frac{-a_e - \alpha \operatorname{sgn} a_e}{1 + \alpha^2 + \rho^2},$$

$$\ddot{\varphi} = \frac{a_e + \alpha \operatorname{sgn} a_e}{1 + \alpha^2 + \rho^2}$$

Thus, in case of the large enough friction the block can't start sliding (even accompanied with rotation) from the "nominal" initial condition. Sliding can only begin when the block makes a non-zero angle with the supporting plane.

Now, it is necessary to consider the case when the angular speed of the body is not zero.

2.4. Collisions

If the angle φ becomes zero, and the angular speed is not zero, then collision takes place. In order to describe it, we'll use the Routh hypothesis about the relation between the normal and tangential impulses. The collision should be subdivided into two steps: deformation and restitution. First, consider the deformation phase.

Under the assumptions made earlier, the angular speed and the contact point velocity are of different sign before the collision (that is, the block slides on its rear edge). Let, for definiteness, $\varphi > 0$ before the collision, and, hence, the pre-collision angular speed be negative ($\omega_- < 0$). At the end of the deformation phase, the vertical speed of the new contact point becomes zero.

Impact theory yields the following equations:

$$\rho^2\ \omega' - \omega_-\ = \Delta Q_x^d + \alpha \Delta Q_y^d$$
$$\Delta Q_x^d = \omega_- - \omega' + v_C' - v_{C-}, \quad \Delta Q_y^d = -\alpha\ \omega_- + \omega' \tag{7}$$

Here ΔQ_x^d and ΔQ_y^d are horizontal and vertical impulses; "$-$" sign denotes values before the collision, and prime denotes values after the deformation phase.

Suppose that the contact point velocity becomes zero by the end of this phase. Then from (7) we obtain the following relations:

$$v_C' = 0, \quad \omega' = \frac{\rho^2 - \alpha^2 + 1}{\rho^2 + \alpha^2 + 1}\omega_- - \frac{1}{\rho^2 + \alpha^2 + 1}v_{C-}$$

Hence,

$$\Delta Q_y^d = -\frac{2\alpha\left(1 + \rho^2\right)}{1 + \rho^2 + \alpha^2}\omega_- + \frac{\alpha}{1 + \rho^2 + \alpha^2}v_{C-}, \quad \Delta Q_x^d = \frac{2\alpha^2}{1 + \rho^2 + \alpha^2}\omega_- - \frac{\rho^2 + \alpha^2}{1 + \rho^2 + \alpha^2}v_{C-}$$

Taking into account (4), one can readily show that

$$\left|\Delta Q_x^d\right| \le f \Delta Q_y^d$$

This means that friction is sufficient to maintain zero velocity of the contact point during the deformation phase.

Now consider the restitution phase. From Newton's hypothesis we obtain

$$\Delta Q_y^d = k \Delta Q_y^r$$

Here k is the restitution coefficient, ΔQ_y^r is the vertical impulse for the restitution phase.

Suppose that the horizontal velocity of the contact point by the end of the restitution phase is zero. Impact theory yields the following equations:

$$\rho^2 \, \omega_+ - \omega' = \Delta Q_x^r + \alpha \Delta Q_y^r$$

$$\Delta Q_x^r = \omega' - \omega_+ + v_{C+}, \quad \Delta Q_y^r = u_+ - \alpha \omega_+ + \alpha \omega' \tag{8}$$

Here u_+ is the vertical speed of the contact point after the restitution phase, and "+" sign denotes values after the collision.

From (8) we obtain:

$$\omega_+ = \frac{\rho^2 - \alpha^2 + 1 - 2\alpha^2 k}{1 + \alpha^2 + \rho^2} \omega_- - \frac{1 + \rho^2 - k\alpha^2}{\left(1 + \alpha^2 + \rho^2\right)\left(1 + \rho^2\right)} v_{C-}$$

$$u_+ = \frac{k\alpha^3}{1 + \rho^2}\left(-2\frac{\rho^2 + h^2 m}{1 + \alpha^2 + \rho^2} \omega_- + \frac{1}{1 + \alpha^2 + \rho^2} v_{C-}\right)$$

One can readily show that for $f \geq \alpha$ the inequality $\left|\Delta Q_x^r\right| \leq f \Delta Q_y^r$ holds.

Hence, the horizontal speed of the contact point remains zero during the restitution phase. As for the vertical speed, it has the third order of smallness under the assumption that $\alpha \ll 1$, which allows neglecting the free flight phase.

3. Numerical simulation

Basing on the above mathematical model, numerical simulation was performed of the block behavior for different laws of motion of the supporting plane (piecewise-constant and harmonic). We assumed that the collisions are perfectly inelastic ($k = 0$). The following values of parameters (satisfying (4)) were used for calculations:

$$\alpha = 0.1, \quad \rho = 0.3, \quad f = 1.5$$

Some results of computations are presented in Fig. 2-5. Blue lines denote the time-dependence of the angle φ, and green lines denote the time-dependence of the contact point speed v_C.
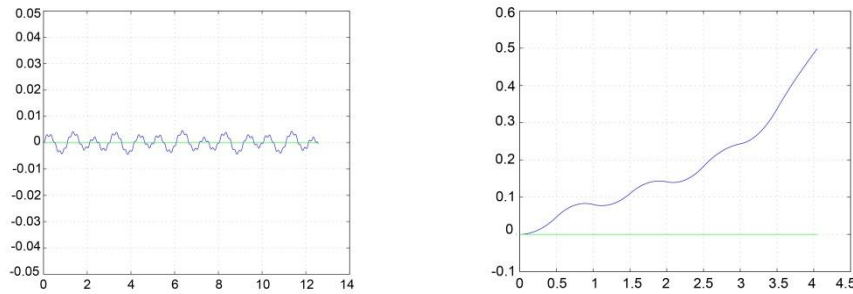

Figure 2. *a)* $a_e = \begin{cases} 0.5, & 2n-2 \leq 10t < 2n-1 \\ -0.5, & 2n-1 \leq 10t < 2n \end{cases}$, $n \in \mathbb{N}$; *b)* $a_e = \begin{cases} 0.5, & 2n-2 \leq 2t < 2n-1 \\ -0.5, & 2n-1 \leq 2t < 2n \end{cases}$, $n \in \mathbb{N}$.
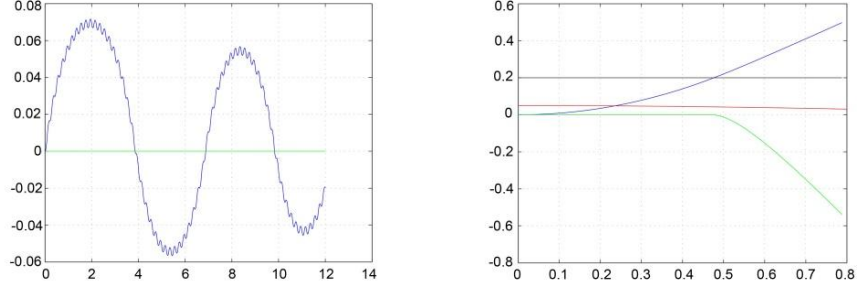
Figure 3. *a)* $a_e = \begin{cases} 2, & 2n-2 \le 10t < 2n-1 \\ -2, & 2n-1 \le 10t < 2n \end{cases}$, $n \in \mathbb{N}$; *b)* $a_e = \begin{cases} 2, & 2n-2 \le t < 2n-1 \\ -2, & 2n-1 \le t < 2n \end{cases}$, $n \in \mathbb{N}$.
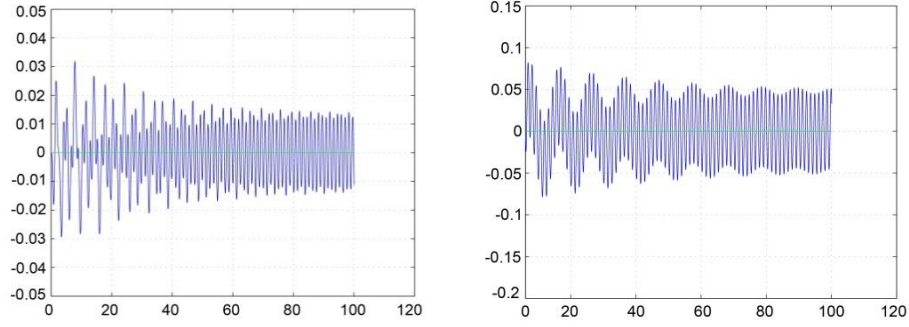

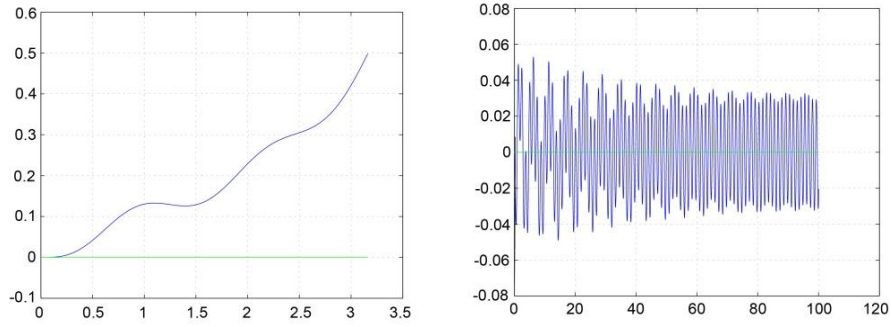**Figure 4.** *a)* $a_e = 0.25\sin(5t)$; *b)* $a_e = 0.5\sin(5t)$.

Figure 5. *a)* $a_e = 0.75\sin(5t)$; *b)* $a_e = 0.75\cos(5t)$.

The friction coefficient is large, so the block starts sliding only at high external acceleration, which leads to its overturning. For moderate accelerations, it performs pure rocking.

For periodic external acceleration, it is the relation between the magnitude of the acceleration and the period that determines if the block will overturn. Note, however, that the behavior of the block depends considerably not only on the amplitude and frequency of the excitation acceleration, but also on its phase (see Fig. 5).

A series of calculations was performed where the external acceleration was given by the formula $a_e = A\omega^2 \sin \omega t$. Basing on these computations, the boundary values of parameters A and ω were determined, for which rocking motion without overturning is still possible (so to speak, numerical criteria of overturning).
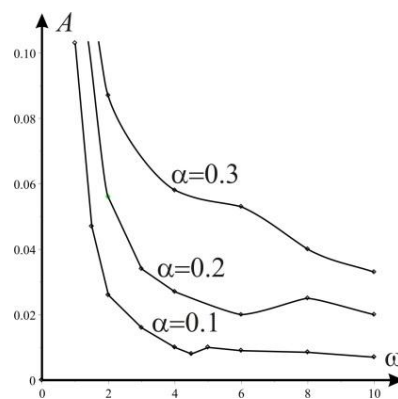

Figure 6. *Area of possible rocking without overturning in the plane of amplitudes and frequencies of the supporting plane displacement*

In Fig. 6, these boundaries are shown the areas in the plane of the mentioned parameters for different values of α. Motion without overturning is possible below corresponding curves. Note that they practically do not depend on friction coefficient in the considered range of f.

4. Conclusions

Dynamics of a rigid block on moving horizontal plane is studied with consideration of effects due to dry friction and collisions. Different phases of motion, including collisions, are considered for the case of large enough friction. Specific features of behavior of the block related with the presence of the dry friction are described. Influence of amplitudes and frequencies of the external acceleration upon the block motion is studied.

Acknowledgments

References

[1] Goyal, S., Ruina, A., Papadopoulos, J. Planar sliding with dry friction Part 2. Dynamics of motion. *Wear*, 143 (2) (1991), 331-352.

[2] Ivanov, A.P. A dynamically consistent model of the contact stresses in the plane motion of a rigid body. *J. Appl. Math. and Mech.,* 73 (2009), 134–144.

[3] Samsonov, V.A. On sliding of a puck. *Mechanics of Solids*, 48(5) (2013), 581-583.

[4] Stronge, W.J. Friction in collision: resolution of a paradox. *J. Appl. Phys.* 69(2), (1991), 610–612.

[5] Djerassi, S. Collision with friction; Part A: Newton's hypothesis. *Multibody Syst. Dyn.*, 21 (2009), 37–54.

[6] *Housner, G. W.* The behaviour of inverted pendulum structures during earthquakes. *Bull. Seism. Soc. Am.* 53, (1963), 403 417.

[7] Yim, C.-S., Chopra, A. K., Penzien, J. Rocking response of rigid blocks to earthquakes. *Earthquake Engineering & Structural Dynamics* 8 (6), (1980), 565–587.

[8] Ishiyama, Yu. Motions of rigid bodies and criteria for overturning by earthquake excitations. *Earthquake engineering and structural dynamics* 10, (1982), 635-650.

[9] Hogan, S.J. On the dynamics of rigid block motion under harmonic forcing. Earthquake Engineering, X World conference, (1992), 2817-2821.

[10] Lipscombe, P., S. Pellegrino, S. Free rocking of prismatic blocks. *J. of Engineering Mechanics*, 119 (7), (1993), 1387–1410.

[11] Peña, F., Prieto, F., Lourenço, P. B., Campos-Costa, A., and Lemos, J. V. On the dynamics of rocking motions of single rigid-block structures. *Earthquake Eng. Struct. Dyn.,* 36 (2007), 2383-2399.

[12] Andreaus, U., Casini, P. On the rocking-uplifting motion of a rigid block in free and forced motion: influence of sliding and bouncing. *Acta Mechanica*, 138 (3), (1999), 219-241.

Yury Selyutskiy, Ass. Professor: Institute of Mechanics of Lomonosov Moscow State University, Michurinsky prosp. 1, 119192, Moscow, Russia (*seliutski@imec.msu.ru*). The author gave a presentation of this paper during one of the conference sessions.

Rinaldo Garziera, Professor: University of Parma, via Università, 12 - I 43121 Parma, Italy (*rinaldo.garziera@unipr.it*).

Luca Collini, Ass. Professor: University of Parma, via Università, 12 - I 43121 Parma, Italy (*luca.collini@unipr.it*).

Long-term behavior of adaptive strategies for artificial sensors due to receptors
(CON047-15)

Konrad Siedler, Carsten Behn

Abstract: The paper is devoted to the problem of identification of ground excitations which force a sensor and its seismic masses, respectively. Precisely, a control strategy is sought such that acting forces on a sensor can be measured and identified. The sensor is modeled by a mechanical system in form of a spring-mass-damper system within a rigid frame with degree of freedom two and strict relative degree two, which is forced by a (supposed unknown) ground excitation to the frame. We further suppose, that the seismic masses are under the load of internal control forces to achieve the prescribed goal. The sensor properties are derived from the natural behavior of mechanoreceptors from biology, which can adapt their reactions to several stimuli caused by the environment. For this reason, adaptive control strategies with time-varying controller gains are applied to ensure the sensor behavior. While not changing excitations have to fade out by the controller, further stimulus from the environment has still to be perceptible and absolute values has to be identified. Additionally, the sensor has to be as universal as possible and the lowest possible value of the controller gain has to be ensured. For this, existing control strategies from literature are analyzed and modified. Then, the most effective control strategies are applied to the sensor system. Finally, the controllers with the best results of the identification of excitations are successfully and powerfully verified in long-term behavior and their response to different kinds of excitations using random system parameters.

1. Motivation

To establish contact with the environment, every organism has sensory organs. They are highly specialized biological sensors which have been perfected and still get perfected in the course of the evolution, by natural selection sorting poorly or faulty functional systems. As a result, the animals evolve excellently adapted skills for their habitats, whose functional components are limited to the essential. So its worth to take a look at the animal kingdom to deduce existing solutions for our technical world on the model of the nature.

An interesting species is the phylum of arthropods (lat. arthropoda). They have to rely on a perfect workable vibration sense. This works in a way that animal hairs (distributed everywhere on the body – primary concentrated on the legs in case of arachnids) get into vibration due to changes in the environment. Then, these vibrations are noticed and "measured" by

mechanoreceptors inside, [2]. These hair-sensors are so sensitive, that air turbulence of approaching objects can be detected as they can decided between approaching enemies and victims. For example, the air turbulence caused by a fly can be detected in a distance of up to 30 cm. These sensory hairs are called "Trichobitria" for arachnids, [1].

1.1. Mechanoreceptors

In the moment of an incoming stimulus, i.e., when a change of the environment gets registered, forces are transferred by the sensory hair to the tissue. The receptors therein notice the changes and react with different characteristics. Therefore, the hair is only a lever to transfer stimuli. For the stimulus perception, only the support of the hair is important. The mechanoreceptors serve as stimuli converters or processing units. They are responsible for the registration of physical stimuli. If such a mechanoreceptor is excited by a constant excitation, it reacts with a short and quick answer. This signal falls off continuously. The reachable activity rate or running time for such a reaction is the so-called adaption and is the base of the following classification, [8]:

- Fast-Adapting Mechanoreceptor (FAM): Once developed an excitation, a FAM responds only to changes of the excitation with a short and fast series of pulses, followed by a equally rapid decline of the activity. While the excitation remains constant only pulses with long offset occurs.

- Slow-Adapting Mechanoreceptor (SAM): The reaction of this type shows a similar course as the FAM, but far slower. Furthermore, it offers a continuous reaction at constant excitations. In figure 1, it can be seen that the SAM has a much higher activity rate, while the constant excitation continues in contrast to FAMs, [8].

So fast adapting mechanoreceptors exhibit the sensitivity to react to changes, but to ignore a constant signal. Nevertheless, they have the adaptability to perceive a change during a constant signal.

1.2. Aims

The properties of FAMs should be mimicked by a (technical) sensor, e.g. in robotics. Therefore, it is considered in the modeling to implement the essential functionalities of the sensor (its sensory behavior) in a suitable mechanical control system. Excitations should be *identified* using as few as possible known system parameters. Adaptive control strategies transpose the biological behavior, in the following points:

- By occurring of constant excitations (e.g. wind) the system still has to be *sensitive for other acting stimuli (e.g. air turbulence).*
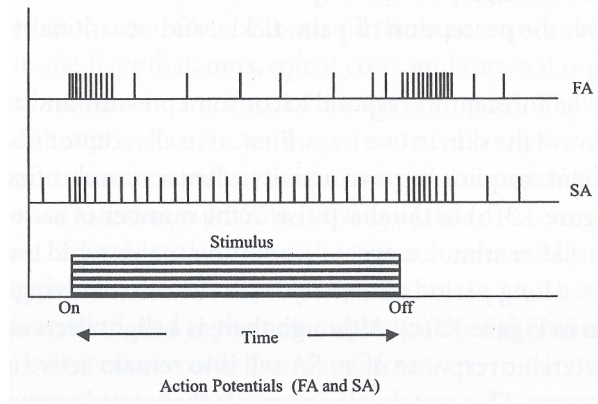
Figure 1. Reaction of fast/slow adapting (FA/SA) mechanoreceptors during a constant excitation, [8].

- In contrast to the biological paradigm *absolute values has to be identifiable*.

- The controller gain has to be as low as possible, so *as little as possible raised energy* has to be needed for this.

Using the time-varying and self adapting gain $k(\cdot)$, the controller should get the ability to "learn". These points are analyzed via a simulation and parameter study. To implement these points, different control strategies are applied to a sensor model with a degree of freedom (DoF) two and tested for their possible use in, e.g., a long-term behavior. We try to use the identification ideas in [3,4,6], but apply the developed adaptive strategies therein to a system of $DoF = 2$ in order to achieve more promising results. The best strategies are then used to analyze and investigate the long-term behavior of the modeled system.

2. Sensor model with degree of freedom two

A promising way to achieve a very good identification of ground excitations is a spring-mass-damper model with $DoF = 2$. With a two-mass-system, there exist a variety of ways to implement a strategy for the identification of ground excitations, for example, the second mass can serve as an absorber mass, or more options for the introduction of the gain factor $k(\cdot)$ exists.

2.1. Modeling

We consider a sensor system consisting of two visco-elastically (with parameters c_1, c_2, d_1 and d_2) interconnected mass points m_1 and m_2 within a rigid frame, which is forced via a

553

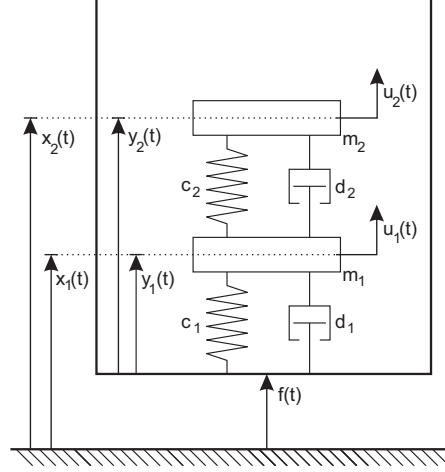(unknown) ground excitation $f(\cdot)$, see figure 2.

Figure 2. Sensor system with degree of freedom two.

The variables $x_1(t)$ and $x_2(t)$ represent the absolute coordinates of the masses m_1 and m_2 at time t, whereas $y_1(t)$ and $y_2(t)$ represent the relative ones. With the regulating forces $u_1(t)$ and $u_2(t)$ it is tried to influence the masses m_1 and m_2 in that way to identify the unknown ground excitation.

2.2. Model equations

The equations of motion are derived using Newton's second law for the masses m_1 and m_2. In absolute coordinates x_1 and x_2 we get:

$$\left.\begin{aligned}
m_1\,\ddot{x}_1 &= -c_1\left(x_1(t) - f(t)\right) - d_1\left(\dot{x}_1(t) - \dot{f}(t)\right) \\
&\quad + c_2\left(x_2(t) - x_1(t)\right) + d_2\left(\dot{x}_2(t) - \dot{x}_1(t)\right) + u_1(t)\,, \\
m_2\,\ddot{x}_2 &= -c_2\left(x_2(t) - x_1(t)\right) - d_2\left(\dot{x}_2(t) - \dot{x}_1(t)\right) + u_2(t)\,.
\end{aligned}\right\} \tag{1}$$

With the transformation $y_i(t) := x_i(t) - f(t)$ for all t and $i \in \{1, 2\}$, the absolute coordinates x_i are replaced by the relative ones y_i, we get:

$$\left.\begin{aligned}
m_1\,\ddot{y}_1 &= -(d_1 + d_2)\,\dot{y}_1 + d_2\,\dot{y}_2 - (c_1 + c_2)\,y_1 + c_2\,y_2 - m_1\,\ddot{f}(t) + u_1(t)\,, \\
m_2\,\ddot{y}_2 &= -d_2\,\dot{y}_2 + d_2\,\dot{y}_1 - c_2\,y_2 + c_2\,y_1 - m_2\,\ddot{f}(t) + u_2(t)\,,
\end{aligned}\right\} \tag{2}$$

with (dimensionless) parameters given in table 1.

Table 1. Parameters chosen for all following simulations.

$m_1=1$	$m_2=1$
$d_1=5$	$d_2=5$
$c_1=10$	$c_2=10$

3. Control strategies

Numerous adaptive control strategies in different versions with different feedback laws were studied for their quality in the identification of ground excitations in [7], inspired by strategies for a system of $DoF = 1$ in [3,4,6]. The best resulting control strategies are listed in table 2 and explained in the following.

Table 2. Summary of the most effective control strategies.

	Advanced $\lambda-$Stabilisation	Offset-Control
Feedback law	PD-Feedback	PD-Feedback
Gain factor	scalar	vectorial, 2-Norm
Evaluating regulation force	$u_1(t)$	$u_1(t)$

3.1. Control goal

With two masses m_1 and m_2, there are different ways to act on the system with the regulating forces $u_i(t)$: control the movement of only *one* mass, or the movement of *both* masses, or regulate the distance between the masses. For this, we consider the following PI-feedback laws

- feedback laws with *different* gain factors:

$$u_i(t) = -k_i(t)\, e_i(t) - \kappa\, k_i(t)\, \dot{e}_i(t)\,, \quad i \in \{1,2\} \tag{3}$$

with $\quad k_i(t) = f_i\big(e_i(t), t\big)$

- feedback laws with *one common* gain factor:

$$u_i(t) = -k(t)\, e_i(t) - \kappa\, k(t)\, \dot{e}_i(t) \tag{4}$$

with $\quad k(t) = f\big(||e(t)||, t\big)$

The larger the value of κ is chosen, the more is the settling time increased. Therefore, this value is as low as possible to choose, but even so, that: $\kappa > 0$. So the stabilizing effect of the D-term is obtained. For this reason $\kappa = 0.1$ is sufficient, see [5].

3.2. The adaptation laws

The gain parameter is determined via a so-called *adaptation law*. In this paper, we focus on the following two:

- Advanced λ-Stabilization:

  First versions of advanced λ-stabilization were set in [6]. In [5], this adaptation law was further developed. Here, it is adapted to the new system:

$$
\dot{k}_i(t) \quad = \quad
\left.
\begin{cases}
\gamma \left(|e_i(t)| - \varepsilon\lambda \right)^2 & \text{for} \quad \varepsilon\lambda + 1 \le |e_i(t)| \\[2mm]
\gamma \left(|e_i(t)| - \varepsilon\lambda \right)^{\frac{1}{2}} & \text{for} \quad \varepsilon\lambda \le |e_i(t)| < \varepsilon\lambda + 1 \\[2mm]
0 & \text{for} \quad |e_i(t)| < \varepsilon\lambda \,\wedge\, t - t_e < t_d \\[2mm]
-\delta(|e_i(t)|, \varepsilon\lambda)\, k(t) & \text{for} \quad |e_i(t)| < \varepsilon\lambda \,\wedge\, t - t_e \ge t_d
\end{cases}
\right\} \qquad (5)
$$

$$
\delta(|e_i(t)|, \varepsilon\lambda) := \sigma \cdot \left(1 - \tfrac{|e_i(t)|}{\varepsilon\lambda} \right)
$$

with $\varepsilon = 0.7$, $\sigma = 0.5$, $t_d = 2$, $\gamma = 100$ and $\lambda = 0.2$

- Offset-Control:

  Initially, the idea is only to use the error value $e(t)$ (P-Gain). But, in this adaptation law, there does not exist a possibility to decrease the gain factor. The gain factor increases all the more, the further the position of the mass m is away from the reference position ($y_{Ref}(t) = 0$). Afterwards, the gain factor keeps the foregoing values of the adaptation law in mind and increases this value only to the next one. One way to make the adaptation law forget these previous values is to give the position of the mass m from the "past" with a delay of the value t_{off} and negated back to the input of the controller. So, the reduction of the gain factor depends on the value which it had to increase before. The time t_{off} is called "offset-time":

$$
\dot{k}(t) \quad = \quad
\left.
\begin{cases}
\gamma \, ||e(t)||_j & \text{for} \quad t \le t_{off} \\[2mm]
\gamma \, ||e(t)||_j - \rho \, ||e(t - t_{off})||_j & \text{for} \quad t > t_{off}
\end{cases}
\right\} \qquad (6)
$$

with $\rho = \gamma = 100$ and $t_{off} = 5.0$

The value $e(t_{off})$ shows the error of the position of the mass m to the time t_{off}. The higher this value is chosen, the higher increases the gain factor $k(t)$, because the adaptation law keeps more past values in mind, before being demount. The smaller the time t_{off} is chosen the restless will the course of the gain factor be and so the course of the regulating force, too.

4. Tests of the chosen control strategies

For the long-term behavior investigations, a new excitation function $f_{200}(t)$ (see (7) and figure 3) is introduced, which helps to study the behavior of the system to different excitation pattern.

$$t \longmapsto f_{200}(t) = \left. \begin{array}{c} \left(1 + 10\,e^{-(t-13)^2} + 10\,e^{-(t-31.4)^2} + 5\,e^{-(t-75.5)^2} + 5\,e^{-(t-81.7)^2} \right. \\ \left. +5\,e^{-(t-88.5)^2} \right) \cos\left(t\left(0.5\,e^{\frac{-(t-55)^2}{50}}\right) + 1\right)\left(-\frac{1}{\pi}\arctan\left(\frac{t-155}{2.5}\right) + 0.5\right) \end{array} \right\}$$
$$(7)$$

This excitation function is used for the following simulations. Both masses are controlled to
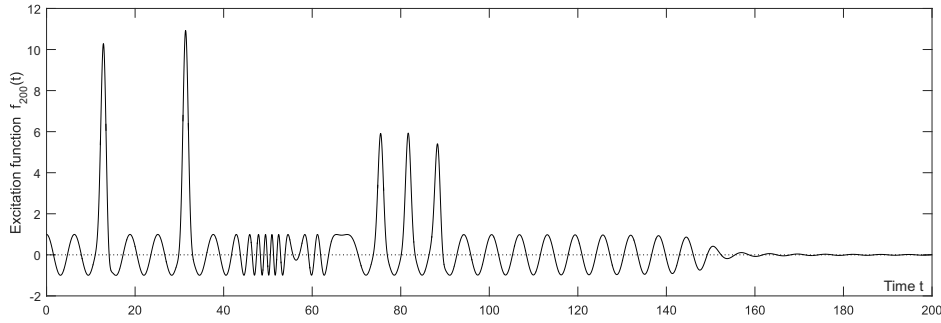
Figure 3. The excitation function $f_{200}(t)$.

their rest positions and we observe the quality of the approximation of the regulating force $u_1(t)$ via the excitation $m_1\,\ddot{f}(t)$ (for randomly selected system parameters). Moreover, for brevity, we focus on feedback structure (3) and apply both adaptation laws to point out the main difference.

4.1. Long-term behavior

To look at the quality of the identification in observing the regulating forces $u_1(t)$ compared to the excitation force on mass m_1, we get the following simulation results. Figure 4 shows the excitation force to mass m_1.

If we apply the adaptation law of the advanced λ-stabilization (5), than figure 5 shows the necessary control force $u_1(t)$ in this case.

Like the characteristic of this adaptation law, little excitations (low values of its amplitude) on mass m_1 are filtered by the property of the λ-tolerance area. Since the regulating force drops from $t = 100$ so, that a little bit later no regulating force exists and so it is assumed that no (relevant) excitation acts on the system. This property is to qualify: In the high frequency area (about $t \in [40; 60]$) the excitation can drive out the mass m_1 from
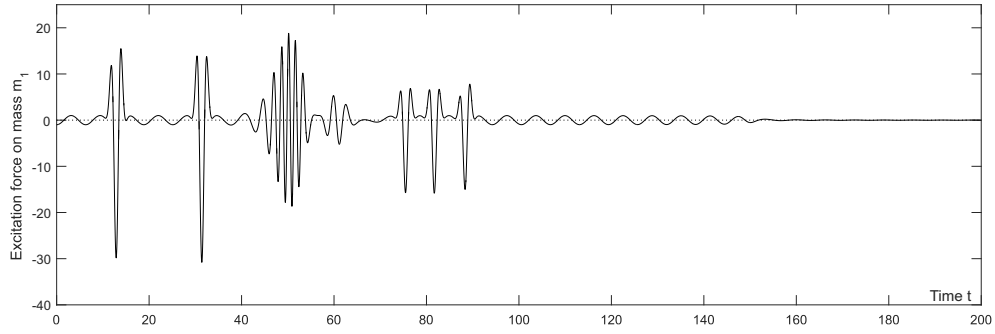
557

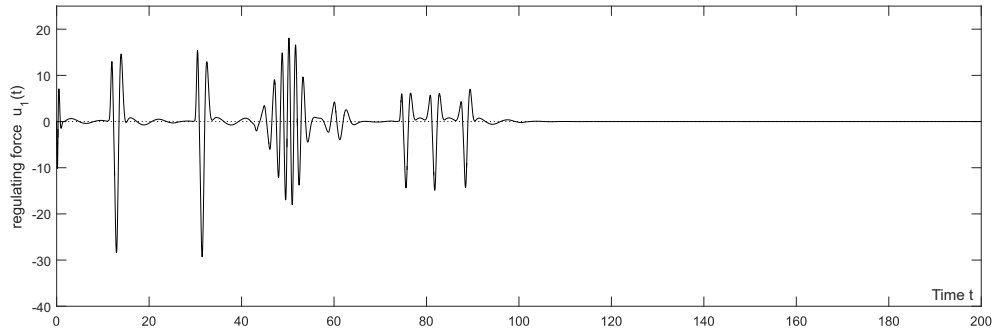**Figure 4.** The excitation force on mass m_1: $m_1 \ddot{f}(t)$.

Figure 5. The regulating force $u_1(t)$, advanced λ−Stabilisation.

the tolerance area, although the amplitude of the excitation is identical to $t \approx 100$ at this moment. Because of the periodical and fast leaving of the tolerance area, it is not enough time to decrease and so the gain factor increases down-welling. This area is very good to identify in observing the regulating force.

The cosine wave around the peaks is only to imagine, so long no other event after a short time drives the mass out of the tolerance area.

Altogether, the form of the excitation can be clearly seen, in observing the regulating force $u_1(t)$. Corresponding to the biological ideal, low excitations are only for short time visible, so that they can only be suggested (adjustable over the parameters: waiting time t_d, factor σ) and afterwards gradual filtered (adjustable over the factor σ). For example, at the moment $t \approx 90$, one can see a cosine wave which dies down. Its amplitude or frequency is not high enough that it can leave the tolerance area. Only for the time t_d the gain factor is high enough, that the regulating force can show the excitation, after that δ is working. The real end of the cosine wave is not visible.

Figure 6 presents the necessary control force in case of applying the adaptation law of the offset-control (6).
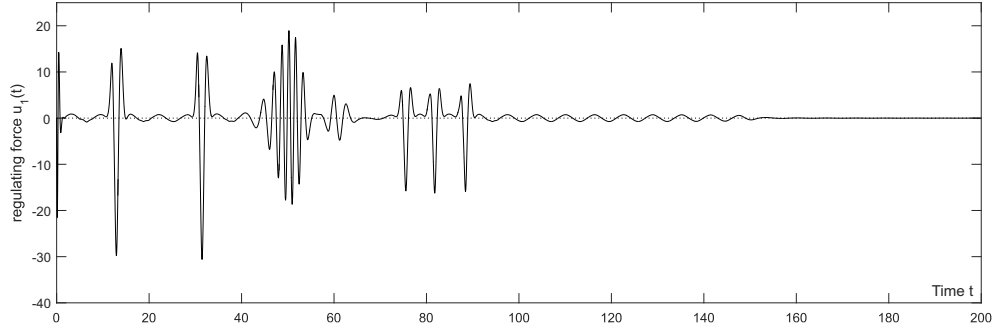

Figure 6. The regulating force $u_1(t)$, Offset-Control.

Its a very good coincidence of the forces. Both the moments of low excitations and the high peaks are good to see in the regulating force $u_1(t)$. As long as the excitation is not exactly $f_{200}(t) \equiv 0$, every time a value for the gain factor exists $k(t) > 0$.

4.2. Behavior in case of randomly chosen system parameters

In subsection 4.1, one can see the behavior of both control strategies to different kinds of excitations. According to subsection 1.2, the sensor system has to give a reliable identification of excitations, without knowledge about the system parameters. Therefore, the behavior of the sensor system is now examined with randomly chosen system parameters[1].

For this purpose, three simulations for every control strategy are presented.

Advanced $\lambda-$Stabilization   For the control with adaptation law (5), the randomly chosen system parameters are given in table 3. To evaluate the quality of the identification of

Table 3.   Random system parameters, simulation with advanced $\lambda-$Stabilization.

Parameter	Simulation $i = 1$	Simulation $i = 2$	Simulation $i = 3$
Masses 1/ 2	1.7264/1.0679	0.8389/1.1535	0.6482/1.5196
Damper 1/ 2	6.1793/6.2463	3.6828/4.2444	4.0475/3.5462
Springs 1/ 2	11.4432/10.3283	7.2766/14.2338	8.3536/12.2123

the excitation in observing the regulating force $u_1(t)$, the time histories of these quantities are given in one figure 7. For comparability the courses are scaled with their mass m_1, so

---

[1]The ranges are: for both masses $0.5 \leq m \leq 2.0$, damper $3.0 \leq d \leq 7.0$ and springs $5.0 \leq c \leq 10.0$.
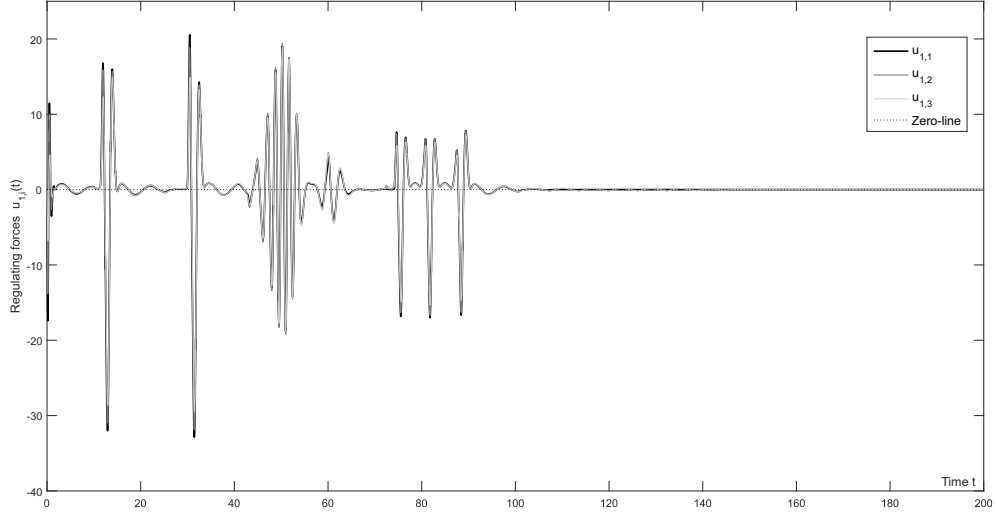
Figure 7. Regulating forces $u_{1,i}(t)$: Red - $u_{1,1}(t)$, green - $u_{1,2}(t)$, blue - $u_{1,3}(t)$.

that the value of the regulating force at the moment t is divided by the mass m_1. The courses from figure 7 are illustrated in the same axis scaling as the appearing force by the excitation from figure 4.

It is easy to see a very good approximation of the forces, which differ only rarely despite different system parameters.

With decreasing mass one can see an increase of the extreme values of the regulating forces. Thereby in the settling area, there is a faster settling to $y = 0$ for regulating force $u_{1,3}(t)$, than the other regulating forces. So from the moment of about $t \approx 110$, it takes a value of $u_{1,3}(t > 110) \equiv 0$, while the regulating force minor swings for the other simulations. With the chosen parameters, the mass m_1 leaves the λ-tolerance area for a very small interval of about 0.3 to 0.4, by what the gain factor takes values between $k(t) \in [2.5; 3.5]$. So, a regulating force $u_1(t)$ exists for these simulations.

In view of the randomly chosen system parameters, the differences between the regulating forces $u_{1,1}(t)$ to $u_{1,3}(t)$ are very small. That means the results point out, that adaptation law (5) represents a very good opportunity for implementing the functionality of a FAM.

Table 4. Random system parameters, simulation with Offset-Control.

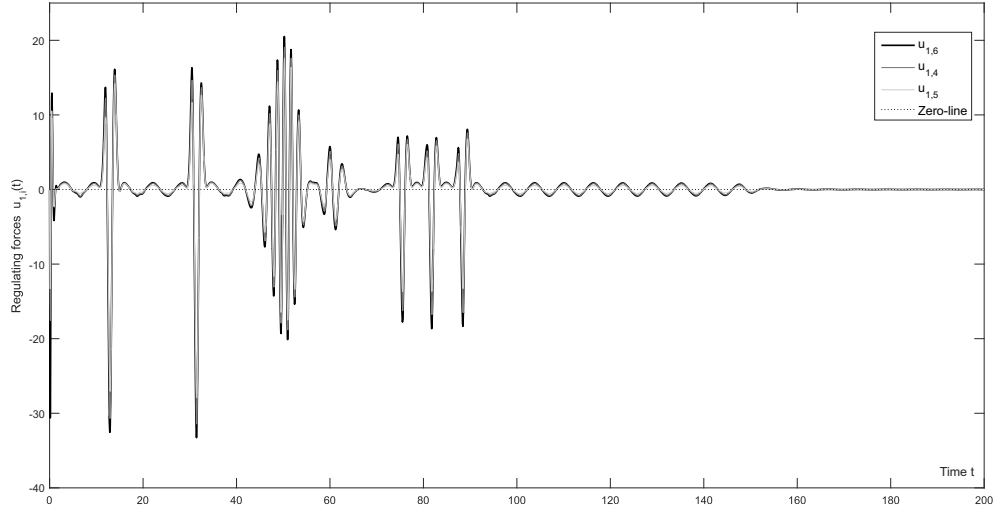| Parameter	Simulation $i = 4$	Simulation $i = 5$	Simulation $i = 6$
Masses 1/ 2	1.5181/1.0883	1.5422/0.5517	0.6453/1.3849
Damper 1/ 2	6.0310/5.6219	4.2684/4.7550	6.3116/3.2715
Springs 1/ 2	6.7119/12.4313	14.5022/8.8156	14.3791/11.4593

Figure 8. Regulating forces $u_{1,i}(t)$: Red - $u_{1,4}(t)$, green - $u_{1,5}(t)$, blue - $u_{1,6}(t)$.

Offset-Control   For the simulations using adaptation law (6), the randomly chosen system parameters are now given in table 4. To study the behavior of the Offset-Control, the results of the simulations are presented in the same way as already the advanced λ-stabilization ones, see figure 8. The courses are very similar to each other. Above all, the courses of the regulating forces $u_{1,4}(t)$ and $u_{1,6}(t)$ exhibit a very good agreement. Only the course of the regulating force $u_{1,5}(t)$ shows a clear less amplitude. This behavior exists at every time t. The best approximation of the force of the excitation $m_1 \ddot{f}_{200}(t)$ shows the blue one.

The similarity of the courses reflects the behavior of the gain factor $k(t)$, it appears to have only a vertical offset. The same happens to the position of the mass m_1, only with variation of the amplitude.

For the Offset-Control, one can see a very good approximation of the respective regulating forces $u_{1,i}(t)$ to the resulting force of the excitation $m_1 \ddot{f}_{200}(t)$. The characteristic property of the Offset-Control allows a good identification for any excitation type (wether weak or strong), but it needs at any time where the excitation function has a value of $f_{200}(t) \neq 0$ a value for the gain factor of $k(t) > 0$. Thereby, the control strategy requires more energy as the advanced λ-stabilization one.

5. Conclusion

Concerning the adaptation and identification behavior of animal mechanoreceptors, the two

561

presented adaptation laws for PD-control of an artificial mechanical sensor system worked successfully and effectively. The identification scheme was based on observing the regulating force and on comparing it with the excitation force on the corresponding mass point. In view to the specific properties of the adaptation laws, they showed a very good functionality. With the advanced λ-stabilization one can filtrate dispensable signals, by adjust of the value λ for the tolerance area. Thereby, too little changes can not be seen. Using the Offset-Control, a very good identification of all occurring signals was possible, but that led to ongoing energy requirements. Depending on the information needed, one can insert an appropriate adaptation law, without changing the feedback law. In both cases, only observing of the regulating force $u_1(t)$ on the mass m_1 is necessary.

References

[1] BARTH, F. *Sinne und Verhalten aus dem Leben einer Spinne.* Springer, Berlin (Germany), 2001.

[2] BARTH, F. Spider mechanoreceptors. *Current Opinion in Neurobiology 14* (2004), 415–422.

[3] BEHN, C. Adaptive λ-tracking-control for relative degree two systems with applications to bio-inspired sensors. *Nonlinear Dynamics 50*, 4 (2007), 817–828.

[4] BEHN, C. Modeling the adjustment of receptor cells via adaptive λ-stabilizing control. *Journal of Mechatronics 2*, 4 (2014), 275–290.

[5] BEHN, C., AND LOEPELMANN, P. Adaptive vs. fuzzy control of uncertain mechanical systems. *International Journal of Applied Mechanics 4*, 2 (2012), 28 pages.

[6] BEHN, C., AND STEIGENBERGER, J. Improved adaptive controllers for sensory systems - first attempts. In *Modeling, Simulation and Control of Nonlinear Engineering Dynamical Systems* (2009), J. Awrejcewicz, Ed., Springer, pp. 161–178.

[7] SIEDLER, K. Simulation studies of control strategies for a bio-inspired mechanical sensor system for the identification of ground excitations. Master's thesis, Ilmenau University of Technology, 2015. Dept. of Technical Mechanics.

[8] SODERQUIST, D. *Sensory Processes.* Sage Publications, Thousand Oaks (USA), 2002.

Konrad Siedler, B.Sc.: Ilmenau University of Technology, Department of Technical Mechanics, Max-Planck-Ring 12 (Building F), 98693 Ilmenau, Germany (*konrad.siedler@tu-ilmenau.de*).

Carsten Behn, Associate Professor: Ilmenau University of Technology, Department of Technical Mechanics, Max-Planck-Ring 12 (Building F), 98693 Ilmenau, Germany (*carsten.behn@tu-ilmenau.de*). The author gave a presentation of this paper during one of the conference sessions.

Mechanical systems with two nonlinear springs connected in series
(ASY251-15)

Roman Starosta, Grażyna Sypniewska-Kamińska, Jan Awrejcewicz

Abstract: The aim of the paper is analysis of dynamical regular response of the nonlinear oscillator with two serially connected springs of cubic type nonlinearity. Behaviour of such systems is described by a set of differential-algebraic equations (DAEs). Two examples of systems are solved with the help of the asymptotic multiple scales method in time domain. The classical approach has been appropriately modified to solve the governing DAEs. The analytical approximated solution has been verified by numerical simulations.

1. Introduction

The linear simplification is sometimes too rough to describe the behavior of a physical object with sufficient accuracy. Therefore, models of nonlinear oscillators have been widely considered in physics and engineering. Nonlinear oscillators with serially connected springs were investigated by many authors mostly numerically. Most papers concern a case, when one of the springs is linear and the second one is nonlinear [1, 2, 3].

Telli and Kopmaz [1] showed that the motion of a mass mounted via linear and nonlinear springs in series, is described by a set of differential-algebraic equations. Similar situation occurs in our investigation. It implies a need of a modification of the standard multiple scale method in time domain (MMS). Two examples of the system with two nonlinear springs are presented and analyzed using appropriately adopted MMS. That are one-dimensional oscillator and a spring pendulum.

2. One-dimensional oscillator

Let us consider the one-dimensional motion of a body of mass *m* attached by massless nonlinear springs to an immovable support. The studied system is shown in the Figure 1.

The restoring force of the springs with cubic nonlinearity are

$$F_i = k_i \left(Z_i + \Lambda_i Z_i^3 \right), \quad i = 1,2 \tag{1}$$

where Z_i is the elongation of the *i*-th spring, k_i is the constant stiffness and Λ_i is the nonlinearity parameter. Lengths of untensioned springs are L_{10} and L_{20}.
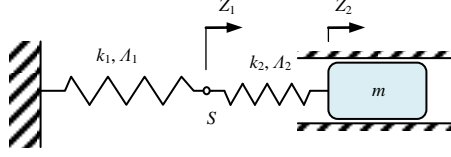
Figure 1. Oscillator with series connection of two nonlinear springs.

Such type of nonlinear elasticity is widely discussed in the papers concerning nonlinear dynamics [1, 4]. When $\Lambda_i > 0$ the characteristics of the spring is called "hard", while for $\Lambda_i < 0$ the characteristics is called "soft". Hereafter we consider only the case $\Lambda_i > 0$.

2.1. Mathematical model

Two equations describe behaviour of the system. One of them is the differential equation of the body motion

$$m\left(\ddot{Z}_1 + \ddot{Z}_2\right) + k_2 Z_2\left(1 + \Lambda_2 Z_2^{\,2}\right) = 0 . \tag{2}$$

The second one is the algebraic equation describing equilibrium at the massless connection point S and reads

$$k_1 Z_1\left(1 + \Lambda_1 Z_1^2\right) - k_2 Z_2\left(1 + \Lambda_2 Z_2^{\,2}\right) = 0 . \tag{3}$$

The above equations are supplemented by the initial conditions

$$Z_2(0) = X_0, \; \dot{Z}_2(0) = V_0 . \tag{4}$$

After transformation of the governing equations to the more convenient dimensionless form they read

$$\ddot{z}_1 + \ddot{z}_2 + (1 + \lambda) z_2\left(1 + \alpha_2 z_2^2\right) = 0 , \tag{5}$$

$$\lambda z_2\left(1 + \alpha_2 z_2^2\right) - z_1\left(1 + \alpha_1 z_1^2\right) = 0 , \tag{6}$$

$$z_2(0) + z_1(0) = z_0, \; \dot{z}_2(0) + \dot{z}_1(0) = v_0 , \tag{7}$$

where z_0 and v_0 are initial displacement and velocity of the body, $z_i = Z_i / L$, $\alpha_i = \Lambda_i L^2$ for $i = 1, 2$, $L = L_{10} + L_{20}$, $\lambda = k_2 / k_1$. Dimensionless time $\tau = t\,\omega_1$ where $\omega_1 = k_e / m$ and $k_e = k_1 k_2 / (k_2 + k_1)$ have been assumed as characteristic quantities.

2.2. Approximated analytical solution

The problem (5)–(7) can be solved using MSM [4], although the approach requires some significant modification. The assumptions of smallness of the nonlinearity parameters are proposed in the form

$$\alpha_1 = \tilde{\alpha}_1 \varepsilon, \, \alpha_2 = \tilde{\alpha}_2 \varepsilon \,, \tag{8}$$

where ε is a small perturbation parameter.

The solution is searched in the form of series with respect to the small parameter

$$z_2(\tau;\varepsilon) = \sum_{k=0}^{k=1} \varepsilon^k z_{2k}(\tau_0, \tau_1), \quad z_1(\tau;\varepsilon) = \sum_{k=0}^{k=1} \varepsilon^k z_{1k}(\tau_0, \tau_1). \tag{9}$$

Introducing (8) and (9) into (5) – (6) we obtain two equations in which the small parameter ε appears. These equations should be satisfied for any value of the small parameter, so after sorting them with respect to the powers of ε we get the differential equations of the first and second order. After eliminating secular terms and solving the equations, the approximate solution takes the form:

$$z_1(\tau) = b_0 \lambda \cos(B\tau + \psi_0) + \frac{b_0^3 \lambda \big(3\alpha_2(5+8\lambda) - \alpha_1 \lambda^2(16+25\lambda)\big)}{32(1+\lambda)} \cos(B\tau + \psi_0)$$
$$+ \frac{2b_0^3 \lambda \big(9\alpha_2 + \alpha_1(\lambda-8)\lambda^2\big)}{32(1+\lambda)} \cos(B\tau + \psi_0)\cos(2B\tau + 2\psi_0), \tag{10}$$

$$z_2(\tau) = b_0 \cos(B\tau + \psi_0) + \frac{b_0^3 \big(\alpha_2 - 8\alpha_2 \lambda + 9\alpha_1 \lambda^3\big)}{32(1+\lambda)} \cos(3B\tau + 3\psi_0), \tag{11}$$

where $B = 1 + 3b_0^2 \big(\alpha_2 + \alpha_1 \lambda^3\big)/8(1+\lambda)$, while b_0 and ψ_0 are the initial amplitude and phase.

2.3. Results

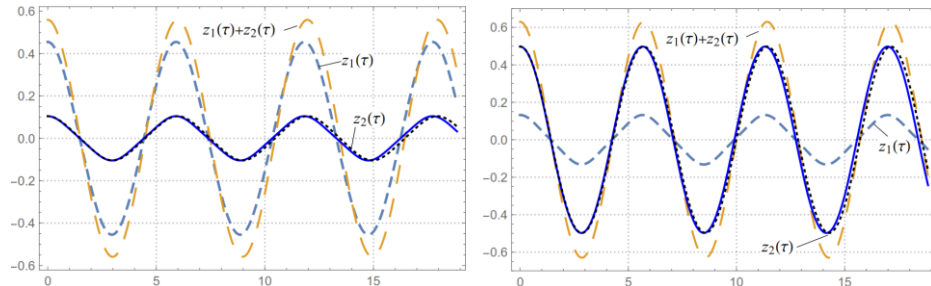In Figure 2 the time history of the generalized co-ordinates and their sum are presented.

Figure 2. Time history of the motion of the system for $\alpha_1 = 0.8$ $\alpha_2 = 1.4$; a) $\lambda = 8$, $b_0 = 0.05$;

$\alpha_2 = 1.4$; b) $\lambda = 0.1$, $b_0 = 0.5$; dotted line – numerical solution.

The comparison between numerical and analytical solutions confirms correctness of the asymptotic calculations. The explicit form of the solution allows for deeper analysis of the motion of the body.

From solution (10) the period of the primary vibration can be derived

$$T = \frac{16\pi(\lambda+1)}{3\alpha_1 b_0^2 \lambda^3 + 3\alpha_2 b_0^2 + 8(\lambda+1)}.$$

(12)

Expression (12) quantitatively describes dependence of the period with respect to amplitude, involved nonlinearities and the parameter λ. When the springs are nonlinear with hard characteristics ($\alpha_i > 0$), the period is smaller than 2π. In Figure 3 the value of period of the vibration versus nonlinearity parameters α_1 and α_2 is shown.
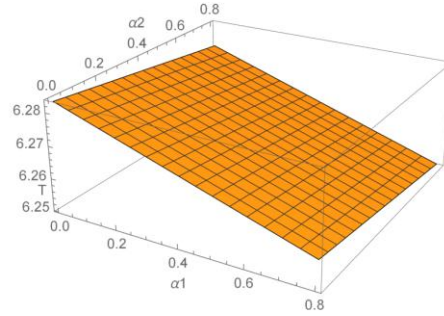
Figure 3. Period vs. nonlinearity parameters; $\lambda = 1.5$, $b_0 = 0.1$.

The dependences of the vibration period and amplitude versus λ obtained from (12) are presented in Figure 4.
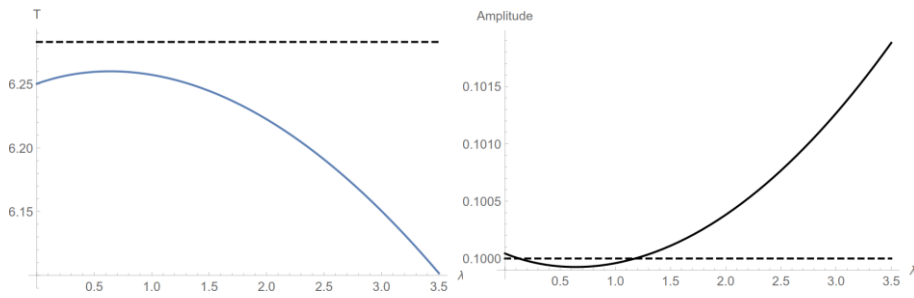

Figure 4. Period and amplitude vs. λ; $\alpha_1 = 0.8$, $\alpha_2 = 1.4$; dashed line – linear case $\alpha_1 = 0$, $\alpha_2 = 0$.

The position of the extremum value in Figure 4 depends on nonlinearity of springs α_1, α_2.

3. Spring pendulum

The dynamics of the nonlinear spring pendulum presented in Figure 5 is investigated in this point. Such quite simple and intuitive system serves as a very good example of a study of non-linear phenomena exhibited by two degrees-of-freedom mechanical systems.
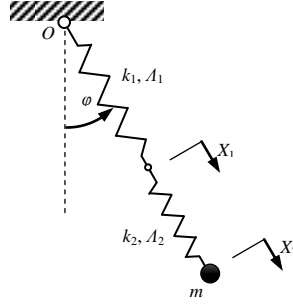

Figure 5. The pendulum with two nonlinear springs connected in series.

The investigated pendulum-type system consists of the small body of mass m suspended at a fixed point on the two nonlinear springs of the length L_{01}, and L_{02} whose elastic constants are denoted by k_1, Λ_1 and k_2, Λ_2. Due to the introduced constraints, the body can move only in the fixed vertical plane. Moreover we assume that the springs are straight and collinear. We are interested in free motion of the system, thus no external force or damping are admitted. The total springs elongation Z_1, Z_2 and the angle φ describe unambiguously the position of the system.

3.1. Mathematical model

The equations of motion are obtained with the help of the Lagrange equations of second kind. Similarly as in previous section, the differential equations are supplemented by the algebraic one, which describes equilibrium of the spring's connecting point S. The restoring forces in the springs are of the same type as previously. They are described by eq. (1). The dimensionless form of the mathematical model is as follows

$$\ddot{z}_1 + \ddot{z}_2 + \left(1 + 3z_{2r}^2\alpha_2\right)(1 + \lambda)z_2 + 3z_{2r}\alpha_2(1 + \lambda)z_2^2 + \alpha_2(1 + \lambda)z_2^3 - w^2(\cos\varphi - 1)$$
$$- (1 + z_1 + z_2)\dot{\varphi}^2 = 0, \tag{13}$$

$$(1 + z_1 + z_2)\left((1 + z_1 + z_2)\ddot{\varphi} + 2(\dot{z}_1 + \dot{z}_2)\dot{\varphi} + w^2\sin\varphi\right) = 0, \tag{14}$$

$$\lambda z_2\left(\alpha_2 z_2(z_2 + 3z_{2r}) + 3\alpha_2 z_{2r}^2 + 1\right) - z_1\left(\alpha_1 z_1(z_1 + 3z_{1r}) + 3\alpha_1 z_{1r}^2 + 1\right) = 0. \tag{15}$$

The initial conditions reads

$$z_2(0) + z_1(0) = z_0, \dot{z}_2(0) + \dot{z}_1(0) = v_0, \varphi(0) = \varphi_0, \dot{\varphi}(0) = \omega_0. \tag{16}$$

The dimensionless parameters are defined in the same way as above, in section 2. The elongations of the springs at the static equilibrium position z_{1r} and z_{2r} fulfill the following additional conditions

$$z_{2r}\left(1+z_{2r}^2\alpha_2\right)=w^2/(1+\lambda) \quad \text{and} \quad z_{1r}\left(1+z_{1r}^2\alpha_2\right)=\lambda w^2/(1+\lambda) . \tag{17}$$

The trivial solution of Eq. (14), which fulfills $z_1+z_2+1=0$, is omitted.

3.2. Approximated analytical solution

The problem (13)–(16) can be solved analytically using the multiple scale method [4], although the approach requires some significant modification. The assumptions of smallness of the nonlinearity parameters are proposed now in the form

$$\alpha_1 = \tilde{\alpha}_1\varepsilon^2, \alpha_2 = \tilde{\alpha}_2\varepsilon^2 , \tag{18}$$

In this problem three time scales should be used, so the solutions are searched in the form

$$z_2(\tau;\varepsilon)=\sum_{k=1}^{k=3}\varepsilon^k z_{2k}(\tau_0,\tau_1,\tau_2), \quad z_1(\tau;\varepsilon)=\sum_{k=1}^{k=3}\varepsilon^k z_{1k}(\tau_0,\tau_1,\tau_2), \quad \varphi(\tau;\varepsilon)=\sum_{k=1}^{k=3}\varepsilon^k z_{1k}(\tau_0,\tau_1,\tau_2). \tag{19}$$

Adopting the MSM we obtain the asymptotic analytical solution in the form:

$$
\begin{aligned}
z_1 &= a_{10}\lambda\left(1-3\left(z_{1r}^2\alpha_1-z_{2r}^2\alpha_2\right)\right)\cos\left((\Gamma_1+\Gamma_2)\tau+\psi_{10}\right)+a_{20}^2w^2\lambda\left(3\cos(2(\Gamma_5+\Gamma_6)\tau+2\psi_{20})\right. \\
&\left.+4w^2-1\right)/4\left(4w^2-1\right)(1+\lambda)-3a_{10}a_{20}^2w\lambda\left(\left(1+w-2w^2\right)\cos\left((\Gamma_2+\Gamma_3+2\Gamma_4)\tau+\psi_{10}-2\psi_{20}\right)\right. \\
&\left.+\left(-1+w+2w^2\right)\cos\left((\Gamma_2+\Gamma_3-2\Gamma_4)\tau+\psi_{10}+2\psi_{20}\right)\right)/\left(16\left(4w^2-1\right)\right)
\end{aligned} \tag{20}
$$

$$
\begin{aligned}
z_2 &= a_{10}\cos\left((\Gamma_1+\Gamma_2)\tau+\psi_{10}\right)+\frac{a_{20}^2w^2\left(4w^2-1+3\cos(2(\Gamma_5+\Gamma_6)\tau+2\psi_{20})\right)}{4\left(4w^2-1\right)(1+\lambda)} \\
&-3a_{10}a_{20}^2w\left(\left(1+w-2w^2\right)\cos\left((\Gamma_2+\Gamma_3+2\Gamma_4)\tau+\psi_{10}-2\psi_{20}\right)\right. \\
&\left.+\left(-1+w+2w^2\right)\cos\left((\Gamma_2+\Gamma_3-2\Gamma_4)\tau+\psi_{10}+2\psi_{20}\right)\right)/\left(16\left(4w^2-1\right)\right)
\end{aligned} \tag{21}
$$

$$
\begin{aligned}
\varphi &= a_{20}\cos\left((\Gamma_5+\Gamma_6)\tau+\psi_{20}\right)+a_{10}a_{20}w(1+\lambda)\left(\left(-2-3w+2w^2\right)\cos\left((-\Gamma_1-\Gamma_2+\Gamma_5+\Gamma_6)\tau-\psi_{10}+\psi_{20}\right)\right. \\
&\left.+\left(2-3w-2w^2\right)\cos\left((\Gamma_1+\Gamma_2+\Gamma_5+\Gamma_6)\tau+\psi_{10}+\psi_{20}\right)\right)/\left(2\left(4w^2-1\right)\right) \\
&+a_{20}a_{10}^2w\left(6-5w+w^2\right)(1+\lambda)^2\cos\left((-2(\Gamma_2+\Gamma_3)-\Gamma_4/2)\tau-2\psi_{10}+\psi_{20}\right)/16(2w-1) \\
&+a_{20}a_{10}^2w\left(-6+7w+9w^2+2w^3\right)(1+\lambda)^2\cos\left((2(\Gamma_2+\Gamma_3)-\Gamma_4/2)\tau+2\psi_{10}+\psi_{20}\right)/192\left(4w^2-1\right) \\
&+a_{20}^3\left(1-49w^2\right)\cos(3(\Gamma_5+\Gamma_6)\tau+3\psi_{20})/192\left(4w^2-1\right)
\end{aligned} \tag{22}
$$

where $a_{10},a_{20},\psi_{10},\psi_{20}$ are the initial values of amplitudes and phases of z_2 and φ respectively. They are related to the initial values z_0, v_0, φ_0 and ω_0 by the conditions (16) and eqs.(20) – (22) at instant $\tau=0$. The shortening denotations $\Gamma_1,\Gamma_2,\Gamma_3,\Gamma_4,\Gamma_5,\Gamma_6$ have the following form

$$\Gamma_1 = 1 + \frac{3\left(z_{2r}^2 \alpha_2 + z_{1r}^2 \alpha_1 \lambda\right)}{2(1+\lambda)}, \quad \Gamma_2 = \frac{3a_{20}^2 w^2 \left(w^2 - 1\right)}{4\left(4w^2 - 1\right)}, \quad \Gamma_3 = \frac{2 + 3z_{2r}^2 \alpha_2 + 2\lambda + 3z_{1r}^2 \alpha_1 \lambda}{2(1+\lambda)},$$

$$\Gamma_4 = \frac{12a_{10}^2 (1+\lambda)^2 \left(w - w^3\right) + w\left(8a_{20}^2 w^4 + \left(16 - a_{20}^2\right) - w^2 \left(64 + 7a_{20}^2\right)\right)}{8\left(4w^2 - 1\right)},$$

$$\Gamma_5 = \frac{12w a_{10}^2 (1+\lambda)^2 \left(w^2 - 1\right)}{64w^2 - 16}, \quad \Gamma_6 = \frac{-8a_{20}^2 w^5 - w\left(16 - a_{20}^2\right) + w^3 \left(64 + 7a_{20}^2\right)}{64w^2 - 16}.$$

3.3. Results

Time histories of the coordinates describing position of the body are presented in Figure 6. In both graphs, the solid line represents the asymptotic solution according to (20) – (22).
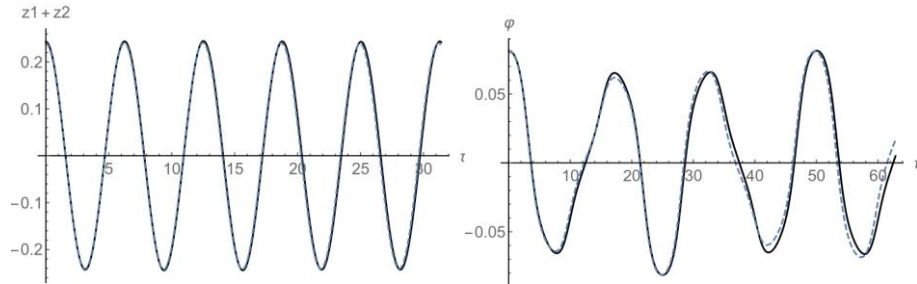
Figure 6. Time history of the body position for $\alpha_1 = 0.35$, $\alpha_2 = 0.25$, $\lambda = 2.5$, $a_{10} = 0.07$, $a_{20} = 0.07$, $\psi_{10} = 0$, $\psi_{20} = 0$; dashed line – numerical solution.

The period of the first term of the asymptotic solution for longitudinal as well as swing vibration as a function of the parameter λ are presented in Figure 7.
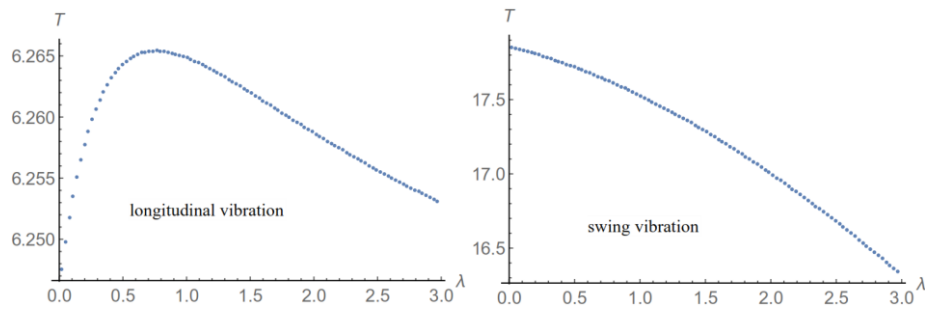

Figure 7. Period vs. λ for longitudinal and swing vibration; for $\alpha_1 = 0.35$, $\alpha_2 = 0.25$, $a_{10} = 0.07$, $a_{20} = 0.07$, $\psi_{10} = 0$, $\psi_{20} = 0$.

4. Conclusions

The mathematical model of the mechanical systems containing two serially connected nonlinear springs consists of the differential and algebraic equations. Properly modified multiple scales method in time domain allows to solve effectively this problem and to obtain the approximate asymptotic solutions. The range of parameters, for which the error is reasonably small, is limited according to the assumptions of the MSM. The correctness of the results has been confirmed by numerical simulation.

The analytical solution allows to analyse the influence of the parameters on the studied system motion. The influence of some parameters on the period and amplitude has been discussed in the case of free vibration.

Finally, we confirmed that the applied software Wolfram Mathematica has been very helpful in the analytical transformations and simplification of the derived and studied DAEs.

Acknowledgments

References

[1] Telli, S. and Kopmaz, O., Free vibrations of a mass grounded by linear and nonlinear springs in series, *J. Sound Vib.,* 289, (2006), 689-710.

[2] Lai, S.K. and Lim, C.W., Accurate approximate analytical solutions for nonlinear free vibration of systems with serial linear and nonlinear stiffness, *J. Sound Vib.*, 307 (2007), 72-736,.

[3] Bayat, M., Pakar, I. and Cveticanin L., Nonlinear free vibration of systems with inertia and static type cubic nonlinearities: An analytical approach. *Mech. Mach. Theory,* 77 (2014), 50-58.

[4] Awrejcewicz, J. and Krysko, V.A., *Introduction to Asymptotic Methods*, Chapman and Hall, Boca Raton, 2006.

Roman Starosta, Ph. D: Poznań University of Technology, Institute of Applied Mechanics, ul. Piotrowo 3, 60-965 Poznań, Poland (*roman.starosta@put.poznan.pl*). The author gave a presentation of this paper during one of the conference sessions.

Grażyna Sypniewska-Kamińska, Ph. D: Poznań University of Technology, Institute of Applied Mechanics, ul. Piotrowo 3,60-965 Poznań, Poland, (*grazyna.sypniewska-kaminska@put.poznan.pl*).

Jan Awrejcewicz, Professor: Technical Universityof of Łódź, Department of Automatics and Biomechanics, ul. Stefanowskiego 90-924, Łódź, Poland (*awrejcew@p.lodz.pl*).

Rollers vibration of conveyor belt
(STA194-15)

Martin Svoboda, Frantisek Klimenda, Jan Kampo, Josef Soukup

Abstract: The article is deals of measurement of vibrations on a roller conveyor stand. These vibrations have a significant influence on the noise of the conveyor. For the two sets of rollers were determined the vibrations by experimentally. Difference between individual set of rollers is in used of semi finished product of the outer shell. The design of the rollers is the same. One set has a shell from convectional tube and the second set from accuracy tube. The vibrations were measured by six-channel analyzer Brüel&Kjær (PULSE). Acceleration and natural frequency were measured by using a three-axis accelerometer. In the conclusion of the article is an evaluation of vibration. Three the highest acceleration values in depending on the frequency of vibration in individual directions are given. From this evaluation are selected rollers with minimal and maximal acceleration.

1. Introduction

The rollers, respectively his fixing on the support structure are the priority source of noise of tube belt conveyors. The rollers are in operation dynamically loaded by a tensile force of belt and vertical force from the conveyed material. None of these forces is not constant, are varies at a given time. This load causes vibration of the rollers in x, y and z-axis. The vibrations of the rollers are transmitted over their fixed on the supporting structure. The supporting structure vibrates and it is the noise source [2, 3]. The pipe conveyor uses a rubber belt that is rolled into a tube. This construction uses six rollers for rolling and maintaining the belt in the desired transverse profile (tube). It means that on one supporting are installed twelve rollers. This leads to relatively considerable vibrations and hence to noise of supporting structure. By a covers are covering the exposed places for noise reduction. The noise pollution may be also increased at the improper fixing. The article is deals by the measurement of rollers vibration which have a different semi finished product of shell and thus a balancing. Measurement of two set of rollers ($\varnothing$ 89 x 214 mm) is presented.

2. Vibration measurement

Measurement was performed on stand measuring which is composed of a part of the tube belt conveyor (Fig. 1). The stand uses a three supports on which can be fixed the roller holders for rollers$\varnothing$ 89 x 214 mm and $\varnothing$ 112 x 224 mm. The roller holders are made from sheet metal with thickness 5 mm. The weight of whole construction (stand) without the rollers is 369 kg. The lower

longitudinal members are provided with adjusting screws (two on each side) which is used to set the stand horizontally. The rollers are fixed to holders by screws which are placed in the roller axis. These holders are made from metal sheet (thickness 5 mm). The axis of roller is fixed displaceable in the holder. Fixation of the roller on the holder is shown on Fig. 2.

Figure 1. Stand measuring

Figure 2. Fixation of the rollers on the stand

Each set of the rollers includes three rollers of identical design ($\varnothing$ 89 x 214 mm). The bearings with inner diameter 20 mm (6204) have the all rollers. Both sets of the rollers differ by used semi finished product of rollers shell. The rollers the first set (1.X) is made from convectional tube and the second set (2.X) is made from accuracy tube. The basic parameters of rollers for measuring are shown in Tab. 1.

From Tab. 1 it is apparent that set 1 which is made from convectional tube, showing large weight dispersion. The difference between the heaviest and the lightest roller is 75.7 g (roller 1.2 and 1.3). It is evident that the roller 1.2 which has the lowest weight having different tolerance of the individual parts. Different tolerance of the shafts and the bearings housings is haven. Conversely the rollers of set 2 have a very small weight difference (the difference between the max. and min weight is only 2.1 g).

Table 1. Rollers parameters

Name	Number of pieces	Internal indication	Weight [g]
Roller from convectional tube	3	1.1	2431,6
		1.2	2352,2
		1.3	2427,9
Roller from accuracy tube	3	2.1	2538,4
		2.2	2540,5
		2.3	2539,8

Belt speed in operation is 2.5 m.s^{-1}. This speed was maintained for all measurement and corresponds of revolutions 563.75 rev.min^{-1} for rollers $\varnothing$ 89 mm. These revolutions were measured continuously by laser tachometer Brüel&Kjær type 2981 (CCLD). The vibrations of the individual rollers were measured by three-axis piezoelectric accelerometer. The acceleration and the own angular frequency is calculated by equations

$$a = \frac{dv}{dt} = -\omega^2 y_0 \sin\omega t = a_0 \sin\omega t, \tag{1}$$

$$\Omega = \sqrt{\frac{k}{m}}, \tag{2}$$

were v - speed, ω - angular frequency, y_0 - displacement amplitude, a_0 - acceleration amplitude, t – time, k – rigidity of the system, m – weight of the system.

The accelerometer was placed on the roller holder (Fig. 3) and it measured the vibration in three mutually orthogonal axes. The vibrations are transmitted through the holders to the support and to the all constructions. The construction is vibrated. Also it was measured the acceleration on the supports and the longitudinal members of construction, simultaneously was the noise measured.

The acceleration sensor and the noise sensors were involved in the analyzer PULSE 3060-B-120 and evaluation by program. Sensing vibration time was 30 s. Each roller was measured by 10 times and were own (dominant) frequency in each axis evaluated including the size of the acceleration.
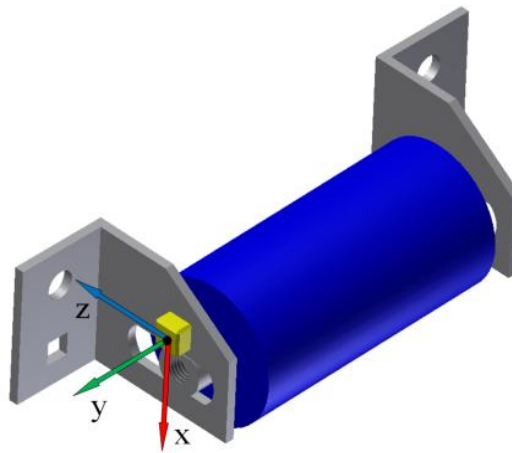
Figure 3. Location of the accelerometer on the roller holder

3. Measurement evaluation and discussion

Evaluation of the acceleration and vibration frequency of individual rollers is shown in Tab. 2. The first three natural frequencies and maximum amplitude of acceleration in individual directions are given. All frequency are placed in the zone where is the sensitivity of the ear human is high.

On Fig. 4, Fig. 5 and Fig. 6 are shown graphs of the acceleration and frequency of roller 1.1 in x, y and z-axis direction.

The Fig. 4 is shown that the maximum acceleration (the largest acceleration amplitude) achieved at a frequency of 1064 Hz which is the dominant (the value of the acceleration is 0.0101 m.s^{-2}). Other two own frequencies are 64 and 352 Hz.
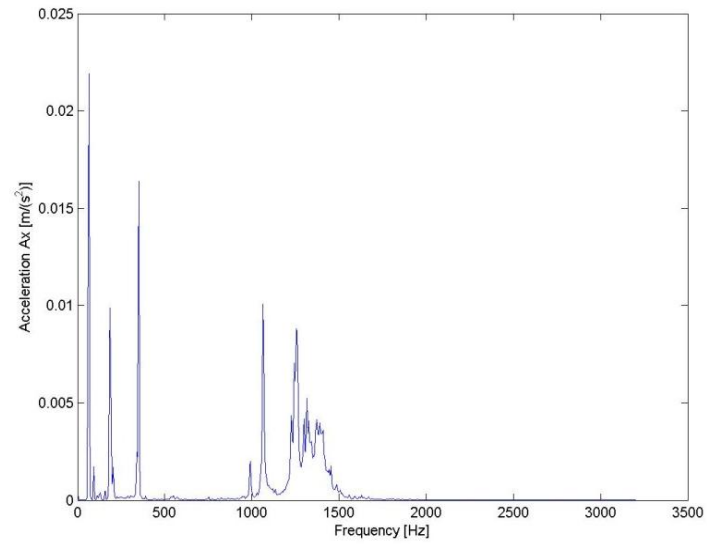
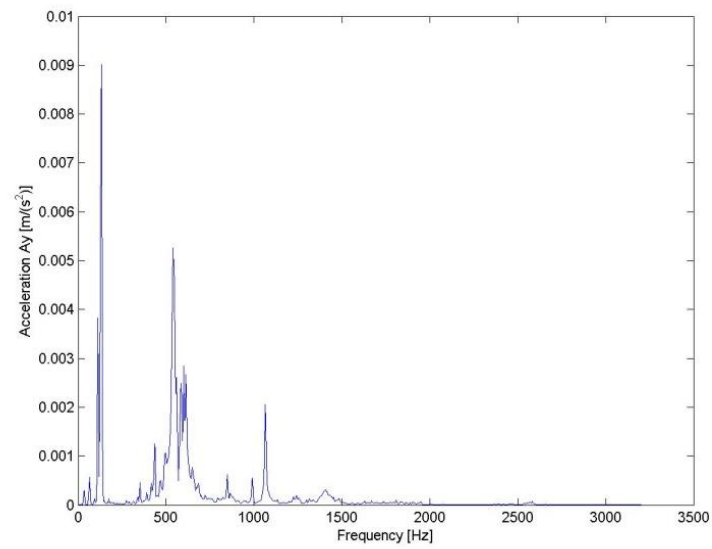**Figure 4.** Acceleration and frequency of roller 1.1 in *x*-axis direction

Figure 5. Acceleration and frequency of roller 1.1 in *y*-axis direction
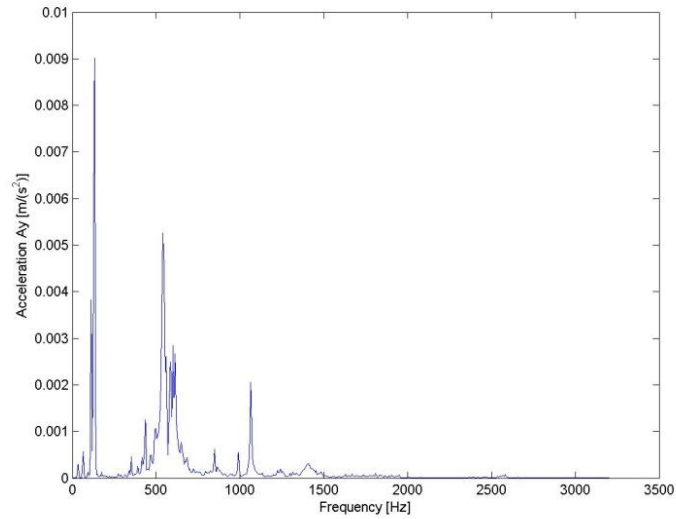
Figure 6. Acceleration and frequency of roller 1.1 in *z*-axis direction

The Tab. 2 shows that the rollers of set 2 exhibit the high vibrations in the *y*-direction, i.e. in the shaft axis (particularly roller 2.2). This roller has an erroneous the imposition. These vibrations are vibrating the steel frame of the conveyor and increase the overall noise of devices. Conversely the roller of set 2 in the *x*-direction has lower frequencies. The dominant frequency of the individual rollers is significantly different. This indicates of their bad balance.

Table 2. Vibration of roller (own frequency and acceleration of roller)

Roller	Dominant frequency	Frequency and acceleration *x* direction		Frequency and acceleration *y* direction		Frequency and acceleration *z* direction	
		f_x [Hz]	a_x [m.s^{-2}]	f_y [Hz]	a_y [m.s^{-2}]	f_z [Hz]	a_z [m.s^{-2}]
1.1	f_1	64	0,0219	132	0,0090	64	0,0459
	f_2	352	0,0164	540	0,0053	188	0,0099
	f_3	1064	0,0101	112	0,0038	92	0,0076
1.2	f_1	352	0,1932	128	0,0121	64	0,0776
	f_2	64	0,0352	528	0,0120	92	0,0601
	f_3	1220	0,0299	536	0,0119	160	0,0582
1.3	f_1	64	0,0480	1176	0,0323	64	0,1733
	f_2	356	0,0286	1168	0,0257	160	0,0125
	f_3	832	0,0106	1264	0,0148	872	0,0057

Table 2. Vibration of roller (own frequency and acceleration of roller) - continue

Roller	Dominant frequency	Frequency and acceleration x direction		Frequency and acceleration y direction		Frequency and acceleration z direction	
		f_x [Hz]	a_x [m.s^{-2}]	f_y [Hz]	a_y [m.s^{-2}]	f_z [Hz]	a_z [m.s^{-2}]
2.1	f_1	804	0,0178	132	0,0585	64	0,0253
	f_2	840	0,0173	1088	0,0366	176	0,0130
	f_3	824	0,0164	996	0,0156	156	0,0130
2.2	f_1	780	0,3361	1088	0,6222	820	0,1759
	f_2	772	0,0270	1004	0,2804	440	0,1563
	f_3	344	0,0288	996	0,0279	156	0,0882
2.3	f_1	904	0,0483	944	0,0101	64	0,0241
	f_2	944	0,0316	904	0,0100	156	0,0117
	f_3	868	0,0278	128	0,0080	864	0,0072

4. Conclusion

The article deals with the measurement of noise two sets of rollers for conveyor belt. The one set is made from the normal tube and the second tube is made from the precision tube. The all rollers have the parameter $\varnothing$ 89 × 214 mm. From the Tab. 1 it is evident that the individual sets of rollers have their weight differ. The measured vibrations (Tab. 2) have an effect on the vibration of the whole construction. The total noise is increases. The maximum size of the acceleration of the roller is in the *x*-axis direction of roller 2.2 (dominant frequency is 780 Hz, acceleration is 0.3361 m.s^{-2}), the minimum size of the acceleration of the roller is in the *x*-axis direction of roller 1.1 (dominant frequency is 1064 Hz, acceleration is 0.0101 m.s^{-2}). In the *y*-axis direction is the maximum acceleration of roller at the roller 2.2 (dominant frequency is 1088 Hz, acceleration is 0.6222 m.s^{-2}), the min. size of the acceleration of the roller is in the *y*-axis direction of roller 1.1 (dominant frequency is 112 Hz, acceleration is 0.0038 m.s^{-2}). In the *z*-axis direction is the maximum acceleration of roller at the roller 2.2 (dominant frequency is 820 Hz, acceleration is 0.1759 m.s^{-2}), the min. size of the acceleration of the roller is in the *z*-axis direction of roller 2.3 (dominant frequency is 864 Hz, acceleration is 0.0072 m.s^{-2}). In the next stage will be measured the rollers driven by a conveyor belt which is not burdened by the transported material.

References

[1] Nový, R.: *Hluk a chvění*, ČVUT Praha, 2000. ISBN 80-02246-3

[2] Apetaur, M.: *Akustika výrobních strojních celků a výrobních prostor*, UJEP Ústí nad Labem, 2007, ISBN 978-80-7044-933-2

[3] Baron, R.: *Industrial Noise Control and Acoustic,* New York, Marcel Deckker, 2003, ISBN 0-8247-0701-X

[4] Nový, R., Kučer, M.: *Snižování hluku a vibrací,* ČVUT Praha, 2009

[5] Klimenda, F., Svoboda, M., Rychlíková, L., Petrenko, A.: Investigation of Vertical Vibration of a Vehicle Model Driving Through a Horizontal Curve, *Manufacturing Technology*, Vol 15, No 2, ISSN 1213-2489

[6] Gerlici, J., Lack, T., Harušinec, J.: The Test Stand Load Modulus Implementation for the Realistic Railway Operation in the Laboratory Conditions, *Manufacturing Technology*, Vol 13, No 4, ISSN 1213-2489

[7] Dižo, J.: Evaluation of Ride Comfort for Passengers by Means of Computer Simulation, *Manufacturing Technology*, Vol 15, No 1, ISSN 1213-2489

Martin Svoboda, Ph.D.: University of J. E. Purkyne in Usti nad Labem, Faculty of Production Technology and Management, Department of Machine and Mechanics, Na Okraji 1001, 400 96, Usti nad Labem, Czech Republic, (*svoboda@fvtm.ujep.cz*).

Frantisek Klimenda, M. Sc.(Ph.D student).: University of J. E. Purkyne in Usti nad Labem, Faculty of Production Technology and Management, Department of Machine and Mechanics, Na Okraji 1001, 400 96, Usti nad Labem, Czech Republic, (*klimenda@fvtm.ujep.cz*).

Josef Soukup, Asocc. Prof.: University of J. E. Purkyne in Usti nad Labem, Faculty of Production Technology and Management, Department of Machine and Mechanics, Na Okraji 1001, 400 96, Usti nad Labem, Czech Republic, (*soukupj@fvtm.ujep.cz*).

Jan Kampo, M. Sc.(Ph.D student).: University of J. E. Purkyne in Usti nad Labem, Faculty of Production Technology and Management, Department of Machine and Mechanics, Na Okraji 1001, 400 96, Usti nad Labem, Czech Republic, (*kampo@fvtm.ujep.cz*). The author gave a presentation of this paper during one of the conference sessions.

Wave-based control of strongly non-uniform lumped flexible systems
(CON295-15)

Joseph W. Thompson, William J. O'Connor

Abstract: Wave-Based Control (WBC) is particularly effective for rest to rest maneuvers of under-actuated, uniform, cascaded, lumped flexible systems. WBC sees the motion as a superposition of rightwards and leftwards travelling mechanical waves. The actuator simultaneously launches and absorbs these waves, to combine position control and active vibration damping. The method has many advantages. It is robust to modelling errors and system changes. It requires minimal sensing, all done at the actuator. Because it is robust, WBC also achieves good control for mildly non-uniform, lumped systems. When highly non-uniform however, control becomes difficult. Wave dispersion then causes trapping of vibrations. A wave model which accurately represents the dynamics must deal with these non-uniformities. In continuous systems non-uniformities cause partial reflection and transmission of waves. This paper examines ways of modelling a similar phenomenon in lumped systems. These models are then used to modify the traditional WBC scheme to achieve good control of strongly non-uniform lumped systems. Applications include control of launch vehicles for spacecraft payload comfort and reduction of propellant sloshing.

1. Introduction

Consider a generic under-actuated flexible system, such as that shown in figure 1, which has a single actuator, with displacement x_0, controlling the motion, x_i, of a cascade of masses and springs, of arbitrary length. This arrangement represents a range of flexible systems of practical engineering interest, including robotic arms, cranes, space structures and disk drive heads. Typically the actuator must directly control x_0 to achieve a desired motion of the tip mass, x_n, and so it must combine position control and active vibration damping. For rest-to-rest manoeuvres to a new target position, these two tasks must be completed simultaneously. If for example it reaches the right position while still vibrating, subsequent vibration absorption will probably move it away from target, and further motion will start the vibration again.

Of the many approaches to date to designing controllers [4, 5], Wave-Based Control (WBC) has been shown to have many advantages [1, 3], including robustness to modelling errors, to actuator limits and to system changes; rapid responses; ease of implementation;
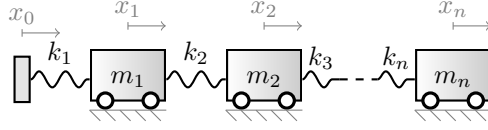
Figure 1. Non-uniform lumped system with one free and one moving boundary

and minimal sensing. Any motion of the actuator is envisaged as launching a wave (or motion disturbance) into the system, which travels to the tip and back, dissipating as it goes. The control system measures the returning wave and gets the actuator to absorb it. This process of absorption provides active vibration damping. If the launch wave has a net (DC) displacement, the process of absorption will also involve a further net displacement which, in the absence of external disturbances, will equal the net displacement of the launch wave. So at steady state, the system will come to rest at a displacement of twice the final value of the launch wave.
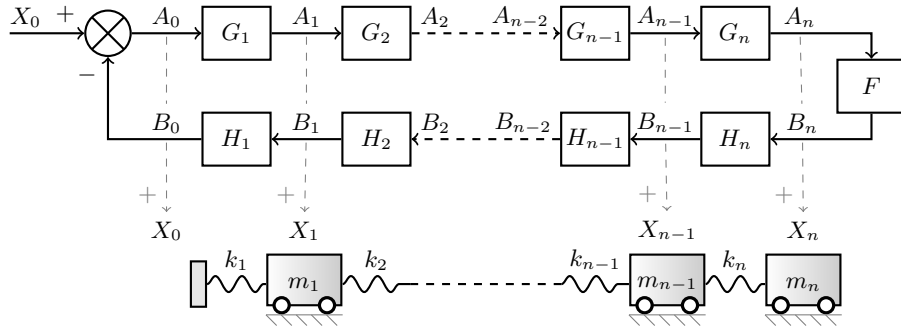
Figure 2. Series wave model of lumped system

Implicit in the design of WBC is some kind of wave model of the lumped system. Figure 2 shows what we call a "series" model for the n-mass system in figure 1, comprising a loop of $2n + 1$ wave transfer functions (WTFs). The upper loop models the outgoing waves (or propagating motion) from actuator to tip, with WTFs G_i, while the lower loop models the waves returning from the tip to the actuator, with WTFs H_i. The motion of each mass, x_i, corresponds to the sum of the corresponding outgoing component, a_i, and the returning component b_i. For the model to be considered valid, the x_i should obey the equations of motion of the system. Using capitals to indicate the Laplace Transform of the corresponding

time-domain variables, the wave model is described by:

$$A_i = G_i A_{i-1} \tag{1}$$

$$B_{i-1} = H_i B_i \tag{2}$$

and the validity condition that the X_i satisfy the equations of motion is:

$$X_i = A_i + B_i \tag{3}$$

The summing junction at the left ensures that, for the actuator, $X_0 = A_0 + B_0$. The free (unconstrained) tip is modelled by the transfer function F, joining the outgoing loop to the returning loop such that:

$$B_n = F A_n \tag{4}$$

WBC works especially well for uniform systems, with equal masses and springs. In this case, all the WTFs in the wave model can be set equal to each other, and then they take the form:

$$G(s) = 1 + \frac{ms^2}{2k} - \sqrt{\frac{ms^2}{k} + \frac{m^2 s^4}{4k^2}} \tag{5}$$

It is easy to verify that figure 2 is then a valid model of figure 1, in the sense that the sum $A_i + B_i$ obeys the same equations of motion as X_i. Thus the wave model provides a new way of understanding the dynamics of the system, an alternative to modal analysis, for example. It resolves the motion into two counter-propagating components passing over, or through, each other. This in turn leads to good controller design.

The inherent robustness of WBC also ensures that this model leads to good control for mildly non-uniform systems. However, as the system becomes strongly non-uniform, control becomes more difficult, resulting for example in longer settling times for rest-to-rest manoeuvres. This challenge is not unique to WBC. Any control system for a system such as figure 1 would experience major problems when x_0 is trying to control x_n and, for example, one of the masses between them is much larger than the rest, causing an inertial blockage, dynamically isolating the tip from the actuator.

As part of ongoing research into WBC, this paper explores ways to model non-uniform mass-spring cascades in a wave-like manner, mainly to help in the design of controllers to deal better with strongly non-uniform systems.

Even in the uniform case, the lumped system is dispersive. The loop model in figure 2 captures this dispersion in the form of the transfer functions, $G(s)$ in equation 5. As the non-uniformity of the system becomes more pronounced, the dispersion increases. Classical

wave analysis would suggest modelling strong non-uniformities using "shunt" transfer functions, interconnecting the upper and lower loops in figure 2, especially at points of greater discontinuity, modelling partial transmission and partial reflection of waves. Such shunt models can, and have been, developed, and are a topic of on-going research [2].

However a series model is still possible, even with strongly non-uniform systems with strong dispersion. For reasons of brevity, this paper focuses on purely series models, that is, models such as figure 2 forming a single loop. One reason for this is to facilitate WBC, which precisely seeks to cause waves to enter the system at the actuator, travel to the tip and then back again, to leave the system through the actuator, leaving the desired motion behind, while damping vibration. The paper will consider the ambiguities in the model, and propose how these might be resolved, and then how they might be applied to control. (Shunt models will be presented in other work.)

2. Resolving the ambiguity in the series wave model

The model shown in figure 2 consists of $2n + 1$ WTFs yet the system has just n equations of motion. As a consequence any $n + 1$ of these WTFs may be chosen arbitrarily and the remaining n may be calculated to satisfy the equations of motion. Therefore there is an infinity of choices for the transfer functions G_i, H_i and F, all giving valid series models of the system. Not all of them, however, will exhibit wave-like behaviour. Although the motion in a lumped system may not be considered as waves in the classical sense, it has already been shown that the motion has certain wave like properties that are useful for designing controllers. The subject of this section is to define these useful wave-like properties, and to use them as validity conditions for the series wave model, thereby removing the ambiguity in WTFs G_i, H_i and F.

2.1. System equations of motion

Figure 3(a) shows a typical internal mass mass m_i, $(1 < i < n - 1)$, for the flexible system of figure 1. Each of these masses m_i has another mass m_{i-1} (or for $n = 1$ the actuator) to its left connected by spring k_i and also a mass to its right m_{i+1} connected by spring k_{i+1}. Figure 3(b) shows the boundary mass m_n which has no mass and spring opposing its motion to the right. The equations of motion of these internal and boundary masses will now be considered separately.

The internal section of the system shown in figure 3(a) has six components of motion: A_{i-1}, A_i, A_{i+1}, B_{i-1}, B_i and B_{i+1}. The components A_{i-1} and B_{i+1} may be thought of as the inputs to this sub-system. They are the motion components (waves) incident from the left and from the right into this sub-system. Equation 6 shows the four remaining motion
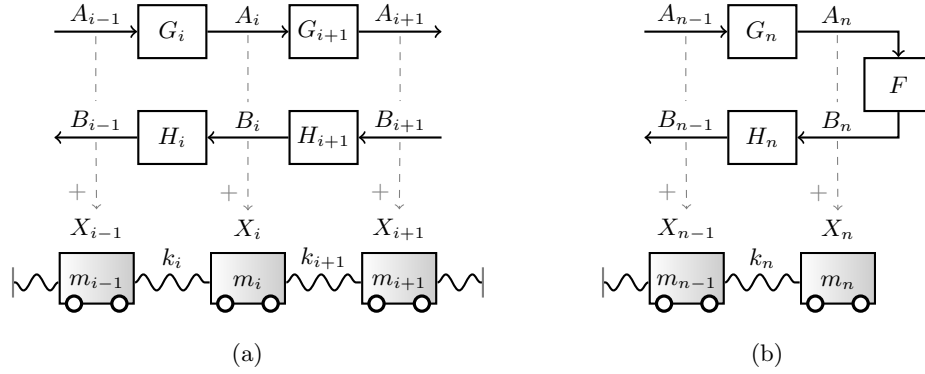
Figure 3. (a) Internal mass subsystem, and (b) Boundary mass subsystem

components written in terms of these inputs, A_{i-1} and B_{i+1}.

$$
\begin{bmatrix} A_{i+1} \\ A_i \\ B_{i-1} \\ B_i \end{bmatrix} = \begin{bmatrix} G_i G_{i+1} & 0 \\ G_i & 0 \\ 0 & H_i H_{i+1} \\ 0 & H_{i+1} \end{bmatrix} \begin{bmatrix} A_{i-1} \\ B_{i+1} \end{bmatrix}
\tag{6}
$$

The motion of mass m_i is described by:

$$
m_i s^2 X_i - k_i \left(X_{i-1} - X_i \right) - k_{i+1} \left(X_{i+1} - X_i \right) = 0
\tag{7}
$$

Using equations 4 and 6 to substitute for the displacements X_{i-1}, X_i and X_{i+1} we obtain:

$$
A_{i-1} \left[G_i \left(s^2 m_i - \left(G_{i+1} - 1 \right) k_{i+1} \right) + \left(G_i - 1 \right) k_i \right]
$$
$$
+ B_{i+1} \left[H_{i+1} \left(-H_i k_i + k_i + k_{i+1} + s^2 m_i \right) - k_{i+1} \right] = 0 \quad (8)
$$

This equation represents the $n - 1$ equations of motion for masses m_1 to m_{n-1}.

The subsystem at the boundary shown in figure 3(b) has four components of motion, A_{n-1}, A_n, B_{n-1} and B_n. The component A_{n-1} may be thought of as the input to this sub-system. It is the motion component (wave) incident from the left hand side. In a similar fashion to the non-boundary masses, the three remaining motion components may be written in terms of A_{n-1} as follows:

$$
\begin{bmatrix} A_n \\ B_{n-1} \\ B_n \end{bmatrix} = \begin{bmatrix} G_n \\ F G_n H_n \\ F G_n \end{bmatrix} A_{n-1}
\tag{9}
$$

583

The motion of mass m_n is described by:

$$s^2 m_n X_n - k_n (X_{n-1} - X_n) = 0 \tag{10}$$

Using equations 4 and 9 to substitute for displacements X_{n-1} and X_n we obtain:

$$A_{n-1} \left(k_n \left[G_n (F H_n - F - 1) + 1 \right] - (F+1) s^2 G_n m_n \right) = 0 \tag{11}$$

2.2. Towards a unique series wave model

To help resolve ambiguities, we propose two constraints on the model, based on desired wave-like properties. Firstly, each subsection of the system, such as shown in figure 3(a), should work independently of the rest of the system and thus must itself be a valid series model. Secondly, the model should allow superposition, so that counter-propagating wave components at any point should not interfere with each other. These constraints imply that the equation of motion of each internal mass m_i must hold for any possible values of A_{i-1} and B_{i+1}, i.e. any motion incident from the left and any motion incident from the right. Similarly at the boundary we require that the equation of motion for the boundary mass m_n should hold for any possible value of A_{n-1}. For equation 8 to hold for any values of A_{i-1} and B_{i+1}, two independen equations emerge, one describing a recursion relation between G_i and G_{i+1} and one describing a recursion relation between H_i and H_{i+1}.

$$G_i = \frac{k_i}{k_{i+1} (1 - G_{i+1}) + k_i + s^2 m_i} \tag{12}$$

$$H_{i+1} = \frac{k_{i+1}}{-H_i k_i + k_i + k_{i+1} + s^2 m_i} \tag{13}$$

If equation 11 is to hold for any value of A_{n-1} then the boundary WTF F must be

$$F = \frac{(G_n - 1) k_n + s^2 G_n m_n}{G_n \left[(H_n - 1) k_n - s^2 m_n \right]} \tag{14}$$

Now if any G_i is known, all the other G_i may be calculated according to equation 12 and similarly if any H_i is known then all the other H_i may be calculated according to equation 13. The chosen constraints supply an extra $n - 1$ equations, bringing the total number to $2n - 1$. But two more equations are still needed. There is still a free choice for one of the G_i and one of the H_i, any combination of which will yield a valid series model. It is here proposed that a very good choice is to make the upper and lower loops behave as if they were parts of systems extending to infinity in a uniformly, periodic way. For this to be true the G_i and H_i must cycle and to return back to the same transfer function at the start of each new appended system. In other words, the dynamic load seen by the actuator, looking

584

forward, is the non-uniform cascade of masses and springs of the actual system, followed by a (notional) repetition of this system in a periodic way, for ever. This can be achieved by making G_n and G_1 also follow the recursion given by equation 12 such that:

$$G_n = \frac{k_n}{-\left(G_1 - 1\right)k_1 + k_n + s^2 m_n} \tag{15}$$

In this way the G_i are made to cycle periodically. This can be thought of as making the system as close to uniform as possible, by repeating the (non-uniform) sub-system, uniformly, to infinity. It is conjectured that such an arrangement, for example, may maximise power flow, and yield the flattest possible frequency response, between actuator and tip. It also helps design very good control systems. Similar arguments apply for the return loop. By making H_1 and H_n follow the recursion given by equation 13, the return loop is made uniformly periodic in the same sense, where now the notional extension to infinity is through the actuator to the left.

$$H_n = \frac{k_n}{-\left(G_1 - 1\right)k_1 + k_n + s^2 m_n} \tag{16}$$

These two equations bring the total to $2n + 1$ and provide an unambiguous way to arrive at a wave model for a non-uniform system.

Comment 1

Whether or not the choices just described are the best possible, and how exactly one might define "best", are still open questions. As a minimum, however, we can certainly be sure that these choices lead to valid, well-defined, series wave models of non-uniform systems.

Comment 2

When these criteria are implemented in practice, the mathematics can become tedious, especially for cascades with more than a few masses and springs. But at least three interesting features emerge. Firstly, as will be seen in section 2.4 a quadratic equation is obtained in the WTFs, with two solutions, one of which is proper (with phase lag and finite gain for all frequencies), the other not. This is exactly what happened in the uniform case. The appropriate choice between the two solutions is obvious. Secondly, the order of the WTFs does not grow with the length of the system, but remains "close to" second order (with terms in s^2 plus fractional powers of s), for all the resulting G_i and H_i. Thirdly, the procedure leads to WTFs which become identical to those of the previous uniform model when the masses and springs are equal.

2.3. Uniform case

In the uniform case, where all springs are of stiffness k, all masses are m and $G_i = H_i = G$, equations 12 and 13 reduce to the same quadratic in G.

$$G^2 - \left(2 + \frac{ms^2}{k}\right) G + 1 = 0 \tag{17}$$

This has two solutions given by:

$$G = 1 + \frac{ms^2}{2k} \pm \sqrt{\frac{ms^2}{k} + \frac{m^2 s^4}{4k^2}} \tag{18}$$

These two solutions correspond to motion propagating in two different directions. At a given complex frequency s, one of these solutions is strictly proper, and causal. This solution corresponds to a forward propagating wave and the other to a wave propagating in the opposite direction. Equation 14 for the boundary WTF then gives $F = G$ so that all WTFs including F are equal in the uniform case.

2.4. Two-mass system

The simplest non-uniform system consists of two masses ($n = 2$). The series model for this system consists of five transfer functions, G_1, G_2, F, H_2 and H_1. In this case equations 12 and 15 may be simplified to a quadratic in G_1:

$$G_1^2 - \left(\frac{(k_1 + k_2)\left(2k_1 + m_1 s^2\right)}{k_1\left(k_1 + k_2 + m_1 s^2\right)} + \frac{m_2 s^2}{k_1}\right) G_1 + \frac{k_1 + k_2 + m_2 s^2}{k_1 + k_2 + m_1 s^2} = 0 \tag{19}$$

This has solutions:

$$G_1 = \frac{(k_1 + k_2)\left(m_1 + m_2\right)s^2 + 2k_1\left(k_1 + k_2\right) + m_1 m_2 s^4}{2k_1\left(k_1 + k_2 + m_1 s^2\right)}$$

$$\pm \frac{\sqrt{\left(m_2 s^2\left(k_1 + k_2 + m_1 s^2\right) + \left(k_1 + k_2\right)\left(2k_1 + m_1 s^2\right)\right)^2 - 4k_1^2\left(k_1 + k_2 + m_1 s^2\right)\left(k_1 + k_2 + m_2 s^2\right)}}{2k_1\left(k_1 + k_2 + m_1 s^2\right)} \tag{20}$$

and the corresponding solutions for G_2 are:

$$G_2 = \frac{(k_1 + k_2)\left(m_1 + m_2\right)s^2 + 2k_2\left(k_1 + k_2\right) + m_1 m_2 s^4}{2k_2\left(k_1 + k_2 + m_2 s^2\right)}$$

$$\pm \frac{\sqrt{\left(m_2 s^2\left(k_1 + k_2 + m_1 s^2\right) + \left(k_1 + k_2\right)\left(2k_1 + m_1 s^2\right)\right)^2 - 4k_1^2\left(k_1 + k_2 + m_1 s^2\right)\left(k_1 + k_2 + m_2 s^2\right)}}{2k_2\left(k_1 + k_2 + m_2 s^2\right)} \tag{21}$$

where the plus or minus sign before the radical must be the same as in G_1. So, as in the uniform case, there are two solutions for G_1 and G_2 corresponding to waves propagating in
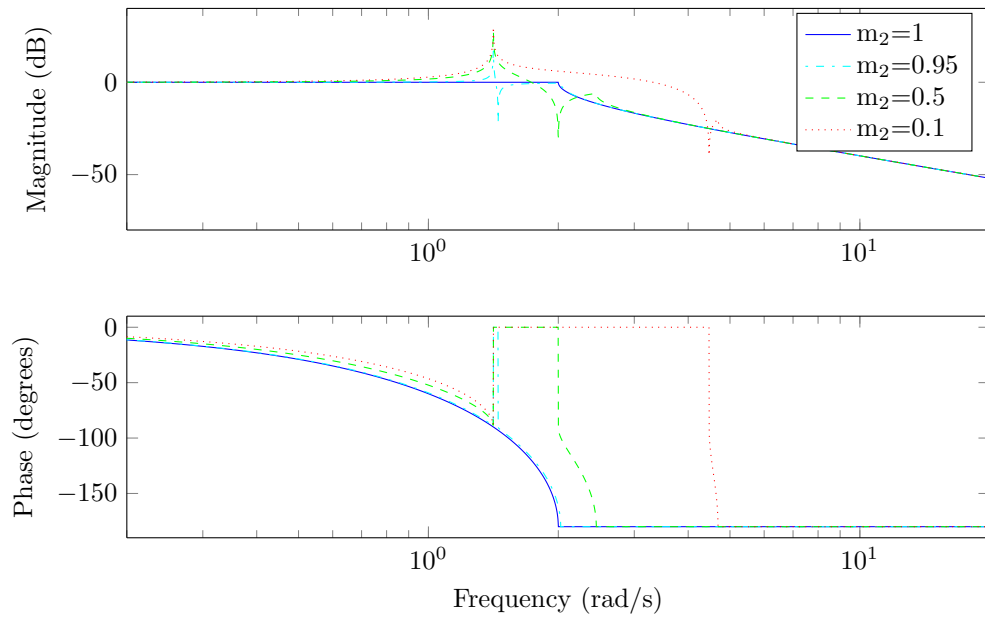
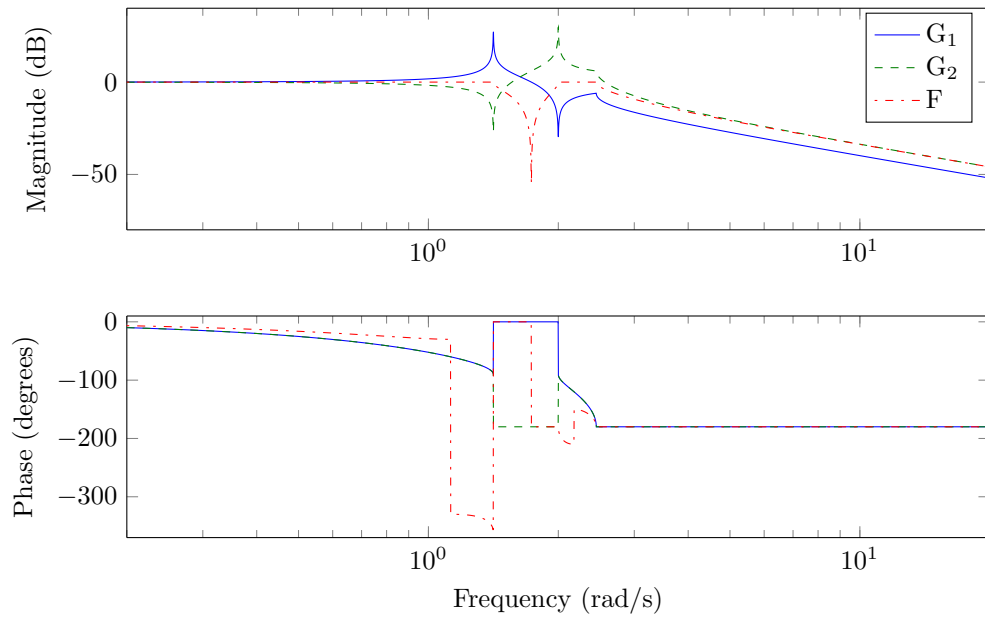**Figure 4.** Bode plots for WTF G_1 as system becomes non-uniform

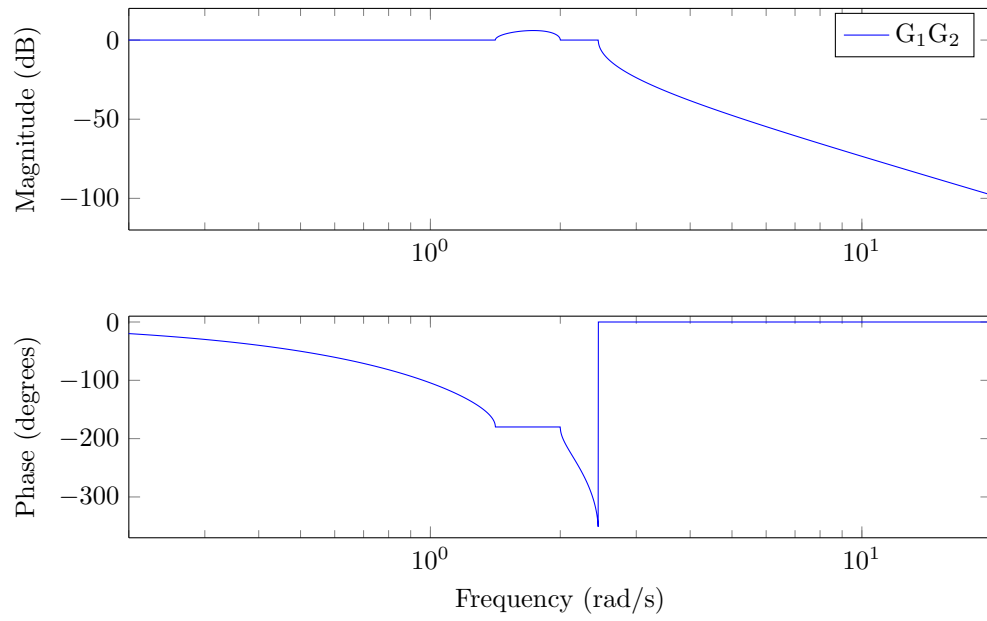**Figure 5.** Bode plots for WTFs G_1, G_2 and F

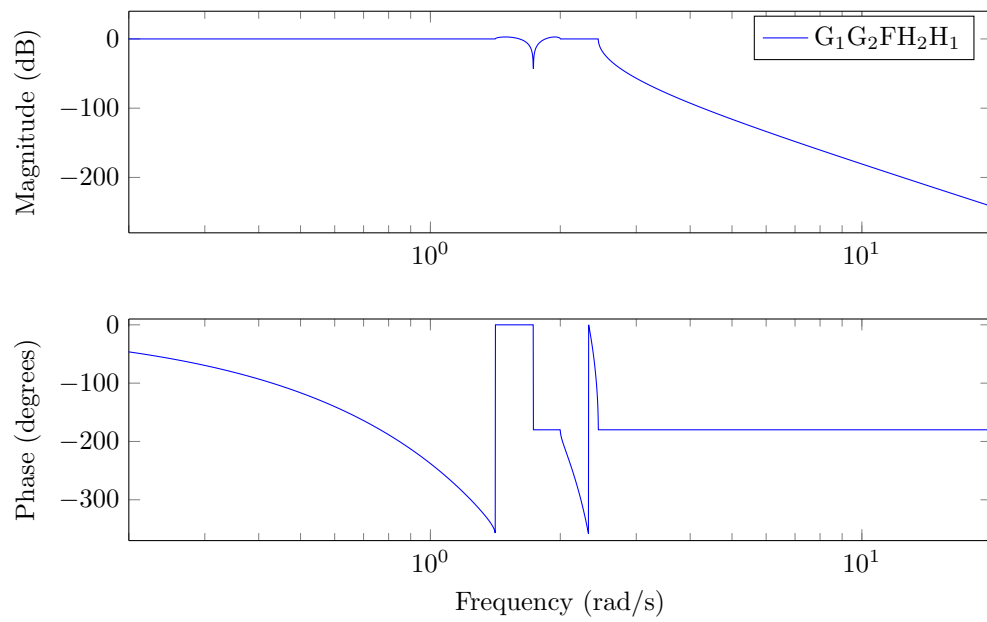**Figure 6.** Bode plots for transfer function G_1G_2

Figure 7. Bode plots for transfer function $G_1G_2FH_2H_1$

two directions. Equations 13 and 16 may be solved in the same way. It is easy to show that the solutions for H_1 and H_2 will be the same as equations 20 and 21 but with k_1 and k_2 interchanged. The boundary transfer function F may then be calculated using equation 14. It can be seen that all the WTFs in this model are global, or in other words they depend on all the parameters of the system: k_1, k_2, m_1 and m_2. In the uniform case, the solutions for G_1 and G_2 reduce to the uniform WTF of equation 18. Changes in the Bode magnitude and phase plots for G_1 are shown in figure 4, as the system departs from the uniform case ($k_1 = k_2 = 1$, $m_1 = m_2 = 1$). The system is made gradually more non-uniform by reducing the value of m_2, the tip mass. The springs are kept equal, implying that $H_1 = G_2$ and $H_2 = G_1$ in all cases. It can be seen that the low and high frequency behaviour is the same in all cases and is that of the uniform WTF of equation 18 with $k = k_1$ and $m = m_1$. When the system becomes non-uniform a finite pole and zero appear in The pole and zero occur at frequencies, $\sqrt{\frac{k_1+k_2}{m_1}}$ and $\sqrt{\frac{k_1+k_2}{m_2}}$ respectively.

The Bode magnitude and phase plots for G_1, G_2 and F are shown in figure 5 for $m_2 = 0.5$. At high and low frequencies both G_2 and F approach the uniform WTF with $k = k_2$ and $m = m_2$ It can be seen that G_2 also has a single pole and zero but interestingly where G_1 has a pole, G_2 has a zero and vice versa. It can also be seen that F has a zero at frequency $\sqrt{\frac{(k_1+k_2)(m_1+m_2)}{2m_1 m_2}}$.

The Bode plots for the product $G_1 G_2$ are shown in figure 6. This is the transfer function from actuator to tip and for the system in question is equal to $H_2 H_1$, the transfer function from tip back to actuator. In the product $G_1 G_2$ a cancellation of poles and zeros occurs so that it has a very flat frequency response with a small hump between frequencies $\sqrt{\frac{k_1+k_2}{m_1}}$ and $\sqrt{\frac{k_1+k_2}{m_2}}$. The magnitude plot has a maximum at frequency $\sqrt{\frac{(k_1+k_2)(m_1+m_2)}{2m_1 m_2}}$.

The magnitude and phase plots for the product $G_1 G_2 F H_2 H_1$ are shown in figure 7. The flatness of the response and unity gain, despite the non-uniformity, are conjectured to be ideal for optimising wave-based control as they suggest "unhindered", uniform motion propagation around the loop, from actuator to tip and back to actuator.

3. Conclusions and future work

The model of figure 2 is not uniquely defined and many possible WTFs lead to valid series wave models. Proposals have been presented here to remove the ambiguities, leading to a unique series wave model of the non-uniform system. In the uniform case the series model proved useful in designing control systems and it is expected the same will apply to the non-uniform case .

This series model is made possible by imagining the non-uniform system as one unit of a system that is extended uniformly to infinity. The new wave model consists of non-uniform

WTFs each of which depends on all the dynamic parameters of the system. In this sense the series model is global rather than local. If a purely local model is desired (one where each WTF depends only on local m_i and k_i), shunt WTFs must be added to the model. Such shunts would represent partial reflection and partial transmission of wave components at points within the system.

The non-uniform WTFs have some interesting properties. Unlike in the uniform case, they have finite poles and zeros. Interestingly however the products of the series of WTFs from actuator to tip and tip to actuator have no poles or zeros. Similarly the overall transfer function from actuator to the tip and back again has a very flat frequency response.

Future work will include: investigations into higher order non-uniform systems; the modification of existing wave based control schemes using the non-uniform WTFs; and further development of the shunt wave model.

Acknowledgments

References

[1] O'CONNOR, W. J. Excellent control of flexible systems. *Control* (2005), 6181–6186.

[2] O'CONNOR, W. J. Wave-like modelling of cascaded, lumped, flexible systems with an arbitrarily moving boundary. *Journal of Sound and Vibration 330*, 13 (2011), 3070–3083.

[3] O'CONNOR, W. J., AND FUMAGALLI, A. Refined Wave-Based Control Applied to Non-linear, Bending, and Slewing Flexible Systems. *Journal of Applied Mechanics 76*, 4 (2009), 041005.

[4] PAO, L. Y. Minimum-time control characteristics of flexible structures. *Journal of Guidance, Control, and Dynamics 19*, 1 (1996), 123–129.

[5] ROBINETT III, R. D., FEDDEMA, J., EISLER, G. R., DOHRMANN, C., PARKER, G. G., WILSON, D. G., AND STOKES, D. *Flexible robot dynamics and controls*, vol. 19. Springer Science & Business Media, 2012.

Joseph W. Thompson, BSc, ME (PhD student): University College Dublin, School of Mechanical and Materials Engineering, Belfield, Dublin 4, Rep. of Ireland
(*joseph.thompson@ucdconnect.ie*).

The author gave a presentation of this paper during one of the conference sessions.

William J. O'Connor, BE, PhD, FIEI, CEng: University College Dublin, School of Mechanical and Materials Engineering, Belfield, Dublin 4, Rep. of Ireland (*william.oconnor@ucd.ie*).

On the mathematical analysis of vibrations of axially moving strings and beams
(ASY239-15)

Wim T. van Horssen

Abstract: In this paper the transversal vibrations of an axially moving string or beam with constant or time-varying length, time-varying velocity, and/or time-varying tension are studied. By using a multiple timescales perturbation method, asymptotic approximations of the solutions of the formulated initial-boundary value problems are constructed. The applicability of Galerkin's truncation method and the applicability of the method of characteristic coordinates for these types of problems are discussed. The presence of internal resonances and autoresonances are described in detail. For conveyor belt problems it will be shown how the two timescales perturbation method in combination with the method of characteristic coordinates can be used to construct asymptotic approximations of the solutions on long timescales. Also for these conveyor belt problems it turned out that Galerkin's truncation method was not applicable to obtain asymptotic results on long timescales.

1. Introduction

Over the last sixty years a huge amount of papers was published on the transversal vibrations of axially moving strings or beams. This was and still is partly due to the enormous variety in engineering applications such as conveyor belts, chair lifts, pipes transporting liquids and gases, band saws, elevator cables, crane and mining hoists, and so on. The relatively simple, mathematical description by means of string-like or beam-like models was and is another reason to consider these vibration problems. The reader is referred to the following, rather recent papers [1-27] and the references therein to have a quick overview what was studied in the past, and how it was studied. Usually an initial-boundary value problem for an axially moving , tensioned string or for a tensioned Euler-Bernoulli beam equation is studied. These string and beam equations can be linear or nonlinear. As linear string and beam equation one has

$$u_{tt} + 2Vu_{xt} + V_t u_x + \left(V^2 - c^2\right)u_{xx} = 0, \text{ and} \tag{1}$$

$$u_{tt} + 2Vu_{xt} + V_t u_x + \left(V^2 - c^2\right)u_{xx} + \frac{EI}{\rho A}u_{xxxx} = 0 \tag{2}$$

respectively, where $u(x,t)$ is the displacement of the string or beam in vertical direction, $V(t)$ is the time-varying string or beam speed in horizontal direction, $c > 0$ is the wave speed due to a pretension in the string or beam, x is the coordinate in horizontal direction, E is the modulus of elasticity, I is the second moment of inertia with respect to the string/beam middle plane, ρ is the mass density of the string/beam, A is the cross-sectional area of the string/beam, t is the time, and L is the distance between the pulleys (see figure 1).
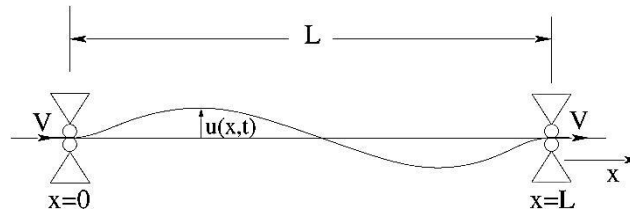
Figure 1. Schematic model of the axially moving continuum with axial speed V in x-direction and transversal displacement $u(x,t)$.

When small (geometrical) nonlinearities are introduced in the model equations (1) and (2), or when small axial speed fluctuations in V (due to belt system imperfections such as pulley eccentricities, and so on) are considered, one can apply perturbation methods to approximate the solution of an initial-boundary value problem for Eq. (1) or Eq. (2). The reader is referred to [28-25] to have a good idea about the available perturbation methods for these types of problems. For the aforementioned problems it is usually assumed that the solution $u(x,t)$ can be written in an infinite series representation, that is, in a Fourier series

$$u(x,t) = \sum_{n=1}^{\infty} a_n(t)\, \phi_n(x) \quad , \tag{3}$$

where $\phi_n(x)$ are the eigenfunctions of the eigenvalue problem corresponding to the linear, unperturbed boundary value problem for Eq. (1) or Eq. (2). By substituting the infinite series (3) into the initial-boundary value problem for $u(x,t)$ one obtains an infinite dimensional system of ordinary differential equations for the functions $a_n(t)$. This infinite dimensional system is usually truncated to only the first few oscillation modes, that is, the infinite series (3) is truncated to $\sum_{n=1}^{N} a_n(t)\phi_n(x)$ with $N = 1, 2,$ or $3.$ For beam-like problems this approach seems to be working when the bending

592

stiffness is sufficiently large and the initial energy is restricted to the first few modes. For string-like problems, however, is has to been shown in [5, 6, 7, 14, 24] that application of Galerkin's truncation method may lead to inaccurate results on long time-scales. This is primarily caused by the fact that by truncating the system to a finite number of oscillation modes, one in fact neglects the presence of infinitely many internal resonances in the system. In this short paper it will be shown how string-like problems can sometimes be solved by using a multiple timescales perturbation in combination with the method of characteristic coordinates. This paper is organized as follows. In section 2 of this paper an initial-boundary value problem for an axially moving string with a low and harmonically time-varying axial velocity will be formulated. In section 3 it will be shown that application of Galerkin's truncation method in combination with the multiple timescales perturbation method leads to inaccurate results on long timesscales. In section 4 it will be shown how accurate results on long timescales can be obtained by introducing characteristic coordinates in the multiple scales approach. Finally, in section 5 some conclusions will be drawn, and some remarks will be made.

2. Formulation of the problem

In this paper the following initial-boundary value problem in non-dimensional form (see also [5, 6, 7, 14, 24]) is considered for the function $u(x,t)$:

$$u_{tt} - u_{xx} = -V_t u_x - 2V u_{xt} - V^2 u_{xx} \quad , \quad t > 0 \, , \, 0 < x < 1 \, , \tag{4}$$

$$u(x,0) = \phi(x) \, , \, u_t(x,0) = \psi(x) \, , \, 0 < x < 1 \, , \tag{5}$$

$$u(0,t) = u(1,t) = 0 \, , \quad t \geq 0 \, , \tag{6}$$

where the axial velocity $V(t)$ of the string is assumed to be a harmonically varying function about a mean velocity of order ε. The velocity variation frequency is Ω, and its amplitude $\varepsilon \alpha$, and one writes

$$V(t) = \varepsilon \left(V_0 + \alpha \sin(\Omega t) \right), \tag{7}$$

where $\varepsilon, V_0, \alpha,$ and Ω are constants with $V_0 > |\alpha|, \Omega > 0,$ and ε is a dimensionless small parameter with $0 < \varepsilon \ll 1$. The condition $V_0 > |\alpha|$ implies that the string will always move forward in one direction. The functions $\varphi(x)$ and $\psi(x)$ in (5) are the initial displacement and the initial velocity of the string, respectively.

3. A Fourier series approach and Galerkin's method

In this section an approximation of the solution of the initial-boundary value problem (4) – (6) will be constructed in Fourier series form by using a two-timesscales perturbation method. It is assumed that $u(x,t)$ can be written in the following form

$$u(x,t) = \sum_{n=1}^{\infty} u_n(t,\tau;\varepsilon)\sin(n\pi x),$$ (8)

with $\tau = \varepsilon t$. By substituting the series (8) into the partial differential equation (4), by using the orthogonality properties of the sin-functions, and by approximating $u_k(t,\tau;\varepsilon)$ by $w_{k0}(t,\tau) + \varepsilon w_{k1}(t,\tau) + O(\varepsilon^2)$, the following $O(1)$-problem and $O(\varepsilon)$-problem for w_{k0} and w_{k1} can be obtained

$$O(1): \quad \frac{\partial^2 w_{k0}}{\partial t^2} + (k\pi)^2 w_{k0} = 0,$$ (9)

$$O(\varepsilon): \frac{\partial^2 w_{k1}}{\partial t^2} + (k\pi)^2 w_{k1} = -2\frac{\partial^2 w_{k0}}{\partial t\partial \tau} + \sum_{\substack{n=1 \\ n\pm k \\ \text{is odd}}}^{\infty} \frac{nk}{n^2 - k^2}\left[4\alpha\Omega\cos(\Omega t)w_{n0} + 8(V_0 + \alpha\sin(\Omega t))\frac{\partial w_{n0}}{\partial t}\right].$$

(10)

The solution of the $O(1)$-problem can be written as follows:

$$w_{k0}(t,\tau) = A_{k0}(\tau)\cos(k\pi t) + B_{k0}(\tau)\sin(k\pi t),$$ (11)

where $A_{k0}(\tau)$ en $B_{k0}(\tau)$ are still arbitrary functions, which are so determined as to make the solution of the $O(\varepsilon)$-problem for $w_{k1}(t,\tau)$ free of secular terms. Since it assumed that $w_{k0}(t,\tau)$ and $w_{k1}(t,\tau)$ are bounded on timescales of $O(\varepsilon^{-1})$, these secular (unbounded) terms may destroy the accuracy of the approximations on long timescales, so they should be avoided. From Eq. (10) it can readily be seen that resonances will occur when $\Omega = (k+n)\pi, \Omega = (k-n)\pi$ or $\Omega = (n-k)\pi$ with $k\pm n$ is odd. So, secular terms in the solution of the $O(\varepsilon)$-problem will occur when Ω is an odd multiple of π. When Ω is equal to $m\pi$ with m odd and fixed it follows from (10) (see also [5, 6, 7, 14, 24]) that $A_{k0}(\tau)$ and $B_{k0}(\tau)$ have to satisfy:

594

$$\frac{dA_{k0}}{d\tau} = -\frac{\alpha}{m}\Big[(m-k)B_{(m-k)0} - (k+m)B_{(k+m)0} - (k-m)B_{(k-m)0}\Big],$$

$$\frac{dB_{k0}}{d\tau} = -\frac{\alpha}{m}\Big[(m-k)A_{(m-k)0} - (k+m)A_{(k+m)0} + (k-m)A_{(k-m)0}\Big], \tag{12}$$

for $k = 1, 2, 3,\dots$ And for non positive indices k, the functions A_{k0} and B_{k0} are defined to be zero. System (12) is an infinite dimensional system of coupled ordinary differential equations. It is clear from the structure of the system (12) that infinitely many interactions between the vibration modes occur.

3.1. Application of the truncation method

In this section system (12) with $m = 1$ will be studied by using Galerkin's truncation method, that is, the infinite dimensional system is truncated to a finite dimensional one (that is, only a finite number of vibration modes is considered). For example truncating, the infinite dimensional system (12) to the first three modes gives $\dot{X} = AX$, where

$$X = \begin{bmatrix} A_{10} \\ B_{10} \\ A_{20} \\ B_{20} \\ A_{30} \\ B_{30} \end{bmatrix}, \ \ and \ A = \begin{bmatrix} 0 & 0 & 0 & -2 & 0 & 0 \\ 0 & 0 & 2 & 0 & 0 & 0 \\ 0 & -1 & 0 & 0 & 0 & -3 \\ 1 & 0 & 0 & 0 & 3 & 0 \\ 0 & 0 & 0 & -2 & 0 & 0 \\ 0 & 0 & 2 & 0 & 0 & 0 \end{bmatrix}.$$

This system has eigenvalues $2\sqrt{2}i, -2\sqrt{2}i,$ and $0,$ all with multiplicity 2. By using the computer software package MAPLE, the eigenvalues of system (12) with $m = 1$ have been computed and are (up to the first 10 modes) listed in Table 1.

No. of modes	Eigenvalues of matrix A (all multiplicity 2)	Dimension eigenspace of A
1	0	2
2	$\pm\sqrt{2i}$	4
3	$0, \pm 2\sqrt{2i}$	6
4	$\pm 1.13i, \pm 4.33i$	8
5	$0, \pm 2.30i, \pm 5.89i$	10
6	$\pm 7.50i, \pm 1.00i, \pm 3.56i$	12
7	$0, \pm 9.15i, \pm 2.05i, \pm 4.90i$	14
8	$\pm 10.83i, \pm 0.93i, \pm 3.18i, \pm 6.30i$	16
9	$0, \pm 12,54i, \pm 1.89i, \pm 4.38i, \pm 7.74i$	18
10	$\pm 14.26i, \pm 0.87i, \pm 5.65i, \pm 9.23i, \pm 2.93i$	20

Table 1. Approximations of the eigenvalues of the truncated system (12).

From Table 1, it can be seen that the eigenvalues of the truncated system are always either zero or purely imaginary. It is well known in mathematics that in this case no conclusion can be drawn for the infinite dimensional system.

3.2. Analysis of the infinite dimensional system (12)

In this section, we shall show that the results obtained by applying the truncation method are not valid on timescales of $O\left(\varepsilon^{-1}\right)$ in all cases. By introducing $X_{k0}\left(\tau\right) = kA_{k0}\left(\tau\right)$ and $Y_{k0}\left(\tau\right) = kB_{k0}\left(\tau\right)$, system (12) becomes:

$$\begin{cases} \dfrac{dX_{k0}}{d\tau} = k\left[-Y_{(m-k)0} + Y_{(k+m)0} + Y_{(k-m)0} \right], \\ \dfrac{dY_{k0}}{d\tau} = -k\left[X_{(m-k)0} + X_{(k+m)0} + X_{(k-m)0} \right], \end{cases} \qquad (13)$$

for $k = 1, 2, 3, \ldots$, and the functions X_{k0} and Y_{k0} are zero for non positive indices k. Then it can be deduced that:

$$\begin{cases} X_{k0}\dot{X}_{k0} = k\left[-X_{k0}Y_{(m-k)0} + X_{k0}Y_{(k+m)0} + X_{k0}Y_{(k-m)0} \right], \\ Y_{k0}\dot{Y}_{k0} = -k\left[Y_{k0}X_{(m-k)0} + Y_{k0}X_{(k+m)0} + Y_{k0}X_{(k-m)0} \right]. \end{cases} \tag{14}$$

By adding both the equations in (14), and by taking the sum from $k = 1$ to ∞, it follows that:

$$\begin{aligned} \frac{1}{2}\sum_{k=1}^{\infty}\frac{d}{d\tau}\left(X_{k0}^2 + Y_{k0}^2 \right) = \quad & m\sum_{k=1}^{\infty}\left(X_{(k+m)0}Y_{k0} - Y_{(k+m)o}X_{k0} \right) \\ & +(1)\left(-X_{(m-1)0}Y_{10} - Y_{(m-1)0}X_{10} \right) \\ & +(2)\left(-X_{(m-2)0}Y_{20} - Y_{(m-2)0}X_{20} \right) \\ & \qquad\qquad \vdots \\ & +(m-2)\left(-X_{20}Y_{(m-2)0} - Y_{20}X_{(m-2)0} \right) \\ & +(m-1)\left(-X_{10}Y_{(m-1)0} - Y_{10}X_{(m-1)0} \right). \end{aligned} \tag{15}$$

By differentiating Eq. (15) with respect to τ on both sides, we obtain:

$$\frac{1}{2}\sum_{k=1}^{\infty}\frac{d^2}{d\tau^2}\left(X_{k0}^2 + Y_{k0}^2 \right) = 2m^2\sum_{k=1}^{\infty}\left(X_{k0}^2 + Y_{k0}^2 \right), \tag{16}$$

and then by putting $\sum_{k=1}^{\infty}\left(X_{k0}^2 + Y_{k0}^2 \right) = W(\tau)$ into Eq. (16) yields:

$$\frac{d^2W(\tau)}{d\tau^2} - 4m^2W(\tau) = 0. \tag{17}$$

The solution of (17) is: $\qquad W(\tau) = C_1 e^{2m\tau} + C_2 e^{-2m\tau},$

where C_1 and C_2 are arbitrary constants and can be determined by using the initial conditions.

The energy of the system can be approximated using the function $W(\tau)$. For $C_1 \neq 0, W(\tau)$ (so the energy) increases exponentially if τ increases. Thus $W(\tau)$ is unbounded in τ and increases as τ increases. This behavior is different from the behavior of A_{k0} and B_{k0} as obtained by applying the truncation method.

This implies that the approximations obtained by applying the truncation method to system (12) are not accurate on long timescales, that is, on timescales of order ε^{-1}.

4. The method of characteristic coordinates

In this section a two-timescales perturbation method will be used to construct asymptotic approximations of the solution of the initial-boundary value problem (4)-(7), which are valid on long timescales, that is, on timescales of order ε^{-1}. To avoid errors due to truncation in the Fourier series approach (see the previous section) it will turn out that the use of characteristic coordinates $\sigma = x - t, \xi = x + t$ is an appropriate approach to construct asymptotic approximations on long timescales. In this approach the initial-boundary value problem is transformed into an initial value problem by extending the dependent variables as well as the initial values $\phi(x)$ and $\psi(x)$ to odd and 2-perodic functions in x. This is accomplished by multiplying each term in Eq. (4) which is not already odd in x (i.e. terms like u_x and u_{xt}) with $H(x)$, where H is an odd and 2-periodic function in x, and on $0 < x < 1$ H is equal to 1. So, Eq.(4) becomes

$$u_{tt} - u_{xx} = \varepsilon\left[-\alpha\Omega\cos(\Omega t)H(x)u_x - 2(V_0 + \alpha\sin(\Omega t))H(x)u_{xt}\right]$$
$$+O(\varepsilon^2).$$

By assuming that the function u is a function depending on the characteristic variables σ, ξ, and the slow time $\tau = \varepsilon t$, that is, $u(x,t) = v(\sigma,\xi,\tau)$, and by assuming that $v(\sigma,\xi,\tau)$ has the following formal expansion in ε

$$v(\sigma,\xi,\tau) = v_0(\sigma,\xi,\tau) + \varepsilon v_1(\sigma,\xi,\tau) + \cdots,$$

one obtains in the usual way the following $O(1)$-problem, and $O(\varepsilon)$-problem:

$O(1)$:

$$-4v_{0\sigma\xi} = 0, \qquad\qquad \sigma < \xi, \qquad\qquad \tau > 0, \tag{18}$$

$$v_0(\sigma,\sigma,0) = \phi_0(\sigma), \qquad\qquad \sigma = \xi, \qquad\qquad \tau = 0, \tag{19}$$

$$-v_{0\sigma}(\sigma,\sigma,0) + -v_{0\xi}(\sigma,\sigma,0) = \psi_0(\sigma), \qquad \sigma = \xi, \qquad \tau = 0, \tag{20}$$

$O(\varepsilon)$:

$$-4v_{1\sigma\xi} = -2v_{0\xi\tau} + 2v_{0\sigma\tau} - \alpha\Omega\cos\left(\frac{\Omega(\xi-\sigma)}{2}\right)H\left(\frac{\xi+\sigma}{2}\right)(v_{0\sigma}+v_{0\xi})$$

$$+2(V_0 + \alpha\sin\left(\frac{\Omega(\xi-\sigma)}{2}\right)H\left(\frac{\xi+\sigma}{2}\right)(v_{0\sigma\sigma}+v_{0\xi\xi}), \qquad (22)$$

$$v_1(\sigma,\sigma,0) = \phi_1(\sigma), \qquad \sigma = \xi \qquad \tau=0, \qquad (22)$$

$$-v_{1\sigma}(\sigma,\sigma,0) + v_{1\xi}(\sigma,\sigma,0) = -v_{0\tau}(\sigma,\sigma,0) + \psi_1(\sigma), \quad \sigma = \xi, \quad \tau=0, \qquad (23)$$

where $\phi_i(\sigma)$ is the $O(\varepsilon^i)-$ part of $\phi(\sigma)$, and $\psi_i(\sigma)$ is the $O(\varepsilon^i)-$ part of $\psi(\sigma)$. The general solution of (18)-(20) is obtained by direct integration. Hence, the solution of Eq. (18) can be expressed as

$$v_0(\sigma,\xi,\tau) = f_0(\sigma,\tau) + g_0(\xi,\tau), \qquad (24)$$

where f_0 and g_0 are arbitrary functions of the characteristic variables σ and ξ and the slow time τ , which in turn are functions of x and t . The functions f_0 and g_0 can be obtained by demanding that v_1 does not contain secular terms and that v_0 satisfies the initial conditions (19) and (20), implying that f_0 and g_0 have to satisfy $f_0(\sigma,0)+g_0(\sigma,0)=\varphi_0(\sigma)$ and $f'_0(\sigma,0)+g'_0(\sigma,0)=\psi_0(\sigma),$ where the prime indicates a derivative with respect to the first argument. By eliminating $g_0(\sigma,0)$ from the previous two equations, it follows that $f_{0\sigma}(\sigma,0) = \frac{1}{2}(\phi_{0\sigma}(\sigma)-\psi_0(\sigma))$. From the odd and 2-periodic extension of the dependent variable of the problem (4)-(7), it also follows that f_0 and g_0 have to satisfy $g_0(\sigma,\tau) = -f_0(-\sigma,\tau)$ and $f_0(\sigma,\tau) = f_0(\sigma+2,\tau)$ for $-\infty < \sigma < \infty$ and $\tau \geq 0.$ Now the $O(\varepsilon)$-problem (21)-(23) can be solved in such a way that v_1 does not contain secular terms. Then, it turns out that $f_0(\sigma,\tau)$ has to satisfy

$$f_{0\sigma\tau} - 2\alpha\sin((2m-1)\pi\sigma)f_{0\sigma} + \frac{2\alpha}{(2m-1)\pi}\cos((2m-1)\pi\sigma)f_{0\sigma\sigma} = 0 \qquad (25)$$

when $\Omega = (2m-1)\pi$ with $m \in \mathbb{Z}^+$. The reader is referred to [25] for details of the computations.

Now it should be observed that Eq. (25) is a first order partial differential equation in $f_{0\sigma}$, which can be solved exactly by using the method of characteristics for first order PDEs. In [25] some examples are given how these exact solutions can be obtained.

5. Conclusions and remarks

In this paper the transversal vibrations of an axially moving continuum (string) with time-varying velocity have been discussed in detail. The drawbacks of the truncation method for these string-linke problems are indicated, and it has been shown how these drawbacks can be prevented by using the method of characteristic coordinates.

Up to now only a few problems have been investigated in this way, but the applicability of the method of characteristic coordinates for these types of problems will be studied further in the near future.

References

[1] Wickert, J.A., and Mote Jr., C.D. Travelling load response of an axially moving string. *Journal of Sound and Vibration* 149 (1991), 267-284.

[2] Kaczmarczyk, S. The passage through resonance in a catenary-vertical hoisting system with slowly varying length. *Journal of Sound and Vibration* 208 (1997), 243-265.

[3] Pakdemirli, M., and Ulsoy, A.G. Stability analysis of an axially accelerating string, *Journal of Sound and Vibration* 203 (5) (1997), 815-832.

[4] Öz, H.R., and Boyaci H. Transverse vibrations of tensioned pipes conveying fluid with time-dependent velocity. *Journal of Sound and Vibration* 236 (2) (2000), 259-276.

[5] Suweken, G., and van Horssen, W.T. On the transversal vibrations of a conveyor belt with a low and time-varying velocity. Part I: the string-like belt case. *Journal of Sound and Vibration* 264 (1) (2003,) 117-133.

[6] Suweken, G., and van Horssen, W.T. On the transversal vibrations of a conveyor belt with a low and time-varying velocity. Part II: the beam-like case. *Journal of Sound and Vibration* 267 (2003), 1007-1027.

[7] Suweken, G., and van Horssen, W.T. On the weakly nonlinear, transversal vibrations of a conveyor belt with a low and time-varying velocity. *Nonlinear Dynamics* 31 (2003), 197-223.

[8] Karzmarczyk, S., and Ostachowicz, W. Transient vibration phenomena in deep mine hoisting cables. Part 1: mathematical model. *Journal of Sound and Vibration* 262 (2003), 219-244.

[9] Karzmarczyk, S., and Ostachowicz, W. Transient vibration phenomena in deep mine hoisting cables. *Journal of Sound and Vibration* 262 (2) (2003), 219-244.

[10] Zhu, W., and Xu, G. Vibrations of elevator cables with small bending stiffness. *Journal of Sound and Vibration* 263 (3) (2003), 679-699.

[11] Kuiper, G.L., Metrikine, A.V.: On stability of a clamped-pinned pipe conveying fluid. *Heron* 49(3) (2004), 211-231.

[12] Zhu, W.D., and Chen, Y. Forced response of translating media with variable length an tension: Application to high-speed elevators. *Proc. Inst. Mech. Eng. KJ. Multi-body Dyn.* 219 (2005), 35-53.

[13] Chen, L., and Yang, X. Stability in parametric resonance of axially moving viscoelastic beams with time-dependent speed. *Journal of Sound and Vibration* 284 (3-5) (2005), 879-891.

[14] Ponomareva, S.V., and van Horssen, W.T. On transversal vibrations of an axially moving string with a time-varying velocity. *Nonlinear Dynamics* 50 (2007), 822-829.

[15] Andrianov, I.V., and van Horssen, W.T. On the tranversal vibrations of a conveyor belt: Applicability of simplified models. *Journal of Sound and Vibration* 313 (3-5) (2008), 822-829.

[16] Ghayesh, M.H., and Khadem, S.E. Rotary inertia and temperature effects on non-linear vibration, steady-state response and stability of an axially moving beam with time-dependent velocity. *International Jounal of Mechanical Sciences* 50 (3) (2008), 389-404.

[17] Pakdemirli, M., and Őz, H.R. Infinite mode analysis and truncation to resonant modes of axially accelerated beam vibration. *Journal of Sound and Vibration* 311 (3-5) (2008), 1052-1074.

[18] Ponomareva, S.V., and van Horssen, W.T. On the transversal vibrations of an axially moving continuum with a time-varying velocity: Transient form string to beam behavior. *Journal of Sound and Vibration* 325 (4-5) (2009), 959-973.

[19] Brake, M.R., and Wickert, J.A. Model analysis of a continuous gyroscopic second order system with nonlinear constraints. *Journal of Sound and Vibration* 329 (2010), 893-911.

[20] Sandilo, S.H., and van Horssen, W.T. On boundary damping for an axially moving tensioned beam. *Journal of Vibration and Acoustics, Transactions of the ASME* 134 (1) (2012), 0110051-0110058.

[21] Zhang, Y.L., and Chen, L.Q. Internal resonance of pipes conveying fluid in the supercritical regime. *Nonlinear Dynamics* 67 (2012), 1505-1514.

[22] Chen, L.Q., Tang, Y.Q., and Zu, J.W. Nonlinear transverse vibration of axially accelerating strings with exact internal resonances and longitudinally varying tensions. *Nonlinear Dynamics* 76 (2014), 1443-1468.

[23] Sandilo, S.H., and van Horssen, W.T. On a cascade or autoresonances in an elevator cable system. *Nonlinear Dynamics* 80 (2015), 1613-1630.

[24] Malookani, R.A., and van Horssen, W.T. On the asymptotic approximation of the solution of an equation for a non-constant axially moving string with time-varying velocity. *Journal of Sound and Vibration* 344 (2015), 1-17.

[25] Malookani, R.A., and van Horssen, W.T. On the asymptotic approximation of the solution of an equation for a non-constant axially moving string. (2015), submitted for publication.

[26] Gaiko, N.V., and van Horssen, W.T. On the lateral vibrations of a vertically moving string with a harmonically varying length. *Proceedings of the ASME IMECE2015 conference*, Houston (2015),1-7.

[27] Gaiko, N.V., and van Horssen, W.T. On wave reflections and energetics for a semi-infinite traveling string with a nonclassical boundary support (2015), submitted for publication.

[28] Nayfeh, A.H., and Mook, D.T. *Nonlinear Oscillations.* Wiley, New York, 1979.

[29] Murdock, J.A. *Perturbations: Theory and Methods.* Wiley, New York, 1991.

[30] Kevorkian, J., and Cole, J.D. *Multiple Scale and Singular Perturbation Methods.* Springer-Verlag, New York, 1996.

[31] Neyfeh, A.H. *Perturbation Methods.* Wiley, New York, 2000.

[32] Andrianov, I.V., and Awrejcewicz, J. New trends in asymptotic approaches: Summatio and interpolation methods. *Applied Mechanics Reviews* 54 (2001), 69-91.

[33] Andrianov, I.V., and Manevitch, L.I. *Asymptotology.* Kluver Academic Publishers, Dordrecht, 2002.

[34] Andrianov, I.V., Awrejcewicz, J., and Barantsev, R.G. Asymptotic approaches in mechanics: new parameters and procedures. *Applied Mechanics Reviews* 56 (2003), 87-109.

[35] Verhulst, F. *Methods and Applications of Singular Perturbations.* Springer-Verlag, 2005.

Wim T. van Horssen, Associate Professor: Delft University of Technology, Delft Institute of Applied Mathematics, Mekelweg 4, 2628 CD Delft, The Netherlands (w.t.vanhorssen@tudelft.nl).

The author gave a keynote presentation of this paper during one of the conference sessions.

A chain of FPU cells
(BIF212-15)

Ferdinand Verhulst

Abstract: In contrast to the classical Fermi-Pasta-Ulam (FPU) chain, the in-homogeneous FPU chain shows nearly all the principal resonances. Using this fact, we can construct a periodic FPU chain of low dimension, for instance a FPU cell of four degrees-of-freedom, that can be used as a building block for a chain of FPU cells. Differences between chains in nearest-neighbour interaction and those in overall interaction are caused by symmetry. We will also show some results on the dynamics of a particular chain of FPU cells where different kinds of chaos play a part.

1. Introduction

The Fermi-Pasta-Ulam (FPU) chain or lattice is an n degrees-of-freedom (dof) Hamiltonian system that models a chain of oscillators with nearest-neighbour interaction, see [3] and [4]. In the classical (symmetric) case all the masses $m_i, i = 1, \ldots, n$ of the chain are equal. To find prominent resonances in the inhomogeneous case poses an inverse problem for the spectrum of the linearized equations of motion. Inhomogeneous nonlinear FPU chains were studied in [1] with emphasis on the case of four particles with mass distribution producing the $3 : 2 : 1$ resonance. For any periodic inhomogeneous FPU α-chain (quadratic nonlinearities) with four dof and masses m_i, $i = 1, \ldots, 4$ we have, putting $a_i = 1/m_i$, the system:

$$
\begin{cases}
\dot{q_1} &= v_1, \ \dot{v_1} = [-2q_1 + q_2 + q_4 - \varepsilon((q_1 - q_4)^2 - (q_2 - q_1)^2)]a_1, \\
\dot{q_2} &= v_2, \ \dot{v_2} = [-2q_2 + q_3 + q_1 - \varepsilon((q_2 - q_1)^2 - (q_3 - q_2)^2)]a_2, \\
\dot{q_3} &= v_3, \ \dot{v_3} = [-2q_3 + q_4 + q_2 - \varepsilon((q_3 - q_2)^2 - (q_4 - q_3)^2)]a_3, \\
\dot{q_4} &= v_4, \ \dot{v_4} = [-2q_4 + q_1 + q_3 - \varepsilon((q_4 - q_3)^2 - (q_1 - q_4)^2)]a_4.
\end{cases}
\tag{1}
$$

The q_i indicate the positions of the particles, the v_i their velocity, ε is a small parameter; sometimes it is convenient to use momentum-position variables p, q. We call the case with quartic terms in the Hamiltonian added (cubic terms in the equations of motion) a β-chain. It was shown in [8], that in the classical periodic FPU problem with four identical particles the normal form of the system is integrable, see also [9]. The implication is that for ε small, the measure of chaos is in this classical case $O(\varepsilon)$.

We assume that the Hamiltonian can be expanded in homogeneous polynomials as $H = H_2 + \varepsilon H_3 + \varepsilon^2 \ldots$ with the index indicating the degree of the polynomial. Apart from the Hamiltonian H we have as a second (translational) momentum integral of system (1):

$$m_1 v_1 + m_2 v_2 + m_3 v_3 + m_4 v_4 = \text{constant}. \tag{2}$$

The expression for the quadratic part of the Hamiltonian H_2 is:

$$H_2 = \frac{1}{2} \sum_{i=1}^{4} a_i p_i^2 + \frac{1}{2}[(q_2 - q_1)^2 + (q_3 - q_2)^2 + (q_4 - q_3)^2 + (q_1 - q_4)^2]. \tag{3}$$

H_2 is a first integral of the linearized system (1), it is also a first integral of the normal form of the full system (1). This has the following implication: When using H_2 from the solutions of the truncated normal form indicated by: $\bar{H}(p,q) = H_2(p,q) + \varepsilon \bar{H}_3(p,q)$, we obtain an $O(\varepsilon)$ approximation of the (exact) $H_2(p(t), q(t))$ valid for all time; for a proof see [10] chapter 10.

2. Transformation to a quasi-harmonic form

The presence of the momentum integral enables us to reduce system (1) to a three dof system. It has been shown in [1] that the $\omega_1 : \omega_2 : \omega_3 = 3 : 2 : 1$ resonance arises in a one-parameter family of Hamiltonians; many other resonances can be found. Without loss of generality we choose

$$\omega_1^2 = \frac{9}{14}, \ \omega_2^2 = \frac{4}{14}, \ \omega_3^2 = \frac{1}{14}. \tag{4}$$

The one-parameter family of $3 : 2 : 1$ resonances can be generated by the real parameter $u \in [0, u_1)$ with $u_1 = 0.887732$. In an application later on we will choose a particular value of u, called case 1 in [1]. To put system (1) in the standard form of quasi-harmonic equations we have to apply a suitable symplectic transformation $L(u)^{-1} : p, q \to y, x$ with x the vector of the new position variables that is three-dimensional because of the reduction by the momentum integral (2). This leads to a transformed Hamiltonian $H_2 + \varepsilon H_3$:

$$H_2 = \frac{1}{2}(\dot{x}_1^2 + \frac{9}{14}x_1^2 + \dot{x}_2^2 + \frac{4}{14}x_2^2 + \dot{x}_3^2 + \frac{1}{14}x_3^2)$$

and H_3 a cubic expression containing 10 terms, see for details [1]. Because of the $3 : 2 : 1$ resonance, only two terms will be active in the normalized H_3; an intermediate normal form will be:

$$\begin{cases} \ddot{x}_1 + 9x_1 &= -\varepsilon 14 d_6 x_2 x_3, \\ \ddot{x}_2 + 4x_2 &= -\varepsilon 14 (d_6 x_1 x_3 + d_9 x_3^2), \\ \ddot{x}_3 + x_3 &= -\varepsilon 14 (d_6 x_1 x_2 + 2 d_9 x_2 x_3), \end{cases} \tag{5}$$
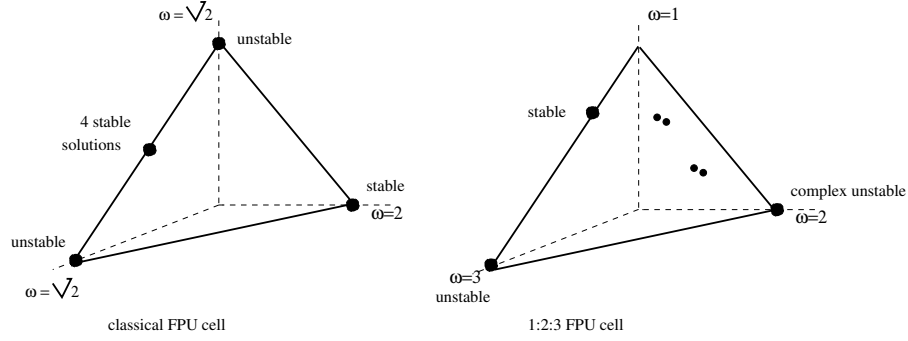
Figure 1. Action simplices. A dot indicates one or more periodic solutions, at the vertices one finds the normal modes if these exist. Left the actions of the classical FPU chain with four particles, the $\sqrt{2} : \sqrt{2} : 2$ resonance has two unstable normal modes. Right the case of the FPU chain with four particles in $1 : 2 : 3$ resonance. The normal modes corresponding with $\omega = 3$ and 2 exist but are unstable, in the second case with complex eigenvalues.

It was shown in this case that for nearly all parameter values, one of the short-periodic solutions is complex unstable. This is highly relevant for the characterization of the chaotic dynamics of the system as it was shown in [5] that a Shilnikov-Devaney bifurcation [2] can take place in the $3 : 2 : 1$ resonance. For a summary of the results in the parameter case $0 < u < u_1$ see the action simplex in fig. 1 (right).

In the sequel we will treat such a FPU chain with 4 particles as a FPU cell, and we will construct a chain of FPU cells. Such a chain is depicted in fig. 2.
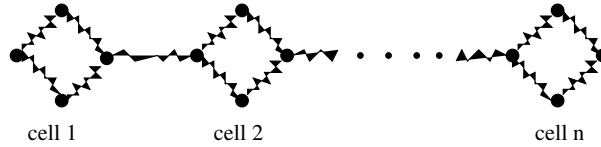
Figure 2. A chain of FPU cells, each consisting of four particles.

3. Energy exchange and recurrence in PFU cells

We will use particular values for the masses, in [1] denoted by "case 1". We choose:

$$a_1 = 0.00510292, a_2 = 0.117265, a_3 = 0.0854008, a_4 = 0.292231,$$

leading to the frequencies (4). With these mass ($a_i = 1/m_i$) values the symplectic transformation of the four-particles system produces :

$$d_6 = -0.0306229, \ d_9 = -0.0089438.$$

The analysis in [1] for case 1 shows that the x_2 normal mode of an isolated cell is complex unstable. We will study a chain of FPU cells with this choice of masses; the cells interact weakly by the mass points $q_2, q_6, \ldots$ etc. so that the $3 : 2 : 1$ resonances of the cells experience only a slight detuning. Consider as an illustration the case of two cells with:

$$\begin{cases} H_2 = & \frac{1}{2} \sum_{i=1}^{8} \frac{v_i^2}{a_i} + \frac{1}{2}[(q_2 - q_1)^2 + (q_3 - q_2)^2 + (q_4 - q_3)^2 + (q_1 - q_4)^2] + \frac{1}{2}\varepsilon\mu(q_2 - q_6)^2 \\ & + \frac{1}{2}[(q_6 - q_5)^2 + (q_7 - q_6)^2 + (q_8 - q_7)^2 + (q_5 - q_8)^2], \end{cases} \tag{6}$$

and $a_i = a_{i+4}$, $i = 1, \ldots, 4$; ε scales the nonlinearities, $\varepsilon\mu$ scales the detuning. The equations of motion produce a 16-dimensional phase-space and become:

$$\begin{cases} \dot{q}_1 & = v_1, \ \dot{v}_1 = [-2q_1 + q_2 + q_4 - \varepsilon((q_1 - q_4)^2 - (q_2 - q_1)^2)]a_1, \\ \dot{q}_2 & = v_2, \ \dot{v}_2 = [-2q_2 + q_3 + q_1 - \varepsilon\mu(q_2 - q_6) - \varepsilon((q_2 - q_1)^2 - (q_3 - q_2)^2)]a_2, \\ \dot{q}_3 & = v_3, \ \dot{v}_3 = [-2q_3 + q_4 + q_2 - \varepsilon((q_3 - q_2)^2 - (q_4 - q_3)^2)]a_3, \\ \dot{q}_4 & = v_4, \ \dot{v}_4 = [-2q_4 + q_1 + q_3 - \varepsilon((q_4 - q_3)^2 - (q_1 - q_4)^2)]a_4, \\ \dot{q}_5 & = v_5, \ \dot{v}_5 = [-2q_5 + q_6 + q_8 - \varepsilon((q_5 - q_8)^2 - (q_6 - q_5)^2)]a_1, \\ \dot{q}_6 & = v_6, \ \dot{v}_6 = [-2q_6 + q_7 + q_5 + \varepsilon\mu(q_2 - q_6) - \varepsilon((q_6 - q_5)^2 - (q_7 - q_6)^2)]a_2, \\ \dot{q}_7 & = v_7, \ \dot{v}_7 = [-2q_7 + q_8 + q_6 - \varepsilon((q_7 - q_6)^2 - (q_8 - q_7)^2)]a_3, \\ \dot{q}_8 & = v_8, \ \dot{v}_8 = [-2q_8 + q_5 + q_7 - \varepsilon((q_8 - q_7)^2 - (q_5 - q_8)^2)]a_4. \end{cases} \tag{7}$$

The recurrence theorem for volume-preserving maps was formulated by Poincaré in 1890 in his prize essay for Oscar II; it can also be found in [7] vol. 3. It implies, loosely formulated, that for Hamiltonian systems on a compact energy manifold, nearly all solutions return after a finite time arbitrarily close to their original position in phase-space. Analysis of recurrence adds to our understanding of the dynamics.

For a one dof system on a compact domain recurrence is trivial as under these conditions nearly all solutions are periodic. For two dof systems that are integrable, recurrence behaviour is relatively simple near a stable periodic solution. In nearly-integrable two dof systems a similar result can be obtained using the KAM theorem, but in general this is already not so easy for chaotic two dof systems.

To measure recurrence for a system of two FPU cells we will start with zero energy in the second cell and consider energy exchange between the FPU cells. To study recurrence we will also use the Euclidean norm:

$$d = \left[\sum_{i=1}^{4} (q_i(t) - q_i(0))^2 + \sum_{i=1}^{4} v_i^2 + c \sum_{i=5}^{8} (q_i(t)^2 + v_i(t)^2) \right]^{1/2}. \tag{8}$$

In the case of one cell, $c = 0$, for two cells $c = 1$. It would be natural to apply weights, based on the masses, to the displacements but this does not change the picture qualitatively.

3.1. Set-up of the experiments

We will start with initial values in cell 1 and will be interested in the energy transfer to cell 2. The initial values of the velocities were chosen to be zero. As the chain is Hamiltonian, the flow will be recurrent, but we expect differences between the classical case of equal masses and the case of the $3 : 2 : 1$ resonance where the flow is chaotic. We restrict ourselves to initial values in a neighbourhood of the normal modes indicated in the second and fourth column of table 1. As the phase-flow is chaotic, see [5], we expect the transfer of energy between the cells and the recurrence to be different from the case of a nearly integrable cell system like the classical FPU chain with all masses equal. The numerics involves a $[0, 5000]$ time interval with relative tolerance e^{-7}, absolute tolerance e^{-10}.

The $3 : 2 : 1$ resonance will be detuned by the interaction between the cells. Keeping the interaction small by choosing $\varepsilon = 0.2, \mu = 0.1$, the detuning does not disturb the qualitative picture of the resonance. With the mass distribution of case 1 we have for the frequencies of the linearized system $\omega_1 = 0.8019 \, (0.8018), \omega_2 = 0.5487 \, (0.5345), \omega_3 = 0.2742 \, (0.2673)$ with between brackets the frequencies of isolated cells ($\varepsilon = \mu = 0$).

For the instantaneous energy E_{c1} stored in cell 1 we have:

$$\begin{cases} E_{c1} = & \frac{1}{2} \sum_{i=1}^{4} \frac{v_i^2}{a_i} + \frac{1}{2}[(q_2 - q_1)^2 + (q_3 - q_2)^2 + (q_4 - q_3)^2 + (q_1 - q_4)^2] \\ & + \frac{\varepsilon}{3}[(q_2 - q_1)^3 + (q_3 - q_2)^3 + (q_4 - q_3)^3 + (q_1 - q_4)^3]. \end{cases} \tag{9}$$

The energy of cell 2 is obtained from E_{c1} by adding 4 to all the indices.

3.2. Energy transfer between two cells

We compare the energy transfer to cell 2 between the $1 : 2 : 3$ resonance of case 1 with the behaviour of the classical FPU chain with four equal particles. In this classical case the frequencies of the linearized system are $\sqrt{2}, \sqrt{2}, 2, 0$. For reasons of comparison we choose for the masses in the classical case $m = 0.1$. The symmetry induced by the equal masses means that we have to choose the initial conditions in the classical FPU case with care. For

Table 1. The eigenmodes **e** of the system in **x** variables transformed to **q** variables for the $1 : 2 : 3$ resonance (case 1, 2nd column) and the classical FPU case (4th column). Because of the presence of the momentum integral (2), the reduction to three dof makes the values produced for the 4th eigenvector redundant. The initial values of the positions for the numerical integrations have been chosen near the eigenmodes; the initial velocities are zero. The symplectic transformation $L(u)$ from [1] discussed in section 2 gives us the relation between the normal modes of the system in quasi-harmonic coordinates $(x, \dot{x})$ and the initial conditions in the variables (q, v) of system (7). This means that a given position vector $(q_1, q_2, q_3, q_4) = \mathbf{q}$ is obtained from the **x** normal modes by putting $\mathbf{q} = L(u)\mathbf{x}$.

	Case 1	Initial values case 1	Classical FPU	Initial values classical FPU
$L(u)\mathbf{e_1}$	$\begin{pmatrix} -0.00432273 \\ 0.0290855 \\ -0.0969556 \\ 0.506839 \end{pmatrix}$	$\begin{pmatrix} -0.1 \\ 0.1 \\ -0.2 \\ 0.3 \end{pmatrix}$	$\begin{pmatrix} -0.5 \\ 0.5 \\ -0.5 \\ 0.5 \end{pmatrix}$	$\begin{pmatrix} -0.4 \\ 0.45 \\ -0.4 \\ 0.42 \end{pmatrix}$
$L(u)\mathbf{e_2}$	$\begin{pmatrix} 0.00315777 \\ -0.297518 \\ 0.126704 \\ 0.127029 \end{pmatrix}$	$\begin{pmatrix} 0.1 \\ -0.2 \\ 0.3 \\ -0.1 \end{pmatrix}$	$\begin{pmatrix} 0 \\ 1/\sqrt{2} \\ 0 \\ -1/\sqrt{2} \end{pmatrix}$	$\begin{pmatrix} 0.1 \\ 0.6 \\ -0.1 \\ -0.65 \end{pmatrix}$
$L(u)\mathbf{e_3}$	$\begin{pmatrix} -0.0228266 \\ 0.152804 \\ 0.235358 \\ 0.121061 \end{pmatrix}$	$\begin{pmatrix} -0.1 \\ 0.3 \\ 0.4 \\ 0.05 \end{pmatrix}$	$\begin{pmatrix} -1/\sqrt{2} \\ 0 \\ 1/\sqrt{2} \\ 0 \end{pmatrix}$	$\begin{pmatrix} -0.65 \\ 0.1 \\ 0.6 \\ -0.1 \end{pmatrix}$
$L(u)\mathbf{e_4}$	$\begin{pmatrix} 0.0674775 \\ 0.0674775 \\ 0.0674775 \\ 0.0674775 \end{pmatrix}$	$\begin{pmatrix} 0.0 \\ 0.0 \\ 0.0 \\ 0.0 \end{pmatrix}$	$\begin{pmatrix} 0.5 \\ 0.5 \\ 0.5 \\ 0.5 \end{pmatrix}$	$\begin{pmatrix} 0.0 \\ 0.0 \\ 0.0 \\ 0.0 \end{pmatrix}$

608

instance there exists the family of periodic solutions defined by:

$$q_2(t) = q_4(t) = 0, \ q_1(t) = -q_3(t), \ \ddot{q}_1 + 2q_1 = 0, \ \ddot{q}_3 + 2q_1 = 0.$$

As the link between the cells involves the second particle, this means that there is no energy transfer between the cells when starting with these solutions. It is easy to obtain a few exact solutions by generalizing this result for the classical FPU chain with $2n$ dof.
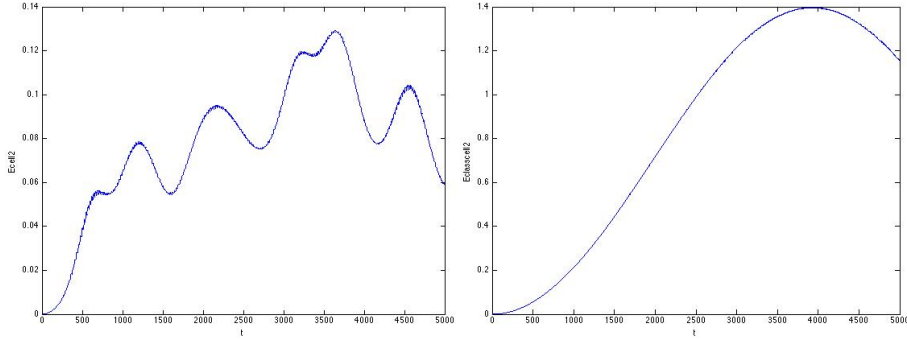
Figure 3. Time series ($[0, 5000]$) of the energy of the second cell, left the $1 : 2 : 3$ resonance (scale $[0, 0.14]$), right the classical case (scale $[0, 1.4]$). The link is linear and exists between q_2 and q_6; The initial conditions of the first cell start near the eigenmode x_1 and are given in table 1, the second cell starts with zero energy; $\varepsilon = 0.2, \mu = 0.1$.

In the figs 3 - 5 on the left we have energy transfer starting near respectively 3 unstable solutions in a chaotic dynamical system; the transfer is irregular but assumes at certain times a considerable part, more than 90 % of the energy of cell 1. On the right side of the figs 3 - 5 we have energy transfer starting in the classical FPU case showing a rather regular pattern. The (ir)regularity of the energy transfer is the main difference.

3.3. The recurrence of an solution

We will explore recurrence phenomena for our systems of one cell ($c = 0$, 8-dimensional) and two FPU cells ($c = 1$, 16-dimensional) using the Euclidean distance d, see eq. (8). Increasing the dimension will in general increase the recurrence times but other aspects of the dynamics play a part. We will use again the initial values given in table 1. We explore the recurrence in the first cell with the initial conditions near the complex unstable x_2 normal mode, see fig. 6 (left) and for two cells (right). In the classical FPU system we have rather regular recurrence near the x_2 normal mode, see fig. 7.

609
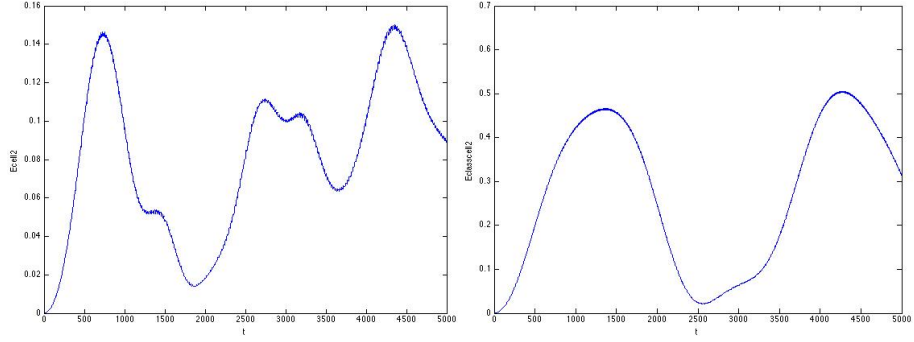
Figure 4. Time series ($[0, 5000]$) of the energy of the second cell, left the $1 : 2 : 3$ resonance (scale $[0, 0.16]$), right the classical case (scale $[0, 0.7]$). The link is linear and exists between q_2 and q_6; The initial conditions of the first cell start near the eigenmode x_2 and are given in table 1, the second cell starts without energy; $\varepsilon = 0.2, \mu = 0.1$.
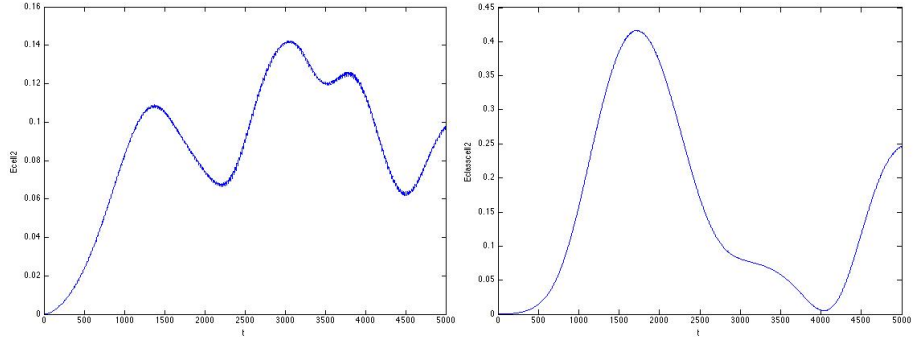
Figure 5. Time series ($[0, 5000]$) of the energy of the second cell, left the $1 : 2 : 3$ resonance (scale $[0, 0.16]$), right the classical case (scale $[0, 0.45]$). The link is linear and exists between q_2 and q_6; The initial conditions of the first cell start near the eigenmode x_3 and are given in table 1, the second cell starts without energy; $\varepsilon = 0.2, \mu = 0.1$.
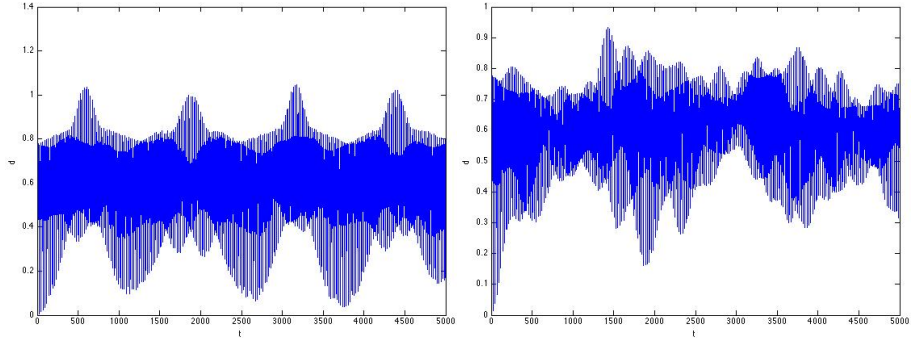
Figure 6. Time series ($[0, 5000]$) of the Euclidean distance d starting near the complex unstable normal mode x_2 in the first FPU cell in $1 : 2 : 3$ resonance (left, scale $[0, 1.4]$). The recurrence for 5000 time steps is delayed on the right (scale $[0, 1]$) where we started with the same initial conditions (table 1) for two cells.
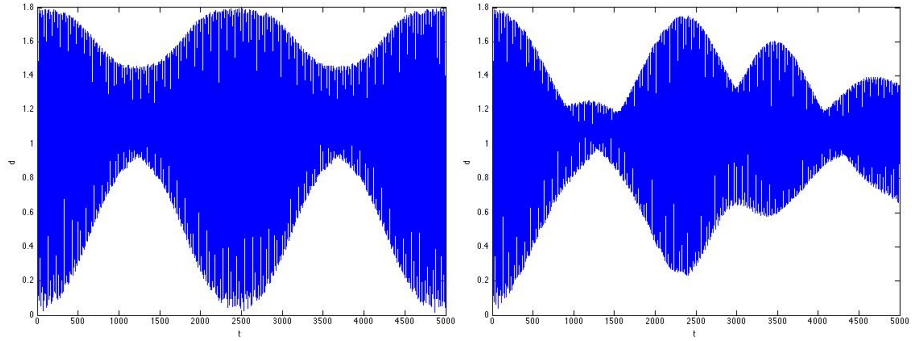
Figure 7. Time series ($[0, 5000]$) of the Euclidean distance d starting near the x_2 eigenmode in the first classical FPU cell (left, scale $[0, 1.8]$). For the initial conditions indicated in table 1 the recurrence is quite good. On the right (scale $[0, 1.8]$) the time series for two cells with the same initial conditions; the recurrence is delayed.

Acknowledgements

References

[1] Roelof Bruggeman and Ferdinand Verhulst, *The inhomogeneous Fermi-Pasta-Ulam chain*, submitted for publ. (2015).

[2] R.L. Devaney, *Homoclinic orbits in Hamiltonian systems*, J. Diff. Eqs. 21, pp. 431-438 (1976).

[3] E. Fermi, J. Pasta and S. Ulam, *Los Alamos Report LA-1940*, in "E. Fermi, Collected Papers" 2, pp. 977-988 (1955).

[4] J. Ford, Physics Reports 213, pp. 271-310 (1992).

[5] Igor Hoveijn and Ferdinand Verhulst, *Chaos in the* $1:2:3$ *Hamiltonian normal form*, Physica D 44, pp. 397-406 (1990).

[6] E. Atlee Jackson, Perspectives of nonlinear dynamics (2 vols.), Cambridge University Press (1991).

[7] Henri Poincaré, *Les Méthodes Nouvelles de la Mécanique Céleste*, 3 vols. Gauthier-Villars, Paris, 1892, 1893, 1899.

[8] Bob Rink and Ferdinand Verhulst, *Near-integrability of periodic FPU-chains*, Physica A 285, pp. 467-482 (2000).

[9] B. Rink, *Symmetry and resonance in periodic FPU-chains*, Comm. Math. Phys. 218, pp. 665-685 (2001).

[10] J.A. Sanders, F. Verhulst, and J. Murdock, *Averaging methods in nonlinear dynamical systems*, Applied Mathematical Sciences vol. 59, 2d ed., Springer, 2007.

[11] Ferdinand Verhulst, *Methods and applications of singular perturbations*, Springer, 2005.

[12] Ferdinand Verhulst, *Integrability and non-integrability of Hamiltonian normal forms*, Acta Applicandae Mathematicae vol. 137, pp. 253-272 (2015)

Ferdinand Verhulst, Ph.D.: University of Utrecht, Mathematisch Instituut, PO Box 80.010, 3508 TA Utrecht, The Netherlands (*f.verhulst@uu.nl*). The author gave a presentation of this paper during one of the conference sessions.

Active control of a rotating composite thin-walled beam structure (CON074-15)

Jerzy Warminski, Jarosław Latalski

Abstract: Dynamics of a rotating composite beam attached to a hub and controlled by active element is studied in the paper. The considered beam is modelled as a thin-walled structure made of composite material. A specific structural laminate configuration resulting in a strong coupling of specimen lead-lag bending and twisting has been assumed. This structural property allows controlling both coupled modes by just a single actuator. To reduce structural vibrations, induced by external excitation, a non-linear saturation control strategy is applied. Effectiveness of the proposed non-linear control method is tested taking into account the dynamic properties of the combined hub-beam system. The importance of the hub inertia in controller frequency tuning is underlined.

1. Introduction

Rotating beams are often used as models for studying the dynamic properties and behaviour of turbomachinery blades, helicopter rotor blades, flexible links of robotic manipulators or lightweight satellite structure appendages. The primary interest is usually aimed at planar bending of rotating links, often coupled to torsional deformation due to e.g. aerodynamic or fluid-to-structure interactions. The effect of vibration mode coupling may be also observed for modern lightweight structures made of composite materials as a result of inherent directional properties of multilayered laminates. Moreover, the discussed mode coupling phenomena may be also observed due to a non-uniform and/or non-symmetric specimen cross-section, or due to beam pretwisting.

On the other hand the discussed feature of vibrations mode coupling in orthotropic materials is a promising concept of material tailoring that plays a significant role in modern structures design. This refers particularly to advanced mechanical and aerospace designs.

Further enhancement of structural performance may be achieved by the concept of intelligent structures. The idea of smart systems requires integration of sensory capabilities and actuation authority within the host structure combined with appropriate control strategy. The possible use of this technology opens new research areas and new design perspectives. The concept is receiving considerable attention in recent years. Apart from classical control methods, recently nonlinear control strategy with application of active elements is proposed in literature [4, 8, 13, 14]. One of the most attractive methods is the so called saturation

based control, which due to nonlinear coupling allows transfer vibration from a plant (host structure) to the controller [10, 11]. The proposed strategy can also be modified by adding time delay to the control signal. The nonlinear saturation control has been applied mainly for oscillating structures fixed to a immovable base.

The main goal of this paper is to study the non-linear vibration control strategy in order to reduce structural vibrations of a rotating hub–composite beam system. As opposed to classical cases where the single vibration mode is addressed this paper discusses the control of the structural coupled vibrations by using just a single active element. The considered structural mode coupling results from the orthotropic properties of the composite and cross-sectional circumferential lamination scheme as well. The results of the analysis are presented for circumferentially asymmetric stiffness (CAS) which leads to coupled flexural-torsional vibrations of the rotating thin-walled beam. The study is a continuation of the previous authors research, reported in publications [3, 4, 13].

2. Mathematical model

Let us consider a slender, straight and elastic composite, single cell thin-walled beam clamped at the rigid hub of radius R_0 and inertia J_h experiencing rotational motion about fixed axis Z_0 as shown in Figure 1. The composite material is linearly elastic (Hookean) and its properties are constant in spanwise direction. The beam is clamped to the rigid hub at the arbitrary presetting angle θ. It is assumed the beam profile is neither tapered nor pretwisted.

An active element (patch) is embedded onto the specimen flange right at the clamping as shown in Figure 1. In order to reduce beam oscillations, the system is controlled through a nonlinear control unit (controller).

In the structural analysis of the system the transverse beam shear deformations are taken into account and these are assumed to be uniform over the beam cross-section. In the analysis of torsional deformation the non-uniform model is assumed, thus the rate of beam twist $\varphi' = \frac{d\varphi}{dx}$ depends in general on the spanwise coordinate x. Moreover, the elastic warping deformation of the cross-section is taken into account and both kinds of this phenomena are considered i.e. due to cross-section shape (primary warping effect) as well as due to the wall thickness (secondary warping). More detailed information on adopted assumptions is given in paper [2].

In the foregoing calculations the graphite-epoxy laminate material is considered and the following material data is used $E_1 = 206.75 \cdot 10^9$ Pa, $E_2 = E_3 = 5.17 \cdot 10^9$ Pa, $G_{23} = 3.1 \cdot 10^9$ Pa, $G_{13} = G_{12} = 2.55 \cdot 10^9$ Pa, $\nu_{32} = 0.25$, $\nu_{21} = \nu_{31} = 0.00625$, $\rho = 1528.15$ kg/m³. Dimensions of the beam are as follows: cross-section height $c = 0.00508$ m, width of the cross-section $d = 0.0254$ m, wall thickness $h = 0.001$ m, beam length $l = 0.254$ m and hub
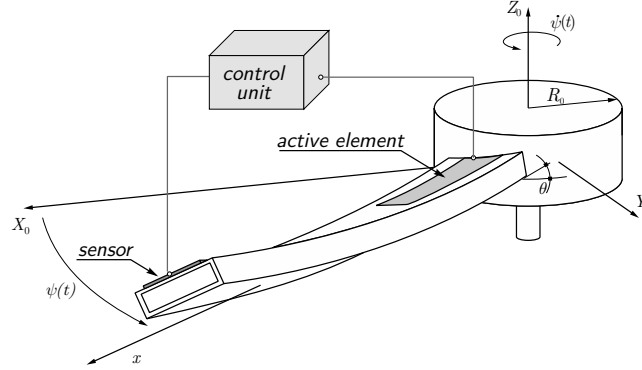
Figure 1. Model of a rotating composite thin-walled beam-hub structure.

radius is $R_0 = 0.1 \cdot l$. This data comes from [12] and it is used to compare the natural frequencies of the hub-beam system if hub inertia is neglected.

3. Governing equations

The equations of motion of the rotating beam and hub sub-system are derived according to the extended Hamilton principle of the least action. Setting formula for potential and kinetic energy results in a set of seven partial differential equations of motion mutually coupled. Three equations correspond to displacements of the beam cross-section reference point (transverse and axial one), two equations for shear deformations and one corresponds to the beam twist. The seventh equation is related to the hub rotation $\psi(t)$ about fixed inertial reference frame axis. Full step-by-step derivation of these equations of motion is presented in previous authors papers [2, 5].

In connection to the derivation procedure several comments are in order. Firstly – although the developed model is a linear one, the expression for the axial strain should include the higher order terms associated with the transverse and lateral beam deformations. These approach enables capturing in equations of motion the stiffening effect due to centrifugal forces which, for rotating systems, is crucial. Other methodologies that might be used to capture the stiffening effect in dynamics of rotating systems are reported in papers [7, 9].

Second – invoking the facts that the blade is much stiffer in the longitudinal direction than in the flapping and lagging ones, and that the effect of the axial inertia is much smaller than the others, the original axial dynamic equation may be simplified to a quasi-static one by discarding axial inertia term. This approach enables to relate the axial deformation with the transversal ones, and subsequently to express the formulas for centrifugal stiffening effect terms which are present in bending and twisting equations.

The third comment is that significant simplification of this full system of equations may be obtained by setting fibers in the laminate to be oriented according to the circumferentially asymmetric stiffness (CAS) configuration scheme. This arrangement implies the ply-angle distribution $\alpha(z) = -\alpha(-z)$ in the top and bottom walls of the box beam (flanges) and $\alpha(y) = -\alpha(-y)$ in the lateral walls (webs) – see Figure 2. As reported in the literature
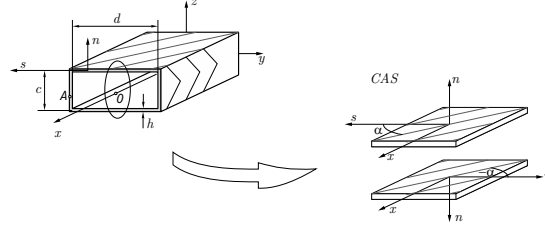
Figure 2. CAS lamination scheme for upper/lower and side beam walls

(see e.g. [1,6,15]) the discussed fabric configuration decouples the full set of six equations of motion (6 DOF) into two independent sub-systems: one exhibiting flapwise bending–shear–twisting coupling and the second one where axial stretching and chordwise bending–shear modes coexist. Thus, clamping the beam to the hub at $\theta = 90°$ angle makes the flexible body to exhibit lead-lag deformation to be coupled with twisting. The magnitude of the coupling effect depends on the fiber orientation angle. It has been shown in papers [5,15] that the maximum is observed for fiber orientation angle $\alpha \approx 75°$. This orientation is used in performed numerical simulations.

The originally derived partial differential equations of the system have been simplified according to the postulated above assumptions. Next, they were reduced to ordinary differential ones using Galerkin's procedure for a single coupled flexural-torsional mode. Details considering the functions (mode shapes) used in the procedure are given in paper [4].

Finally, the dynamics of the beam-hub system with the added controller is given by a set of dimensionless ODEs

$$
\ddot{q}_1 + \zeta_1 \dot{q}_1 + \alpha_{12} \ddot{\psi} + \left(\alpha_{11} + \alpha_{13} \dot{\psi}^2 \right) q_1 + \alpha_{14} \dot{\psi} \dot{q}_1 = g_1 q_c^2,
$$
$$
\ddot{q}_c + \zeta_c \dot{q}_c + \omega_{0c}^2 q_c = g_2 q_c q_1, \tag{1}
$$
$$
\left(1 + J_h + \alpha_{h2} \right) \ddot{\psi} + \zeta_h \dot{\psi} + \alpha_{h1} \ddot{q}_1 + \alpha_{h3} \dot{\psi} \dot{q}_1 = \mu,
$$

where: q_1 is a coordinate corresponding to the first flexural-torsional mode, q_c is the coordinate of the controller and ψ angle of rotation of the hub (Fig.1a). Coefficients α_{1i}, $i = 1, \ldots, 4$, α_{hj}, $j = 1, \ldots, 3$ are computed from Galerkin procedure and then transformed to dimensionless form, ζ_1, ζ_c, ζ_h are damping coefficients of the beam, the controller and

the hub respectively, J_h is the relative dimensionless mass moment of inertia of the hub expressed with respect to the beam inertia and μ is the torque imposed to the hub.

The set of equations (1) governs full system dynamics. All equations are coupled however, we can notice that the first equation is related to coupled flexural-torsional beam vibration, the second equation represents the controller dynamics and the third is the driving equation which arises from the hub rotation.

4. Nonlinear control of the rotating beam structure

In order to reduce vibrations of the combined hub-beam structure we apply an active element which affects beam dynamics, if the input voltage is supplied. In this paper we propose strategy based on nonlinear quadratic coupling of the plant and the controller. This kind of coupling under some conditions may transfer energy from the hub-beam system to the controller and, if tuned properly, the so called saturation phenomenon takes place.

The controller is designed as a linear oscillator nonlinearly coupled with the beam. The signal from controller is squared and multiplied by gain g_1. On the other hand the controller is coupled with the beam by the gain g_2 and product of coordinates q_1 and q_c.

The natural frequency of the controller is tuned to the beam natural frequency satisfying the condition $\omega_{0c} = 1/2\omega_{01}$, where ω_{01} is the first natural frequency of the combined hub-beam system, which depends on the angular velocity $\dot{\psi}$ and the mass moment of inertia of the hub and is defined as [5]

$$\omega_{01} = \sqrt{\frac{\alpha_{11} + \alpha_{13}\dot{\psi}^2}{1. - \frac{\alpha_{12}\alpha_{h1}}{1.+J_h}}} \qquad (2)$$

As we can notice the controller tuning depends on the angular velocity of the rotating hub. In the present study we assume that the hub-beam system is excited by external torque expressed as a sum of a constant and a periodic component: $\mu = \mu_0 + \rho \cos \omega t$. The numerical dimensionless coefficient adopted from paper [5] take values

$$\alpha_{11} = 3.2651, \alpha_{12} = -2.9063, \alpha_{13} = 0.3527, \alpha_{14} = 0.4602,$$

$$\alpha_{h1} = -0.3202, \alpha_{h2} = -0.14637, \alpha_{h3} = -0.1464,$$

$$\zeta_1 = 0.01 \times \omega_{1beam} = 0.01807, \zeta_h = 0.1, \zeta_c = 0.001$$

$$g_1 = 0.01, g_2 = 1.0, \mu_0 = 0.0, \rho = 0.01.$$

$$(3)$$

The effectiveness of the proposed control method is analysed for varied driving torques as defined by parameters of the amplitude ρ and the frequency ω of periodic excitation but assuming the constant component μ_0 to be equal to zero. In practice the discussed control can be realized by an active element and a sensor placed on the beam (Fig.1).
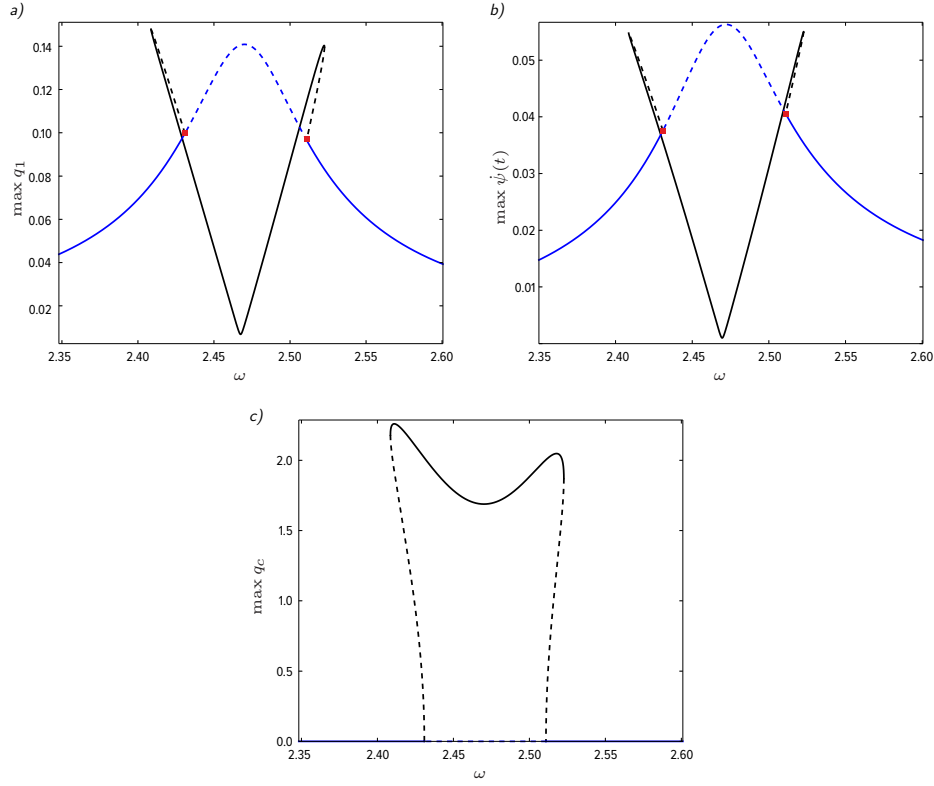
Figure 3. Amplitude-frequency curves of the beam (a), the hub (b) and the controller (c); numerical data given in (3) .

At first we test the proposed control strategy considering the periodic excitation and data given in (3). The resonance curve for the system without control is presented by blue curve in Fig.3(a,b) and it corresponds to a classical linear system characteristics. However, due to nonlinear coupling and the requested controller frequency tuning, the controller is activated in the resonance zone which is demonstrated by coordinate q_c in Fig.(3c). This phenomenon leads to energy transfer from the plant (the hub-beam system) to the controller. Both the resonance curves in Fig.3(a,b) show system vibrations to be evidently suppressed and both the beam and the hub oscillations are reduced almost to zero nearby the natural frequency of the system (black curve). The arising new branches of the characteristic lead to unstable solutions of the original resonance curve without control (blue dashed line). The branch points are indicated by red squares.

In order to take the full benefit from the control strategy, it is crucial to set the control parameters properly. There are two gains g_1 and g_2 which mutually couple the plant and
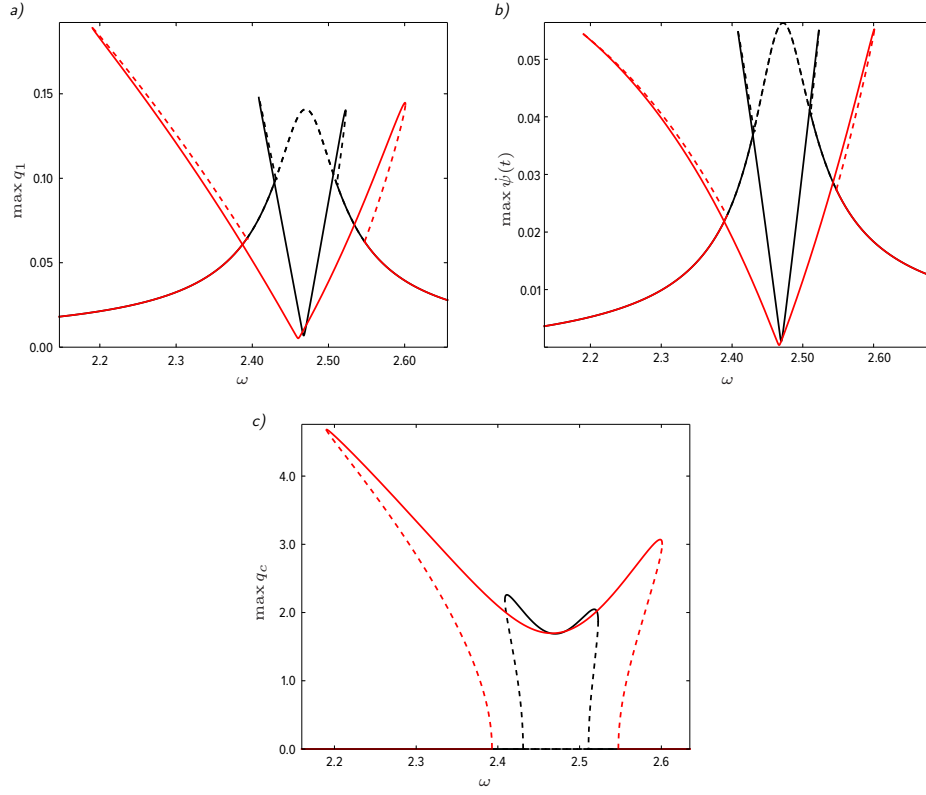
Figure 4. Amplitude-frequency curves of the beam (a), the hub (b) and the controller (c) obtained for gain $g_2 = 1$ - black colour, $g_2 = 3$ - red colour; rest data as in (3).

the controller. It has been observed in numerical tests performed for various values of the gain g_1 that the system is not sensitive for the variation of this parameter. However, the influence of gain g_2 is essential. In Fig.4 we present a comparison for two various values of the gain g_2: $g_2 = 1$ - black colour, $g_2 = 3$ - red colour. The higher gain value results in larger amplitudes of the controller. The profit of higher gain magnitude is that the controller is activated in the wider frequency zone (red curve in Fig.4) and thus, the region of vibrations suppression is larger too (see red curves in Fig.4 a and b). However there is also a negative effect, visible out of the rezonanse zone where oscillations of the hub-beam system are much higher than for the uncontrolled system. This is observed by branches on the outer left and right side of the rezonanse zone. For the gain $g_2 = 3$ branches (in red) are significantly wider than for the gain $g_2 = 1$ case. It means that the system is highly sensitive to the gain g_2, thus this parameter has to be properly tuned according to the real plant dynamics.

The second aspect of the analysis is the controller frequency tuning. It is necessary to take into account the fact that both the angular velocity and the mass moment of inertia of the hub essentially influence system dynamics. Therefore, both these parameters need to be considered while designing the controller. In given above examples the equation (2) has been used to tune the controller to the structure. However, in classical approach, for a non-rotating cantilever beam, the controller frequency is fixed as a half of the separated beam natural frequency [13]. This approach may be ineffective for rotating flexible structures.

Let us consider the same system governed by equations (1) with parameters (3), but now we tune the controller assuming $\omega_{0c} = \frac{1}{2}\sqrt{\alpha_{11}}$. As we can see in such a case there is no vibration suppression near the resonance zone (see Fig.5). Instead of this, near the natural frequency of the beam $\omega_{1beam} = \sqrt{\alpha_{11}} = 1.0807$ we observe an additional resonance with large amplitudes indicated by red colour for beam response in Fig.5 (a) with zoom in
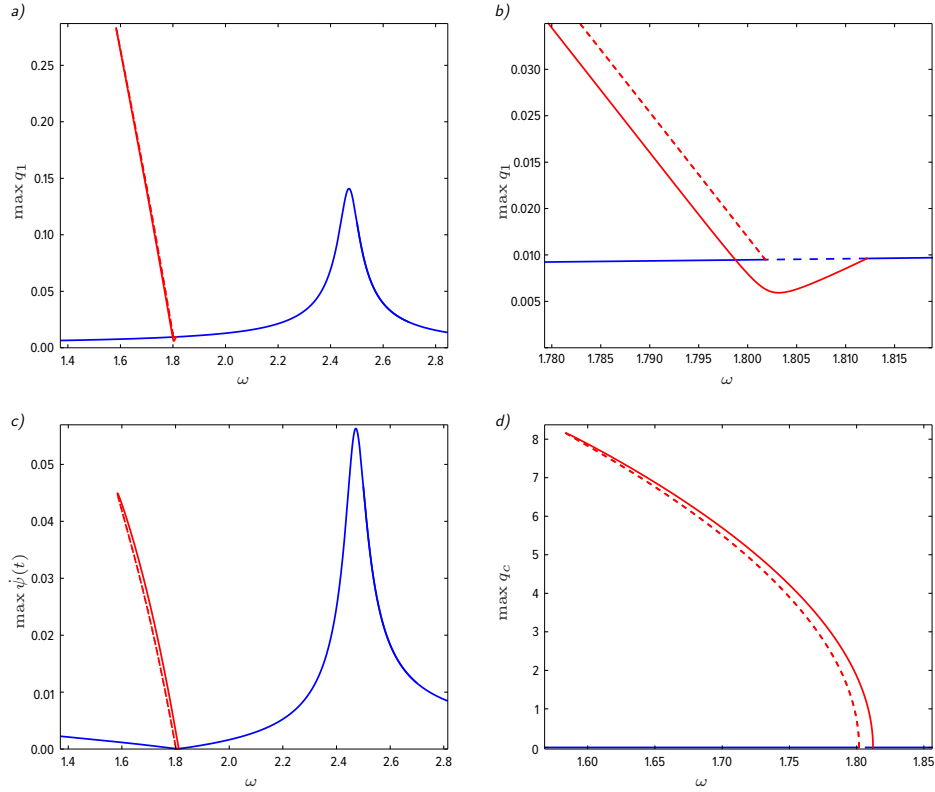
Figure 5. Amplitude-frequency curves of the beam (a) and zoom around natural frequency of the beam (b), the hub (c) and the controller (d) obtained for $\omega_{0c} = \frac{1}{2}\sqrt{\alpha_{11}}$; data as in (3); red colour - controller activation.

(b), and for the hub in Fig.5(c). This is the direct result of wrong controller tuning and its activation in improper frequency range, presented in Fig.5(d).

5. Conclusions

In this paper we proposed the application of the nonlinear saturation control strategy for vibration suppression of the rotating hub-beam structure. The model of the system has been derived in papers [2,5] considering composite thin-walled beam specimen and rigid hub dynamics. The governing PDEs equations of motions have been reduced to ODEs using Galerkin procedure. Next, the saturation controller has been adopted and the equations of the system complemented. It has been shown that the proposed control strategy is effective if gains of the control signal are properly chosen. Performed numerical tests allow to conclude the system is sensitive to the gain g_2, where the changes in system response are observed for different g_2 values. Thus this parameter has to be set according to the resonance characteristics of the combined hub-beam rotating system.

A crucial factor is the proper tuning of the controller frequency to the frequency of the rotating structure. The mass moment of inertia of the hub has to be taken into account as well as system angular velocity. If the controller is tuned in a classical way, i.e. considering only dynamics of a separated cantilever beam, the undesirable results are obtained. The controller is activated in improper zone and furthermore an additional resonance with large amplitudes is observed.

References

[1] ARMANIOS, E. A., AND BADIR, A. M. Free vibration analysis of anisotropic thin-walled closed-section beams. *AIAA Journal 33*, 10 (1995), 1905–1910.

[2] GEORGIADES, F., LATALSKI, J., AND WARMINSKI, J. Equations of motion of rotating composite beam with a nonconstant rotation speed and an arbitrary preset angle. *Meccanica 49*, 8 (2014), 1833–1858.

[3] LATALSKI, J. Modelling of macro fiber composite piezoelectric active elements in ABAQUS system. *Eksploatacja i Niezawodnosc - Maintenance and Reliability*, 4 (2011), 72–78.

[4] LATALSKI, J., BOCHEŃSKI, M., AND WARMINSKI, J. Control of Bending-Bending Coupled Vibrations of a Rotating Thin-Walled Composite Beam. *Archives of Acoustics 39*, 4 (2014), 605–613.

[5] LATALSKI, J., AND WARMINSKI, J. Bending-twisting coupled vibrations of a rotating shear-flexible thin-walled composite beam. *Mathematics and Mechanics of Solids (submitted, under review process)* (2015).

[6] LIBRESCU, L., AND SONG, O. *Thin-Walled Composite Beams: Theory and Application.* Springer, Dordrecht and the Netherlands, 2006.

[7] MAYO, J., GARCÍA-VALLEJO, D., AND DOMÍNGUEZ, J. Study of the geometric stiffening effect: comparison of different formulations. *Multibody System Dynamics 11*, 4 (2004), 321–341.

[8] PAI, P., F., WEN, B., NASER, A., S., AND SCHULZ, M., J. Structural vibration control using PZT patches and non-linear phenomena. *Journal of Sound and Vibration 215*, 2 (1998), 259–282.

[9] PIEDBŒUF, J.-C., AND MOORE, B. On the foreshortening effects of a rotating flexible beam using different modeling methods. *Mechanics of Structures and Machines 30*, 1 (2002), 83–102.

[10] QUEINI, S., S., AND NAYFEH, A., H. A Theoretical and Experimental Implementation of a Control Method Based on Saturation. *Nonlinear Dynamics 13* (1997), 189–202.

[11] QUEINI, S., S., NAYFEH, A., H., AND PRATT, J., R. A nonlinear vibration absorber for flexible structures. *Nonlinear Dynamics 15* (1998), 259–282.

[12] SONG, O., AND LIBRESCU, L. Free vibration of anisotropic composite wthin-walled beams of closed cross-section contour. *Journal of Sound and Vibration 167*, 1 (1993), 129–147.

[13] WARMINSKI, J., BOCHENSKI, M., JARZYNA, W., FILIPEK, P., AND AUGUSTYNIAK, M. Active suppression of nonlinear composite beam vibrations by selected control algorithms. *Communications in Nonlinear Science and Numerical Simulation 16*, 5 (2011), 2237–2248.

[14] WARMINSKI, J., CARTMELL, M. P., MITURA, A., AND BOCHENSKI, M. Active vibration control of a nonlinear beam with self- and external excitations. *Shock and Vibration 20* (2013), 1033–1047.

[15] WARMINSKI, J., LATALSKI, J., AND SZMIT, Z. Coupled flexural-torsional vibrations of a composite beam attached to a rotating hub. In *Eurodyn 2014*, Á. Cunha, Caetano, Elsa de Sá, P. Ribeiro, and G. Müller, Eds. European Association for Structural Dynamics, Porto, 2014, pp. 1883–1889.

Warminski Jerzy, Ph.D., D.Sc. Prof.: Lublin University of Technology, Department of Applied Mechanics, Nadbystrzycka St. 36, 20-618 Lublin, Poland (*j.warminski@pollub.pl*). The author gave a presentation of this paper during one of the conference sessions.

Latalski Jarosław, Ph.D.: Lublin University of Technology, Department of Applied Mechanics, Nadbystrzycka St. 36, 20-618 Lublin, Poland (*j.latalski@pollub.pl*).

INDEX OF AUTHORS

627